

Papers from U.S. Department of Energy  
Science Undergraduate Laboratory Internship Program (SULI) 2005

---

*Stanford Linear Accelerator Center, Stanford University, Stanford, CA 94309*

Work supported by Department of Energy contract DE-AC02-76SF00515.

**Balloon-Borne Gamma-Ray Polarimeter (PoGO) to study Black Holes, Pulsars, and AGN**

**Jets: Design and Calibration**

Zachary Apte

Office of Science, SULI Program

Hampshire College

Stanford Linear Accelerator Center

Menlo Park, California

July 11, 2005

Prepared in partial fulfillment of the requirements of the Office of Science, U.S. Department of Energy Science Undergraduate Laboratory Internship (SULI) Program under the direction of Dr. Tsunefumi Mizuno, Dr. Tsuneyoshi Kamae, and Dr. Grzegorz Madejski in the Astro Gamma group of the Stanford Linear Accelerator Center.

Participant:

\_\_\_\_\_  
Signature

Research Advisor:

\_\_\_\_\_  
Signature

## Table of Contents

Abstract	iii.
Introduction	1
Flight Instrument	3
Materials and Methods	4
Results	6
Discussion and Conclusions	7
Acknowledgements	8
References	8
Tables	10
Figures	10

## ABSTRACT

Gamma-Ray Polarimeter to study Black Holes, Pulsars, and AGN Jets: Design and Calibration.

ZACHARY APTE (Hampshire College, Amherst, MA 01002) Tsuneyoshi Kamae (Stanford Linear Accelerator Center, Menlo Park, CA 94025)

Polarization measurements at X-ray and gamma-ray energies can provide crucial information on the emission region around massive compact objects such as black holes and neutron stars. The Polarized Gamma-ray Observer (PoGO) is a new balloon-borne instrument designed to measure polarization from such astrophysical objects in the 30-100 keV range, under development by an international collaboration with members from United States, Japan, Sweden and France. The PoGO instrument has been designed by the collaboration and several versions of prototype models have been built at SLAC. The purpose of this experiment is to test the latest prototype model with a radioactive gamma-ray source. For this, we have to polarize gamma-rays in a laboratory environment. Unpolarized gamma-rays from Am241 (59.5 keV) were Compton scattered at around 90 degrees for this purpose. Computer simulation of the scattering process in the setup predicts a 86% polarization. The polarized beam was then used to irradiate the prototype PoGO detector. The data taken in this experiment showed a clear polarization signal, with a measured azimuthal modulation factor of  $0.35 \pm 0.02$ . The measured modulation is in very close agreement with the value expected from a previous beam test study of a polarized gamma-ray beam at the Argonne National Laboratories Advanced Photon Source. This experiment has demonstrated that the PoGO instrument (or any other polarimeter in the energy range) can be tested in a laboratory with a simple setup to a similar accuracy.

## INTRODUCTION

Accreting black holes, isolated pulsars, and jet-dominated active galactic nuclei (AGN) are among the many exotic objects of great astronomical interest which can emit polarized x-rays and gamma rays; measurements of the polarization in the Compton scattering energy range (30-100keV) can reveal important information about the conditions in and around these mysterious objects. The Polarized Gamma-ray Observer (PoGO) project is an international effort to send a very sensitive instrument to the top of the atmosphere (overburden of  $3 \text{ g/cm}^2$ ) to measure polarization of these sources.

Polarization of astrophysical gamma-rays arises through a variety of well-understood processes. Synchrotron radiation arises due to high energy electrons orbiting in an ordered magnetic field [3]. All synchrotron radiation is polarized perpendicular to the magnetic field revealing information about the orientation of the magnetic field around the source. Compton scattering of unpolarized photons from the accretion disk or surrounding clouds around a black hole or an active galactic nucleus by high energy electrons can also produce polarized gamma-rays[9]. The absorption cross-section of photons traveling through a strong magnetic field ( $>10^{12}$  Gauss) depends on the polarization direction making it possible to measure the strong-field near the surface of a neutron star [1,2]. In all of these cases, the orientation of the polarization plane (the plane on which the electric field vector lies) depends on the orientations of the magnetic field or the accretion disk; therefore polarization measurement is a powerful probe of the emission mechanism and the source geometry[9]. Due to the lack of sensitivity, there has been no measurement of polarization in X-ray and gamma-ray bands except for that on Crab Nebula in early 1970s[6].

Despite the importance of the x-ray and gamma-ray polarization measurement, it has only been measured only once by the OSO-8 satellite which studied the Crab Nebula at 2.6 and 5.2 keV. We note that the RHESSI satellite reported a polarization measurement using Bragg diffraction [5,6,7] 2 years ago for a gamma-ray burst [8] but the validity of the measurement has been severely challenged.

To examine the PoGO flight instrument's capability, a simplified prototype detector array was recently tested at the Advanced Photon Source (APS) at Argonne National Laboratories [9]. The detector array consisted of seven hexagonally configured fast plastic scintillators coupled with PMTs [figure 2] and was irradiated by polarized photon beams at 60, 73 and 83 keV. The data showed an azimuth-angle modulation factor of  $0.42 \pm .01$ . Computer simulations of this experiment using a modified Geant4 simulation package showed a modulation factor of  $0.488 \pm .006$  for a fully polarized 73 keV photon beam [9].

The experiment reported here will focus on repeating the capability tests previously conducted at APS in the laboratory using a simple laboratory setup which utilizes the radioactive source Americium 241 (59.5 keV): if we obtain a similar result in this experiment, it will become a very powerful verification method in the laboratory during development of the PoGO flight instrument.

To create a polarized beam, Compton photons scattered around 90 degrees are selected in a double scattering setup [figure 3]. Polarization is a function of scattering angle and reaches 100% at 90 degrees. The Klein-Nishina cross section (1) takes the following formula

$$\frac{d\sigma}{d\Omega} = \frac{1}{2} r_0^2 \frac{k^2}{k_0^2} \left[ \frac{k}{k_0} + \frac{k_0}{k} - 2 \sin^2 \theta \cos^2 \phi \right] \quad (1)$$

where  $\theta$  is the scattering angle, or angle between the incident and the scattered gamma-rays,  $\phi$  the angle between the electric field plane and the scattered gamma ray

direction. The notation is defined as in Figure 2. There, one completely linearly polarized photon is scattered by a free electron at point O. The momentum vector of incident and scattered photon are  $k_0$  and  $k$ , respectively, and the unit vector along the polarization vector before the scattering is  $e_0$ .  $\theta$  and  $\varphi$  are the polar and azimuth angle of the scattering. Here,  $k_0$  and  $e_0$  are assumed to be along z-axis and x-axis, respectively.

Because we are scattering at 90 degrees, the value for  $\theta$  is 90 degrees (from horizontal to vertically down), making sine squared go to 1. Then after that photon scatters off the central scintillator (back to horizontal) the cosine squared value goes from zero to one, creating an angular modulation in the differential cross-section.

Another important Compton equation is (2) which describes the energy of the scattered photon ( $E'$ ) as a function of the scattering angle  $\theta$  and the initial energy  $E$ .

$$E' = \frac{E}{1 + \frac{E}{M_e c^2} (1 - \cos \theta)} \quad (2)$$

## **FLIGHT INSTRUMENT**

To carry out polarization measurements we are constructing a new balloon-borne instrument, the Polarized Gamma-ray Observer (PoGO) [9, 10] which employs coincident detection of Compton scattering and photo-absorption to measure polarization in the 30-100 keV range [9]. The flight instrument will carry 217 bundled well-type phoswich counters with PMTs (Photo Multiplier Tubes). Each counter will consist of three types of scintillation material: one Bismuth germinate crystal (BGO) and two types of plastic scintillators, one with a fast response (fast plastic) and another with a slow response (slow plastic). The 217 phoswich counters will be surrounded by the side BGO scintillators [Figure 1].

The instrument employs a well-type phoswich active shielding design to produce high quality data (high signal-to-noise factor) from low flux sources[11]: each type of scintillation material has a very different temporal response to incident x-rays; making discrimination between the location of a scintillation signal possible. The BGO scintillators are used to block background x-rays from the bottom and sides: any event detected in coincidence with an event in the BGO scintillators it is discarded. The slow plastic scintillators (60 cm long and hollow ) with tin and lead foils wrapped around them define the field of view of the instrument to about two degrees by two degrees. The only x-rays which will produce a signal at a fast scintillator but not at slow plastic will be recorded as “valid” events[Figure 1].

The fast plastic scintillators are the main detector of the instrument. X-rays that enter a fast scintillator, Compton-scatter into another fast scintillator, and are photo-absorbed there will make a valid event. From the coincident set of fast scintillators, the path of the x-ray can be reconstructed and the direction of the Compton scattering determined. Because the asymmetry (modulation) in azimuth angle of Compton scattering is directly related to the polarization of the x-rays, the polarization (magnitude and orientation) of the x-rays can be determined.

## **MATERIALS AND METHODS**

To create a mono-energetic, collimated, polarized gamma ray source a strong Americium <sup>241</sup> source was placed inside a lead container with a 5 mm wide and 39.5 mm long hole in it. The small hole leads to a fast scintillator, also contained in the lead, with another hole (5mm by 50mm) at 90 degrees to the first, leading out of the container. This setup should only allow events Compton scattered at 90 degrees out, creating a mono-energetic beam (53.3 keV, post

scattered energy see eq. 2) that has a high degree of polarization and is highly collimated[Figure 3].

The PoGO Prototype Detector was arranged as an array of 7 hexagonal plastic Saint-Gobain BC-404 scintillators, each 2.68 cm wide and 20 cm long, as shown in Figure 4, 5 (which includes the numbering scheme). Each scintillator was glued directly to a Hamamatsu R580 PMT (3.4 cm photocathode diameter, larger than that of PMTs used for PoGO flight). The center scintillator acted as a Compton scattering target and the outer six scintillators, separated from the center scintillator by 2.2 cm, detected the scattered photons. In the final PoGO instrument the hexagonal detector units will be tightly bundled together in a close-packed hexagonal array figure [1][12]. However, photons scattered in one detector are likely to pass through to its nearest neighbors before being photo-absorbed. Thus, the prototype array approximates a region of the final PoGO instrument[9].

The array was mounted on a rotation stage, as shown in Figure 5, to allow measurement of the modulation factor by rotating about the center scintillator aligned to the incident photon beam. To measure the detector response to relative to the polarization plane, the instrument was rotated in 30 degree steps covering the azimuthal angle range of 0–150 degrees. Each run took about 60 hours. Energy measured by the fast scintillator was calibrated by irradiating each detector with  $^{241}\text{Am}$ [figure 11]. The energy resolution (full width at half maximum) at 59.5 keV spanned the range of 31 % to 39 % and were assumed to scale with the inverse square root of energy [9]. Coincidence triggering was used to gate our data acquisition system as shown in figure 12.

To eliminate background events which were not removed by hardware triggering, several different data selection criteria were used finally producing a clean data set of approximately 20

Compton events per hour. To remove background from cosmic-rays an initial set of selection criteria were used to analyze the waveform output from the PMTs, only events which had the temporal response corresponding to a scintillation event were selected. Those data were then converted from volts to keV and further event selection criteria were applied to select only valid Compton events (photons scattered off the central scintillator and absorbed by a peripheral one): requiring that exactly 2 PMTs had an energy greater than 3 keV, and that the total energy in all the PMTs must be between 39.5 and 79.5 keV ( $59.5 \pm 20$ ). The events in each of the peripheral scintillators which made it through all the criteria were then summed to give the number of events in each peripheral scintillator.

A modified Geant4 toolkit [13] was used to find a modulation factor for a Monte Carlo simulation of the prototype configuration being irradiated with polarized 53.3 keV photons. The simulation didn't take into account the Gaussian energy response of the scintillation materials so a Gaussian pseudo-random number generator was used to apply a Gaussian energy distribution.

We normalized the number of events in each scintillator to the integration time and then fit the result to a sinusoidal curve and obtained a modulation factor ( $M_p$ ) from the maximum ( $R_{\max}$ ) and minimum ( $R_{\min}$ ) rates measured as a function of azimuthal angle by [Figure 8]:

$$M_p = \frac{R_{\max} - R_{\min}}{R_{\max} + R_{\min}} \quad (3)$$

## RESULTS

Using the aforementioned software event selection we obtained a clean data set with around 20 recorded Compton events per hour. A plot of the energy distribution of events recorded in PMT8, the fast scintillator in the lead brick used to create the polarization (triggered with PMT4, the central scintillator), shows the expected Poisson energy distribution around 6.2

keV for Compton scattering of 59.5 keV photons at 90 degrees [Figure 7]. The event selection used can be clearly seen superimposed over the plot of energy deposited in the central scintillator versus the total deposited energy [Figure 8]. There are several structures visible in Figure 8 that we used event selection to exclude. The clear line along the bottom of the cluster of data points is composed of events which only include PMT4; the higher energy ones are photo-absorption and the lower energy ones are escaped Compton events. Table 1 is a table of the all the modulation factors acquired over the course of this experiment. The modulation factor acquired over this experiment is 86% of the one acquired one at the Argonne beam test [9] and 74% of the value indicated by the simulation [Figure 9].

## **DISCUSSION AND CONCLUSION**

We succeeded in measuring polarization in the laboratory which was the motivation of this paper has implications into the PoGO project as a whole. The characterization of this method is important because for development of the PoGO flight instrument because instrument development demands a much more flexible schedule of testing than available at a source such as APS. Computer simulation using the Geant4 analyses package indicates double scattering events will lead to an 86% polarized beam [Figure 10]. Because we measured the polarization to be about 86% of the one measured at the Argonne APS, and simulations indicate that double scattering events inside the scattering scintillator lead to an 86% polarization, our data seem to validate this method.

Because of the angular width of the central scintillator and the angular size of the holes in the lead brick, the scattering angle is not truly 90 degrees but is the whole range of 80-100 degrees. The maximum and minimum normalized differential cross-sections for this situation

range from .96 to 1 and 0 to .04 respectively, leading to  $\pm 4\%$  difference in polarization. This is for a scintillator perfectly aligned with the beam; if the scintillator was not perfectly aligned the overall error could increase to  $\pm 5\%$ .

Our result normalized to the Argonne beam test result ( $0.36/0.42 = 0.86$ ) matches closely with the simulation's value for polarization (86%), confirming the validity of this method as a development tool for the PoGO flight instrument.

## ACKNOWLEDGEMENTS

I would like to thank the U.S. Department of Energy for giving me the opportunity to participate in the SULI program, the experience had been invaluable. Dr. Tsunifume Mizuno deserves special thanks for working closely with me on this project. Additionally, many thanks to both Dr. Tsuneyoshi Kamae, and Dr. Grzegorz Madejski who helped extensively with the editing of this paper.

## REFERENCES

- [1] A. K. Harding, Physics in Strong Magnetic Fields in Science, vol. 251 pp 1033 March 1991
- [2] A. K. Harding, The Physics of Gamma-ray Bursts Physics Reports vol. 206 pp. 327-291 February 1991
- [3] G.B. Rybicki, A.P. Lightman, Radiative Processes in Astrophysics, New York: Wiley, 1979
- [4] K. Makishima et al., A. S. P Conf. Proc. 251, ed. H. Inoue and H. Kunieda, Astr. Soc. of the Pacific (2001) 564.
- [5] M. C. Weisskopf, et. Al, Measurement of the X-ray Polarization of the Crab Nebula, Astrophysical Journal, vol. 208, pp L125-L128, June 1976.
- [6] M. C. Weisskopf, et. Al, A Precision Measurement of the X-ray Polarization of the Crab Nebula without Pulsar Contamination, Astrophysical Journal vol. 220 pp. L117-L121 March 1978
- [7] E. H. Silver, et. Al, Search for X-ray polarization in the Crab Pulsar, Astrophysical Journal, volume 225 pp. 221-225, October 1978.
- [8] W. Coburn, S. Boggs, Polarization of the prompt -ray emission from the -ray burst of 6 December 2002 Nature, vol. 423 pp 415-417 May 2003
- [9] T. Mizuno, et. Al. Beam Test of a Prototype Detector Array for the Pogo Astronomical Hard X-Ray/Soft Gamma Ray Polarimeter, Nuc. Inst. Met'd. phys res 540 (2005) 158-168
- [10] V. Andersson, et. Al Large-Area Balloon-Borne Polarized Gamma Ray Observer (PoGO) 22<sup>nd</sup> Texas Symposium, Stanford, December 13-17 2004

- [11] T Kamae, et. Al., Well-Type Phoswich Counter for Low-Flux X-Ray/  $\gamma$  Detection, IEEE Trans. Nucl Sci., vol. 40, no. 2, pp. 204-207, Apr. 1993
- [12] P. Chen et al., in Proc. IEEE Nuclear Science Symp., Portland, Oregon, October 2003
- [13] S. Agostinelli et Al, Geant4 - a simulation toolkit, Nucl. Instr. and Meth., vol. 506 pp. 250 - 303 August 2003

## TABLES

Table 1

### Results over different runs

Data Source	offset from initial position(degrees)	Modulation factor	total counts	time period (hr)	compton events/hr
AM241	0	0.39±0.04	1343	65.5	20.5
AM241	30	0.33±0.038	1192	63	18.9
AM241	60	0.32±0.042	1289	66	19.5
AM241	90	0.35±0.036	1158	60	19.3
AM241	120	0.36±0.044	1141	58.5	19.5
AM241	150	0.39±0.036	1113	60	18.6
Average	NA	.036±.002	7236	373	19.4
SIMULATION	30	0.488±0.001	13959	NA	NA

## FIGURES

Figure 1. Conceptual design of PoGO. It consists of an array of well-type phoswich detector units, each made of a fast plastic scintillator, a slow plastic scintillator tube, a thin high-Z metal foil and a bottom BGO. A set of side anti-coincidence detectors made of BGO surrounds the array of phoswich units. In the figure, representative passages of gamma-rays are shown with energy deposition marked by circles. The trigger scheme accepts only the ones marked as “Fully contained gamma-ray”.

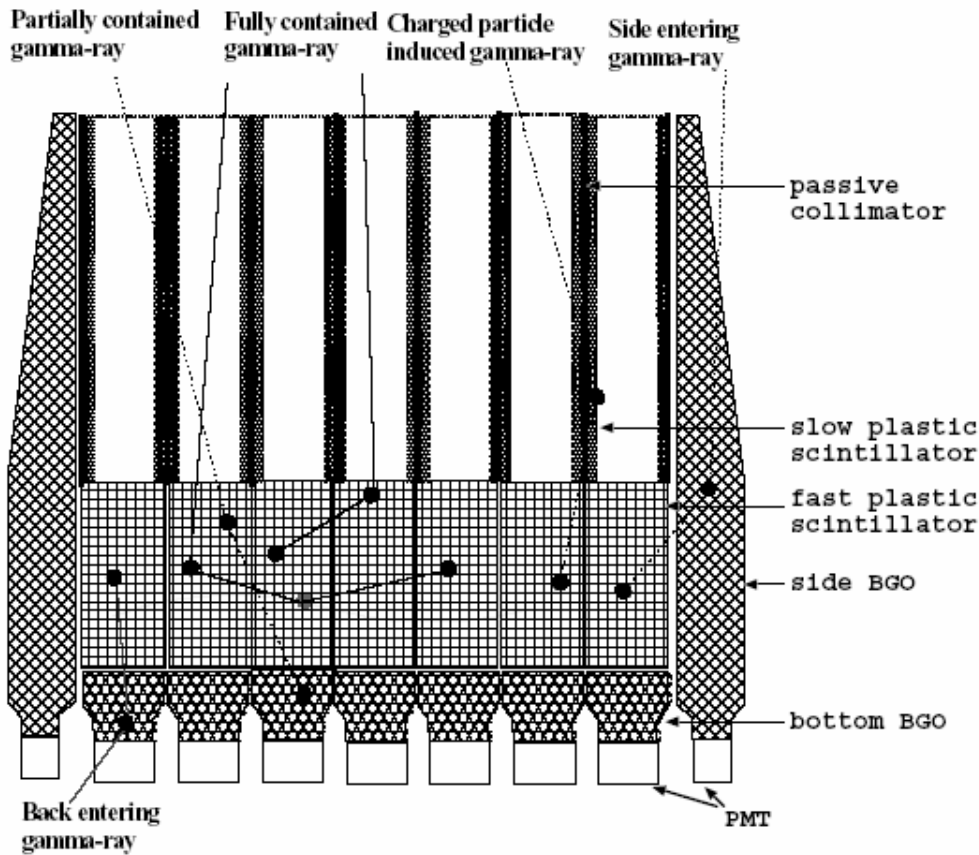


Figure 2. A photon scattering at point O. The momentum vector ( $k_0$ ) and the polarization vector ( $e_0$ ) of an incident photon are along z- and x-axis, respectively.  $\theta$  and  $\varphi$  are the scattering polar and azimuth angle. Plane S is constructed by  $e_0$  and  $k$ , the momentum vector after the scattering.  $e$  is in plane S.

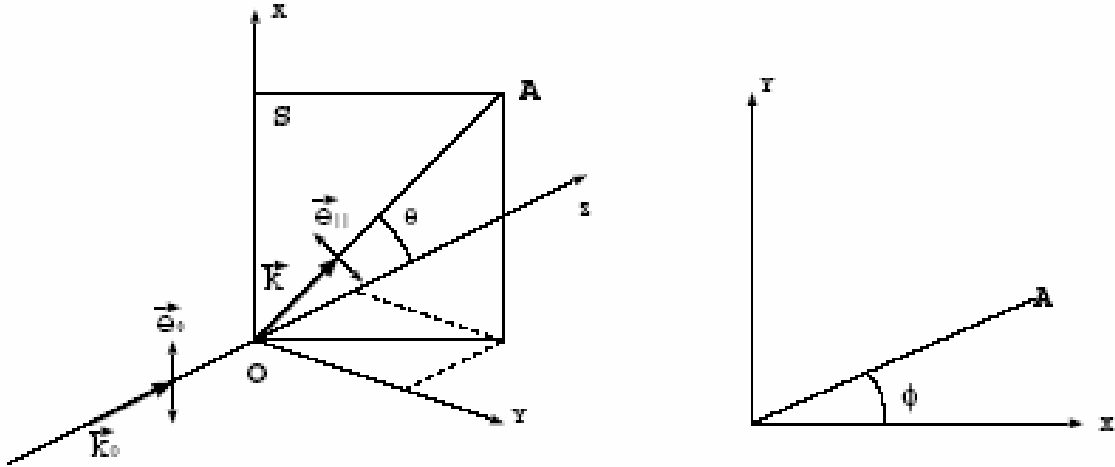


Figure 3. A Simplified drawing of the scattering apparatus. The large green block represents the lead block that the Americium (blue) and PMT8 (red) are embedded in. The white tubes represent the holes in the lead block. The dashed red line represents a possible gamma ray path. The jagged shape represents the Compton event.

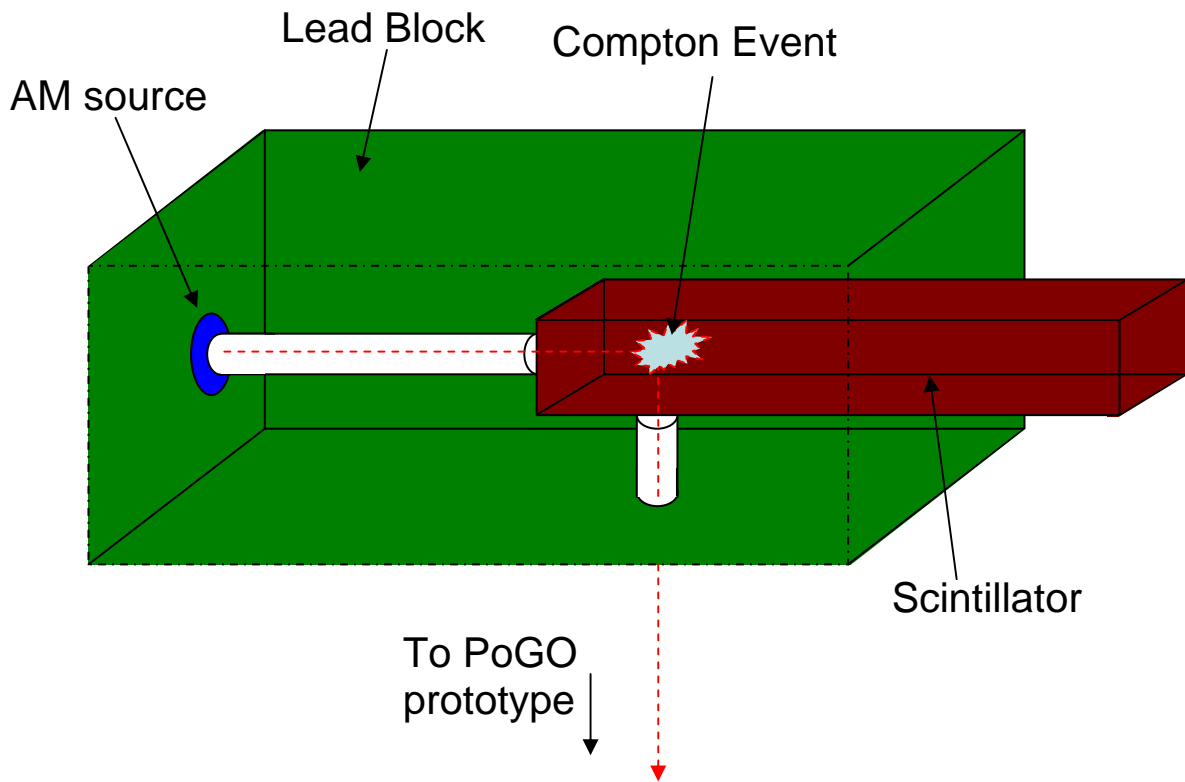


Figure 4. The layout and numbering scheme of scintillators viewed from the beam origin. Detector rotation angle is defined to be  $0^\circ$  when scintillators channels 3, 4 and 5 are along the horizontal (x-axis), and to be  $30^\circ$  when channels 1, 4 and 7 are along the vertical (y-axis).

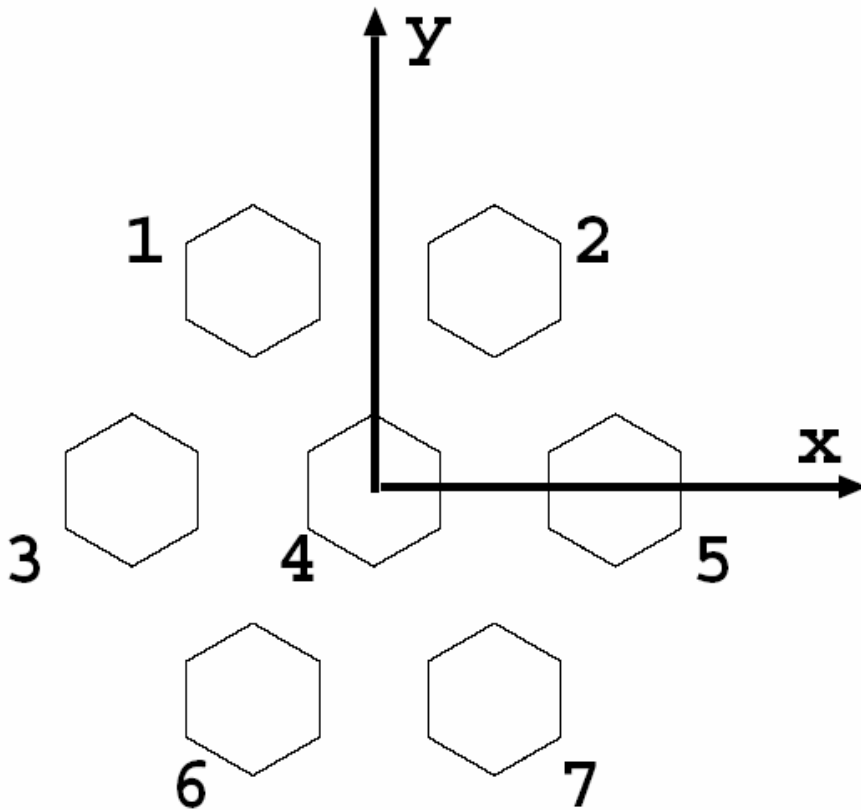


Figure 5. The rotation frame containing the 7 PMTs.



Figure 7. This plot shows Poisson distribution of energy for 90 degree Compton events in PMT8, the polarization apparatus (~6.2 keV absorption). As well the higher peak for the double scattering can be seen.

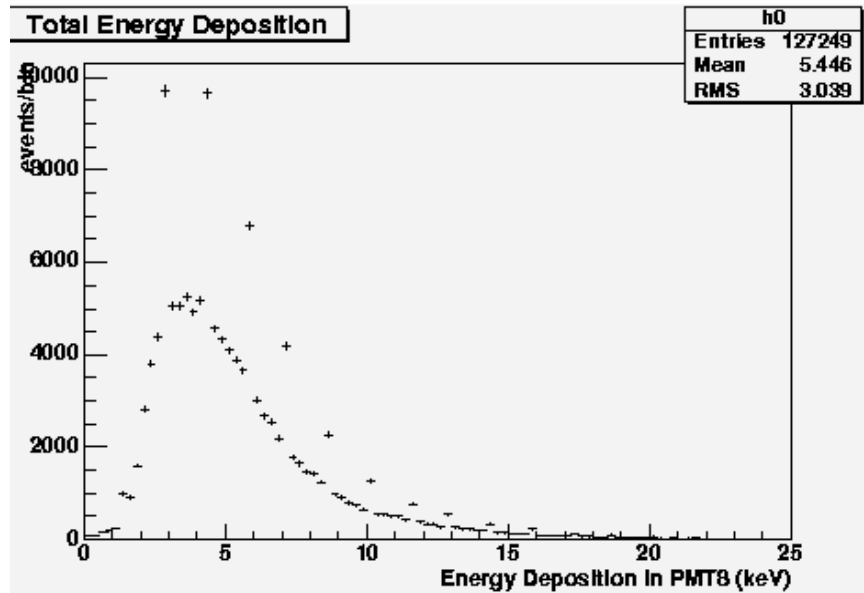


Figure 8. Relation of deposit energy in the central scintillator and total energy deposition for 59.5 keV run at 0-degree rotation. Event selection criteria used in data analysis are also shown by dotted lines. (see text)

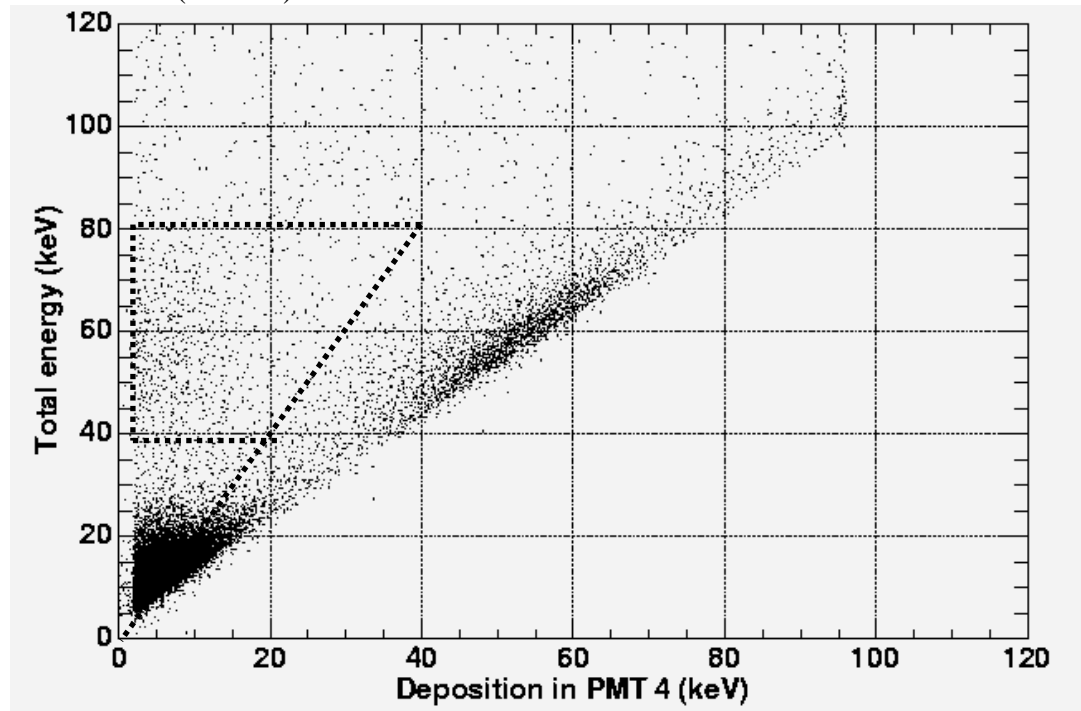


Figure 9. Simulation of polarization from lab setup using taking double scattering into account leads to an 86% polarization.

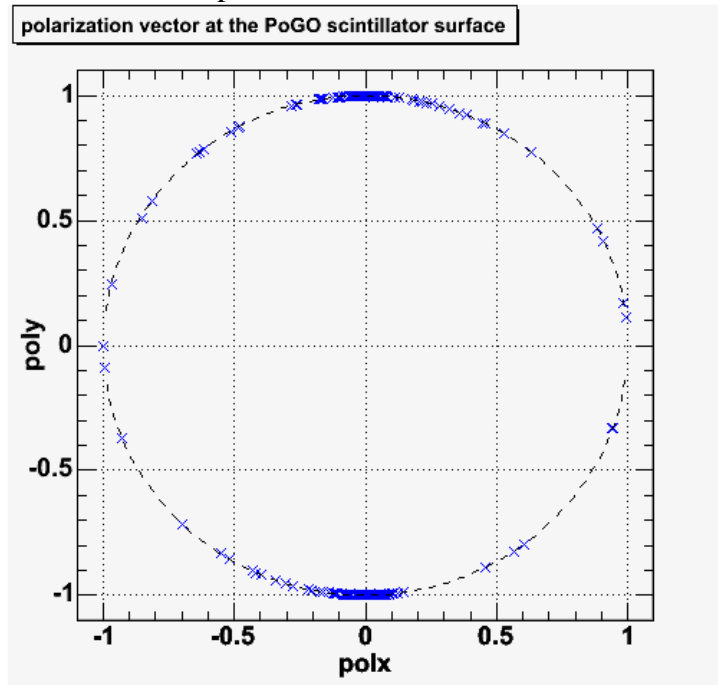


Figure 10. Modulation curves for PMTs, and overlaid with the simulation curve.

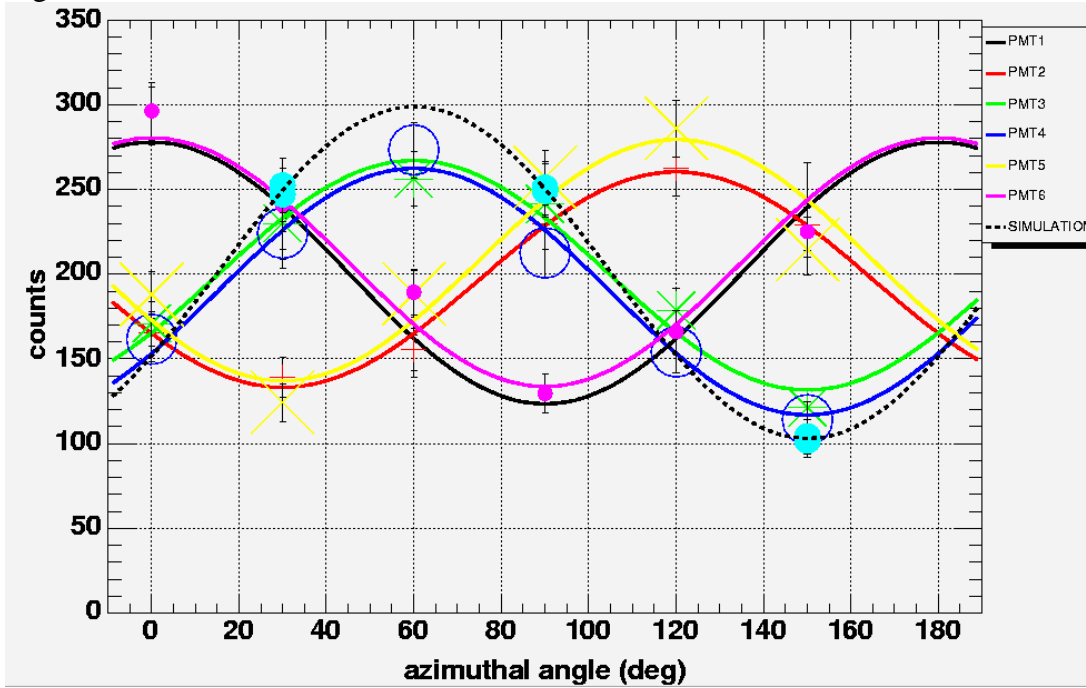


Figure 11. Calibration curve of a PMT scintillator pair. Obtained by irradiating the PMT with 59.5 keV photons.

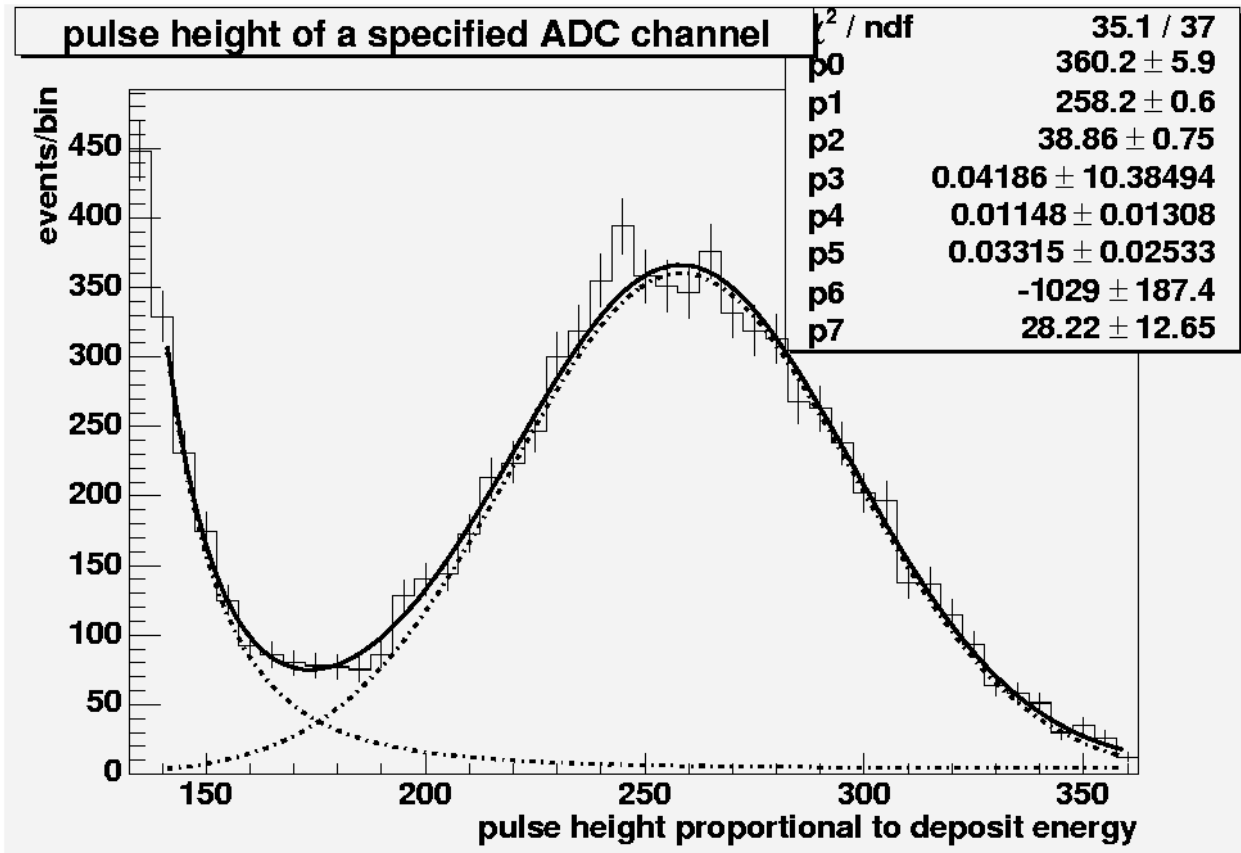
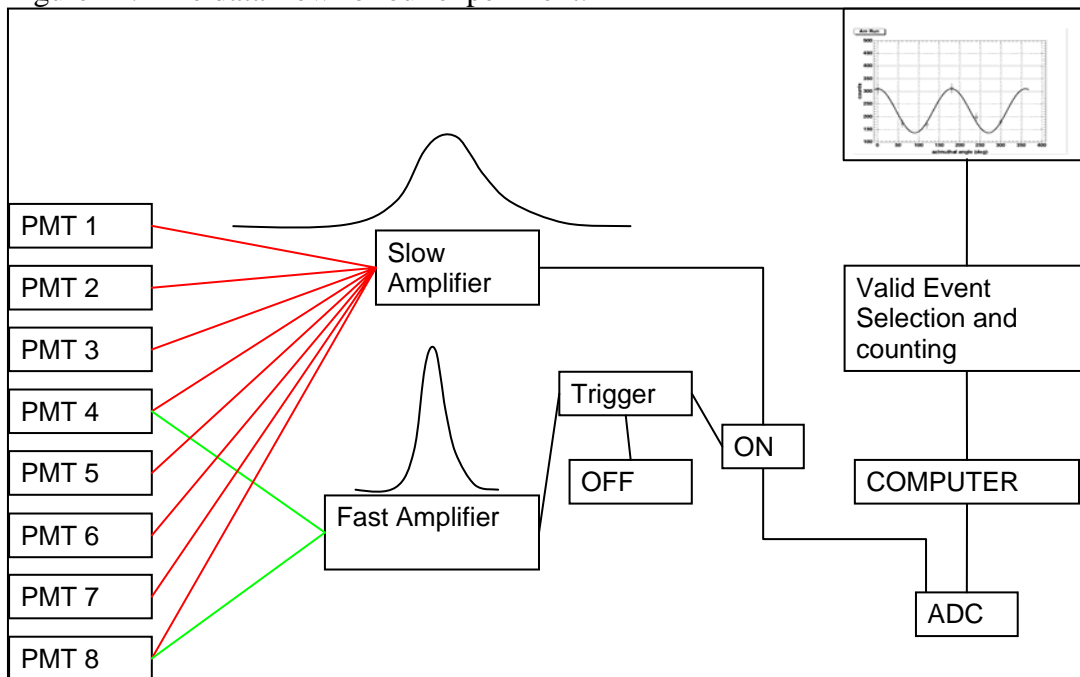


Figure 12. The data flow for our experiment.



# The SPEAR 3 Vacuum System

## An Analysis of the First Two Years of Operation (2004 and 2005)

Rebecca Armenta

Office of Science, SULI Program

University of California at Los Angeles

Stanford Linear Accelerator Center

Menlo Park, California

August 18, 2005

Prepared in partial fulfillment of the requirements of the Office of Science, U.S. Department of Energy Science Undergraduate Laboratory Internship (SULI) Program under the direction of Mr. Harold A. Morales and Mr. Benjamin D. Scott in the Engineering and Technical Services Division of the Stanford Synchrotron Radiation Laboratory (SSRL) at the Stanford Linear Accelerator Center.

Participant: \_\_\_\_\_  
Signature

Research Advisors: \_\_\_\_\_  
Signature

\_\_\_\_\_  
Signature

# *Table of Contents*

---

<b>Abstract</b>	<b>3</b>
<b>Introduction</b>	<b>5</b>
<b>Methods and Materials</b>	<b>9</b>
<b>Discussion</b>	<b>11</b>
<b>Conclusion</b>	<b>15</b>
<b>Tables and Figures</b>	<b>16</b>
Figure 1	<b>16</b>
Figure 2	<b>16</b>
Figure 3	<b>17</b>
Figure 4	<b>18</b>
Figure 5	<b>18</b>
<b>Literature Cited</b>	<b>19</b>
<b>Acknowledgements</b>	<b>19</b>

## *Abstract*

---

SPEAR 3, a synchrotron radiation source at the Stanford Linear Accelerator Center, has been in operation for the past two years. SPEAR 3 was designed to achieve high beam lifetimes while operating at a higher current level than previously achieved with SPEAR 2. Maintaining high electron beam lifetimes within the ring allows users to perform their experiments with a consistent supply of high current synchrotron radiation. The purpose of this analysis is to evaluate the SPEAR 3 vacuum system's performance during the 2004 and 2005 runs while considering methods to optimize and improve vacuum system conditioning, especially within the pumping system, so that a recommended plan of action can be created for the FY 2006 run. Monitoring the dynamics of the electron beam within the ring can be a difficult task. Pressure data obtained from the gages attached to pumps, temperature data obtained from thermocouples located at various locations around the ring, and beam lifetime projections help to provide some indication of the health of the electron beam, but the true conditions within the beam chamber can only be extrapolated. Data collected from sensors (gauges, thermocouples, etc.) located around the ring can be viewed and extracted from a program created at the Stanford Synchrotron Radiation Laboratory (SSRL) called *Historyplot*. Manipulation and analysis of data was performed with the commercially available programs *Matlab* and *Excel*. The data showed that the beam lifetimes in 2005 were much greater than they were in 2004, but it did not provide a clear indication as to why this occurred. One variable of major importance between the 2004 and 2005 runs is the Titanium Sublimation Pump (TSP) flash frequency (flashing is the process in which Titanium from filaments within the pump is sublimated onto the wall surfaces of the

pump, where it removes gas molecules from the system by chemisorption). The data indicated that pressures in 2005 could have been lower, based on a comparison between 2004 pressures, if the TSPs were flashed more frequently than they were in 2005. However, the data from 2004 and 2005 does not provide enough information to accurately determine an optimal conditioning frequency, though it does provide enough information to formulate a recommended plan of action for the next run. It appears that flashing at a high rate during the beginning of a run and at a lower rate as the run progresses may be the most effective pumping approach to further improve the vacuum level of the ring. It is recommended that the SPEAR 3 vacuum system should be operated in this way next year.

## *Introduction*

---

The Stanford Positron Electron Asymmetric Ring (SPEAR) is currently a third generation synchrotron radiation source. SPEAR 3 replaced SPEAR 2 during the period of April to October, 2003, and has been operating for two years. It was designed to run at 500mA, a much higher current level than the SPEAR 2 maximum current level of 100mA. The 2004 and 2005 runs were primarily 100mA runs, but tests at 200mA and 500mA during the 2005 run have proven that SPEAR 3 is ready for 500mA in 2006.

In addition to 500mA design objective, SPEAR 3 was designed to have an increased beam lifetime and much lower beam emittance than the SPEAR 2 ring produced (lower beam emittance is equivalent to a more focused electron beam ). A new vacuum system, along with a new magnet lattice system and several new insertion devices were designed to achieve these performance goals and operational efficiency. As a result, scientists can perform “the next generation of experiments” with fewer obstacles than in the past.

Maintaining consistent beam life for users (increasing beam lifetime) is one of the main performance goals of the system. The vacuum system has much to do with maintaining the beam life. The objective of this project is twofold: one, to analyze the vacuum system and either confirm or refute that the vacuum system is operating as expected according to its design and two, to determine if it is performing optimally.

Optimal performance of the vacuum system is highly dependent upon its vacuum pumping capabilities. Maintaining a very low pressure within the beam chamber helps to

prevent beam current losses that would occur when electrons composing the beam collide with the molecules of the residual gases remaining in the chamber. Less collisions and, subsequently, less losses corresponds directly to high beam lifetime, or high vacuum quality. The SPEAR 3 ring utilizes both sputter ion pumping (using noble diode pumps) and titanium sublimation pumping to achieve ultra high vacuum (UHV) levels (pressures  $< 10^{-10}$  Torr). SPEAR 3 uses 74 Titanium Sublimation Pumps (TSPs) and 129 Noble Diode Ion Pumps (IPs) to create the UHV environment for the electron beam.

The two types of pumps are used in combination because each is more effective at pumping different gas molecules from the vacuum chamber. TSP pumps are capable of operating at high pumping speeds for “getterable” gases (chemically active gases such as  $N_2$ ,  $O_2$ ,  $H_2$ ,  $CO$ ,  $CO_2$ ,  $H_2O$ ), but do not efficiently remove noble gas molecules (Ar, He,  $CH_4$ ,  $C_2H_6$ ) from the chamber. Noble ion pumps are much more effective at pumping the noble gas molecules from the vacuum chamber than the TSPs are (noble gas molecules are present during leaks).

The “batch deposition method” is the procedure used for operating the TSP pumps in the SPEAR 3 ring. In this method, the sublimation of Titanium onto the pumping surface (in this case, the pumping surface is extruded aluminum fins) is induced periodically, and the film deposited on the surface will trap gas molecules and eventually saturate (resulting in a reduction of pumping capacity) with those trapped gas molecules between sublimations [1]. The optimum SPEAR 3 TSP flash frequency for maximum vacuum pressure improvement has not yet been determined. It is the common belief that frequent flashing results in favorable performance characteristics. However, this assumption overlooks disadvantages that may be presented by this practice. Flashing too

often may increase the titanium film thickness on the walls of the chamber to a point where it may begin to flake off (or to peel away from the surface), thus producing additional surfaces that may introduce more gas molecules (and possibly particulates) into the chamber. In addition, the flashing process is quite time consuming—flashing the 74 TSP pumps can take up to 8 hours. This time spent on flashing the TSPs takes away from the time that could be dedicated to accelerator physics applications or to the extension of the user run.

A major component of this project will be the determination of an optimal flash frequency for the TSPs. It is appealing to determine this optimal flash rate because when implementing it, it will not be necessary to perform any extra physical work on the apparatus. Scientists and engineers have direct control over how the TSPs are utilized in the system, so an optimized flashing scheme can be achieved quite simply by just a change in procedure.

The SPEAR 3 vacuum system consists of a series of copper chambers (which incorporate an antechamber design) with discrete absorbers, masks, and pumps. All of these are supported, along with the magnets, on girder sections around the 234.126 meter circumference ring. A benefit of the SPEAR 3 copper chamber with antechamber design is that high gas loads produced from photon stimulated desorption (PSD) at the masks and absorbers are located close to the high speed TSP pumps; the TSPs should be able to pump these gas molecules out of the chamber with ease. A disadvantage of this antechamber design is that the chamber has more surface area, and thus the thermal gas load (from desorption) is increased. The copper chambers and various interior devices are connected with bellows, which are designed to aid installation and assembly, and to allow

a smooth transition for the electron beam to and from different devices in the ring that may require different aperture configuration. Because the bellows are part of the beam aperture transition devices, they are also often locations of higher order mode (HOM) heating and can contribute to losses in beam lifetime. During the analysis, the temperatures at these locations will be reviewed.

## *Methods and Materials*

---

In order to achieve the objectives of this project, it is pertinent to first determine if, as predicted by design, optimal performance is being achieved by the vacuum system. Performance predictions can be found in the Conceptual Design Report [2] and in released documents on the vacuum group network. However, not all aspects of the vacuum system can be easily measured for comparison. For example, a test chamber was used to determine much of the preliminary data on the TSPs used in the system. The test chamber was equipped with gages not present on all TSPs within the ring. Uncertainty about what occurs within the chamber during periods of normal operation is part of the motivation for this project. The next step toward completing the objectives of this project is analyzing the relationship between the vacuum system components and losses in beam lifetime. This analysis will determine if the vacuum system itself contributes to beam lifetime losses. A somewhat comprehensive grasp on the vacuum system is necessary to make such an assessment. If a relationship exists, further work can be undertaken to determine methods of prevention or modification. It would also be helpful to be able to develop a relationship between measurable vacuum system parameters and overall system performance parameters, the most obvious one being beam lifetime. It is convenient and reasonable to assume that the vacuum pressure has a direct effect on the beam lifetime, however, this is not always the case. The relationship between these two parameters is much more complicated to assess because many other parameters have an effect on beam lifetime.

The majority of the system analysis requires run data obtained in the last two years of operation. Data from SPEAR 3's database will be extracted using a program

called Historyplot and imported into other graphing programs such as Excel and Matlab. The data will be explored and relationships between pertinent parameters may be drawn.

Preliminary data procured from the database has been organized into graphs. There are no experimental findings, as no experiment was actually performed, but many helpful observations have been made as a result of the rearrangement of the raw data into graphs revealing salient information. The data procurement process is a tedious one. Extracting information from the SPEAR 3 database proved to be the most time consuming activity of the whole analysis process. Several methods of extracting the data from the current system were pursued (methods in Matlab), but none provided a significant advantage over the system's default program (Historyplot) for viewing and extracting data. Although inconvenient, Historyplot did provide the information needed to assess the subject at hand.

## *Discussion*

---

SPEAR 2 maintained lifetimes of about 40 hours while operating at 3GeV and 100mA. SPEAR 3 currently maintains lifetimes of over 40 hours, even at the beginning of a run, when beam scrubbing has not yet rid the chamber of residual gas molecules within the chamber. {Beam scrubbing is a phenomenon that highly affects the performance of the system, but it is not easily measured as a parameter. Beam scrubbing is the phenomena described as reductions in dynamic pressure rise (due to photon stimulated desorption) with increasing integrated photon dose (Amp-hours) [2]}. It is obvious that the performance of SPEAR 3 surpasses that of SPEAR 2. What is not obvious, however, is whether or not SPEAR 3 can perform even better. If it can operate more efficiently, it would be helpful to know before the machine begins its 500mA run. Hopefully, this can be determined from the data that is available from the past two years.

Figure 5 shows the lifetimes achieved in 2004 and 2005 as functions of integrated run current. Integrated run current is a better parameter than time to consider when analyzing the development of the system because it represents events in terms of how much current had run through the chamber at that point of time, and therefore gives an indication of how much beam scrubbing may have occurred in comparison to other events plotted against integrated run current. The figure clearly shows that higher lifetimes were achieved more quickly in 2005 than in 2004. Additionally, the 2004 data shows a much smoother curve than the 2005 data. There are many reasons/combinations of reasons why this may have occurred. The first is that the ring chambers had already been exposed to a whole year of beam scrubbing by the beginning of the 2005 run, and, therefore, could have experienced lower desorption rates during the 2005 run than during

the 2004 run. Another factor that may have contributed to the large differences in lifetimes is the TSP flash sequence for 2005. The flash frequency for the 2005 run and the 2004 run are very different. In 2004, the TSPs were flashed as many as 20 times, while the TSPs were only flashed a maximum of 5 times in 2005. The flash frequency, however, could not have contributed to such large differences in lifetimes all on its own. Figure 1 shows that the pressure for the TSP settles to about the same final pressure level after a certain integrated run current level is reached. If the lifetimes were solely affected by the vacuum pressures, they would have settled at similar values towards the end of the runs. HOM heating doesn't explain this jump in lifetime either; the temperatures measured at aperture transition areas (especially at BL11 upstream bellows) indicate that the temperatures were actually lower at these locations in 2004 than they were in 2005. Therefore, high occurrences of HOM heating could not have been the only reason for the lower lifetimes in 2004. Information about the nature of the dominant gas molecules within the chamber during the different runs might provide an explanation for the lifetime differences. However, only two Residual Gas Analyzers (RGAs) have been attached to the ring of which one is non-operational and the other is attached to the back end of a TSP (so it cannot accurately analyze the gas composition within the beam chamber). Clearly more information is needed to explain the differences shown in Figure 5.

Other information that can be drawn from Figure 1 is that the multiple flashings of 2004 created a smooth pumpdown curve for the whole year. The sparse flashings of 2005 created large steps in the pressure profile for 14G-TSP1. These pressures are at times higher than pressures at the same integrated run current levels in 2004. The profile of 03G-TSP1 is less dramatic. This may have to do with the fact that its pressure was

significantly lower before and after each flash. Its pressure reading was initially lower than the pressure at 14G-TSP1 because it was actually flashed an extra time before the 2005 run started. It is difficult to say whether or not the 2005 run would have benefited significantly from multiple flashings, but it is definitely an issue that needs to be looked into more closely.

Figure 2 shows the 2004 and 2005 pressure profiles of the girder 14 ion pumps. It is interesting to note that although the 2004 and 2005 pressures for ion pumps 2 and 3 end up with approximately the same final pressures at the end of each respective run, while the final pressures for ion pump 1 do not.

Figure 3 and Figure 4 show the relationship between certain TSP pressures and beam lifetime. Flashes are indicated on the graphs by vertical red lines. These figures help to map out a relationship between the flash pattern and the pressure profiles of these pumps. The flash patterns in 2004 and 2005 are obviously quite different. The TSPs were flashed 20 times in 2004 (14 times during beam current operation) and 5 times in 2005 (3 times during beam current operation). The contrast between these two figures strongly suggests that multiple flashings in 2004 contributed significantly to the smooth pumpdown curve shown in the figure. However, it is not evident that flashing multiple times throughout the *whole* run is entirely necessary. The sizable amount of time spent flashing the TSPs during the middle and tail end of the run (6-8 hours per flash), during the time when beam time is needed to run and complete experiments, may have been wasted since it may not have been necessary to flash so often in order to maintain the shape of the curve. The data from 2004 and 2005 is not sufficient enough to determine

whether or not this is so. More data from future runs will have to be scrutinized in the same way to determine a definitive solution to this flash pattern puzzle.

.

## *Conclusion*

---

As of yet, the only definitive conclusions that can be made are that the vacuum system is performing quite well at 100mA and that it is capable of safely handling 500mA current levels since no dramatic beam losses occurred during tests. However, much more work on the subject is currently in progress, and data from future runs will aid in determining the optimal performance conditions of the system. From the data that is available, it appears that the TSPs may not have been utilized at their maximum efficiency in either 2004 or 2005. The most effective approach may be to flash often during the initial pumpdown and during the beginning of the run in order to develop the “smooth curve” trend, and to flash less often once the run progresses. Vacuum pressure, lifetime, and RGA data from the next few runs will be analyzed to determine whether or not this is the best TSP flashing method.

# Tables and Figures

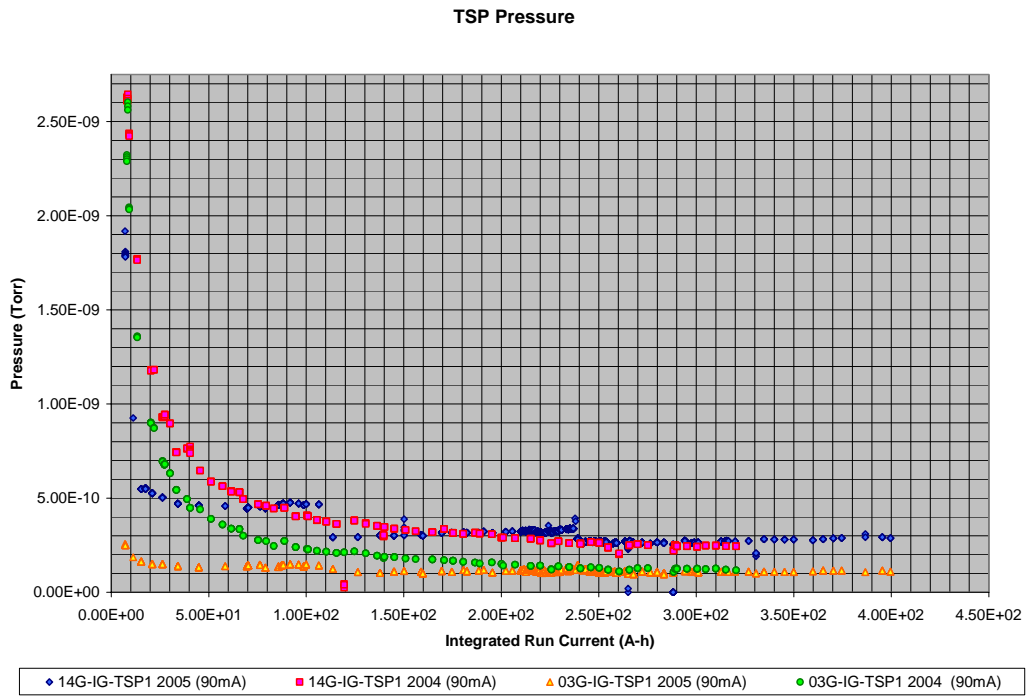


Figure 1: TSP pressures for certain pumps in 2004 and 2005

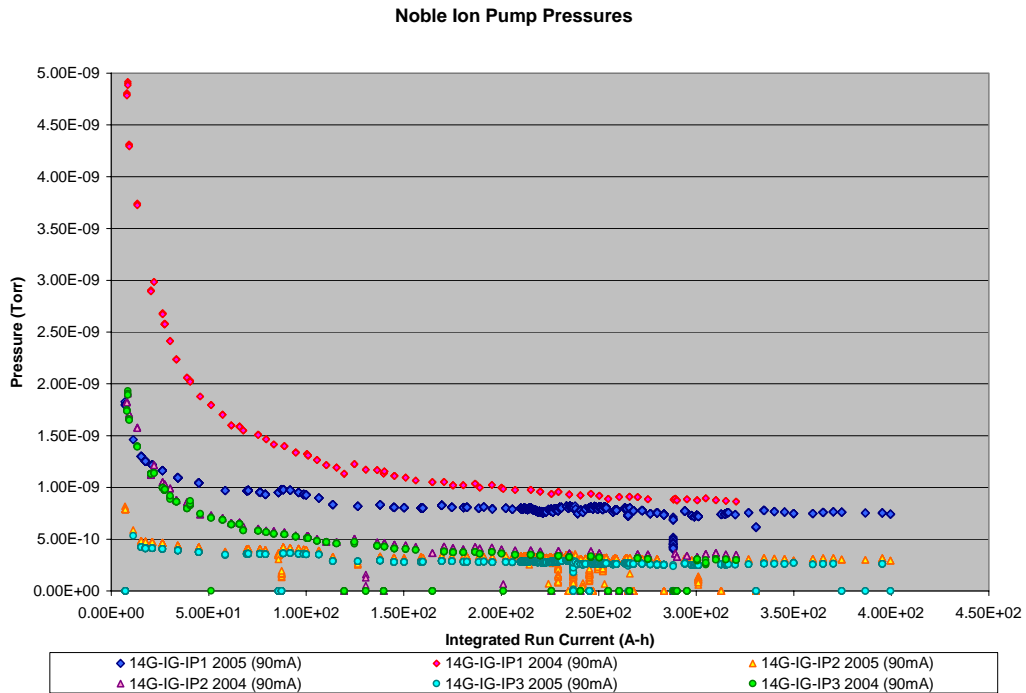


Figure 2: Ion pump pressures for certain pumps in 2004 and 2005

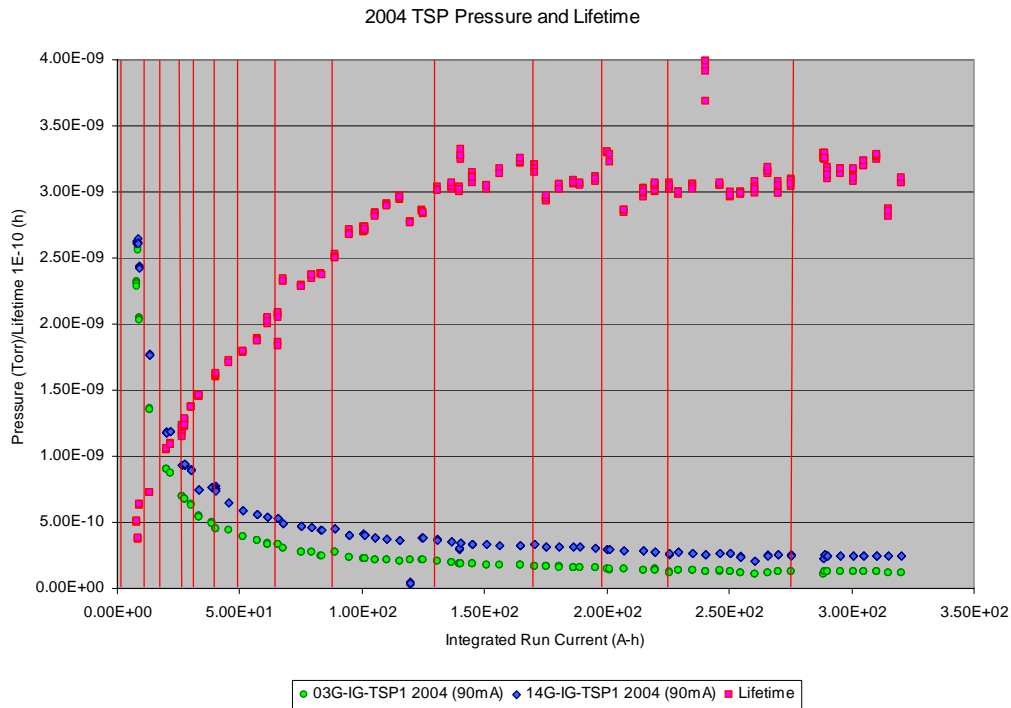


Figure 3: Relationship between the pressure profile of certain TSPs in 2004 (14G-TSP1 and 03G-TSP1) and beam Lifetime. Red vertical lines are locations of TSP flashes.

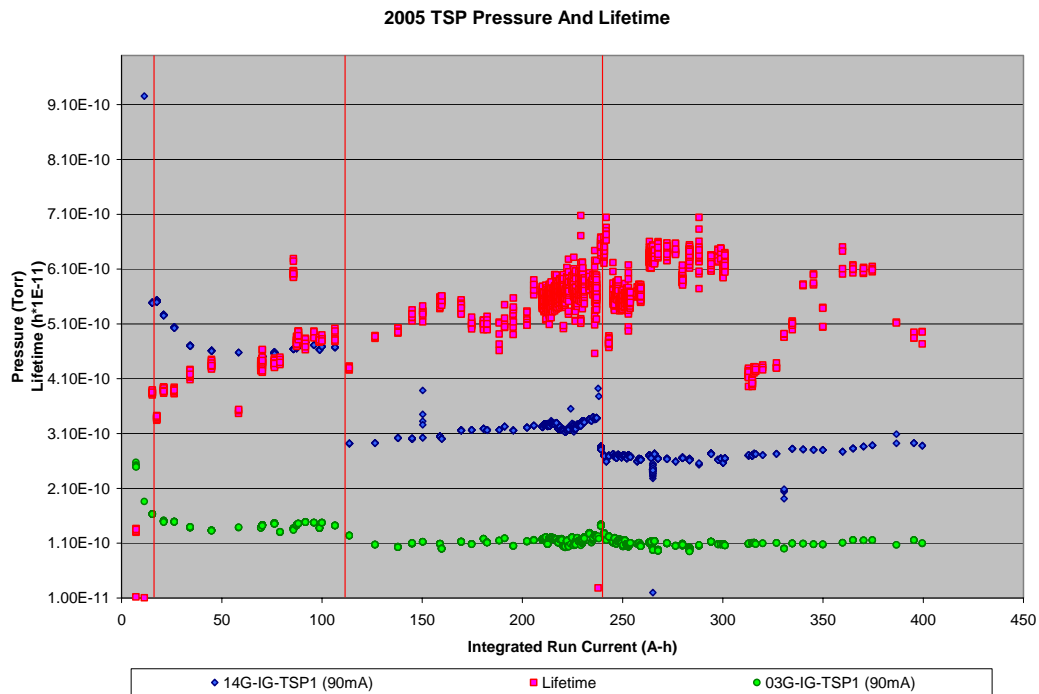


Figure 4: Relationship between the pressure profile of certain TSPs in 2005 (14G-TSP1 and 03G-TSP1) and beam Lifetime. Red vertical lines are locations of TSP flashes.

### Beam Lifetime

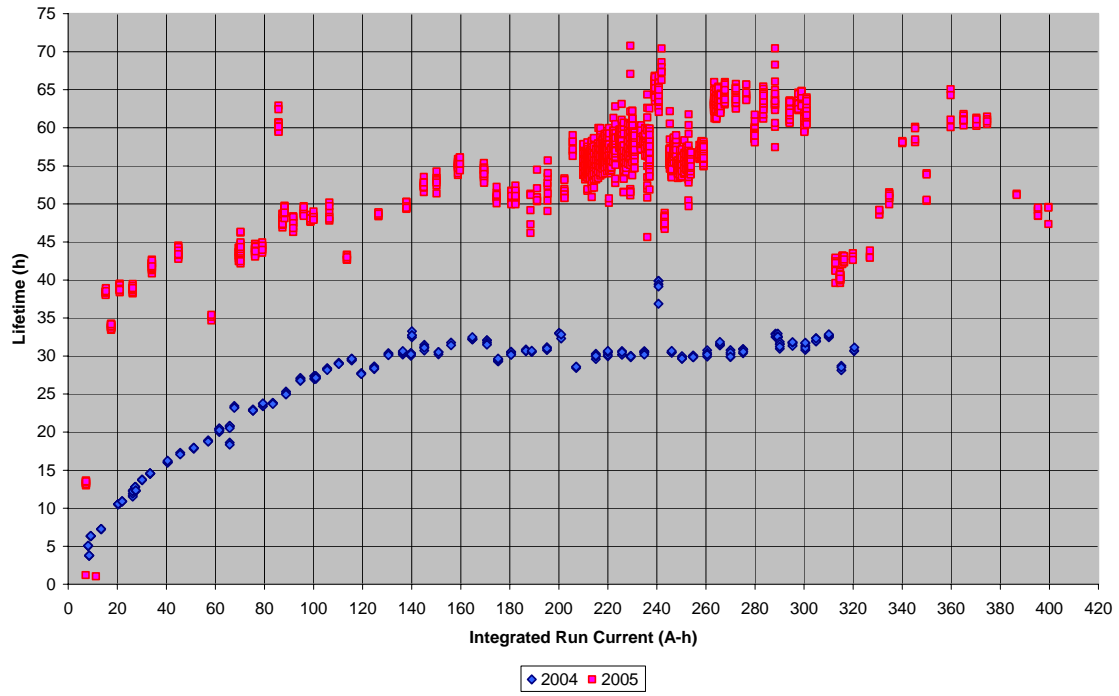


Figure 5: Electron Beam Lifetimes in 2004 and 2005 as Functions of Integrated Run Current

## *Literature Cited*

---

- [1] Welch, K. M., *Capture Pumping Technology, An Introduction*. Pergamon Press (2000) pp. 185-208
- [2] P. Bellomo, R. Boyce, J. Corbett (Deputy Editor), P. Corredoura, E. Daly, D. Dell'Orco, T. Elioff, I. Evans, A. Fisher, R. Hettel (Editor), N. Kurita, J. Langton, G. Leblanc, C. Limborg, D. Martin, Y. Nosochkov, T. Rabedeau, S. Park, J. Safranek, H. Schwarz, J. Sebek, J. Tanabe, C. Wermelskirchen, K. Wille, R. Yotam, F. Zimmermann, *SPEAR 3 Design Report*. Stanford Linear Accelerator Center, Stanford University, Stanford, California. (1999)

## *Acknowledgments*

---

I would like to thank my mentors, Mr. Harold A. Morales and Mr. Benjamin Scott, as well as everybody at the Engineering and Technical Services Department of the Stanford Synchrotron Radiation Lab at the Stanford Linear Accelerator Center. I would also like to thank the U.S. Department of Energy, the Office of Science, and the SULI program (especially James Lindesay, Helen Quinn, and Pauline Wethington) for providing me with the opportunity to learn all that I did as an intern this summer.

## The Heat Loss Analysis and Commissioning of a Commercial Helium Dewar

Marcus Bellamy

University of New Mexico

U.S. Department of Energy

Stanford Linear Accelerator Center

Menlo Park, California

Science Undergraduate Laboratory Internship (SULI) Program

August 15, 2005

Prepared in partial fulfillment of the requirements of the Office of Science, Department of Energy's Science Undergraduate Laboratory Internship under the direction of Helen Quinn at Stanford Linear Accelerator Center.

Participant: \_\_\_\_\_  
Signature

Research Advisor: \_\_\_\_\_  
Signature

# Table of Contents

Abstract .....	iii.
Introduction .....	1
Materials and Methods .....	2
Results .....	5
Discussion and Conclusion .....	8
Acknowledgements .....	9
References .....	9
Tables .....	10
Figures .....	11

## **Abstract**

A low temperature cryostat suitable for many different experiments will be commissioned at the cryogenic test facility at SLAC. The scope of the project is to make commission a commercial Helium dewar. The building of the top flange will be followed from its design phase through to its finished assembly. In addition, diagnostic tools such as thermometry, level detector, pressure gauge, transfer lines for He and N<sub>2</sub>, vent lines with relief valves for He and N<sub>2</sub> will be incorporated. Instrumentation to read and plot this data will also be included. Once the cryostat is assembled, we will cool down the cryostat to measure its performance. A typical consumption rate of Helium will be measured and from this, the overall heat leak to the dewar will be calculated.

A processing instrumentation diagram (PID) of the dewar system was created with SolidEdge and was later approved and published as an official SLAC document. The plots comparing the liquid level changes of the 36 inch probe with the time and the heat loss as a function of time proved to be a valid indication that the data was interpreted and recorded correctly and that the dewar was put together successfully.

## Introduction

A cryostat is a mechanism used to operate something under a controlled low temperature. A dewar is a form of a cryostat that is used to hold a liquid cryogen. In this case, the dewar will hold both liquid nitrogen and liquid helium. Between the two liquids are insulation and two vacuums. Insulation is needed to help remove existing paths of infrared radiation, while the vacuums are needed to minimize convection and conduction by removing air. Intermediate thermal temperature shields, which are made of materials with low emissivity, are also put into place to ward off radiation. A good portion of the dewar material is stainless steel, due to its low conductivity, good impact strength and a high tensile modulus.

While in the designing process of a dewar, it is important to understand and consider the many thermodynamic, chemical, physical, mechanical, and safety properties, in order to optimize the performance of the dewar and to maintain its reliability. While in the process of fine-tuning the design, one method of examining the performance could be to determine the typical consumption rate of Helium and compare it with a heat loss calculation.

The two primary fluids used in the cryostat design are liquid nitrogen and liquid helium. Nitrogen, as a gas, makes up 80% of the atmosphere. Liquid nitrogen is an essential intermediate chemical (precoolant) used for helium liquefaction. Some safety issues directly related with the managing of liquid nitrogen include asphyxiation, overpressure and frostbite. Overpressure could occur if the liquid nitrogen is enclosed in a container where there is no outlet or vent line (such as a relief valve) in place. If not given some path to allow the evaporation to leave, the pressure may soon build up to the

point where the container will explode. Frostbite can occur if proper handling of the liquid nitrogen is not undertaken. At the normal boiling point of nitrogen, its temperature is 77.347 K and its pressure is 1 atm. While the temperature outside of the dewar will be ambient, the inner nitrogen jacket will be cooled down by the liquid nitrogen to a consistent temperature very close to 77 K. The low temperature of liquid nitrogen will be used to maintain the very low temperature of liquid helium.

Helium is the second most common element in the universe. However, it is uncommonly found on earth because it does not combine with other elements and it is very light and very fast, allowing much of it to escape. Helium's boiling point at 1 atm is 4.224 K. Liquid helium has a high compressibility and a low viscosity. Helium also has the ability to become a superfluid, in which the thermal conductivity approaches infinity and the viscosity approaches zero. It is considered to be a superfluid if cooled below a temperature of 2.177 K (considered to be at its lower Lambda point). Normal helium is regarded as He I, while superfluid helium is regarded as He II.

Given the precautions and necessities of safely maintaining these two elements in their liquid state and maintaining consistent temperatures at designated areas, reasonable assumptions can be made on the ramifications of the dewar's performance.

## **Materials and Methods**

Before the manufacturing process, the cryostat assembly was designed using the advanced CAD software known as Solid Edge. The CAD design included the dewar, top flange, thermometry, level detector, pressure gauge, transfer lines for He and N<sub>2</sub>, and the vent lines with relief valves for He and N<sub>2</sub>. This design was called a processing

instrumentation diagram (PID). Designing the top assembly on computer-based software before manufacturing is a safe, logical, and cost-effective way to understand the feasibility behind the design.

The manufacturing process initiated by welding the utility ports and installing the baffles to the top flange. The first baffles made were simply test baffles used only while examining the cryostat's viability. These test baffles were made of fiber glass and were encased with aluminum sheets, in order to improve reflectivity. There were a total of 8 baffles in a layered sequence, connected to the top flange by steel rods and bolts. An assembly stand was constructed to elevate the top flange while adding/modifying its surrounding components and to safely store the flange with baffles when removed from the inside of the dewar. Since the dewar height (without the adapter and top flange) is 60 inches, the assembly stand was set to be 59 inches. The inside of the depth of the dewar is 48 inches, so the inner components of the top flange were kept well below this dimension to provide sufficient space for the liquid helium.

The top flange is comprised of stainless steel with a cylindrical base and several ports, which are suitable for housing of relief valves, a pressure gage, liquid-level indicators, and a He transfer line. The ports were welded on the flange and the regions along connecting edges were fused to assure minimal leakage. The adapter flange (riser), also made of stainless steel, was also fabricated and is connected to the bottom surface of the top flange. The riser is a wide-body, hollow cylinder with 6 input/output ports, in place for additional feedthroughs to carry out the experiment. Each of the flange and riser parts underwent cold tests, to ensure that their material composition could handle the low

temperatures involved in the experiment. When each of the flange and riser ports are not being used, they are blanked off with a metal plate and an o-ring.

Next, the riser was fastened onto the dewar and the top flange was fastened onto the riser, in order to first ensure that the dewar was vacuum tight by pumping out any accumulated air. The pumping process was done by connecting a Tops turbo pump to the dewar vacuum. The Tops base pressure was  $5 \times 10^{-5}$  Torr, while the dewar base pressure was  $2.8 \times 10^{-4}$  Torr. The vacuum pump was then disconnected and the vacuum port was blanked off. A Lexan (polycarbonate) cover was made for the top of the dewar when missing the flange and riser.

Once the vacuum check was complete, the part for liquid helium level probe was machined and assembled. The probe needed to be surrounded by a metal covering in order to manage the extremely low temperature. The baffles were initially greater in diameter than necessary, and their diameter length was abated and tailored to fit scarcely smaller than that of the riser's inner diameter.

Following this, the main vacuum valve, along with blank flanges, were installed onto the flange for leak testing. The UL 100 leak checker was connected to the dewar's inside via transfer line through valves and the dewar was then pumped down. The vacuum pump was used to draw out any moisture and atmospheric build-up in the dewar. The leak detector was then used to find any leaking joints which were then fixed until the dewar was vacuum (leak) tight.

After the vacuum leaks were adequately minimized, tubing from the helium feed on the dewar was connected to the helium suction line to provide helium backfill. The manufactured liquid level probe was also installed onto the cryostat as well as a liquid

level probe used in previous cryogenic experiments. The newer probe has six pins, and only four were needed. Therefore, to avoid heat leak from the two unused pores, the remaining pins were filled with epoxy. The helium vessel was pumped via a vacuum pump and backfilled with helium three times to reach a desired pressure below  $2 \times 10^{-1}$  Torr. Alongside the dewar nitrogen fill line was gradually filled with liquid nitrogen, to get down to a temperature of 77 K. The excess liquid nitrogen was sent through copper tubing, which led to the outside. A T-valve was attached to the copper tubing, in order to have the ability to open the valve and know when to stop cooling when the temperature reached 77 K. The first pump down reading was  $2.6 \times 10^{-1}$  Torr, the second at  $2.2 \times 10^{-1}$  Torr, and third at  $1.9 \times 10^{-1}$  Torr.

After the cooling process brought the inside of the dewar near 77 K, the liquid helium was transported to the dewar helium fill port using a transfer line secured by two flanges at each end. Beside the liquid helium tank was a helium gas tank, which fed to the liquid helium tank to maintain a high enough pressure to transfer the helium to the dewar.

After reaching a temperature close to 4.2 K, the helium liquid levels were monitored and recorded using the two intact liquid level probes. Each of the two liquid level probes were pin-connected to an electrical output, which relayed the level of the liquid helium.

## **Results**

Two liquid level probes were installed onto the dewar, one 30 inches long and the other 36 inches long. When the reading of the 30 inch probe was 100% (99.9%), the reading of the 36 inch probe was at about 83% (82.7%), which was a good signification that the probes were displaying accurate level indications. The 36 inch probe was filled to

90.4%, and the corresponding time, pressure inside the dewar system, and liquid levels were recorded. After this point, the time, pressure and liquid levels were recorded every half an hour at first, and then every hour after the rate of helium loss decreased. The pressure stayed between 814-824 Torr. Periodically, the liquid nitrogen jacket was re-filled to maintain the low temperature. It took about four days and 8 hours (104 hours) for the liquid helium to completely run out.

Since the desired units were metric, the pressure was converted from Torr to pascals. The lower and upper pressures were converted as follows:

$$814\text{Torr} \times \frac{1\text{atm}}{760\text{Torr}} \times \frac{1.013 \times 10^5 \text{ Pa}}{1\text{atm}} = 1.085 \times 10^5 \text{ Pa}$$

$$824\text{Torr} \times \frac{1\text{atm}}{760\text{Torr}} \times \frac{1.013 \times 10^5 \text{ Pa}}{1\text{atm}} = 1.098 \times 10^5 \text{ Pa}$$

The *Handbook of Cryogenic Engineering* provided a table of different densities and latent heat (heat of vaporization) values in correspondence to various temperatures and pressures. An average pressure value of  $1.089 \times 10^5 \text{ Pa}$  was a good estimate for reference to the tabulated values. For a liquid helium pressure of  $1.089 \times 10^5 \text{ Pa}$  (which is equal to a temperature of about 4.3 K), the liquid density is  $123.4 \frac{\text{kg}}{\text{m}^3}$ , the saturated density is  $18.17$

$\frac{\text{kg}}{\text{m}^3}$ , the liquid heat of vaporization is  $0.1045 \times 10^5 \frac{\text{J}}{\text{kg}}$ , and the saturated heat of

vaporization is  $0.3071 \times 10^5 \frac{\text{J}}{\text{kg}}$ . Latent heat (heat of vaporization) is the amount of heat

required to convert the unit mass of a liquid into the vapor without a change in

temperature. It requires converting something in a more organized state (as a liquid) to something with more spontaneity.

The volumetric flow rate was also calculated, which involved using the probe height of 30 inches, the dewar's inner jacket diameter, and the time. The 36 inch probe was primarily used to test against the 30 inch probe, so only the liquid levels of the 30 inch probe were used for further analysis. Steps to obtaining the volumetric flow rate and sample volume flow rate calculations are below:

Volume when 30 inch level probe at 100%:

$$V = \pi r^2 h = \pi \times \left[ 14 \text{in} \times \frac{.0254 \text{m}}{1 \text{in}} \right]^2 \times 30 \text{in} \times \frac{.0254 \text{m}}{1 \text{in}} = 0.303 \text{m}^3$$

Volume when 36 inch level probe at 100%

$$V = \pi r^2 h = \pi \times \left[ 14 \text{in} \times \frac{.0254 \text{m}}{1 \text{in}} \right]^2 \times 36 \text{in} \times \frac{.0254 \text{m}}{1 \text{in}} = 0.363 \text{m}^3$$

The volumetric flow rate from 11:20-12:20pm:

$$q = \frac{\Delta V}{\Delta t} = \frac{(0.1850 - 0.1825) \text{m}^3}{3600 \text{s}} = 6.73 \times 10^{-7} \frac{\text{m}^3}{\text{s}}$$

After calculating the volumetric flow rate, and looking up the corresponding densities and latent heat values, the heat loss,  $Q$ , was found using the following equation:

$$Q = q \rho H_{\text{vapor}} = q \rho (H_{\text{SAT}} - H_{\text{LIQ}})$$

The units for heat loss are joules, and a sample calculation of the heat loss for the same time increment above (11:20-12:20pm) is shown below:

$$Q = 6.73 \times 10^{-7} \frac{\text{m}^3}{\text{s}} \times 123.4 \frac{\text{kg}}{\text{m}^3} \times (0.3071 - 0.1045) \frac{\text{J}}{\text{kg}} = 1.682 \times 10^{-5} \text{W}$$

A graph of  $Q$  vs.  $t$  (time) was created to find out if the plot characteristics were typical or desired for dewar experimentation.

## Discussion and Conclusion

After several drafts, a processing instrumentation diagram (PID) was successfully created with SolidEdge. It was later approved and published as an official SLAC document. This drawing will serve as a good reference for any future experiments on the blue dewar.

Because of recurring leaks in the beginning, the dewar components were disassembled and reassembled several times, which was the longest process of the project. However, it is common for leak checking to be a lengthy process to ensure the viability of the dewar, and therefore obtaining accurate results in experiments and it is worth the extra time reserved to this process.

There was a minor set-back of having to disassemble the baffles, which involves talking them apart individually, simply because they were not covered with aluminum sheeting. Having covered them prior to connecting them to the flange rods would have saved time. Another minor set-back was the waiting process for the liquid helium to arrive.

A plot was created comparing the liquid level changes of the 36 inch probe with the time, in order to ensure that the points fashioned a gradually sloping curve. Since the graph did indeed reveal a steadily sloping curve, it was a good indication that the data was interpreted and recorded correctly.

As viewed from the plot of the heat loss as a function of time, there were no major fluctuations in heat loss. Theoretically, the heat loss should decrease as the path from the top flange extends down to the helium jacket, since the top of the flange is close to room temperature (298 K), while the bottom is close to 4.2 K. Moreover, the heat loss also

lowers after passing the baffles. The plot validated this idea because the heat loss did decrease considerably with time, meaning that as time passed, the heat loss was closer to the bottom of the helium jacket. Although some of the points were noticeably out of the realm the fit curve, the heat loss scale is in 0.2 increments, meaning that the points that were away from the expected flow of the curve were only off by a small fraction of a watt.

### **Acknowledgements**

I offer my thanks to the U.S. Department of Energy and the SULI program for granting me the opportunity to undergo research here at the Stanford Linear Accelerator Center. A special thanks to my mentors, EunJoo Thompson and John Weisend, for providing me with their knowledge, support, and a meaningful experience through this research project. I appreciate the efforts that Michael Racine and Ron Rogers put in helping me with the project and their continuous patience and comedy. I would like to thank James Lindesay and Helen Quinn for optimizing my overall interning experience. Finally, I would like to thank each individual of the SULI program and each member of the French House for making this a memorable and fun summer.

### **References**

- [1] Flynn, M. Thomas, "Cryogenic Engineering," Marcel Dekker, Inc., 1997
- [2] Weisend II, G. John, "Cryogenic Properties of Materials," 2003 CA Short Course Symposium, September 16, 2003.
- [3] Weisend II, G. John, "Handbook for Cryogenic Engineering," Taylor and Francis, 1998.

## Tables

<u>Time (hr)</u>	<u>36in LL (%/100)</u>	<u>30in LL (%/100)</u>	<u>Pressure (kPa)</u>	<u>36in Volume Flow Rate (m<sup>3</sup>/s)</u>	<u>30in Volume Flow Rate (m<sup>3</sup>/s)</u>	<u>36in Heat Loss (W)</u>	<u>30in Heat Loss (W)</u>
0.00	0.904	0.996	109.30	0.000000000	0.000000000	0.000	0.000
1.00	0.899	0.996	109.03	0.000000420	0.000000000	1.051	0.000
2.00	0.892	0.996	109.70	0.000000294	0.000000000	0.736	0.000
3.00	0.884	0.996	109.83	0.000000224	0.000000000	0.561	0.000
4.00	0.873	0.996	109.16	0.000000231	0.000000000	0.578	0.000
5.00	0.860	0.995	109.03	0.000000219	0.000000020	0.547	0.050
6.00	0.851	0.993	108.76	0.000000126	0.000000034	0.315	0.084
15.50	0.824	0.881	110.23	0.000000146	0.000000729	0.366	1.823
16.50	0.777	0.874	109.56	0.000000240	0.000000043	0.599	0.107
17.25	0.737	0.872	109.43	0.000000195	0.000000012	0.487	0.029
18.75	0.734	0.867	109.70	0.000000013	0.000000027	0.034	0.067
19.75	0.730	0.863	109.30	0.000000017	0.000000020	0.043	0.051
20.75	0.727	0.856	109.56	0.000000012	0.000000034	0.030	0.085
30.95	0.721	0.843	109.43	0.000000016	0.000000042	0.041	0.106
31.15	0.718	0.841	108.50	0.000000008	0.000000006	0.020	0.016
32.15	0.712	0.835	108.90	0.000000016	0.000000019	0.039	0.047
33.35	0.705	0.826	108.63	0.000000018	0.000000027	0.044	0.068
46.10	0.687	0.810	109.83	0.000000033	0.000000035	0.082	0.088
49.60	0.666	0.801	109.30	0.000000036	0.000000018	0.089	0.046
50.80	0.623	0.747	108.76	0.000000071	0.000000107	0.178	0.268
60.80	0.603	0.714	109.83	0.000000028	0.000000055	0.069	0.137
61.80	0.597	0.707	109.43	0.000000008	0.000000011	0.020	0.029
65.00	0.589	0.699	109.30	0.000000010	0.000000012	0.026	0.031
68.75	0.582	0.687	109.43	0.000000009	0.000000018	0.021	0.044

**Table 1.** Time, liquid level, pressure, volume flow rate, and heat loss analysis of the blue dewar system.

# Figures

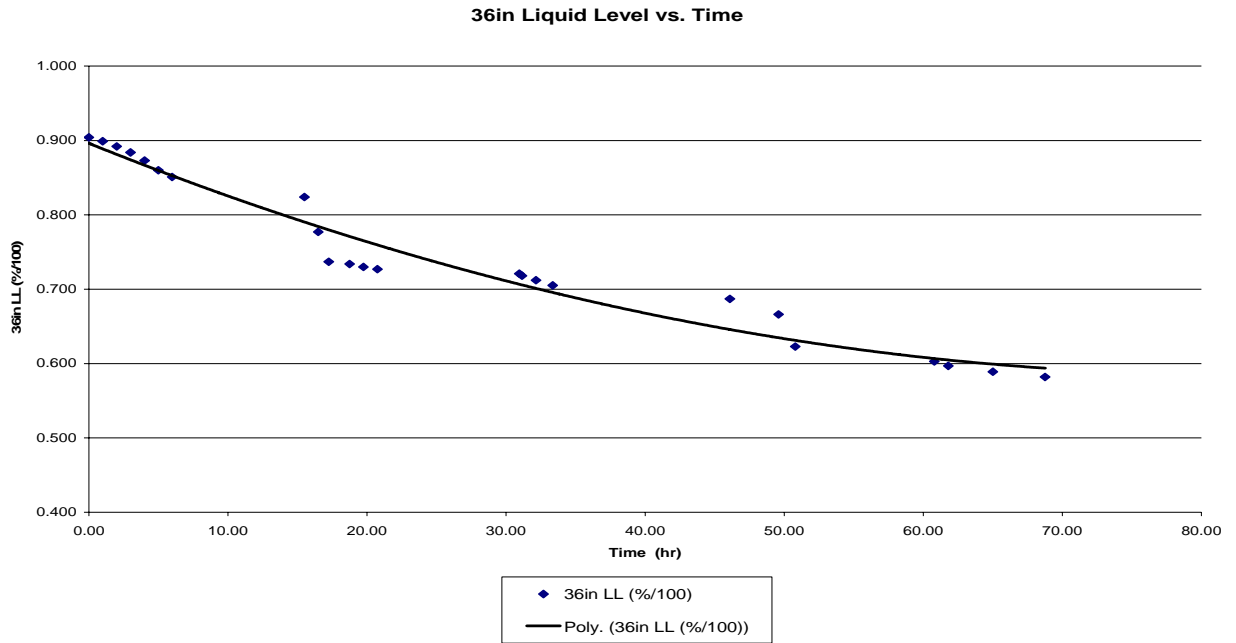


**Figure 1.** Plot of the liquid level changes of the 36 inch probe with respect to time.

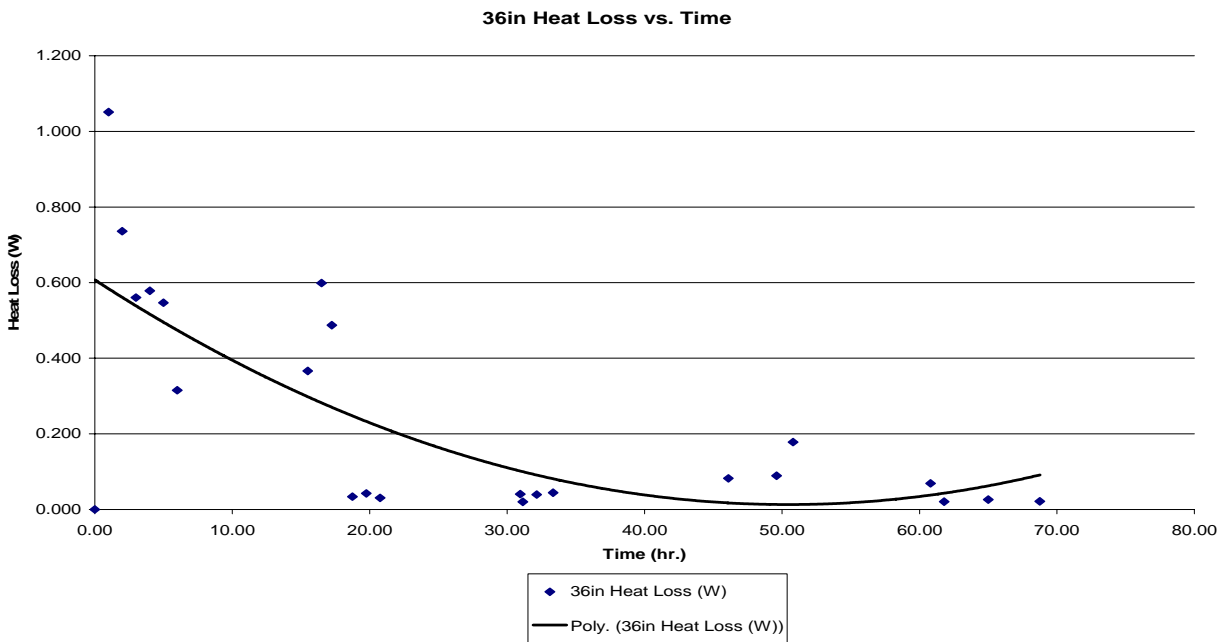


**Figure 2.** Plot of the heat loss along the 36 inch depth with respect to time.

## Mapping Strain in Nanocrystalline Nitinol: an X-ray Diffraction Method

Matthew Bibee

Office of Science, SULI Program

University of California, San Diego

Stanford Linear Accelerator Center

Menlo Park, California

August 19, 2005

Prepared in partial fulfillment of the requirements of the Office of Science, U.S. Department of Energy Science Undergraduate Laboratory Internship (SULI) Program under the direction of Dr. Apurva Mehta in the of the Stanford Synchrotron Radiation Laboratory (SSRL) at the Stanford Linear Accelerator Center (SLAC).

Participant:

\_\_\_\_\_

Signature

Research Advisor:

\_\_\_\_\_

Signature

## Table of Contents

Abstract	iii.
Introduction	1
Materials and Methods	3
Results	7
Discussion and Conclusions	8
Acknowledgements	10
References	10
Figures	11

## ABSTRACT

Mapping Strain in Nanocrystalline Nitinol: an X-ray Diffraction Method. MATTHEW BIBEE (University of California, San Diego, La Jolla, CA 92093) APURVA MEHTA (Stanford Linear Accelerator Center, Menlo Park, CA 94025).

Understanding the mechanical properties of biomedical devices is critical in predicting and preventing their failure in the body. Such knowledge is essential, for example, in the design of biomedical stents, which must undergo repeated strain over their ten year lifetimes without breaking. Computational models are used to predict mechanical response of a device, but these models are not complete; there are significant deviations from the predictions, especially when devices are subjected to repeated multi-axial loads. Improving these models requires comparisons with actual measurements of strained nitinol. Local measurements of the full strain tensor can be made using X-ray diffraction techniques, but they are currently limited to materials whose grain size is larger than the X-ray beam size or require several diffraction patterns produced by rotation of the sample. Nitinol stents are nanocrystalline, with grains smaller than any available X-ray beam. We present a method for measuring the local strain in a nanocrystalline material from a single X-ray diffraction pattern by extending current powder diffraction techniques. The components of the strain tensor are mapped onto a displacement ellipsoid, which is then reconstructed from diffraction data through Bragg's law and least-squares fitting. Using simulated diffraction data, we performed sensitivity tests to examine how the accuracy of the method depends on how much of the diffraction pattern is measured. We found that strain can be accurately calculated from measurements of at least three

diffraction arcs of at least  $20^\circ$  in length. Thus we believe that our method is a viable approach to calculating strain provided a sufficient amount of diffraction pattern is recorded.

## INTRODUCTION

Designing biomedical devices requires a detailed understanding of the materials from which they are constructed in order to minimize the risk of failure inside the body. One vital property that affects a device's durability is the material's stress-strain behavior. For instance, a biomedical stent (a metal mesh tube used to prop open a collapsed artery) must expand and contract each time the heart beats. Thus, over a stent's FDA-required lifetime of ten years, it must undergo more than four-hundred million strain cycles without breaking. Thus knowledge of how strain affects the integrity of a material is critical for stent design.

Designing a device to withstand such large amounts of repeated strain is complicated, but powerful computational finite element models exist to predict the strain behavior of nitinol in biomedical stents [1]. These models aid greatly in stent design, but the fact that stent failures still occur shows that the models are not complete. Incompleteness of the FEA models also arises from the fact that more and more biomedical devices are made from advanced materials, such as nitinol. Nitinol, an equiatomic alloy of nickel and titanium, is used in stent production because of its unique properties of superelasticity and shape memory. While these properties are an asset in the creation of stents, they also cause nitinol's strain behavior to differ markedly from that of more well-studied materials such as steel. In addition to the reversible elastic and nonreversible plastic deformation documented in steel, nitinol can also deform by a reversible, temperature dependent transformation between austenite and martensite phases. It is this extra mechanism of deformation that provides nitinol with its unusual superelastic and shape

memory properties and also contributes to less than adequate understanding of its mechanical response under repeated multi-axial load.

In order to improve the models it is necessary to directly measure strain in a real device. X-ray diffraction, being non-contact and non-destructive, is a useful method for measuring local strain on a device which is still under a complex multi-axial load. However, its usefulness is currently limited by the size of the X-ray beam (currently about 1  $\mu\text{m}$  at U.C. Berkeley's Advanced Light Source). Successful strain measurements have been made for materials whose grains are larger than the beam size [2]. In this arrangement, the beam is incident on a single crystallite, creating a Laue diffraction pattern that can be used to calculate the second rank (three-by-three) strain tensor. However, when the grains are smaller than the beam size, the beam is diffracted by many crystallites at once. This is the case for nanocrystalline nitinol, which is the primary material for stent production. Strain has not yet been measured in these materials, but we propose that it is possible to calculate the local strain tensor of nanocrystalline nitinol using powder diffraction techniques similar to those described by [3] and [4]. However, in contrast to their techniques, we calculate the strain tensor from a single diffraction pattern rather than a series of patterns recorded at different sample orientations. Measuring local strain at many locations in a sample produces a strain map of the material's response to a given stress condition. Comparison of strain maps from measurement and modeling helps to improve the models, resulting in the creation of more reliable stents.

## MATERIALS AND METHODS

### *Effects of Strain on a Material*

While bulk strain is easily measurable using a strain gauge, local strain measurements are considerably more difficult. The imposition of stress on a material produces changes in the material's macroscopic dimensions, which manifest themselves on the atomic level as alterations to the crystal lattice. A material under elastic strain will deform due to the compression and stretching of atomic bonds, which alters the spacing of the crystal lattice planes. Strain is represented mathematically by a symmetric second order tensor consisting of six independent terms: three terms representing normal strain and three representing shear strain. However, the strain tensor may always be transformed by coordinate system rotation into a system where shear strains vanish and the normal strains are defined as the principal strains. With no shear strain, it is evident that a tensile normal strain represents an increase in atomic spacing along the axis of the strain, whereas a compressive normal strain represents a corresponding decrease in atomic spacing. Thus we can conceive of a displacement ellipsoid, oriented along the three principal strain axes, whose deviations from a sphere correspond to the principle strains. The ellipsoid will be thinner than the unstrained sphere along axes of compressive strain and thicker along axes of tensile strain. The addition of shear strain produces a rotation of the ellipsoid.

### *X-ray Diffraction*

X-ray diffraction is an excellent tool for examining the spacing between atoms and, by extension, strain. When an X-ray beam is incident upon a single crystal, the radiation that is

scattered from each atom will interfere constructively only at certain angles relative to the crystal lattice, creating a series of diffraction spots. For a comprehensive explanation of scattering and diffraction, see [5]. The angles at which the spots will appear are given by Bragg's law,

$$\frac{2d \sin \theta}{\lambda} = n,$$

where  $\lambda$  is the X-ray wavelength,  $d$  is the spacing of the diffraction planes,  $\theta$  is the angle of beam incidence and diffraction, and  $n$  is an integer.  $d$  is measured along the bisector of the incident and diffracted beams. Following conventions of diffraction notation, we will refer henceforth to the angle  $2\theta$  rather than  $\theta$ . The spacing of the diffraction spots, measured by  $2\theta$ , is thus inversely proportional to the crystal lattice spacing  $d$ .

Nanocrystalline nitinol by definition is made of grains on the order of several nanometers, much smaller than the beam size of 1  $\mu\text{m}$ . Thus the X-ray beam is incident upon many small crystallites at once. We assume that the crystal lattices of the crystallites are oriented randomly with respect to one another. In this situation, often called powder diffraction, each grain illuminated by the beam produces its own set of diffraction spots with the same angle  $2\theta$  from single crystal diffraction. Assuming the crystallites are randomly oriented with respect to one another, each diffraction spot smears out into a ring (Figure 2), with each point on a ring corresponding to the diffraction spot produced by the crystallites sharing a certain orientation. The orientation of the crystallite is represented by the angle  $\phi$ , which is the angle that the crystallite's diffraction spot has been rotated away from vertical. Several distinct rings will be present in the pattern, corresponding to  $d$  spacings of the different sets of diffraction planes defined by the crystal's specific Bravais lattice type [5]. Typically

only part of each ring is captured by a detector, so that a powder diffraction pattern appears as a set of “-arcs,” each of which represents a constant  $2\theta$  value and a range of  $\chi$  values (Figure 1).

### ***Calculation of the Strain Tensor***

Techniques exist for calculating local strain in materials using single crystal diffraction [2] and from powder diffraction patterns using multiple beam shots at a number of different incident angles [3,4]. Our method extends the work of [3] and [4] to allow the local strain tensor to be calculated from a single diffraction pattern, which not only eliminates the technical challenge of focusing the X-ray beam on a single area of sample while changing the angle of incidence, but it also reduces the time required to complete a measurement.

The key to our technique is the fact that crystallites with different orientations will have different responses to an applied strain. The magnitude and sign of the change in spacing between the lattice planes is dependent on the relative orientation of the lattice planes and the local principal strain axes. The change in diffraction plane spacing along a given axis is directly equivalent to the deviation of the displacement ellipse from the unstrained sphere along that axis. Importantly, the lattice spacing  $d$  now varies with angles  $2\theta$  and  $\chi$ , meaning the -arcs no longer represent constant  $2\theta$  values. Each point on each arc provides information about the local strain along a particular axis specified by  $2\theta$  and  $\chi$ . The strain can be calculated from

$$\epsilon_{2\theta,\chi} = \frac{d_{2\theta,\chi} - d_0}{d_0},$$

where  $d_{2,}$  is the lattice spacing measured along this axis and  $d_0$  is the unstrained lattice spacing, which can be measured from an unstrained sample.  $d_{2,}$  and  $d_0$  can be calculated using Bragg's law.

A single  $\chi$ -arc provides  $d$  values over a range of  $\omega$ 's, and several  $\chi$ -arcs together provide  $d$  values over a range of  $\omega$ 's at several  $2\theta$  values. Each  $\chi$ -arc is produced by a different set of diffraction planes, meaning each arc has a different  $d$  value, however the  $d$  values are not independent and can be normalized using a single multiplicative factor derived from the crystal lattice structure (for nitinol, these factors are  $1, \sqrt{2}, \sqrt{3}, 2, \dots$ ). When normalized, the diffraction arcs can be transformed into arcs that can be thought of as lying on a single displacement ellipsoid (Figure 3).

[3] and [4] describe how to calculate the six terms of the strain tensor given a set of normalized  $d$  values measured at different angles. However, the coordinate system used by [3] and [4] is designed to accommodate measurements made by rotating the sample or X-ray beam, not measurements extracted from the  $\chi$ -arcs. Therefore, we derived a transformation between the coordinate system of [3] and [4] (shown in Figure 3) and a coordinate system more appropriate for describing  $\chi$ -arcs (Figure 4). Modifying equation 5.4 from [4] to use the

angles  $\omega$  and  $\chi$ , where  $\omega = \Theta - \frac{2\theta}{2}$  ( $\Theta$  being the incident angle of the X-ray beam), we get:

$$\begin{aligned} \varepsilon_{\omega, \chi} = & \varepsilon_{11} \frac{\tan^2 \omega}{\tan^2 \omega + \sec^2 \chi} + \varepsilon_{22} \frac{\tan^2 \chi}{\tan^2 \omega + \sec^2 \chi} + \varepsilon_{33} \frac{1}{\tan^2 \omega + \sec^2 \chi} \\ & + \varepsilon_{12} \frac{2 \tan \omega \tan \chi}{\tan^2 \omega + \sec^2 \chi} + \varepsilon_{23} \frac{2 \tan \chi}{\tan^2 \omega + \sec^2 \chi} + \varepsilon_{13} \frac{2 \tan \omega}{\tan^2 \omega + \sec^2 \chi} \end{aligned}$$

where  $\epsilon_{11}$ ,  $\epsilon_{22}$ ,  $\epsilon_{33}$ ,  $\epsilon_{12}$ ,  $\epsilon_{23}$ , and  $\epsilon_{13}$  are the six terms of the strain tensor. Each point on each arc yields values for  $\omega$ ,  $\chi$ , and  $\epsilon_{\omega\chi}$ . The non-linear equation in two terms can be transformed into a linear equation in 6 terms,

$$\epsilon_{\omega\chi} = \epsilon_{11}a_1 + \epsilon_{22}a_2 + \epsilon_{33}a_3 + \epsilon_{12}a_4 + \epsilon_{23}a_5 + \epsilon_{13}a_6$$

where  $a_1$  to  $a_6$  are defined as follows:

$$a_1 = \frac{\tan^2 \omega}{\tan^2 \omega + \sec^2 \chi}$$

$$a_2 = \frac{\tan^2 \chi}{\tan^2 \omega + \sec^2 \chi}$$

$$a_3 = \frac{1}{\tan^2 \omega + \sec^2 \chi}$$

$$a_4 = \frac{2 \tan \omega \tan \chi}{\tan^2 \omega + \sec^2 \chi}$$

$$a_5 = \frac{2 \tan \chi}{\tan^2 \omega + \sec^2 \chi}$$

$$a_6 = \frac{2 \tan \omega}{\tan^2 \omega + \sec^2 \chi}$$

The terms of the strain tensor can be found by a least squares fit of the diffraction data to the equation above.

A strain map can be obtained by measuring the local strain tensor at a series of grid points along the sample. The map is then created by plotting the values of each component of the tensor spatially.

## RESULTS

In order to determine how much data is required for an accurate and robust determination of the strain tensor, we performed several sensitivity tests using simulated diffraction data. We created simulated data of various sizes in order to test the method's

dependence on space coverage. The data was simulated from a tensor with normal strains along the X, Y, and Z axes but no shear strains. Various amounts of Gaussian error were added to the data. Even with perfect data points (no simulated error), tests showed that data from one or two arcs was insufficient for calculating the full strain tensor. With two arcs, it was possible to calculate the terms  $\epsilon_{22}$ ,  $\epsilon_{12}$ , and  $\epsilon_{23}$  but not  $\epsilon_{11}$ ,  $\epsilon_{33}$ , and  $\epsilon_{13}$ . With error-free data and at least three arcs, it was possible to calculate all six terms as long as at least nine data points were available. The results in Figure 5a-f were obtained from simulated data that included points from 3 arcs with Gaussian errors (standard deviation of  $0.1^\circ$ ) added to the values of the simulated data set. The vertical axis shows the deviation of the calculated strain values from the true strain values, and the X axis shows the length of the arcs in degrees. It was possible to calculate the full strain tensor from the three arcs, but as can be seen in Figure 5b, the accuracy of  $\epsilon_{22}$  declined dramatically for arc lengths of less than  $20^\circ$ .

## DISCUSSION AND CONCLUSION

Our tests show that this method is applicable to nanocrystalline materials if sufficient diffraction data is available. There must be at least three measurable diffraction arcs in the pattern, and the arcs must have sufficient extent. It is evident from the sensitivity tests that the number of arcs sets the goodness of the fit in the XZ plane (where  $\epsilon_{11}$  and  $\epsilon_{33}$  were located), and the length of the arcs sets the goodness of the fit in the Y direction (where  $\epsilon_{22}$  was located). The question is essentially how much of the displacement ellipsoid needs to be measured, and at what accuracy, in order to correctly extrapolate the rest of the ellipsoid. Our results show that at least three arcs  $20^\circ$  in length are necessary.

The method is also limited by several assumptions. The first assumption is that strain in the material is continuous, so that neighboring crystallites experience the same local strain. If this were not so, then there would be no correlation between different points on the diffraction pattern, and no strain information could be extracted. The grain-to-grain strain discontinuity would result in discrete “jumps” in the diffraction ring. The fact that these jumps are not observed in the diffraction pattern shows that this assumption is mostly true, however, the jumps could still exist on a small scale, manifesting themselves as error in ring measurements. Another assumption is the random orientation of crystallites. In fact, most materials have preferred crystallite orientations due to rolling and other metallurgical shaping processes. Such texture properties lead to imperfections in the diffraction pattern, such as the irregularities in intensity across the diffraction arcs evident in Figure 1. Gaps in the diffraction arcs may be present if there are crystallite orientations which are not sufficiently populated in the material. Such gaps reduce the space available for measurement and thus affect the accuracy of the fit. An additional assumption is the absence of plastic strain. This method measures only elastic strain, as this is the mechanism that affects lattice spacing. A real device under complex multi-axial load undergoes both plastic and elastic deformations, so it is important to minimize the amount of plastic strain by simplifying the load geometry and limiting the total strain on the material. The austenite-martensite transition also occurs as strain increases, so that in some cases the cubic austenite arcs may be replaced with monoclinic martensite arcs. One must be vigilant for this transition, but new arcs are easily discernable and can be incorporated into the method, yielding a measure of the strain associated with the phase transition.

There is still a need to examine the influence of the detector resolution on the goodness of the fit. Once the errors are well understood, the next step is to measure real local strain values and compare the resulting strain maps to the predictions of FEA models such as those in [1]. This will allow refinement of the models, which will provide insight into the physical mechanisms behind nitinol deformation. Understanding these mechanisms is vital to producing safer and longer lasting stents.

### **ACKNOWLEDGEMENTS**

I would like to thank Apurva Mehta, a great mentor in every sense of the word, both scientifically and personally. Xiao-Yan Gong, Alan Pelton, and others at Nitinol Devices and Components were very supportive and provided motivation and background for this research. I would also like to thank the U.S. Department of Energy for providing this research experience, as well as James Lindsay and Helen Quinn for organizing it.

### **REFERENCES**

- [1] A. R. Pelton, X. Y. Gong, and T. Duerig, "Fatigue testing of diamond-shaped specimens," *Proceedings of the International Conference on Shape Memory and Superelastic Technology Conference*, 2003.
- [2] A. A. MacDowell, R. S. Celestre, N. Tamura, R. Spolenak, B. C. Valek, W. L. Brown, J. C. Bravman, H. A. Padmore, B. W. Batterman, J. R. Patel, "Submicron X-ray diffraction," *Nuclear Instruments and Methods in Physics Research A*, vol. 467-468, 2001, p. 936-943.

- [3] V. Hauk, *Structural and residual stress analysis by nondestructive methods*, 1997, pp. 132-133.
- [4] I. C. Noyan and J. B. Cohen, *Residual Stress: measurement by diffraction and interpretation*, 1987, pp. 117-130.
- [5] B.E. Warren, *X-ray diffraction*, 1990.

### Figures

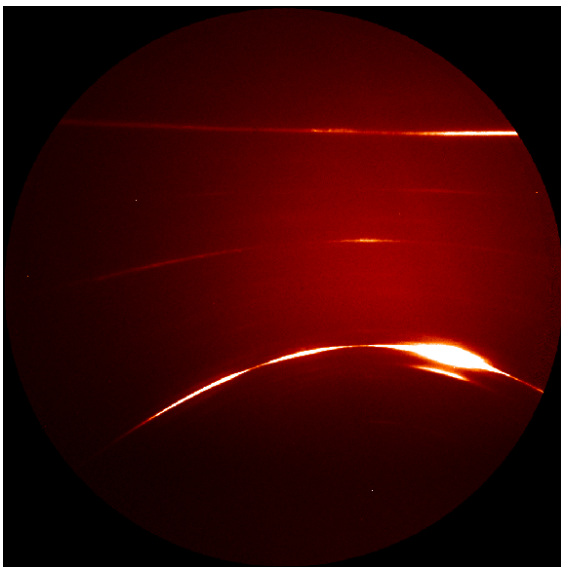


Figure 1. Example of nanocrystalline X-ray diffraction pattern with  $\gamma$ -arcs.

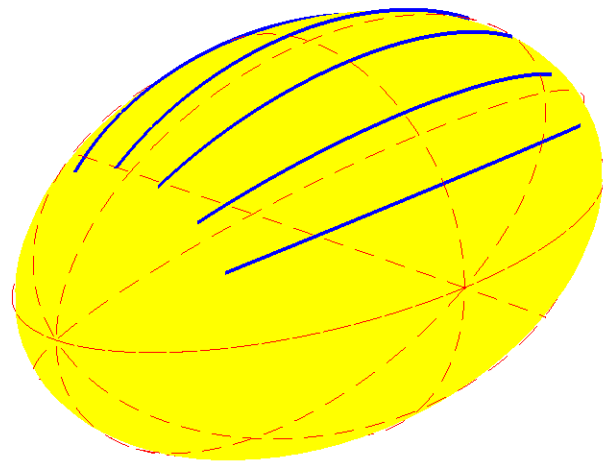


Figure 2. Displacement ellipsoid with  $\gamma$ -arcs.

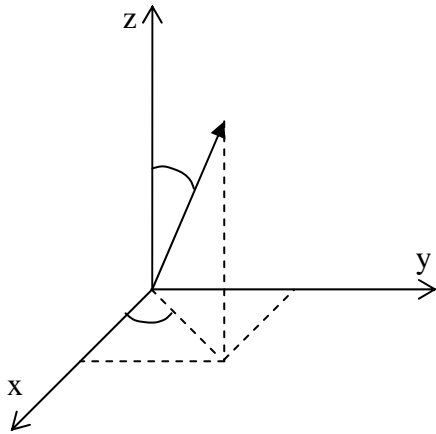


Figure 3. Coordinate system used by [4] and [5].

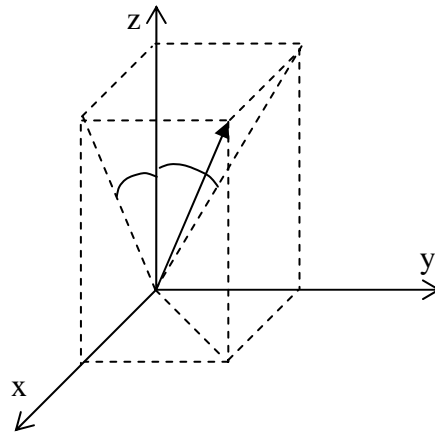


Figure 4. Coordinate system for describing -arcs.

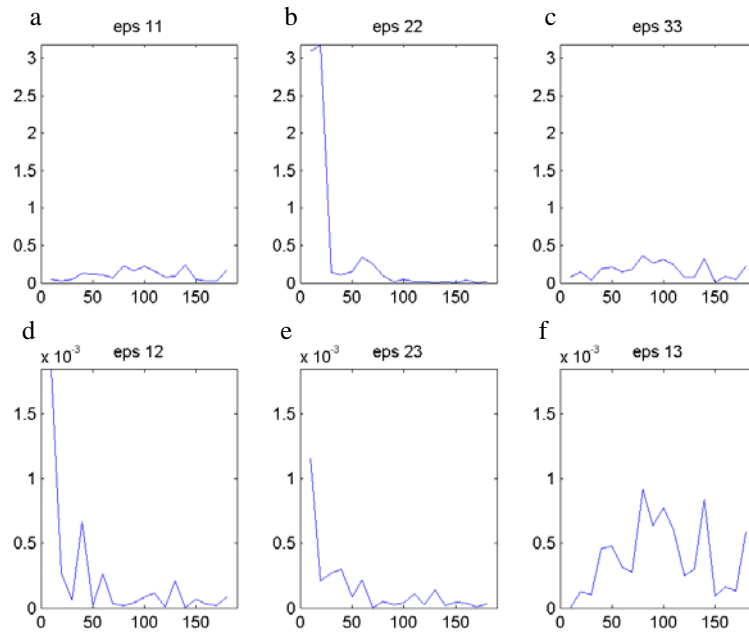


Figure 5. Error in strain term vs. coverage

## 2-D Modeling of Energy-z Beam Dynamics Using the LiTrack Matlab Program

Sean K. Cauley

Office of Science, SULI Program

Paine College

Stanford Linear Acceleration Center

Menlo Park, California

August 19, 2005

Prepared in partial fulfillment of the requirements of the Office of Science, U.S. Department of Energy Science Undergraduate Laboratory Internship (SULI) Program under the direction of Michael Woods in the Particle Physics Division of Stanford Linear Acceleration Center (SLAC).

Participant:

\_\_\_\_\_

Signature

Research Advisor:

\_\_\_\_\_

Signature

## Table of Contents

Abstract	iii.
Introduction	1
Material and Methods	3
Results	6
Discussions and Conclusions	8
Acknowledgement	9
References	9
Tables	10
Figures	13

## ABSTRACT

2-D Modeling of Energy-z Beam Dynamics Using the LiTrack Matlab Program. SEAN K. CAULEY (Paine College, Augusta, GA 30901) MICHAEL WOODS (Stanford Linear Acceleration Center, Menlo Park, CA 94025).

Short bunches and the bunch length distribution have important consequences for both the LCLS project at SLAC and the proposed ILC project. For both these projects, it is important to simulate what bunch length distributions are expected and then to perform actual measurements. The goal of the research is to determine the sensitivity of the bunch length distribution to accelerator phase and voltage. This then indicates the level of control and stability that is needed. In this project I simulated beamlines to find the rms bunch length in three different beam lines at SLAC, which are the test beam to End Station A (ILC-ESA) for the ILC studies, Linac Coherent Light Source (LCLS) and LCLS-ESA. To simulate the beamlines, I used the LiTrack program, which does a 2-dimensional tracking of an electron bunch's longitudinal ( $z$ ) and the energy spread beam ( $E$ ) parameters. In order to reduce the time of processing the information, I developed a small program to loop over adjustable machine parameters. LiTrack is a Matlab script and Matlab is also used for plotting and saving and loading files. The results show that the LCLS in Linac-A is the most sensitive when looking at the ratio of change in phase degree to rate of change. The results also show a noticeable difference between the LCLS and LCLS-ESA, which suggest that further testing should go into looking the Beam Switch Yard and End Station A to determine why the result of the LCLS and LCLS-ESA vary.

## INTRODUCTION

The electron bunch distribution generated by the linear accelerator (linac) at Stanford Linear Accelerator Center (SLAC) can be described by a 6-parameter “phase space”  $(x, x', y, y', z, E/E)$ . The X coordinate represents the horizontal transverse distribution with characteristic rms spotsize  $\sigma_x$ ;  $X'$  is the horizontal angular distribution with characteristic rms angular divergence  $\sigma_{x'}$ . The Y coordinate represents vertical transverse distribution with characteristic rms spotsize  $\sigma_y$ ;  $Y'$  is the vertical angular distribution with characteristic rms angular divergence  $\sigma_{y'}$ . Z is the longitudinal distribution with characteristic rms bunch length  $\sigma_z$ . The sixth coordinate in the 6-parameter “phase space” is  $E/E$ .  $E/E$  represents the energy spread of the beam. The fifth and sixth coordinate ( $z$  and  $E/E$ ) determine the beam’s longitudinal emittance, which is given by the product of the bunch length and energy spread distributions. In this project, I am studying the longitudinal emittance of electron bunch distributions for 3 planned beamlines at SLAC.

The three beamlines that will be used to analyze the longitudinal emittance of electron bunch distribution are i) Linac Coherent Light Source (LCLS), with beam from a new rf gun at the 2/3 point of the SLAC Linac to the end of the Linac, ii) LCLS-ESA, with the beam in i) transported through the A-line to End Station A, and iii) International Linear Collider (ILC) test beam using the full existing SLAC Linac and Damping Rings with beam transported from the end of the Linac through the A-line to End Station A (ILC-ESA) (see Figure 1).

For the LCLS beam study, we track the beam in the last third of the linac; it has a beam energy of 14.1 GeV at the end of the Linac (see Figure 2). The LCLS project will use the 14.1 GeV electron beam and pass it through a new 100-meter wiggler section to be constructed to generate an intense short pulse x-ray laser. Short electron bunches enable short x-ray pulses.

For the ILC-ESA, we tracked the beam from the existing electron damping ring through the full linac and to ESA, with a final beam energy of 28.5 GeV. This test beam has similar bunch charges and bunch lengths as will be used in the proposed ILC project.

The LCLS-ESA beamline adds the A-line to the LCLS beamline, with a final beam energy of 14.1 GeV.. This last beamline simulation will be to study how an LCLS test beam could replace the ILC-ESA beam for ILC tests.

Short bunches and the bunch length distribution have important consequences for both the LCLS project at SLAC and the proposed ILC project. For both these projects, it is important to simulate what bunch length distributions are expected and then to perform actual measurements. Here I report on simulation studies. At ILC, intense short bunches generate wakefields. Wakefields arise from image charges generated in material (collimators, beampipes) close to the electron bunch [1]. The image charges generate electromagnetic wakefields that act back on the bunch, in particular on the tail of the bunch, increasing both the transverse and longitudinal beam emittance [2]. These wakefields can cause a change in the longitudinal energy distribution of a bunch. Wakefields generated by short bunches can also escape from the beampipe (from ports for cables or vacuum pumps for example) and generate electromagnetic interference to detector electronics (2). At LCLS, short bunches will be used to see real time chemical and biological reactions [3]. Chemical and biological reaction occur at sub-picosecond time scale; therefore, it is important to generate bunches which are equivalent to 300 m or 1 picoseconds. One example of an LCLS experiment is to use an x-ray laser, which will hit a target material and detectors will take pictures of the resulting diffraction pattern. Short bunches and precise timing at the femtosecond level will be used to take digital images [4]. Images from different beam pulses with femtosecond timing information will then be put together to show

how the reaction occurred in real time (3).

The tools to accomplish this task will be the Matlab and the Litrack programs. Litrack was specifically designed to study the electron beam's longitudinal emittance and how it evolves during beam transport through SLAC's linac [5]. Litrack program can adjust parameters (such as phase of the beam with respect to the accelerating rf in different sections of the Linac) of different beamlines to study the dependence of the bunch length distribution on these (2) LiTrack is run from Matlab, which is an analysis package using linear algebra and matrix manipulation for modeling and creating output files and plots (1).

## **MATERIALS AND METHODS**

For these simulations, we used the Matlab and the LiTrack programs to simulate the ILC-ESA beamline, LCLS beamline, LCLS-ESA beamline and there parameters.

To determine the sensitivity of the rms bunch length, we looked at the effects caused by changes in certain parameters. The first parameter changed was the phase degree of the acceleration phase, which determines where the electron bunch is located with respect to the peak of the rf voltage wavelength (Figure 3). The phases degree was adjusted for the acceleration phase of Sector 2 thru Sector 10 for the ILC-ESA beamline and Linac-A for the LCLS and LCLS-ESA beamlines. The next parameter to be varied was the phase degree of the acceleration phase of Sectors 10-30 for the ILC beamline and Linac-B for the LCLS and LCLS-ESA beamlines. The last parameter to be studied is the compressor voltage. The compressor voltage is the voltage that an electron bunch has when the bunch reaches the peak of the rf voltage (see Figure 3).

Table 1 show the basic command and code for the beamline. The first column displays

the specific action that will be carried on. These names are not included in beamline matrices. The second column shows the specific number code for the action. The other five columns describe distinct characteristics of the particular code at that given moment. The 10 and 11 code show how where the beam is located (last value in the row). This is significant for changing parameter in given sections.

Using the LiTrack program, we changed the acceleration phase for ILC-ESA beamline file in Sector 2 thru Sector 10 of the Linac from the default value of  $10^\circ$  to values  $+1^\circ$ ,  $+2^\circ$ , and  $+3^\circ$  of the default value. The default value was found by looking at Table 2 for a phase value in Sector 2. The change in phase degree value illustrates how the rms bunch length, FIT ( a Gaussian fit that compare the Zpos and current in the form of a bell curve), and peak current are affected. The data was collected form the figure which shows the result that would be produced in ESA. From the information gathered, we noticed the fit value had a negative slope. This information caused for the inquiry of the further information about the phase at it increase by increments greater than  $3^\circ$ . Information was gathered for the ILC-ESA until slope of the fit became positive. The information was then recorded; we continued collecting data for the ILC-ESA for Sector 10 thru Sector 30 of the Linac. In these sectors, we changed the default phase  $17.5^\circ$  to values  $+1^\circ$ ,  $+2^\circ$ , and  $+3^\circ$  of the default values. The default value was found by looking at Table # for a phase value in Sector 11. The results can be seen in figure 5 and 6.

We now look at the effects that the compressor voltage has on the FIT, rms bunch length and peak current in the ILC-ESA. The phase degree in the acceleration phase was left at  $10^\circ$  in Sector 2 thru 10 and at  $16.5^\circ$  degrees in Sectors 10 thru 30 of Linac. The compressor voltage was change from  $+1\text{MeV}$ ,  $+2\text{MeV}$ , and  $+3\text{MeV}$  of the default value, which is  $38.5\text{MeV}$ . The default value was found by looking at Table 2 for a phase value in Sector 2. The data was

collected from the figure, which displayed the results that are produced in ESA. The results are seen in Figure 11.

After testing the ILC, we now test the sensitivity of the LCLS. Using Table 3 we found the acceleration phase for Linac-A of LCLS. We then changed the phase degree of the LCLS  $+1^\circ$ ,  $+2^\circ$ , and  $+3^\circ$  of the default value of  $40.8^\circ$ . The results used are the ones that correspond with the end of the LCLS and can be seen in Figure 7. Next, we repeated the procedure for the LCLS, except changing the default value ( $13.58^\circ$ ) of Linac-B by  $+1^\circ$ ,  $+2^\circ$ , and  $+3^\circ$ . The default value was found in Table 3. The results used are the ones that correspond with the end of the LCLS and can be seen in Figure 8.

The last beamline tested was the LCLS-ESA. The LCLS-ESA test methods are similar to the LCLS beamline, but a few differences. The default values came from Table 4 and are  $10.8^\circ$  for the Linac-A and  $11^\circ$  for Linac-B. The results correspond to the results produced in ESA and found in Figures 9 and 10.

Next we look at the longitudinal position (Zpos) and the relative energy ( ) of the bunches generated from LiTrack. This part of the simulation involved some computer programming using C++ in Matlab. In order to complete the task we must first add a code 2 (code 2 is a code that dumps Zpos and relative energy into an ASCII file) to the beamline parameter file [5]. Once this is complete, run LiTrack and a new file called "litrack\_zd\_output.dat" is generated. The next step was to create a program called "Zpos&E" that would use the litrack\_zd\_output file to calculate the standard deviation (std), mean, a Zpos histogram, a histogram, and a plot showing Zpos versus . Once the program was completed, we began working on creating a program called "LiTrack-loop" that will repeat LiTrack a finite number of

times. The next step was to make a program called “G-Fit” that would create a Gaussian Fit for the zpos and place the Fit over a plot of the current vs. the Zpos. The final step was to add the 3 small programs created and make one program that will complete all these task.

## RESULTS

Figure 5 shows the rms bunch length and peak current for the ILC in Sectors 2-10. The peak current ( $I_{pk}$ ) increases until the phase degree reaches  $18.5^\circ$  at the point the peak reaches a high of 1.42 kA. The fit (fit rms) starts with a value of 0.468mm at  $8^\circ$  and continues to decrease until the phase degree reaches  $19.5^\circ$  at this particular point the fit is a value of 0.128mm. In Figure 4, we see that the phase degree has to decrease by  $5^\circ$  before the bunch length decrease by a little more than half. This rate continues until the bunch length reaches its relative minimum value. Once the relative minimum is achieved, the bunch length began increasing at the same rate.

Figure 6 shows the rms bunch length and peak current for the ILC in Sectors 10-30. The  $I_{pk}$  show an increasing current until the current reaches a value of 1.4403 kA. The current occurs when the phase is at  $19.5^\circ$ . The rms fit begins at  $15.5^\circ$  with a magnitude of 0.497mm. At  $19.5^\circ$ , the rms fit stops decreasing and reaches a relative minimum of 0.132mm. Figure 5 shows the phase degree Sectors 10 – 30, which decrease by half every two degrees. As with Sector 2- 10, this continues until it reaches the minimum. The  $I_{pk}$  for both sections is at a relative max around the same time the bunch length reaches their minimal values.

Figure 11 displays the results for the ILC when the compressor voltage is varied. The rms fit goes up and down from 1.933 mm to 0.212 mm, until 41.5 MeV. At 41.5 MeV, the rms fit shoots up to 22017 mm. The  $I_{pk}$  shows a curve similar to trig function with a maximum of 0.9615

kA at 38.5 kA. The minimum values occur at 35.5 MeV and 40.5 MeV with a corresponding voltage of 0.1762 kA and 0.1870 kA. Figure 10 shows the affects that a change in compressor voltage would have on the ILC. The figure shows a very unstable rms bunch length, which seems to increase and then decrease at a random length each change. The  $I_{pk}$  increase about 1kA every three degrees and then follow by decreasing at the same rate.

The LCLS, shown in Figure 7, starts with a rms bunch length of 40.821 m and an  $I_{pk}$  of 4.318 kA at a phase degree of  $38.8^\circ$ . The rms's relative minimum is 3.549 m, which occurs at  $41.8^\circ$ . At the same point, the  $I_{pk}$  reaches it relative maximum of 36.728 kA. The LCLS results for Linac-A show that the rms bunch length decreased to one-tenth of the bunch length at  $38.8^\circ$  in a three degree change (see Figure 7). The  $I_{pk}$  experience the same change in values except the change was an increase in kA. Figure 8 explains the results for Linac-B. In this figure, we see a change of 0.4 m in  $6^\circ$ . The peak current a change of -4 kA occur in the same duration.

Figure 9 shows the LCLS-ESA beamline for Linac-A. In this figure, the rms and rms fit seems to be a constant function set at 183 m and 0.018 mm. The  $I_{pk}$  oscillates between 3.3 kA and 3.5 kA during the different phases. In Figure 9 we see the results of the LCLS-ESA for Linac A. The figure shows that rms bunch length is not affected by a change in degree phase. The peak current shows similar result to the rms bunch length.

In Figure 10, the rms fit starts at mm and the  $I_{pk}$  starts at 2.142kA for the LCLS-ESA in Linac-B. The rms fit reaches a relative minimum of 0.018 mm when the phase is  $11^\circ$ . At  $11^\circ$ , the  $I_{pk}$  reaches a relative maximum of 3.506 kA. The rms bunch length in Linac-B shows the length decreasing to one-fourth of the value at  $9^\circ$  in two degrees (see Figure 10). Yet, the length increase at an even larger rate. The current continues the trend of acting opposite of the rms bunch length.

## DISCUSSION AND CONCLUSION

The results show the bunch length being affected most when the acceleration phase for Linac-A of the LCLS were changed. This was determined by looking at the ratio for the change in phase degree to rate of change in bunch length. The ratio for the LCLS in Linac-A was an astonishing 3:10. The LCLS-ESA in Linac-B was the next in sensitivity having a ratio of 2:4. The rest in order of sensitivity were the ILC in Sectors 10 – 30, ILC in Sectors 2 – 10, LCLS in Linac-B, and LCLS-ESA in Linac-A (see Table 5). The LCLS-ESA in Linac-A was the least sensitive having a ratio of 6:0<sup>+</sup>. The compressor voltage showed very rapid changes in bunch length; however, the rate of change was so sporadic that I was unable to clarify a clear rate of change. The peak current for the change in phase degree showed the same rate of changes as the bunch length. The peak current for the compressor voltage show a ratio of change equivalent to 3:5.

The results from Figure 5-10, show that peak current was inversely proportional to the fit rms value. This property suggests that the current might be able to detect when the bunch will have the lowest length. If this property holds true, then the absolute minimum in rms bunch length can be calculated by observing the peak current as the phase degree change. The highest peak current should be around the area of the lowest bunch length.

The LCLS beamline and LCLS-ESA beamline are identical lines, except for the LCLS-ESA continuing down to ESA and different compressor voltage. The compressor voltage for the LCLS and LCLS-ESA only varies in the Linac-A section. In this section, the voltage is 4.5 GeV in LCLS and 5.7 GeV in the LCLS-ESA. This gives a small explanation for the different results, but does not explain the result thoroughly because the changes caused by the ESA are not shown.

Suggesting further looks at the affects of the A-line and ESA

In this project, we have studied the sensitivity of bunch length distribution for three planned beamlines at SLAC to different acceleration phase and compressor voltage.

### **ACKNOWLEDGEMENT**

This research was conducted at the Stanford Linear Accelerator Center. I would like to thank the Department of Energy, Office of Science for allowing me to participate in the SULI program and giving me an exciting and knowledgeable experience. I would also like to Helen Quinn, James Lindesay, and the SULI participants for 2005, who got me involved in this program and gave me words of wisdom when they were needed. Special thanks go to my mentor Michael Woods, who share his knowledge in 2-D simulation, computer programming, and Linear Accelerators.

### **REFERENCES**

- [1] M. Woods, R. Erickson, J. Frisch, "A test facility for the ILC at SLAC ESA, for prototypes of beam Delivery and IR components," for Particle Accelerator Conference (PAC), Knoxville, TN, May, 2005
- [2] P. Emma, M. Woods, "Electron bunch length compression in the SLAC A-line," IPBI TN-2004-8, August, 2004
- [3] P. Krejcik, "Short bunch beam diagnostics," SLAC-PUB-9527, September, 2002
- [4] J. Galayda, H.R Woods, "Linac Coherent Light Source: New tools create new science," April, 2005
- [5] K.L.F. Banes, P. Emma, "*LiTrack*: A fast longitudinal phase space tracking code with graphical user interface," for PAC, Knoxville, TN, May, 2005

## TABLES

descrip.	code	$p_1$	$p_2$	$p_3$	$p_4$	$p_5$
mark	1					
dump	2					
compr.	6	$R_{56}$	$T_{566}$	$E_0$	$U_{5666}$	
chicane	7	$R_{56}$	$E_0$			
linac	10	$E_{final}$	$\phi$	$\lambda$	$i_{wake}$	$L$
linac	11	$V_0$	$\phi$	$\lambda$	$i_{wake}$	$L$
rw-wake	15	$\tau$	$L$	$\sigma_c$	$\tau$	1/0
ISR	22	$\sigma_\delta$				
$E$ -cuts	26	$\delta_{min}$	$\delta_{max}$			
$z$ -cuts	36	$z_{min}$	$z_{max}$			
STOP	99					

**Table 1.** List of function-codes and their parameters for LiTrack. All units are marked except energy, voltage, and phase, which are GeV, GV, and degrees, respectively;  $\pm \phi E=E_0$ . Blank parameter slots are not used by the code.

-11	0	0	0.104969	0	0
-11	0.385	90.0	0.104969	1	2.13
26	-0.021	0.021	0	0	0
-6	0.590	1.0535	1.190	0	0
-10*	9.000	-10.5	0.104969	1	809.5
-10^	28.500	-17.5	0.104969	1	1872.4
-6	0.465	2.744	28.500	0	0
-22	1.0E-4	0	0	0	0
-26	-0.005	0.005	5	0	0
2	0	0	0	0	0
-99	0	0	0	0	0

**Table 2.** Shows the beamline code use to simulate the ILC in LiTrack program. \* = Sector 2-10, ^= Sector 10-30

-11	0	0	0.104969	0	0.1
-11	0.12959	-1.1	0.104969	1	6.1
22	3.50E-4	0	0	0	0
-6	0.0063	0.140	0.135000	0	0
-11	0.14739	-20	0.104969	1	8.78
-11	0.0190	-160	0.026242	2	0.60
-7	-0.03905	.25	0	0	0
-11*	5.71031	40.8	0.104969	1	329.1
7	-0.0247	4.54	0	0	0
-22	0.80E-5	0	0	0	0
11^	9.9145	13.58	0.104969	1	552.9
11	0	0	0.105	5	76
11	0	0	0.105	6	275
6	0.000133	0.0063	14.1	0	0
-22	1.32E-5	0	0	0	0
27	0.020	1	0	0	0
-99	0	0	0	0	0

**Table 3.** Shows the beamline code use to simulate the LCLS in LiTrack program. \* = Linac-A, ^= Linac-B



Beamline	Minimum Bunch Length ( m )	Sensitivity Ratio (degrees : rate of change)
ILC Sectors 2-10	128	5:2
ILC Sectors 10-30	132	2:2
LCLS Linac-A	3.549	3:10
LCLS Linac-B	16.438	6: 0.9
LCLS-ESA Linac-A	15	6:0
LCLS-ESA Linac-B	18	2:4
ILC voltage	212	NA

**Table 5.** Show the sensitivity ratio for each beam line and the lowest bunch length produced by each beamline.

### FIGURES

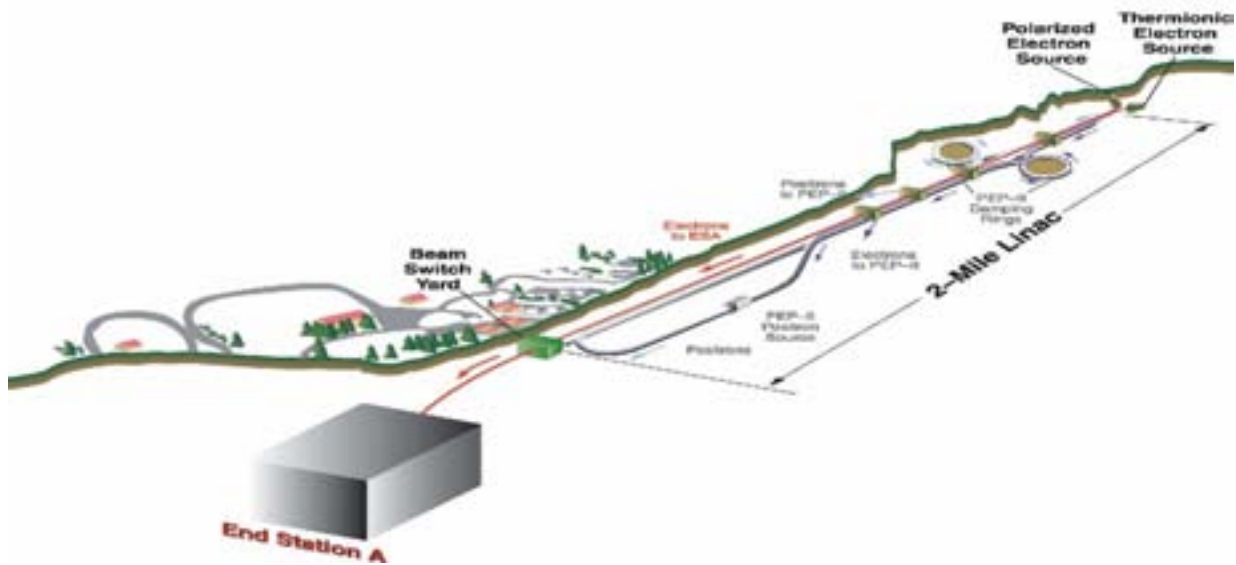


**Figure 1.** The Set up of the Linear Accelerator at SLAC.

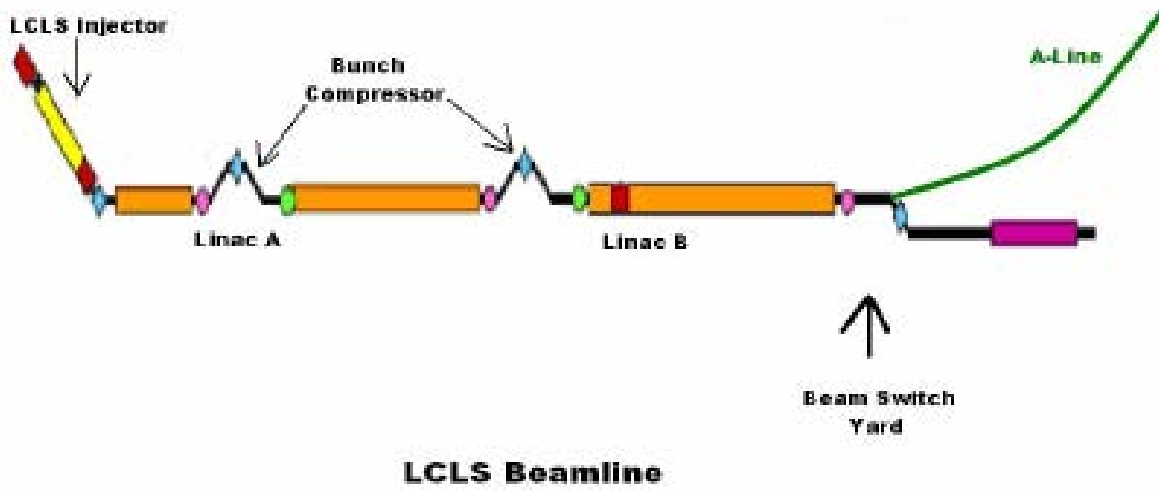


Figure 2.

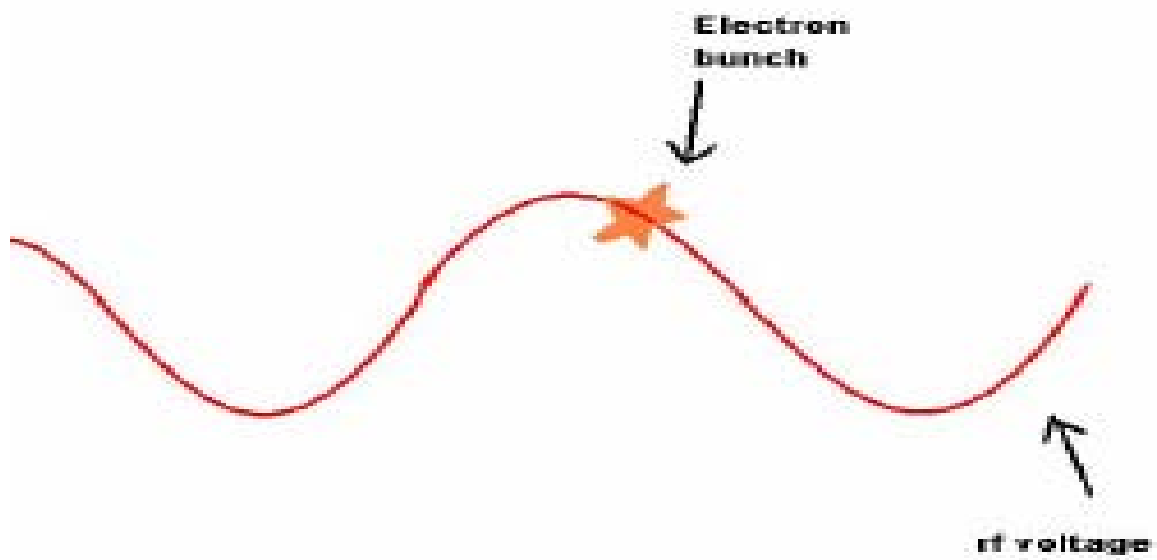
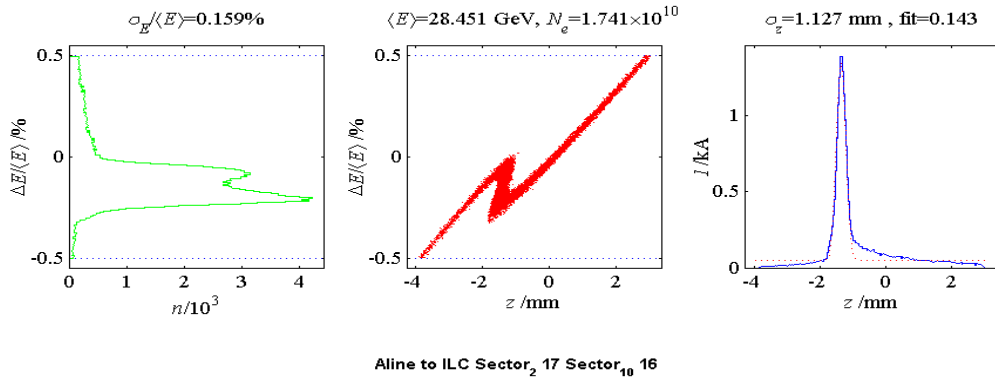
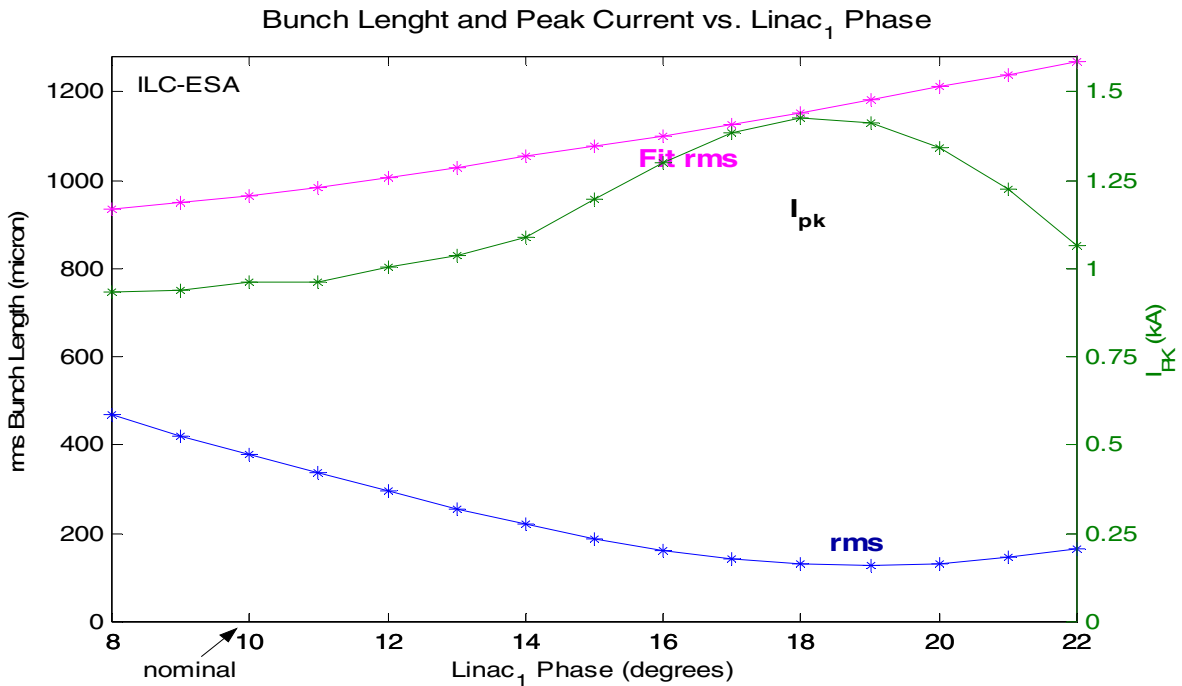


Figure 3.



**Figure 4.** Example of the results produced LiTrack program.. The left figure shows a histogram of  $E/E$ . The center figure shows a plot of  $E/E$  vs.  $Z_{pos}$ . The figure on the right shows a plot of  $Z_{pos}$  vs. current. The fit and rms fit are located above the figure on the far right.



**Figure 5.** Compares the rms bunch length, fit, and peak current as the phase changes Sector 2 thru 10 of the ILC-ESA. In Sectors 10 – 30 the phase is  $16.5^\circ$  and the compressor voltage is 38.5 MeV

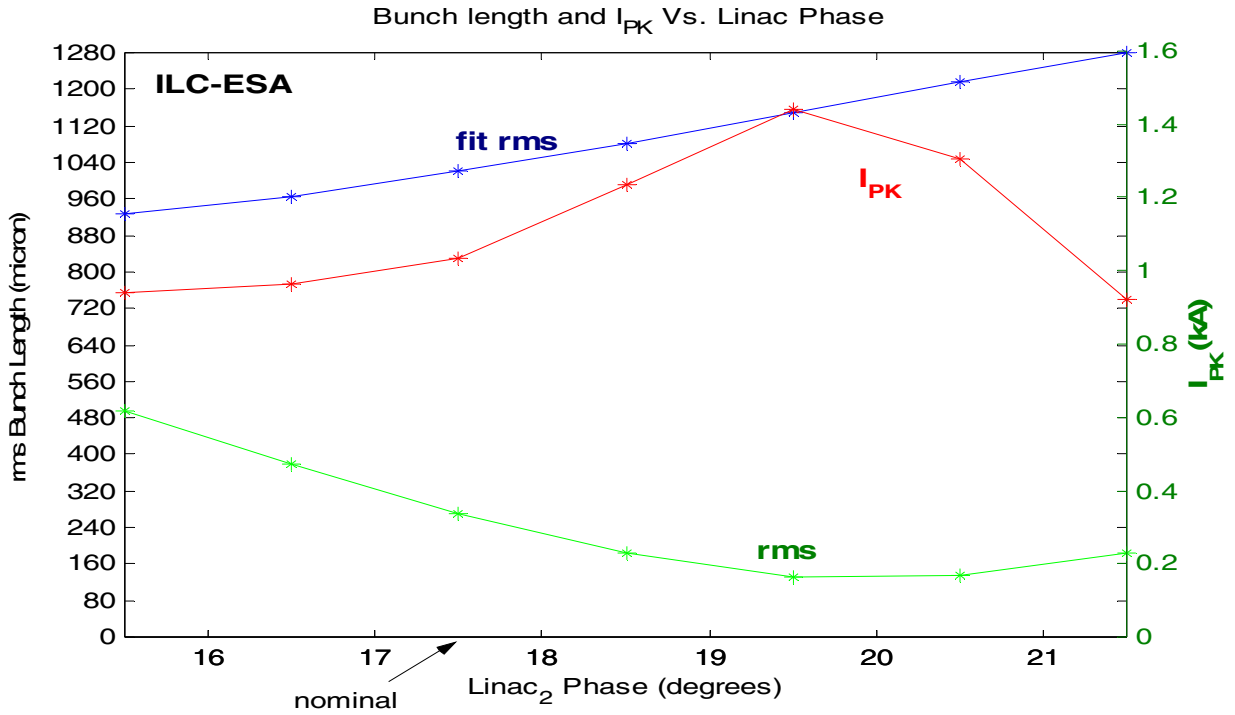


**Figure 6.** Compares the rms bunch length, fit, and peak current as the phase changes Sector 10 thru 30 of the ILC-ESA. . In Sectors 2 – 10 the phase is  $10^\circ$  and the compressor voltage is 38.5 MeV

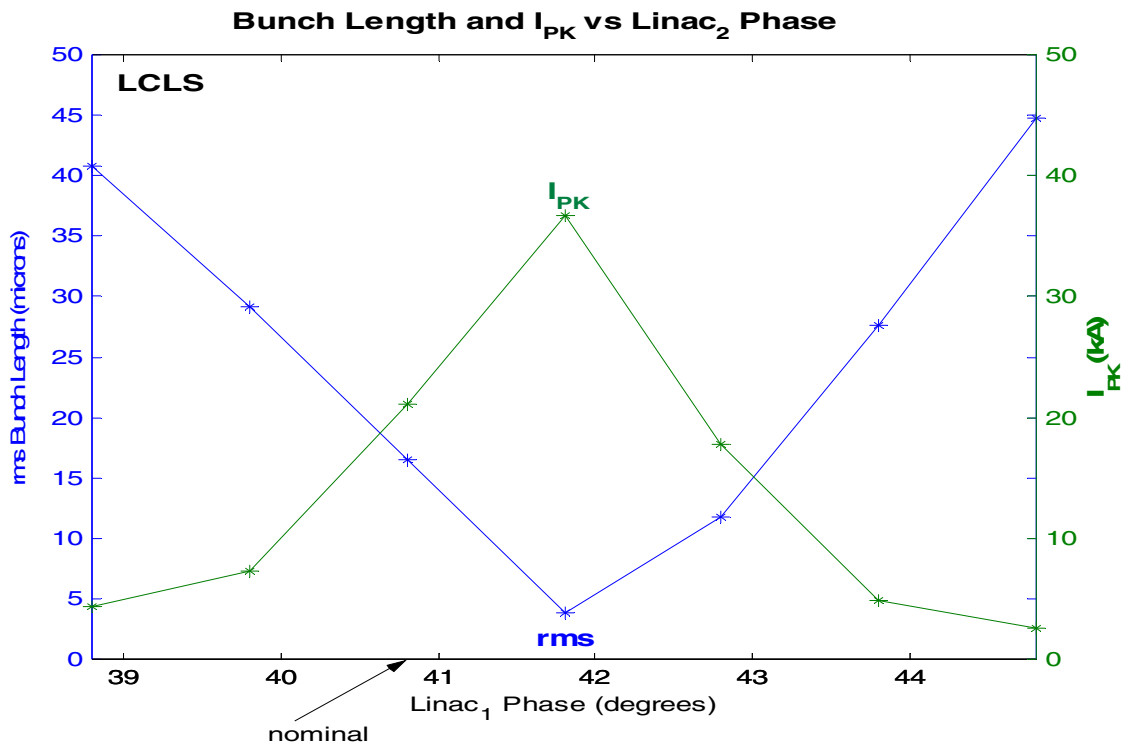


**Figure 7.** Compares the rms bunch length, fit, and peak current as the phase changes in Linac-A of the LCLS. In Linac-B the phase is  $13.58^\circ$  and the compressor voltage is 4.5 GeV

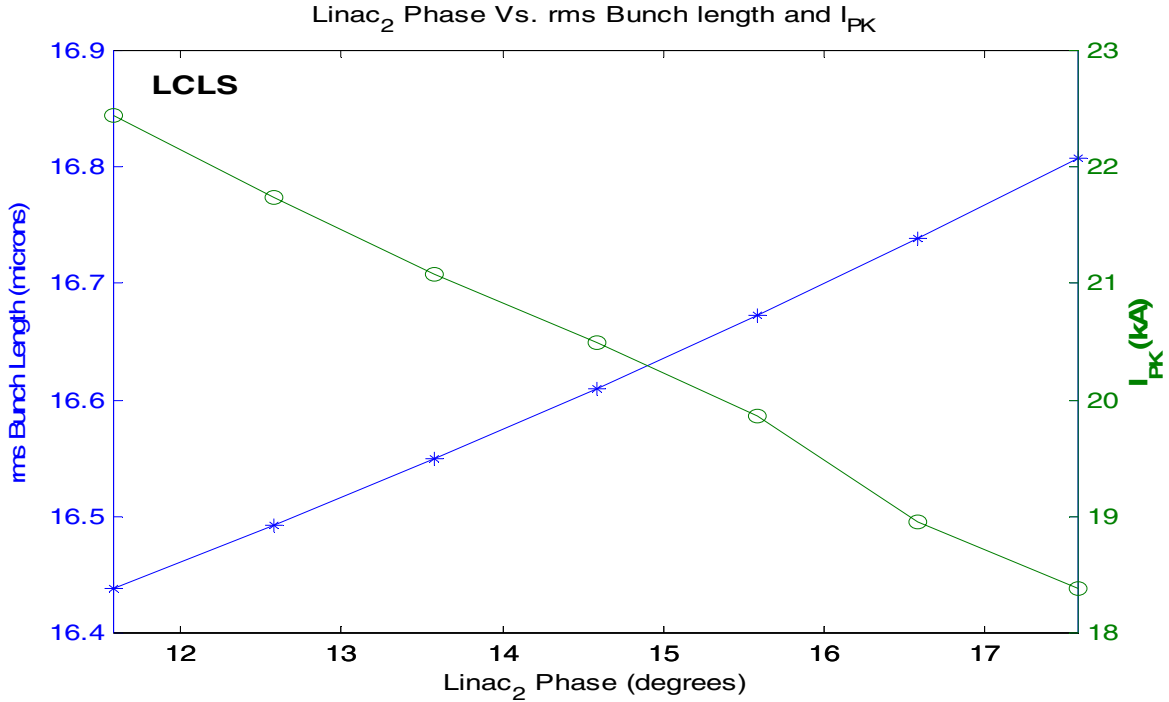


**Figure 8.** Compares the rms bunch length, fit, and peak current as the phase changes in Linac-B of the LCLS. . In Linac-A the phase is  $40.8^\circ$  and the compressor voltage is 9.5 GeV

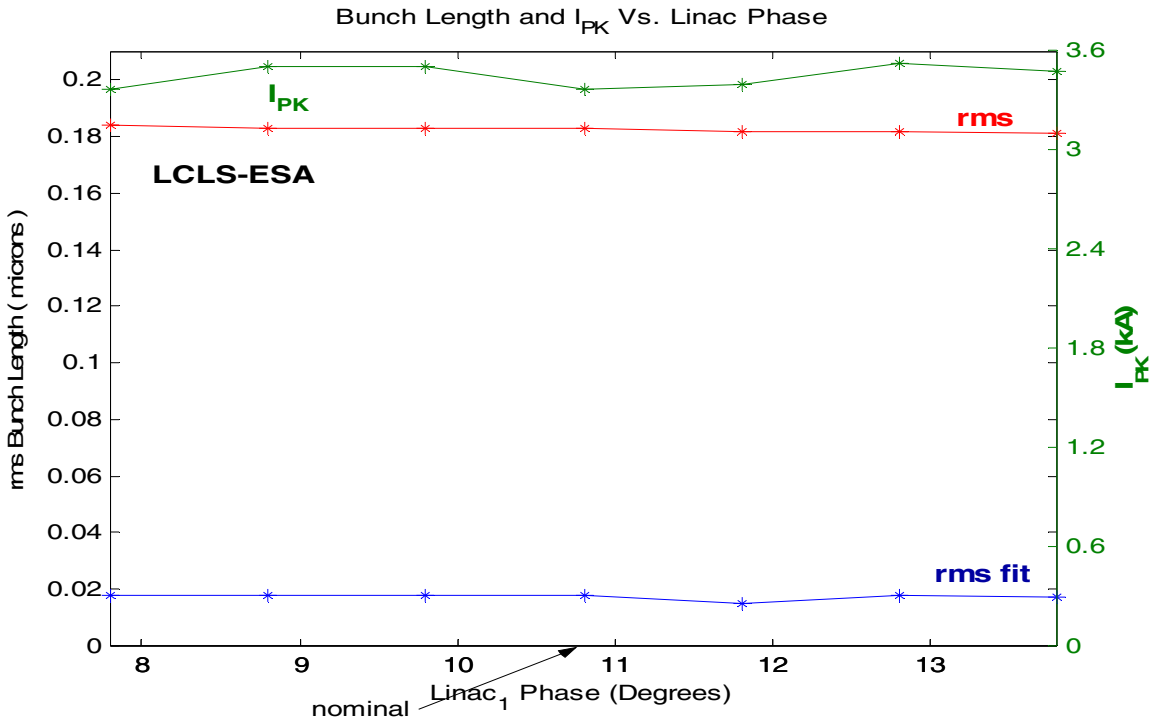


**Figure 9.** Compares the rms bunch length, fit, and peak current as the phase changes in Linac-A of the LCLS-ESA. In Linac-B the phase is  $10^\circ$  and the compressor voltage is 9.9 GeV

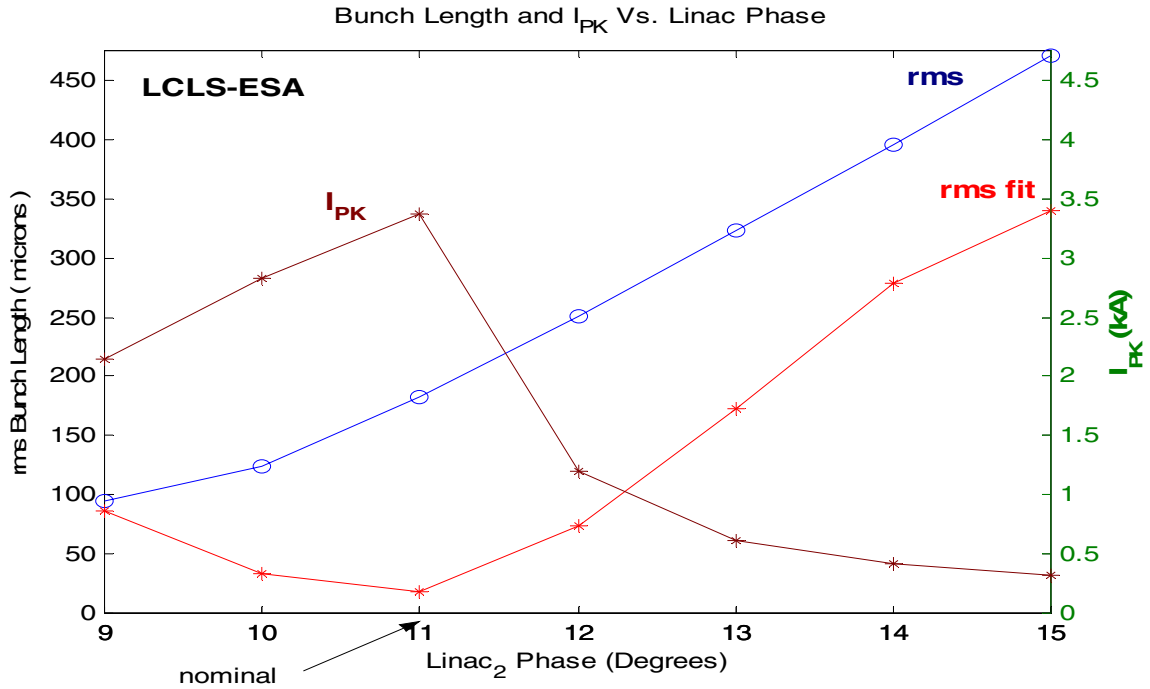


**Figure 10.** Compares the rms bunch length, fit, and peak current as the phase changes in Linac-B of the LCLS-ESA. . In Linac-A the phase is  $10.8^\circ$  and the compressor voltage is 14.1 GeV

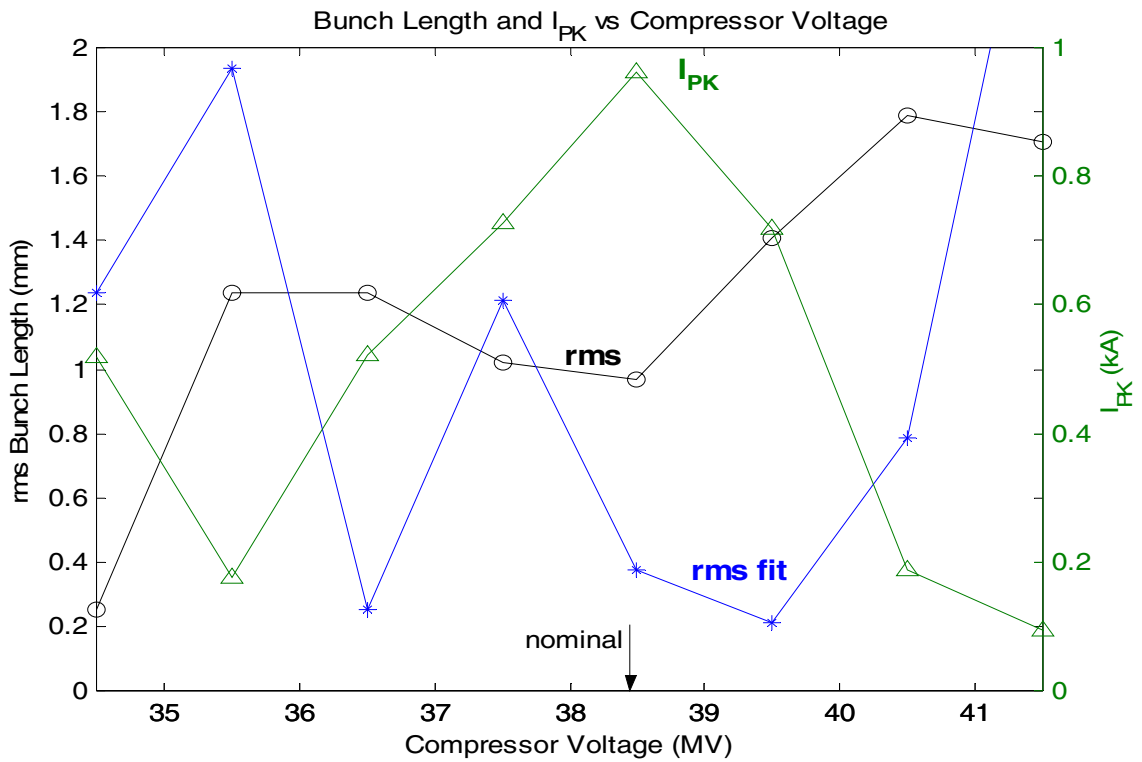


**Figure 11.** Compares the rms bunch length, fit, and peak current as the compressor voltage of the ILC-ESA changes. Sectors 2 -10 phase is  $10.8^\circ$  and Sectors 10 – 30 phase is  $16.5^\circ$ .

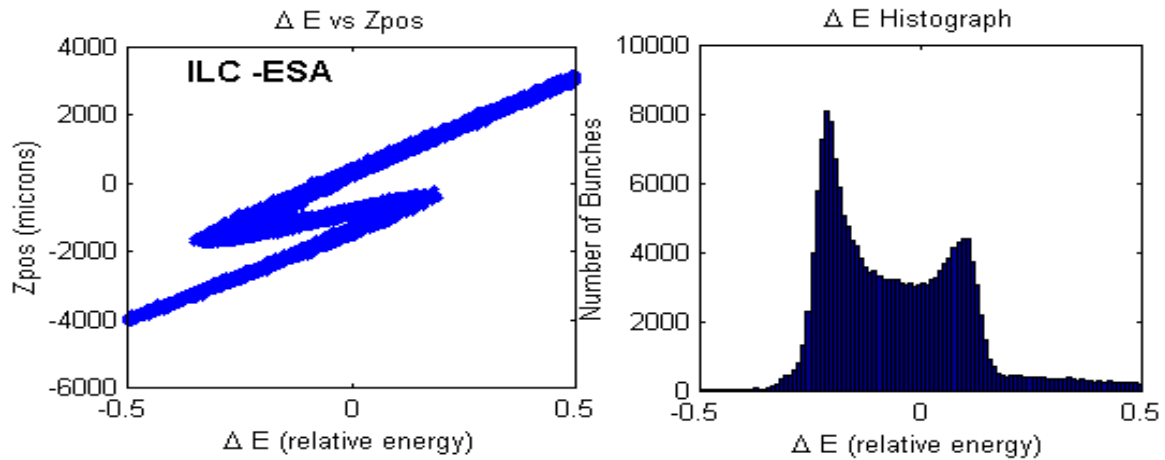


**Figure 12.** Example of histogram and plot generated from Program 1. The figure on the left show the relationship between the Zpos and relative energy. The figure on the right shows a histogram of the relative energy.

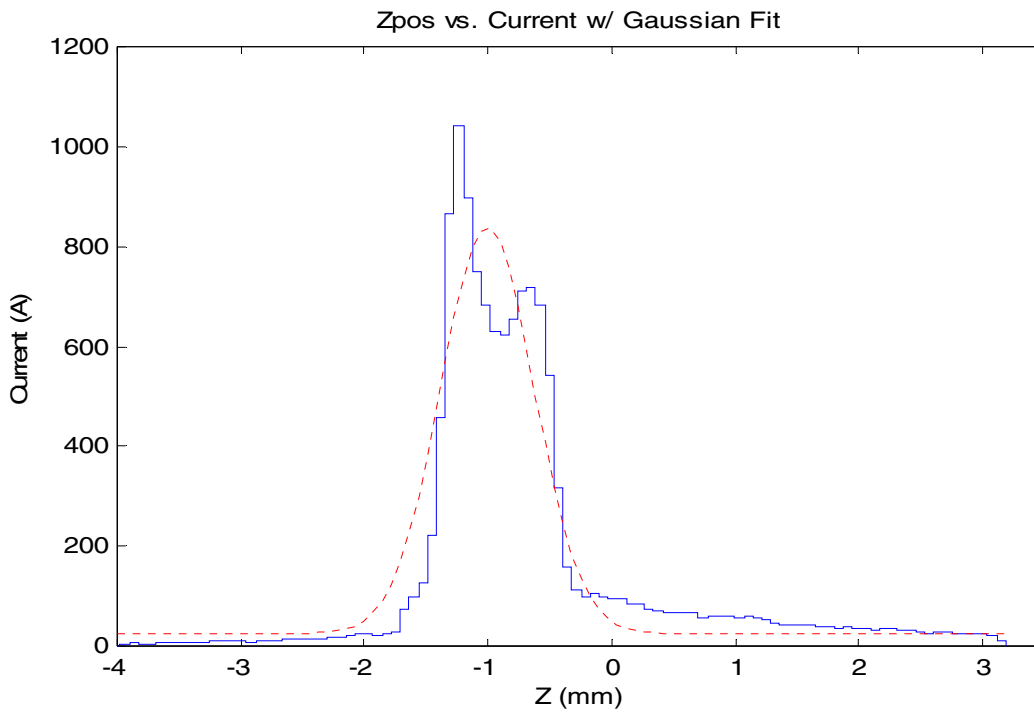


**Figure 13.** Example of plot generated from Program 3. The plot show the relation ship between the Zpos and Current. The red dotted line is a Gaussian fit for the relationship between the Zpos and Current



# Weak lensing PSF correction of wide-field CCD mosaic images

Marissa Cevallos

*California Institute of Technology*

Office of Science, SULI Program  
Stanford Linear Accelerator Center  
Menlo Park, California

August 20, 2005

Prepared in partial fulfillment of the requirements of the Office of Science, U.S. Department of Energy Science Undergraduate Laboratory Internship (SULI) Program under the direction of Dr. Phil Marshall, at the Kavli Institute for Particle Astrophysics and Cosmology (KIPAC) at the Stanford Linear Accelerator Center (SLAC).

Participant:

\_\_\_\_\_  
Signature

Research Advisor:

\_\_\_\_\_  
Signature

# Contents

<b>1</b>	<b>Introduction</b>	<b>4</b>
1.1	Gravitational lensing . . . . .	5
1.2	Characterizing the point spread function . . . . .	5
<b>2</b>	<b>Methods</b>	<b>6</b>
2.1	Extracting galactic and stellar objects . . . . .	6
2.1.1	Separating stars from galaxies . . . . .	6
2.2	Object shape estimation and PSF correction . . . . .	7
2.3	Efficient computing . . . . .	7
2.4	Correlation functions . . . . .	8
2.5	Mass maps . . . . .	9
<b>3</b>	<b>Results</b>	<b>9</b>
<b>4</b>	<b>Discussion and Conclusions</b>	<b>10</b>
<b>5</b>	<b>Acknowledgments</b>	<b>12</b>
<b>6</b>	<b>Figures</b>	<b>13</b>

# Weak lensing PSF correction of wide-field CCD mosaic images

Marissa Cevallos

*California Institute of Technology, Pasadena, CA 91125*

## Abstract

Gravitational lensing provides some of the most compelling evidence for the existence of dark matter. Dark matter on galaxy cluster scales can be mapped due to its weak gravitational lensing effect: a cluster mass distribution can be inferred from the net distortion of many thousands of faint background galaxies that it induces. Because atmospheric aberration and defects in the detector distort the apparent shape of celestial objects, it is of great importance to characterize accurately the point spread function (PSF) across an image. In this research, the PSF is studied in images from the Canada-France-Hawaii Telescope (CFHT), whose camera is divided into 12 CCD chips. Traditional weak lensing methodology involves averaging the PSF across the entire image: in this work we investigate the effects of measuring the PSF in each chip independently. This chip-by-chip analysis was found to reduce the strength of the correlation between star and galaxy shapes, and predicted more strongly the presence of known galaxy clusters in mass maps. These results suggest correcting the CFHT PSF on an individual chip basis significantly improves the accuracy of detecting weak lensing.

# 1 Introduction

Dark matter is predicted to compose as much as 90 percent of the Universe's baryonic matter, yet experimentalists have yet to detect the actual dark matter particle. Dark matter's presence is suggested in the analysis of the large-scale structure of the Universe, but was first postulated by Fritz Zwicky in the 1930s as non-luminous material to account for the extra gravitational pull in the Coma cluster of galaxies. When scientists in the 1960s began making galactic observations similar to Zwicky's, the concept of dark matter became a real cosmological area of interest, and alternate methods were sought to detect its elusive presence.

Weak gravitational lensing is one of these methods. In weak gravitational lensing, dark matter halos act as lenses to distort light from background sources. The lensing effect is similar to that of classical optics, but caused by the gravitational field of the dark matter—Figure 1 depicts an object that has been lensed by a massive source. Weak gravitational lensing attempts to use a net statistical lensing distortion over a field with large numbers of galaxies to predict the regions and amounts of dark matter. We assume that in a large sample of elliptical galaxies *without* gravitational lensing that the average shape of a galaxy would be a circle<sup>1</sup>. Therefore, any net ellipticity is a lensing effect of primarily dark matter (1).

Weak gravitational lensing has only recently stemmed from its precursor, strong gravitational lensing. Strong gravitational lensing occurs when a single massive object, such as a star or galaxy, bends light from a source to form another image. These curved images are known as *Einstein rings*, as they were predicted by Einstein's theory of general relativity. The first such lens was discovered in 1979 at Kitt Peak Observatory, though Fritz Zwicky confidently and correctly wrote forty years earlier that such a lens would not be difficult to detect (2). The important difference between weak and strong gravitational lensing is the absence of Einstein rings in weak methods. One cannot distinguish a single weakly lensed galaxy from a single unlensed galaxy—it is only by understanding the correlation between thousands of galaxy shapes that one can observe a weak lensing signal.

Recent observational progress in weak lensing has been rapid, with good use being made of the large format CCD mosaic cameras now installed at many telescopes: these permit the observation of a good fraction of a square degree of sky in a single exposure, and so are well-suited to weak lensing observations requiring the measurement of many thousands of background galaxy shapes.

---

<sup>1</sup> In three dimensions, a sphere, but our images are two-dimensional.

In particular, a wide field of view is required to match the outer radii of nearby clusters, for which good data exist in other wavebands but have been lacking a lensing mass determination (1).

## 1.1 Gravitational lensing

Ellipticity is a critical property of the weakly lensed galaxies that we seek to measure. The ellipticity of an object due to gravitational influence can be derived from a few equations. Assuming an ellipse with a semi-major axis  $a$ , semi-minor axis  $b$ , and orientation angle  $\phi$ , the ellipticity  $\epsilon$  of an object is given by

$$\epsilon = \frac{a - b}{a + b} e^{2i\phi}. \quad (1)$$

This ellipticity is what we measure for each galaxy. For a large number of galaxies, we can estimate the ensemble average ellipticity,  $g$ , or reduced shear:

$$\langle \epsilon \rangle = g. \quad (2)$$

The reduced shear is proportional to the shear  $\gamma$  and convergence  $\kappa$  by

$$g = \frac{\gamma}{1 - \kappa}, \quad (3)$$

where  $\gamma$  and  $\kappa$  are linear combinations of second derivatives of the projected, scaled gravitational potential:  $\kappa$  is in fact proportional to the projected total mass density. Equations (1), (2), and (3) provide the link between measurable ellipticities and projected mass distribution.

## 1.2 Characterizing the point spread function

As weak lensing is an intrinsically weak effect, slight error might distort what we interpret as gravitational lensing—these problems hail mostly from the detector and atmospheric distortion. A space-based telescope, such as the Hubble Space Telescope, can ignore the problems associated with atmospheric distortion, but the images we consider in this research come from the ground-based Canada-France-Hawaii Telescope (CFHT). Therefore, it is necessary to characterize the point-spread-function (PSF) in order to describe the unwanted distortion and eliminate it from the fields of interest. The PSF is convolved with the true, undistorted image to produce the image that is actually seen by the detector. Because we know nothing of the intrinsic ellipticities of the galaxies we study, we must calibrate the galaxy field using a PSF derived from images of stars (which are intrinsically point-like).

The images we consider in this research come from the Canada-France-Hawaii Telescope (CFHT) in Hawaii. The CFHT uses the CFH12K camera (3), a CCD mosaic camera with 12 chips arranged in two rows of six as seen in Figure 1. Though there is no reason to suspect that atmospheric distortion will be more prevalent in one chip over another, the flaws in individual pixels may present errors unique to each chip. Moreover, slight deviations from planarity across the mosaic could introduce systematic ellipticity in the PSF—the CFH12K camera has a tilt height of about 20 microns. However, when performing weak lensing analysis, one typically corrects the PSF averaged over the entire image. This research aims to characterise the PSF in each chip, as we suspect the concatenation of the 12 PSF corrections will be different from the PSF of the entire image.

## 2 Methods

### 2.1 Extracting galactic and stellar objects

In order to create a comprehensive catalog of objects in a given field, it is necessary to extract objects through an automated method. `Source Extractor`, or `SExtractor`, is a program that estimates shapes rather poorly, but accurately and rapidly locates the centers of all objects in an image – it is the  $(x, y)$  coordinates we are interested in determining from `SExtractor`. `SExtractor` creates a catalog with not only the position of each object, but the Full Width at Half Maximum (FWHM) of the object’s brightness profile. This is useful information—we will use it to differentiate between stars and galaxies.

#### 2.1.1 Separating stars from galaxies

The question of how to separate stars from galaxies in an object catalog is a pertinent one. Because the PSF of the stars will be used to calibrate the PSF of the galaxies, it is important that one maintains two catalogs for stars and galaxies. Unfortunately, with limited resolution from the detector, it is often unclear whether a high magnitude object is a star or a galaxy, since there is no definitive algorithm for such a classification. However, it is known that stars must appear point-like, such that stars at varying magnitudes will have about the same full width at half maximum (FWHM), while the FWHM of a galaxy will vary along with its magnitude. By plotting magnitude against FWHM, regions of objects with similar FWHM values can be selected from the graph and placed in a star catalog.

In Figure 3, magnitude and FWHM are compared for a given catalog containing both stars and galaxies. Though stars may be present throughout the plot, it is a safer bet to assume that all of the objects in the vertical band—the stellar locus—between about  $x = 4$  and  $x = 5$  are stars which reached the CCD’s saturation point. Under close inspection, one notices that Figure 3 has a double stellar locus, or two vertical bands. After closer inspection<sup>2</sup>, it appeared that both bands contained stellar objects, so the chosen star catalog was composed of objects from both bands.

It is trickier to extract galaxies. Not all of the “leftover” objects in Figure 3 are galaxies—the lower left corner between  $x = 0$  and  $x = 4$  is most likely full of very faint stars, galaxies, and noise peaks, which are undesirable in weak lensing. Galaxies were chosen by constructing a rectangular region to the right of the stellar locus, but above very high magnitudes (note that the vertical axis in Figure 3 is reversed, running up from high magnitude to low magnitude). It is almost inevitable that one will include stars in the galaxy catalog and likewise mask potential galaxies by labelling them as stars. This small error is expected and does not significantly change the result of the weak lensing data.

## 2.2 Object shape estimation and PSF correction

Objects detected with SExtractor were re-measured using the tools in the imcat package (4), yielding accurate ellipticities for both stars and galaxies. The PSF patterns were characterized by applying a polynomial fit of degree  $n$  to give a smoothly interpolated stellar ellipticity pattern – in this research, we take  $n = 5$ . The Perl script `psfcorrect` performs this polynomial fit, and then uses the model stellar ellipticity field to correct the catalog of galactic objects, using the scheme derived by (5). The corrected galaxy ellipticities are then taken to be estimates of the local weak lensing shear.

## 2.3 Efficient computing

Analyzing an image for weak lensing involves both manual and automated methods—the researcher inevitably has to mask images by hand to eliminate spurious objects, but after selecting stars and galaxies, the process of creating a mass map involves no manual decisions. Thus, creating an algorithm to automate the process in between is a time-saving task that minimizes the chance that the researcher introduces more error. In addition, because we are not only interested

---

<sup>2</sup> We select objects in one band and replot them over the original image to see whether they correspond to stellar objects; we repeat for the other locus.

in the PSF correction across the total image, but the correction in all 12 chips, analyzing each chip individually is a tedious process. For the purposes of this research, several Perl scripts were written to run pre-existing code. Most involved reading in a directory of catalogs, and then iteratively running the appropriate process for each catalog.

Code now exists to divide a catalog into separate catalogs according to chip, run `psfcorrect` on these individual catalogs, and concatenate the catalogs into one catalog (of the same size as the original). After running the scripts, the only difference between the resulting catalog and one run through `psfcorrect` normally is when the objects underwent PSF correction chip-by-chip or with the entire catalog.

## 2.4 Correlation functions

A correlation function relates how closely two quantities are correlated. If the PSF alters the apparent ellipticity of a star, then every nearby object should be more or less affected in the same way. This is a correlation we can measure and attempt to reduce by correcting the galaxy images for the PSF.

The ellipticity vectors of two objects can be compared by taking the dot product between them. For two ellipticity vectors  $\epsilon^a$  and  $\epsilon^b$  with components  $\epsilon_1$  and  $\epsilon_2$ , the dot product is given by

$$\epsilon^* = \epsilon^a \cdot \epsilon^b = |\epsilon_1^a \epsilon_1^b + \epsilon_2^a \epsilon_2^b|.$$

We take the magnitude because we do not care about the direction of the vectors: if  $\epsilon^*$  is 1 or -1, then the vectors are parallel. However, the ellipticity values found by `psfcorrect.pl` are not strictly vectors, so we have to use a more sophisticated product that is dependent on the position angle  $\phi$  between the two objects.

Incorporating the angle between ellipticity “vectors”, we have

$$\gamma\gamma_+ = (\epsilon_1^A \cos 2\phi + \epsilon_2^A \sin 2\phi) \times (\epsilon_1^B \cos 2\phi + \epsilon_2^B \sin 2\phi) \quad (4)$$

$$\gamma\gamma_x = (\epsilon_1^A \sin 2\phi - \epsilon_2^A \cos 2\phi) \times (\epsilon_1^B \sin 2\phi - \epsilon_2^B \cos 2\phi) \quad (5)$$

in which  $\gamma\gamma_+$  represents the “E-mode” and  $\gamma\gamma_x$  is the “B-mode” correlation. In weak lensing with exactly calculated PSF corrections, the correlation function given by the B-mode should be zero, while the E-mode should be some non-zero (positive) number. If the two quantities compared are stars against stars, then the E-mode and B-mode correlation strengths should be ap-

proximately equal, assuming there is no reason for stars to be aligned in one formation more than the other.

The star-galaxy correlation function will show a similar, although much noisier) shape, since the galaxies (before PSF correction) have ellipticities partially due to the PSF. After a perfect PSF correction, the star-galaxy correlation function should fall to zero, as there is no other physical connection between the apparent shapes of the stars and galaxies. If there *is* a correlation between the two, then this indicates that the applied PSF correction was not accurate enough.

A Perl script was written to read in two catalogs and computes both their E-mode and B-mode correlation functions, comparing the ellipticity between every pair of objects using Equations (4) and (5) and binning the pairs as a function of the distance by which the pair is separated.

For a pair of galaxy catalogs with thousands of objects, the required run-time (which scales as  $O(n^2)$ ) presented a difficulty; an option was introduced to eliminate duplication of comparisons, lowering the run time when using two identical catalogs by a factor of two. However, in investigating the correlation between stars and galaxies, the star catalog generally contains an order of magnitude less objects, so the runtime is reasonable.

## 2.5 Mass maps

Though it is straightforward to predict galaxy ellipticities from a mass distribution, performing the inverse operation is non-trivial. We must first crudely estimate mass from ellipticities, and then iteratively refine the mass map to improve the match between predicted and observed ellipticities. One such code to do this is LensEnt2 (6). More specifically, LensEnt2 infers  $\kappa$  from solving the system of equations (Equations (1), (2), and (3)), but because of the presence of noise, the solution must be found iteratively.

In order to compare the chip-by-chip analysis to the standard method of weak lensing, we may use mass maps as a test. This requires running both catalogs through LensEnt2 and compare the resulting mass maps. If one method clearly predicts known mass clusters more than the other, then it may be the more useful method.

## 3 Results

In order to compare the PSF pattern of the entire detector to that of the individual chips, three approaches were used: plotting ellipticity components, analyzing the correlation function between

catalogs of stars and galaxies, and testing the level of observed signal (believable and spurious) in the resulting mass maps. A wide-field image of Abell 399 was used for the tests.

Figure 4 presents four plots of ellipticity against position, with the magnitude and angle of the ellipticity represented by sticks centered on the object positions. The left-most plots show stellar ellipticities before PSF correction, and the right-most plots shows ellipticities after PSF correction. The top-right plot has chip-by-chip PSF correction, while the bottom-right plot has the traditional whole-image PSF correction.

In Figure 5, a statistical argument is unnecessary to convince the reader that the correlation functions resulting from the chip-by-chip method are less noisy than the original method. All four graphs are correlation functions between the same stars and galaxies. The top two plots used catalogs that had corrected for the PSF on a chip-by-chip basis; the bottom two plots used catalogs with traditional PSF corrections. The plots to the left are of E-mode correlation, and the ones to the right are of B-mode correlation: both show a significant improvement when moving to the chip-by-chip correction scheme.

LensEnt2 generates a reconstructed projected mass map at a user-defined angular resolution: typically the data quality favours a low resolution map, but the higher resolution maps provide useful diagnostics when trouble-shooting. Figure 6 shows mass maps derived from chip-by-chip catalogs and traditional catalogs. The top two maps are at a higher angular resolution (3 arcmin FWHM) than the bottom two (9 arcmin FWHM). The left-most plots are from chip-by-chip corrected catalog, while the right-most maps are from the traditionally-corrected catalog. The red outline is tilted by about 5 degrees to compensate for the tilt in the original image. The center of the mass maps is the position of the brightest cluster galaxy.

## 4 Discussion and Conclusions

In two of the three tests—correlation functions and mass maps—the PSF correction appears to have been significantly improved by splitting the image by chip. It is especially evident in Figure 5 that the chip-by-chip plots are less noisy than the other two. In fact, it even appears that the bottom two plots still contain some smooth, large-scale PSF variation, which is exactly what the PSF correction tries to eliminate. Because such a pattern is not present in the chip-by-chip plots, one can conclude that the PSF correction in these plots is better.

It is not obvious whether the ellipticity plots show improvement because of the presence of

high-ellipticity objects that were not filtered out during an earlier stage of the analysis. The results are reasonable, however—the left-most plots are identical (they both represent the uncorrected ellipticities), while the plots on the right are difficult to distinguish between and would require further study in order to reach solid conclusions about the effectiveness of splitting catalogs by CCD chips.

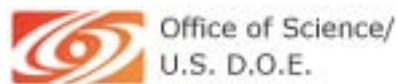
While a quick glance at the correlation functions can show that one is clearly better, it is not so intuitive to understand the mass maps. Because the mass maps are supposed to show where regions of dark matter are located, and we cannot see dark matter, it seems to be difficult to gauge whether a mass mapping was successful. However, we can look at where we know there are high-density regions of mass (for example, the central galaxy cluster) and compare how strongly the mass map predicts its presence. The left-most maps, from chip-by-chip catalogs, more strongly predict a single mass in the center than the other maps—the right-most maps predict a single mass in the center, but with fewer contour lines (bottom right of Figure 6) or as two masses in the center (top right of Figure 6). It would be too great a coincidence to have the PSF correction of 12 different chips conspire to give a residual PSF pattern that mimicked and increased weak lensing signal at the center of the map!

We must then ask why these differences arise: the 20 microns in tilt height is perhaps a factor, as is the make-up of individual chips. If a better PSF correction is obtained simply by regionalizing the image, but not necessarily by chips, then one could entertain the possibility of splitting the chips into even smaller regions. However, this leaves each region with fewer objects with which to do a PSF correction. The problem then becomes one of optimization—at what point (ie, how many galaxies, or at what fraction of the sky) does it become disadvantageous to split the image into smaller regions? This could be explored in future work.

It may be the case that a higher order polynomial fit ought to be used. Future work should test the outcomes of PSF corrections with  $n$  degree fits other than  $n = 5$ . It is not always advantageous to use very high order polynomials: we are seeking a smooth characterization of the PSF, not one that fluctuates with the stellar shape estimation noise. However, it may be that the tests devised here would show further improvement in the PSF correction if the polynomial order were to be varied. The analysis pipeline put in place in the course of this work will allow this, and other subtle effects, to be rigorously investigated.

## 5 Acknowledgments

I would like to thank the Department of Energy Office of Science for the funding to participate in the SULI program – it is a wonderful program and great learning experience. I would like to thank my mentors Phil Marshall and Maruša Bradač and for their time, patience, and good advice. In addition, I would like to thank Helen Quinn and James Lindesay for their tireless efforts in running the SULI program, and the Stanford Linear Accelerator Center for hosting me. This work was supported in part by the U.S. Department of Energy under contract number DE-AC02-76SF00515.



## References

- [1] Philip Marshall. *Bayesian Analysis of Clusters of Galaxies*. PhD thesis, Cavendish Astrophysics and King's College, Cambridge, September 2003.
- [2] Peter Schneider. Introduction to gravitational lensing and cosmology. In *Gravitational Lensing: Strong, Weak and Micro*. Springer-Verlag: Berlin, 2003.
- [3] Jean-Charles Cuillandre. Cfh12k: a 12,288 by 8,192 pixel ccd mosaic camera for high resolution wide field imaging.
- [4] Nick Kaiser. Available as <http://www.ifa.hawaii.edu/~kaiser/imcat/>.
- [5] N. Kaiser, G. Squires, and T. Broadhurst. A method for weak lensing observations. *The Astrophysical Journal*, pages 460–475, August 1995.
- [6] Phil Marshall. Lenseint version 2. Available as <http://www.mrao.cam.ac.uk/projects/lenseint/version2/>.

## 6 Figures

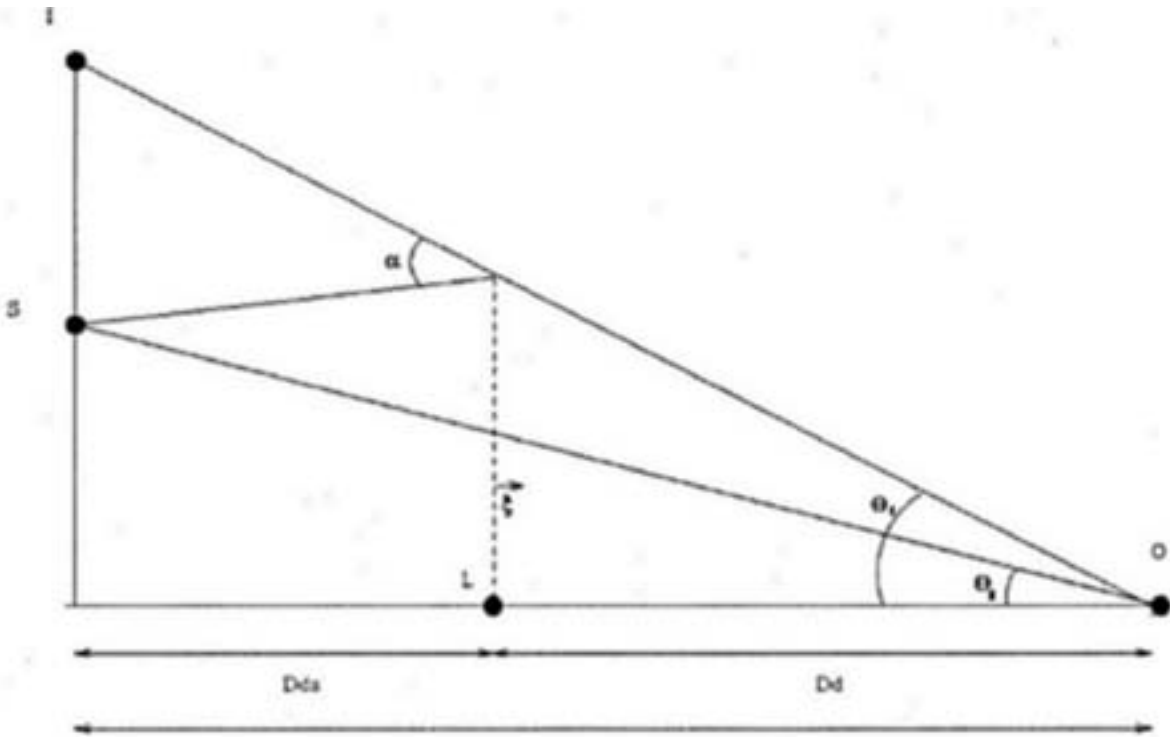


Figure 1: Gravitational lens geometry.  $D_s$  is distance between observer and source;  $D_d$  is the distance between observer and lens, and  $D_{ds}$  is the distance between the source and lens. In the absence of the lens, the angle between the observer and source is  $\theta_S$ ; with the lens, the image appears at an angle of  $\theta_I$ .

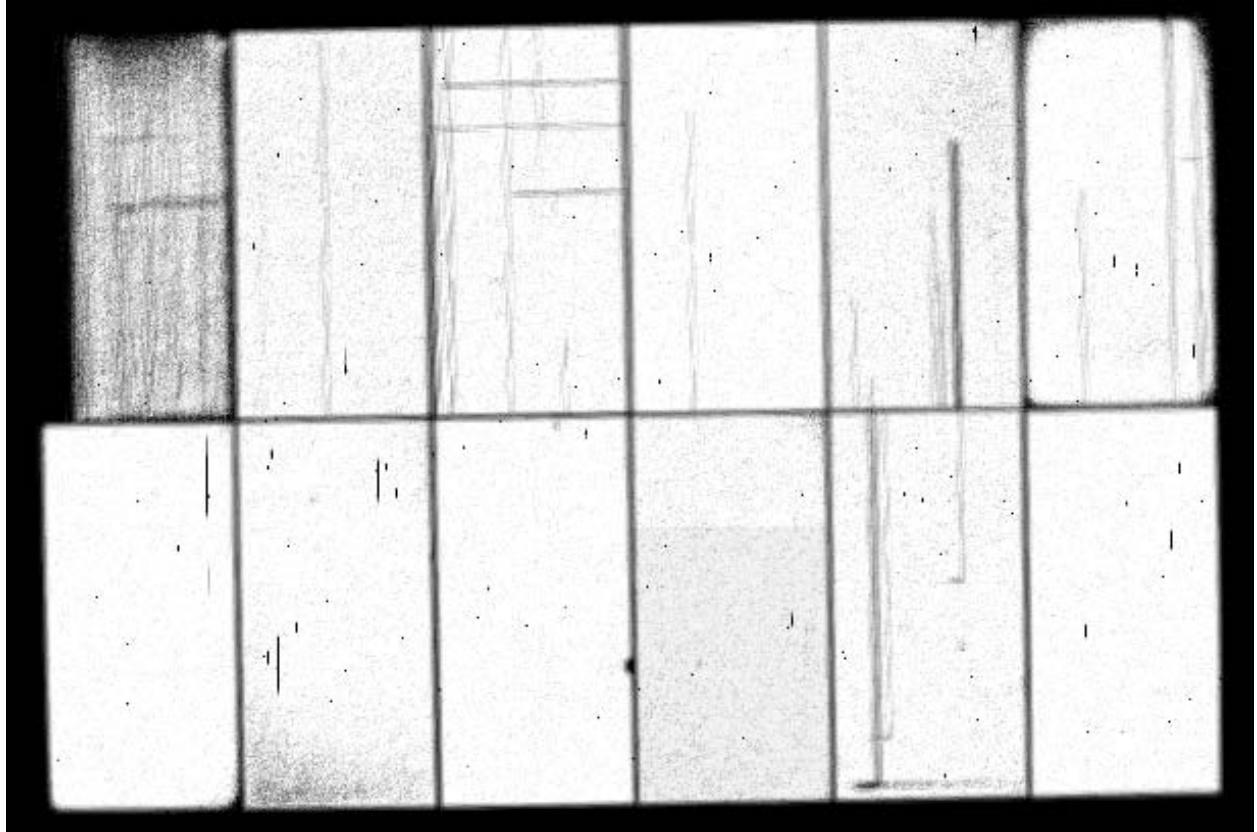


Figure 2: Weight image of A399. The gaps between chips are clearly visible as under-exposed regions.

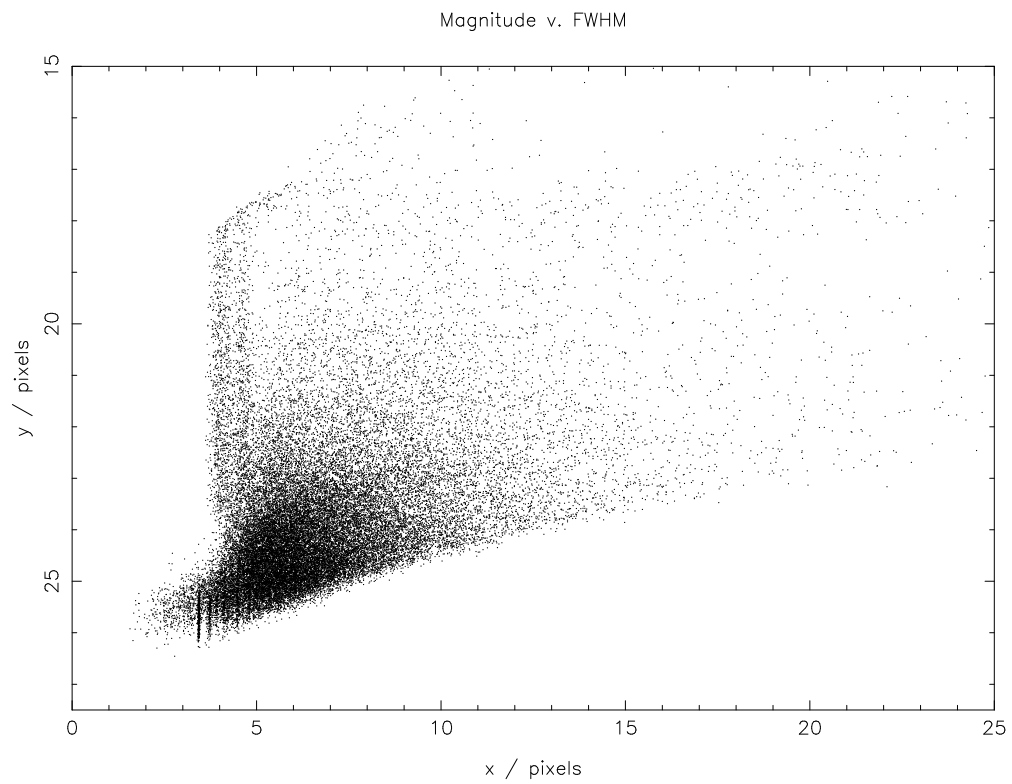


Figure 3: Object magnitude vs. FWHM. Stars are selected from the vertical band between about  $x = 4$  and  $x = 5$ .

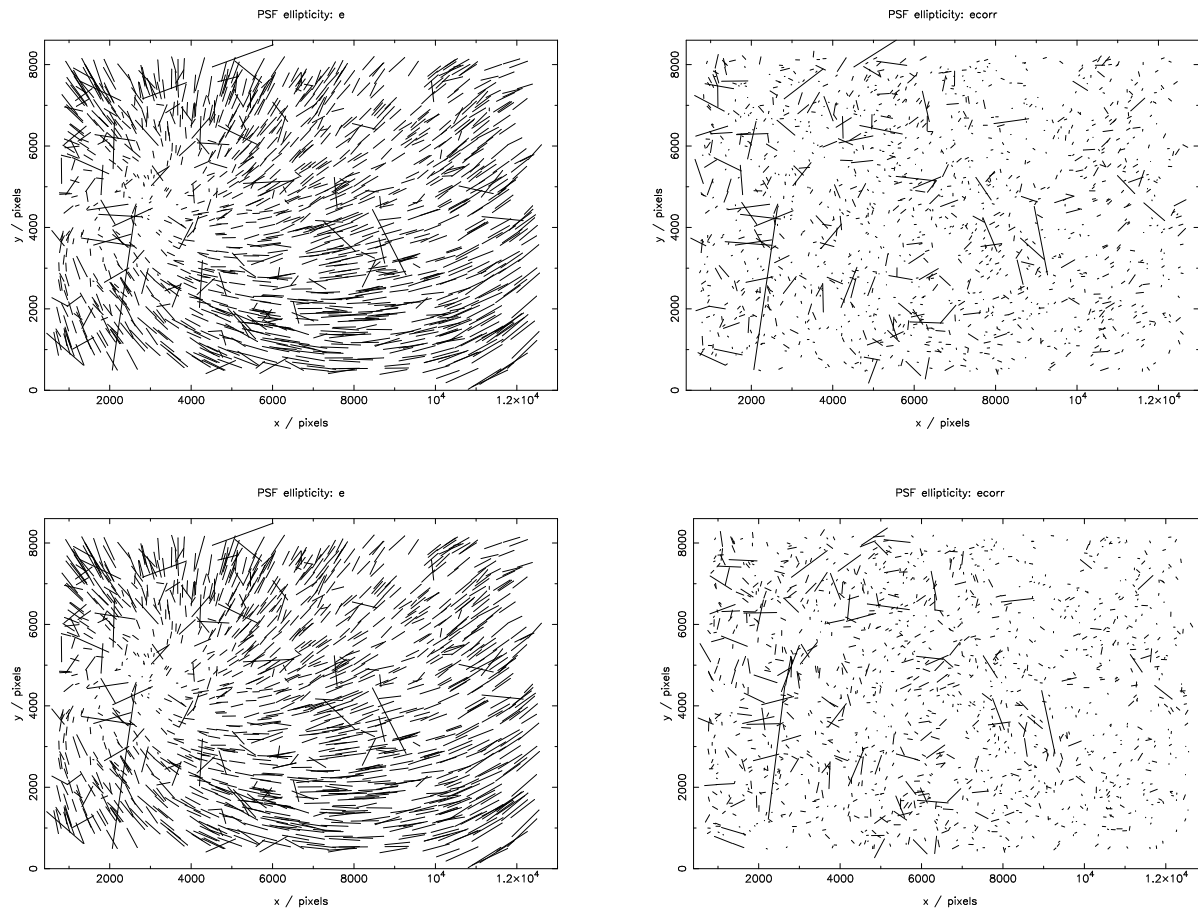


Figure 4: Stellar ellipticity vs. position. Left-hand plots show raw ellipticity plotted as vectors; the plots on the right show the same stars after ellipticity correction. Top row: traditional whole-image correction; bottom row: chip-by-chip analysis.

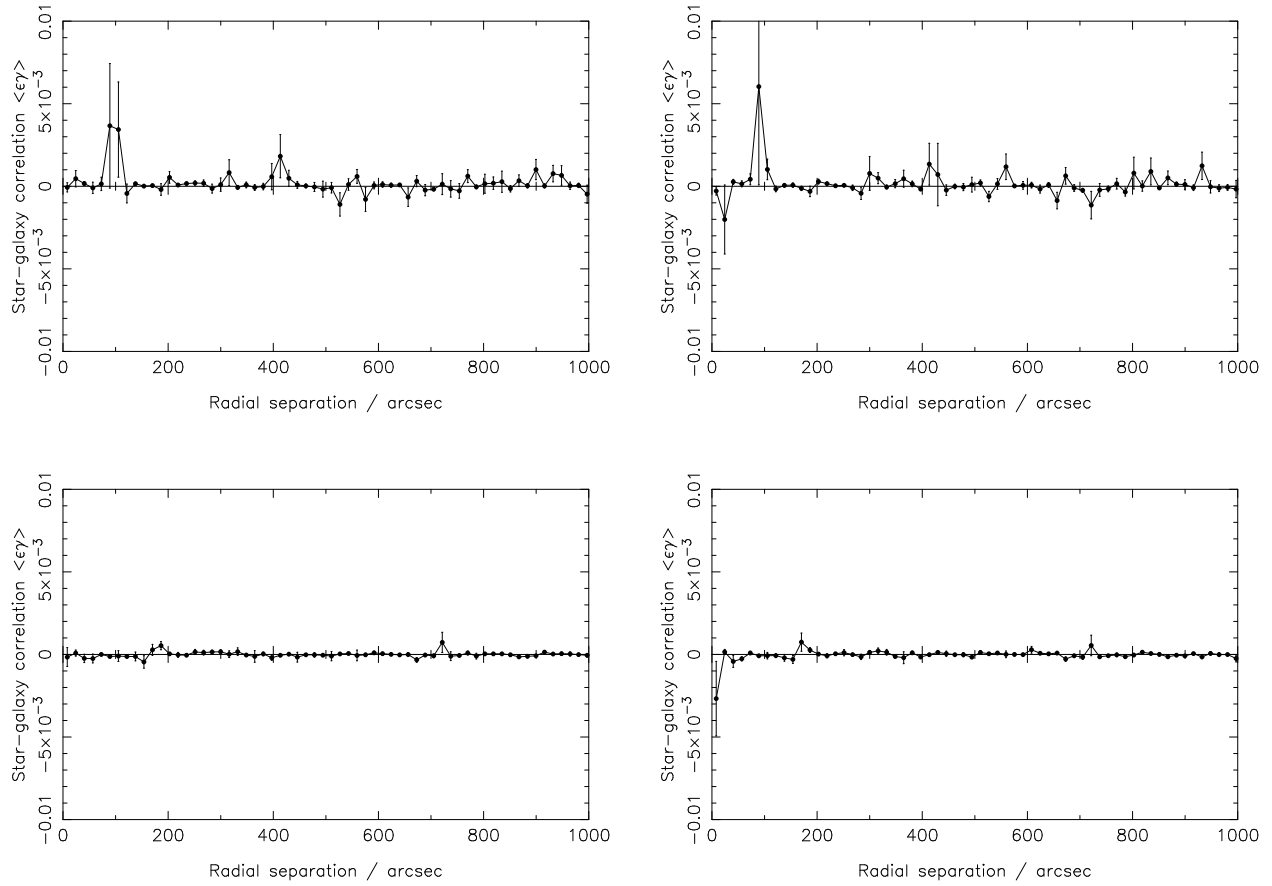


Figure 5: Correlation functions between star and galaxy catalogs. Left-hand plots show E-mode correlation, right-hand ones show B-mode. Top row: traditional whole-image correction; bottom row: chip-by-chip analysis.

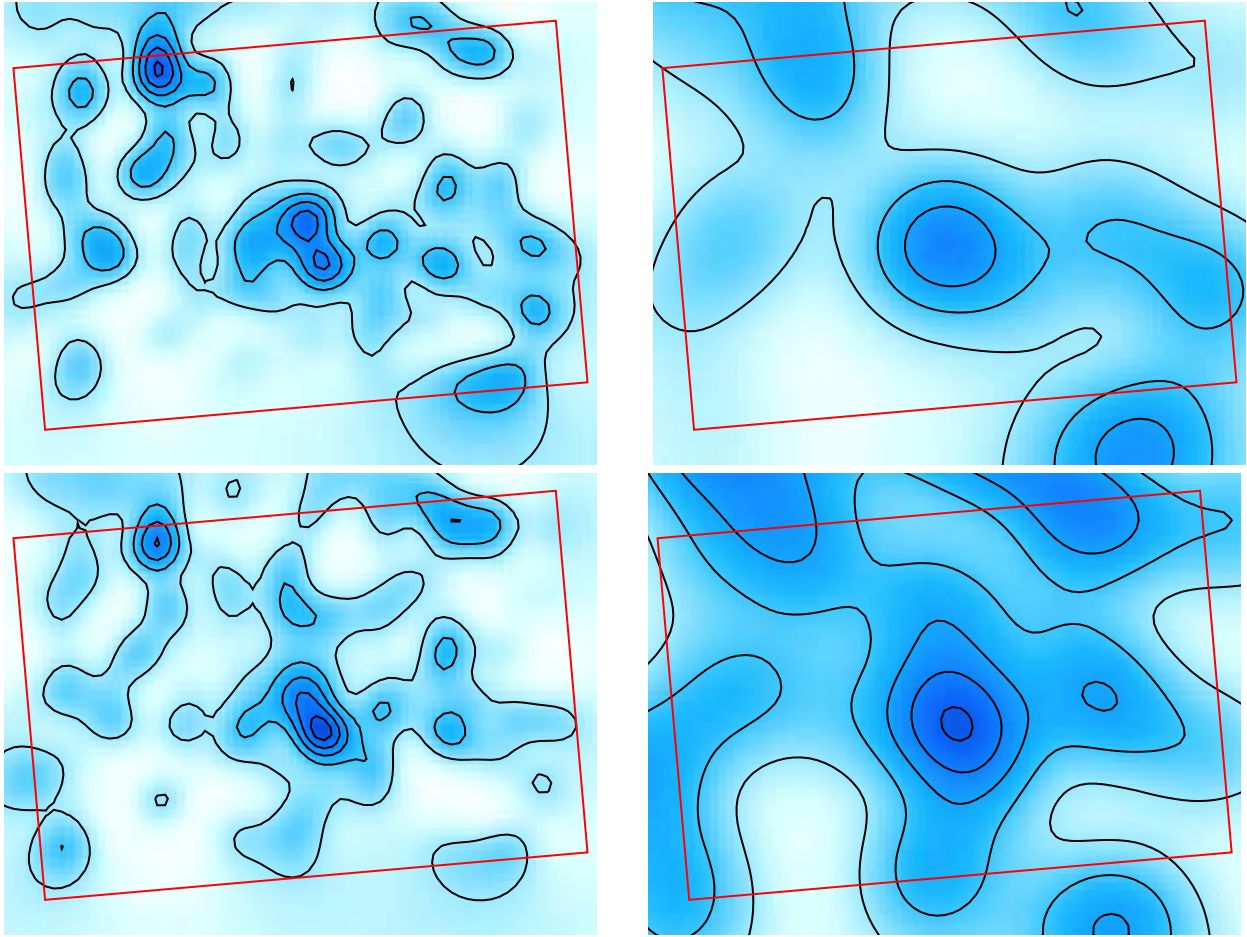


Figure 6: LensEnt2 mass maps inferred from the PSF-corrected A399 galaxy catalogues. Left-hand maps are at 3 arcmin resolution, right-hand ones 9 arcmin. Top row: traditional whole-image correction; bottom row: chip-by-chip analysis.

**Analysis of  $B \rightarrow \omega l \nu$  Decays With BaBar**Yiwen Chu<sup>1</sup>, Bryce Littlejohn<sup>2</sup>

Office of Science, SULI Program

<sup>1</sup>Massachusetts Institute of Technology, <sup>2</sup>Principia College

Stanford Linear Accelerator Center

Menlo Park, California

August 29, 2005

Prepared in partial fulfillment of the requirements of the Office of Science, U.S. Department of Energy Science Undergraduate Laboratory Internship (SULI) Program under the direction of Jochen Dingfelder in Experimental Group C at the Stanford Linear Accelerator Center (SLAC).

Participants:

-----

Signature

Research Advisor:

-----

Signature

# Contents

<b>1</b>	<b>Abstract</b>	<b>3</b>
<b>2</b>	<b>Introduction</b>	<b>4</b>
<b>3</b>	<b>Analysis Methods</b>	<b>6</b>
3.1	Neutrino Reconstruction . . . . .	7
3.2	Background Suppression and Signal Selection . . . . .	9
3.3	Signal Extraction . . . . .	16
<b>4</b>	<b>Results and Discussion</b>	<b>16</b>
<b>5</b>	<b>Acknowledgements</b>	<b>20</b>

# 1 Abstract

Analysis of  $B \rightarrow \omega l \nu$  Decays With BaBar. YIWEN CHU(Massachusetts Institute of Technology, Cambridge, MA 02139) BRYCE LITTLEJOHN(Principia College, Elmhurst, IL 60120) JOCHEN DINGFELDER(Stanford Linear Accelerator Center, Menlo Park, CA 94025).

As part of the BaBar project at SLAC to study the properties of  $B$  mesons, we have carried out a study of the exclusive charmless semileptonic decay mode  $B \rightarrow \omega l \nu$ , which can be used to determine the Cabibbo-Kobayashi-Maskawa matrix element  $V_{ub}$ . Using simulated event samples, this study focuses on determining criteria on variables for selection of  $B \rightarrow \omega l \nu$  signal and suppression of background from other types of  $B\bar{B}$  events and continuum processes. In addition, we determine optimal cuts on variables to ensure a good neutrino reconstruction. With these selection cuts, we were able to achieve a signal-to-background ratio of 0.68 and a signal efficiency of the order of 1%. Applying these cuts to a sample of 83 million  $B\bar{B}$  events recorded by BaBar in  $e^+e^-$  collisions at the  $\Upsilon(4S)$  resonance, we obtain a yield of  $115 \pm 19$   $B \rightarrow \omega l \nu$  decays.

## 2 Introduction

The BaBar experiment at SLAC studies the properties of  $B$  mesons in  $B\bar{B}$  events produced in  $e^+e^-$  collisions on the  $\Upsilon(4S)$  resonance. We study the particular exclusive decay  $B \rightarrow \omega l\nu$ , which is called a charmless semileptonic decay due to the presence of two leptons and the  $\omega$  meson in the final state. The study of charmless semileptonic decays allows for the determination of the Cabbibo-Kobayashi-Maskawa (CKM) matrix element  $|V_{ub}|$ , which determines the probability of a  $b \rightarrow u$  transition in a weak interaction and is one of the smallest and least known elements. In the Standard Model, the

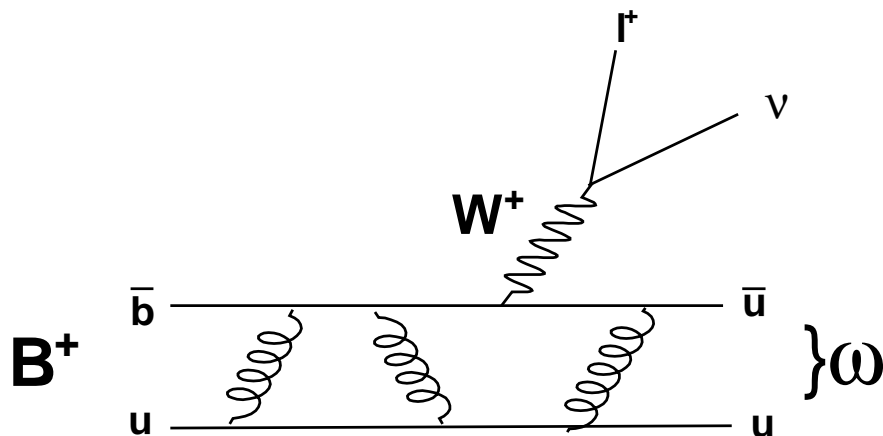


Figure 1: Feynman diagram of a  $B \rightarrow \omega l\nu$  decay.

CKM matrix is unitary, and this condition can be graphically represented as the Unitarity Triangle in the complex  $(\rho - \eta)$  plane [1].  $|V_{ub}|$  indicates the length of one side of this triangle. A precise measurement of  $|V_{ub}|$  would significantly improve the constraints on the Unitarity Triangle and provide a stringent test of the Standard Model mechanism for Charge-Parity (CP) violation.

The BaBar collaboration has already measured several other charmless

semileptonic decays, such as  $B \rightarrow \pi l \nu$  and  $B \rightarrow \rho l \nu$  [2]. However, the  $B \rightarrow \omega l \nu$  mode is experimentally more difficult and has not yet been studied in detail with sufficient signal statistics by BaBar. Recent studies at Belle have been able to identify these events and measure a branching fraction of  $(1.3 \pm 0.4 \pm 0.3 \pm 0.3) \times 10^{-4}$  [3].

In this study, we focus on improving the selection of  $B \rightarrow \omega l \nu$  decays by reducing the background from other processes and ensuring a reliable reconstruction of the neutrino kinematics. In the complex process of analyzing data, discrimination between signal and background is particularly important and challenging for a rare process such as  $B \rightarrow \omega l \nu$ . By looking at tracks made in different parts of the BaBar detector, we can reconstruct and identify the particles produced in the  $e^+e^-$  collision, thereby selecting signal decays. However, background events can be misidentified as signal, or a real signal decay may be wrongly reconstructed. The latter case may occur by, for example, assigning a particle from the other  $B$  decay to the signal  $B$  decay. Significant backgrounds include  $B \rightarrow X_c l \nu$  decays, where  $X_c$  stands for a meson that contains a  $c$  quark, and  $e^+e^- \rightarrow q\bar{q}$  processes (“continuum events”). Fortunately, the features of the signal events we are interested in differ in many ways from those of the background, which allows us to enhance the signal by applying selection cuts on variables that exhibit these differences. Another challenge of the analysis process involves the reliable reconstruction of the semileptonic decay kinematics. In particular, we study the quality of the neutrino reconstruction. Since these particles are not directly detectable, their kinematics must be inferred indirectly from the missing momentum and energy of the entire event, causing much room for error. We study several variables that can be used to ensure a good quality of the neutrino reconstruction.

After performing the above studies using Monte Carlo simulated samples, we can determine the number of signal events in a sample of 83 million  $B\bar{B}$  events recorded with the BaBar detector.

### 3 Analysis Methods

To identify a  $B \rightarrow \omega l \nu$  decay, we look for the presence of a lepton with center-of-mass momentum greater than 1.3 GeV/c, a substantial missing momentum as indication of a neutrino in the event, and a reconstructed hadron consistent with an  $\omega$  meson. The  $\omega$  is reconstructed in its dominant decay mode  $\omega \rightarrow \pi^+ \pi^- \pi^0$ , where the  $\pi^+$  and  $\pi^-$  are identified as charged tracks in the drift chamber not consistent with a lepton or kaon and the  $\pi^0$  as two photons in the electromagnetic calorimeter produced in the decay  $\pi^0 \rightarrow \gamma\gamma$ .

The data and Monte Carlo samples used in our analysis have been applied with preliminary selection criteria (“preselection”). In order to reduce continuum background events that are not produced on the  $\Upsilon(4S)$  resonance, the preselection uses loose cuts on the number of charged tracks ( $N_{track} > 3$ ),  $R2 < 0.6$ ,  $|\cos \theta_{BY}| < 1.5$  (see section 3.2 for definitions of  $R2$  and  $|\cos \theta_{BY}|$ ). In addition, we apply a loose cut on the invariant mass of the three pions forming the omega candidate of  $0.70 < m_{\pi^+ \pi^- \pi^0} < 0.86$  GeV and a cut on the  $\omega$  decay amplitude of the three pions produced, given by

$$\lambda = \frac{|\vec{p}_{\pi^+} \times \vec{p}_{\pi^-}|^2}{\frac{3}{4}(\frac{1}{9}m_{3\pi}^2 - m_{\pi^+}^2)^2} > 0.25 \text{ GeV}^{-2}. \quad (1)$$

These criteria significantly reduce the requirements on CPU time and disk space and yield a data sample of manageable size for this analysis.

### 3.1 Neutrino Reconstruction

In addition to the energetic charged lepton, the presence of a neutrino in the decay products of the  $B$  meson is a characteristic feature of semileptonic modes, so we first try to isolate events with a well reconstructed neutrino. Since neutrinos cannot be detected, we must infer their mass and kinematics from all reconstructed particles. The four-momentum of the neutrino is taken to be the missing four-momentum of the event, given by

$$(\vec{p}_\nu, E_\nu) = (\vec{p}_{miss}, E_{miss}) = (\vec{p}_{beams}, E_{beams}) - \left( \sum_i \vec{p}_i, \sum_i E_i \right), \quad (2)$$

where  $\vec{p}_{beams}, E_{beams}$  are the sums of the known momenta and energies of the colliding  $e^+$  and  $e^-$ , and  $\vec{p}_i, E_i$  are the momentum and energy of the  $i^{th}$  reconstructed particle [4]. We also reject events with  $|\vec{p}_{miss}| < 0.7$  GeV. The missing-mass squared of the neutrino is then calculated as

$$m_{miss}^2 = E_{miss}^2 - |\vec{p}_{miss}|^2. \quad (3)$$

In the simulated events, these reconstructed quantities can be compared to the true values for each event, which tells us how well the neutrino has been reconstructed. In particular, we are interested in the following resolutions:

1.  $|\vec{p}_{miss}| - |\vec{p}_{\nu,true}|$ : The difference in the magnitudes of the lab-frame momenta.
2.  $q_{reco}^2 - q_{true}^2$ : Here  $q^2$  is the four-momentum transfer of the decay, given by

$$q^2 = (p_{lepton} + p_\nu)^2 = (p_B - p_{hadron})^2. \quad (4)$$

It is equivalent to the invariant mass squared of the virtual W boson involved in the production of the lepton and neutrino.

We try to quantify the quality of the neutrino reconstruction by fitting the  $|\vec{p}_{miss}| - |\vec{p}_{\nu,true}|$  distribution with a Gaussian function for the peak and

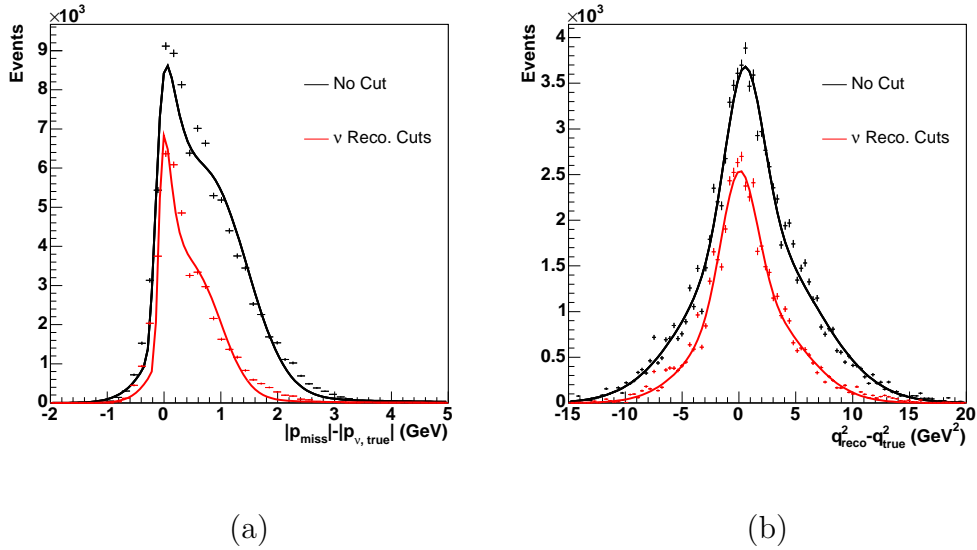


Figure 2: Resolutions (a)  $|\vec{p}_{miss}| - |\vec{p}_{\nu,true}|$  and (b)  $q_{reco}^2 - q_{true}^2$ . Crosses are simulated signal events with statistical error and lines are fits. Black: No cuts applied. Red: Resolutions after chosen cut of  $\frac{m_{miss}^2}{E_{miss}} < 2.6$  GeV,  $\theta_{miss} > 0.5$  rad, and  $Q_{tot} \leq 1$ .

a Landau function for the tail. The  $q_{reco}^2 - q_{true}^2$  distribution was fitted with two Gaussian functions, one for the peak and the other to describe the tails. Although the fits are not perfect, they approximately quantify the quality of the reconstructed neutrino. We then study the width ( $\sigma_{peak}$ ) and mean ( $\mu_{peak}$ ) of the peak Gaussian functions, along with the ratio  $\frac{N_{tail}}{N_{all}}$ , where  $N_{all}$  is the number of events in both the Gaussian and Landau functions, and  $N_{tail}$  is the number of events in the tail with selection criteria (as explained below) outside  $2\sigma$  of the Gaussian peak without selection criteria.

As can be seen in Fig. 2, there are significant resolution tails due to poorly reconstructed events. These tails are mostly caused by events where particles are lost outside the detector acceptance region or by the production of an additional neutrino from, for example, the decay of the other  $B$  meson. By discarding events that do not satisfy selection criteria on the following

variables that are directly affected by the neutrino reconstruction, we can reduce the resolution tails.

1.  $Q_{tot} = \sum_i Q_{track,i}$ : If a charged particle was lost, the total charge of the event will generally no longer be zero. To reduce the effect of losses due to detector acceptance, we use the typical cut of  $Q_{tot} \leq 1$ .
2.  $m_{miss}^2/E_{miss}$ :  $m_{miss}^2$  should be  $m_\nu^2 = 0$ . Since the  $m_{miss}^2$  resolution broadens linearly with  $E_{miss}$ , a cut on this variable is more effective than a cut on  $m_{miss}^2$ .
3.  $\theta_{miss}$ : This variable indicates the angle between the missing momentum and the  $e^-$  beam. When this angle is close to  $0^\circ$  or  $180^\circ$ , it is likely that the missing momentum was caused by a particle other than a neutrino traveling in the direction of the beamline, where it cannot be detected.

We vary the cuts from  $m_{miss}^2/E_{miss} < 1.0$  GeV to  $m_{miss}^2/E_{miss} < 3.8$  GeV and from  $\theta_{miss} > 0$  rad to  $\theta_{miss} > 0.6$  rad and then plot the signal efficiency  $\epsilon_{sig} = N_{cut}^{sig}/N_{uncut}^{sig}$  and the characteristic parameters of the resolutions as functions of cut values in order to find the best combination of cuts (see Fig 3). While we see only a moderate improvement when tightening the cut on the missing mass, a tighter cut on  $\theta_{miss}$  significantly improves the resolution. We choose the cuts  $m_{miss}^2/E_{miss} < 2.6$  GeV,  $\theta_{miss} > 0.5$  rad, and  $Q_{tot} \leq 1$ . This optimum combination of cuts, along with other cuts of similar efficiency, are presented in Table 1 for comparison.

### 3.2 Background Suppression and Signal Selection

The background for  $B \rightarrow \omega l \nu$  decays can be categorized into several sources. Continuum background consisting of  $e^+e^- \rightarrow q\bar{q}$  processes are the largest contribution, while another significant source is semileptonic  $B \rightarrow X_c l \nu$  events

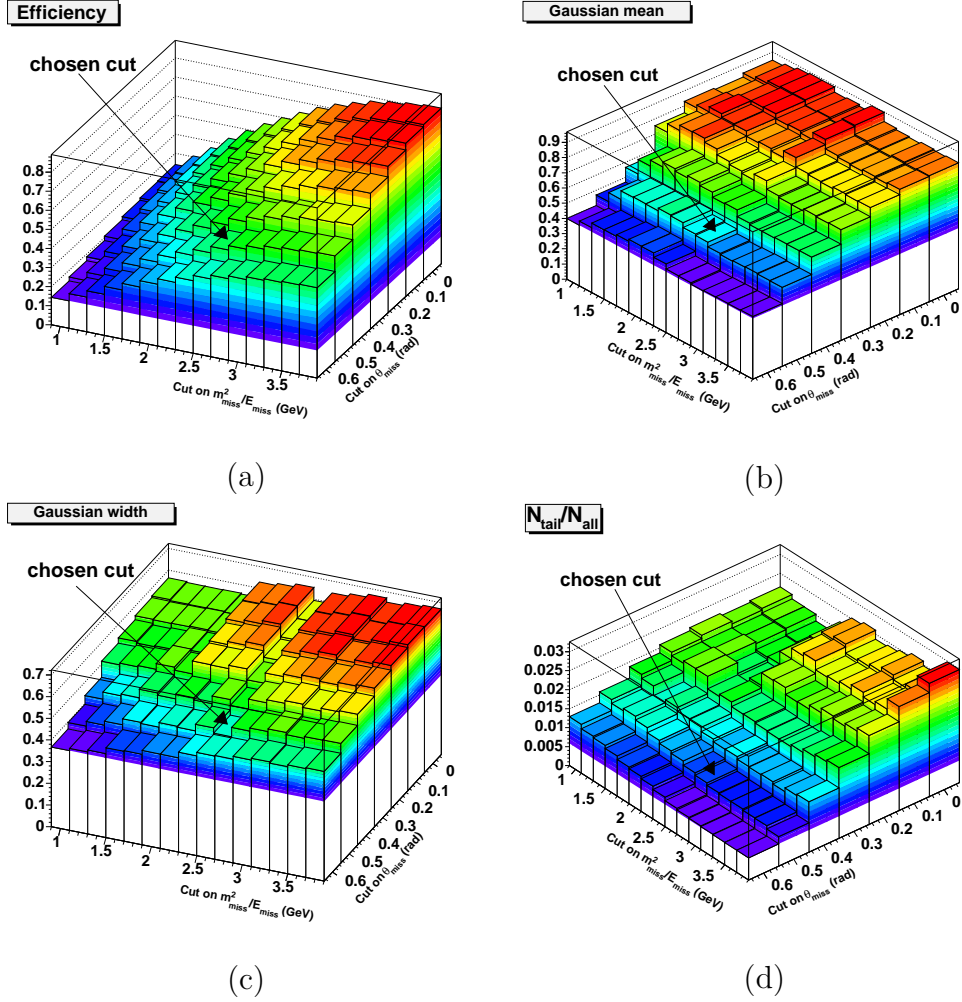


Figure 3: Characteristic quantities of  $\nu$  momentum resolution for all combinations of cuts on  $m_{miss}^2/E_{miss}$  and  $\theta_{miss}$ . (a) Signal efficiency with preselection, (b) Peak Gaussian mean  $\mu_{peak}$ , (c) Peak Gaussian width  $\sigma_{peak}$ , and (d) the ratio  $\frac{N_{tail}}{N_{all}}$ . Similar plots were used with the  $q^2$  resolution to determine the optimal cut.

	Sets of Cuts			Signal Efficiency	$ \vec{p}_{miss}  -  \vec{p}_{\nu,true} $ (GeV)			$q_{reco.}^2 - q_{true}^2$ (GeV)		
	$Q_{tot}$	$\theta_{miss}$ (rad)	$\frac{m_{miss}^2}{E_{miss}}$ (GeV)		$\sigma_{peak}$	$\mu_{peak}$	$\frac{N_{tail}}{N_{all}}$	$\sigma_{peak}$	$\mu_{peak}$	$\frac{N_{tail}}{N_{all}}$
No Cut:	-	-	-	1	0.66	0.848	0.03	1.659	0.474	0.41
Chosen Cuts:	$\leq 1$	$> 0.5$	$< 2.6$	0.552	0.481	0.554	0.010	1.556	0.0192	0.172
Cuts w/ Similar Eff.:	$\leq 1$	$> 0$	$< 1.8$	0.574	0.556	0.889	0.0187	1.834	0.489	0.27
Cuts w/ Similar Eff.:	$\leq 1$	$> 0.3$	$< 2$	0.559	0.597	0.783	0.0178	1.911	0.27	0.241

Table 1: Four combinations of  $m_{miss}^2/E_{miss}$ ,  $\theta_{miss}$ , and  $Q_{tot}$  cuts with their effect on  $\nu$  resolutions and signal efficiencies. The chosen set of cuts is compared to the uncut signal Monte Carlo sample along with two other sets of cuts with similar signal efficiencies

with a charm meson in the final state. The continuum background has a more jet-like topology than  $B\bar{B}$  events, which are isotropic in the center-of-mass frame. The continuum background is therefore significantly suppressed by preselection. However, preselection is not as effective on  $B \rightarrow X_c l \nu$  decays, which are also much more abundant than the signal. In addition there is background from other  $B \rightarrow X_u l \nu$  modes where  $X_u$  is  $\pi^\pm, \pi^0, \rho^\pm, \rho^0$ , etc. Even after applying the neutrino reconstruction cuts, the background completely overwhelms the signal (Fig. 4). Selection criteria on top of the neutrino reconstruction cuts must be applied to reduce these various backgrounds with respect to the  $B \rightarrow \omega l \nu$  signal.

We first studied the agreement between Monte Carlo and BaBar data for the two main background sources by comparing them using  $B \rightarrow X_c l \nu$  and continuum enhanced samples. There was a relatively uniform normalization discrepancy in the continuum background, which may be caused by unsimulated continuum processes in the Monte Carlo. We simply scaled the continuum background by a factor of 1.1 in order to match the data. The shapes of the distributions for several kinematic variables in the  $B \rightarrow X_c l \nu$  enhanced sample were also slightly different between data and Monte Carlo (at the 10% level). Within the scope of this study, we could not further investigate these deviations.

We define several variables that characterize each reconstructed event and will be used for selection cuts. The first three variables below describe the topology of the event.

- $|\cos \theta_{thrust}|$ , where  $\theta_{thrust}$  is the angle between the thrust axis [5] of the so-called Y system, consisting of the  $\omega$  and lepton, and the thrust axis of the rest of the event. Here the thrust axis is the direction that maximizes the total longitudinal components of the particle momenta.

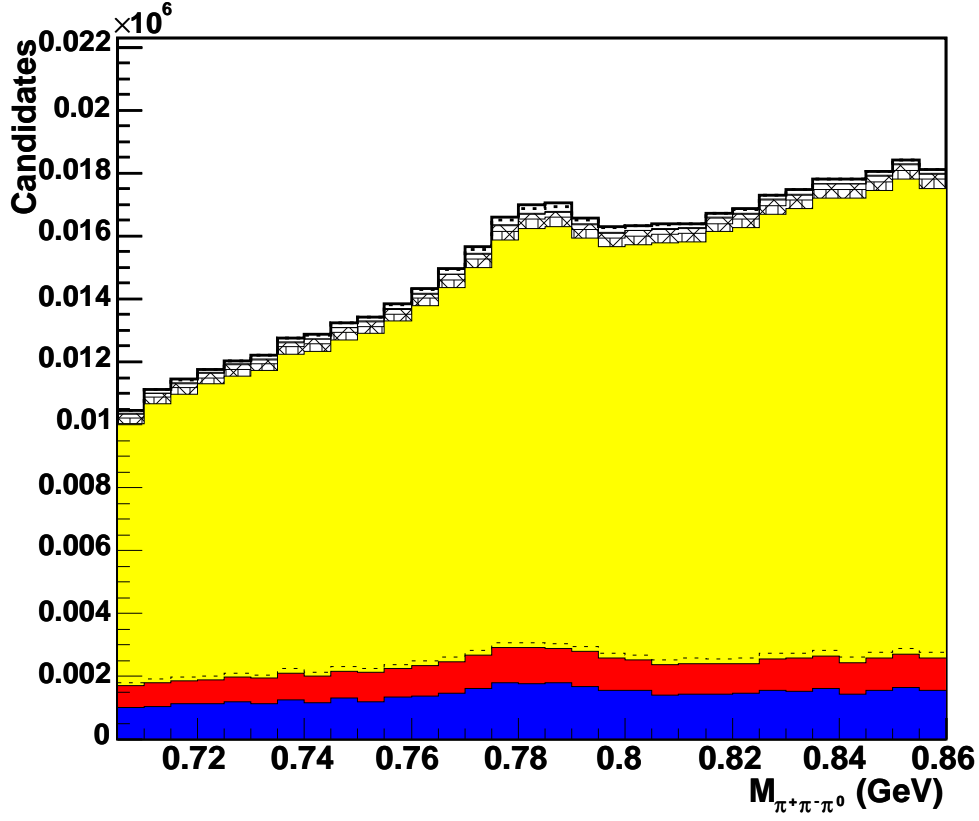


Figure 4: Invariant mass  $m_{\pi^+\pi^-\pi^0}$  after only preselection and neutrino reconstruction cuts. Red and blue histograms are  $e^+e^- \rightarrow q\bar{q}$  events with a real and fake lepton, respectively. Yellow histograms are  $B\bar{B}$  background, dominated by  $B \rightarrow X_c l \nu$  decays (above dotted line). Hatched histograms are other  $B \rightarrow X_u l \nu$  decays. Simulated signal is shown as white histogram with the contribution from combinatoric signal (see last sentence before Sec. 3.3 for definition) marked as dotted line.

This variable peaks around 1 for jet-like events like  $e^+e^- \rightarrow q\bar{q}$ .

- $L2 = \sum_i |\vec{p}_i^*| \cos^2 \theta_i^*$  where  $|\vec{p}_i^*|$  is the momentum of the  $i^{th}$  particle in the center-of-mass frame, and  $\theta_i^*$  is the angle of the momentum with the thrust axis of the  $Y$  system. This quantity is large for jet-like events and small for isotropic ones such as semileptonic  $B$  decays.
- $R2$ : the ratio of the  $2^{nd}$  to  $0^{th}$  Fox-Wolfram moments [6]. It is close to 0 for isotropic events and close to 1 for jet-like events.
- The cosine of the angle between the  $Y$  system and the  $B$  meson, given by

$$\cos \theta_{BY} = (2E_B^* E_Y^* - M_B^2 - M_Y^2) / (2|\vec{p}_B^*| |\vec{p}_Y^*|), \quad (5)$$

where the  $B$  momentum and energy are calculated from the known beam four-momenta and the  $Y$  momentum and energy are determined through the reconstruction of the lepton and  $\omega$ . For correctly constructed  $B \rightarrow \omega l \nu$  decays,  $\cos \theta_{BY}$  should be between -1 and 1 so that  $\theta_{BY}$  corresponds to a physical angle. The backgrounds, on the other hand, should have a broader distribution.

- $\Delta E = E_B^* - \sqrt{s}/2$ , where  $E_B^*$  is the energy of the reconstructed  $B$  meson and  $\sqrt{s}$  is the mass of the  $\Upsilon(4S)$ .
- $m_{ES} = \sqrt{s/4 - (\vec{p}_B^*)^2}$ , the beam energy substituted mass of the reconstructed  $B$  meson.

We use the preselected Monte Carlo samples to determine which variables show a discrimination between signal and background and are therefore useful for selection cuts. We first optimized cuts on topology and kinematics variables. The topology variables showed significant differences between the signal and continuum backgrounds, while kinematic variables such as lepton

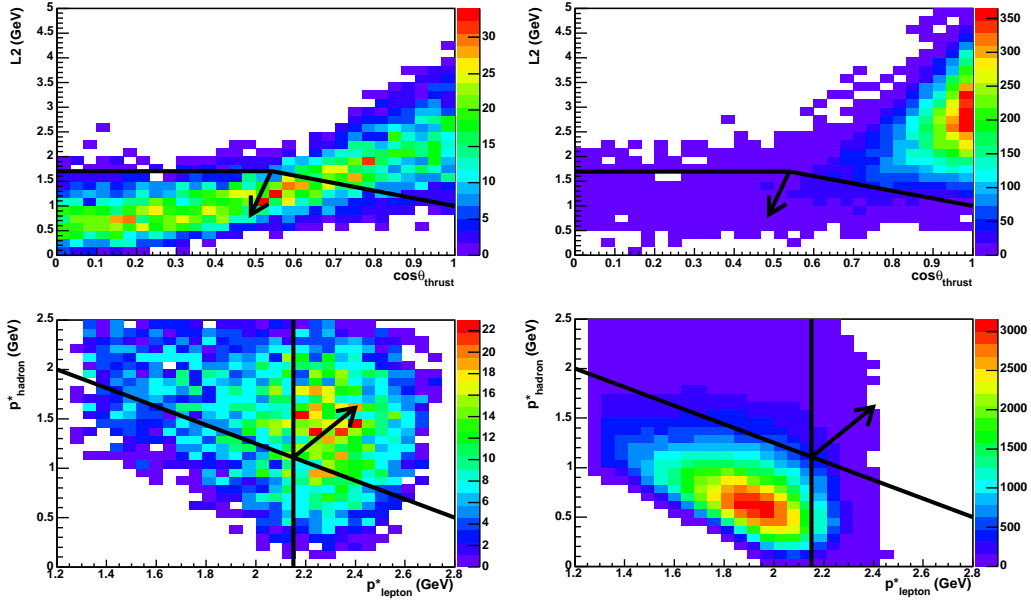


Figure 5: Top: Distributions of L2 vs.  $\cos\theta_{thrust}$  for simulated signal (left) and continuum background (right). Bottom: Distributions of lepton vs. hadron momentum for simulated signal (left) and  $B \rightarrow X_c l \nu$  background (right). Black arrow points to region selected.

and hadron momentum were very effective in suppressing other semileptonic decays (see Fig. 5). For example,  $B \rightarrow X_c l \nu$  background tends to have lower lepton and hadron momenta than the  $B \rightarrow \omega l \nu$  signal due to the heavier quark produced. Distributions for some of these variables can be found in Fig. 6. A list of selection cuts along with signal efficiencies and approximate amount of background reduction is given in Table 2. Fig. 6 also compares simulation with data selected from a sample of 83 million  $B\bar{B}$  events. Simulated samples have been scaled to the data statistics. We see reasonable agreement between data and simulation and a clear excess of signal events above the dominant background. There are also contributions from other  $B \rightarrow X_u l \nu$  decays, as well as a contribution from signal decays where the reconstructed  $\omega$  includes a background pion or photon (“combinatoric sig-

nal”).

### 3.3 Signal Extraction

After all other cuts have been optimized, we extract the  $B \rightarrow \omega l \nu$  signal from the  $\Delta E$ ,  $m_{ES}$ , and  $m_{\pi^+\pi^-\pi^0}$  distributions. For signal decays, we expect  $\Delta E$  to be close to 0;  $m_{ES}$  and  $m_{\pi^+\pi^-\pi^0}$  should correspond to the  $B$  mass and the  $\omega$  mass, respectively. We require that  $-0.3 < \Delta E < 0.5$  GeV,  $m_{ES} > 5.23$  GeV, and  $0.75 < m_{\pi^+\pi^-\pi^0} < 0.81$  GeV. These three cuts had the most significant effects on our signal-to-background ratio. Fig. 6 and 7 show the distributions of these variables with their corresponding cuts.

## 4 Results and Discussion

After all cuts we were able to see a distinct mass peak around the omega mass of 782 MeV in the  $m_{\pi^+\pi^-\pi^0}$  distribution (Fig. 7). This shows that we have effectively reduced the background and can extract the desired  $B \rightarrow \omega l \nu$  signal. The final Monte Carlo signal efficiency is of the order of 1%, while the various backgrounds have been reduced by roughly  $10^{-4}$  to  $10^{-6}$ . A comparison between the effects of signal extraction on the Monte Carlo signal and background is given in Table 3. The final number of signal events predicted by the Monte Carlo simulation is 133, and the total number of expected background events is 195, giving a signal-to-background ratio of 0.68. This ratio is more than sufficient for isolating the signal processes above background uncertainties.

We determine the number of signal events in the data by subtracting out the Monte Carlo simulated background distributions. We find  $115 \pm 19$   $B \rightarrow \omega l \nu$  decays in the data, where the error includes the statistical

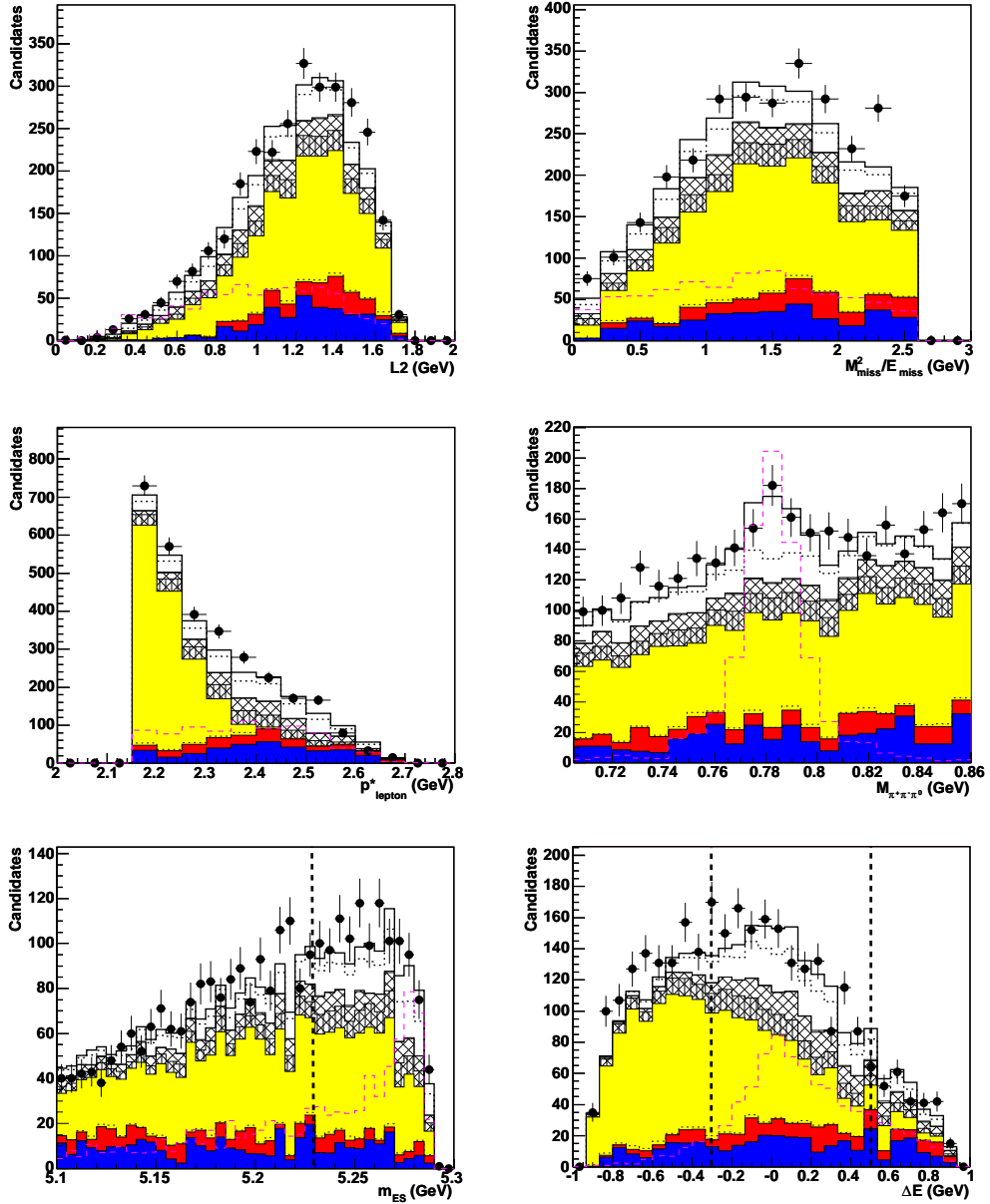


Figure 6: Distributions before signal extraction for six variables used in the selection cuts.  $\Delta E$  and  $m_{ES}$  are shown with corresponding cuts indicated by vertical lines. Monte Carlo simulation (histograms) is compared to BaBar data (points). Magenta dashed histograms with arbitrary normalization indicate the signal shapes. See Fig. 4 caption for details.

	signal	$B \rightarrow X_c l \nu$	$B \rightarrow X_u l \nu$	$e^+ e^- \rightarrow q \bar{q}$
preselection	35	1.8	6.1	0.4
	Efficiencies of individual cuts on top of preselection(%)			
$ p_\nu  > 0.7 \text{ GeV}$	96	99	99	85
neutrino reconstruction	50	29	42	33
$R2 < 0.4$	92	99	97	64
$ \cos \theta_{BY}  < 1$	92	66	71	73
$p_{hadron}^* + 0.94 p_{lepton}^* > 3.125 \text{ GeV}; p_{lepton}^* > 2.15 \text{ GeV}$	43	1.4	11	31
$L2 + 1.5 \cos \theta_{thrust} < 2.5; L2 < 1.7 \text{ GeV}$	63	47	49	7.8

Table 2: Cut efficiencies for simulated signal and background samples.

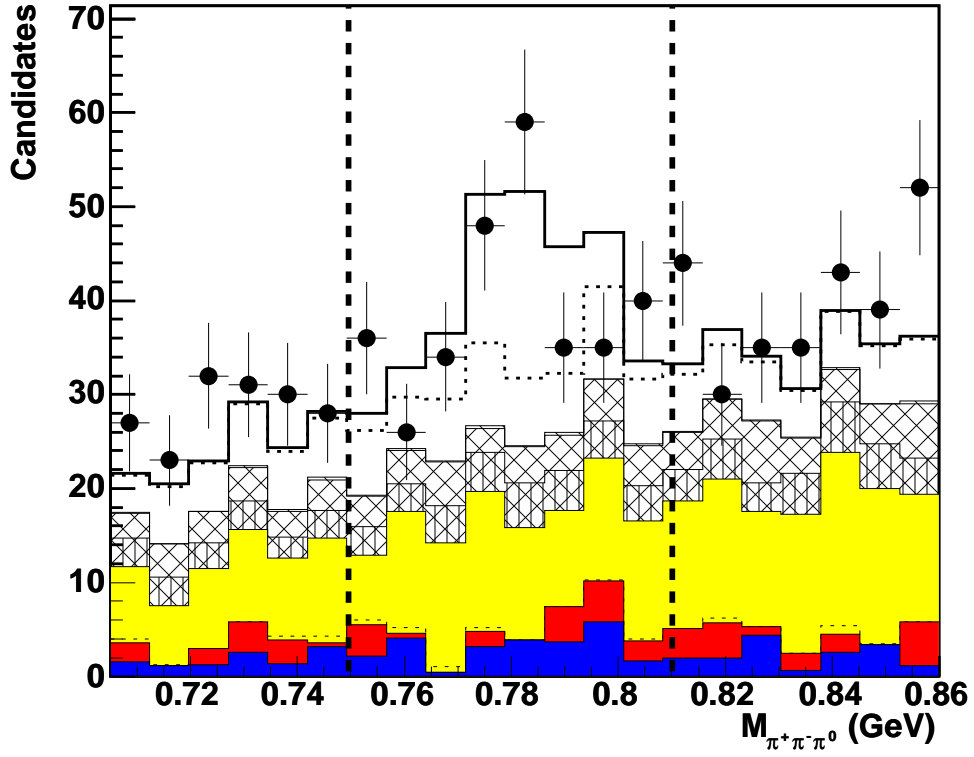


Figure 7: Invariant mass  $m_{\pi^+\pi^-\pi^0}$  after all selection cuts but the one on the mass itself. The final mass cut is indicated as vertical lines. The raggedness of the continuum background distribution is due to the low statistics of the Monte Carlo sample. See Fig. 4 caption for details.

	Before Sig. Extr.	After Sig. Extr.
Signal Events	482	133
Background Events	2386	195
Signal-to-background ratio	0.20	0.68
Signal Efficiency (approximate)	0.04	0.01
Background Efficiency (approximate)	$10^{-5}$	$10^{-6}$

Table 3: Effects of signal extraction along with final numbers of events and efficiencies.

uncertainties of the data and Monte Carlo samples.

We hope to use the work presented here to calculate the  $B \rightarrow \omega l \nu$  branching fraction, which can be obtained using the exact signal efficiency along with the number of signal events in the data. Another feature that calls for further investigation is the discrepancies between the data and  $B \rightarrow X_c l \nu$  and continuum backgrounds observed in the dedicated background-enhanced samples. Eventually, the analysis of this decay mode can be used to extract the CKM matrix element  $|V_{ub}|$  and thus constrain the Unitarity Triangle.

## 5 Acknowledgements

We would like to thank the Department of Energy, Office of Science and SLAC for this opportunity to participate in the SULI program. We would especially like to express our gratitude to our mentor, Jochen Dingfelder, who always took time out of his extremely busy schedule to help us with our programming and explain the physics behind what we were doing. We would also like to thank Vera Lüth, Mike Kelsey, Kai Yi, and the rest of our colleagues in Group C for providing valuable help and advice.

## References

- [1] L. Wolfenstein, *Phys. Rev. Lett.* **51**, 1945 (1983).
- [2] *BABAR* Collaboration, B. Aubert *et al.*, hep-ex/0507003, (Submitted to *Phys. Rev. Lett.* D Rapid Communications).
- [3] Belle Collaboration, C. Schwanda *et al.*, *Phys. Rev. Lett.* **93**, 131803 (2004).
- [4] A.J. Weinstein, “Study of Exclusive Charmless Semileptonic Decays of the B Meson”, PhD thesis, Stanford Linear Accelerator Center (2004).
- [5] E. Farhi, *Phys. Rev. Lett.* **39**, 1587(1977).
- [6] G.C. Fox and S. Wolfram, *Nucl. Phys.* **B149**, 413 (1979).

**"B" Values – 1st Leg**

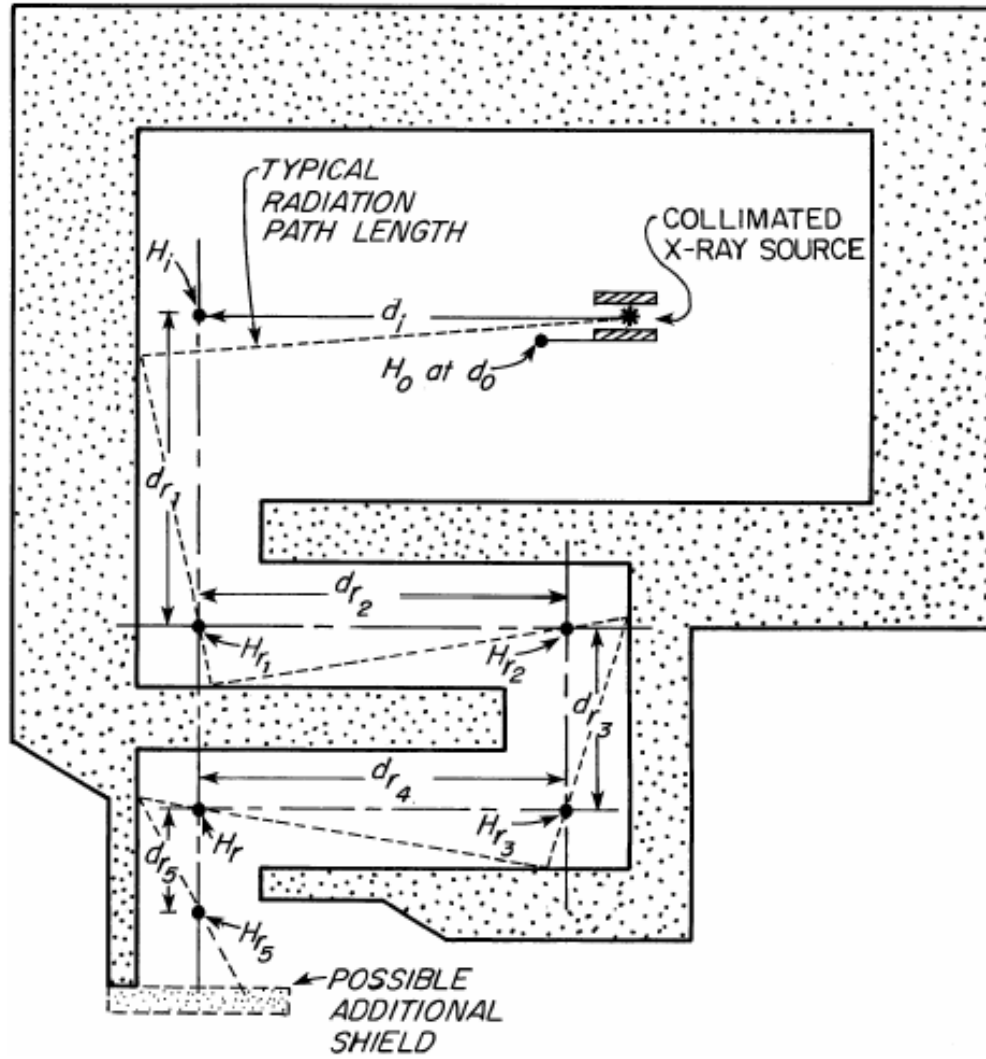
Cross-section Length	Energy		
	1 GeV	100 MeV	30 MeV
	1.00E+09	1.00E+08	3.00E+07
50	1.6987 ± .0007	1.6805 ± .0005	1.7301 ± .0005
100	1.8384 ± .0007	1.7293 ± .0005	1.7442 ± .0003
200	1.8751 ± .0006	1.7284 ± .0003	1.7547 ± .0004
300	1.8854 ± .0009	1.7424 ± .0003	1.7812 ± .0005
400	0.635146 ± .000856	1.7481 ± .0004	1.8011 ± .0004
	10 MeV	3 MeV	1 MeV
	1.00E+07	3.00E+06	1.00E+06
50	1.6951 ± .0004	1.7849 ± .0005	1.7523 ± .0003
100	1.7040 ± .0003	1.7895 ± .0003	1.8208 ± .0002
200	1.7174 ± .0002	1.8019 ± .0004	1.9012 ± .0003
300	1.7470 ± .0002	1.8337 ± .0003	1.9719 ± .0002
400	1.7690 ± .0002	1.8578 ± .0003	1.9762 ± .0003
	100 KeV	12 KeV	1200 eV
	1.00E+05	1.20E+04	1.20E+03
50	1.8426 ± .0003	1.9777 ± .0006	2.0307 ± .0007
100	1.8773 ± .0003	2.0306 ± .0007	2.0934 ± .0008
200	1.9484 ± .0002	2.1424 ± .0005	2.2223 ± .0004
300	2.0326 ± .0004	2.2683 ± .0008	2.3652 ± .0007
400	2.1116 ± .0004	2.3832 ± .0009	2.4991 ± .0007
	120 eV	12 eV	thermal
	120	12	0.025
50	2.0179 ± .0005	2.0051 ± .0005	2.1196 ± .0007
100	2.0844 ± .0006	2.0706 ± .0004	2.2014 ± .0006
200	2.2140 ± .0008	2.2057 ± .0006	2.3500 ± .0008
300	2.3621 ± .0007	2.3511 ± .0006	2.511 ± .001
400	2.5013 ± .0007	2.4914 ± .0009	2.6569 ± .0015

**Table 3**  
**Calculated *b* values from the first leg with propagated error.**

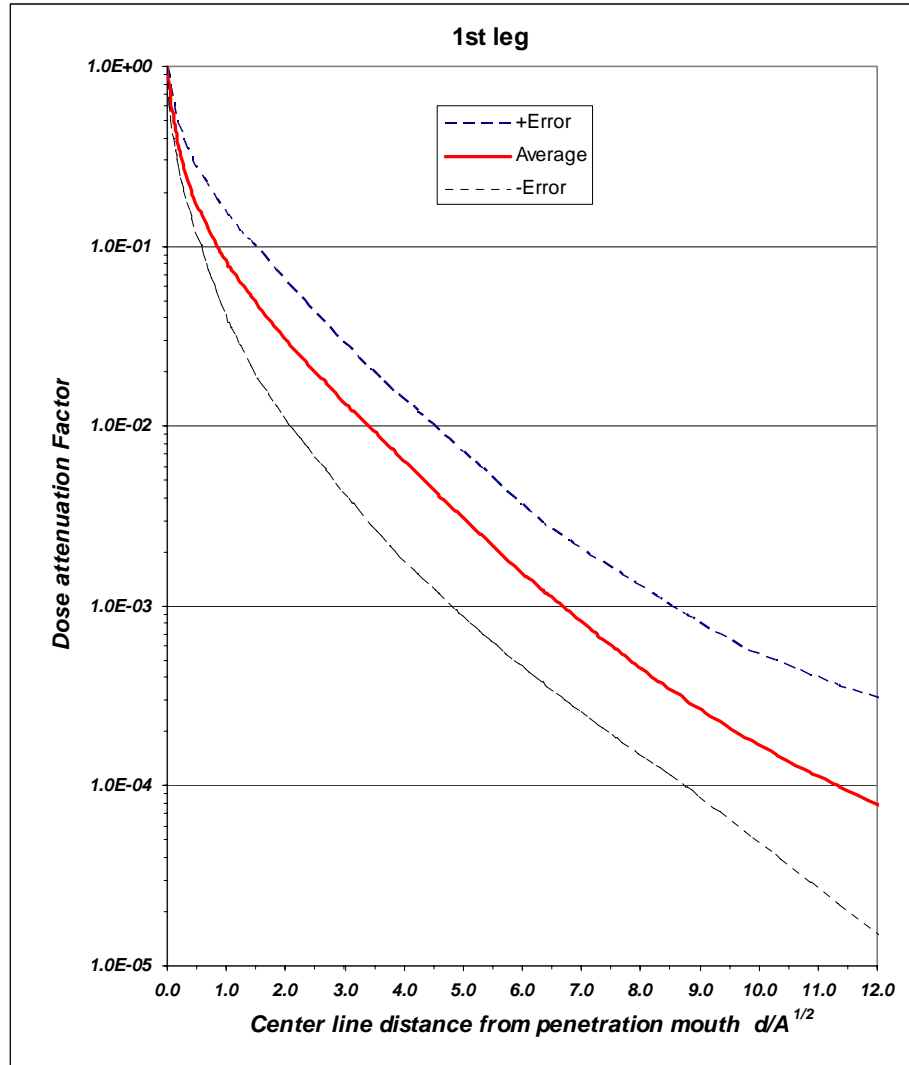
"B" Values - 2nd Leg

Cross-section Length			
	1 GeV	100 MeV	30 MeV
	1.00E+09	1.00E+08	3.00E+07
50	2.7405 ± .0088	3.2142 ± .0114	3.1927 ± .0121
100	2.6785 ± .0105	2.9335 ± .0150	3.0047 ± .0050
200	2.9672 ± .0111	2.7024 ± .0077	2.7108 ± .0097
300	2.7552 ± .0112	2.8368 ± .0085	2.6838 ± .0079
400	2.7097 ± .0101	2.8785 ± .0121	2.8963 ± .0112
	10 MeV	3 MeV	1 MeV
	1.00E+07	3.00E+06	1.00E+06
50	2.5605 ± .0063	2.7672 ± .0078	2.7336 ± .0044
100	2.4777 ± .0051	2.7531 ± .0113	2.7886 ± .0046
200	2.6469 ± .0062	2.805 ± .011	2.8245 ± .0051
300	2.5891 ± .0057	2.7765 ± .0088	2.9824 ± .0068
400	2.8354 ± .0081	2.805 ± .009	2.9805 ± .0057
	100 KeV	12 KeV	1200 eV
	1.00E+05	1.20E+04	1.20E+03
50	2.8148 ± .0058	2.8931 ± .0112	2.9745 ± .0138
100	2.8708 ± .0062	2.9772 ± .0111	3.1134 ± .0121
200	3.3451 ± .0062	3.362 ± .012	3.0547 ± .0195
300	3.6073 ± .0059	3.616 ± .012	3.6491 ± .0118
400	3.7186 ± .0157	3.9623 ± .0205	3.7931 ± .0238
	120 eV	12 eV	thermal
	120	12	0.025
50	2.978 ± .006	2.8859 ± .0115	2.9353 ± .0108
100	2.9139 ± .0065	3.1396 ± .0124	3.0329 ± .0111
200	3.2406 ± .0136	3.6434 ± .0157	3.4723 ± .0138
300	3.571 ± .019	3.663 ± .014	4.0157 ± .0198
400	3.7558 ± .0225	4.1401 ± .0241	4.0245 ± .0186

**Table 4**  
**Calculated *b* values from the second leg with propagated error.**

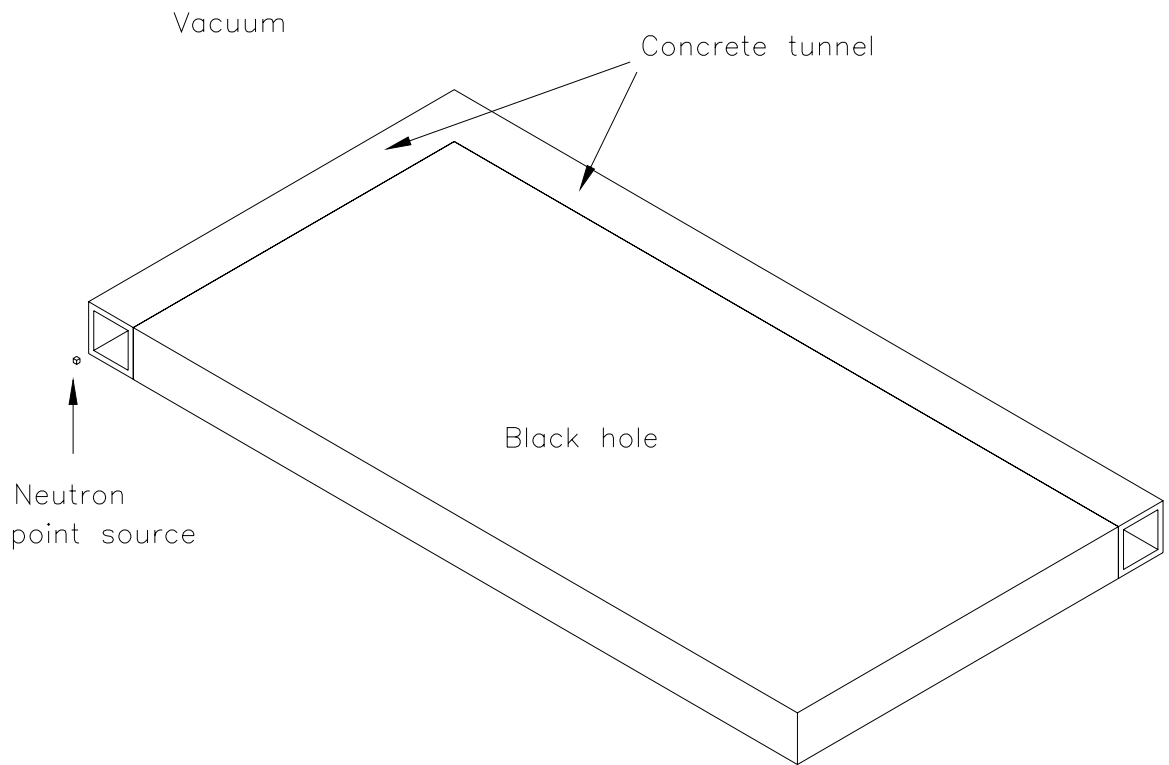


**Figure 1**  
**Dangerous radiation is attenuated by multiple reflection through a series of tunnels.**

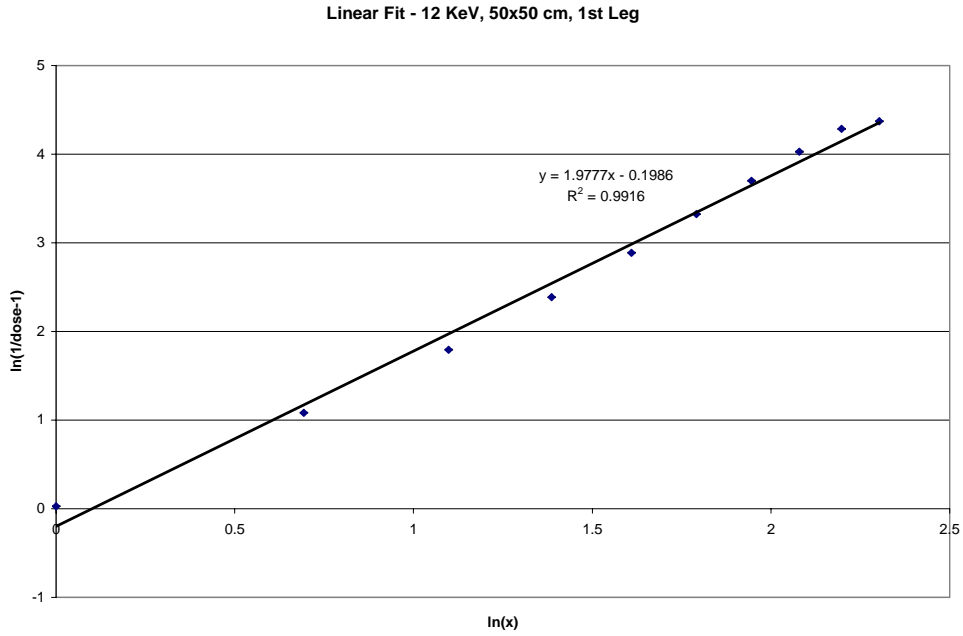


**Figure 2**

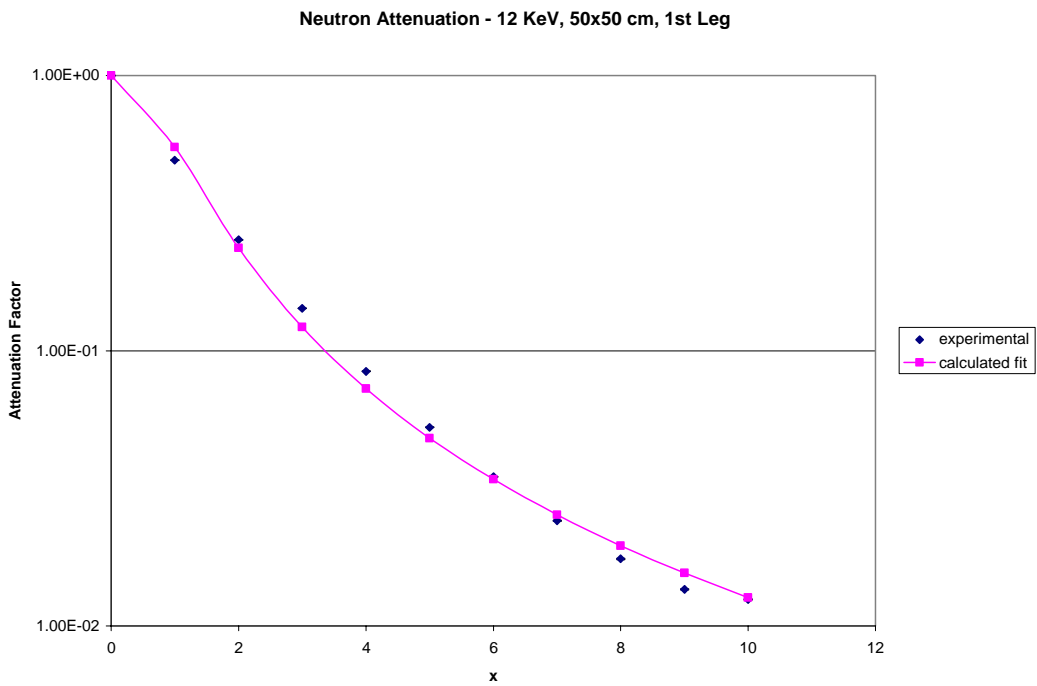
**One version of the universal transmission curve, created by K. Goebel et al. at CERN in 1975 and included for publication in “Radiological Safety Aspects of the Operation of Proton Accelerators” by R. H. Thomas et al. for the IAEA in 1988.**



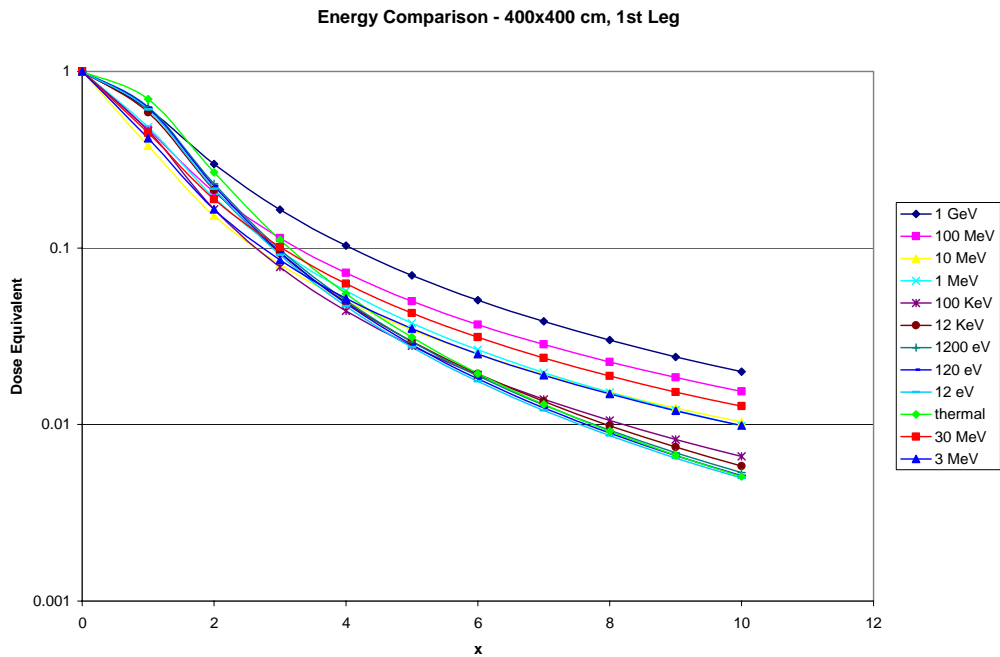
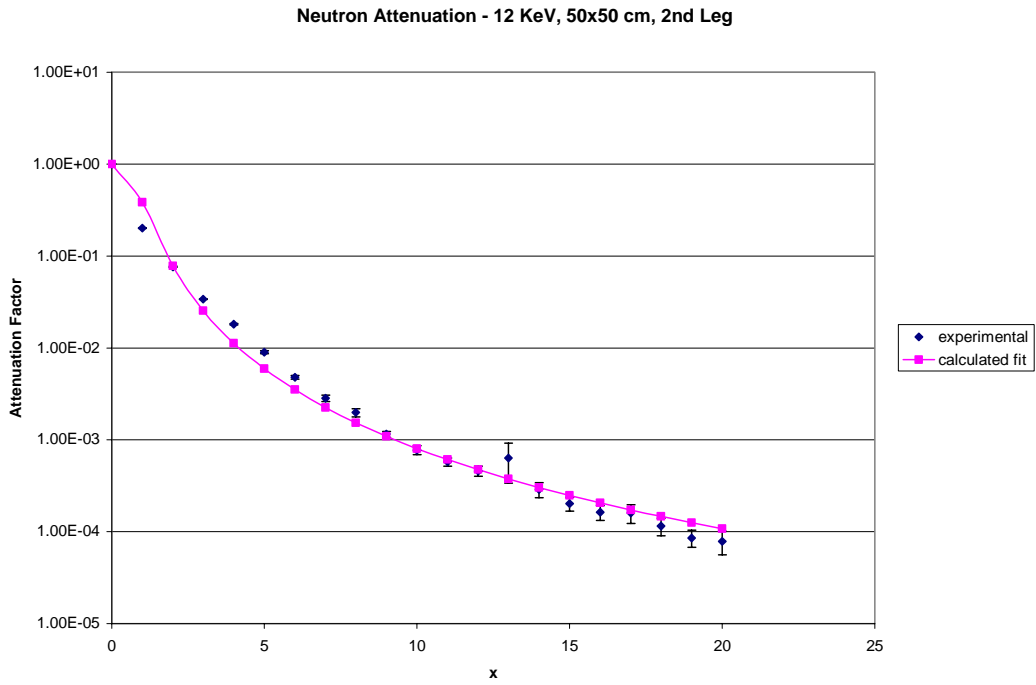
**Figure 3**  
**This simulated labyrinth model was designed to experiment with neutron attenuation.**



**Figure 4**  
**A plot of attenuation data in the form of Eq. 4, producing a linear relationship.**



**Figure 5**  
**An example of a curve of the form of Eq. 2**  
**matched to some experimental data from the first leg.**



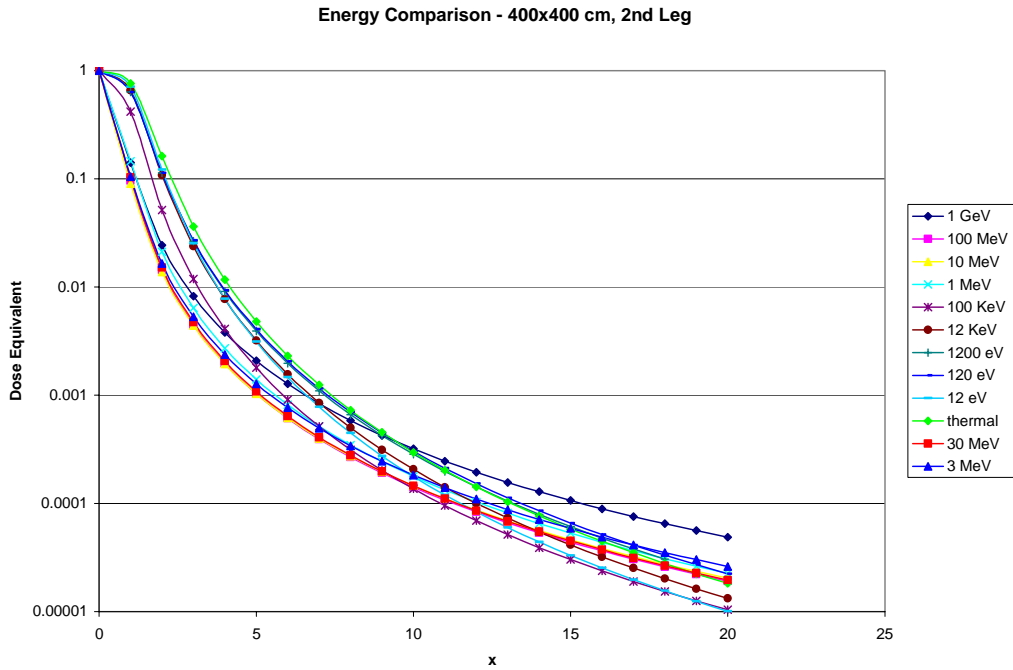


**Figure 8**  
An energy comparison in the second leg for the 400x400 cm geometry.

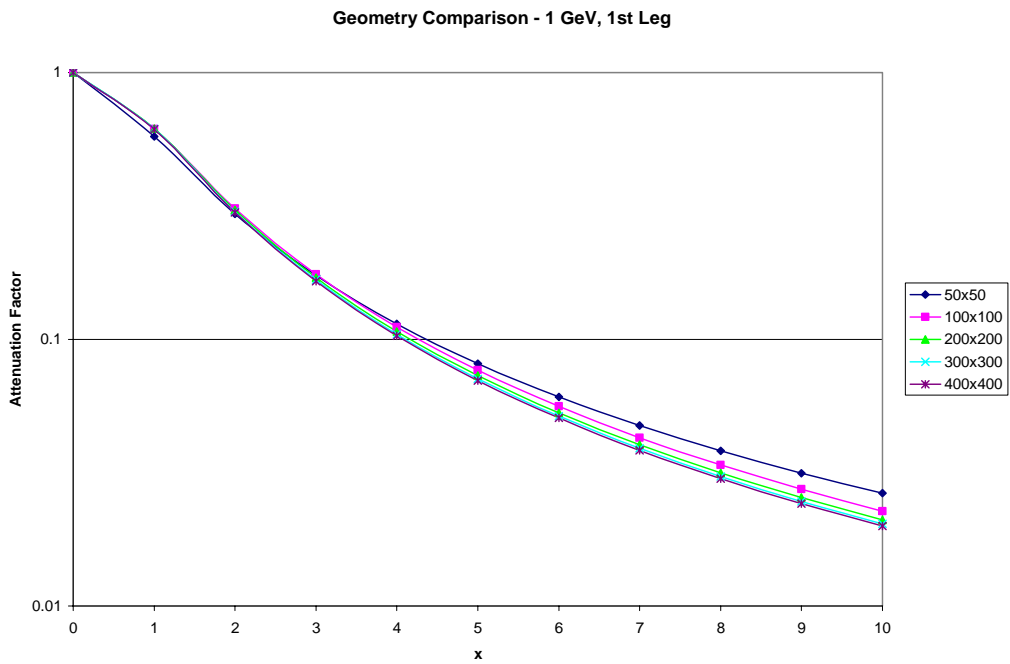


**Figure 9**  
A comparison of the geometry curves in the first leg for 1 GeV.

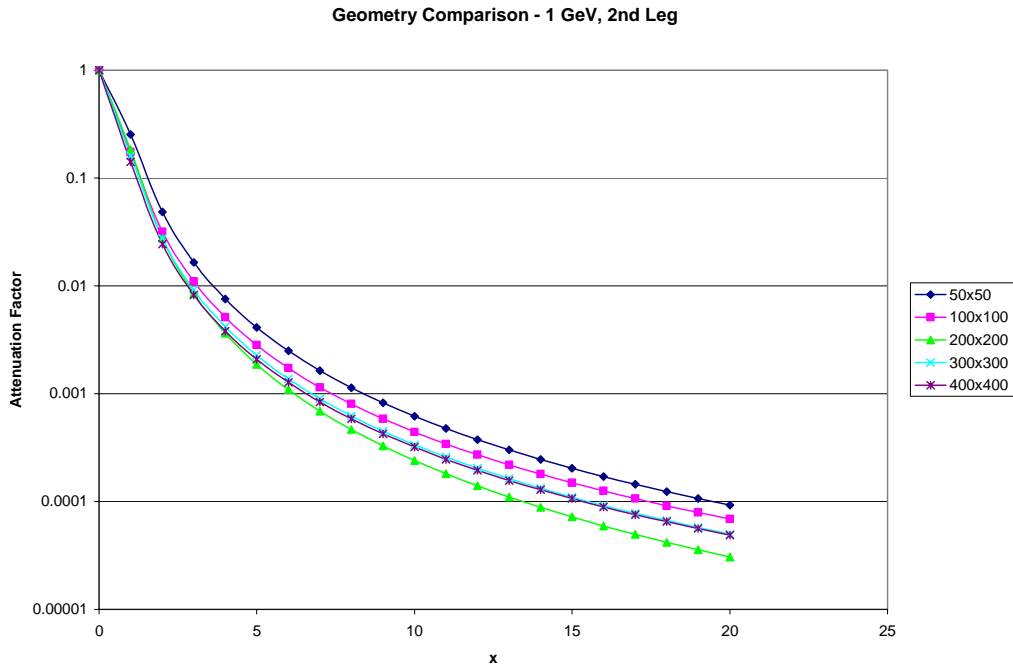


**Figure 10**  
A geometry comparison in the second leg for 1 GeV.

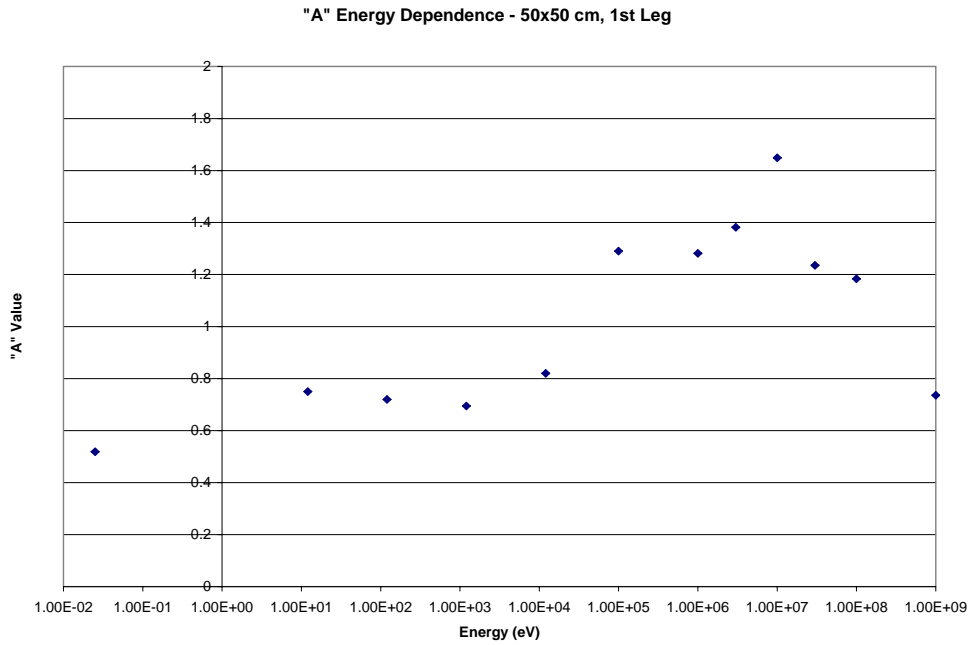


**Figure 11**  
 $a$  as a function of energy in the first leg.  
The sudden drop may be a sign of neutron scattering.

"A" Energy Dependence - 50x50 cm, 2nd Leg

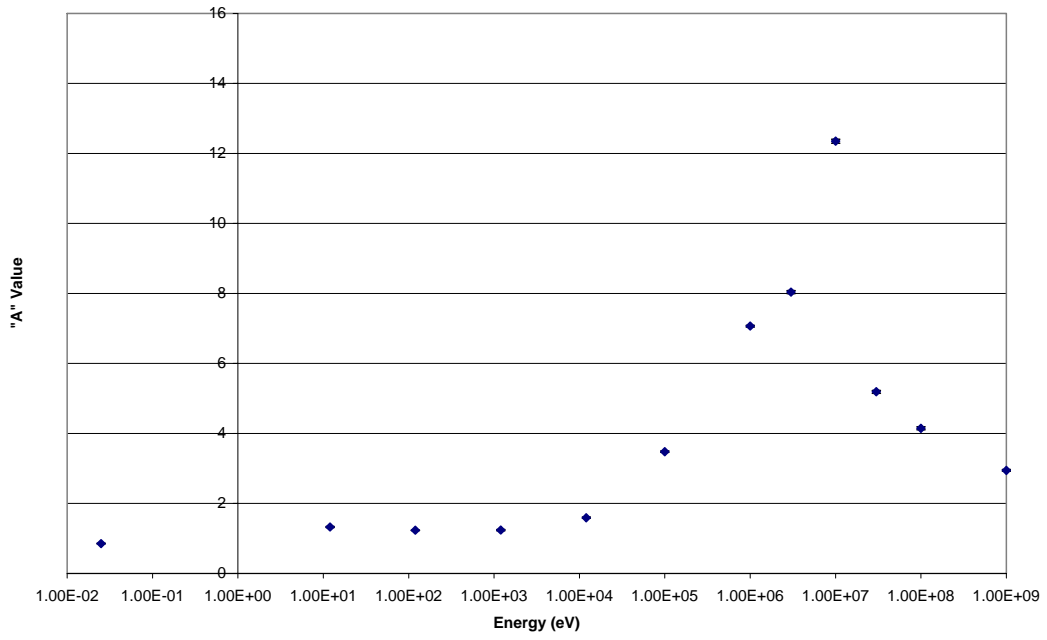


**Figure 12**  
*a* as a function of energy in the second leg.

"A" Geometry Dependence - 100 MeV, 1st Leg

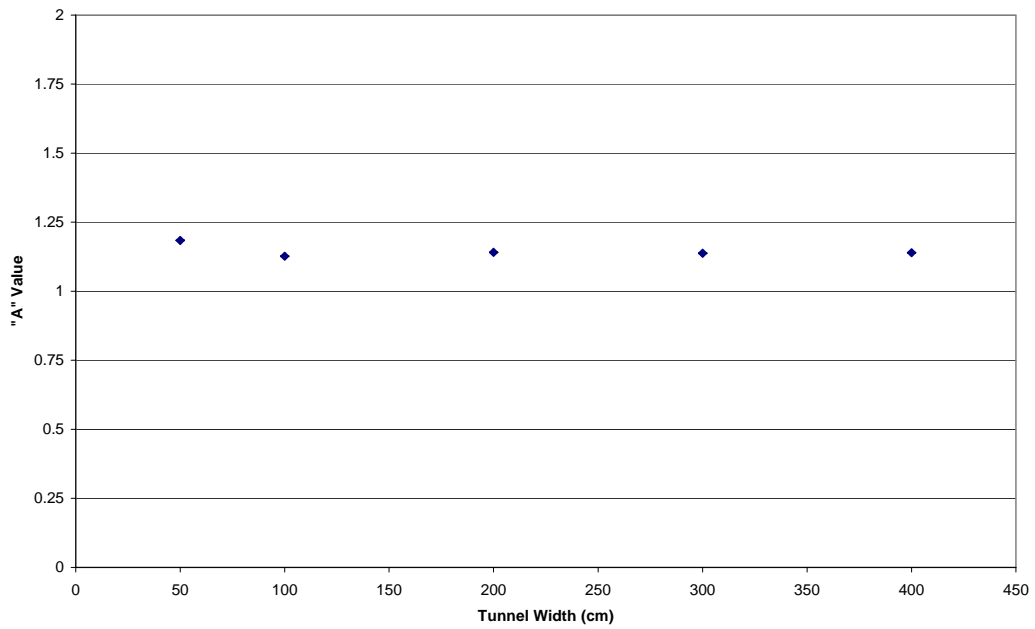


**Figure 13**  
*a* remains relatively constant throughout the different geometries.

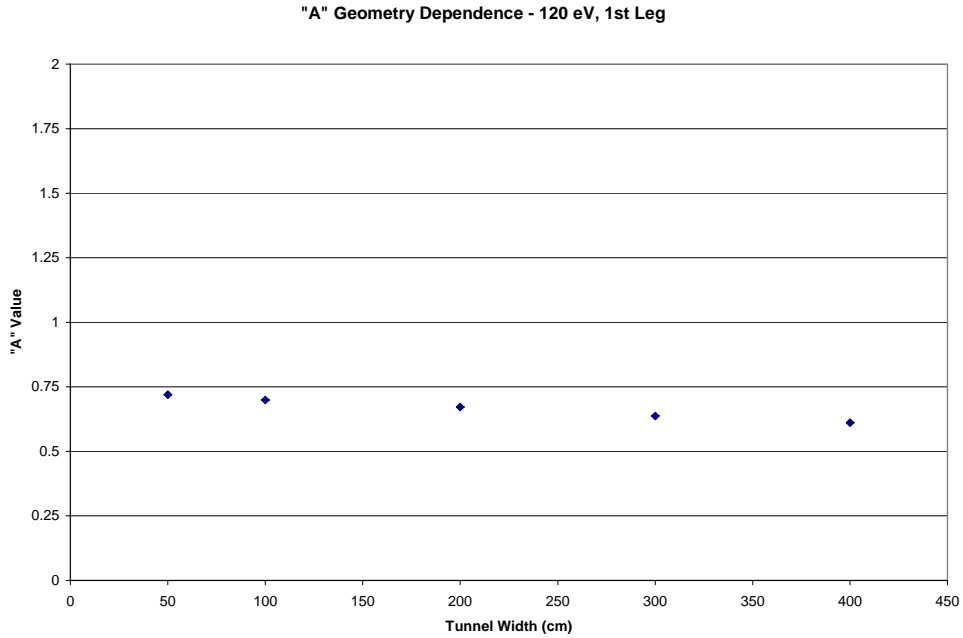


**Figure 14**  
*a* seems to decrease linearly, although the change is still very small.  
 This pattern was observed at all energies below 1 MeV.

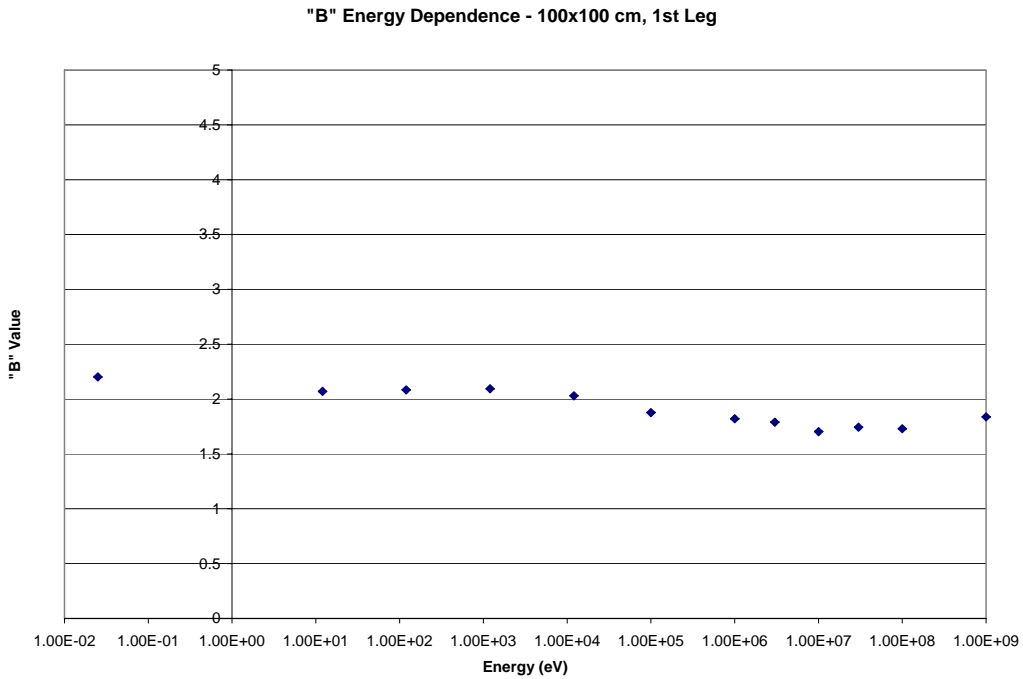


**Figure 15**  
*b* as a function of energy in the first leg of the 100x100 cm geometry.  
 The value remains fairly constant.

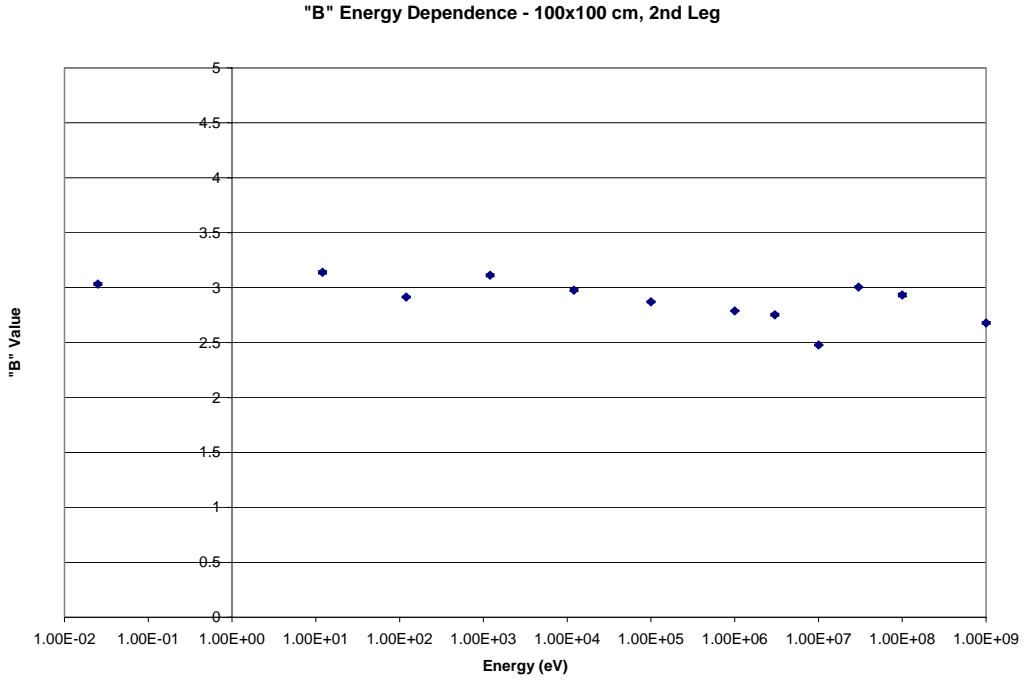


**Figure 16**  
***b* as a function of energy in the second leg of the 100x100 cm geometry.**

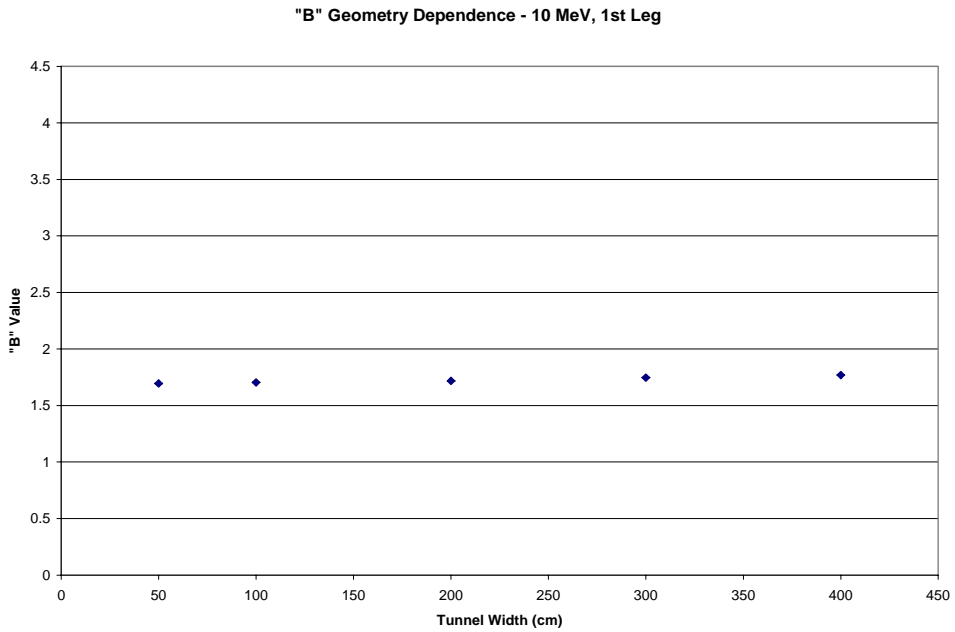


**Figure 17**  
***b* as a function of geometry in the first leg at 10 MeV. Changes in the value are minute.**

"B" Geometry Dependence - 120 eV, 1st Leg

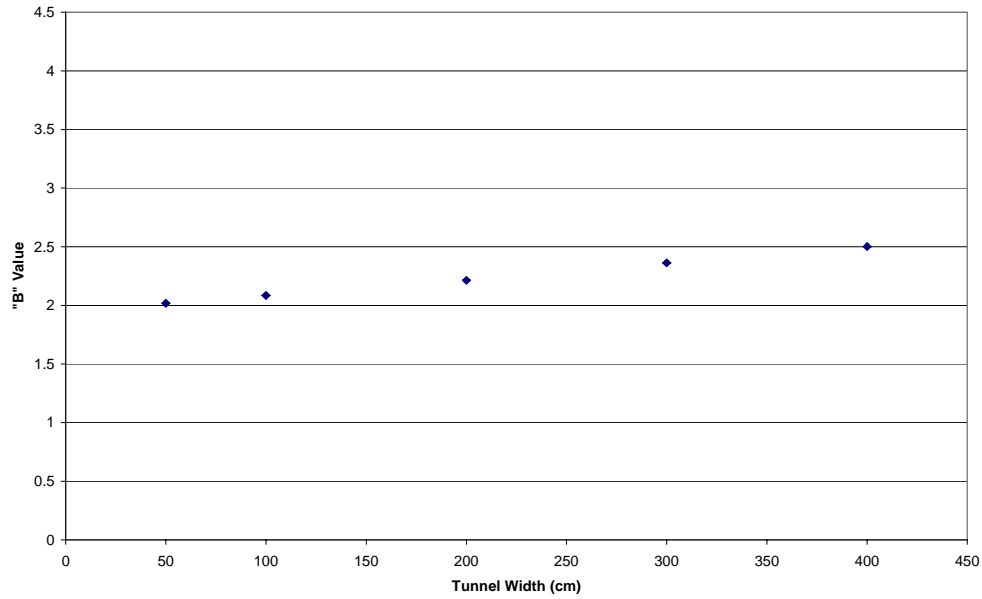


Figure 18

*b* as a function of geometry in the second leg at 120 eV. Although still fairly constant, the value appears to linearly increase at a gradual rate. This pattern was observed at all energies below 1 MeV.

Linear Fit - Thermal, 300x300 cm, 2nd Leg

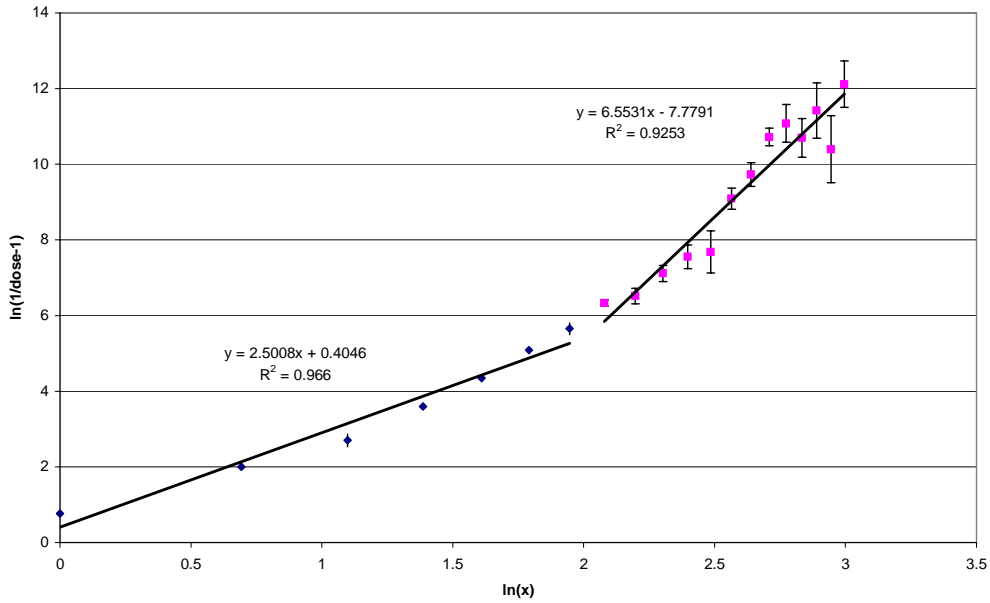
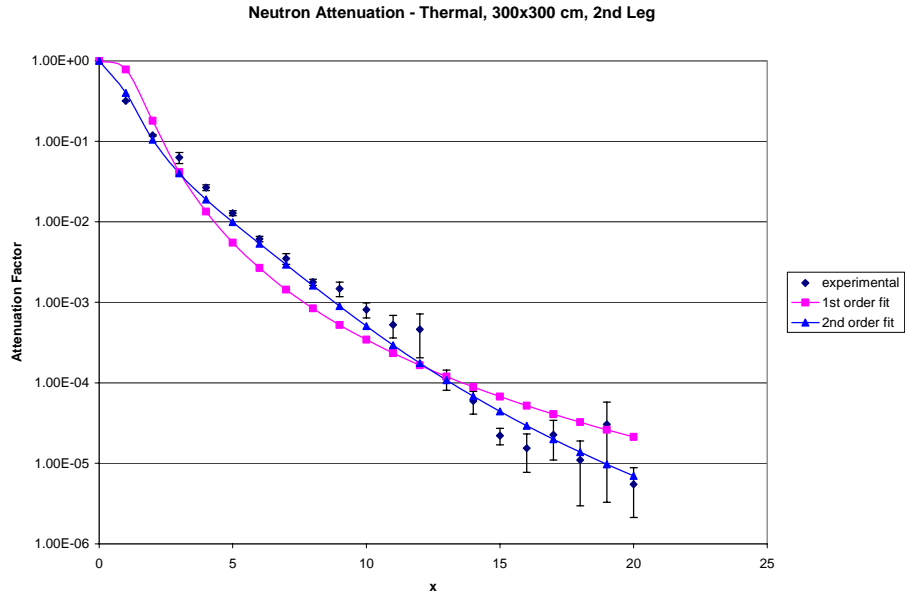
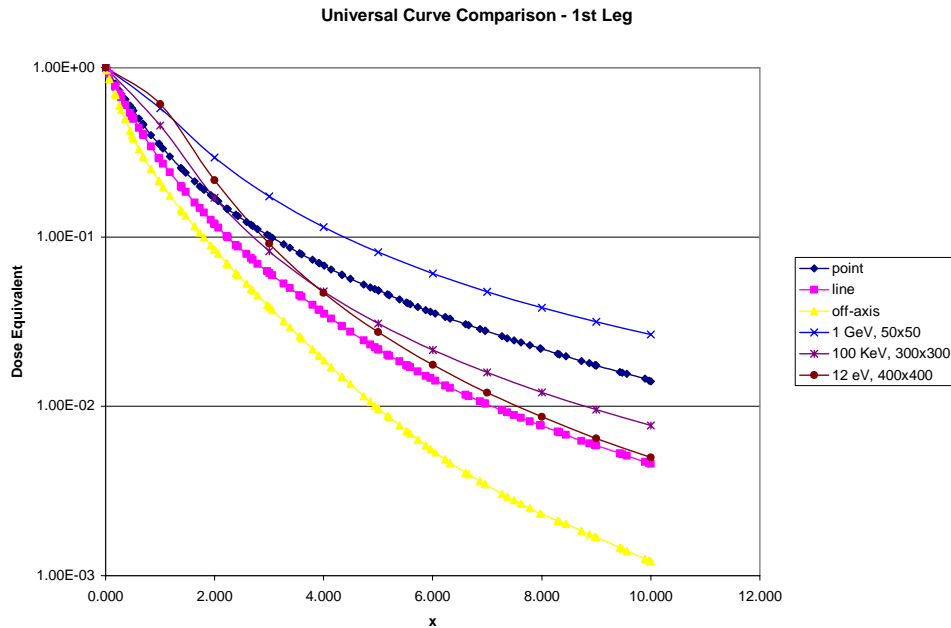


Figure 19

The logarithmic data is matched more accurately with two lines rather than one.



**Figure 20**  
**A comparison of the original fit using Eq. 2 and the new fit using Eq. 5. The second-order fit follows the data more closely, and the inflection is less apparent.**



**Figure 21**  
**Three experimental curves compared to curves from three types of sources. The point source curve appears to be an accurate average of the experimental curves across the energy spectrum.**

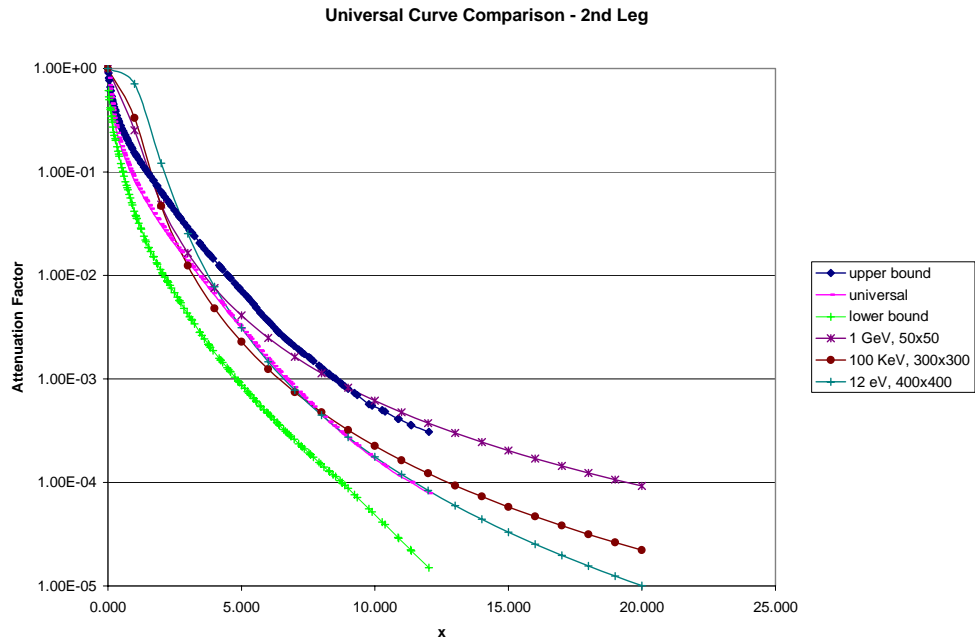


**Figure 22**  
**Three curves at different energies superimposed on the universal transmission curve. For the most part, the curves stay within the bounds, but there is some straying at large distances.**

**A Fast Monte Carlo Simulation for the  
International Linear Collider Detector**

Daniel Furse

Office of Science, SULI Program

Georgia Institute of Technology

Stanford Linear Accelerator Center

Menlo Park, California

August, 2005

Prepared in partial fulfillment of the requirements of the Office of Science, U.S. Department of Energy Science Undergraduate Laboratory Internship (SULI) Program under the direction of Dr. Timothy Barklow in the Particle Physics Division of Stanford Linear Accelerator Center.

Participant:

\_\_\_\_\_  
Signature

Research Advisor:

\_\_\_\_\_  
Signature

# A Fast Monte Carlo Simulation for the International Linear Collider Detector

Daniel Furse

3 Aug 2005

## **Abstract**

The following paper contains details concerning the motivation for, implementation and performance of a Java-based fast Monte Carlo simulation for a detector designed to be used in the International Linear Collider. This simulation, presently included in the SLAC ILC group's `org.lcsim` package, reads in standard model or SUSY events in STDHEP file format, stochastically simulates the blurring in physics measurements caused by intrinsic detector error, and writes out an LCIO format file containing a set of final particles statistically similar to those that would have found by a full Monte Carlo simulation. In addition to the reconstructed particles themselves, descriptions of the calorimeter hit clusters and tracks that these particles would have produced are also included in the LCIO output. These output files can then be put through various analysis codes in order to characterize the effectiveness of a hypothetical detector at extracting relevant physical information about an event. Such a tool is extremely useful in preliminary detector research and development, as full simulations are extremely cumbersome and taxing on processor resources; a fast, efficient Monte Carlo can facilitate and even make possible detector physics studies that would be very impractical with the full simulation

by sacrificing what is in many cases inappropriate attention to detail for valuable gains in time required for results.

# 1 Background

The International Linear Collider collaboration was officially formed in 1998 following a meeting of the group's inaugural committee at ICHEP in Vancouver and has persisted ever since at the forefront of the worldwide effort toward the eventual construction of a TeV range  $e^+e^-$  linear collider. This group is secondarily split along continental lines into three main semi-autonomous collaborations. In Europe and centered at Hamburg (part of the DESY group) is the ECFA collaboration, which did a great deal of work early on in designing a mid-size,  $B = 4T$  detector; their main design report [1] continues to be a good source of ballpark figures and parameterizations for detector performance. In Asia and centered in Japan at KEK is the ACFA collaboration, which mainly works on a lower B-field, larger tracker detector design. Finally, strongly represented at SLAC and with groups scattered over most of North America is the ALCPG group, with whom this project has been conducted.

Clearly, most of the attention given to plans for this future accelerator falls on the design of the detector itself, which is natural given its proportionately higher cost and complexity. Since the energy ranges in which this collider will be operating demand a linear design, this reduces the number of possible detector sites to one (compare, say, CERN with four different detectors), which in turn forces a number of compromises to be drawn. The detector that is finally built must have good position and energy resolution in all of its component parts (rather than, say, using different detectors for different types of measurements) and be nearly hermetically sealed in order to ensure an accurate characterization of collision events. This all must be done while optimizing cost: a task which demands high-quality, easily accessible knowledge of what an arbitrary detector design is capable of. It is the pursuit of this sort of performance data that drives almost all the computer simulation efforts for the ILC here at SLAC.

## 2 Motivation

The task of fully simulating the response of a particle detector to a high energy physics event is, without a doubt, computationally daunting; so much so in fact that it must be handled as a set of separate problems. The entire task is quite naturally broken down into three phases, each with an independent goal and different file type, allowing for analysis code to be conveniently run at points in the middle of the full process. The first of these phases is event generation, whereby a physicist can produce a file containing potentially millions of different instances of a particular high-energy event. Event generation programs offer varying degrees of control over the type and realism of events produced, allowing a user to condition the output according to his needs. This flexibility is extremely important in producing meaningful statistical studies of detector behavior, and we exploit it fully in conducting the studies in the subsequent sections on performance. The particular event generation program used here is called Whizard, which uses Monte Carlo methods to simulate many details of particle events, including decay chains, bremsstrahlung, and gluon radiation. Whizard will typically take electrons and positrons and produce a specific type of event, which it then naturally simulates on through decays down to particles stable enough to interact with a normal particle detector; this list of particles includes photons, electrons, muons, neutrinos, pions,  $K_{long}^0$ -s, protons and neutrons. All of this event information (particle types, momenta, energies, parentage information, etc.) is written to an output file in STDHEP format, which is the input file for the next stage.

The next step is to take the final state particles and simulate the minute details of their interaction with the detector. The program we typically use for this is a variant of the widely-known Geant4 program made at CERN for their simulation studies; its installation at SLAC is called SLIC. SLIC will take an STDHEP file and detector description (usually formatted as Java code) as input, producing raw detector hits as information in the output file.

These hits are really just singlets or doublets of data, being either only an id flag identifying which part of the detector was activated (tracker elements produce such hits) or an id flag and a value (such as a calorimeter cell would produce). In order to produce such a file, Geant4 takes the final state particles and swims them through the simulated detector, allowing photons to randomly pair-produce as they pass detector components, allowing neutrons to produce showers of hits in the calorimeter, among other things, all in a very realistic and exhaustive way, particle by particle.

The final step in a full simulation is reconstruction; this section is different than the other two in that the algorithms implemented are also used in reconstructing events that produced actual detector data. The goal of the reconstruction programming is to take the raw data in the LCIO file produced by SLIC and reproduce the STDHEP events as closely as possible, thus giving a good measure of how well detector and code are working together to extract physics from data. To be most accurate, the reconstruction code is really part of the detector itself, as weak points in the algorithms are manifestly indistinguishable from errors intrinsic to the detector—it is therefore of utmost importance to have the best possible reconstruction code with little regard for speed. Currently, the ILC group at SLAC is still fine-tuning the calorimeter cluster reconstruction portions of their code, which gives a sense of the seriousness of this step.

Clearly, this is a long and complicated process (a flowchart of the data path can be found in the appendix) where accuracy is absolutely the first priority, a fact which meets many needs very well. But there is also a large and important set of information concerning general detector properties and dependences of physics data quality on said properties that elicits a much different priority ordering. When trying to get a good range for the solenoidal field needed in the detector or when trying to estimate what the best size is for a tracking chamber in a detector looking for certain Higgs events, a tool like the full SLIC + reconstruction is far from ideal. It is this type of data

and the need for it that is best addressed by a fast Monte Carlo simulation, one that statistically matches the full Monte Carlo as closely as possible in important areas without getting into the details of raw data. A good Monte Carlo simulator will be readily reconfigured to simulate different detector descriptions, all while remaining fast and satisfactorily faithful to the full simulation. Bringing to fruition such a simulator and optimizing it has been the primary task of this project.

### 3 Implementation

The group at the spearhead of SLAC's ILC-related simulation efforts is currently developing a Java-based reconstruction and analysis package called `org.lcsim`, which can be run either stand-alone or plugged into the Java Analysis Studio (JAS) 3 framework. From JAS3, one can load and run analyses on almost any section of the full `org.lcsim` package of classes and generate histograms and fitted curves for any set of data. The fast Monte Carlo simulator will be a part of this package, and itself can be run either stand-alone or inside of JAS3. Also presently included in the `org.lcsim` package is a snippet of analysis code written to evaluate the performance of the fast MC. This code divides the detector into thrust hemispheres using the plane normal to the thrust axis calculated for particles created in the detector and then generates histograms for the jet energy resolution by calling all the particles in each thrust hemisphere members of a jet. Histograms generated by this code for two-jet  $e^+e^- \rightarrow u\bar{u}$  events can be found in the performance section of the paper.

The fast MC itself, being an alternative to SLIC + reconstruction, needs to take the type of input SLIC works with and generate files similar to those the reconstruction algorithm generates. Hence, the fast MC will read in STDHEP files, then directly smear each final state particle and create a detector object appropriate for the particle type and charge, along with a

reconstructed particle object for all particles except neutrinos. This means that different sets of smearing algorithms are needed depending on the part of the detector a specific particle interacts with, the different detector component behaviors being governed by independent sets of parameters. A good initial source for developing effective methods has again been provided by the DESY group's TESLA design report[1]. This report provides some excellent information as to the dependences of detector component resolutions on event variables as well as the dependences of these resolutions on construction variables, which while not directly accessible in the fast MC do provide realistic limits on the MC parameter ranges. Another good source of implementation examples is an older fast MC program written in FORTRAN called SIMDET[2]; we borrow lightly from this program and actually have used its performance characteristics as a baseline goal which we hoped to surpass. All of the different methods we implemented are outlined in the sections below, which break down the mathematical core of the program by detector components.

### 3.1 Calorimeter Methods

For all of the dynamical variables measurable from a cluster of calorimeter hits associated with a particle (energy, momentum direction and particle species, to a degree), we take the STDHEP particle's properties and smear them according to various stochastic formulae:

- Energy Smearing:

$$E_{recon} = E + \mathcal{R}_g \cdot \left\{ E \left( \frac{a}{\sqrt{E}} + b \right) \right\} \quad (1)$$

Where  $\mathcal{R}_g$  is a gaussian random number with a standard deviation of one and a mean of zero, and  $E$  is the energy of the STDHEP file

particle for which we're generating a cluster. There are separate parameters  $a$  and  $b$  for both the electromagnetic calorimeter and the hadronic calorimeter.

- Position (Momentum) Smearing:

$$\vec{r}_{recon} = r_{det}(\theta, \phi) \cdot \left\{ \frac{a}{\sqrt{a^2 + b^2 \mathcal{R}_g^2}} \hat{r} + \frac{b \mathcal{R}_g}{\sqrt{a^2 + b^2 \mathcal{R}_g^2}} (\sin(\mathcal{R}\phi) \hat{v}_1 + \cos(\mathcal{R}\phi) \hat{v}_2) \right\} \quad (2)$$

Where again  $\mathcal{R}_g$  is a gaussian random number, plain  $\mathcal{R}$  is a random number flatly distributed between zero and one,  $\hat{r}$  is a unit vector pointing from the interaction point to the STDHEP particle's actual position at the face of the calorimeter,  $\theta$  is the angle  $\hat{r}$  makes with the beampipe,  $\phi$  is the azimuthal angle of  $\hat{r}$ ,  $\hat{v}_{1,2}$  are any unit vectors that along with  $\hat{r}$  comprise an orthonormal set, and finally where the function  $r_{det}(\theta, \phi)$  describes the shape of the inside of the calorimeter.

- Efficiency:

$$P(E) = 1 - \frac{1}{1 + e^{b \cdot (E-a)}} \quad (3)$$

This equation gives the probability of a particle of energy  $E$  to be observed in a calorimeter. The parameters  $a$  and  $b$  are called, respectively, the onset and the sharpness. It may be immediately clear, but  $a$  is the energy at which a particle will be observed half of the time, and the parameter  $b$  is  $2 \cdot \frac{dP}{dE} |_{E=a}$ .

This function may be made arbitrarily close to step-like as the user wants simply by increasing  $b$  to a very high value, normally 10,000. A picture of the function can be found below, in Figure 1:

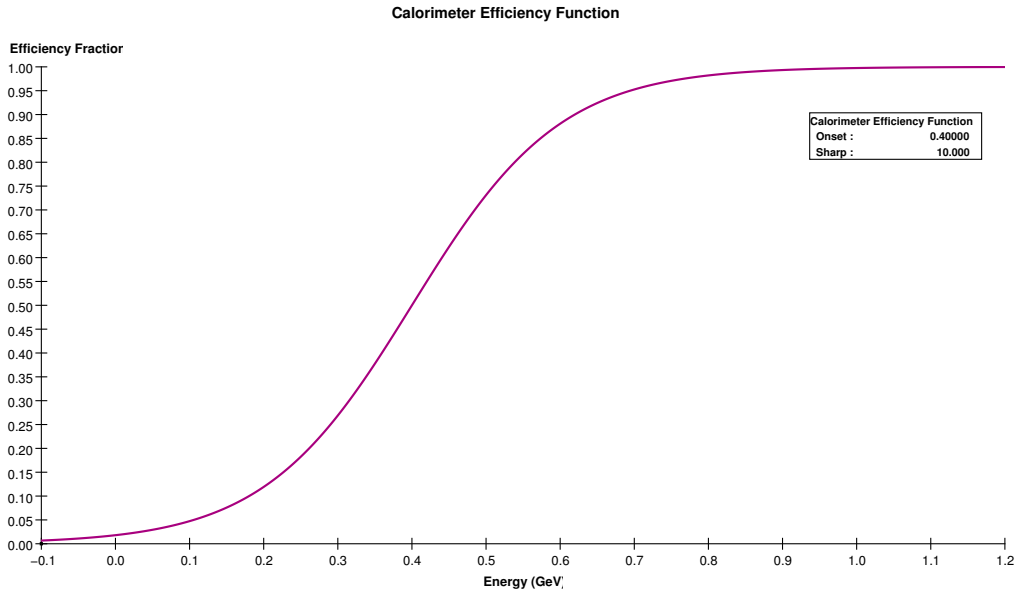


Figure 1: The basic efficiency function used in the org.lcsim fast MC; this function is incidentally called the Woods-Saxon potential and is used to model the strong-force binding potential nucleons feel inside heavy nuclei.

This concludes the list of methods that are easily associated with a single formula. The following sections concern smearing methods that are more programmatic; incidentally, these phenomena affect the physical results the detector can deliver to a much lesser degree than those described above.

- Particle Identification:

The ability of the detector to correctly identify particles is modeled according to the following prescription. All stable, charged tracks

are at first assumed to be pions (this is, statistically, an excellent assumption), but if the particle actually is not a pion the program will throw a flatly distributed random number to determine whether or not the particle is correctly identified, with separate efficiencies for protons, electrons, and muons. If the random number is below the efficiency for the particle specified, the fast MC identifies the non-pion particle correctly in the output file. Similarly, all neutral clusters are assumed to be associated with  $K_{long}^0$  impacts, but there is an efficiency for correct neutron identification. Photons leave such a distinctive burst in the electromagnetic calorimeter that they are assumed to be correctly identified 100% of the time, which is again an excellent assumption. Currently, all identification efficiencies are constant throughout the energy range of the detector, due to the fact that the actual efficiencies and dependences we are trying to mimic are completely dependent on the quality of the reconstruction algorithms which, as mentioned previously, are still being developed. As soon as we can assess the function that best matches the identification quality's dependence, it can be easily included in the program.

- Cluster Overlap Compensation

While the effects of having clusters overlap are quite small (by design) in the current ILC detector, the method is so mathematically interesting that it has been included anyway. There are, fundamentally, two separate phenomena that can occur as a result of clusters landing on top of each other. The more severe of these two processes is complete cluster confusion, in which two clusters of hits are in such close proximity and so entangled with each other that a reconstruction program will more than likely confuse them as one large cluster. This effect is simple to model, with the probability for any two clusters  $i$  and  $j$  being confused

given by:

$$P_{ij} = \iint_{Cal} d^2r \left( \frac{1}{\sqrt{2\pi b_i^2}} e^{-\frac{(\vec{r}_i - \vec{r})^2}{4b_i^2}} \right) \cdot \left( \frac{1}{\sqrt{2\pi b_j^2}} e^{-\frac{(\vec{r}_j - \vec{r})^2}{4b_j^2}} \right) \quad (4)$$

Where the integral is over the surface of the calorimeter face, and the parameter  $b_i$  could potentially depend on particle  $i$ 's energy and type. In a current version (still in testing), all  $b_i$  are constant, and set to the same value as the  $b$  mentioned parameter in the momentum smearing section. Since the gaussians are symmetrical, the probability of confusion only depends on the separation of the centroids; the formula resulting from evaluating the integral above is how the dependence is actually implemented in the program:

$$P_{ij} = e^{-\frac{\|\vec{r}_i - \vec{r}_j\|^2}{8b^2}} \quad (5)$$

To actually simulate confusing clusters and make use of the probability formula stated above, the program makes a list of integers with as many elements as there are clusters, and then runs through all possible combinations of clusters. If a flat random number compared with  $P_{ij}$  as calculated above indicates that a certain combination  $ij$  should be confused, the program will put the value of the lower of the two indices  $i$  and  $j$  into the slot in the list corresponding to the higher index, then proceed to the next combination; proceeding in this manner causes trees of confused hits to branch outward toward higher numbers, with the base node of the tree having the lowest index of all the cluseters it contains. After this process is complete, the program runs backwards over the list containing the confusion information conveniently enabling the program to run over any trees of hits it has created from branch to root, since a lower-numbered node will be closer to the

root of a given tree. While scanning, if bin  $i$  contains a value  $j$  different from -1, the program reassigns the position of cluster  $j$  as an energy-weighted average of  $i$ 's position and  $j$ 's position, dumps  $i$ 's energy into cluster  $j$ , and then removes cluster  $i$  from the list. The list containing the confusion data is then dumped, and the remaining list of clusters represents the list of clusters that the reconstruction program actually has a chance of generating.

The other aspect of cluster confusion is the difficulty in dividing energy up between clusters that lie in close proximity. In order to simulate this effect accurately, we will remind ourselves of the fact that if a group of clusters is reasonably isolated, one can very accurately know the total energy of the cluster while still making significant errors in assigning partial energies to the individual clusters in the group. We can take such a group of isolated clusters and let it include the entire calorimeter, and then we arrive at the fact that the total energy deposited in the calorimeter should be an invariant quantity under any reasonable cluster confusion simulation. When we look (quite suggestively) at cluster confusions as transformations acting on the configuration of hits in the detector that must preserve a certain kind of sum, we see that energy partitioning errors for  $n$  calorimeter clusters can be very well modeled by transformations belonging to the group  $SO(n)$ . This is done by introducing a stochastic  $SO(n)$  smearing operator which acts on an energy vector defined as having elements  $\sqrt{E_i}$ , where  $E_i$  is the energy of the  $i$ th cluster; hence  $\vec{\sqrt{E_i}} \cdot \vec{\sqrt{E_i}} = \sum_i E_i$  is preserved. Since we demand that the smearing operator be part of  $SO(n)$ , we know it will have the following form:

$$\mathcal{O} = e^{c_{ij}g_{ij}} \tag{6}$$

where  $g_{ij}$  are the  $\frac{n(n+1)}{2}$  generators of  $SO(n)$  and the coefficients  $c_{ij}$  are free for us to define as we choose. Since  $c_{ij}$  represents the angle through which we want to rotate or smear the energy between clusters  $i$  and  $j$ , we will want to restrict  $c_{ij}$  to be on the interval  $[-\frac{\pi}{2}, \frac{\pi}{2}]$ , since the functions  $\cos^2 \theta$  and  $\sin^2 \theta$  are bijective on  $[0, \frac{\pi}{2}]$  and we want to allow the vector to smear symmetrically in both directions without double counting any particular configuration. Hence, we choose our angle to be:

$$c_{ij} = P_{ij} \mathcal{R}_g - \frac{\pi}{2} \cdot \left\lfloor \frac{P_{ij} \mathcal{R}_g}{\pi/2} \right\rfloor \quad (7)$$

Where the mean  $P_{ij}$  of the gaussian portion is calculated in exactly the same way as the probability for completely confusing clusters (see Equation 4), except the standard deviations of the gaussians ( $b_{ij}$ ) may be different in this case. Using such a definition for  $c_{ij}$  causes the probability of smearing to an angle  $\theta$  to be given by:

$$P(\theta) = \frac{1}{\sqrt{2\pi P_{ij}^2}} \sum_{n=0}^{\infty} e^{-\frac{(\theta+n\frac{\pi}{4})^2}{2P_{ij}^2}} = \frac{e^{-\frac{\theta^2}{2P_{ij}^2}}}{\sqrt{2\pi P_{ij}^2}} \sum_{n=0}^{\infty} e^{-\frac{n^2\pi^2}{36P_{ij}^2}} \quad (8)$$

The second infinite series on the line is certainly convergent (by the integral test, if you like), and can be readily calculated exploiting the fact that  $P(\theta)$  is normalized over  $[-\frac{\pi}{2}, \frac{\pi}{2}]$ , which is itself easily demonstrated by exploiting the linearity of integrals:

$$\sum_{n=0}^{\infty} e^{-\frac{n^2\pi^2}{36P_{ij}^2}} = \operatorname{erf} \left( \frac{\pi/2}{\sqrt{2P_{ij}^2}} \right)^{-1} \quad (9)$$

which yields an expression for  $P(\theta)$  that has no series in it:

$$P(\theta) = \frac{1}{\sqrt{2\pi P_{ij}^2}} \cdot \operatorname{erf}\left(\frac{\pi/2}{\sqrt{2P_{ij}^2}}\right)^{-1} e^{-\frac{\theta^2}{2P_{ij}^2}} \quad (10)$$

This concludes our exhaustive treatment of the important feature of cluster confusion; an implementation of the methods described here might be made available in a future version of org.lcsim when the opportunity for tailoring the parameters to match the finished reconstruction algorithm exists.

## 3.2 Tracker Methods

The simulation of tracker error is much more modular and direct than the simulation of calorimeter error; indeed, there is one process performed on each track which simultaneously and interdependantly smears all the physical variables we are concerned with. The procedure requires a track to be parameterized as a five element vector, acted upon by a stochastic operator called the covariant error matrix. Complete details of these methods and a simple variation on them are included below.

- Conversion to DOCA Parameters

The acronym DOCA is an abbreviation for “distance of closest approach”, and the DOCA parameters are a set of five variables that specify a helical trajectory winding around the detector’s magnetic field by describing it at the point of closest approach to the beam axis. The DOCA parameters  $x_i$  are defined as follows (references to a cartesian system assume that the z axis is along the detector axis):

- $x_0 = d_0$  is the helix’s distance of closest approach to the z-axis.
- $x_1 = \phi_0$  is the angle the projection of the track in the x-y plane makes with the x-axis at the point of closest approach

to the z axis.

- $x_2 = \Omega$  is the signed curvature of the track, and is directly proportional to the momentum of the track in the x-y plane, which is itself often called the transverse momentum.
- $x_3 = z_0$  is the z coordinate of the track at the point of closest approach.
- $x_4 = \tan \lambda$  where  $\lambda$  is the angle the track makes with the x-y plane at the point of closest approach.

These five variables are exactly enough to specify the position and momentum of the particle track, since the fact that these are defined to specify the closest approach position on the track implies the constraint  $\vec{p}_t \cdot \vec{r} = 0$ , thus eliminating one of the coordinates from the  $\vec{x}, \vec{p}$  set for the particle. The DOCA parameters are especially convenient for calculating the large set of error matrices discussed in the following section, and the DOCA variables are the ones we'll be working in unless otherwise noted.

- Covariant Track Smearing

The DOCA variables are quite natural for the detector, but they are interdependent; a small error in the curvature will certainly result in an erroneous measurement of, say,  $\tan \lambda$ , so it's necessary to treat this aspect of the problem in a valid statistical fashion. The correct formalism is found by calculating a real, symmetric error matrix (which is also known as the covariance matrix) for the detector which describes how errors couple between variables. Given an error matrix, we can get the statistically independent variables by finding the eigenvectors  $\vec{v}_i$  (which correspond to these independent combinations), whose distributions will be governed by eigenvalues  $\sigma_i$ . We then smear the track according to the matrix by using the following procedure:

$$\vec{X}_{recon} = \vec{X} + \begin{pmatrix} | & | & \cdots & | \\ \vec{v}_1 & \vec{v}_2 & \cdots & \vec{v}_5 \\ | & | & \cdots & | \end{pmatrix} \begin{pmatrix} \mathcal{R}_{g1} \cdot \sigma_1 \\ \mathcal{R}_{g2} \cdot \sigma_2 \\ \vdots \\ \mathcal{R}_{g5} \cdot \sigma_5 \end{pmatrix} \quad (11)$$

Where the set  $\mathcal{R}_{gi}$  is a group of 5 independently drawn gaussian random numbers and recall that the set  $\sigma_i$  are the square roots of the eigenvalues. Hence, the components of momentum and position are all simultaneously taken care of. The main drawback of this method, complete and elegant as it is, is the difficulty of calculating the covariance matrices and implementing them. Since the tracker itself is made up of a set of concentric cylinders, the error matrices describing the tracker will change depending on if the track passes through the endcaps or the barrels of the set. Also, there is an energy dependence on the resolution of the tracker for the various physical variables, and since the detector is not spherically symmetric there will also be a dependence in the matrix on the  $\tan \lambda$  variable. These dependences are taken into account not by constructing an appropriate matrix-valued function, but rather by calculating constant matrices on a discrete lattice of points  $(E, \lambda)$  and linearly interpolating matrices as they are needed. Again, we are faced with the problem that changing the description of the detector is quite difficult, and in order for the fast MC to be an effective tool for the types of physics studies it was designed to this cumbersomeness can be a serious drawback. Answering this shortcoming is a method for quickly modifying the distributions the matrices produce without changing the way the errors propagate between variables, the details of which are described in the following section.

- Modified Covariant Track Smearing

Often, the object of a certain physics study of a detector is to determine the dependence of, say, the average mass resolution for a particle on an intrinsic detector resolution. With the present fast MC this is very easy to do with calorimeter resolutions since the user has direct access to these resolutions, but what about studies involving dependences on tracker resolutions? This is much more difficult to do since the matrix smears all the variables simultaneously. However, it should be mathematically possible to modify the matrices in such a way as to *impose* a resolution on a certain variable while leaving the error mixing properties unaffected. This is indeed true, though figuring out the method is somewhat involved. First of all, we must analyze and interpret the covariance matrix itself: how does the probability of adding a small error DOCA vector  $\delta\vec{X}$  to the original DOCA parameter vector  $\vec{X}$  depend on the covariance matrix  $\hat{C}$ ? In order to answer this question, we must take another look at the method described in the previous section. Firstly, we can rewrite Equation 11 in the following way:

$$\vec{X}_{recon} = \vec{X} + \sum_{k=1}^5 \mathcal{R}_{gk} \sigma_k \vec{v}_k \quad (12)$$

Upon inspection we see first of all that the set of vectors  $\vec{v}_k$  form an orthonormal basis, being the eigenvectors of a hermitian matrix; as such they differ from the standard Cartesian set only by a transformation belonging to  $SO(5)$ . Also, we see that the standard deviation of the distribution describing the probability of drawing a certain component in the direction  $\vec{v}_k$  is exactly  $\sigma_k$ . We can assimilate this information in a single statement by writing down the probability of drawing a correction vector  $\delta\vec{X}$ :

$$P(\delta\vec{X}) = \prod_{k=1}^5 \frac{1}{\sqrt{2\pi}\sigma_k} \cdot e^{-\sum_{k=1}^5 \frac{(\delta\vec{X} \cdot \vec{v}_k)^2}{2\sigma_k^2}} \quad (13)$$

Clearly, we now have a statement that tells us how correcting  $\vec{X}$  in a certain way depends on both the covariance matrix  $\hat{C}$  and the DOCA vector  $\delta\vec{X}$ , thus meeting our immediate goal. The most illustrative way to proceed is to geometrically characterize our probability distribution. If we take an isoprobable surface, we will obtain a five-dimensional ellipsoid whose principal axes are oriented along the vectors  $\vec{v}_k$ , which are themselves, recall, mixtures of various DOCA variables. But what if we want to know the distribution a certain matrix will give for a pure DOCA variable, or some other general non-eigenmixture of variables? This is pretty simple if we force  $\delta\vec{X}$  to be of the form  $\xi\vec{u}$ , where  $\vec{u}$  is a vector in the direction of the combination whose distribution we're interested in. Permitting this substitution into Equation 13 and factoring out  $-\xi^2$ , we obtain by inspection the following effective distribution for a combination represented by  $\vec{u}$ :

$$\sigma_{\vec{u}} = \left( \sum_{k=1}^5 \frac{(\vec{v}_k \cdot \vec{u})^2}{\sigma_k^2} \right)^{-\frac{1}{2}} \quad (14)$$

Now that we can say with certainty how a certain matrix is effectively smearing some variable, say  $\Omega$ , we can begin to figure out how to change this distribution without affecting the desirable mixing properties of the covariance matrix. First of all, an object describing the error mixing properties of the covariance matrix must be identified so that we may ensure its invariance. This is done by decomposing a covariance matrix  $\hat{C} = C_{ij}$  in the following way:

$$C_{ij} = \sqrt{C_{ii}}\sqrt{C_{jj}}\Upsilon_{ij} \quad (15)$$

The matrix  $\Upsilon_{ij} = \hat{\Upsilon}$  is the one describing the mixing, and as such we may not touch it; hence we only are allowed to change the elements under the radicals. Since we are mainly going to be worried about forcing distributions on *pure* DOCA variables, we are further constrained to modify only the specific element under the radical corresponding to the variable of interest. For instance, if we're looking to impose a resolution on  $\tan \lambda$ , we only are allowed to modify  $C_{44}$ . So how does changing a single element in the decomposition in Equation 15 affect the effective distribution calculated in Equation 14? Attacking this final, central question analytically is unnatural and cumbersome, and the simple answer can be much more easily obtained by thinking about the problem geometrically. In order to do this, we can rewrite the decomposition in Eq. 15 in matrix form, allowing the matrix  $\hat{\Delta}$  to have diagonal elements  $\sqrt{C_{ii}}$  and off-diagonal elements zero:

$$\hat{C} \rightarrow \hat{\Delta}\hat{\Upsilon}\hat{\Delta} \quad (16)$$

We now allow ourselves to modify the  $j$ th element of  $\hat{\Delta}$  by letting a certain  $\Delta_{jj} \rightarrow \sqrt{a}\Delta_{jj}$ . This can be represented again as a set of matrix operations by introducing a new diagonal matrix  $\hat{A}$  whose single nonunity diagonal element is  $a$ , at the intersection of the  $j$ th row and column. This leads to the identification of the modified covariance matrix  $\hat{C}'$  with the decomposition:

$$\hat{C}' \rightarrow \hat{A}\hat{\Delta}\hat{\Upsilon}\hat{\Delta}\hat{A} \quad (17)$$

Beginning our geometric analysis, we realize first that there is a

certain probability  $\tilde{P}$  whose corresponding isoprobable surface is an ellipsoid with axes whose lengths are themselves the standard deviations for the distribution,  $\sigma_i$ ; in analogy with the one-dimensional distribution this probability  $\tilde{P}$  is shown to be  $1/\sqrt{e}$  times the normalization constant for the function. Hence, calculating distributions of variables is effectively nothing more than measuring “radii” of a certain five-dimensional ellipsoid in various directions. The next necessary realization is that physical equations describing isoprobable surfaces can be obtained by contracting the covariance matrix itself with  $\delta\vec{X}$  enough times and setting that contraction equal to some appropriate constant:

$$(\delta\vec{X})^T \hat{C} \delta\vec{X} = c \tag{18}$$

By plugging in our decompositions of  $\hat{C}$  and  $\hat{C}'$  into the above equation we obtain:

$$\begin{aligned} (\delta\vec{X})^T \hat{\Delta} \hat{Y} \hat{\Delta} \delta\vec{X} &= c \\ (\delta\vec{X})^T \hat{A} \hat{\Delta} \hat{Y} \hat{\Delta} \hat{A} \delta\vec{X} &= c \end{aligned} \tag{19}$$

We can allow the matrices  $\hat{A}$  in the second equation above to act on the vectors  $\delta\vec{X}$  rather than on the matrices, calling the resulting vectors  $\delta\vec{X}'$ . These can be interpreted as vectors belonging to a new coordinate system whose  $j$ th component has been dilated. It takes little convincing to see that the width of an ellipse along a coordinate  $\delta X_i$  which has been stretched by a factor  $\sqrt{a}$  will likewise be stretched by a factor  $\sqrt{a}$ ; furthermore, since the deviations of the full distribution correspond *exactly* to the widths of a particular isoprobable surface, we can say that letting  $\hat{C} \rightarrow \hat{C}'$

as above will cause  $\sigma_{\bar{u}} \rightarrow \sigma'_{\bar{u}} = \sqrt{a}\sigma_{\bar{u}}$ . The problem is therefore solved, with the needed multiplier  $a$  given by:

$$a = \frac{\sigma_{desired}^2}{\sigma_{original}^2} \quad (20)$$

where the deviations are both for the variable of interest. Using this method, we accomplish what we set out to do: we can give the user of the program the same kind of direct access to tracker resolutions as he has to calorimeter resolutions all while preserving the covariance of the tracker smearing method (even though it takes a lot of work to do and a lot of paper to explain).

## 4 Performance

Before releasing any program as a tool intended for general use, thorough testing and characterization must be carried out. In order to test the fast Monte Carlo simulator, a somewhat physically artificial `stdhep` file was written in order to perform debugging and characterization studies; in it an electron-positron pair annihilates to produce an up quark and an anti-up quark, each at exactly 250 GeV. Included in the characterization below performed using this file is an exhaustive group of figures with commentary included demonstrating the capabilities of the simulator at firstly simulating high energy physics events and secondly at extracting meaningful information on how physical results depend on basic detector performance characteristics. In brief, we first show raw particle-by-particle smearing histograms for the set of standard detector parameters, then we show that changing these parameter changes the smearing statistics as advertised in the implementation section. Second we show the results of a simple thrust analysis on the simulated 250 GeV  $u\bar{u}$  events, followed by a study on how changing the detector parameters changes these physical results. Finally, in the last section of the

paper, we perform a simulated measurement of the mass of the  $Z_0$  boson, lightly touching on the dependence of the resolution of this measurement on the detector parameters.

## 4.1 Raw Smearing Results

The standard *sdjan03* detector for the SLAC ILC group currently uses the following fast Monte Carlo parameters:

Electromagnetic Calorimeter Onset:	.1 GeV
EM Cal. Sharpness:	10.0 %/GeV
EM Cal. Minimum: $\theta$ :	$\cos^{-1}$ .95
EM Cal. Energy Resolution Parameter $a$ :	.18
EM Cal. Energy Resolution Parameter $b$ :	0.0
EM Cal. Position Resolution Parameter $a$ :	.10
EM Cal. Position Resolution Parameter $b$ :	0.0
Hadronic Calorimeter Onset:	.2 GeV
H Cal. Sharpness:	10.0 %/GeV
H Cal. Minimum $\theta$ :	$\cos^{-1}$ .95
H Cal. Energy Resolution Parameter $a$ :	.50
H Cal. Energy Resolution Parameter $b$ :	.08
H Cal. Position Resolution Parameter $a$ :	.10
H Cal. Position Resolution Parameter $b$ :	0.0
Tracker Minimum Transverse Momentum:	.2 GeV/c
<i>Normal Tracker Covariance Matrices Used</i>	

Shown below, in Figures 2 and 3, is a set of histograms showing the raw particle-by-particle smearing of the final-state particles in the stdhep file (henceforth called *history particles*) to the reconstructed particle content in the output slcio file using the unmodified *sdjan03* detector.

---

<sup>1</sup>For definitions and implementation of the above variables, see the previous section.

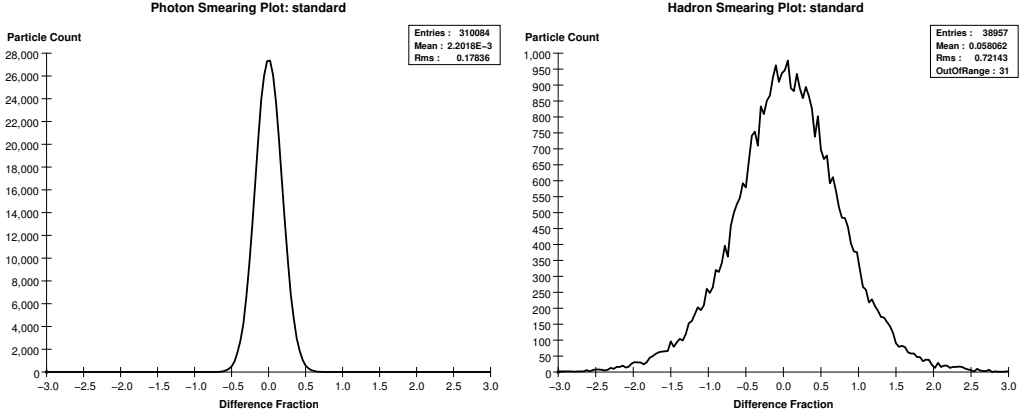


Figure 2: The above plots are histograms of the quantity  $(E_{recon} - E_{hist})/\sqrt{E_{recon}}$  binned for each photon (left) and hadron (right) occurring in a sample of 10,000  $e^+e^- \rightarrow u\bar{u}$  events.

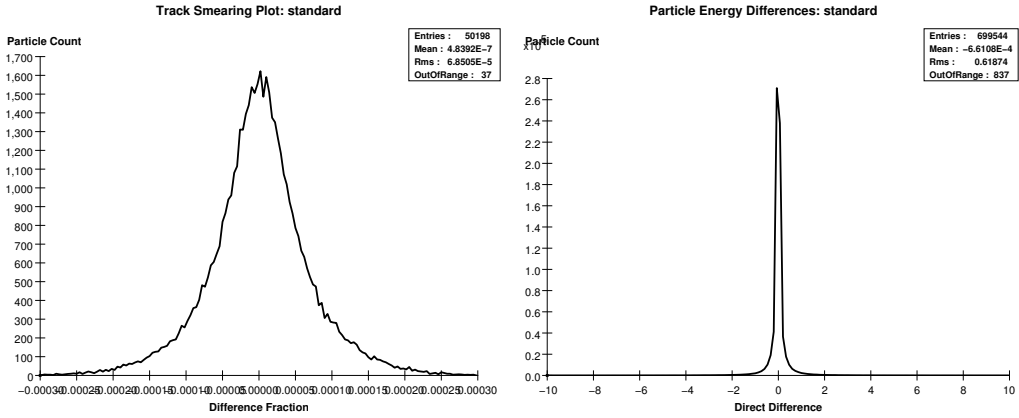


Figure 3: The above left histogram is the quantity  $(Pt_{recon} - Pt_{hist})/Pt_{hist}^2$  where  $Pt$  is the transverse momentum binned for each charged particle, and the above right histogram is  $E_{recon} - E_{hist}$  for each particle of any type that the detector finds.

Upon examining these histograms, the program certainly appears to be smearing as described in the implementation section, though there are a few discrepant features of interest in the figures. Clearly the photon distribution and the hadron distributions above have non-negligible mean values; in the hadronic plot this is due mostly to the fact that the offsetting  $b$  parameter for

the hadronic calorimeter is nonzero, but both have another significant error contribution. The source of this contribution lies in the fact that the program smears the energies of the particles in a gaussian fashion, for which there is a non-zero probability of smearing the particle's energy below its own mass. When this happens, the program simply draws another gaussian random number, effectively cutting off the distribution's tail below the particle mass, consequently modifying the error function for the distribution. Hence, for a particle of mass  $m$ , the error function is modified in the following way:

$$\text{erf}^*(E) = \begin{cases} \frac{\text{erf}(E/\sqrt{2}\sigma) - \text{erf}(m/\sqrt{2}\sigma)}{1 - \text{erf}(m/\sqrt{2}\sigma)} & E > m \\ 0 & E \leq m \end{cases} \quad (21)$$

where the error function we're using is for a normalized distribution centered on  $E_{hist}$ , having domain  $(0, 1)$  and  $\text{erf}(E_{hist}) = \frac{1}{2}$ . These details are complicated by the fact that in our particular choice of event, many more sensitive, low energy photons are created than high energy ones, compounding the effect. Having spoken to this issue, we shall explore the effects of changing the electromagnetic calorimeter parameter  $a$  on the shapes of the smearing histograms, just to ensure that the program is actually smearing energies to model our detector input. Setting  $a = .09$  and letting the rest of the parameters remain as standard produces the histograms found in Figure 4.

Notice in Figure 4 that the hadronic distribution is identical to that found in Figure 2, as expected. Also note that the non-zero mean discussed above is decreased by about an order of magnitude, which is in line with the interpretation of this mean's non-zero divergence given in the comments following Figure 2. Next, in Figures 5 and 6, are the histograms that follow from setting first  $a = .27$  then lastly  $a = .36$ .

Again, the most notable features in Figures 5 and 6 are the small non-zero means in the photon smearing plots; notice that the deviation from zero varies approximately exponentially as  $a$  is changed, achieving ten percent of

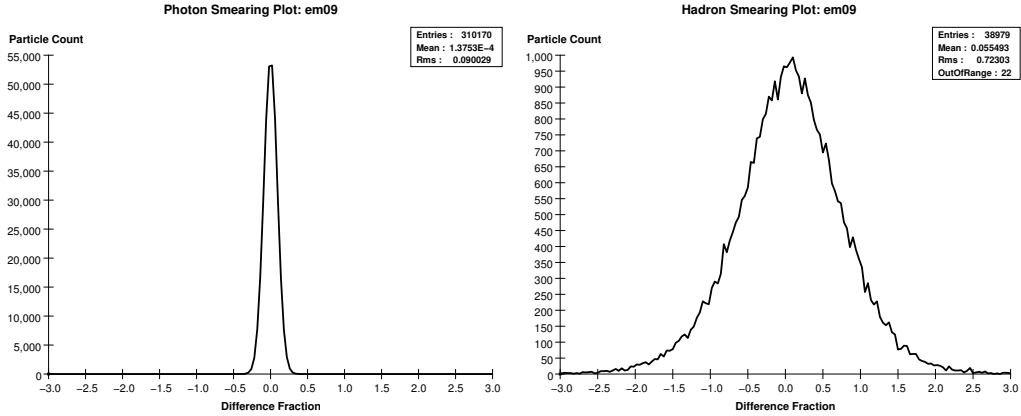


Figure 4: The above plots are histograms of  $\Delta E/\sqrt{E}$  for each photon (left) and hadron (right) in the standard detector, but with electromagnetic calorimeter parameter  $a$  set to .09.

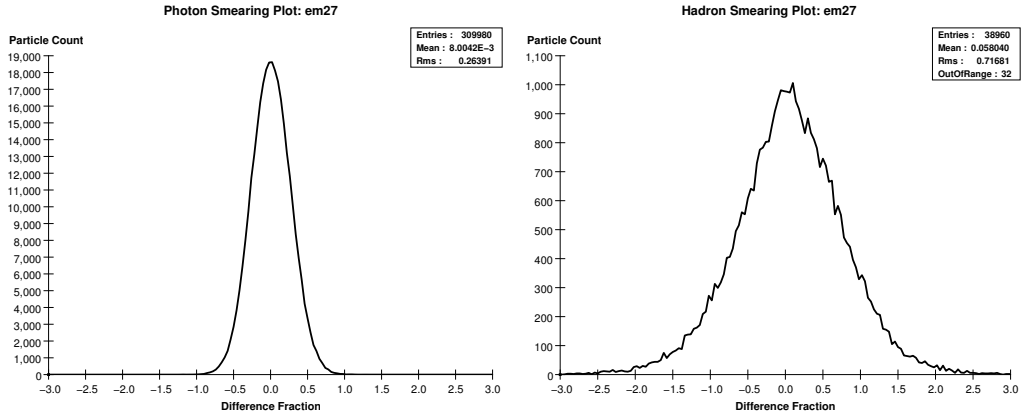


Figure 5: The above plots are histograms of  $\Delta E/\sqrt{E}$  for each photon (left) and hadron (right) in the standard detector, but with electromagnetic calorimeter parameter  $a$  set to .27.

the deviation in the final histogram where  $a = .36$ . Reassuringly we have a very clean, straightforward dependence for the electromagnetic calorimeter deviation on the supplied parameter  $a$ ; in short, we can safely conclude that this aspect of the program is working properly.

Now, let us turn our attention to the hadronic resolution smearing parameter, which, recall, is implemented in an identical fashion to the correspond-

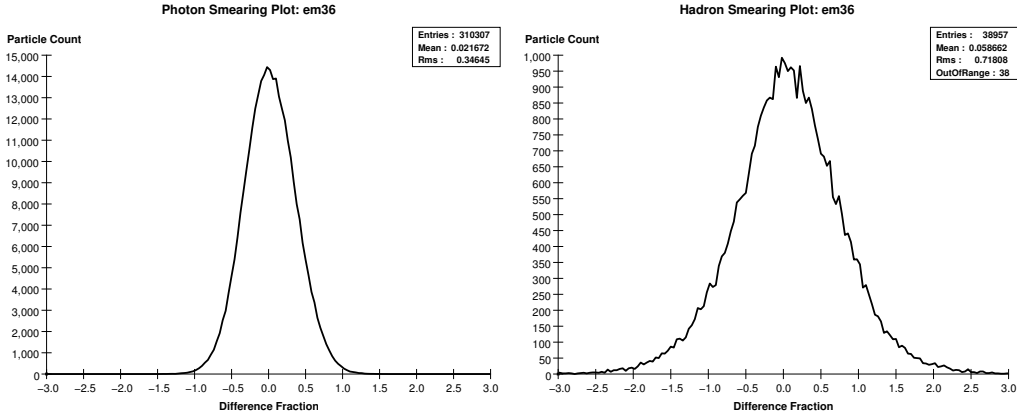


Figure 6: The above plots are histograms of  $\Delta E/\sqrt{E}$  for each photon (left) and hadron (right) in the standard detector, but with electromagnetic calorimeter parameter  $a$  set to .36.

ing electromagnetic calorimeter parameter. The main difference between how these two types particles are smeared lies in the error-function correction effect mentioned above<sup>2</sup>, to which the hadrons are more sensitive due to their significant masses. Nevertheless, the effect of changing the resolution parameter is very similar to that seen in the photonic distributions by changing the corresponding electromagnetic calorimeter parameter; this can be seen in the following histograms, for the first of which  $a = .30$  in Figure 7.

The salient features here are again the mean and the standard deviation, now of the hadronic distribution on the right. Contrast the mean of the standard detector hadronic distribution ( $\sim .05$ , found in Figure 2) with Figure 7's mean value of about .02. This decrease in mean divergence is isomorphic to that which occurs in the photonic distribution when the electromagnetic calorimeter  $a$  is dropped from .18 to .09. The hadronic mean, in keeping with the behavior of the photonic plot, diverges significantly as the resolution is made worse; this effect can be seen in Figure 8, for which  $a = .70$ .

Clearly, as seen in Figure 8, the mean offset issue is much more significant for massive particles (as compared to photons) when the energy resolution is

---

<sup>2</sup>see page XX.

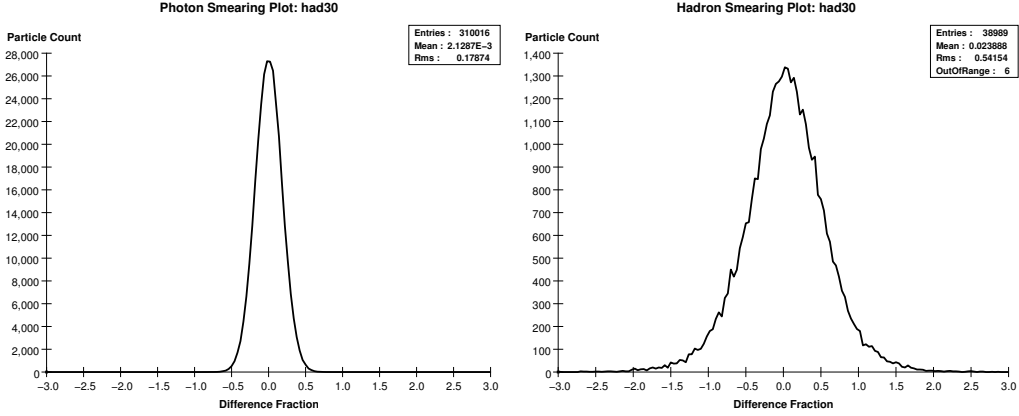


Figure 7: The above plots are histograms of  $\Delta E/\sqrt{E}$  for each photon (left) and hadron (right) in the standard detector, but with hadronic calorimeter parameter  $a$  set to .30.

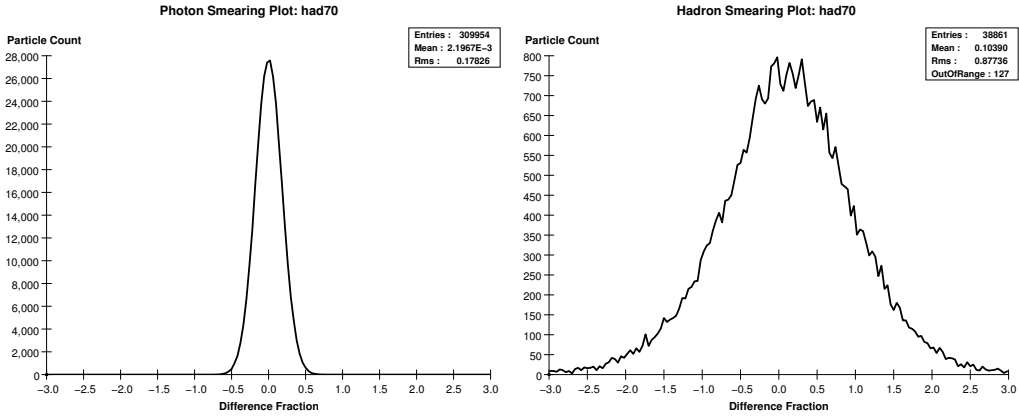


Figure 8: The above plots are histograms of  $\Delta E/\sqrt{E}$  for photons (left) and hadrons (right) in the standard detector with the hadronic calorimeter parameter  $a$  set to .70.

made very bad, indicating the sensitivity of the function  $\text{erf}^*(E)$  to changes in the resolution when  $\text{erf}(m)$  is significantly large.

Finally, let us turn to the performance of the modified tracking parameterization; it is especially important to check the implementation of this feature as its derivation was quite complicated and because it is the only practical way we can directly modify the way the tracker is modeled. A very

useful choice of tracker parameterization (we will want to use our modified tracker smearing method to force the curvature parameter in order to change the energy resolution, of course) is the following:

$$\Delta\Omega \propto \sqrt{(a)^2 + \left(\frac{b}{Pt \cdot \cos\theta}\right)^2} \quad (22)$$

where the constant of proportionality is composed of factors of  $\Omega$  and  $p_{track}$  inserted to correct the units. A nice feature about programming in the modified tracker control is that it gives us great flexibility in not only our choice of specific parameters, but also in our choice of parameterization function itself. Using the above equation for  $\Delta\Omega$ , a choice for the tracker parameters giving very reasonable distributions is  $a = 2.1 \times 10^{-5}$  and  $b = 1.0 \times 10^{-4}$ ; this is the "simple-standard" distribution, and the histograms generated using these choices of parameter appear below, in Figure 9.

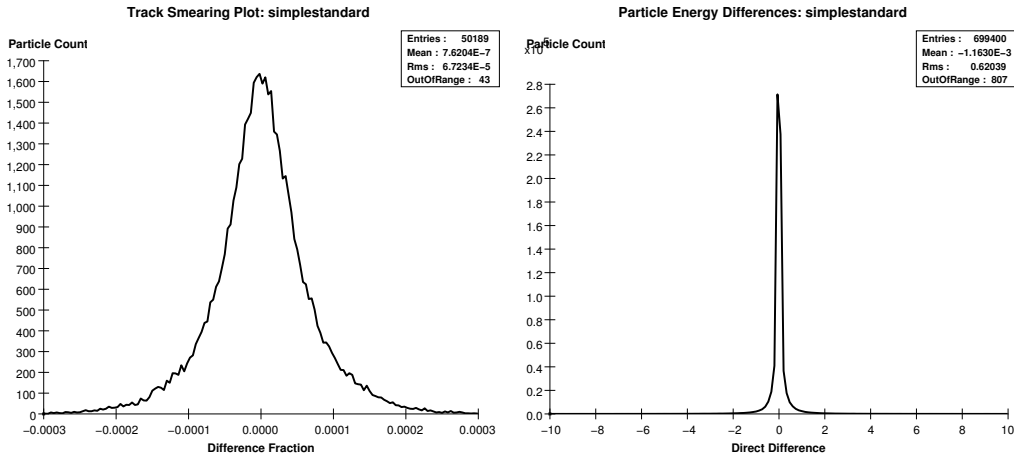


Figure 9: The plots above were generated by forcing  $\Delta\Omega$  as described above, in Eq. 22, with  $a = 2.1 \times 10^{-5}$  and  $b = 1.0 \times 10^{-4}$ . The histograms are of the quantity  $(Pt_{recon} - Pt_{hist})/Pt_{hist}^2$ , again track-by-track over the first 10,000 events in the  $u\bar{u}$  stdhep file where  $Pt$  is the transverse momentum of the track.

It is not immediately apparent in Figure 9, but the tracker smearing plot on the left is (as the parameterization of the curvature resolution introduced above might suggest) a collapsed image of a bivariate distribution that depends both on energy and on the angle  $\theta$  of the tracks; as such it will exhibit some very interesting properties as we vary  $a$  and  $b$  in Equation 22. The distribution itself is only approximately gaussian at the core; the large tails on the distribution betray that it would be more accurately fitted to  $e^{-\sqrt{a^2(E-b)^2+c^2}}$  (an exponentiated hyperbola). A quick comparison with the standard detector tracker distribution in Figure 3 justifies our decision to call these values of  $a$  and  $b$  the standard set, as the difference of the deviations of the two distributions is only  $1.3 \times 10^{-6}$ . Let us now vary the  $a$  parameter and observe the changes incurred in the distribution for tracking momentum. Below are histograms constructed by letting  $a = 1.0 \times 10^{-5}$ ,  $4.0 \times 10^{-5}$ , and  $8.0 \times 10^{-5}$ , contained in Figures 10–12.

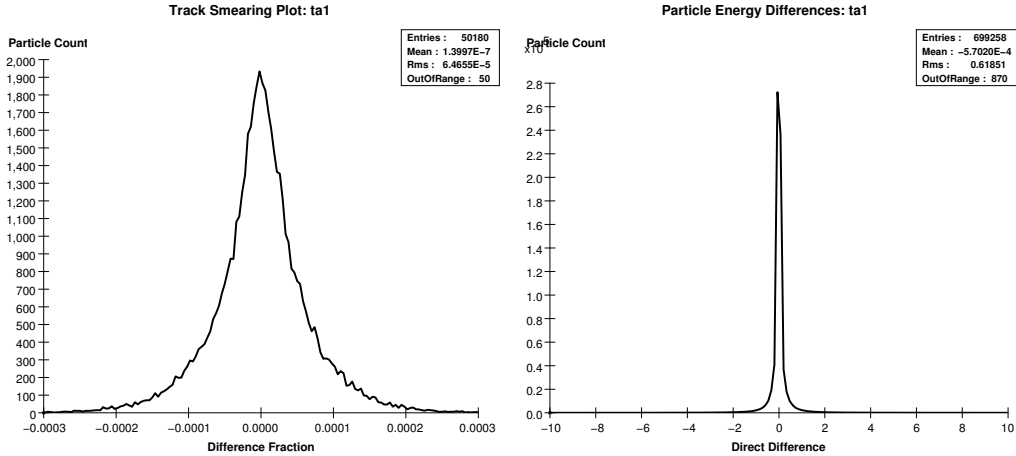


Figure 10: The above left histogram is the quantity  $\Delta Pt/Pt^2$  (where  $Pt$  is the transverse momentum) generated with tracker parameter  $a$  (see Eq. 22) set to  $1.0 \times 10^{-5}$  and  $b$  left at its simple-standard value.

In Figures 10–12, the previous comment on the tracker histogram being a collapsed projection of a bivariate distribution gains a great deal of meaning, with manifestly concrete consequences. First of all, we see in the histogram

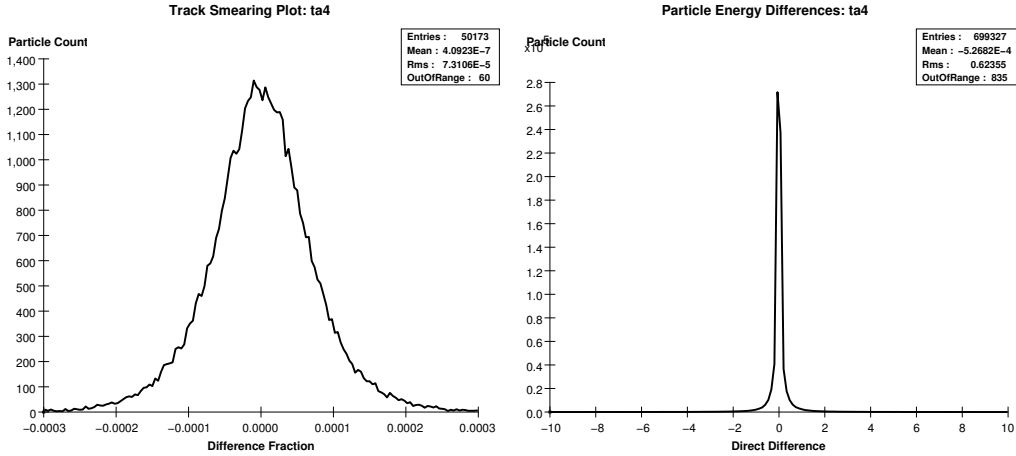


Figure 11: The above left histogram is the quantity  $\Delta Pt/Pt^2$  (where  $Pt$  is the transverse momentum) generated with tracker parameter  $a$  (see Eq. 22) set to  $4.0 \times 10^{-5}$  and  $b$  left at its simple-standard value.

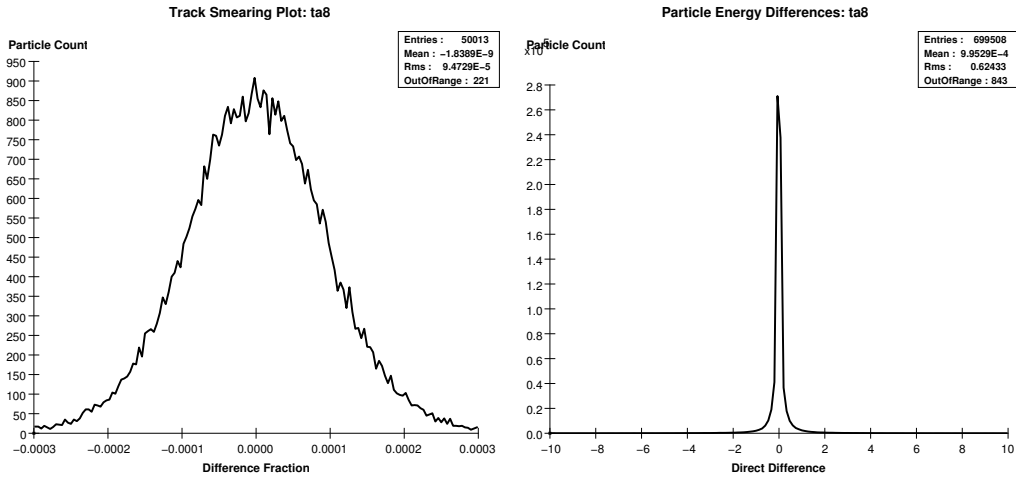


Figure 12: The above left histogram is the quantity  $\Delta Pt/Pt^2$  (where  $Pt$  is the transverse momentum) generated with tracker parameter  $a$  (see Eq. 22) set to  $8.0 \times 10^{-5}$  and  $b$  left at its simple-standard value.

for which  $a = 1.0 \times 10^{-5}$  (Figure 10) that the core of the histogram is much more sharply peaked than in Figure 9; If the distribution were in fact gaussian we'd expect a situation where the derivative of the distribution smoothly

crosses zero at the mean, but instead we get a situation where the resulting histogram is quite “pointy”, elucidating the fact that we’re only allowed to glimpse a shadow of what is really happening. Looking at the other end of the resolution spectrum in Figures 11 and 12, we see that the opposite happens. The core of the distribution gets much blurrier, with the top smoothing out and gaining statistical fuzziness; generally the hits are less localized around a clear mean as  $a$  increases. These are all very good signs that the smearing procedure is working as designed, and certainly we can, if we wish, arbitrarily let  $a$  change until we get a distribution that looks appropriate for whatever purpose. Now let us turn our attention to the  $b$  parameter, whose smearing term depends on  $\cos\theta$ . Again, we must bear in mind the multivariate nature of these distributions, and as we will see, the phenotype for changing the  $b$  parameter is much different than that for changing  $a$ . To illustrate this, below are histograms constructed by letting  $b = 0.5 \times 10^{-3}$ ,  $2.0 \times 10^{-3}$ , and finally  $4.0 \times 10^{-3}$ , contained in Figures 13–15.

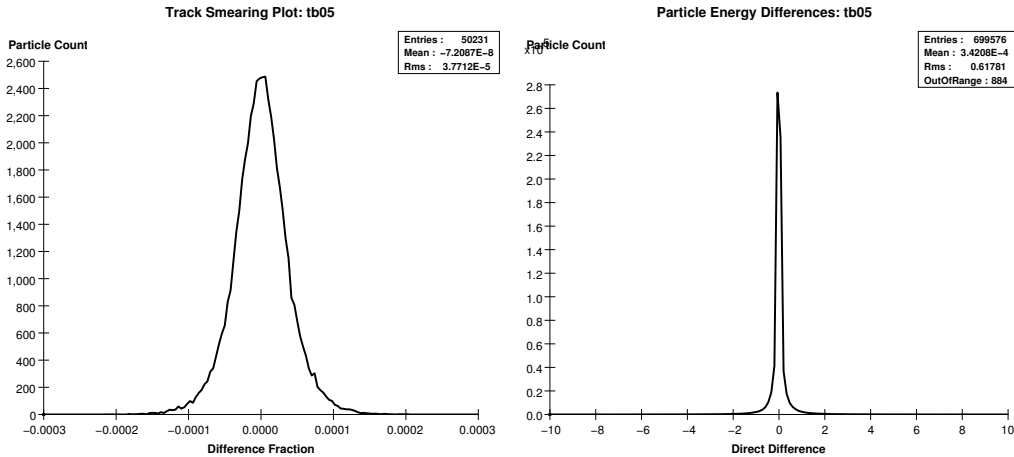


Figure 13: The above left histogram is the quantity  $\Delta Pt/Pt^2$  (where  $Pt$  is the transverse momentum) generated with tracker parameter  $b$  (see Eq. 22) set to  $0.5 \times 10^{-3}$  and  $a$  left at its simple-standard value.

As claimed, changing the parameter  $b$  in Eq. 22, put bluntly, looks very different than does changing the parameter  $a$ . The parameter  $b$  too *physically*

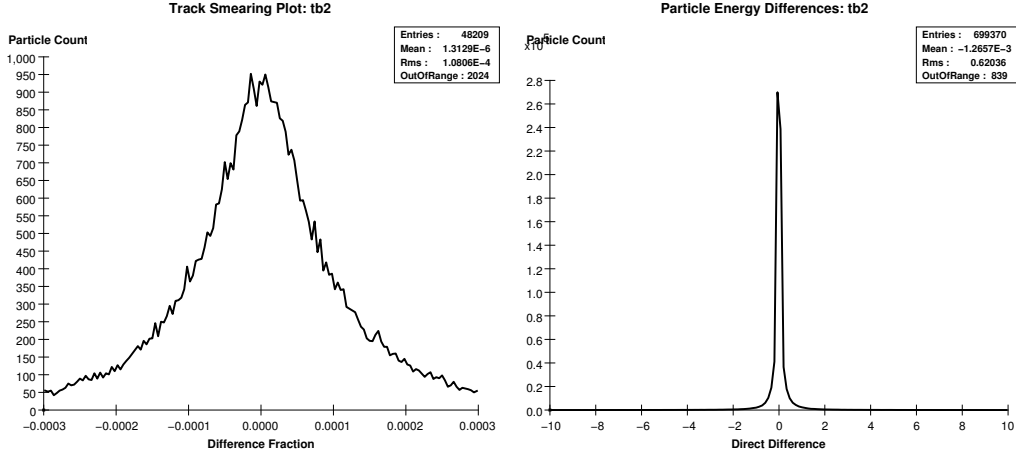


Figure 14: The above left histogram is the quantity  $\Delta Pt/Pt^2$  (where  $Pt$  is the transverse momentum) generated with tracker parameter  $b$  (see Eq. 22) set to  $2.0 \times 10^{-3}$  and  $a$  left at its simple-standard value.

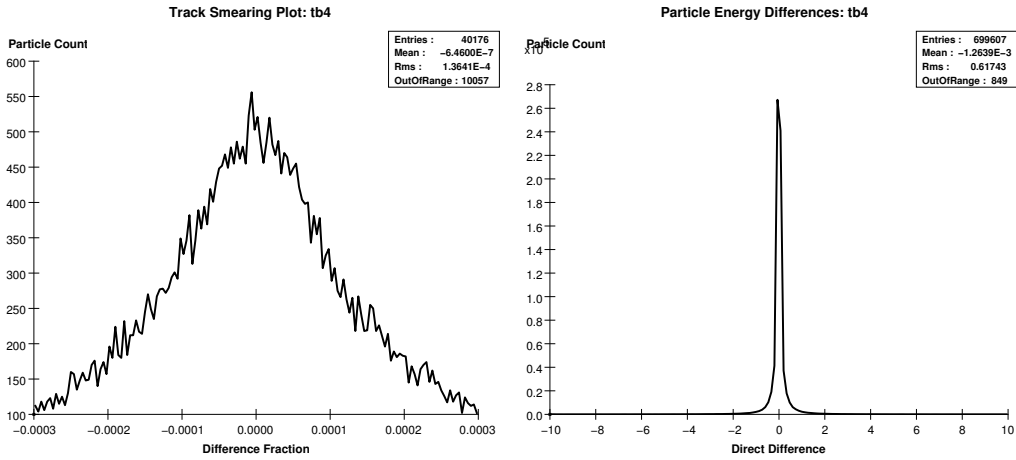


Figure 15: The above left histogram is the quantity  $\Delta Pt/Pt^2$  (where  $Pt$  is the transverse momentum) generated with tracker parameter  $b$  (see Eq. 22) set to  $4.0 \times 10^{-3}$  and  $a$  left at its simple-standard value. Note the vertical scale.

has a different role from that of  $a$ , describing how the accuracy in measuring the curvature is reduced as the track becomes more and more in line with the beam pipe. This is certainly a realistic dependence to expect, since as

the angle  $\theta$  decreases, so does the fraction of the total momentum that we're able to measure. This of course has the effect of amplifying the error in the measurement of the total momentum, which is the quantity of greatest interest here. We can see in the histograms for varied  $b$  that increasing this parameter tremendously increases the significance of, primarily, the tail of the distribution, producing histograms that are decidedly non-gaussian. Nonetheless, we do achieve the expected overall effect, with the net resolution plummeting as  $b$  is increased.

## 4.2 $u\bar{u}$ Events at 500 GeV: Thrust Analysis

Our next task, having shown that the program is performing properly, is to assess how changing the detector parameters affects measurable physical quantities in a realistic event analysis. Since the stdhep file we're using has each quark at 250 GeV, the event should be boosted enough to keep each quark jet relegated to one thrust hemisphere, just by conservation of momentum. By calculating the thrust axis  $\vec{T}$  for each event, we should be able to divide up all the particles in the detector as belonging to one quark or the other by determining the sign of  $\vec{T} \cdot \vec{p}_{recon}$  for each reconstructed particle, where  $\vec{p}_{recon}$  is the full 4-momentum. After performing the above analysis on both the set of reconstructed particles and the set of history particles, we can bin the differences between the energies summed up in each thrust hemisphere for each type of particle in order to get a histogram of the jet energy resolution for the detector. Since the measured jet energy contains measurements from the tracker and both calorimeters, the jet energy resolution is going to be a highly composite plot; thus it will have some very interesting behavior as the properties of the various components of the detector are changed. Determining this behavior is exactly the goal of the fast Monte Carlo; with our present experience we can already see how sensitively this is going to depend on the types of particles produced in the events we're studying, among other things.

First of all, let us examine the results of such a thrust analysis performed on an slcio file generated using the standard detector description. Below, in Figures 16-18, are histograms of the measured jet energies for both the reconstructed particles and history particles, the total jet energy resolution, the photonic and hadronic jet energy resolutions, the charged jet energy resolution, and finally a plot showing measured photon energies.

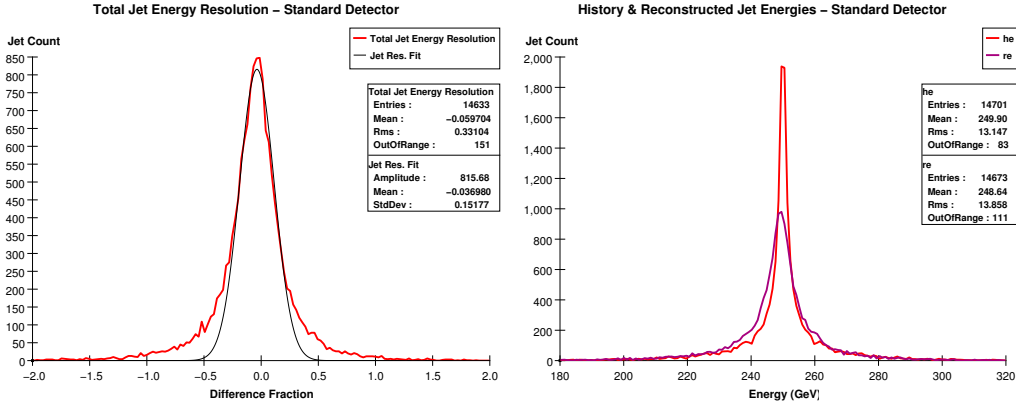


Figure 16: The above right histogram shows simply the measured jet energies for both the history particles and the reconstructed particles, whereas the left histogram shows the jet energy resolution, and is a binning of the quantity  $(E_{recon} - E_{hist})/\sqrt{E_{hist}}$ . As the jet energy resolution for the detector, this is going to be the figure of primary interest.

In Figure 16 we see our first jet energy resolution plot, which is the quantity which will be of greatest interest to us in the remainder of the paper. Again, it's a highly composite distribution, with an only approximately gaussian shape. The fit that has been applied was calculated using a QR factorization, and for each jet energy resolution the fit will be calculated using only the core of the distribution, a decision justified firstly on the non-gaussian nature of the distribution and secondly on the fact that when looking for particle masses with this program, only the core of a mass peak is important. On the right we see the raw jet energy measurements; of greatest interest here are the losses that occur in the detector during the simulation process.

This is the first indication we see of the efficiency function mentioned in the implementation section. We will look further into this loss by hermetically sealing the detector in the next group of histograms we analyze.

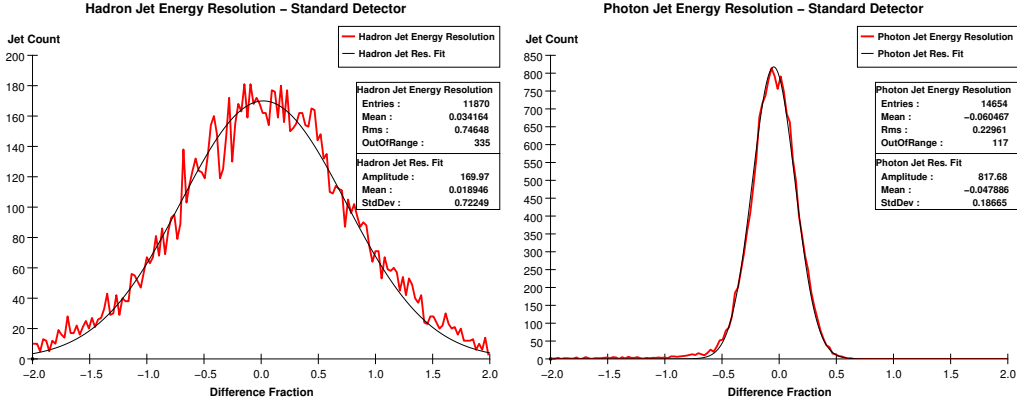


Figure 17: The above figure contains a plot of the photonic and the hadronic jet energy resolutions for the standard detector parameterization.

In Figure 17 we see the isolated photonic and hadronic components of the jet energy. These histograms will naturally be of direct interest when we start varying the parameters for the different calorimeters again in order to see what effect changing the resolution has on the total jet energy plot. Here too, albeit in a very muted way, we can see the non-hermeticity of the detector. This effect shows up as a tiny asymmetry in the tails of the photonic distribution; clearly a few more reconstructed jets are coming in at lower energy with respect to the history jets than at higher energy. Were our statistics higher, we could also observe this tail asymmetry effect in the hadronic energy resolution plot. Again, we can investigate this effect further by making the detector hermetic.

Finally, in Figure 18 we have a plot of the tracker energy resolution as well as a photon spectrum for the  $u\bar{u}$  event. The tremendous negative tail on the tracker energy resolution makes fitting gaussians to this distribution especially problematic, but again we will see that this tail is completely due to

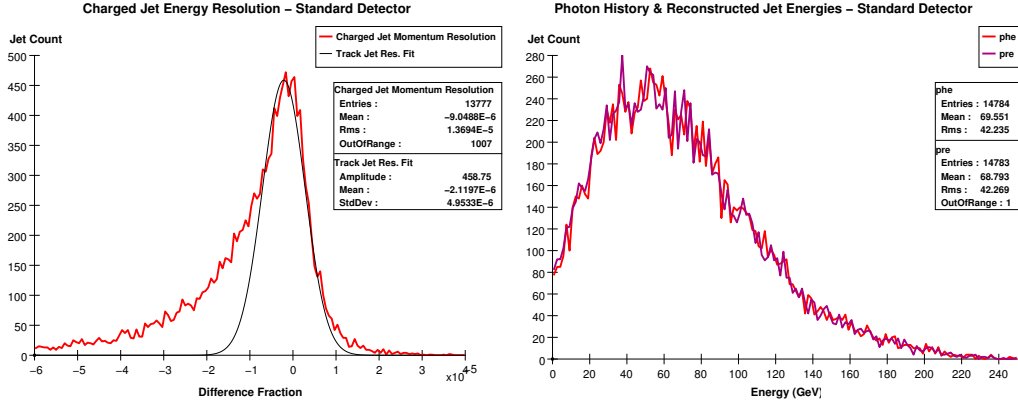


Figure 18: The above figure contains on the left a plot of the charged component of the jet energy resolution, whereas on the right appears a spectrum of the total jet energy contained in the photon radiation from the event.

particle escape or efficiency losses, and that this effect completely disappears when we make the detector hermetically sealed. On the right we see a plot of the photon spectrum, and notably, the total photon energy is more likely to be at the low-energy end of the spectrum. The total tracker spectrum (not shown) is much like the photon spectrum, only it is weighted more toward the high-energy end of the spectrum.

Now, after finally being able to observe effects due to particle loss, let us take a look at what occurs when we try to prevent this by making the detector perfectly efficient and removing all beam-pipe losses. We call such a detector configuration “hermetically sealed”, which is *almost* true since we shall still let neutrinos escape. Below are the same histograms as appear in Figures 16–18, only now we will force different values for a few the parameters found in the table on page 22:

Electromagnetic Calorimeter Onset:	.1 GeV $\rightarrow$ 0.0 GeV
EM Cal. Sharpness:	10.0 %/GeV $\rightarrow$ 10,000 %/GeV
EM Cal. Minimum: $\theta$ :	$\cos^{-1}.95 \rightarrow \cos^{-1} 1.00$
Hadronic Calorimeter Onset:	.2 GeV $\rightarrow$ 0.0 GeV
H Cal. Sharpness:	10.0 %/GeV $\rightarrow$ 10,000 %/GeV
H Cal. Minimum $\theta$ :	$\cos^{-1}.95 \rightarrow \cos^{-1} 1.00$
Tracker Minimum Transverse Momentum:	.2 GeV/c $\rightarrow$ 0.0 GeV/c

The resulting histograms can be found below, in Figures 19-21.

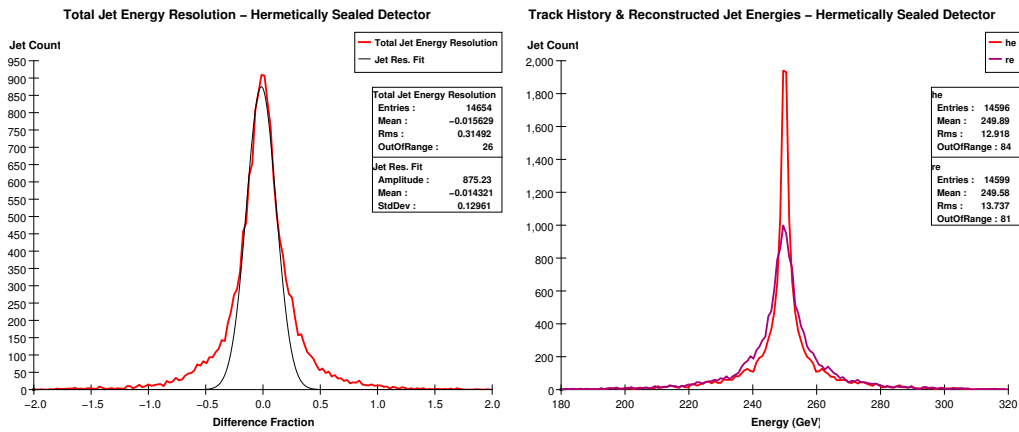


Figure 19: The above figure contains a plot of the total jet energy resolution and the raw history and reconstructed jet energies as generated by the hermetically sealed detector; this detector is described by the table on page 22 with the changes included in the table above.

The left plot in Figure 19 contains the total jet energy resolution after sealing the detector; upon comparison with the standard jet energy resolution in Figure 16 we see a marked improvement. (The fitted resolutions are 15.177% as compared to 12.963%). Also, we see that the peak difference between the history particles and the reconstructed particles in the raw jet energy plot has appreciably disappeared.

Figure 20 contains the photonic and hadronic energy resolutions. Recall that the photonic energy resolution had a small negative tail in Figure 17;

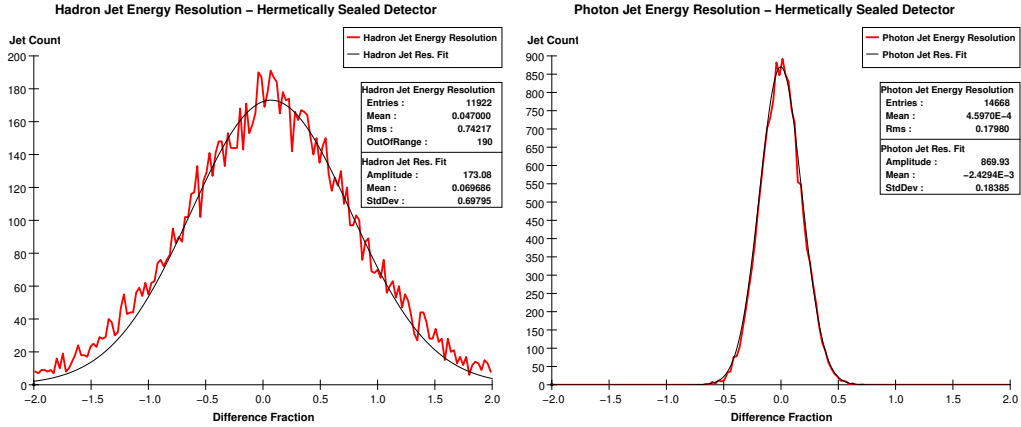


Figure 20: The above figure contains a plot of the photonic and the hadronic jet energy resolutions for the standard detector parameterization.

by sealing up the detector completely we were able to make this effect cease to appreciably exist. Also, notably, the resolution is not much improved at all: the standard detector is able to deliver a resolution of 18.665%, while the sealed calorimeter delivers 18.385%.

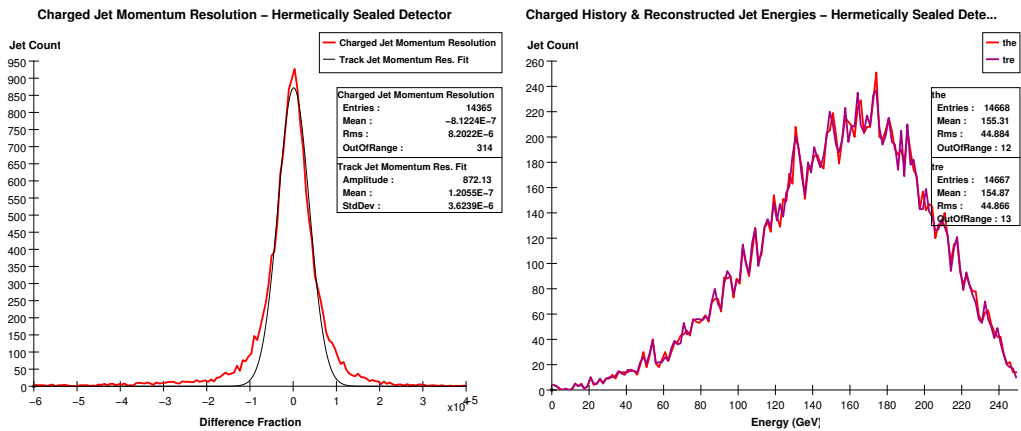


Figure 21: The above figure contains a plot of the photonic and the hadronic jet energy resolutions for the standard detector parameterization.

Finally, looking at Figure 21, we see a huge change in the appearance

of the tracker energy resolution plot: the daunting negative tail found in the standard detector plot (Figure 18) has completely disappeared. From the changes we've observed in this set of data, we can confidently conclude that the offset from zero in the standard detector energy resolution is almost entirely due to loss/efficiency effects, and that among these the most significant contributor is the loss of particles in the tracker due to the transverse momentum minimum parameter.

Having established this important causal point on detector performance, let us now proceed with observing the dependence of the physics performance on the most important variables; the resolution parameters. This is the primary task this program will be used to complete, only our particular choice of event is probably the simplest type of event analysis possible to conduct while still achieving some level of realism. Below, in Figures 22–27, we can find a group of two pertinent thrust analysis figures for each of three different values of the electromagnetic resolution parameter  $a$ , followed by commentary. The values  $a$  assumes are  $a = .09$ ,  $.27$ , and  $.36$ .

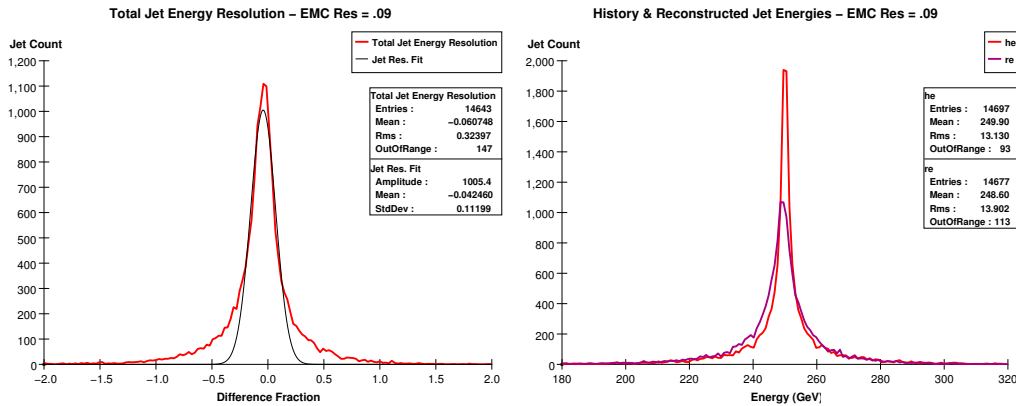


Figure 22: The above figure contains a plot of the photonic and the hadronic jet energy resolutions for the standard detector parameterization.

The histograms contained in Figures 22–27 themselves contain a great deal of important physics results. Since photons are a major component of

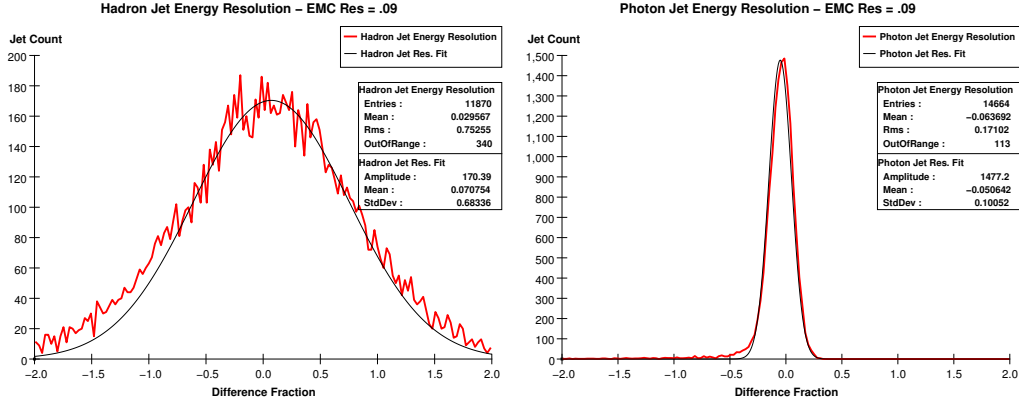


Figure 23: The above figure contains a plot of the photonic and the hadronic jet energy resolutions for the standard detector parameterization.

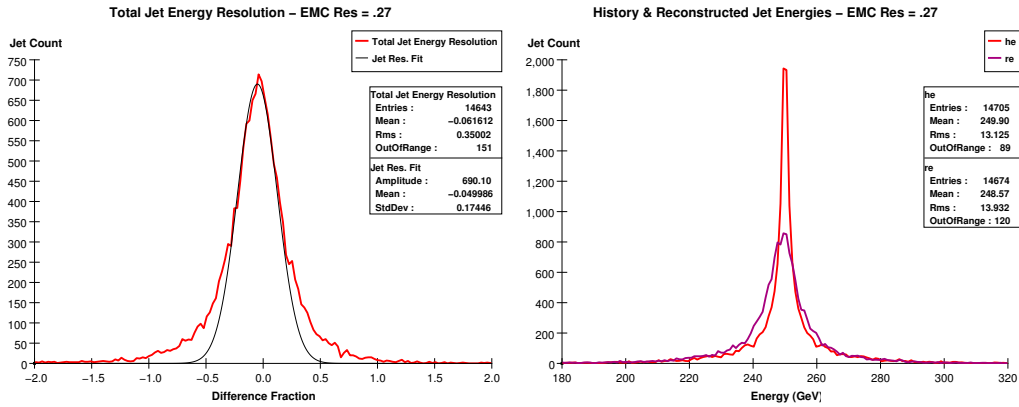


Figure 24: The above figure contains a plot of the photonic and the hadronic jet energy resolutions for the standard detector parameterization.

the  $u$  quark jets we observe, we see that varying the electromagnetic calorimeter resolution has a significant effect on the total jet energy resolution. However, we can also see that the blurriness of the jet energy resolution does have a maximum limiting value (with respect to changes in the electromagnetic parameter  $a$ ), as evidenced by the fact that the change in jet energy resolution between the standard value for  $a$  and  $a = .27$  is greater than the

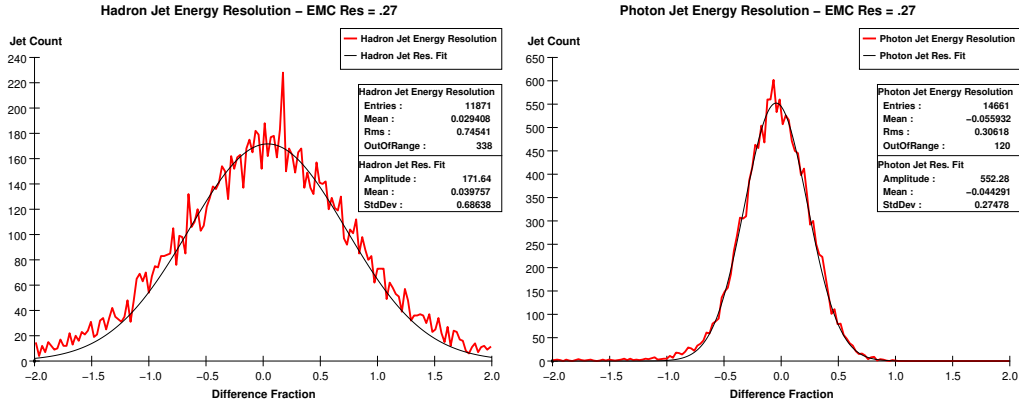


Figure 25: The above figure contains a plot of the photonic and the hadronic jet energy resolutions for the standard detector parameterization.

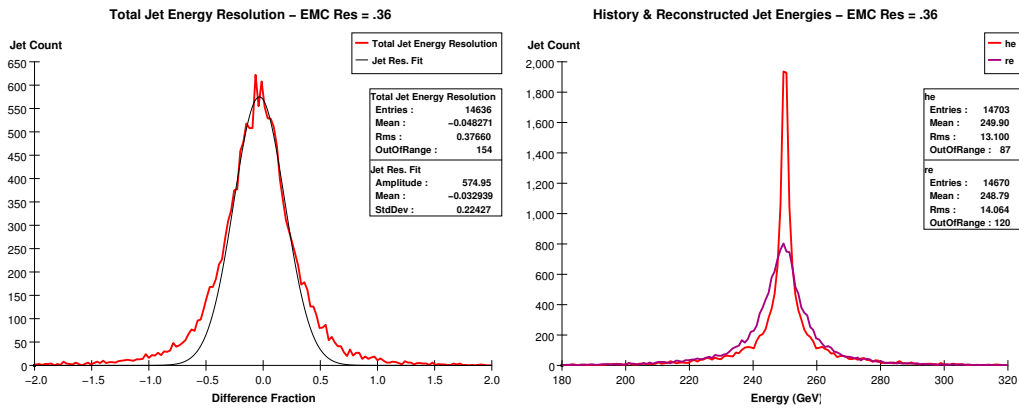


Figure 26: The above figure contains a plot of the photonic and the hadronic jet energy resolutions for the standard detector parameterization.

change observed between  $a = .27$  and  $a = .36$ . This is a consequence of the important multicomponent nature of the total resolution; as the electromagnetic calorimeter gets blurrier, the sharpness of the peak depends more and more heavily on the other components of the detector, finally being carried completely by the tracker, which is the most accurate component. The effect of changing  $a$  at high  $a$  does still show itself, but now also as an increase

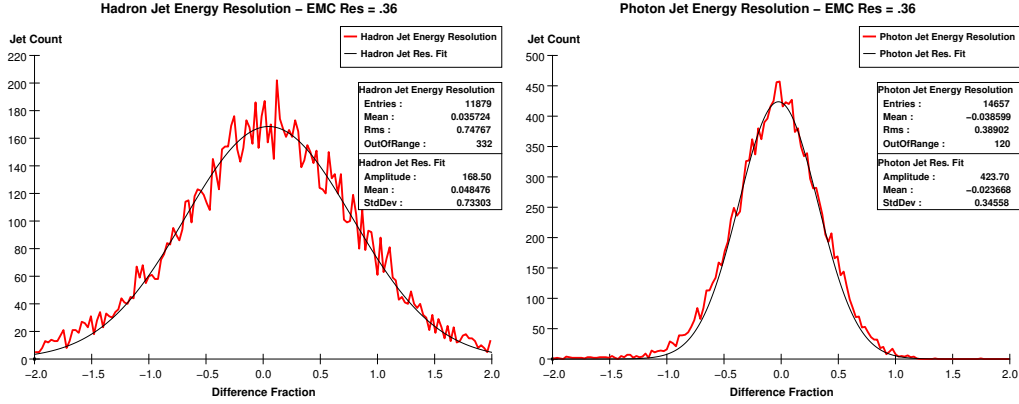


Figure 27: The above figure contains a plot of the photonic and the hadronic jet energy resolutions for the standard detector parameterization.

in the bulk of the “haunches” of the distribution, outside the core but not properly called part of the tail. Again, notice the effects of particle loss in the distributions. The most prominent Landau-esque non-hermeticity tail can be observed in the photon jet resolution plot for which  $a = .09$ ,<sup>3</sup> this is a clear feature in this case mostly because the statistics are the best for this plot. However, we must be mindful that this effect is occurring in *all* histograms, and that this effect is responsible for the nonzero and negative means of the various distributions.

Now, let us turn our attention to the behavior of the resolution results as we change the *hadronic* calorimeter resolution. The plots below, namely Figures 28-33, contain again the total energy resolution, hadronic and photonic resolution, and raw energy peak for each parameter value we choose; values for the hadronic  $a$  parameter in these figures include  $a = .30$  and  $a = .70$ .

The effects of changing the hadronic resolution parameter  $a$ , though implemented almost identically in the program, come in sharp contrast to the behavior observed as we varied the electromagnetic parameter in Figures 22-27. Most prominently, the total jet energy resolution reaches a limiting

<sup>3</sup>see Figure 23

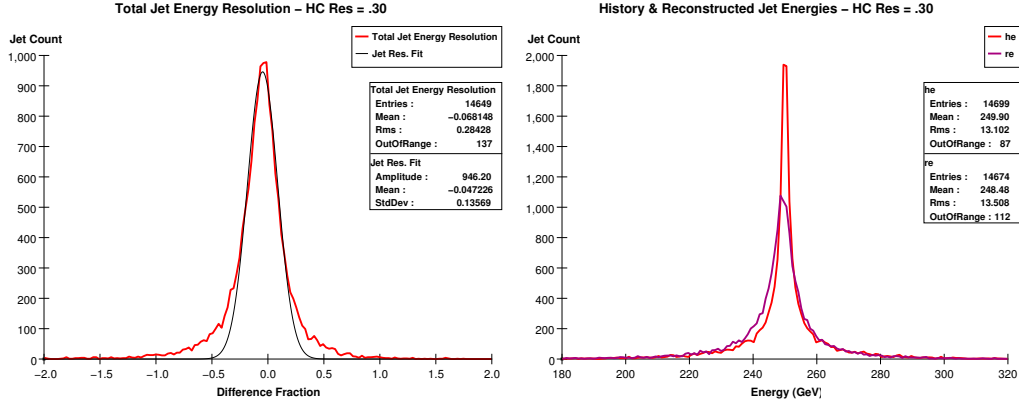


Figure 28: The above figure contains a plot of the photonic and the hadronic jet energy resolutions for the standard detector parameterization.

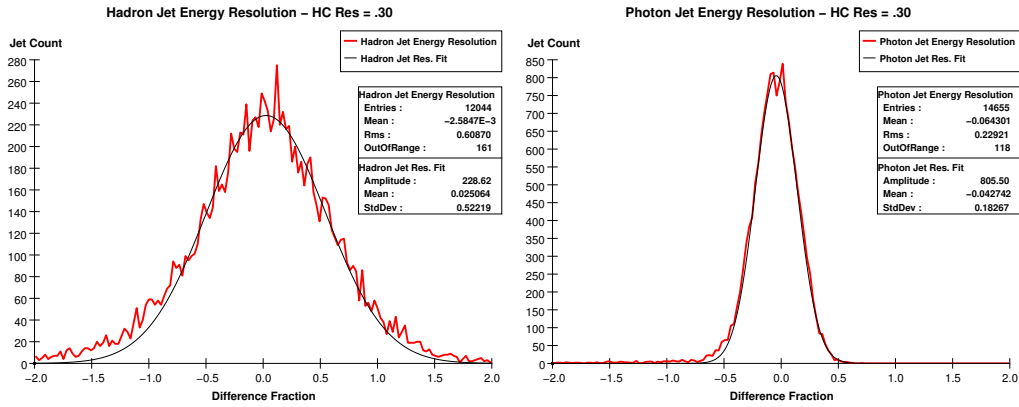


Figure 29: The above figure contains a plot of the photonic and the hadronic jet energy resolutions for the standard detector parameterization.

value much more rapidly than in the electromagnetic case, actually reversing direction by the time  $a = .70$ : the sequence of total jet resolutions as  $a$  is varied is, shockingly 13.569%, 15.177%, and 15.033%! The reversal of the trend requires the illumination of several points in order to become satisfactorily clear, the first of these points is the particle content in the particular events we've chosen to simulate. Roughly speaking, in 10,000  $u\bar{u}$  events, only

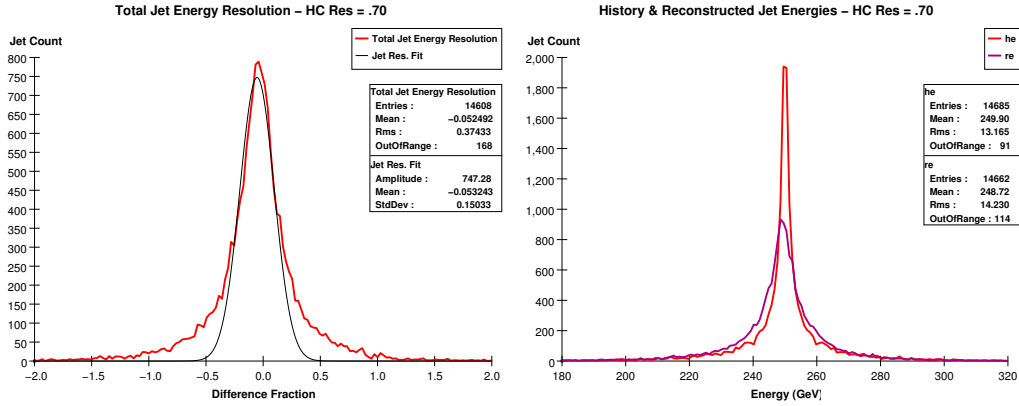


Figure 30: The above figure contains a plot of the photonic and the hadronic jet energy resolutions for the standard detector parameterization.

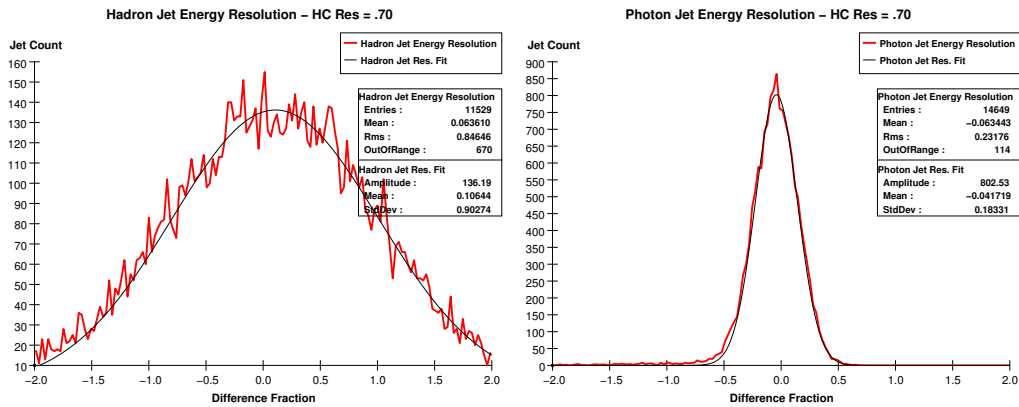


Figure 31: The above figure contains a plot of the photonic and the hadronic jet energy resolutions for the standard detector parameterization.

5.3% of the particles produced are neutral hadrons, with the remainder about equally split between the charged particles and the photons. Consequently, we can reasonably expect that changing the hadronic calorimeter resolution will not affect the total jet resolution very much when compared with the effects of changing other components. However, an interesting thing occurs as we make the hadronic resolution very bad; The component of the total jet

resolution due to hadrons becomes so spread out and consequently of such low amplitude that the core of the distribution to a good approximation is dominated by the photonic and charged components of the jets. Oddly, then, making the hadronic resolution very bad has the counterintuitive effect of actually improving the total jet resolution by effectively removing itself from the region of the distribution whose shape defines the resolution. As we would expect from the behavior we observed when the electromagnetic resolution was pushed up to .36, the “haunches” and tail region of the jet resolution histogram gain a great deal of bulk as the hadronic  $a$  is set to .70.<sup>4</sup>

Let us lastly again turn our attention to effects incurred as a result of changing the tracker resolution parameters. Using again the parameterization set out in Equation 22, we generate Figures 32–39 found below by letting the parameters assume their “simple-standard” values<sup>5</sup>, but with the  $a$  parameter varying between the values  $1.0 \times 10^{-5}$ ,  $2.1 \times 10^{-5}$ ,  $4.0 \times 10^{-5}$ , and  $8.0 \times 10^{-5}$ .

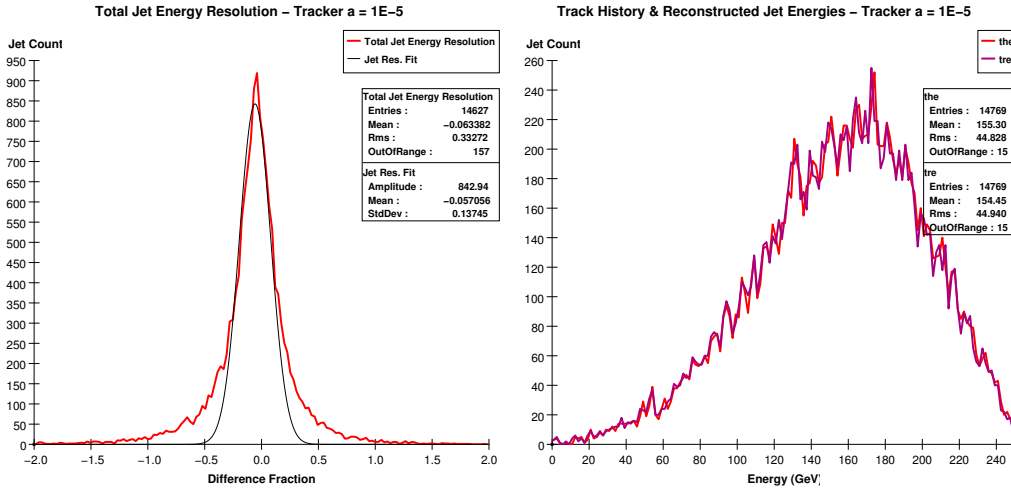


Figure 32: The above figure contains a plot of the photonic and the hadronic jet energy resolutions for the standard detector parameterization.

<sup>4</sup>see Figures 26 and 27.

<sup>5</sup>these are defined on page XX.

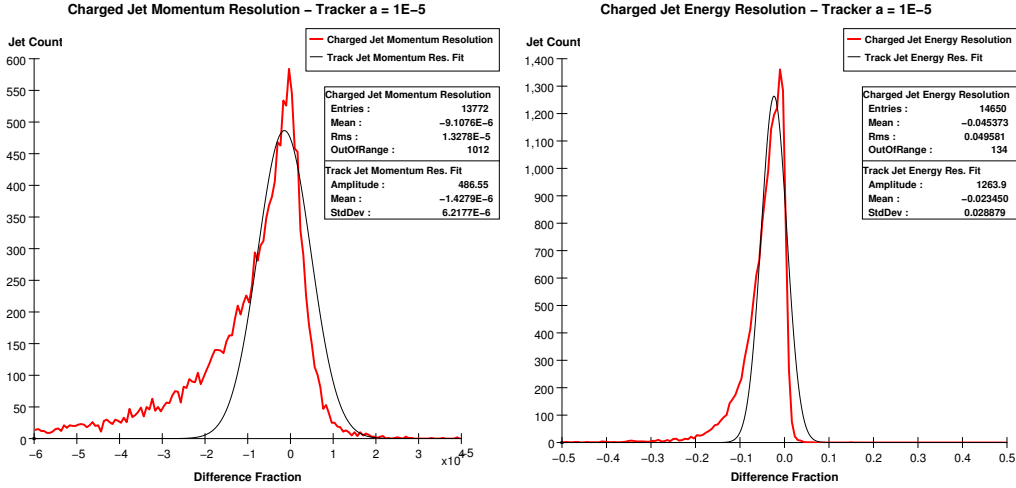


Figure 33: The above figure contains a plot of the photonic and the hadronic jet energy resolutions for the standard detector parameterization.

Right away, in the plots of the charged component of the jet resolution we can see that we are going to be severely handicapped by the tails that particle loss and inefficiency effects cause; this is especially true with respect to defining fits for the tracker resolution histograms. Also in Figure 32 we see the familiar “pointiness” at the mean of the jet resolution distribution that is the hallmark of a multivariate distribution that has a very sharply defined component. This feature will actually persist as we vary the tracker parameters, since the range of  $a$  values we go through doesn’t make the tracker less precise than the calorimeters.

After this first round of tracker examination histograms, we see that the effect of changing the tracker is, as expected, quite different from that of changing either of the calorimeters. Considering that we have two variables working synchronously to shape a single component of the complicated multivariate jet energy resolution, we should certainly be prepared to see some nontrivial dependences on the parameters that appear strange at first glance, requiring further explanation; thankfully, though, the behavior we observe

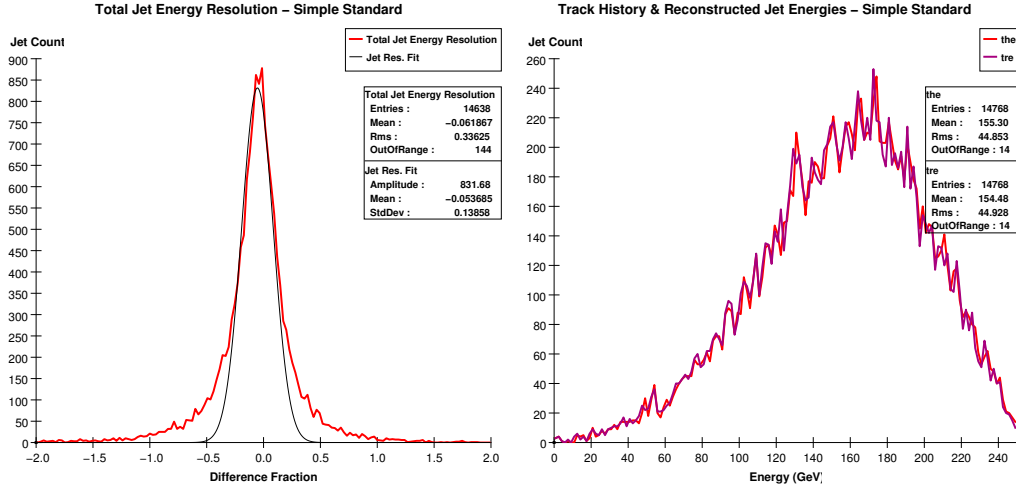


Figure 34: The above figure contains a plot of the photonic and the hadronic jet energy resolutions for the standard detector parameterization.

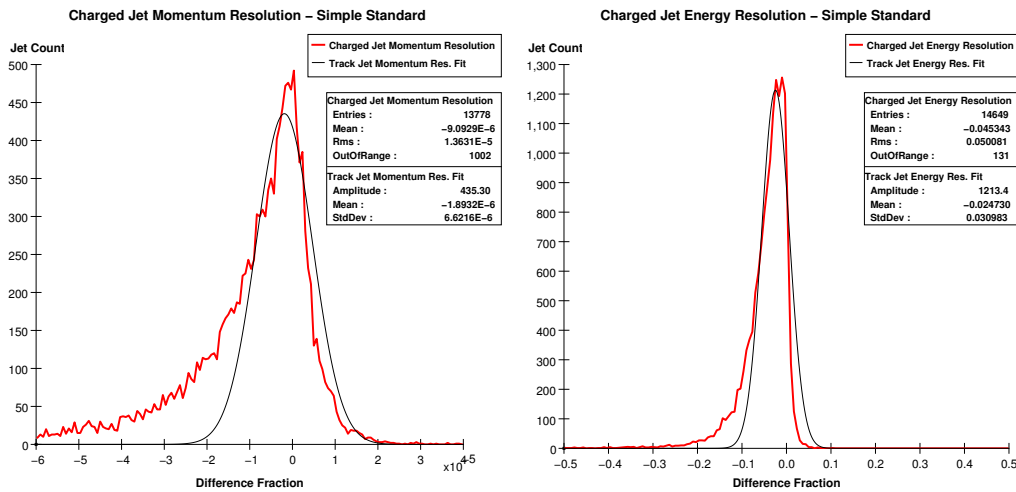


Figure 35: The above figure contains a plot of the photonic and the hadronic jet energy resolutions for the standard detector parameterization.

can be understood in the context of effects we have observed before (especially dependences seen on the hadronic calorimeter parameter). The jet energy resolutions we observe are, in order of increasing tracker  $a$ : 13.745%,

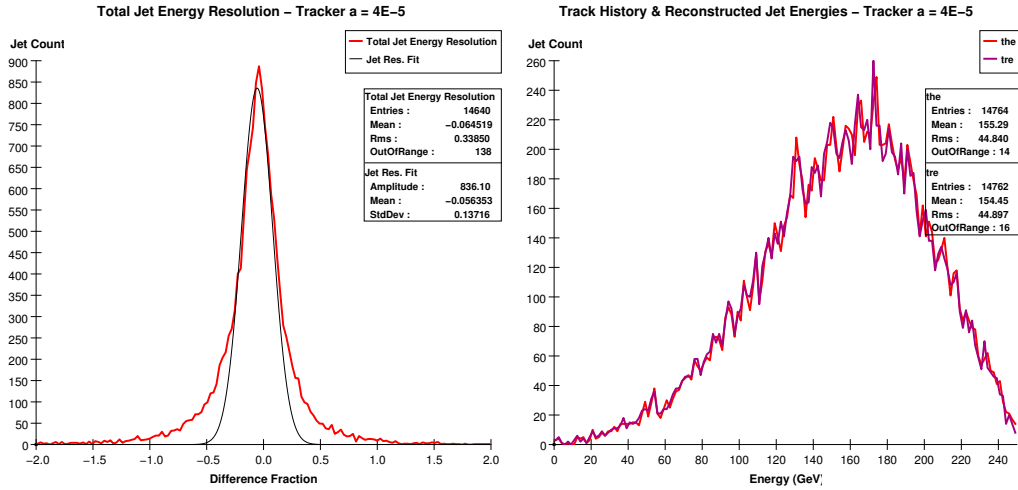


Figure 36: The above figure contains a plot of the photonic and the hadronic jet energy resolutions for the standard detector parameterization.

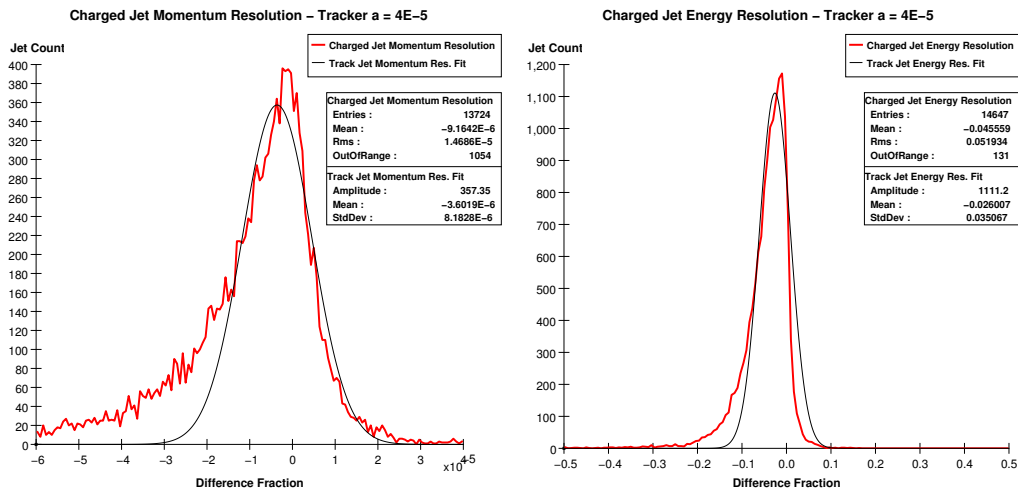


Figure 37: The above figure contains a plot of the photonic and the hadronic jet energy resolutions for the standard detector parameterization.

13.858%, 13.716%, and 15.014%. Clearly this is a strange dependence, and we cannot just sweep it under the rug by calling it statistics since we have more than thirteen thousand jets going into each of these measurements.

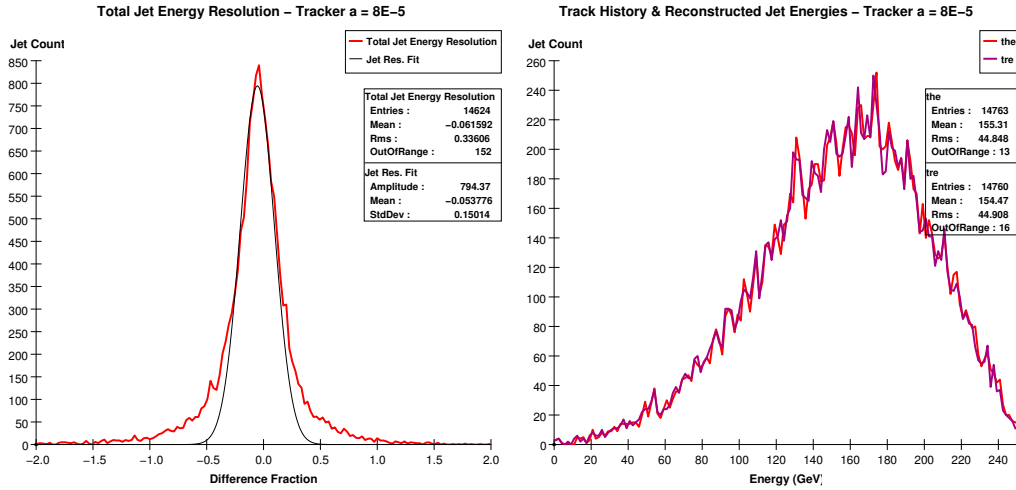


Figure 38: The above figure contains a plot of the photonic and the hadronic jet energy resolutions for the standard detector parameterization.

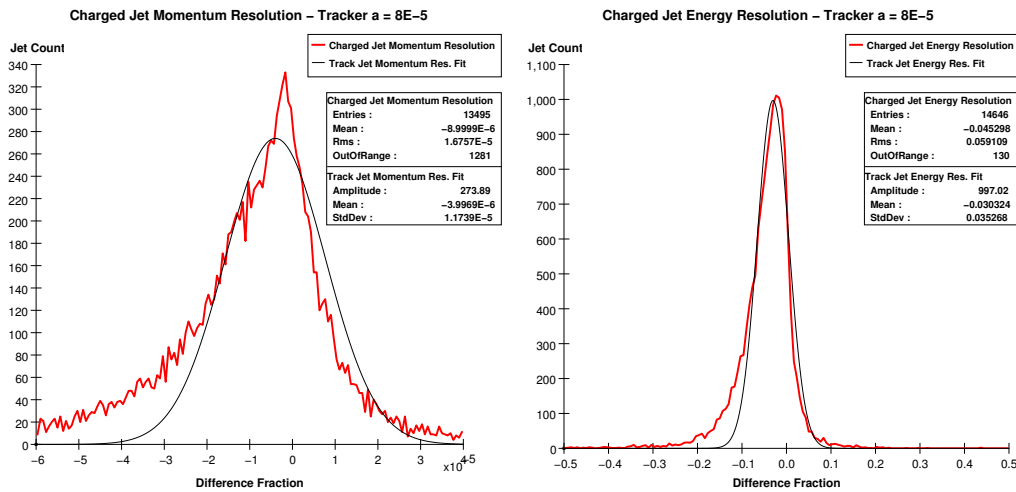


Figure 39: The above figure contains a plot of the photonic and the hadronic jet energy resolutions for the standard detector parameterization.

The key to this dependence is related to the sudden improvement observed in the jet energy resolution as the hadronic calorimeter parameter  $a$  reached its upper limit: a situation in which we were looking at a distribution with

several added components naturally falling into groups with quite different deviations. Whenever one examines a one dimensional distribution that is some kind of collapsing or projection of a distribution of two variables in which the deviation of thin, one dimensional cuts on the collapsed variable depends heavily on the actual position of the cut along the collapsed axis, the width of the core of the fully collapsed distribution will depend, to an excellent approximation, *only* on the parts of the original two dimensional distribution where the collapsed variable cuts had tight deviations, provided the dependence on the collapsed variable isn't so great as to make this sharp region negligibly small. We can put this important general statement into context by looking at the charged component of the jet energy resolution in this way; the distribution for the charged jet energy resolution is, as Equation 22 suggests, a distribution in two variables: the energy  $E$  and the angle  $theta$ . The degree to which the distribution depends on  $theta$  is given by tracker parameter  $b$ , so in light of the above statement, if we have a large  $b$ , the resulting charged jet energy resolution should have a core that is really only a picture of the regions in  $theta$  where the jet energy resolution is good. However, if we make  $a$  (not  $b$ !) large enough that we can say  $a \gg b$ , then the well-defined  $\theta$  dependence on which the selection phenomenon depends will be swamped out. Also, we expect that if we make  $b$  very large we can cause a similar effect, only this time the resulting distribution will have such a small region in  $theta$  for which the resolution is good that a projection onto the energy axis will not have a well-defined core. So, as we change parameters, we expect four distinct regimes: if the resolution is just plain good enough, the core will be very tight; as the resolution gets worse but not too bad, the variations along the collapsed axis serve to smear this resolution around further, without "selecting" a particular region to define a core; as we make the resolution yet worse the selection phenomenon occurs, causing a sharpening of the core, as observed when the hadronic calorimeter parameter  $a$  reached its highest value; finally we expect as the resolution gets yet worse, the selec-

tion will be on such a small region that the collapsed distribution's core will lose out to the enormous, encroaching haunches that the heavy dependence causes. We can see an example of the selection phenomenon occurring in Figures 33, 35, 37, and 39 in the rightmost histogram. However, since our total jet energy resolution is a composite distribution of a few one dimensional distributions (the calorimeters) *anda* collapsed two dimensional distribution (the tracker) we expect end behavior in the extreme fourth regime where the tracker resolution gets so bad that the total jet energy resolution's core becomes almost totally photonic. All of this, to complicate things even more, occurs in the presence of a debilitating Landau-type particle loss tail in the tracker that skews everything, weakening any quantitative arguments based on gaussian fits. Having finally dealt fully with the complex statistical concepts necessary for understanding these collapsed distributions, we can turn our attention to  $b$ -parameter dependence, Figures 40–45.

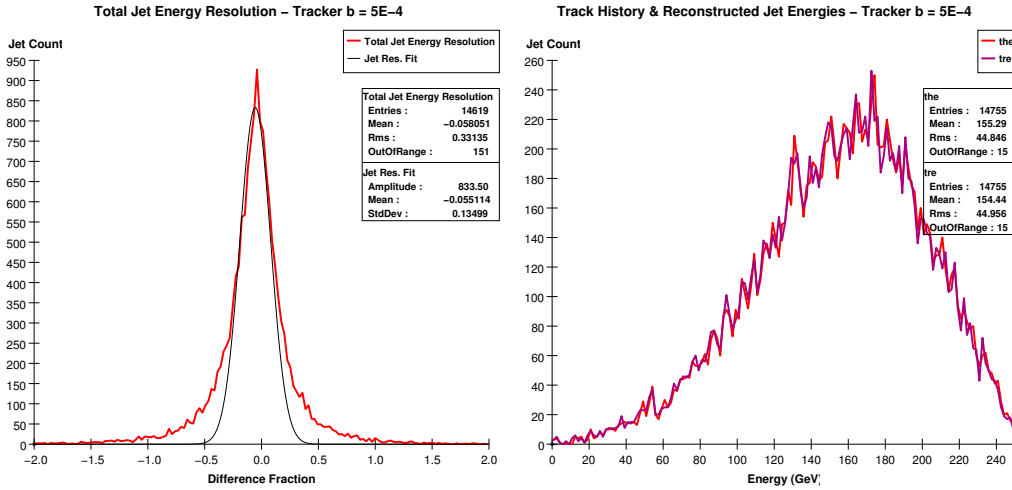


Figure 40: The above figure contains a plot of the photonic and the hadronic jet energy resolutions for the standard detector parameterization.

Note that in the sequence of Figures 40–45 the Simple Standard Figures 34 and 35, for which  $b = 1 \times 10^{-3}$ , should come between Figures 41 and 42

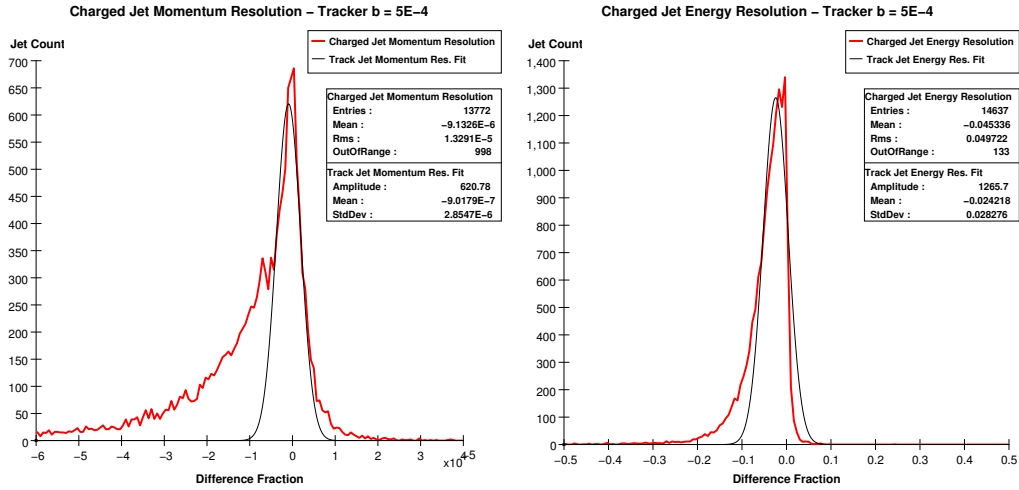


Figure 41: The above figure contains a plot of the photonic and the hadronic jet energy resolutions for the standard detector parameterization.

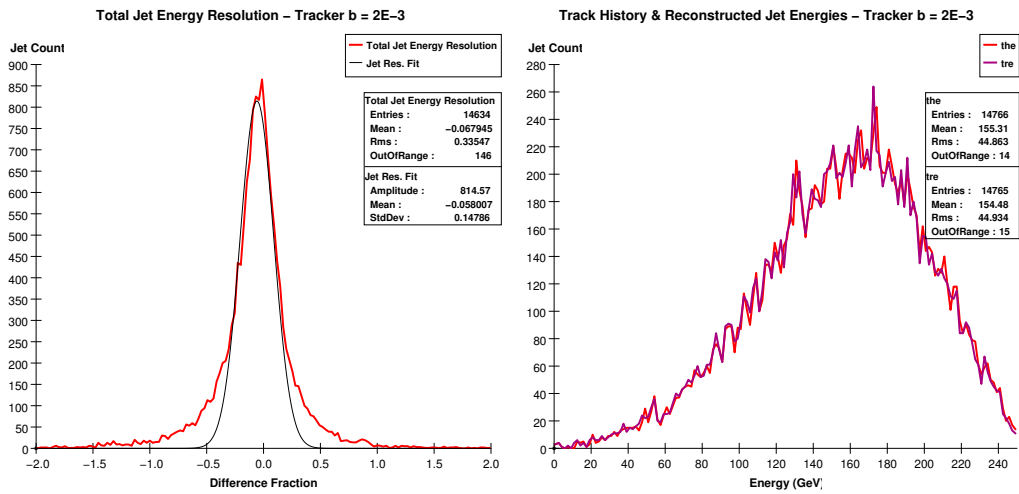


Figure 42: The above figure contains a plot of the photonic and the hadronic jet energy resolutions for the standard detector parameterization.

in order to complete the sequence. Just as in the histograms where the  $a$  parameter was varied, we see the “selection?? process occurring in the total jet energy resolution plots (the left histogram in the even numbered figures).

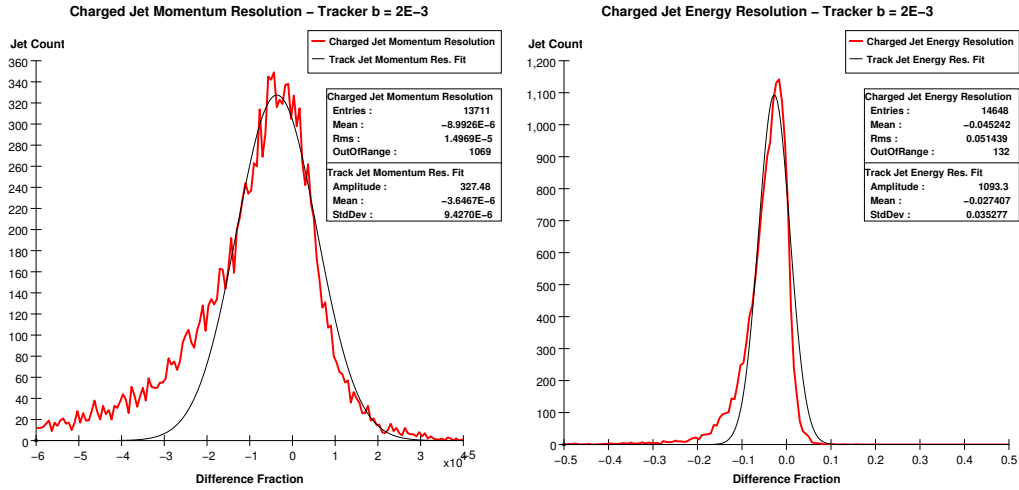


Figure 43: The above figure contains a plot of the photonic and the hadronic jet energy resolutions for the standard detector parameterization.

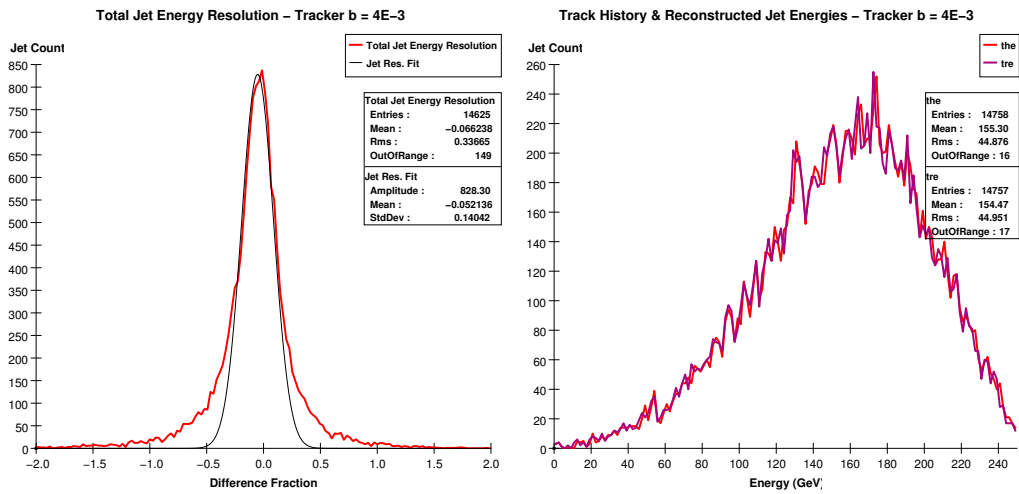


Figure 44: The above figure contains a plot of the photonic and the hadronic jet energy resolutions for the standard detector parameterization.

Interestingly though, in this set of histograms we don't see the selection phenomenon losing out to poor resolution for high values of  $b$ , something we must account for. By looking at Equation 22, we see that near  $\theta = 0$ ,  $P_t$  will

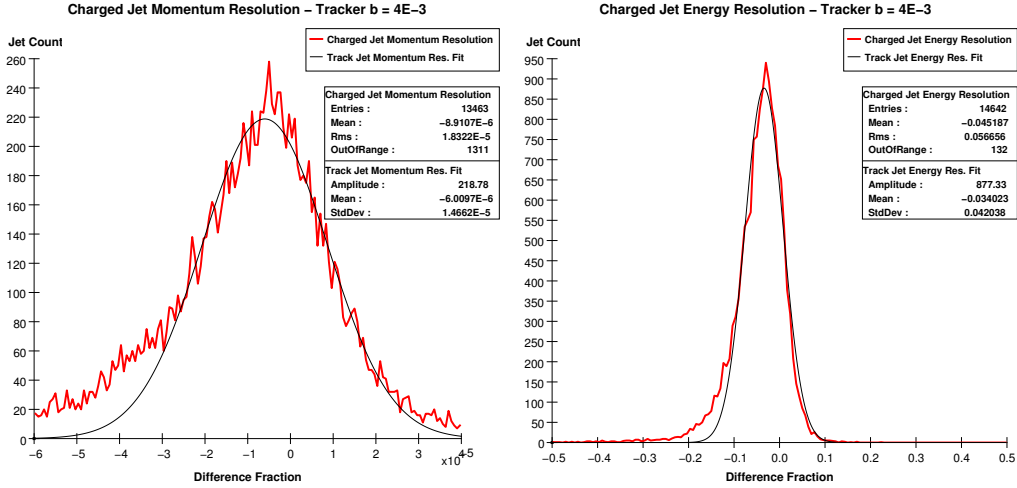


Figure 45: The above figure contains a plot of the photonic and the hadronic jet energy resolutions for the standard detector parameterization.

be maximized for a particle of some arbitrary energy, thus minimizing the contribution from the  $b$  parameter over a range of angles centered around  $\theta = 0$ . Parameter  $a$ , being isolated as a constant term, exhibits no such behavior; making  $a$  large will after a certain point affect all particles equally. The fact that we have particles selecting to minimize their errors if they come in at small angles and reasonably high energies will cause the selection phenomenon to persist over a much greater range of  $b$  values than  $a$  values. This is in agreement with the statistical exposition above; we cite  $a$  and  $b$  as affecting the total distribution in different ways, and even though the final effects are similar we shouldn't expect the different regimes to partition the  $a$  and  $b$  continuums identically. That being said, if we increased  $b$  enough, we should see the resolution trend inverting and getting worse, then finally settling on whatever value the photonic calorimeter and hadronic calorimeter can support. A final note, we can see that there are less and less counts in the core of the total jet energy distribution by looking at the peak values at the centers of the plots, supporting our ideas behind the cause of the selection

phenomenon.

## 5 Physics Analysis

Finally, after having put the program through extensive analysis and testing, we will use it to perform a somewhat more realistic analysis; in this section we present plots and results from analyzing a T-channel process in which an electron positron pair produce a pair of  $Z_0$  bosons. The lowest-order Feynman diagram for this process appears below, in Figure 46. Our particular simulated event takes place at 500 GeV center-of-mass energy, making the results appropriate for a thrust analysis as the jets from the  $Z_0$  particles will have good separation at this energy. In order to “measure” the masses of the  $Z_0$  bosons generated, we simply use the thrust axis of the event to divide the detector up into thrust hemispheres, then sum up the measured four-vectors of the final-state jet particles over each hemisphere. The end result will, of course, be two composite four vectors for each jet; we simply call the measured masses of these composite vectors the measured mass of the  $Z_0$  particle which creates the jet. Below, we present histograms of these measured  $Z_0$  masses generated at various detector parameters (we use the same set from the previous section), along with a rudimentary analysis of the results we have obtained.

In this section of the paper, we shall choose not to undergo the exhaustive and laborious analysis of each detector component undertaken in the sections dealing with the  $u\bar{u}$ -type events. Instead, we will simply note the similarities in statistical changes for the histograms as we vary a detector parameter, letting the exhaustiveness of the former treatment argue that the causes must be the same, as these two-jet events are quite similar from the detector’s point of view. If anything, the fact that the pair of  $Z_0$  bosons has a much higher mass than the  $u\bar{u}$  pair will only slightly affect the validity of our choice to treat these events with a thrust analysis. Again, the purpose of this section

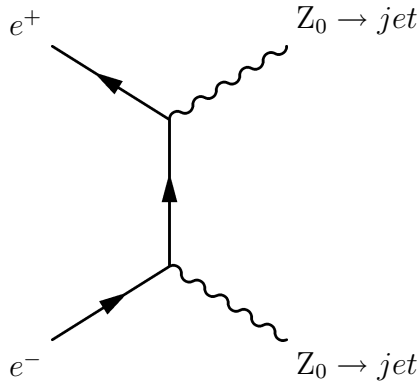


Figure 46: The above diagram depicts the T-channel  $e^+e^- \rightarrow Z_0Z_0$  process simulated to create the figures in this section.

of the paper is just to show that the program can similarly handle a slightly more sophisticated event.

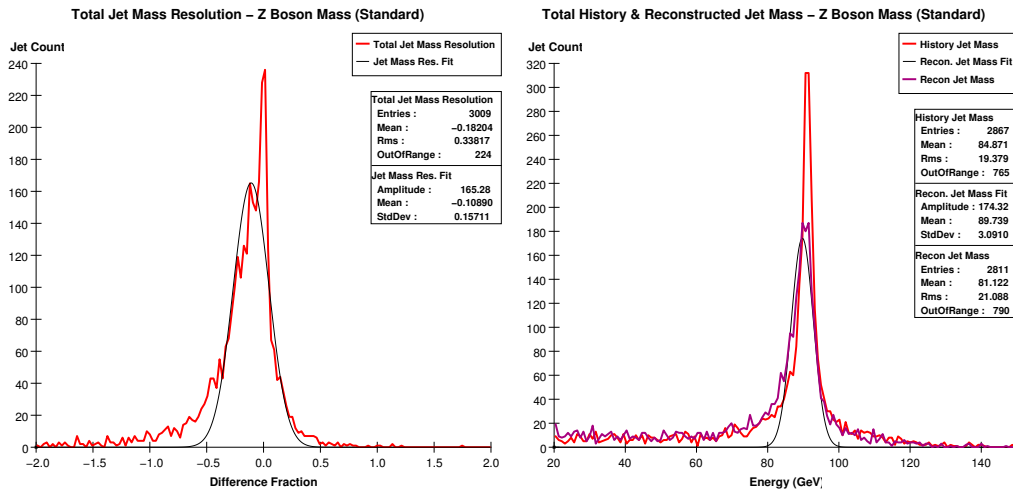


Figure 47: The above figure contains a plot of the photonic and the hadronic jet energy resolutions for the standard detector parameterization.

With the purpose of simple exposition in mind, we present firstly in Figure 47 two histograms summarizing the results of the  $e^+e^- \rightarrow Z_0Z_0$  event simulated with standard detector parameters. Comparing this diagram with its

$u\bar{u}$  analogue, Figure 16, proves especially useful. Both simulations, using the standard detector parameters, are subject to particle loss in the beampipe, the calorimeter because of minimum energy requirements, and the tracker because of minimum transverse momentum requirements; these losses manifest themselves in the negative shift of the reconstructed jet mass peak as compared with the history jet mass peak. Our standard detector reports a  $Z_0$  boson mass of 89.739 GeV, as compared with the modern measured value of 91.2 GeV. This does not seem spectacular, but the reader will notice that the center of the Gaussian fit in Figure 47 is certainly a bit below the center of the reconstructed mass peak, pushing our actual measured value a bit up and hence into a bit better agreement. This discrepancy is entirely due to the definition of the core of the peak, which is arbitrarily chosen to be all the distribution that falls above half the maximum height. This type of definition for the core is, unfortunately, necessarily somewhat blunt with the simple QR decomposition we've chosen to use. However, considering the complexity of the peak to which we must fit and the simplicity of the QR fitter, a disagreement of 1.6% should really be interpreted as very reassuring.

The next figure we present, Figure 48, summarizes a simulation for which the detector was hermetically sealed. Again, we can compare to the corresponding  $u\bar{u}$  histograms, found in Figure 19 for some useful conclusions. As compared with their standard detector counterparts, both of these histograms exhibit much better agreement between the reconstructed mass/energy peaks and the history mass/energy peaks. We conclude, then, that in the simulation of the two  $Z_0$  jets, the somewhat anemic mass measured with the standard detector parameters is due to particle loss. Confirming this hypothesis is the measured  $Z_0$  boson mass, reported in the hermetically sealed detector at 90.5 GeV. Again the reader can visually determine that the fit is again just a tiny bit shy of the position of the actual peak. Note here in comparison with Figure 47 that the peak for the hermetic detector is just a bit tighter than that for the standard detector; this is another trend that carries over

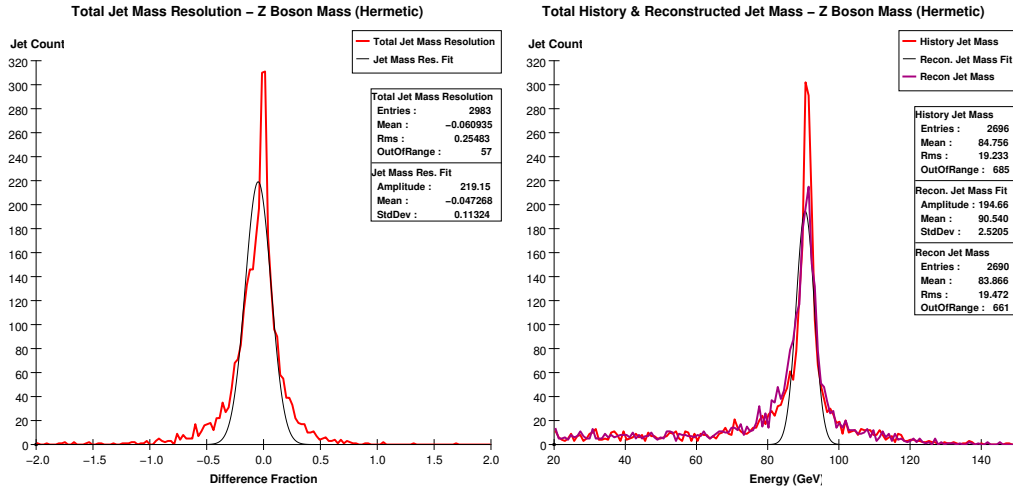


Figure 48: The above figure contains a plot of the photonic and the hadronic jet energy resolutions for the standard detector parameterization.

from the  $u\bar{u}$  simulations.

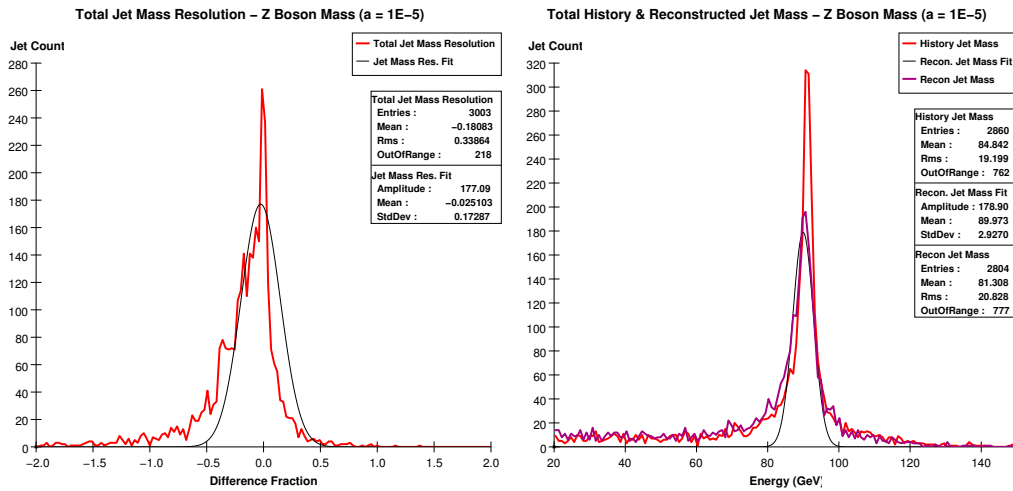


Figure 49: The above figure contains a plot of the photonic and the hadronic jet energy resolutions for the standard detector parameterization.

For the final point in the paper, we shall simply present a series of three

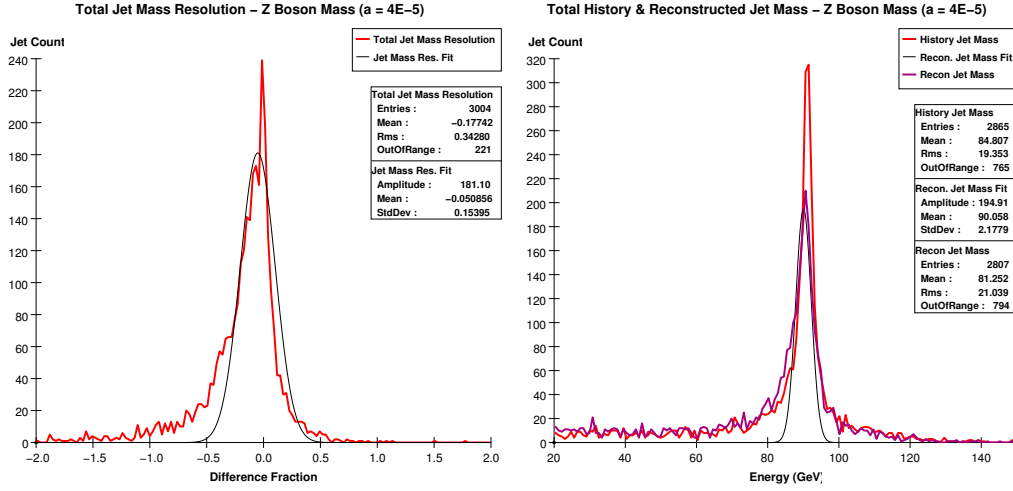


Figure 50: The above figure contains a plot of the photonic and the hadronic jet energy resolutions for the standard detector parameterization.

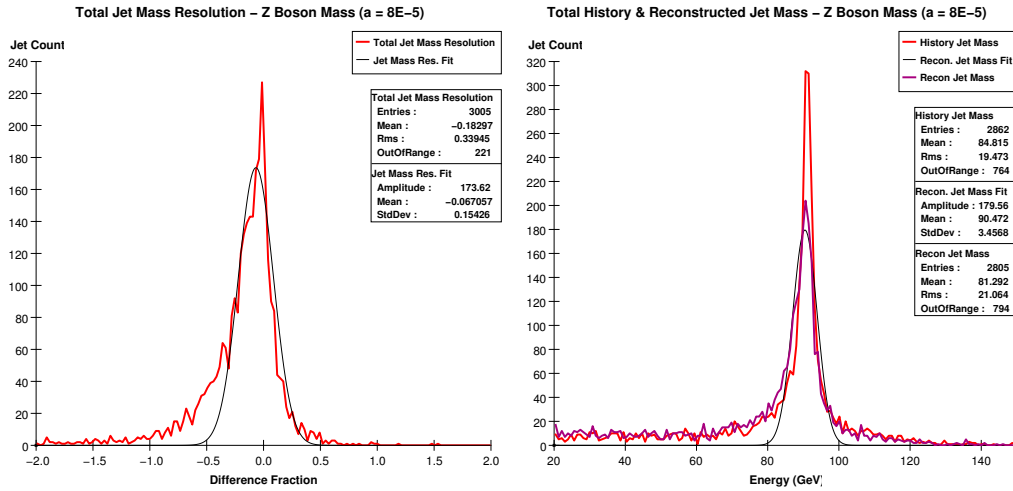


Figure 51: The above figure contains a plot of the photonic and the hadronic jet energy resolutions for the standard detector parameterization.

histograms generated over a range for a single detector parameter. The final histograms, found in Figures 49-51, are generated using the alternative simple tracker parameterization, with the tracker parameter  $a$  as given in Equation

22 acquiring the values  $1 \times 10^{-5}$ ,  $4 \times 10^{-5}$  and  $8 \times 10^{-5}$ , respectively. Recalling the complex discussion about core selection in multivariate statistical distributions given previously in the paper, we should ostensibly be looking for the same features occurring as we vary a parameter in this simulation. However, upon inspection of the histograms, it is immediately apparent that our tails due to particle loss are much too large and our distributions are hence much too non-Gaussian to make any arguments that could be called compelling. Still, we should look for something familiar happening underneath the noise. Firstly, consider the left side Figure 40. This histogram was created by binning jet-by-jet the difference between the reconstructed and the history masses and then scaling appropriately; this is exactly the quantity binned in generating the jet energy resolutions in the  $u\bar{u}$  sections of the paper. First of all, we see a very sharp peak that is clearly centered at 0.0 or somewhere very close to this value. Then, a third of the way down the peak, we see a large mass on the low energy side that is reminiscent of the tail/haunches incurred due to particle losses in the left side of Figure 33. In both of these histograms (each generated using the simple tracker parameterization with  $a = 1 \times 10^{-5}$ ) we have a sharply defined core due to the accuracy of the tracker along with the particle losses, and on top of this we have some selection occurring that sharpens the distribution if  $\theta$  is close to 0. A difference here is that we see the *total* jet mass resolution in a  $e^+e^- \rightarrow Z_0Z_0$  event resembling the *charged* momentum resolution in a  $e^+e^- \rightarrow u\bar{u}$  event; this fact suggests to us that we have a much greater charged component in the  $e^+e^- \rightarrow Z_0Z_0$  type jets as compared to the  $e^+e^- \rightarrow u\bar{u}$  type jets, which of course means that we are really going to be disabled in our analysis by the heavy particle losses in the tracker. Just as expected, for the histograms with the higher values for the  $a$  parameter, we see the resolutions worsening. The main manifestation of this is in the core of the total jet mass resolution; as  $a$  is increased, we see the core spike widening and dropping—by  $a = 4 \times 10^{-5}$  we already see the core at about the same height as the particle loss tail, but

then as we move to double this value at  $a = 8 \times 10^{-5}$ , there isn't a huge difference in the look of the mass resolution plot. This signals us just as in the  $u\bar{u}$  events that we have hit a transitional point where the accuracy of the other components of the detector are beginning to hold up the accuracy of the measurements to a greater degree.

---

This concludes the motivation, theory, implementation, exposition, and analysis of the Fast Monte Carlo simulation for the Linear Collider Detector, written by Daniel Furse during the summer of 2005 on the Department of Energy SULI summer internship at the Stanford Linear Accelerator Center. For any additional questions or comments, please contact Daniel Furse via email at:

<gttg251g@mail.gatech.edu>

## 6 Acknowledgements

First of all, the author would like to thank the Department of Energy, by whose dedication to scientific education this experience was made possible. The author would also like to warmly thank the following persons:

---

James Lindesay	Director of the SULI program at SLAC
Timothy Barklow	The author's mentor at SLAC
Norman Graf	for his extensive help and guidance
Helen Quinn	Official SULI program Contact
Pauline Wethington	SULI administrator

---

The author would finally like to extend his deepest gratitude to the other SULI interns and SLAC employees for making his summer research experience so unbelievably stimulating and truly unforgettable.

## The BaBar Gas Bubbler Upgrade and Evaluation

Yu Gan  
Office of Science, SULI Program  
Princeton University  
Stanford Linear Accelerator Center  
Menlo Park, California

August 9, 2005

Prepared in partial fulfillment of the requirements of the Office of Science, U.S. Department of Energy Science Undergraduate Laboratory Internship (SULI) Program under the direction of Charles Young, part of the BaBar Collaboration at the Stanford Linear Accelerator Center (SLAC).

Participant:

\_\_\_\_\_  
Signature

Research Advisor:

\_\_\_\_\_  
Signature

# Contents

<b>1</b>	<b>Introduction</b>	<b>1</b>
<b>2</b>	<b>Materials and Methods</b>	<b>1</b>
2.1	The Unmodified Gas Bubbler . . . . .	1
2.2	The Oil Trap Design . . . . .	5
2.3	The Retrofit . . . . .	6
2.4	Testing and Calibration . . . . .	7
<b>3</b>	<b>The Retrofitted Gas Bubbler</b>	<b>9</b>
<b>4</b>	<b>Calibration Results</b>	<b>11</b>
<b>5</b>	<b>Discussion and Conclusions</b>	<b>13</b>
<b>6</b>	<b>Acknowledgments</b>	<b>16</b>

## Abstract

The BaBar Gas Bubbler Upgrade and Evaluation. YU GAN (Princeton University, Princeton, NJ 08544) CHARLES YOUNG (Stanford Linear Accelerator, Menlo Park, CA 94025).

The Instrumented Flux Return region (muon and  $K_L$  detection barrel) of the BaBar detector at SLAC requires careful monitoring of the gas flow through the detector array. This is currently done by a system of digital gas bubblers which monitor the flow rate by using photogate technology to detect the presence of bubbles formed by gas flowing through an internal oil chamber. Recently, however, a design flaw was discovered in these bubblers. Because the bubblers are connected directly to the detector array with no filter, during rises in atmospheric pressure or a drop in the gas flow rate (eg. when the gas system is shut off for maintenance), the oil in this chamber could be forced backwards into the detector tubes. To compensate for this problem, we upgraded the existing gas bubbler systems by installing metal traps into the old gas lines to capture the oil. This installation was followed by an evaluation of the retrofitted bubblers during which we determined a relationship between the bubble counting rate and the actual gas flow rate, but encountered recurring problems with baseline fluctuations and unstable bubble counting rates. Future work will involve the study of how these instabilities develop, and whether or not they can be mitigated.

# 1 Introduction

In the data collection for the BaBar detector [1] at Stanford Linear Accelerator Center (SLAC), the outer layer of the detector, the Instrumented Flux Return (IFR), is devoted to the identification of muons and detection of  $K_L$ . Currently, due to the discovery of serious design flaws in the Resistive Plate Chambers (RPC) originally installed in the IFR, the IFR is undergoing a large retrofitting process in which the RPC units are being replaced by the more robust Limited Streamer Tube (LST) modules, a process which started in the summer of 2004 and is scheduled to be completed in the autumn of 2006.

In order to achieve the so-called limited streamer regime required in these modules, the gas mixture (8% isobutane, 3% argon, and 89% carbon dioxide) within these tubes must be carefully regulated; to this end, we have been using a system of digital gas bubblers [2] attached to the end of the gas lines to monitor the outgoing gas rates. The bubblers, however, revealed a serious design flaw recently, wherein certain variations in the ambient atmospheric conditions would be enough to force oil found within the bubbler into the actual modules. This paper outlines the procedures and problems with the retrofitting process designed to mitigate this malfunction of the gas bubblers.

## 2 Materials and Methods

### 2.1 The Unmodified Gas Bubbler

The digital gas bubbler system currently implemented at the BaBar detector is based on a model originally installed at KEK for the Belle detector [3]. A schematic of an unmodified gas bubbler is shown in Figure 1(a), and a photograph can be found in Figure 1(b). A total of 16 gas lines, or channels, can be directed into a gas bubbler at one time. Gas enters the bubbler through gas

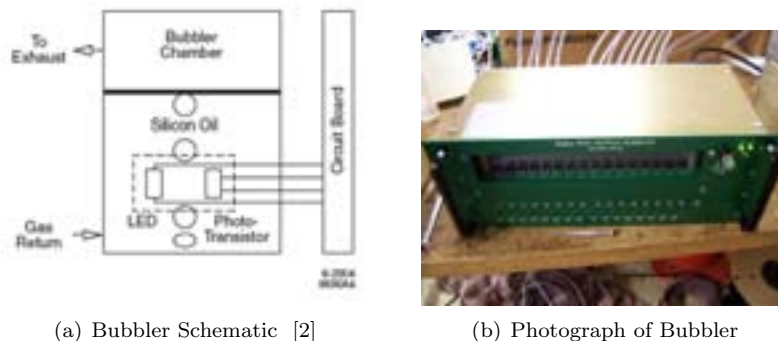
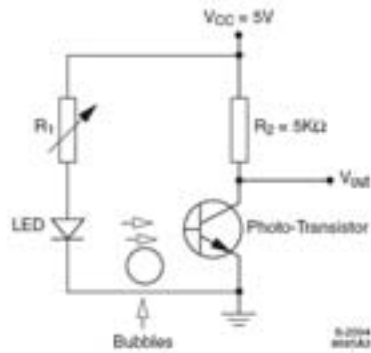


Figure 1: The Gas Bubbler

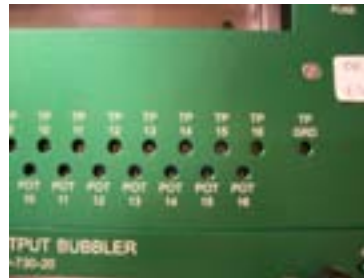
fittings in the rear of the bubbler, and these lines are fed directly into a front-mounted oil chamber. This oil chamber has a small amount of Dow-Corning 704 Diffusion Pump Fluid at the bottom which bubbles when gas is passed into the chamber, and the bubbles are restricted to 16 distinct positions where they pass by a photogate. The gas is then vented out into open air via the exhaust lines.

The photogate consists of a traditional LED and photo-transistor arrangement. The circuit is sketched in Figure 2(a). When a bubble passes through the LED beam, the beam is refracted and fewer photons hit the photo-transistor. This produces a voltage spike which we can read with an oscilloscope or other electronics through test points on the bottom of the front panel (see Figure 2(b)). The voltage spike is inversely proportional to how much light hits the photo-transistor, ie. the more the light is refracted, the greater the signal strength. As seen in Figure 3, the light is refracted the most as the bubble enters and leaves the photogate (when the angle of incidence between the horizontal LED beam and the gas-oil bubble interface is greatest) and is refracted the least as the bubble's center passes the LED (when the LED beam is approximately normal

to the gas-oil interface).



(a) Photogate Circuit (diagram provided by Stephen Foulkes [2])



(b) The Front Panel

Figure 2: The Photogate

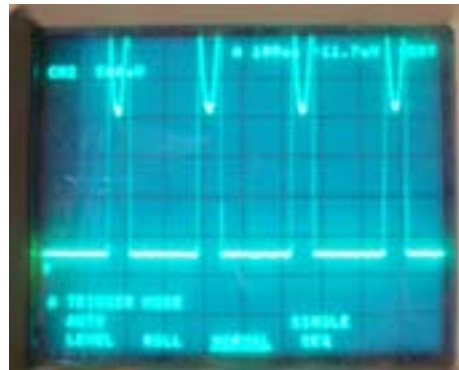


Figure 3: A photogate signal as read out on an oscilloscope

We require for our testing purposes that the spike's valley be between 2 and 2.5V. This is because of the fact that we actually count anything above 1V as a bubble, and by using the 2V threshold, we ensure that the valley will never dip below 1V. If the spike's valley were to fall below 1V, we would double count a single bubble—the first bubble would be the large incoming spike and then the first half of the miniscus before it falls below 1V, and the second would be

the rest of the spike as the voltage climbed above 1V. If the valleys are too low or too high, we can adjust the intensity of the LED by varying the resistance with a potentiometer mounted on the front panel below the oil chamber—if we increase the intensity of the LED beam, the entire amplitude of the spike rises, and the spacing between the valley and the peaks adjusts proportionally.

According to the original design of the bubbler, the incoming gas lines in the interior of the bubbler chassis directly fed into the oil chamber in the front of the chassis. It was soon discovered, however, that because the exhaust line was open to the air and thus sensitive to atmospheric pressure changes, if the ambient air pressure were to rise by one or two inches of water (as it may after a storm front moves out of the area), the pressure of the incoming gas flow may not be enough to prevent the oil in the chamber from flowing back into the gas return line, possibly reaching the connected modules.

This phenomenon has already been witnessed—Figure 4 shows one of the straight gas lines from the interior of the chassis which has several oil droplets within it. If oil were to flow back into the LST modules, the modules could potentially become unusable.



Figure 4: A section of the gas line with oil droplet contamination

It should be noted, however, that we have yet to have such a problem with bubbler performance with the LST modules; four bubblers were retrofitted during last summer's LST installation and they appear to be functioning well.

## 2.2 The Oil Trap Design

In order to compensate for the problem with the original gas bubbler, it was decided that installing cylindrical oil traps between the incoming gas line and the oil chamber would be the most efficient method given the dimensions of the chassis and the dimensions of the rack on which the bubbler is mounted. The traps, as shown in Figure 5, consist of a metal cylinder with two metal caps welded to the top and the bottom, the former having two holes for Poly-Flo gas fittings. The bottoms of these oil traps must be covered with plastic endcaps (Figure 5) to both insulate the metal and physically protect the motherboard underneath gas lines from wear and tear. Each oil trap has a volume exceeding the total volume of fluid in the oil chamber, allowing for the extreme case where 15 channels are functioning properly and all the oil flows back through the last channel. We have no way of checking the traps for oil, so if a major amount of oil were missing, we would have to open up the chassis and check each trap; this procedure will not happen very often if at all.

Gas fittings come in two flavors—the straight connector and the elbow connector (Figure 5). To most efficiently use the volume within the chassis, two oil trap configurations are used—the straight-straight combination, and the elbow-straight combination. In the past there was in fact an oil trap design that allowed the elbow-elbow combination, but this design was eventually replaced by the current oil trap design because this new type was easier to weld and less prone to damage. By using four or five elbow-straight oil traps with the gas channels 1, 2, 14, 15, and 16 (sometimes channel 14 can be done with a straight-straight, depending on how well-packed the middle channels are), and packing the straight-straight cylinders in the middle region as tightly as possible, all 16 channels fit snugly above the motherboard.

Each gas fitting must be screwed into the oil traps with teflon tape. The



Figure 5: Oil trap components clockwise from top-left: Metal Oil Trap, Endcap, Elbow Connector, Straight Connector

teflon tape wrapped around the threads of the gas connectors ensures a gas-tight connection between the oil trap and the gas fittings, sealing any oil into the traps.

### 2.3 The Retrofit

Before full installation can begin, we first had to remove the old gas lines and clean the inside of the chassis. There was frequently a lot of oil lining the inside walls of the chassis, or even the PC board itself. Following this cleaning, we had to cover the PC board and the power supply with insulating plastic to prevent any shorts from occurring between the metal oil traps and the electronics. We used a heat-resistant plastic, and taped the plastic down with 3M 471 Vinyl Tape.

Once the plastic protection had been placed, we replaced the exhaust gas lines first. The long gas line measures 11.25 inches, and the short tube measures around 3 inches. Then, working from Channel 1, we installed each oil trap with tubing along the inside of the chassis. Because of the shortage of space within the chassis, we had to significantly bend some of the tubes to fit them into the box. To avoid putting kinks in the Poly-Flo tubing, the tubes were placed in

boiling water for several seconds before they were installed into the gas fittings, and then bent into shape. This “heat-bending” procedure does place moisture into the tubing, but because the gas bubbler system is placed at the end of the gas line, any moisture retained in the bubbler system should have no effect on LST operation, and in fact, by the time installation occurs, the moisture should have exited the system during testing.

Incidentally, all of the oil traps in the new chassis tend to weigh down the PC board, especially in the middle region where the tube lengths lead to lower-lying oil traps. The PC board could potentially drop so low that the readout and potentiometer access ports on the front of the chassis may drop below the holes in the front panel. Additionally, this added pressure from the traps combined with the warping of the PC board could break some of the more fragile solder joints on the board itself. In order to ensure access to the potentiometers on the front panel, we used styrofoam blocks taped to the bottom of the chassis to support the PC boards from below. These blocks are cut specifically for each chassis, depending on how much the board is pushed down, but the blocks are usually around 1 inch in thickness, and are placed below the potentiometers in the front of the chassis running backwards towards the readout port on the back of the chassis.

## 2.4 Testing and Calibration

After hardware installation, the upgraded chassis are attached to a gas distribution box that can flow gas into all 16 channels (Figure 6). The gas distribution box consists of an incoming gas hose that feeds regular air into 16 Dwyer RMA-151-SSV flow meters, which lead to gas tubes that can attach directly into the rear of the gas bubbler panel of the gas bubbler.

The flow rate for each channel can be set between 30 and 40 cc/min of regular



Figure 6: The Gas Distribution Box

air, and the gas bubbler is tested for any aberrant flow rates. We choose this flow rate because the LST's usually see a gas flow rate such that there is about one volume change per day per gas line. Each gas line services four modules on average, and each module is taken to have an average volume of 15 liters. After conversion, this becomes approximately 41 cc/min (around where we run calibration tests for the bubbler). One chassis, Bubbler 021, was calibrated for this paper.

Rather than use a computer to readout the bubble rate, a rough estimate of the bubble rate by hand is enough to confirm the bubbler's efficiency. We do this by putting test pins in the test points on the front panel of the bubbler and reading out any voltage spikes on the oscilloscope. We set all 16 channels at 10 cc/min and then calibrated each photogate readout until the valley of the spike fell between 2 and 2.5V. After we make this adjustment, we find a suitable viewing window for the oscilloscope display, and froze the display when we could see at least ten distinct spikes caused by bubbles. We then use the cursor function on the scope to find the amount of time we needed to see ten bubbles pass through our photogate, and we then extrapolate the actual count rate from this measurement. We repeated this procedure for 20 cc/min, 30 cc/min, 40 cc/min, and 50 cc/min, the maximum measurable output on the

flow meters.

### 3 The Retrofitted Gas Bubbler

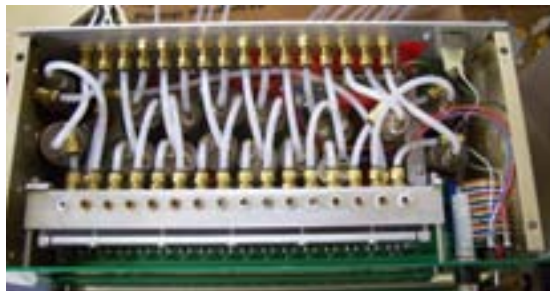


Figure 7: Aerial view of the interior of the retrofitted bubbler

The interior of the upgraded gas bubbler is shown in Figure 7. As can be seen in Figure 8(b), we have generally chosen to cross the gas tubes in the mid-section (ie. we have connected the gas fitting on the rear of the chassis to the oil trap gas fitting that is farthest away, and similarly for the gas fitting on the front of the chassis). This allowed us to bend the tubes with softer curves, and combined with the short lengths of the tubes in the midsection, we greatly reduced the stress on the PC board. The first completed chassis pushed the middle of the PC board down by about 2 mm, but when we shortened the tube lengths in the midsection to 2.5 and 4.5 inches and used the heat-bending technique, we were able to reduce this sagging to about 1 mm.

Indeed, every tube was eventually heat-bent. We had originally planned on only heat-bending the tubes on the left and right sides of the chassis, but when we cut the mid-section tubes to 2.5 and 4.5 inches, the mid-section tubes required heat-bending as well. The tubes on the left and right sides of the chassis (the left side is shown in Figure 8(a)) still demanded the most heat-bending, especially the long tube leading into Channel 2 of the gas bubbler—the tension

within the tube combined with its length forced the tube well above the plane of the box lid, and we eventually decided to heat-bend the tube and then place the lid on the chassis while the tube cooled to condition the Poly-Flo.



(a) Left side



(b) Middle

Figure 8: Closer view of the retrofitted gas bubbler

## 4 Calibration Results

We can use the flow rate reading on the flow meter attached to the distribution box to approximate the correlation between the bubble rate and the flow rate; below is a table of the bubble rates we measured using the techniques outlined in Section 2.4.

	Bubble Rate (bubbles/min) at				
	10 cc/min	20 cc/min	30 cc/min	40 cc/min	50 cc/min
Channel 02	126	174	258	300	366
Channel 03	127	193	267	306	366
Channel 04	115	185	268	306	366
Channel 05	131	200	273	309	364
Channel 06	113	194	250	296	359
Channel 07	117	240	239	300	441
Channel 08	114	162	283	330	444
Channel 09	111	181	245	293	366
Channel 10	112	183	273	314	377
Channel 11	115	206	278	339	375
Channel 12	127	232	303	302	382
Channel 13	131	188	275	319	423
Channel 14	121	173	274	316	380
Channel 15	127	190	274	316	370
Channel 16	112	208	239	302	351

Table 1: Bubble rate vs. flow rate in Bubbler 021

We ignored the data for the first gas channel because the Dwyer flow meter knob was very sticky and the flow rate given on the meter was not very responsive to our turning of the knob. The error on these measurements is approximately  $\pm 5\%$  bubbles/min, which we get from the uncertainties in the cursor placement on the oscilloscope display.

In ramping up the flow rates, we also discovered that as we increased the physical flow rate on the flow meter, the amplitude of the voltage spikes (the initial and final rise as well as the valley) decreased without our adjusting the intensity of the LED beam, and vice versa. In fact, the behavior exhibited by the bubbler readout on the oscilloscope was extremely similar to the kind

of readout one would get from adjusting the LED intensity—changes in the difference between peak and valley of a bubble spike, changes in amplitude, etc. Figure 9 shows this flow behavior at a constant LED intensity.

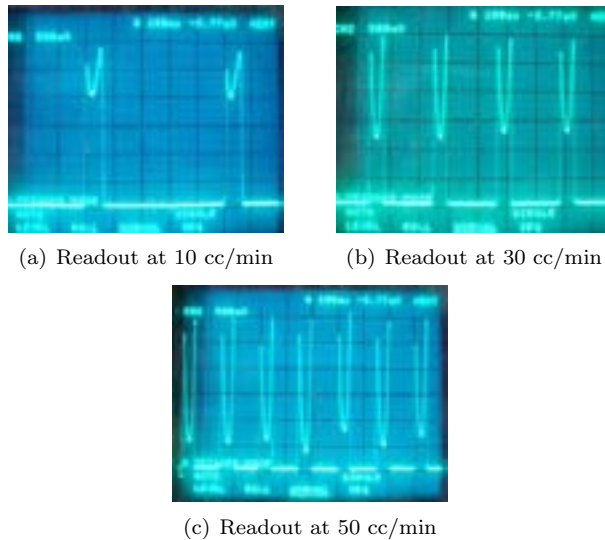


Figure 9: Oscilloscope readouts at constant LED intensity

It is important to note that adjusting the LED will *never* appreciably affect the count rate, so the flow rate affecting the scope readout in a way similar to the LED adjustment is peculiar.

Lastly, we encountered a few temporary instances of “baseline fluctuations” (Figure 10) in 4 of the 64 channels that were retrofitted for this project. As can be seen in Figure 10, baseline fluctuation is a situation in which the usually flat baseline between bubble peaks become jagged and erratic, sometimes jumping beyond the 1V counting threshold. The fluctuations generally disappeared after letting the gas flow for several hours or overnight.

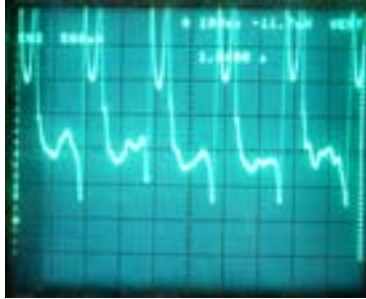


Figure 10: Baseline fluctuation on the oscilloscope readout

## 5 Discussion and Conclusions

We expect that the flow rate is in no way affected by the oil traps. By taking the Reynold's number for the BaBar gas system, we can determine if the flow is laminar or turbulent. The formula for Reynold's number  $Re$  of flow through an arbitrary pipe is

$$Re \equiv \frac{VD}{\nu}$$

where  $V$  is the fluid velocity,  $D$  is the diameter of the pipe through which a fluid is moving, and  $\nu$  is the kinematic viscosity of the fluid [4].

The diameter of the Poly-Flo is documented at  $\frac{1}{4}$  inches, and this converts to 0.625 cm. The kinematic viscosity of the gas is well-documented, and we will assume for simplicity that the gas is 100% carbon dioxide. The kinematic viscosity of carbon dioxide at standard temperature and pressure (1 atm and 273.15 K is  $8.03 \times 10^6$  m<sup>2</sup>/s [5]), and although the conditions in the testing lab are not quite at STP, using this  $\nu$  is a reasonable approximation of the actual  $\nu$  of carbon dioxide in the bubbler. We know the flow rate through each gas line is about 41 cc/min. We can now convert this volumetric flow rate into an average velocity for the gas by using the simple conversion

$$\text{Volumetric Flow Rate} = (\text{Average Velocity}) \times (\text{Cross-Sectional Area of Pipe})$$

which follows from the idea of a cylinder of volume 41 cc with a base area equal to the cross section of the pipe and moving parallel to its height at the average velocity indicated in the formula.

Using this conversion, we get a mean  $V$  of 134 cm/min. If we assume that our flow is turbulent, we approximate  $V$  by doubling 134 cm/min and substitute into our equation for  $Re$  and get 34.8 for our Reynolds number. A Reynolds number below 2320 is considered laminar flow, so even under the assumption that our flow was turbulent, we have a sufficiently low Reynolds number to achieve laminar flow. Often times the limiting factor of flow within a pipe is the pipe diameter, but our flow rate is so low that this is not even an issue.

Given this expectation, adding oil traps into the gas line should have had little effect, because even though we placed more bends in the tubing (which generally increase resistance to flow), our flow rate is so low that any bends the gas sees may be approximated as straight lengths of tubing. Indeed, we see this situation in the retrofitted gas bubblers. If we take the results from Table 1 and use Microsoft Excel 2003's linear regression function to find a linear correlation of the data, we get a reasonably strong correlation between bubble rate and flow rate as read from the flow meters (see Figure 11). This relationship is analogous to the conversion factor found in an earlier study on the unmodified gas bubblers [6].

We do not have error bars drawn on the graph simply because the level of accuracy we need is not remarkably high. The bubblers are not designed to give extremely accurate outputs of the flow rate in the modules; rather, they are designed to confirm that flow is occurring in the gas lines, and also to

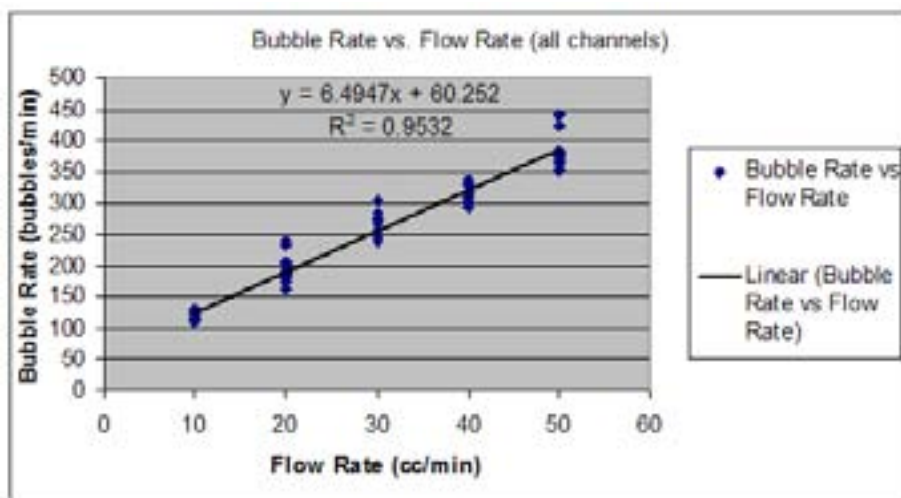


Figure 11: Microsoft Excel output for calibration data of Bubbler 021

give relative flow rates so that changes can be observed in the gas line. The error in fact lies mostly in the Dwyer RMA-151-SSV flow meters attached to the gas distribution box; the oscilloscope readings are reasonably precise, but the fluctuation of the flow meter reading is large (on the order of  $\pm 5$  cc/min at times). It is pointless to try for precise measurements with the Dwyer flow meters; in our evaluation, we intended only to qualitatively confirm that a rough linear fit still exists at these flow rates.

The issue of the changing spike amplitudes is something of a mystery. We currently surmise that it is related to the change in bubble size at different flow rates; when the flow rate increases, the pressure on the tubing outlet would increase, and a slightly larger bubble would form. This larger bubble could deform and become more like an ellipsoid, with the major axis oriented vertically. This way, the refraction at the top of the bubble remains relatively the same, but the rest of the bubble surface is more perpendicular to the LED beam than a sphere's surface, and would thus refract much less. This is pure conjecture at

this point, and further studies may investigate this phenomenon in the future.

The issue of baseline fluctuations does not appear to be a direct result of our installation of oil traps; rather, we believe that baseline spikes may be caused by dust particles that at some point during production were trapped in the bubbler system. These dust particles could conceivably get caught in the photogate apparatus and cause less refraction than the oil-gas film of a bubble, but still enough to register small spikes along the baseline when a bubble is not present. Eventually, the gas flow itself should push this dust particle out of the photogate, thus explaining the temporary nature of the baseline fluctuations. An alternative theory is that a small gas bubble may attach itself to the side of the photogate, and similarly cause smaller but noticeable refraction when a full bubble is not present. Neither of these theories has been confirmed, but as the baseline spikes are a temporary but recurring problem, further experimentation is planned to study this issue.

## 6 Acknowledgments

I would like to thank my mentors Charlie Young, Mark Convery, Sanjay Swain, and Wolfgang Menges, as well as Steve Foulkes and Howard Rogers for all the advice they have given me on physics and research in general. Thank you to my friend Frank Mycroft for his help on fluid mechanics and Reynolds number. Thank you to James Lindesay and Helen Quinn, the two masterminds behind the SLAC SULI program that brought me to California and gave me such a great opportunity to explore the world of modern physics. Thank you to Stew Smith, who let me know about this program. Thank you to Stanford Univ., SLAC, and SULI for providing me with one of the best summers of my life. And finally, I would like to thank the Department of Energy and the Office of Science for supporting this phenomenal program for the last few decades.

## References

- [1] B. Aubert et al. BaBar Collaboration. *Nucl. Instr. and Meth.*, A479:1, 2002.
- [2] S. Foulkes et al. Gas system upgrades for the BaBar IFR detector at SLAC. *Nucl. Instr. and Meth.*, A538:801–809, 2005.
- [3] M. Ahart et al. Flow Control and Measurement for RPC Gases. KEK Belle Note #135, Princeton University, July 1998.
- [4] Eric Weisstein. *Reynolds Number - from Eric Weisstein's World of Physics.* World Wide Web, <http://scienceworld.wolfram.com/physics/ReynoldsNumber.html>, 2005.
- [5] Ken Edwards. *Fluid Properties.* World Wide Web, <https://www.lmnoeng.com/fluids.htm>, 1998-2000.
- [6] Angela Little. Evaluation of the electronic bubbler gas monitoring system for high flow in the BaBar detector. SLAC-TN-03-015.

# An Automated Method for Characterizing the Relaxedness of Galaxy Clusters

MATT GEORGE

HARVARD COLLEGE

OFFICE OF SCIENCE, SCIENCE UNDERGRADUATE LABORATORY INTERNSHIP

STANFORD LINEAR ACCELERATOR CENTER

MENLO PARK, CA 94025

August 19, 2005

Prepared in partial fulfillment of the requirements of the Office of Science, Department of Energy Science Undergraduate Laboratory Internship under the direction of Dr. Steve Allen and Dr. Greg Madejski in the Kavli Institute for Particle Astrophysics and Cosmology at the Stanford Linear Accelerator Center.

Participant: \_\_\_\_\_  
Signature

Advisors: \_\_\_\_\_  
Signature

\_\_\_\_\_  
Signature

# Contents

Abstract	3
1 Introduction	4
2 Procedures	5
2.1 Data Selection and Reduction	5
2.2 Elliptical Isophote Fitting	6
2.3 Power Ratios	7
2.4 Other Tests	8
3 Analysis	9
4 Conclusion	10
5 Acknowledgements	11
References	11

# List of Tables

1 Information about the cluster sample: cluster name, Chandra observation ID, instrument (ACIS-S or ACIS-I), exposure length, redshift, and training group ( <i>Relaxed</i> , <i>Unrelaxed</i> , or none).	14
--	----

# List of Figures

1 Elliptical isophotes fit to A2029, a relaxed cluster (left), and A520, an unrelaxed cluster (right).	15
2 A King model fit to the surface brightness profile of A478	16
3 A plot of power ratios demonstrating the correlation of the decreasing relaxedness of the clusters from bottom left to top right with the increasing values of their power ratios $P_3/P_0$ and $P_2/P_0$ . Figure from [9].	16
4 Index parameter, $\beta$ , plotted against core radius from the King model fits to the catalog. Relaxed clusters exhibit smaller values of $r_c$ than unrelaxed clusters.	17
5 Centroid shifts for the catalog. The relaxed group shows smaller shifts than the group of unrelaxed clusters.	17

# An Automated Method for Characterizing the Relaxedness of Galaxy Clusters

M.R. George<sup>1</sup>, S.W. Allen<sup>2</sup>, G.M. Madejski<sup>2</sup>

1. Harvard College, Cambridge, MA 02138, USA.

2. Kavli Institute for Particle Astrophysics and Cosmology, Stanford University, Menlo Park, CA 94025, USA.

August 19, 2005

## Abstract

Relaxed galaxy clusters are useful tools for probing cosmological parameters like the gas mass fraction of the universe. Selecting relaxed clusters for this purpose can be a time-consuming and subjective task, so we present methods to automate parts of the process. We fit elliptical isophotes to a diverse sample of Chandra cluster data and summarize other methods for quantifying relaxedness which will be included in future work. Analysis of the results of tests from isophote fitting, combined with numerical simulations of cluster structures and comparison to previous classifications will allow us to formulate criteria for selection of relaxed clusters. We find that they tend to have core radii less than approximately 60 kpc from King model fits, shifts in isophote centroids of less than 25 kpc over a range in semi-major axes of several hundred kpc, and significantly greater surface brightness profile gradients within 30 kpc of their cores than unrelaxed clusters. These criteria will help with future cosmological work as larger amounts of cluster data are taken and need objective classification.

# 1 Introduction

Galaxy clusters are important objects for constraining cosmological parameters. Due to their immense size, they are thought to provide a representative sampling of the matter distribution of the universe. The structure within clusters can offer information about evolution over large timescales as well as the dynamics of galaxy interactions. In order to make use of the complex and diverse array of clusters, it is important to have the ability to classify them objectively.

For cosmological purposes, we often wish to select dynamically relaxed clusters for closer study. These objects can be used as a type of standard tool for cosmological mass measurements in the way that Type Ia supernovae have been used as homogeneous candles to study cosmic acceleration. Eliminating clusters with significant structure or activity allows a more careful measurement of the X-ray gas mass fraction, which offers a useful parameter in calculating the densities of matter and dark energy in the universe [2]. Unrelaxed clusters can be physically identified from their spectra if their cores have cooling times greater than the age of the universe, while the cores of relaxed clusters cool on shorter timescales [4]. Relaxed clusters are visually distinguished by their smooth spherical or ellipsoidal gas distributions and relatively sharp central peaks, and they can often be identified optically from a single large galaxy lying at the center of the gravitational well. Unrelaxed clusters may show signs of multiple peaks, asymmetric gas distributions, or merger activity between galaxies.

To date, most classification of clusters has been done by eye. [10] uses a common approach to cluster morphology by analyzing contour lines for multiple brightness peaks, asymmetries, and other irregularities to identify structure. In an effort to reduce the subjectivity introduced by human judgements, [5] presents an attempt to quantify morphologies by measuring the power ratios of polar moments in the x-ray flux distribution. This method has recently been used in a study [4] of the cooling cores of clusters. Another approach involves fitting elliptical isophotes to images of the clusters as originally detailed

for galaxy profiles by [8]. The shifts in centroids and position angles of the ellipses, as well as their ellipticities, offer quantitative details about the shape of the profile which can standardize judgments made by eye. More approaches are presented by [12], which measures deviations from a spherically symmetric profile with  $\beta$ , Lee, and Fourier elongation tests. In this paper, we present an attempt to synthesize some of these techniques with a goal of creating a single automated system for identification of relaxed galaxy clusters.

In the following section, we will outline the tests to be used in our analysis beginning with simpler ones like surface brightness profile fitting from elliptical isophotes. Methods to be implemented in the future like power ratios, as well as more complex techniques such as subtracting a model cluster profile from the data with Markov Chain Monte Carlo analysis will be discussed toward the end of § 2. The results of the tests we have performed will be summarized in § 3. In § 4, we will summarize our findings and discuss future uses for the tools created, including the prospect of creating a unified and efficiently computed index to characterize the relaxedness of a cluster.

## 2 Procedures

### 2.1 Data Selection and Reduction

In order to determine the shapes and evolutionary states of galaxy clusters, we can view the intracluster gas, which has been heated to temperatures sufficiently high to emit x-rays. We use data freely available from the Chandra archive, with clusters in the redshift range  $0.06 < z < 0.45$ . We use Chandra data for its high spatial resolution, which is significantly greater than prior instruments. Clusters were selected from those observed by [1], as well as those listed in the ROSAT Brightest Cluster Sample and its extension, produced by [6, 7] and the REFLEX catalog introduced by [3]. The clusters used in this paper are presented along with their redshifts and other relevant information in Table 1.

With the intention of creating a fast method for selecting relaxed clusters from larger samples or surveys, we wished to minimize the amount of data reduction needed. We chose to use images from the archive's standard processing pipeline which had already been filtered for bad pixels and only contained the two-dimensional spatial information, rather than including the spectral data and reducing the images more thoroughly. Images taken by ACIS-S were preferred over those from ACIS-I due to gaps in the chip layout, but masking will be performed along with the power ratio analysis in order to account for these flaws and to allow for the inclusion of images from both instruments. Additionally, bright sources not belonging to the cluster and regions of high background will be removed using the reduction and power ratio code from [4]. For certain analyses, AGN or other bright sources like central dominant galaxies must be masked from the centers of some clusters.

## 2.2 Elliptical Isophote Fitting

A simple way to extract useful information about the shape of a cluster is to fit elliptical isophotes to images of the profile. We used the *ellipse* function in IRAF to carry out this task, allowing the position angle, ellipticity, and centroid position to vary while fitting ellipses at fixed semi-major axes (SMA) separated in increments of one pixel. Examples of elliptical fits superposed on the Chandra images of a relaxed and an unrelaxed cluster are shown in Figure 1.

This process is not easily automated, since fitting ellipses to a diverse array of clusters requires attention to be given to the program's parameters. For instance, clusters with significant substructure need to have initial ellipses fit at larger distances from the centroid in order to include the whole profile, while more relaxed clusters have smaller core radii and must initially be fit much closer to the center. These differences themselves could provide useful information about the relaxedness of a cluster, but we prefer a more rigorous method than relying on the peculiarities of a fitting program to classify clusters.

Once the information is obtained from the ellipse fitting process, we perform statistical analyses to differentiate between clusters. Using IDL code, we fit a King model of the form  $S(r) = S_0 \left(1 + \left(\frac{r}{r_c}\right)^2\right)^{-3\beta + \frac{1}{2}}$  to the surface brightness profile, where  $S$  is the average number of photon counts across the isophote at semi-major axis  $r$ ,  $S_0$  is a free normalization parameter,  $r_c$  is the core radius in pixels, and the third free parameter is the slope index  $\beta$ . This model was determined to work better than IRAF's built-in galaxy profile model, a sum of two exponentials and a constant, after considering that the King model has half as many free parameters while still providing a good visual fit. A sample comparison of a King model fit to surface brightness profile data is shown in Figure 2.

A related measurement for determining the sharpness of the peak of the surface brightness profile is its gradient. Since relaxed clusters can generally be expected to have strongly centralized luminosity profiles, the magnitudes of their gradients should be greater than those for unrelaxed clusters.

Another useful test for relaxedness that is readily available from the isophote data comes from measuring the distances that the ellipse centroids shift with SMA. Similarly, the changes in relative position angles of the ellipses can also provide information about the structure of a cluster. A relaxed cluster is expected to have a smooth and symmetric spatial distribution of x-ray emitting gas, which would result in concentric ellipses without much variation in position angle. Relaxed clusters can be elliptical rather than spherical because the relaxation time between these states is significantly longer than the age of the universe. Thus, while some may include tests of elongation to characterize relaxedness (e.g. [12]), we generally ignore the ellipticity in our analysis unless it is extreme or highly uncertain, which often indicates an isophote fit of poor quality.

### 2.3 Power Ratios

We intended to apply the method from [5] of multipole expansion of the two-dimensional gravitational potential to calculate power ratios for the sample. Our work with this ap-

proach is presently incomplete, but the process will be explained here because it will be used in future work.

The power of an  $n^{\text{th}}$  order polar moment is denoted as  $P_n$ , and for statistical analysis the power is normalized to become the power ratio  $P_n/P_0$ . More relaxed clusters, having less substructure and greater symmetry, tend to show less power in higher order poles than unrelaxed clusters. [5] and subsequent papers (e.g. [4]) have found a good correlation between the dipole and quadrupole ratios,  $P_2/P_0 - P_4/P_0$ . Other ratios also appear to be correlated, though generally not as strongly. Furthermore, it has been discovered that the position of a cluster along these correlation lines is related to its morphological type as determined by other visual classification schemes. Relaxed clusters have low values for  $P_2/P_0$  and  $P_4/P_0$ , indicating that low power in higher order moments does indeed help to quantify previous classification systems. Despite its success, the significant uncertainties in this method force us to include some of the previously mentioned tests to supplement it as an indicator of relaxedness. Figure 3 shows a plot of power ratios from [9] which graphically summarizes this method.

## 2.4 Other Tests

In an attempt to find a simple yet reliable quantification of relaxedness, we focused our efforts toward elliptical isophote fitting and calculating power ratios. Other methods considered for analysis include modeling the clusters with x-ray emitting blobs using Monte Carlo simulations to determine relevant statistical parameters in the manner of [11]. The ability to compare the results of the morphological tests from this paper with the more physical results from numerical simulations will be important and useful as the methods for using relaxed clusters to constrain cosmological parameters are refined. Other options for quantifying relaxedness include tests outlined by [12] which deal mostly with different analyses of the surface brightness profile, and determination of cooling times from spectral information, as performed by [4]. These procedures have not been included in

this work, but offer further options to supplement our tests at the expense of increased complexity and computing time.

### 3 Analysis

To determine the relaxedness of a galaxy cluster, we use a combination of results from the tests outlined above. For the purpose of comparing values obtained by these tests to previous methods of classification, we identify training sets of clusters commonly accepted as relaxed and unrelaxed. The relaxed group consists of A478, A1835, A2029, and MS2137.3-2353. The clusters identified to be the most unrelaxed are A520, A2163, A2219, and A2744.

The core radius parameter of the King model fit to the surface brightness profile helps to differentiate relaxed and unrelaxed clusters. The relaxed group shows a narrow range of small values for its core radii, while the unrelaxed clusters exhibit a far broader range of higher core radii, as seen in Figure 4. Those clusters not identified as strongly relaxed or unrelaxed lie mostly in the region of the plot near the relaxed ones. As a result of this test, we can filter out clusters with  $r_c \gtrsim 60$  kpc from the subset of relaxed clusters we wish to use to constrain cosmological parameters.

Other parameters from the isophote fits were analyzed, including the variation of centroids and position angles of the ellipses over their range of SMA. Position angles were found to vary widely for the whole catalog, especially at larger SMA where the relative background increased. Position angles and ellipticities did not appear to be independent enough across isophotes to be reliable, and are not used in this analysis. Centroid shifts, however, did show a clear distinction between the relaxed and unrelaxed training groups, with relaxed clusters having smaller centroid shifts. Figure 5 displays the centroid shift (CS) as a function of SMA for each cluster in the catalog. We also define a new measurement, the fractional centroid shift,  $FCS = CS / SMA$ . The mean FCS for a cluster profile

is a simple statistic for comparison of clusters and a useful indicator of relaxedness, with the relaxed group exhibiting values less than  $\approx 0.1$ .

The gradient of the surface brightness profile provides another approach to quantify its peakedness. This statistic measures a morphological characteristic similar to that of the core radius from the King model fit. The relaxed clusters do show significantly larger gradients than the unrelaxed group, but with the current level of sophistication of our analysis, the gradient does not provide any greater distinction between relaxedness than the core radius parameter. Future work will involve a clearer quantification of the gradient and a closer comparison between the results of these two statistics to determine which is more useful and if they can both contribute to our goal of a relaxedness index.

We have not yet been able to synthesize these tests into a single scale for relaxedness. The power ratio method will hopefully provide information about this quality that is more orthogonal to the isophote tests, allowing us to more precisely eliminate the unrelaxed clusters from cosmological studies. The data reduction methods that will be performed with the power ratio analysis will also allow us to use the ACIS-I images more reliably, making available to us a significant number of other clusters from the Chandra archive.

## 4 Conclusion

We have presented several methods of quantifying the relaxedness of galaxy clusters for the purpose of selecting relaxed ones to use in constraining cosmological parameters. These tests will be run periodically on the set of cluster images available from the Chandra archive, and future work may allow the use of data from XMM-Newton or other instruments. The catalog for  $f_{gas}$  measurements in [2] will be updated as new clusters are determined to be sufficiently relaxed and new data demonstrates that clusters already existing in the catalog fail to meet our specified criteria.

Classification of galaxy clusters can now be done without much need for human intervention or subjectivity. As mentioned above, this morphological work will be incorporated with more theoretical and physical models of cluster dynamics and cooling flows in the future. Further refinement of these tests is necessary, but our results show promise for providing an objective measurement of the relaxedness of galaxy clusters. An improved understanding of how galaxy clusters form and evolve will make them better standardized tools for cosmological studies.

## 5 Acknowledgements

This work was made possible by the Office of Science, Department of Energy Science Undergraduate Laboratory Internship program. F. Bauer graciously provided the code for power ratio analysis. M. George would also like to thank his advisors, S.W. Allen and G.M. Madejski, and the program manager, James Lindesay, for their support.

## References

- [1] S. W. Allen and A. C. Fabian. The relationship between cooling flows and metallicity measurements for X-ray-luminous clusters. *MNRAS*, 297:L63–L68, July 1998.
- [2] S. W. Allen, R. W. Schmidt, H. Ebeling, A. C. Fabian, and L. van Speybroeck. Constraints on dark energy from Chandra observations of the largest relaxed galaxy clusters. *MNRAS*, 353:457–467, September 2004.
- [3] H. Böhringer, P. Schuecker, L. Guzzo, C. A. Collins, W. Voges, R. G. Cruddace, A. Ortiz-Gil, G. Chincarini, S. De Grandi, A. C. Edge, H. T. MacGillivray, D. M. Neumann, S. Schindler, and P. Shaver. The ROSAT-ESO Flux Limited X-ray (REFLEX) Galaxy cluster survey. V. The cluster catalogue. *A&A*, 425:367–383, October 2004.

- [4] F. E. Bauer, A. C. Fabian, J. S. Sanders, S. W. Allen, and R. M. Johnstone. The prevalence of cooling cores in clusters of galaxies at  $z \sim 0.15-0.4$ . *MNRAS*, 359:1481–1490, June 2005.
- [5] D. A. Buote and J. C. Tsai. Quantifying the Morphologies and Dynamical Evolution of Galaxy Clusters. II. Application to a Sample of ROSAT Clusters. *ApJ*, 458:27–+, February 1996.
- [6] H. Ebeling, A. C. Edge, S. W. Allen, C. S. Crawford, A. C. Fabian, and J. P. Huchra. The ROSAT Brightest Cluster Sample - IV. The extended sample. *MNRAS*, 318:333–340, October 2000.
- [7] H. Ebeling, A. C. Edge, H. Böhringer, S. W. Allen, C. S. Crawford, A. C. Fabian, W. Voges, and J. P. Huchra. The ROSAT Brightest Cluster Sample - I. The compilation of the sample and the cluster log N-log S distribution. *MNRAS*, 301:881–914, December 1998.
- [8] R. I. Jedrzejewski. CCD surface photometry of elliptical galaxies. I - Observations, reduction and results. *MNRAS*, 226:747–768, June 1987.
- [9] T. E. Jeltema, C. R. Canizares, M. W. Bautz, and D. A. Buote. The Evolution of Structure in X-Ray Clusters of Galaxies. *ApJ*, 624:606–629, May 2005.
- [10] C. Jones and W. Forman. Einstein Observatory Images of Clusters of Galaxies. *ApJ*, 511:65–83, January 1999.
- [11] J. R. Peterson, P. J. Marshall, and K. Andersson. Smoothed Particle Inference: A Kilo-Parametric Method for X-ray Galaxy Cluster Modeling. *ArXiv Astrophysics e-prints*, July 2005.
- [12] P. Schuecker, H. Böhringer, T. H. Reiprich, and L. Feretti. A systematic study of X-

ray substructure of galaxy clusters detected in the ROSAT All-Sky Survey. *A&A*,  
378:408–427, November 2001.

## Tables

Name	ID	ACIS	Exp. (ks)	z	Group
A478	1669	S	42.9400	0.0880000	R
A478	6102	I	10.1300	0.0880000	R
A520	4215	I	67.1500	0.199000	U
A586	530	I	10.1700	0.171000	
A611	3194	S	36.5900	0.288000	
A963	903	S	36.7600	0.206000	
A1068	1652	S	27.1700	0.137500	
A1758a	2213	S	59.0900	0.279000	
A1795	493	S	19.8800	0.0624760	
A1835	495	S	19.7700	0.253200	R
A2029	4977	S	78.9100	0.0770000	R
A2142	1228	S	12.2600	0.0909000	
A2163	1653	I	72.0900	0.203000	U
A2204	499	S	10.2000	0.152300	
A2219	896	S	42.8400	0.228000	U
A2390	4193	S	96.3200	0.228000	
A2744	2212	S	25.1400	0.308000	U
IRAS09104+4109	509	S	9.17000	0.442000	
MS1358.4+6245	516	S	54.7600	0.328000	
MS2137.3-2353	928	S	44.1700	0.313000	R
PKS0745-191	2427	S	18.0900	0.102800	
RXCJ2351.6-2605	2214	S	9.77000	0.230000	
RXJ1347.5-1145	507	S	10.1200	0.451000	
RXJ1532.9+3021	1649	S	9.49000	0.345000	
Z2701	3195	S	27.2700	0.214000	

Table 1: Information about the cluster sample: cluster name, Chandra observation ID, instrument (ACIS-S or ACIS-I), exposure length, redshift, and training group (**R**elaxed, **U**nrelaxed, or none).

## Figures

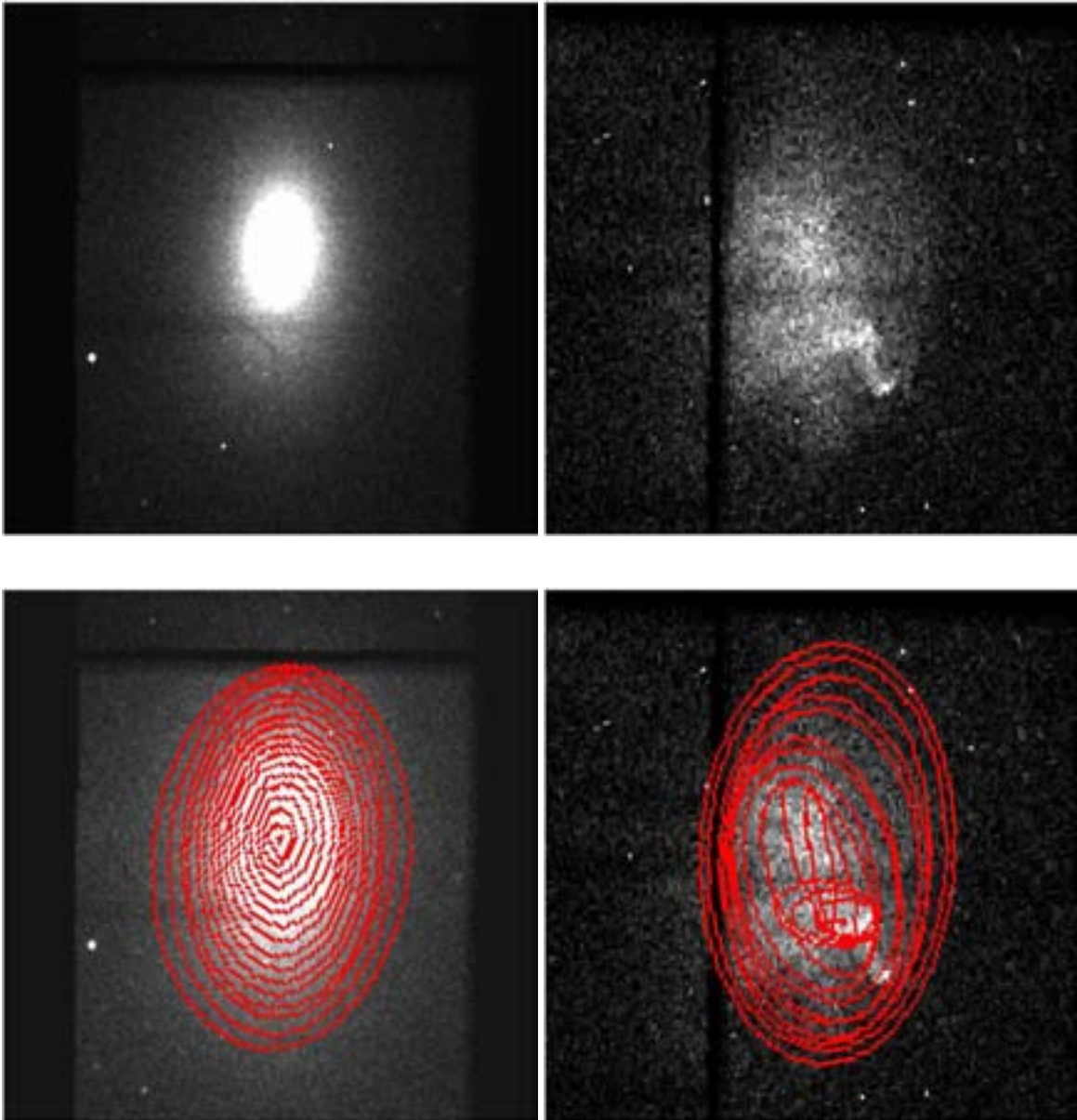


Figure 1: Elliptical isophotes fit to A2029, a relaxed cluster (left), and A520, an unrelaxed cluster (right).

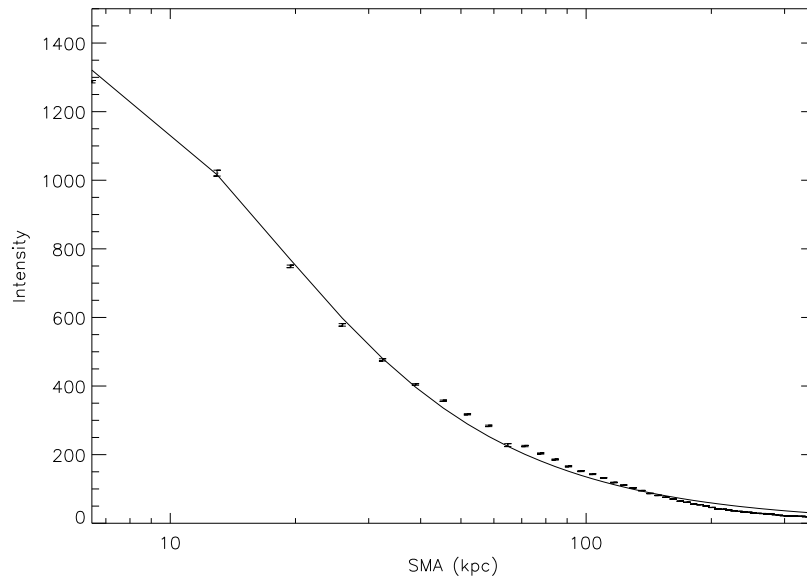


Figure 2: A King model fit to the surface brightness profile of A478

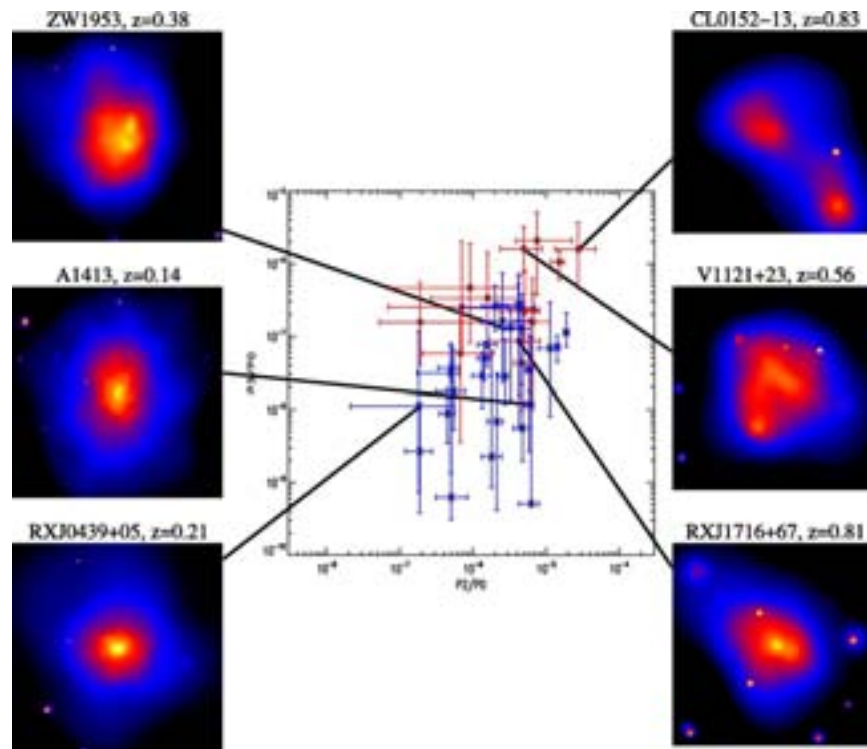


Figure 3: A plot of power ratios demonstrating the correlation of the decreasing relaxed-ness of the clusters from bottom left to top right with the increasing values of their power ratios  $P_3/P_0$  and  $P_2/P_0$ . Figure from [9].

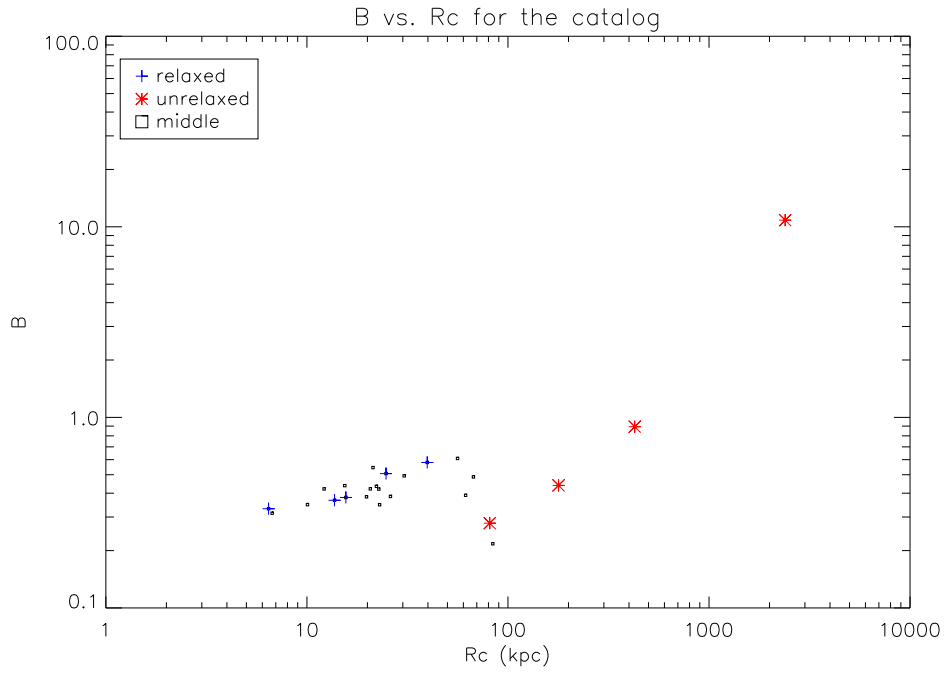


Figure 4: Index parameter,  $\beta$ , plotted against core radius from the King model fits to the catalog. Relaxed clusters exhibit smaller values of  $r_c$  than unrelaxed clusters.

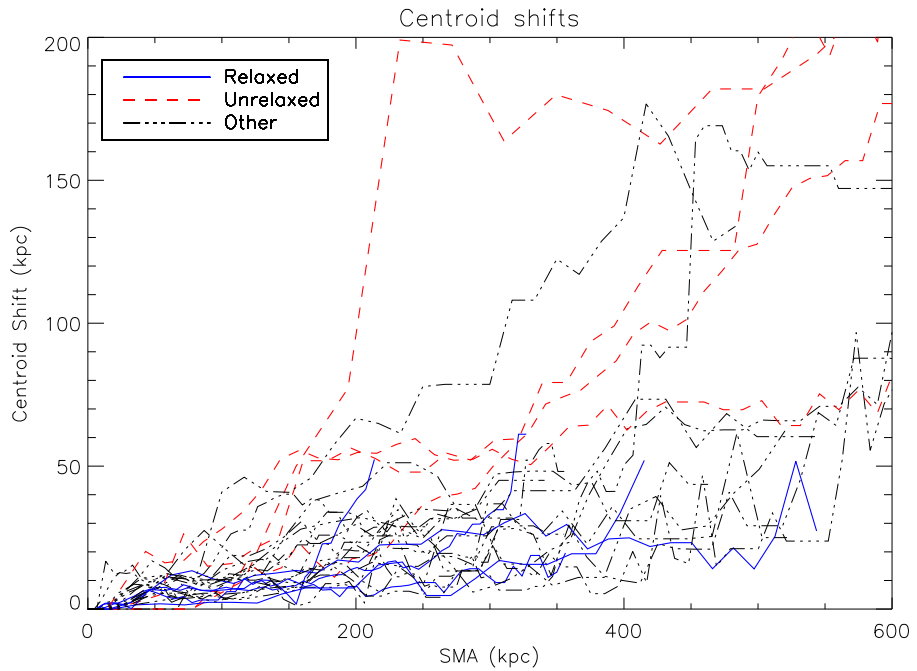


Figure 5: Centroid shifts for the catalog. The relaxed group shows smaller shifts than the group of unrelaxed clusters.

**Improving the Raster Scanning Methods used with X-Ray Fluorescence  
to see the Ancient Greek Text of Archimedes**

Isabella B. Griffin

Office of Science, SULI Program

Norfolk State University

Stanford Linear Accelerator Center

Menlo Park, California

August 20, 2005

Prepared in partial fulfillment of the requirements of the Office of Science  
Undergraduate Laboratory Internship (SULI) Program under the direction of  
Dr. Uwe Bergmann of Stanford Synchrotron Radiation Laboratory.

Participant:

\_\_\_\_\_  
Signature

Research Advisor:

\_\_\_\_\_  
Signature

Any disclaimer(s) required by your host DOE laboratory (if any).

## Table of Contents

Abstract.....	iii
Introduction.....	1
Lab Setup and Equipment.....	3
Results and Discussion.....	7
Conclusion.....	10
Acknowledgements.....	11
References.....	12
Tables.....	12
Formulas.....	13
Figures.....	13

## **ABSTRACT:**

**Improving the raster scanning methods used with x-ray fluorescence to see the ancient Greek copy of Archimedes work. ISABELLA GRIFFIN (Norfolk State University, Norfolk Virginia 23504) DR. UWE BERGMANN (Stanford Synchrotron Radiation Laboratory, Menlo Park California)**

X-ray fluorescence is being used to detect the ancient Greek copy of Archimedes work. The copy of Archimedes text was erased with a weak acid and written over to make a prayer book in the Middle Ages. The ancient parchment, made of goat skin, has on it some of Archimedes most valuable writings. The ink in the text contains iron which will fluoresce under x-ray radiation.

My research project deals with the scanning and imaging process. The palimpsest is put in a stage that moves in a raster format. As the beam hits the parchment, a germanium detector detects the iron atoms and discriminates against other elements. Since the computer scans in both forwards and backwards directions, it is imperative that each row of data lines up exactly on top of the next row.

There are several parameters to consider when scanning the parchment. These parameters include: speed, count time, shutter time, x-number of points, and acceleration. Formulas were made to relate these parameters together. During the actual beam time of this project, the scanning was very slow going; it took 30 hours to scan ½ of a page. Using the formulas, the scientists doubled distance and speed to scan the parchment faster; however, the grey scaled data was not lined up properly causing the images to look blurred. My project was is to find out why doubling the parameters caused blurred images, and to fix the problem if it is fixable.

## **Introduction**

Archimedes was a revolutionary scholar and was centuries ahead of his time. He is responsible for approximating pi, discovering the principles on buoyancy, and was the first to use premature forms of calculus to solve problems. In the 12<sup>th</sup> century, a 10<sup>th</sup> century Greek copy of Archimedes writings was erased with a weak acid, like lemon juice, and written over by a Christian monk to make a prayer book. In the middle ages, parchment was very expensive and hard to come by, therefore when parchment was reused the resulting book was called a palimpsest [1]. The pages of the Archimedes parchment were folded horizontally and bound together so that the Archimedes text lays perpendicular to that of the prayers. These particular writings of Archimedes are very important because they contain the only copy of Archimedes' Method of Mechanical Theorems, in which Archimedes explains how he came up with his theorems. This is also the only document that contains original diagrams of Archimedes [1].

The palimpsest was discovered in 1906 by Johan Ludvig Heiberg in Constantinople, present day Istanbul [1]. He took pictures of the pages because he could not remove the palimpsest from the library. He knew it was the lost Archimedes writings, but he did not have the technology to study it in great detail. After WWI, the palimpsest was lost, not to resurface again till the 1990's in France [1]. The palimpsest was sold on auction by Christies to an anonymous billionaire for \$2 million. The new owner sent it to Walters Art Museum in Baltimore for further study and restoration [1].

Most of the text has been recovered using powerful cameras and special lenses in visible or ultra-violet light and a process known as multi-spectral imaging. This process uses different light of different wavelengths to distinguish between the two different texts

[1]. However, 20-30% of the text could still not been read. Some of the text is too faint, some covered by mold or other obstacles, and four of the pages have forged paintings on them. The big problem was how to get past the paint to see the text. This is when Stanford linear Accelerator Center's (SLAC) Stanford Synchrotron Radiation Laboratory (SSRL) comes into play. The ink used to write Archimedes work contains iron. When put under the x-ray radiation, the iron atoms will fluoresce, or glow, allowing scientist to see beneath the paint and to the original Archimedes text. The work was published in a press release from the journal Nature, SLAC, and from the Walters Art Museum causing enormous media attention (see reference 4).

X-ray beams from SSRL were used to see the hidden text. In a synchrotron, electrons, moving at close to the speed of light, are accelerating in a storage ring. The acceleration causes the electrons to give off x-ray radiation

The ink in the Archimedes text contains iron, which will fluoresce when excited. When an x-ray beam hits an iron atom the x-ray can be absorbed or scattered. If it is absorbed it undergoes a process called the photoelectric effect [2]. In this process, if the x-ray beam has enough energy, electrons in the inner shells are knocked out creating electron holes. These holes put the atom into an excited state. In order to return into the ground state the electrons from the outer shells quickly fill the vacant spots. In doing so, these electrons give off x-rays [2]. Electrons in different energy levels have different binding energies. The energy of the x-rays emitted is the difference in the two binding energies of the shells to and from which the electron jumped. Each element has a characteristic x-ray because each element has a unique set of energy levels. X-ray

fluorescence is the process in which one evokes the emission of the characteristic x-rays known to an element [2].

The pages were put on a stage that moves in the x and y direction on a raster format. As the small x-ray beam hits the page, a germanium detector will detect the fluorescence of the iron and discriminate against that of other elements.

My part in this project is with the scanning procedure. The current problem with our scanning procedure is to synchronize the read out with the scanning speed. Furthermore, we have a dead time at the end of each readout that limits the ultimate imaging speed. I will show experiments that help to improve the scanning procedure's efficiency for future use.

### **Lab Setup and Equipment**

Because my project was to improve the scanning procedure, the original Archimedes Palimpsest and the x-ray beam were not needed. We substituted a class II He Ne laser for the x-ray beam and a photodiode detector instead of the original germanium detector. With this detector we measure the transmission of the laser beam through a self-made stencil. The stencil was made by using a thin, yet sturdy type of cardboard. On it, I cut thin slits in the shape of old English script. I mounted the scroll on a frame that slides into the stage. The laser and detector are lined up with each other so that the laser beam goes directly into the pinhole of the detector. The scroll is scanned on a raster format. When the laser gets to a cutout, the photodiode detector will receive the beam. I scanned the stencil for about 2 weeks, but I was not able to produce a perfectly lined up image. I attributed this to the flaws in my cutout. I then scanned calipers. The advantages with the calipers were they have straight edges, and I was able to control the width of the line. I

then made a transparency with old English text printed on it. The transparency was used to scan full text images.

## The Detector

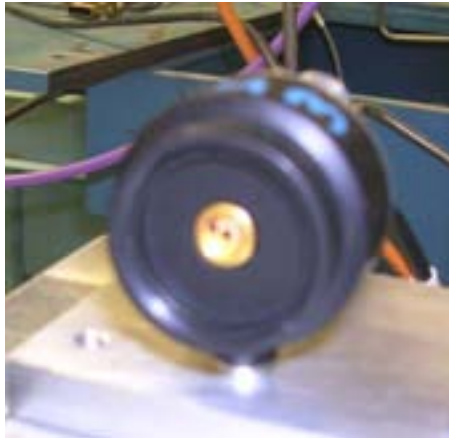


Image 1 : The photodiode detector was mounted behind  
The shutter box, which was removed from the image.

The detector I used in my experiment was a photodiode detector operating in current mode. It sends out a current, that is fed into an amplifier which turns it into a voltage. The voltage signal is then changed into a frequency by a voltage to frequency converter. The frequency is converted into a numerical value when performing a scan. In order to show the image, these numerical numbers are then turned into a grey scale image using a grey scaling program, Rasplot, which will produce an image based on the numerical data. The detector used in the real experiment was a germanium detector.

## The Shutter Box

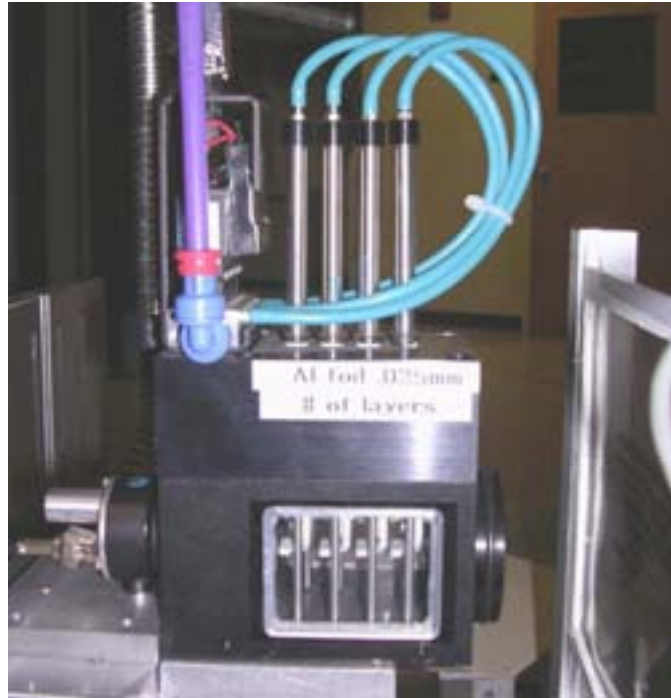


Image 2: The shutter box uses air pressure (in the blue tubes) to open and close the shutters.

The shutter box is used to protect the parchment from radiation damage caused by the x-ray beam. The shutter stays open while the document is scanning, but when the stage gets to the end of the line, the shutter closes and the stage moves to the next line. When the shutter opens again, a new line is scanned. Although the beam is only at the end of the line for a split second, the radiation can still do damage to it. The shutter box will prevent the x-ray beam from being on the endpoints for too long. Formula 1 shows how to calculate the shutter time for a scan.

## The Stage and Motors



Image 3: (above) The stepper motor for the x-direction

Image 4: (below) The experimental set up; the laser, stage, shutter box, and detector



The type of motor used to scan is a stepper motor. 400 steps is one full revolution of the screw or equal to 2.54 mm (1/10 inch) of scan distance. Therefore 157.48 steps

correspond to 1 mm. There were two motors used to scan; one for the x-direction, the other for the y-direction. The x-motor was set to take 100 steps to accelerate to the desired speed, then 100 steps to decelerate to a stop. I hypothesized that the misalignment of the images could be due to a non-constant speed between intervals of acceleration and deceleration. This question prompted me to perform an experiment to see if the speed was in fact “tailing off”, which I will discuss later in the paper.

### **Drivers**

I also experimented with different drivers. The original driver used in the experiment was an E500. This driver has been a standard at SSRL for a decade. It is relatively outdated equipment. I switched to a VXI driver and took scans with it for a few days. The VXI driver is a newer technology. The VXI driver did not produce any clear images, so I switched back to the E500.

## **Results and Discussion**

When the original Archimedes Palimpsest was at SSRL, there were a standard set of parameters used for the x scans. These parameters are: count time, distance, speed, shutter time, and x-number of points (pixels). The count time is simply the time it takes for the parchments to move between readouts. Consequently, the distance the parchment travels during that time corresponds to the pixel size. A pixel size of  $40\mu$  [ $\sim$  600 dpi (dots per inch)] was used, and the actual size of the x-ray beam was slightly larger (50  $\mu$  m diameter). The shutter time is the time period in which the shutter is open (see Formula 1) when scanning one full line. The x-number of points is how many  $40\mu$  pixels are in the desired scanning distance. These parameters relate to each other by a series of formulas (see Formulas Section). Since line scans were taken in both directions, if the timing

between readout time and scanning speed is not perfect, subsequent lines do not line up properly, thus resulting in a blur or even a ghost image. The original parameters used a count time of 0.01ms, a distance of 20mm, a shutter time of 6.12 sec, and a speed of 494 steps/sec (~ 3.14 mm/sec). This resulted in a clear image where subsequent x-lines were aligned. The corresponding time to scan one half of the page of the palimpsest is approximately 30 hours. But it was for example found that doubling the speed did not result in good images and even a change in scan range introduced misalignments. In order to optimize the scanning procedures that result in clear images where subsequent lines are not offset to each other, it was my job to first find out why doubling the parameters did work, and to then produce a clear image with varying distances and speeds.

My first task was to reproduce a clear image using the original parameters from the Archimedes scans. I ran scans with the original parameters and was able to produce a good image (see Figure 1). However, the image showed me that I hadn't been able to cut a straight line. I then replaced my stencil with a set of calipers (see Figure 2). The advantage with the calipers was not only the straight edge but the ability to control the width of the line. In order to scan the calipers I had to change the distance because the width of the calipers was much smaller than that of the stencil. Using the original formula, I changed the distance to 15mm, x-number of points = 375, count time = .01, shutter time = 4.51, speed = 494, acceleration = 100steps to fit the calipers, but subsequent lines were offset. This was when I first notice that the formulas were not quite correct. However, changing the speed slightly to 496 produced a clear image.

I then attempted to produce another lined up image with a distance of 40mm. I was able to do that using the following parameters: distance = 40mm, x-number of points = 1000, count time = .01, shutter time = 12.45, speed = 496, acceleration = 100 steps. Next I tried to scan half the distance using half the speed. I was unsuccessful. When experimenting with different count times, speeds, and accelerations, I was still unable to get a clear image. As it turned out the problem was related to the software as will be discussed below.

In order to test if one reason for misaligned images was related to a non-constant speed, I devised an experiment called the “speed test”. In it, I scanned small distances (i.e. 10mm) and set the acceleration from 100 steps to 10 steps. We hypothesized that if the speed is gradually slowing down, then a scan of a short distance would look significantly better than a scan of a longer distance. I tested a 10 mm distance in great detail in an attempt to get a clear image. I did not get an image that was significantly better than the previous images. A more crucial test is to vary the distances and see which distance produced the best image. This led me to conclude that the speed was constant between intervals of acceleration and deceleration. As an independent test, we hooked up an oscilloscope to both the E500 and the VXI to view the motion of the motors. At this point we changed the acceleration from 100 to 10. We used a faster acceleration so we could have longer periods of constant speed. Both drivers produced the same results: the speed was constant between intervals of acceleration and deceleration. Figure 3 shows a graph of the motion of the motors.

I then tried to scan an image with a faster speed (815) and twice the distance (40mm) of the original parameters. The image did not line up at all, and it was at this

point when we realized that the counting time was not corresponding to the input. My part time mentor, Martin George, wrote a program that checks the count time of each scan. After using this program on several scans, we found out that the count time was not working on the computer. It did not count faster than 0.01 sec even if another value was entered into the computer.

Since the count time did not work, the only way to line up the images at a faster was to change the x-number of points, hence the resolution. With this knowledge, I was able to find parameters that scanned clear images. In Table 1 the different distances, speeds, and x-number of points that produce clear images are summarized.

After taking over 250 scans in the past 4 weeks, I continued scanning with the E500 and have been able to find, for different distances, the speeds and x-number of points that will give lined up images. The distances I tested were 10mm, 20mm, 40mm, 60mm, and 80mm (see Table 1). After I found the correct parameters for each distance I scanned real text on a transparency that I made. I printed Old English text with a high quality printer in transparency paper. I made a frame for it and put it in the stage. I scanned this image when I found a new set of parameters that gave me a straight line after scanning the calipers. I used the transparency to see how well the image lined up over long distances. Figures 4 (before optimizing) and 5 ( optimized parameters) show images from the transparency scanned over a distance of 80mm. I furthermore learned about the mechanical limits of the scanning stage. During one scan a heavy liquid nitrogen dewar was pushed across the experimental floor and an image taken at that time showed a clear degradation in quality. We attributed this to possible vibrations caused by the moving dewar.

## **Conclusion**

At the end of eight weeks, and after nearly 300 scans, I have gained sufficient knowledge of the scanning equipment and procedures in the Archimedes Project. The reason why doubling the parameters did not work was because the count time was at a fixed 0.01 seconds. Unfortunately with the current software shorter readout times cannot be achieved. Faster scans of longer distances can still be accomplished if the pixel size is enlarged. However, varying the pixel size will compromise the resolution. To maintain 600 dpi resolution the standard speed of 496steps/mm must be kept, but the scan distances can now be changed and still produce clear images. I also found that using the formula to find the x-number of points and adding an imperially found 7 to the final number (see formula 3) will give the right x-number of points for the corresponding distance. This additional offset is most likely caused by the acceleration and deceleration that had not previously been taken into account for. The revised formula will now allow us to vary the x-distance without the loss of image quality. This will be very helpful for further imaging when in the Archimedes palimpsest returns to SSRL in early 2006. In the future, it is planned to replace the readout system in order to minimize the dead time and speedup the readout time. This will allow us to perfume faster scans without loss of resolution.

## **Acknowledgements**

I would like to thank my mentor, Dr. Uwe Bergmann, for being a great mentor and choosing me to be apart of the Archimedes project. Special thanks to Martin George for all of our help and support; to the SULI program director, James Lindesay, we could not have asked for a better director; to Helen Quinn, for making this program possible. And I would like to thank the D.O.E for the once in a lifetime opportunity to participate

in the SULI Program. The Archimedes Project is a group collaboration under the direction of Uwe Bergmann. My summer accomplishments at SLAC are a small piece in the over all picture. Special thanks go to the many technicians, engineers and user support personnel at SSRL because without their help, this project would not be possible.

### **References**

- [1] “Infinite Secrets.” Nova. PBS. September 2003
- [2] “X-Ray Fluorescence Spectroscopy.” 2 Aug. 2005  
<<http://www.amptex.com/xrf.html>>
- [3] XRF Corporation. “Radiation Detection.” 17 August 2005.  
<[http://www.xrfcorp.com/technology/radiation\\_detection.html](http://www.xrfcorp.com/technology/radiation_detection.html)>
- [4] <http://home.slac.stanford.edu/pressreleases>  
<http://www.thewalters.org/archimedes/frame.html>  
<http://www.nature.com/news/2005/050516/full/050516-8.html>

### **Tables**

Distance 10mm		Distance 40mm		Distance 80mm	
speed	496	speed	496	speed	830
x-num pts	257	x-num pts	1007	x-num pts	1204
speed	595	speed	595		
x-num pts	215	x-num pts	840		
Distance 20mm		speed	830		
speed	496	x-num pts	606		
x-num pts	507				
		Distance 60mm			
speed	595	speed	595		
x-num pts	424	x-num pts	1257		
speed	830	speed	830		
x-num pts	307	x-num pts	905		

Table1: These are the speeds and x-number of points with different distances.

### Formulas

- 1: Shutter time       $\Delta x \div (v \div s) - .25$  where  $\Delta x$  is the distance of the scan, v is the speed, and s is the device scale for steps in one revolution. (s = 157.48)
  
- 2: Count time       $0.04\text{mm} \div (v \div s)$  where v is the speed and s is the device scale  
For steps in one revolution
  
- 3: X-num points       $\Delta x \div 0.04\text{mm} + 7$  where  $\Delta x$  is the desired scan distance (this formula is only valid when the speed is 496steps/mm)

### Figures

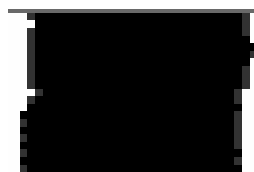


Figure 1: A scan of a line using the stencil. As one can see, neither the left nor the right edge of this line is completely straight.

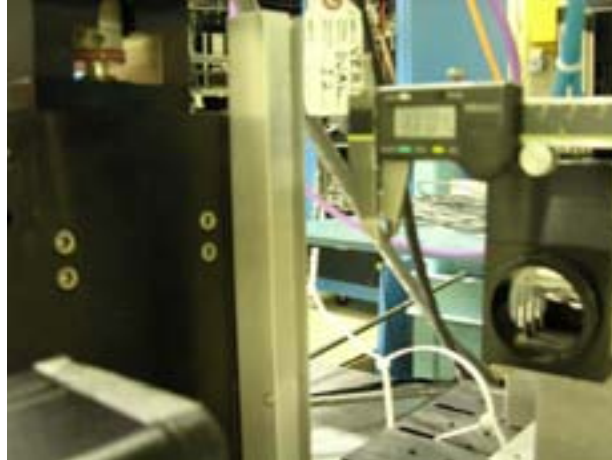


Figure 2: The calipers used to scan

### The Oscilloscope

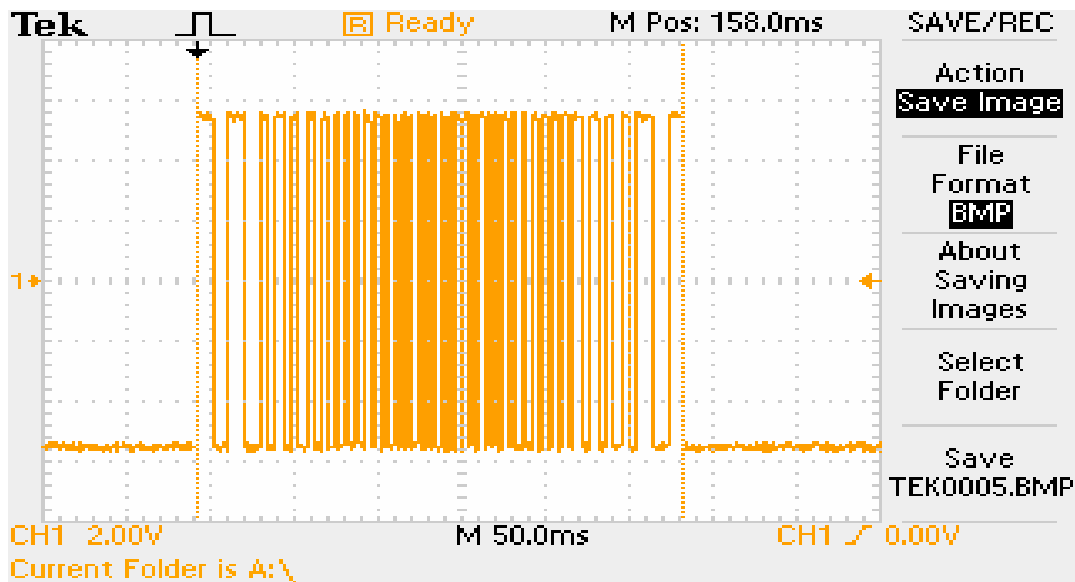
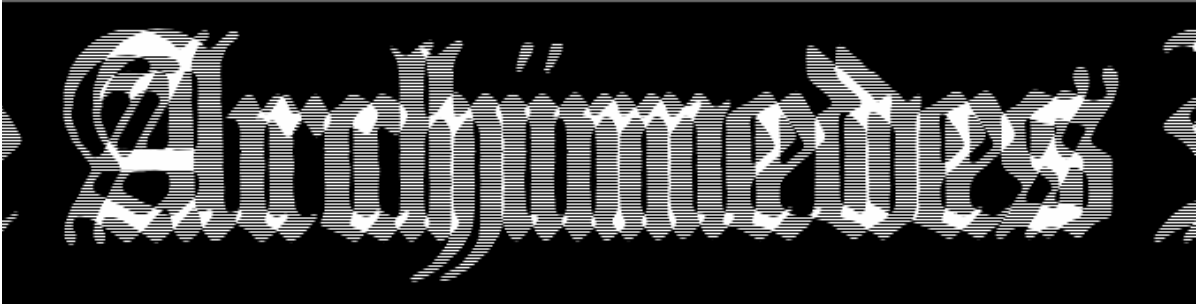


Figure 3: The graph of the motion of the x-motor

The graph shows that the motor had constant speed between intervals of acceleration and deceleration. The reason it is more condensed in the middle is because the graph had to be tightly packed in.



**Figure 4:** This images was scanned on 08-03-05. Filename: cal-238.ras. The parameters are as follows: Distance = 80, x-num pts = 1188, speed = 830, accel. = 10, 377 dpi

This image is considered poor. Subsequent lines do not match up, hence creating a ghost image. It was scanned using the same parameters as the next image, but the x-number of points was changed to 1188.



**Figure 5:** An image scanned on 08-03-05, Filename: cal-229.ras  
The parameters are as follows: distance = 80mm, x-num pts = 1204, speed = 830,  
accel. = 10, 382dpi

This image is considered to be good. The quality is one pixel per point (relatively small). Subsequent lines match to within one to two pixels. This is shown by a closer look at the characters (see Figure 3). This is the scan of a 18 font text.



**Figure 6:**A close up the “Ar” in Archimedes.

As you can see, the pixels are not in a perfectly straight line; however, the image was taken with the optimal scanning parameters for the distance.

**Investigating the Infrared Properties of Candidate Blazars**

Jessica Hall

Office of Science, Science Undergraduate Laboratory Internship Program (SULI)

University of Southern California

Stanford Linear Accelerator Center

Menlo Park, California

August 18, 2005

Prepared in partial fulfillment of the requirements of the Office of Science, U.S.

Department of Energy Science Undergraduate Laboratory Internship (SULI) Program

under the direction of Grzegorz Madejski and Seth Digel in the Gamma-ray Large-Area Space Telescope (GLAST) division at Stanford Linear Accelerator Center.

Participant:

\_\_\_\_\_  
Signature

Research Advisors:

\_\_\_\_\_  
Signature

\_\_\_\_\_  
Signature

## Table of Contents

	<u>Page</u>
Abstract	iii
Introduction	1
Methods	3
Results	6
Discussion and Conclusions	7
Acknowledgments	11
Works Cited	12
Other References	12
Tables	14
Figures	16

## ABSTRACT

Investigating the Infrared Properties of Candidate Blazars. JESSICA HALL (University of Southern California, LA, 90007) GRZEGORZ MADEJSKI (Stanford Linear Accelerator Center, Menlo Park, CA 94025) SETH DIGEL (Stanford Linear Accelerator Center, Menlo Park, CA 94025).

Blazars are active galaxies with super-massive black holes, containing jets that accelerate plasma material and produce radiation. They are unique among other active galaxies for properties such as rapid variability and the lack of emission lines. The double-peaked spectral energy distribution (SED) found for most blazar objects suggests that synchrotron radiation and Compton scattering occurs in the jets. This study is an investigation of the infrared (IR) spectra of a selected population of blazar candidates, focusing on the IR properties of objects within the three types of blazars currently recognized by their spectral characteristics at other wavelengths. Using blazar candidates found in a recent study of the northern sky (Sowards-Emmerd et al., *The Astrophysical Journal*, 2005), IRAS data for 12, 25, 60, and 100  $\mu\text{m}$ , as well as any available data from 2MASS and EGRET, were located. The synchrotron peak of the SED of each object was expected to occur anywhere in the infrared (IR) to soft X-ray range. However, peaks were generally found to lie in the IR range, suggesting potential selection biases. An analysis of selection techniques reveals that the figure of merit used in the original survey is engineered to select objects with a Compton scattering peak luminosity occurring in the GeV range, the energy band most easily detected by the upcoming GLAST mission. Therefore, this figure of merit selection process should be used to compile a list of blazar candidates for further study in anticipation of the launch of the satellite.

## INTRODUCTION

Blazars are active galaxies with super-massive black holes at their cores. The common understanding is that the black holes are rotating and have accretion disks. The physics of this structure often causes jets of high-energy particles that accelerate plasma material out from the nucleus. Compton scattering, and perhaps other processes, creates gamma rays in these jets. One distinguishing characteristic of blazars relative to other active galaxies is that their jets are more or less aligned with the line of sight to the Earth. Relativistic beaming boosts the energy of  $\gamma$ -rays along the jets, making blazars extremely bright sources of high-energy  $\gamma$ -rays. Blazars are unusual among other active galaxies for properties such as rapid variability and the lack of emission lines. They are defined by a flat featureless spectrum, running from the radio range often into the optical, with a strong non-thermal optical component.

Recent research into the methods of identifying blazar candidates has focused on correlation of radio, X-ray, and  $\gamma$ -ray data from different astronomical catalogs to view different characteristics of these objects. Ideally, the data included in such a comparison would be contemporaneous; the variability of blazars makes it difficult to compare properties without obtaining data at all wavelengths at the same time. However, a multi-wavelength data compilation for an object can be useful to analyze the general characteristics of a population of blazar candidates, even if the data are not taken simultaneously.

The unique double-peaked spectral energy distribution (SED) usually observed in multi-wavelength correlations of blazars, typically falling in the infrared (IR) to soft x-ray range for one peak and  $\gamma$ -ray bands for the other peak, suggests that synchrotron

radiation and inverse Compton scattering of electrons occurs in the jets. Based on their SEDs, blazars have been classified into 3 groups: High-energy peaked BL Lacs (HBL), low-energy peaked BL Lacs (LBL), and flat-spectrum radio quasars (FSRQ). Blazars had already been divided into BL Lacs and FSRQ due to certain properties they exhibit, but recent observations have shown that further division was necessary. According to Ghissellini et al. in their unifying scheme for blazars:

- ‘(i) HBL are sources characterized by the lowest intrinsic power and the weakest external radiation field (no or weak emission lines). Consequently the cooling is less dramatic and particles can be present with energies high enough to produce synchrotron emission extending to soft X-ray energies and TeV radiation through the [synchrotron self-Compton] SSC process. [T]he inverse Compton cooling [being] ineffective, the Compton dominance is expected to be small;
- (ii) LBL are intrinsically more powerful than HBL and in some cases the external field can be responsible for most of the cooling. The stronger cooling limits the particle energy implying that the synchrotron and inverse Compton emission peak at lower frequencies, in the optical and GeV bands, respectively, with a larger Compton dominance parameter;
- (iii) FSRQ represent the most powerful blazars, where the contribution from the external radiation to the cooling is the greatest. The emission by synchrotron and [external Compton] EC cannot extend [to] frequencies larger than the IR and MeV-GeV bands and the  $\gamma$ -ray radiation completely dominates the radiative output. Within this class, there is a hint of a further sub-division between low and high polarization objects, with a tendency for LPQ to be more extreme (lower values of  $\gamma_{\text{peak}}$ ...and so on).’ (1: 14)

This study is a follow-up investigation of the IR properties of a blazar candidate population, in hopes of identifying the nature of the double-peaked SED structure in more detail. Other multi-wavelength studies of blazars have been made in the past, with objects selected for their radio, X-ray, or  $\gamma$ -ray properties. However, IR data have been scarce in these surveys, as has sufficient  $\gamma$ -ray coverage of the sky. The limitations of these data will be discussed in the next section. This project focused on expanding on a database already containing data for many wavelengths, provided by Sowards-Emmerd et al. (2). The merit of such a study is obvious; blazars may be very bright in the  $\gamma$ -ray band, but the

limited positional resolution of the former EGRET mission makes a  $\gamma$ -ray selected population impossible to obtain with any accuracy. (Positions of EGRET sources are typically uncertain by 90' or more and the great majority of EGRET sources were still unidentified after the mission.) The Gamma-ray Large Area Space Telescope (GLAST), scheduled to launch in 2007, is expected to detect more than an order of magnitude greater numbers of blazars, and will cover the entire sky approximately every 3 hours. This instrument will greatly improve the study of AGN in general, but until it is in operation, studies of data available in other energy bands are useful to select objects likely to be blazars that GLAST will detect. For this reason, the analysis herein includes any IR and near-IR data available for the objects in question.

## METHODS

A blazar candidate population from a recent study of the northern sky by Sowards-Emmerd et al. (2), selected on a figure of merit (FoM) basis to be similar in property to those blazars that had shown up in the EGRET surveys, was used for analysis. Table 1 of that survey (2:96) was the source database for this study, and included any available radio, X-ray, and red wavelength data for the objects selected by their method. While this method is outlined more in detail within that paper, the definition of FoM they used is as follows (2:96):

$FoM = n_{8.4GHz} * n_{\alpha} * n_{X-ray} * \textit{positional dependence [based on location of radio source]}$ ,  
*where these functions are defined as*

$$n_{8.4GHz} = -3.47 + 2.45 \log s_{8.4} - 0.34(\log s_{8.4})^2,$$

$$n_{\alpha} = \textit{median}(0, 0.19 - 0.35\alpha_{8.4/1.4}, 0.4),$$

$$n_{X-ray} = 0.5 + \textit{median}[0, 0.49 + 0.41 \log(\textit{counts} / s), 0.5]$$

The definition of the figure of merit above made use of the radio flux at 8.4 GHz, as found by the Cosmic Lens All-Sky Survey (CLASS), as well as the radio spectral index.

The x-ray flux was also used, in units of counts per second, and was obtained from the ROSAT All-Sky Survey (RASS). Each of the  $n$  terms described above were calibrated to fall in the range of 0 to 1, defining the FoM as a product probability that would fall in the range of 0 to 1 as well. Because they were searching for EGRET-like sources in this study, instead of matching radio sources to EGRET sources as they had done in a 2003 survey, the positional dependence of the radio source was omitted in their general method, and will not be included further in this survey. Once these objects were chosen by the Sowards-Emmerd et al. figure of merit, the group used different methods, such as archival data, to identify the selected targets as blazar candidates or other phenomena. That study returned a database of over 700 objects, only a portion of which were blazar candidates.

For the purposes of this study, only the objects identified as BL Lac and FSRQ in that survey were considered for infrared analysis. The other objects identified in the northern sky survey were often not considered active galaxies, and many were unidentified, rendering them useless for this study. After obtaining the original database, condensing it to the ~500 objects of BL Lac or FSRQ type and converting all flux values to the Jansky unit, the NASA/IPAC Extragalactic Database (NED) was used to fill in the rest of the broadband data. The Infrared Astronomical Satellite (IRAS) data for 12, 25, 60, and 100  $\mu\text{m}$  wavelengths, as well as near-IR data available from the 2-Micron All-Sky Survey (2MASS) in the J, H, and  $K_s$  bands (1.24, 1.66, and 2.16  $\mu\text{m}$ , respectively) were used in this study. EGRET data were also found for the objects that showed up in the IR or near-IR ranges.

After obtaining all available data in the various wavelength bands, a  $\nu$  vs.  $\nu F_\nu$  graph was created to show the spectral energy distribution (SED) of each source (Figure 1). The frequency values used for each wavelength band are included in Table 1. An algorithm was used to find the effective average frequency  $\langle \nu \rangle$  in the  $\gamma$ -ray band during the conversion of photon count data from EGRET to Janskys, based on the spectral index of the EGRET source. The range of the EGRET flux values for each source was plotted at this average frequency on the SED graph.

Only the graphs with sufficient IR or near-IR data, or a nearly complete SED, were considered for curve-fit analysis. The SEDs of these objects, shown in a log-log scale, had a parabola curve fitted to them (also in log-log scale) to evaluate where the peak synchrotron radiation occurred for the non-simultaneous data. The locations of the synchrotron peak frequencies were noted and used for further analysis.

To see if there was a correlation between the FoM defined in the original data set and the location of the synchrotron peak frequencies found by the graphing program for each object, a  $\nu_{\text{peak}}$  vs. FoM graph was created (Figure 2). The reason why this graph was not considered as sufficient to reveal correlation effects is explained in the following discussion. Because of this, a new graph was created, scaling the FoM for each object by its defined redshift (Figure 3). The FoM was defined using spectral indexes and flux values. To correct for redshift, one must consider the FoM in terms of distance, changing its focus from flux to absolute luminosity. The luminosity distance to be used here can be defined as follows (3:4):

$$D_L = \frac{c}{H_0} (1+z)^2 \int_0^z \frac{dz'}{E(z')} \quad \text{where} \quad E(z) = \sqrt{\Omega_M (1+z)^3 + \Omega_K (1+z)^2 + \Omega_\Lambda}$$

All values for  $D_L$  for the 18 objects that had a defined redshift are included in Table 2.

Here the values of  $\Omega_M = 0.3$ ,  $\Omega_\Lambda = 0.7$ , and  $H_0 = 70$  km/s/Mpc were used.  $\Omega_K$  is

considered negligible here. To change flux values to luminosity:

$$L = \frac{F * 4\pi * D_L^2}{1 + z}$$

$$L_{ratio} = F_{ratio} * \frac{(4\pi * D_L^2) / (1 + z)}{(4\pi * D_{med}^2) / (1 + z)} = F_{ratio} * \left( \frac{D_L}{D_{med}} \right)^2 \quad \text{where } D_{med} \text{ is the median of } D_L \text{ for all objects}$$

Thus, the modified FoM can be defined as:

$$scaled \text{ FoM} = n_{8.4GHz} * n_\alpha * n_{X-ray},$$

where these functions are defined as

$$n_{8.4GHz} = -3.47 + 2.45 \log(s_{8.4} * (D / D_{med})^2) - 0.34 (\log(s_{8.4} * (D / D_{med})^2))^2,$$

$$n_\alpha = median(0, 0.19 - 0.35 \alpha_{8.4/1.4}, 0.4),$$

$$n_{X-ray} = 0.5 + median[0, 0.49 + 0.41 \log((count / s) * (D / D_{med})^2), 0.5]$$

This modified FoM is scaled in terms of luminosity instead of flux values, and is still relatable to the peak frequency. Here the original constants chosen by the Sowards-Emmerd et al. study have not been changed. While this has resulted in n terms that are no longer scaled to fall between 0 and 1, the modified product probability figure of merit is still useful for comparison. The peak frequencies for each object as well as the changed FoM are included in Table 2 for reference. The scaled FoM graph (Figure 3) was more useful to this investigation, and will be discussed further below.

## RESULTS

In the course of searching databases, it became clear that very limited infrared data exist for the objects in this sample. This made the number of objects to be analyzed much smaller than the original sample. About 22 objects out of the original 504 BL Lac and FSRQ sources considered from the survey had adequate data in almost all

wavelengths, only 20 of which had a distinctive synchrotron peak frequency found by the computer curve-fitting procedure. The frequency coverage and sensitivity limit of each instrument used for the data necessary to this project are included in Table 3. Several factors could have brought about the outcome of so little data in the IR and  $\gamma$ -ray bands. The positional accuracy of the source detections for various instruments could have placed the matching object out of the search radius used (about 2 arc minutes). Also, some objects may not have been detected because their cycle of variability was at a low when that portion of the sky was scanned by the telescopes, and so may have been at a low enough energy to be under the instrument detection limit. Also, due to these same effects, only two sources out of the 22 showed up in the EGRET survey. This limited the analysis of the SEDs, reducing the study from considering the double-peak structure to only focusing on where the synchrotron peak would occur for each object.

The first peak frequency vs. figure of merit graph produced showed no correlation between the factors (Figure 2). No dependence on frequency of the synchrotron peak was shown for the FoM, and the BL Lac data points and the FSRQ were not separated in any fashion on the graph. However, the appearance of the graph containing the redshift-corrected FoM (Figure 3) suggests a correlation. Though the location of the synchrotron peak frequency does not seem to depend on the object type, the 18 data points that included redshift data appear to relate  $\nu_{\text{peak}}$  and FoM on the log-log graph. The implications of this will be discussed below.

## **DISCUSSION AND CONCLUSIONS**

Before this study was conducted, it was understood that the synchrotron peak could fall anywhere in the IR to soft x-ray range, depending on the type of object

involved. Such a wide range, however, was not found for the current data. Though a peak frequency varying from IR to x-ray was expected, many sources in the group with sufficient data had a synchrotron peak in IR/near-IR. All but 3 objects of the 20 to which a curve was fitted have synchrotron peaks in this range, suggesting that they fall into the LBL and FSRQ categories.

This effect could have been due to many factors. The first, though the author is not convinced of it, would be that the blazar population in general has an 85% tendency to have the synchrotron peak in the IR range. This is highly improbable due to the current division of blazar types. One type of blazar has not excessively been found over other types in current surveys, suggesting that one category of object is not more likely to occur than another. A more reasonable scenario is that the data source selection methods are biased. Most of the figures plotted were for objects that had data in the IRAS survey, which means that they were selected to be objects that would have a detectable energy emission in the IR. Because blazars are less variable in the IR than in other wavelengths, those which are not too faint to be detected by IR instruments, or those normally peaking in the IR range, would be preferentially selected. Along the same lines, the objects that may have had a peak frequency at another wavelength may have been too faint in the IR to be detected, automatically removing them from this sample.

However, the final result of this survey was also biased in other ways. As mentioned before, a synchrotron peak frequency vs. FoM graph was created to see if there was a correlation between the two factors (Figure 2). If a trend were apparent in such a graph, it would signify that the FoM used to select the sources in the original data list biased the sample toward objects with peaks in the IR or optical wavelengths. Such an

effect has been analyzed for the results of past surveys. For instance, a recent analysis (4: 226) suggests that the different categories of identified blazars found in each survey could be due only to selection criteria biases. As stated in that study, most LBL sources have been identified in the radio range, while HBL are most often found in X-ray surveys.

While no correlation occurs between FoM and the frequency of the synchrotron peak for BL Lacs or FSRQ in the original graph (Figure 2), the dependence of the modified FoM on synchrotron peak frequency (Figure 3) suggests that the FoM is biased to select objects peaking at lower frequencies (i.e. LBL and FSRQ). This selection effect has many different implications. The FoM in the work by Sowards-Emmerd et al. is based on radio fluxes as well as radio spectra, though one term for x-ray flux was included to create less bias. They believed in that study that the radio properties of a blazar object correspond well with the gamma variability and properties, and so it was more worthwhile to focus on that part of the broadband spectra to select blazar candidates. This decision has weighted the survey toward objects with synchrotron peaks in the radio to optical range, as can be seen on the graph. While part of the bias can be explained by the infrared selection of objects in this survey, it cannot be denied that any data input for this model would have a higher figure of merit and be more likely be selected if it were an FSRQ or LBL. Perhaps the inclusion of terms for the IR, near-IR, optical, as well as  $\gamma$ -ray flux in the FoM calculation would make a more broadly based model for the selection of all blazars, or different FoM systems could be determined for pinpointing the three different types. This more inclusive model would be necessary to

continue the study of blazar properties in general, instead of focusing on such a confined sample. For now, this is can only be left up to further study.

If one examines the merits of such a limited set of objects, however, other patterns arise. Another interpretation of the corrected FoM graph would be that, depending on where the synchrotron peak occurred for a blazar candidate, a higher luminosity or intensity of peak would be expected for lower peak frequencies. This effect mirrors that found by Fossati et al. in their 1998 study (5). They discovered a correlation between the luminosity of a blazar and the synchrotron peak frequency of the type of object involved. According to their study, the intensity of the synchrotron and Compton scattering peaks in blazar SEDs are dependent on peak frequency. The linear tendency they found in their  $\nu$  vs.  $\nu L_\nu$  plots (5: 441) is strikingly similar to that found in Figure 3, where the luminosity is expected to be higher for lower frequency peaks. Indeed, the luminosity progression theorized by Fossati et al. can be seen in a luminosity curve plot of each object (Figure 4). As you move to greater frequencies along the plot, the maximum luminosity peak found for the objects lessens.

The objects that fall in the lower frequency range for the synchrotron peak are more likely to show a  $\gamma$ -ray Compton radiation peak in the GeV range, according to the results of the Fossati et al. study. Under this assumption, the FoM defined in the survey by Sowards-Emmerd et al. immediately becomes very important for further observational study of blazar candidates. The objects most likely to be selected by the FoM as it was originally defined would have a  $\gamma$ -ray peak occurring in the GeV, the range most easily detected by the EGRET survey, and most accurately detected by the upcoming GLAST mission. The sensitivity and depth of exposure of the future satellite data will resolve the

issues of discovering objects that are faint in the  $\gamma$ -ray band, as well as making it possible to study variability with its frequent viewings of each source, furthering what we already have discovered about these objects. However, until GLAST has been launched, the FoM defined in the Sowards-Emmerd et al. survey could be used to compile a more complete list of blazar candidates over the entire sky. GLAST will study these objects in more detail, but it would be worthwhile to have a ranked list ready and waiting to be examined. That is the ultimate goal of this study: providing a basis for progress in the study of blazar dynamics with a more sensitive and complete catalogue of blazar-like objects, and being prepared to use advances in technology efficiently, taking advantage of GLAST results as soon as they are available.

### **ACKNOWLEDGMENTS**

This research was conducted at the Stanford Linear Accelerator Center. I thank the U. S. Department of Energy, Office of Science for giving me the opportunity to participate in the SULI program and the chance for me to have a rewarding learning experience. My greatest regards go to Helen Quinn and James Lindesay for running this program. This research has made use of the NASA/IPAC Extragalactic Database (NED) which is operated by the Jet Propulsion Laboratory, California Institute of Technology, under contract with the National Aeronautics and Space Administration. This study would also not have been possible without the use of NASA's Astrophysics Data System Abstract Service. Special thanks go to my mentors Greg Madejski and Seth Digel at the Stanford Linear Accelerator Center for their knowledge, insight, time and patience. I also thank David Sowards-Emmerd et al. for the contribution of data from their recent sky

survey and the enthusiasm shown toward my project idea, Phil Marshall at SLAC for his distance program, as well as my colleagues at SLAC who gladly answered questions.

### **WORKS CITED**

- [1] G. Ghisellini et al., "A Theoretical Unifying Scheme for Gamma-ray Bright Blazars," arXiv: astro-ph/9807317v1, July 30, 1998. 1-24.
- [2] David Sowards-Emmerd et al., "A Northern Survey of Gamma-Ray Blazar Candidates," *Astrophysical Journal*, vol. 626, 95-103, June 10, 2005.
- [3] David W. Hogg, "Distance Measures in Cosmology," arXiv: astro-ph/9905116v4, Dec.16, 2000. 1-16.
- [4] S. Antón and I. W. A. Browne, "The Recognition of Blazars and the Blazar Spectral Sequence," *RAS*, vol. 356, 225-231, Sept. 23, 2004.
- [5] G. Fossati et al., "A Unifying View of the Spectral Energy Distributions of Blazars," *RAS*, vol. 299, 433-448, 1998.

### **OTHER REFERENCES**

M. Böttcher et al., "Coordinated Multiwavelength Observations of BL Lacertae in 2000," *Astrophysical Journal*, vol. 596, 847-859, Oct. 20, 2003.

S. Ciprini et al., "The Infrared Peak of the Blazar Spectral Energy Distribution and the Monitoring from Antarctica," *Mem. S.A.It.*, vol. 74, 70, 2003.

Giovanni Fossati, "Demographics of Blazars," arXiv, Dec 21, 2000.

P. Giommi et al., "The Sedentary Multifrequency Survey, I. Statistical Identification and Cosmological Properties of High-Energy Peaked BL Lacs," *RAS*, vol. 310, 465-475, July 6, 1999.

H. Kubo et al., "ASCA Observations of Blazars and Multiband Analysis," *Astrophysical Journal*, vol. 504, 693-701, Sept. 10, 1998.

Greg M. Madejski, "Black Holes in Active Galactic Nuclei: Observations," *Theory of Black Hole Accretion Disks*, Cambridge University Press. 1-21.

C. von Montigny et al., "High Energy Gamma-Ray Emission from Active Galaxies: EGRET Observations and Their Implications," *Astrophysical Journal*, vol. 440, 525-553, Feb. 20, 1995.

Paolo Padovani and Paolo Giommi, "The Connection Between X-Ray- and Radio-Selected BL Lacertae Objects," *Astrophysical Journal*, vol. 444, 567-581, May 10, 1995.

Marek Sikora and Greg Madejski, "Blazars," arXiv, Jan. 22, 2001.

## Tables

**Table 1- Frequency used to plot each wavelength band**

BAND	FREQUENCY (Hz)
Radio	$8.4 \times 10^9$
100 $\mu\text{m}$	$2.99 \times 10^{12}$
60 $\mu\text{m}$	$4.983 \times 10^{12}$
25 $\mu\text{m}$	$1.196 \times 10^{13}$
12 $\mu\text{m}$	$2.492 \times 10^{13}$
J	$2.411 \times 10^{14}$
H	$1.801 \times 10^{14}$
K <sub>s</sub>	$1.384 \times 10^{14}$
Red	$4.425 \times 10^{14}$
Visible	$6.34 \times 10^{14}$
X-ray	$2.524 \times 10^{17}$
$\gamma$ -ray	Individually determined $\langle \nu \rangle$ for each object

**Table 2- Pertinent data for the FoM graphs and scaled FoM calculations**

Object Name	FoM (S-E, 2005)	S <sub>8.4</sub> (mJy)	$\alpha$	RASS count (ct/s)	z	Type	$\nu_{\text{peak}}$ (Hz)	D <sub>L</sub> (D <sub>med</sub> = 1122.9 Mpc)	Scaled FoM
J003939.61+141157.5	.075	369.8	-0.19	0	1.738	B	$2.91 \times 10^{12}$	6409.262	0.112
J011205.82+224438.7	.105	493.4	-0.15	0.151	-----	B	$1.02 \times 10^{14}$	-----	-----
J024918.01+061951.9	.079	579.3	-0.1	0	1.881	F	$4.88 \times 10^{12}$	7062.936	0.084
J025134.53+431515.8	.079	1174.1	0.01	0.027	1.31	F	$2.68 \times 10^{13}$	4521.92	0.124
J030335.24+471616.2	.132	1616.3	-0.29	0	.475	B	$5.29 \times 10^{12}$	1305.421	0.136
J031948.16+413042.1	.092	34296	-0.23	0	.017	F	$5.02 \times 10^{13}$	36.142	-0.069
J040922.00+121739.8	.103	667.3	-0.25	0	1.02	B	$3.62 \times 10^{12}$	3317.977	0.131
J043311.09+052115.6	.088	2105.2	0.26	1.705	.033	F	$2.03 \times 10^{14}$	71.002	-0.072
J050925.96+054135.3	.093	702.4	-0.16	0.042	-----	B	$3.75 \times 10^{13}$	-----	-----
J075706.64+095634.8	.143	1363.5	-0.23	0.113	.66	B	$7.41 \times 10^{13}$	1942.478	0.206
J082550.33+030924.5	.145	1873.4	-0.18	0.132	.506	B	$3.41 \times 10^{13}$	1408.145	0.169
J140700.39+282714.6	.167	1936.3	-0.49	0	.076	F	$7.26 \times 10^{13}$	168.631	-0.067
J141558.81+132023.7	.119	1564.3	-0.21	0	.246	B	$3.06 \times 10^{12}$	606.272	0.086
J141946.59+542314.7	.219	2248.1	-0.62	0.103	.1153	B	$3.20 \times 10^{13}$	357.109	0.084
J155543.04+111124.3	.195	506.5	-0.28	1.513	.36	B	$3.99 \times 10^{14}$	940.368	0.165
J164258.80+394836.9	.126	6299.8	0.05	0.325	.593	F	$2.47 \times 10^{13}$	1705.328	0.134
J180045.68+782804.0	.117	2874	-0.15	0.066	.68	F	$3.11 \times 10^{13}$	2014.571	0.158
J180650.68+694928.1	.11	1595.5	0	0.154	.05	B	$1.09 \times 10^{14}$	108.921	-0.100
J195959.84+650854.6	.071	222.8	0.04	2.653	.048	B	$1.12 \times 10^{15}$	104.413	-0.244
J221949.74+261327.9	.115	427	-0.41	0.085	.085	F	$7.91 \times 10^{13}$	189.774	-0.203

**Table 3- Statistics on sources from which data was combined.**

<b>Mission</b>	<b>IRAS</b>	<b>2MASS</b>	<b>EGRET</b>
<b>Wavelengths/ energy band</b>	<b>IR- 12, 25, 60, 100 microns</b>	<b>Near-IR- 1.24, 1.66, 2.16 microns</b>	<b><math>\gamma</math>-ray- 20 MeV-30 GeV</b>
<b>Effective Minimum Energy/Flux</b>	<b>.5 Jy at 12 microns to 1.5 Jy at 100 microns</b>	<b>1 mJy</b>	<b>100 MeV</b>
<b>Positional accuracy</b>	<b>20''</b>	<b>.5''</b>	<b>10'</b>
<b>Sky Coverage</b>	<b>96%</b>	<b>~95%</b>	<b>~99%</b>

## Figures

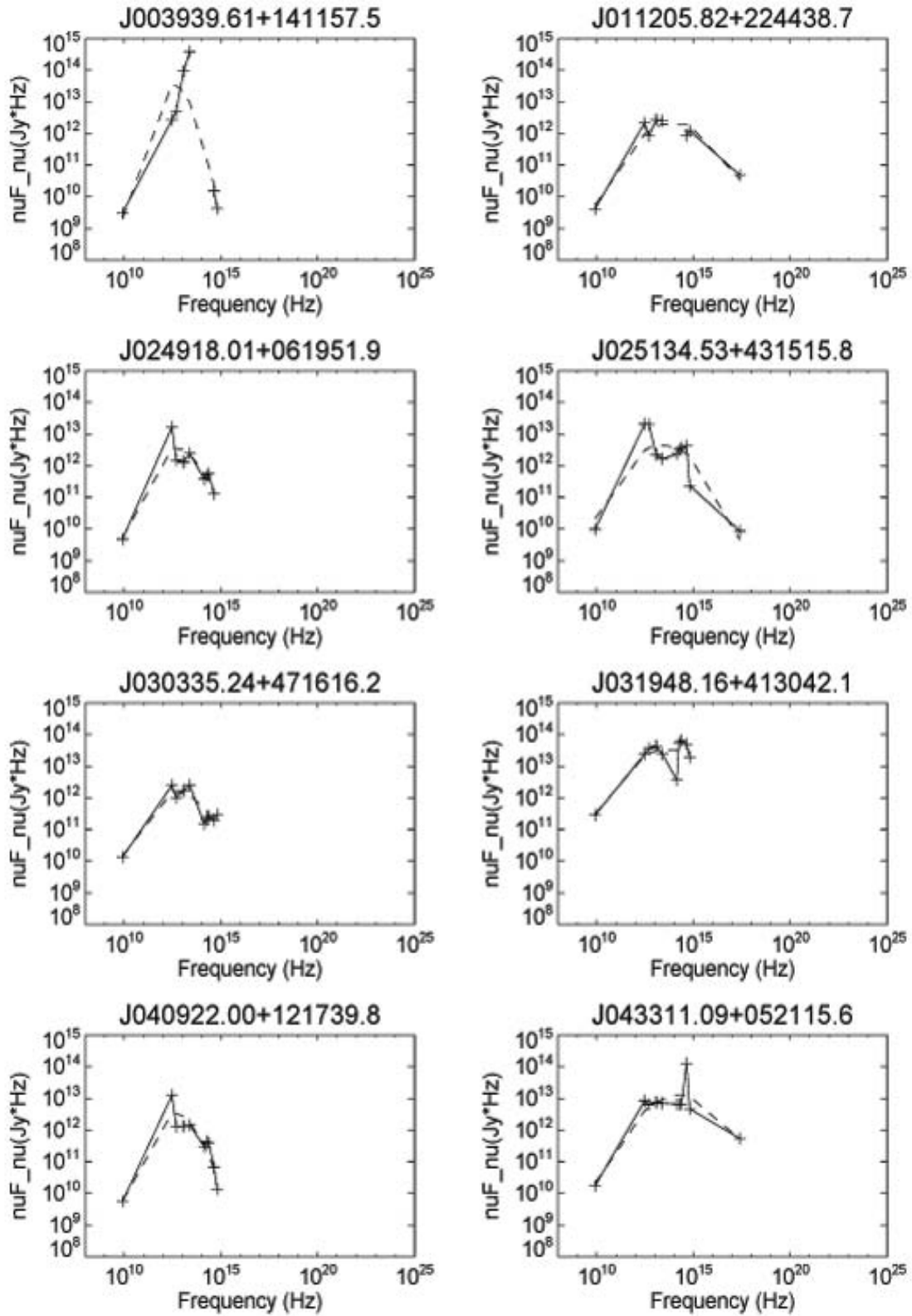


Figure 1- Plotted SEDs of 22 objects with adequate data. Solid lines connect the observed data, dashed lines model the computer-fitted curve.

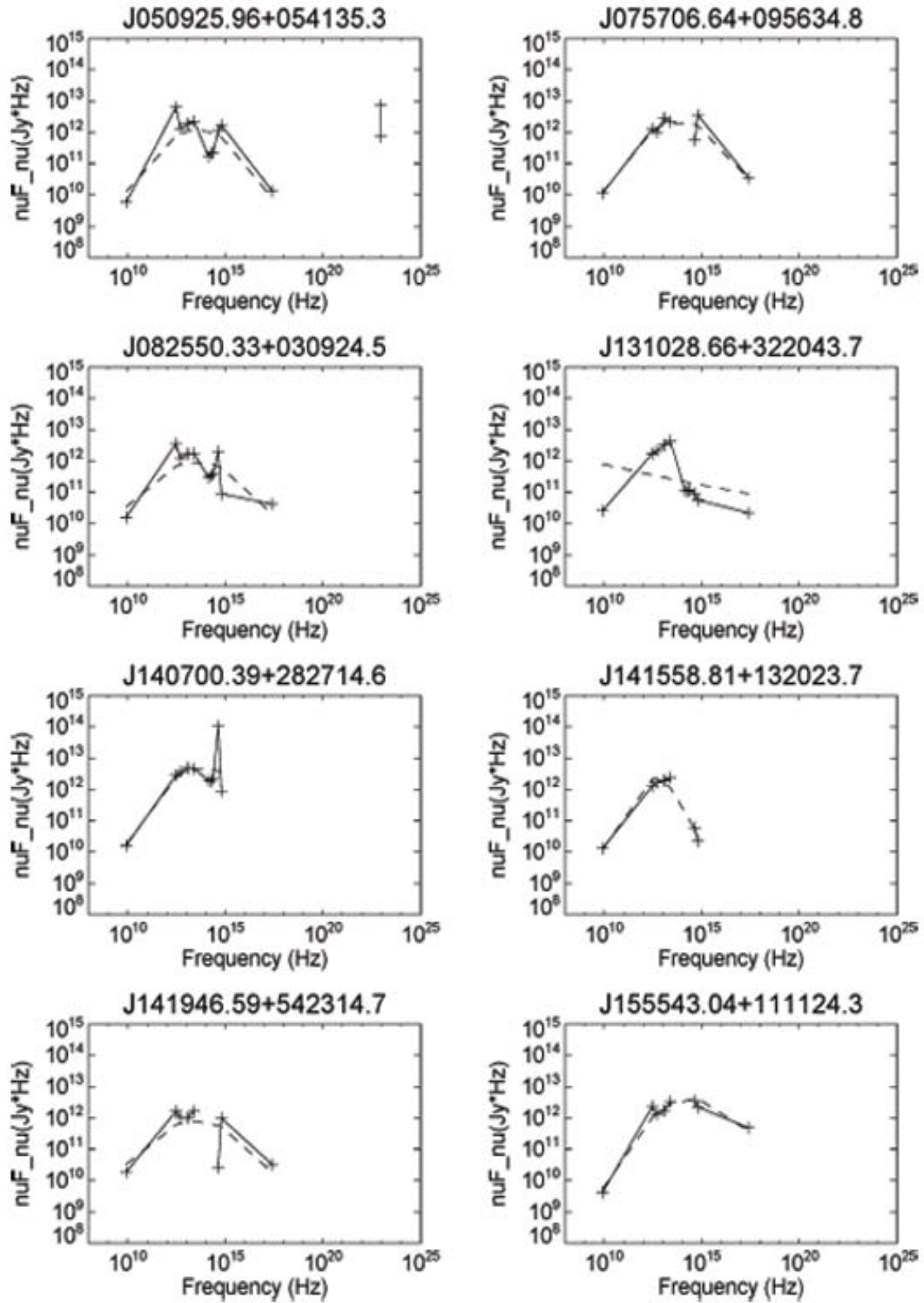


Figure 1- continued

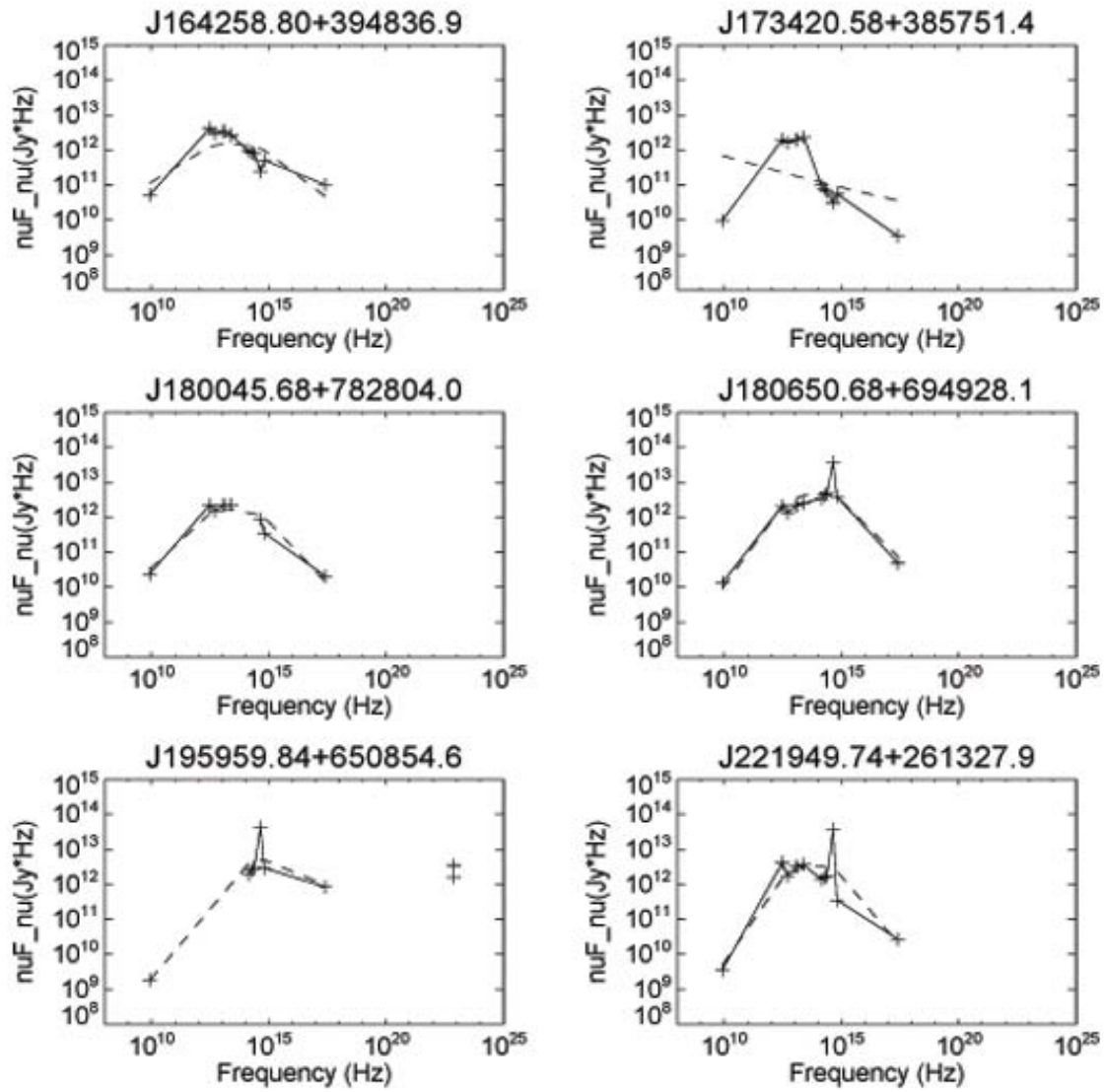


Figure 1- continued

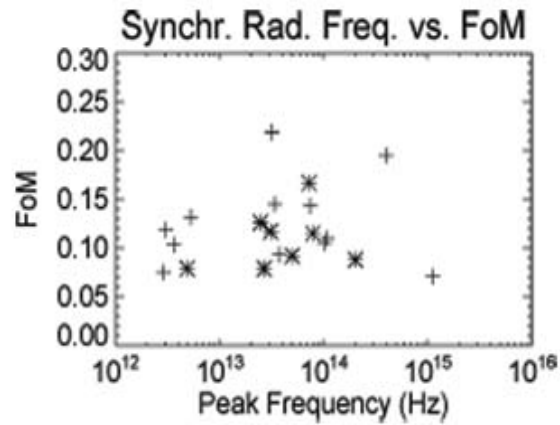


Figure 2- BL Lac plotted as +, FSRQ plotted as \*

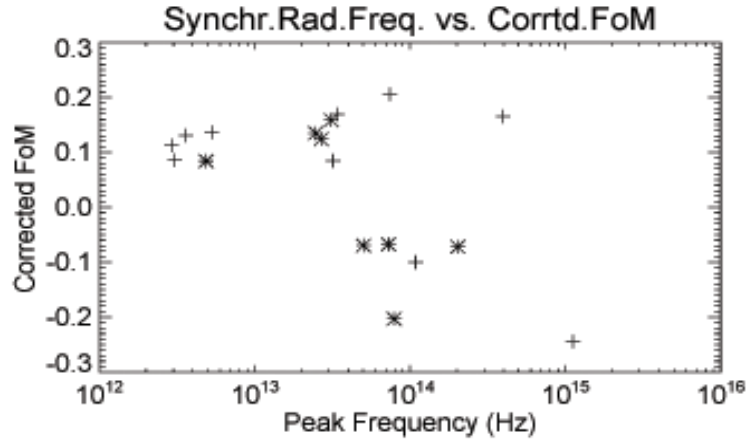


Figure 3- FoM corrected for redshift. As above (Figure 2), BL Lac plotted as +, FSRQ plotted as \*. Only objects with a defined redshift were included in this graph.

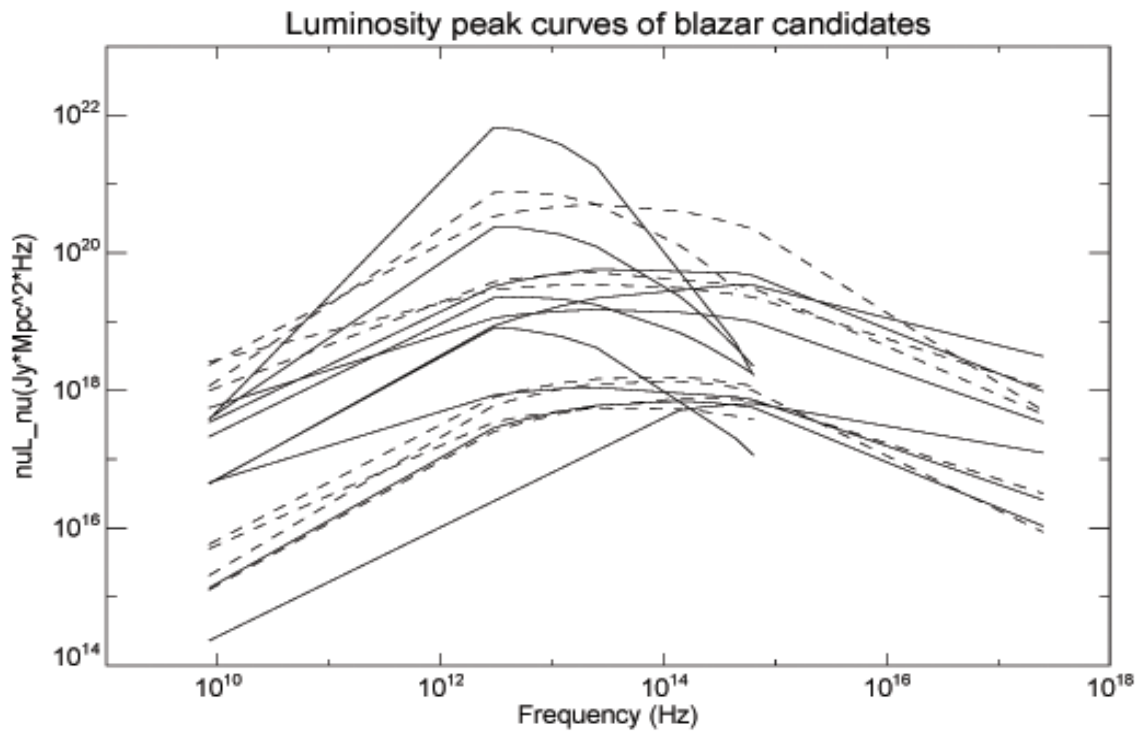


Figure 4- Synchrotron luminosity curves for the 18 redshift-correctable objects, illustrating luminosity progression theory. Parabola curves were fitted to the luminosity data in the same manner as the SED graphs, creating the peaks for each object seen in the compilation plot above.

# Measurement of gravitational lens time delays with LSST<sup>1</sup>

Lowry Anna Kirkby

Magdalen College, Oxford University, United Kingdom

Office of Science, Science Undergraduate Laboratory Internship (SULI)  
Stanford Linear Accelerator Centre  
Menlo Park, California

August 27, 2005

Prepared in partial fulfilment of the requirements of the Office of Science, Department of Energy's Science Undergraduate Laboratory Internship under the direction of Dr. Phil Marshall in the Kavli Institute for Particle Astrophysics and Cosmology (KIPAC) at the Stanford Linear Accelerator Center (SLAC), California.

Participant: \_\_\_\_\_  
Signature

Research Advisor: \_\_\_\_\_  
Signature

---

<sup>1</sup>Large Synoptic Survey Telescope

## Abstract

The proposed Large Synoptic Survey Telescope will be the first to explore multiple dark energy probes simultaneously, including baryon acoustic oscillations, weak lensing, and strong gravitational lensing. The large data sample, covering the entire visible sky every few nights, will allow an unprecedented survey of deep supernova sources and their lensed images. The latter have not yet been observed. Notably, LSST will measure the *time delays* between different strong-lensed images of the same supernova. This will provide a unique probe of dark matter, dark energy, and the expansion rate of the Universe.

By simulating LSST observations under realistic conditions, we determined the time delay precision of multiple images from a representative strong-lensed Type Ia supernova. The output of the simulation was a set of light curves according to field and filter, which were subsequently analysed to determine the experimental time delays. We find that a time delay precision of better than 10% can be achieved under suitable conditions. Firstly, a minimum observed peak-magnitude of 22 is required for the lensed image, corresponding to an intrinsic source magnitude of about 24. The number of such supernova sources expected for LSST is under investigation, but it could amount to several thousand. Secondly, a minimum of about 50 visits per field is required, and, moreover, these visits must be evenly distributed over the duration of the event. The visit frequency should be approximately once per week, or better. Thirdly, the sky brightness should be below 21 magnitude arcsec<sup>-2</sup> to allow sufficient sensitivity to distance sources.

Under the nominal LSST visiting schedule and field conditions, 15% of all fields satisfy these criteria, and allow time delay measurements of better than 10% precision. This performance can be further improved by fitting the predicted supernova light curves to the observations, rather than using the simple weighted mean as in the present study. Of the well-measured fields, 85% involve observations taken with the *r* filter, which has a wavelength acceptance that is well-matched to supernova spectra. This filter therefore represents the best choice for strong gravitational lens observations with LSST.

Our primary conclusion is that the visiting schedule is the single most important parameter to optimise for time delay measurements, and, once a lensed supernova has been detected, that frequent, regular observations should be scheduled to search with the highest sensitivity for multiple, delayed lensed images.

# Contents

<b>1</b>	<b>Introduction</b>	<b>1</b>
1.1	The Large Synoptic Survey Telescope (LSST) . . . . .	1
1.2	Strong gravitational lensing . . . . .	1
1.3	Aim of this study . . . . .	2
<b>2</b>	<b>Experimental methods</b>	<b>2</b>
2.1	LSST simulation . . . . .	2
2.2	Generating a strong lens system . . . . .	3
2.2.1	Modelling System LSN . . . . .	3
2.2.2	Light curve generation . . . . .	4
2.3	Measuring the time delay precision . . . . .	4
2.4	Tests on System LSN . . . . .	6
2.4.1	Run 1 - Threshold source magnitude . . . . .	6
2.4.2	Run 2 - Field conditions and visiting schedule . . . . .	7
<b>3</b>	<b>Results and discussion</b>	<b>8</b>
3.1	Run 1: Threshold source magnitude . . . . .	8
3.2	Run 2: Field conditions and visiting schedule: . . . . .	9
3.2.1	Filter <i>g</i> (400–560 nm) . . . . .	9
3.2.2	Filter <i>r</i> (540–720 nm) . . . . .	9
3.2.3	Filter <i>i</i> (685–870 nm) . . . . .	14
3.2.4	Filter <i>z</i> (840–950 nm) . . . . .	17
3.2.5	Filter <i>Y</i> (945–1030 nm) . . . . .	19
<b>4</b>	<b>Conclusions</b>	<b>22</b>



# 1 Introduction

## 1.1 The Large Synoptic Survey Telescope (LSST)

The proposed LSST is a ground-based telescope currently under study at Stanford Linear Accelerator Center (SLAC) [1]. The telescope is designed to have a large aperture, large field of view and high resolution (Table 1) in order to allow the entire observable sky to be mapped every few nights. Current telescopes either have a collection area large enough to produce deep images over a small field of view, or else can observe large areas of sky quickly but only to shallow depth. With its high etendue,<sup>2</sup> LSST will be able to capture the variation of short-lived stellar objects, such as exploding supernovae—effectively taking a movie of our dynamic Universe.

Table 1: Comparison between LSST and the Sloan Telescope. As a reference point, the field of view of the full moon is  $0.5^\circ$ .

Parameter		LSST	Sloan
Aperture	[m]	8.4	2.5
Field of view	[degrees]	3.5	2.5
CCD pixels	$[\times 10^9]$	3.0	0.1

Table 1 compares the performance of LSST with the current state-of-the-art sky survey, the Sloan Digital Sky Survey, at the Apache Point Observatory, New Mexico. The LSST is aiming for the deepest, fastest, widest and finest imaging ever achieved in one telescope. The images will be recorded using one of five colour filters (designated  $g$ ,  $r$ ,  $i$ ,  $z$  and  $Y$ ). These are weighted towards the red end of the spectrum in order to probe the farthest reaches of the Universe, where objects have a large redshift.

The primary goals of LSST are to explore the dark matter of the Universe, and to shed light on the nature of dark energy. At present, most dark matter and dark energy telescopes probe weak gravitational lensing, i.e. the coherent distortion of background sources, such as galaxies or galactic clusters. Weak lensing surveys are a central goal of LSST. However, LSST will open up a unique window on dark matter and dark energy by its ability to pursue multiple probes simultaneously, such as baryon acoustic oscillations and strong gravitational lensing.

## 1.2 Strong gravitational lensing

Gravitational lensing falls into three regimes: strong lensing, weak lensing and microlensing [2]. Strong lensing is characterised by the formation of multiple images of the source (e.g. the two images shown in Fig. 1). The lens typically consists of a galaxy, or galaxy cluster; the source may be a quasar, a supernova or a distant galaxy. Measurement of the image separation allows reconstruction of the lens's mass distribution, which provides information on its matter and dark matter content. If the lens has an asymmetric mass distribution, or if the source is not directly aligned with the lens (as in Fig. 1), the optical path lengths of the images differ. The arrival time of the light is a result both of geometry (the physical path length difference) and of gravitational effects. If the source is variable, as are quasars and supernovae, the images will also be variable and the time delays between images can be measured. Simultaneous measurement of the time delay and mass distribution allows Hubble's constant,  $H_0$ , to be determined, and thus provides a measure of the expansion rate of the Universe.

---

<sup>2</sup>*Etendue* is the cross-sectional area of a cone of light times the solid angle subtended by the light.

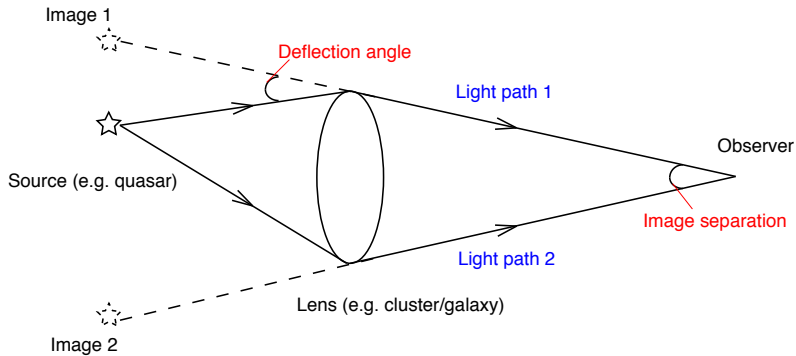


Figure 1: Strong gravitational lensing. Multiple images of the source are seen by the observer, as a result of the deflection of light due to the curvature of spacetime.

### 1.3 Aim of this study

The LSST is estimated to increase the strong-lens sample to at least 10,000 systems—an increase of about two orders of magnitude beyond present world statistics. In addition, LSST is expected to observe the first strong-lensed supernovae and, moreover, to collect a large event sample. Supernovae exhibit well-known light curves with a sharp rise and fall in brightness, providing precise time delay measurements. However, since the telescope will be scanning the sky, there will be gaps in the supernovae light curves, which may reduce the precision of the time delay measurement, and hence reduce the precision of the  $H_0$  determination.

The diverse science goals of LSST involve different spatial, temporal and colour sampling requirements. An optimum observing strategy would maximise the science return from a single set of observations. The aim of our study is to investigate whether the proposed telescope design and operation strategy can deliver the required science from strong lensing surveys.

Our tests and results are described below. The first test involves estimating the threshold source magnitude required for good time delay measurements (§3.1), followed by tests involving the proposed observing strategy (§3.2). In the concluding section (§4), I will discuss the overall results, as well as suggest possible improvements in the observing strategy.

## 2 Experimental methods

### 2.1 LSST simulation

The operation of LSST is currently simulated by the *LSST Observation Simulator*<sup>3</sup>. The Simulator uses real seeing<sup>4</sup> and weather data, taken from the Cerro Tololo Inter-American Observatory (CTIO) [3] in Chile—a site with similar conditions to those proposed for LSST.

The Simulator is able to schedule observations based on a multitude of parameters, such as seeing, airmass, sky brightness, sun and moon angle; it also takes into consideration telescope parameters such as slewing time, shutter time and filter change time. The user is able to run the simulation for as long as desired, and to vary telescope parameters such as exposure time and exclusion zones. The output run history is stored in a MySQL database repository. For each observation, 34 attributes are stored. For this study, we extracted the telescope position

<sup>3</sup>Written by F. Pierfederici and K. Cook, National Optical Astronomy Observatory (NOAO), Tucson, Arizona.

<sup>4</sup>Astronomical *seeing* is the clarity with which the image is observed by a ground-based telescope, primarily determined by Earth’s atmosphere. The seeing is the measured diameter (full width half maximum) of a point source (for example, a star) observed through the atmosphere. The best conditions (e.g. at the Magellan telescope, Chile) reach a minimum seeing of about 0.3–0.4 arcseconds.

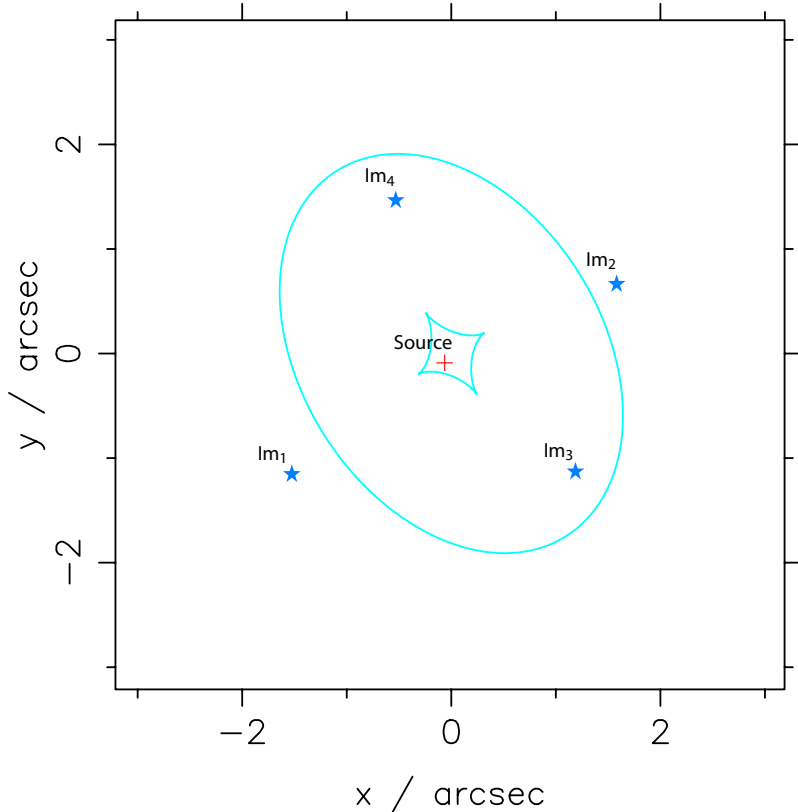


Figure 2: Schematic diagram of System LSN. The turquoise oval and caustic represent the projection of the critical curves in the lens plane (lines of critical density) onto the source plane. These are lines of infinite image magnification. The centre of the lens is positioned at  $(0, 0)$ . The red cross indicates the position of the source (in this case a supernovae), and the four blue stars (labelled  $Im_1$ – $Im_4$ ) indicate the positions of the lensed images of the source.

(the LSST field observed), the filter, the seeing and the sky brightness. We ran the Simulator for an effective operational period of one year.

## 2.2 Generating a strong lens system

A simple mass model for elliptical galaxies and galactic clusters is the *Single Isothermal Ellipsoid* model, in which the density of matter falls off with the inverse of the square of the radius. We simulated a strong lens system using the modelling program *SIElens*,<sup>5</sup> which incorporates the Single Isothermal Ellipsoid mass model. Since strong lensed supernovae have not yet been observed, we modelled and investigated a fictitious system named *System LSN* (Lensed SuperNova).

### 2.2.1 Modelling System LSN

System LSN comprises a Type Ia supernova lensed by an elliptical galaxy, to form a quad image system. A schematic is shown in Fig. 2, and the parameters are summarised in Table 2. For the initial study described here, we designed System LSN to represent a relatively high quality system, with large image separations and long time delays between images (Table 3).

<sup>5</sup>Written by Phil Marshall, SLAC, Stanford, California.

Table 2: Lens and source parameters of System LSN.

System parameter		Value
<b>Lens:</b>		
Position	$\theta_x, \theta_y$	0, 0 arcsec
Redshift	$z_d$	0.40
Velocity dispersion	$\sigma_v$	350.0 km/s
Magnitude	$m_d$	17.68
Effective radius	$r_e$	1.50 arcsec
Axis ratio	q	0.70
Orientation	$\phi$	-58.0 degrees
<b>Source:</b>		
Position	$\beta_x, \beta_y$	-0.06, -0.09 arcsec
Redshift	$z_s$	0.90
Magnitude (unlensed)	$m_s$	25.5

Table 3: Magnitude changes of the four lensed images, and time delays relative to  $Im_1$ .

Image	Magnitude change due to lensing	Time delay (days)
$Im_1$	-1.5	0.0
$Im_2$	-2.0	31.6
$Im_3$	-1.6	42.6
$Im_4$	-1.3	54.8

### 2.2.2 Light curve generation

We generated the system’s four light curves<sup>6</sup> using an idealised, dense time sampling, as shown in Fig. 3a). The same light curves are shown Fig. 3b) assuming measurements with realistic LSST time sampling, using the LSST Observation Simulator. Both sets of light curves correspond to observations taken in the  $r$  filter only. Despite the sparser time sampling, LSST observes the four lensed images with well-resolved time delays and even retains the detailed shape of the supernovae light curves (notice, for example, that the break in the trailing edge is clearly detected).

### 2.3 Measuring the time delay precision

System LSN will have a distinct light curve in each LSST field as a result of the different visiting schedules per field. From these light curves and the weather conditions extracted from

<sup>6</sup>Using the *snlcsim* code written by Liz Rivers, Wellesley College, MA.

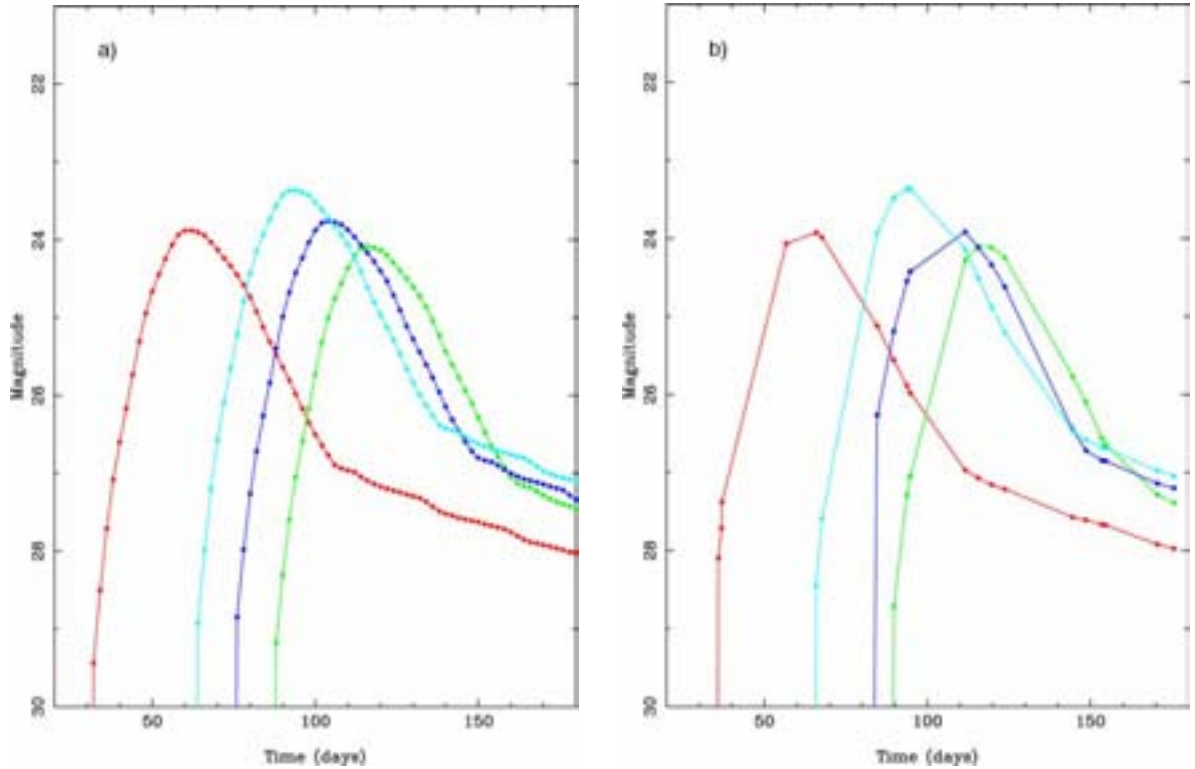


Figure 3: Light curves of System LSN in the  $r$  filter for a) an idealised, dense time sampling and b) a realistic time sampling with LSST. Each curve corresponds to a different lensed image of the supernova. The images are labelled 1 to 4 in order of time (red: 1, turquoise: 2, blue: 3, green: 4). The time delays are 32, 43 and 55 days between images 1–2, 1–3 and 1–4, respectively. Note that the intrinsic source magnitude is about 25.5; the brighter images result from the magnifications due to lensing.

the Observation Simulator, mock LSST images were generated<sup>7</sup> for each day of observation.

We modified the program to produce 4 “fits file” images for each observation day—one of each image in System LSN. We measured the flux and flux error of these images using the Source Extractor astronomical software tool, *SExtractor* [5]. Source Extractor works on both photographic plates and CCDs, and is used for the detection and photometry of sources in fits files.

The time corresponding to the peak magnitude ( $t_{peak}^k$ ) was found for each image,  $k$ , by calculating the weighted mean of each light curve. The accuracy of this value with respect to the true peak (as seen in Fig. 3a) is of course a function of the number of observations made per field per filter (the observing strategy). We thus define the measured time delay ( $\Delta t_{meas}^{1k}$ ) and its fractional error ( $\delta^{1k}$ ) for image  $k$  relative to image 1 to be:

$$\begin{aligned} \Delta t_{meas}^{1k} &= t_{peak}^k - t_{peak}^1 \\ \delta^{1k} &= \frac{\Delta t_{true}^{1k} - \Delta t_{meas}^{1k}}{\Delta t_{true}^{1k}} \end{aligned} \quad (1)$$

where  $\Delta t_{true}^{1k}$  are the true time delays (as given in Table 3) and the image number,  $k = 2, 3, 4$ .

<sup>7</sup>Using the *simlsst* code written by Masao Sako, SLAC.

## 2.4 Tests on System LSN

We wrote a script to execute the previously-described codes in a pipeline, where the output of one program provides the input for the next. The output of the pipeline is a set of light curves, one for each combination of field and filter. These light curves are then analysed to determine the time delay precisions (Eq. 1). The pipeline can be modified in future to study any arbitrary lens system, observed at any position in the sky. The description, inputs and outputs of each piece of code are summarised in Table 4. The pipeline was run twice, as described in §2.4.1 and §2.4.2.

Table 4: Summary of the programs used in the simulation pipeline.

Program	Function	Inputs	Outputs
1. <i>LSST cadence simulator</i>	Extract obs. dates	- LSST parameters - Run time	- Obs. dates per field - Filter used - Seeing - Sky brightness
2. <i>SIElens</i>	Model lens system	- Lens parameters - Source parameters	- Image separation - Image time delays - Magnification factors
3. <i>snlcsim</i>	Generate light curve	- Obs. dates per filter - Image time delays - Magnification factors	- Light curve per filter
4. <i>simlsst</i>	Simulate LSST images	- LSST parameters - Light curve per filter - Lens and source redshift - Seeing - Sky brightness	- Mock LSST image
5. <i>SExtractor</i>	Measure image flux	- Mock LSST image	- No. objects detected - Detected flux - Flux error
6. <i>tdelays</i>	Determine time delay	- Observation dates - Detected flux - Flux error	- Predicted time delay - Fractional error

### 2.4.1 Run 1 - Threshold source magnitude

We selected a single LSST field with a good visiting schedule, the light curve of which is shown in Fig. 3b). We artificially brightened the source by incrementing the magnitude by 0.5 on each loop (equivalent to shifting the light curve vertically upwards by this amount). This data was used to determine the threshold source peak-magnitude for good time delay measurements.

### 2.4.2 Run 2 - Field conditions and visiting schedule

For this run, System LSN was set to the threshold source peak-magnitude for good time delay measurements, as determined from Run 1. This System was placed in each LSST field, to investigate the following variables:

**Field conditions:** During good observation conditions, LSST is expected to image to magnitude 24 in two 15 second exposures. However, in practice, the minimum detectable magnitude will depend on the sky brightness and the seeing, and so the actual detection limit will vary about this value. The minimum detectable magnitude must be well below the threshold source peak-magnitudes to yield useful time delay measurements.

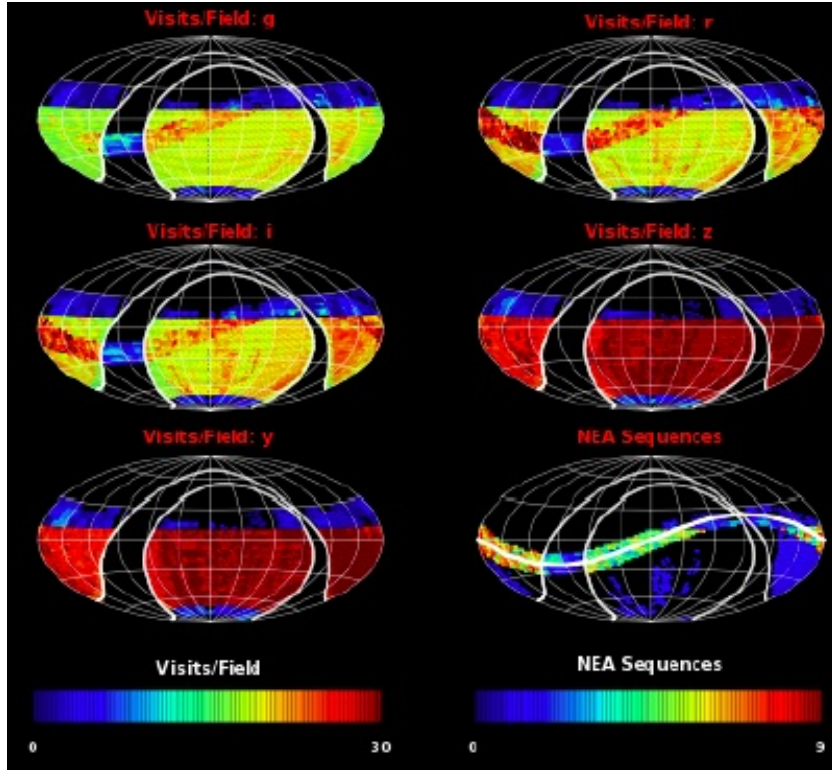


Figure 4: LSST annual sky coverage for Weak Lensing and Near Earth Asteroid (NEA) surveys, in each of the 5 filters ( $g$ ,  $r$ ,  $i$ ,  $z$ ,  $Y$ ), and for the NEA survey alone. Red corresponds to the most frequent visits per field.

**Visiting schedule:** The LSST visiting schedule varies from field to field depending on its primary observation target [4]. Weak Lensing (WL) fields have a highly uneven cadence due to the requirements of the best possible seeing and minimum sky brightness. Such surveys require a minimum of  $\sim 15$ ,  $15$ ,  $15$ ,  $25$  and  $25$  observations per year in filters  $g$ ,  $r$ ,  $i$ ,  $z$  and  $Y$  respectively. Filters  $z$  and  $Y$  are in the infra-red and far infra-red region (840 to 1030 nm). Measurements in these filters are used to reduce end effects, rather than to measure galaxy shapes. In addition, to reduce ellipticity systematics, WL observations must cover many telescope angles. Weak Lensing surveys thus span the entire visible sky. Near Earth Asteroid (NEA) fields require a completely different observing strategy: observations are limited to within  $10^\circ$  of the ecliptic plane, and usually two observations per night are required. These are separated by approximately half an hour, and taken on three nights per month. Figure 4 illustrates the WL and NEA visit

schedules. These plots, extracted from the *LSST cadence Simulator*, depict the number of visits per field made in one year, for each filter. The ecliptic plane corresponds to the wavy band across the center of the plots; the Milky Way corresponds to the large “n-shaped” region where no observations are made. We see that WL sequences (the yellow and red regions) are distributed uniformly across the visible sky, and that all NEA sequences are made within the ecliptic plane.

We investigated the dependence of the precision on the time delays (between image pairs 1–2, 1–3 and 1–4) with this proposed LSST observing strategy.

### 3 Results and discussion

#### 3.1 Run 1: Threshold source magnitude

The variation of fractional time delay error,  $\delta^{1k}$ , as a function of the peak observed magnitude is summarised in Table 5. This data corresponds to a representative field condition and visiting schedule, which are the same for all measurements; only the peak observed magnitude is varied. In this way, the influence of the peak observed magnitude on the time delay error can be isolated. The untouched system,  $\Delta_{mag} = 0$ , corresponds to a peak magnitude in the range, 24.0–23.5. In this case, time delays between image pairs 1–2, 1–3 and 1–4 are measured to a precision of 27%, 36% and 12% respectively. The fractional error of the derived Hubble constant is equal to that of the time delay. Any one such measurement would therefore not improve our knowledge of  $H_0$ , which is currently measured to better than 10% precision. We see that a time delay precision below 10% is achieved when the peak observed magnitudes range from 22.5 to 22.0, or brighter. This corresponds to a magnitude offset relative to the original system (Table 2) of -1.5, i.e. a source magnitude of 24. Several thousand multiply-imaged supernovae with peak intrinsic magnitude of 24 or brighter are expected to be detected with LSST—however, these results show that the number that can be used to measure time delays to better than 10% will be significantly smaller. The threshold measured here will be used in estimating the size of this sub-sample, in future work. Nevertheless, we point out the high statistical precision available with even several hundred measurements of  $H_0$ , each at 10% precision.

Table 5: Variation of fractional time delay error,  $\delta^{1k}$ , for image  $k$  relative to image 1, as a function of the peak observed magnitude. The same, representative, field condition and visiting schedule are used for all measurements; only the peak magnitude is varied.

Peak observed magnitude	Magnitude shift $\Delta_{mag}$	Time delay error, $\delta^{1k}$		
		$k = 2$	$k = 3$	$k = 4$
24.0–23.5	0.0	-.274	-.358	-.124
23.5–23.0	-0.5	-.210	-.152	-.078
23.0–22.5	-1.0	-.172	-.110	-.082
22.5–22.0	-1.5	-.092	-.099	.085
22.0–21.5	-2.0	.044	-.089	.043
21.5–21.0	-2.5	.017	-.010	-.035
21.0–20.5	-3.0	.017	-.005	-.025

### 3.2 Run 2: Field conditions and visiting schedule:

In this run, the influence of the field conditions and visiting schedule were investigated for each of the five filters,  $g$ ,  $r$ ,  $i$ ,  $z$  and  $Y$ , as described below. Following the previous results, System LSN magnitude was set 1.5 brighter for Run 2, corresponding to a source magnitude of 24 and peak observed magnitudes 22.5–22.0.

#### 3.2.1 Filter $g$ (400–560 nm)

**Field conditions:** Figure 5 shows the dependence of the minimum detected magnitude as a function of seeing and sky brightness, in filter  $g$ . It shows that, under conditions of a dim sky background of 21 magnitude arcsec<sup>-2</sup>, and relatively good seeing of 0.7 arcsec, LSST can image to 25 magnitude.

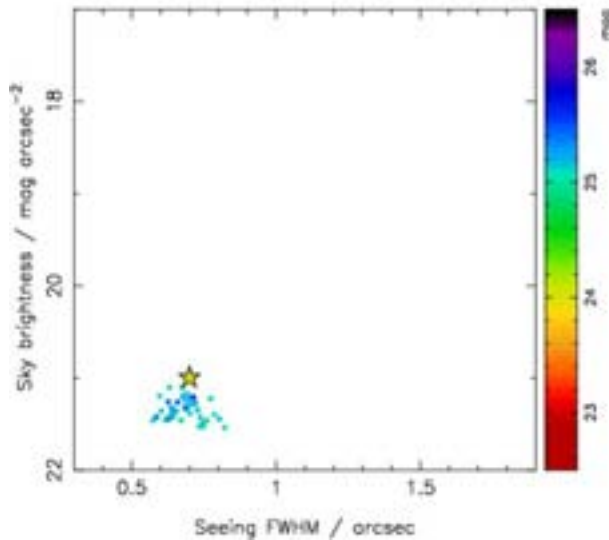


Figure 5: Minimum detected magnitude as a function of seeing and sky brightness, in filter  $g$ . Each data point represents one observation, in a particular field. The colour represents the minimum detected magnitude for that field. The star represents a standard reference point of seeing 0.7 arcsec and sky brightness 21 magnitude arcsec<sup>-2</sup>.

**Visiting schedule:** Despite the good conditions and high minimum observed magnitude, this filter did not yield any time delay measurements. We found that the maximum number of observations per field never exceeded five, and measurements were only ever made of one out of the four images. This was probably because all observations were taken over a short span of days, during which only one of the four images was sufficiently bright. Thus, no time delay between images could be measured. The small number of observations is a direct consequence of the small number of visits per field with filter  $g$ , for the nominal LSST visiting schedule. Since the  $g$  filter (400–560 nm) is not optimised for large redshift sources, it is, in any event, not central to the strong lensing program.

#### 3.2.2 Filter $r$ (540–720 nm)

**Field conditions:** Figure 6 shows the dependence of the minimum detected magnitude as a function of seeing and sky brightness, in filter  $r$ . We see that the minimum detected magnitude

improves with better (smaller) seeing, as expected. All fields include observations on days where the sky brightness has a low value, between about 20.8 to 21.5 mag. On days where the seeing is less than 1 arcsec, LSST can image typically to 24.5 magnitude, or better. Since this is well below the peak threshold magnitude of 22, the supernova light curves should be well measured. At poorer seeings, above about 1 arcsec, the magnitude limit is greater than 24.5. However, only a small fraction of the observations have poor seeing values.

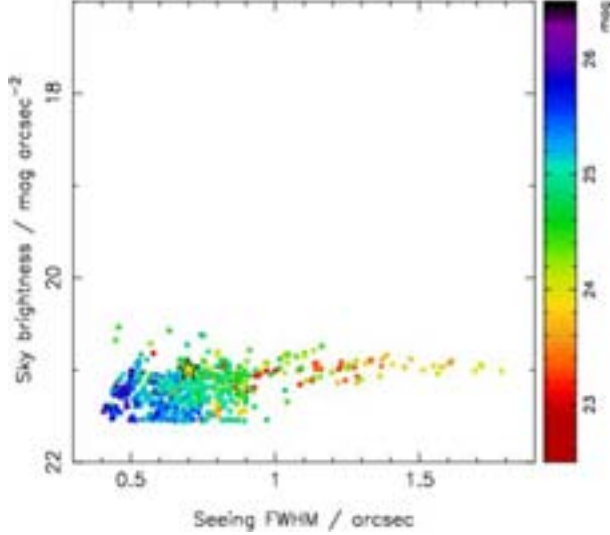


Figure 6: Minimum detected magnitude as a function of seeing and sky brightness, in filter  $r$  (Fig. 5 caption provides more detail).

**Visiting schedule:** Panels a) in Figs. 7–9 show histograms of the fractional time delay error,  $\delta^{1k}$  (Eq. 1), between the image pairs 1–2, 1–3 and 1–4 respectively. The variation of the error with number of visit days per field and number of detections is shown in panels b) of these figures. The large number of data points in panels b) indicate a high frequency of visits with filter  $r$ . The histograms show a peak centered about zero, which corresponds to good time delay measurements. Poorer measurements are indicated by the additional peaks: common to image pairs 1–2 (Fig. 7) and 1–3 (Fig. 8) is a secondary peak at a value of 1; image pair 1–2 has a tertiary peak at a value of -0.7. In panels b), we see that the number of detections increases linearly with number of days, as expected, reaching a maximum of approximately 120 detections for 150 days of observation. The reduced number of detections is the result of poor observation conditions. The general trend is that the time delay error improves with increasing number of detections. This is discussed further in the following section.

**Discussion:** We find that the  $r$  filter provides the best time delay measurements, and as such constitutes the main search filter. It is the principal filter for the weak lensing dataset, due to the low sky brightness, which leads to high numbers of visible faint galaxies. In addition, images taken with this filter have the smallest level of image contamination from internal reflections and diffraction effects in the telescope optics. The weak lensing science therefore dictates  $r$ -filter use when conditions allow—implying frequent, all-sky coverage. For our purposes, the extended red acceptance of the  $r$  filter is well matched to supernovae spectra. Together, these are ideal conditions for time delay measurements of lensed supernovae.

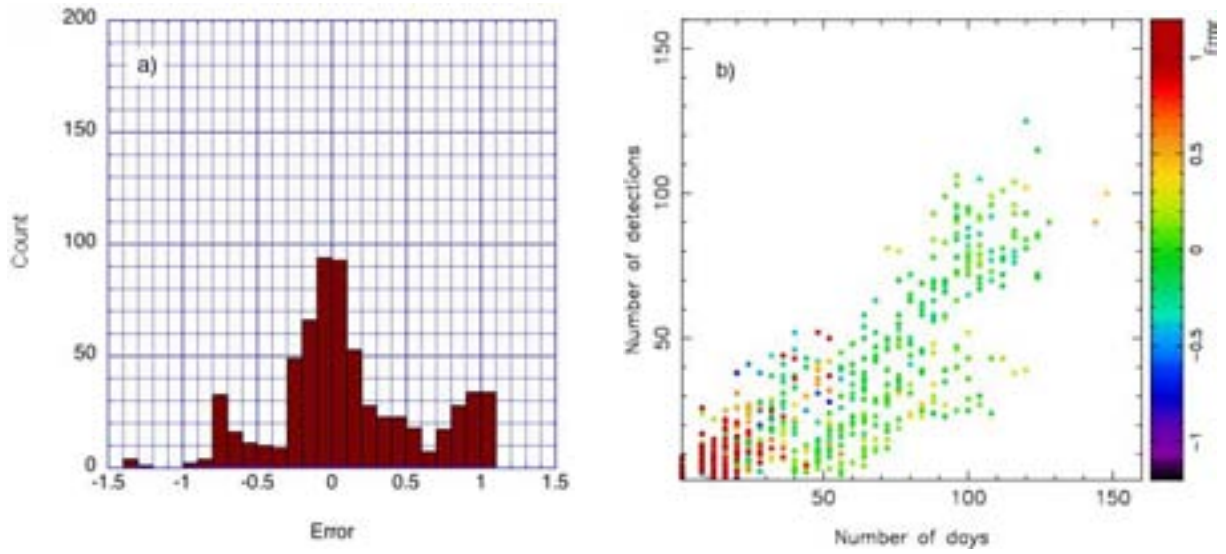


Figure 7: Measurements of image pair 1–2 with filter  $r$ : a) fractional error distribution, and b) number of visit days per field vs. number of detections made. In panel b), the colour of each data point indicates the fractional error obtained in that field.

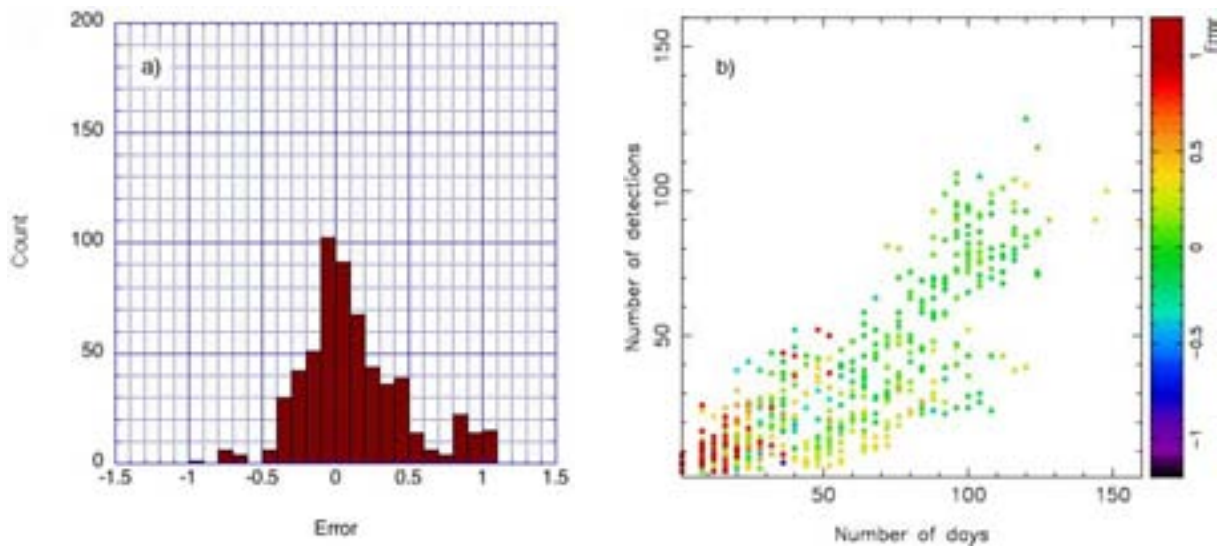


Figure 8: Measurements of image pair 1–3 with filter  $r$ : a) fractional error distribution, and b) number of visit days per field vs. number of detections made. In panel b), the colour of each data point indicates the fractional error obtained in that field.

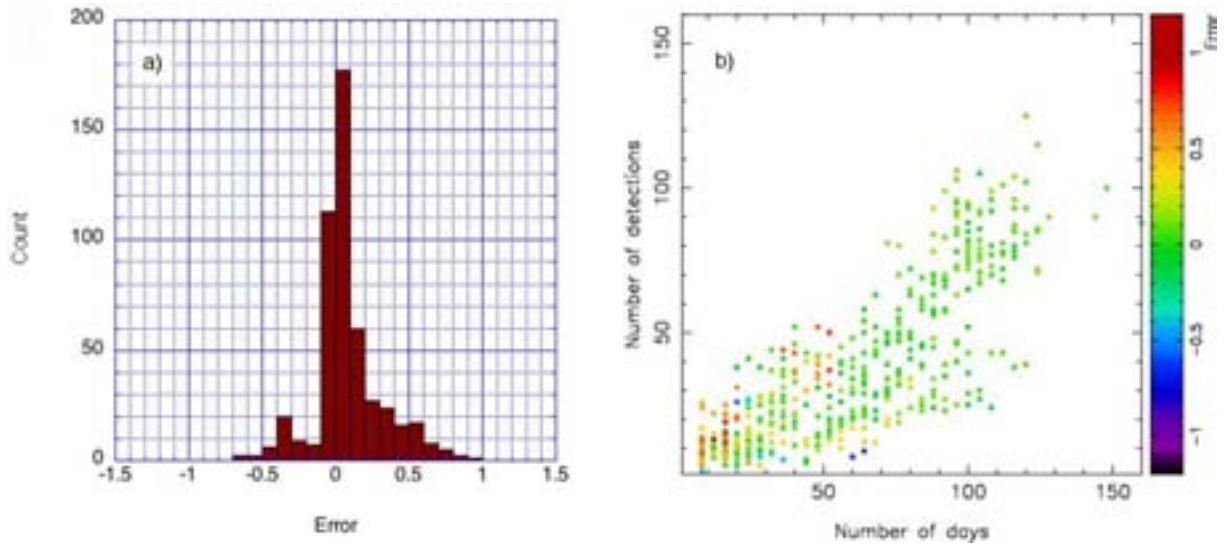


Figure 9: Measurements of image pair 1–4 with filter  $r$ : a) fractional error distribution, and b) number of visit days per field vs. number of detections made. In panel b), the colour of each data point indicates the fractional error obtained in that field.

The central peak seen in panels a) results from fields that have a large number of visit days, and hence a large number of detections. Examples of corresponding light curves are shown in Fig. 10. With the observed sampling interval of about 10–15 days, the time-development of the four images is clearly resolved. Image pair 1–4 (indicated by the black and red curves in Fig. 10) has the longest time delay, thus the fractional errors are smaller than for the other two image pairs. The histogram for image pair 1–4 (Fig. 9a) therefore has the narrowest full-width half-maximum. Good measurements correspond to a time delay measurement error below 10% (Fig. 9a). The necessary conditions are at least about 50 visit days per field (as seen in Fig. 9b), spaced regularly over the observation period so that the curves are well sampled.

The peak at 1, seen for image pairs 1–2 (Fig. 7a) and 1–3 (Fig. 8a), corresponds to a measured time delay of zero (Eq. 1). These measurements occur in fields that have fewer than about 20 visit days, as indicated by the red data points in Figs. 7b) and 8b). Illustrative light curves are shown in Fig. 11. The small number of detections frequently occurs within a short time period, thus all images appear to peak on the same day, leading to a time delay measurement of zero. These poorly-measured delays can easily be eliminated by applying a minimum quality cut on the data. The absence of a peak at 1 in Fig. 9a) is an artefact of the visit schedule: observations fall on days where image 4 (red curve) has zero flux.

The tertiary peak at -0.7 in Fig. 7 is also an artefact of the visit schedule. Examples are shown in Fig. 12. In this class of measurements, there are two predominant observations, separated by an interval of approximately 55 days. The three image pairs thus appear to have the same time delay of about 55 days. This leads to time delay errors of about -0.7, -0.3 and 0 between image pairs 1–2, 1–3 and 1–4, respectively.

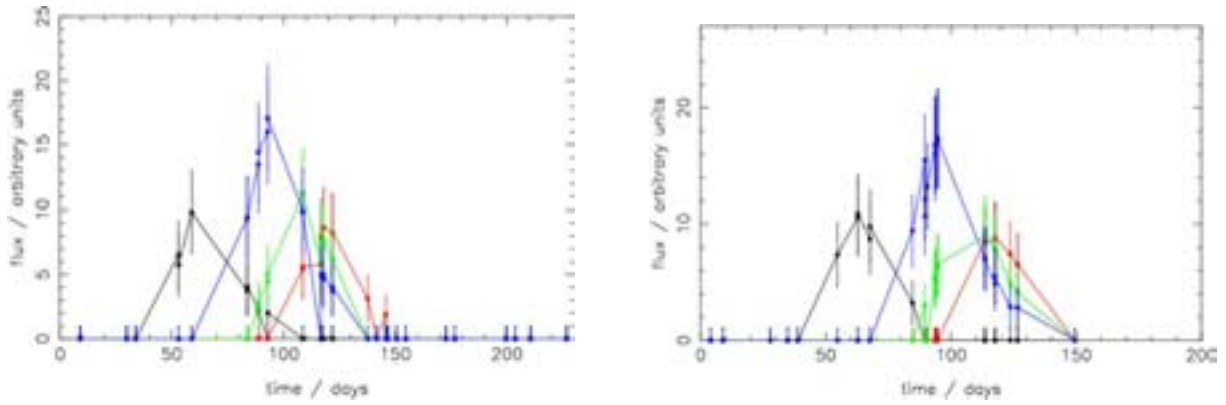


Figure 10: Two examples of measured light curves corresponding to good time delay measurements, with filter  $r$ . The four coloured curves correspond to the four lensed images (as in Fig. 3).

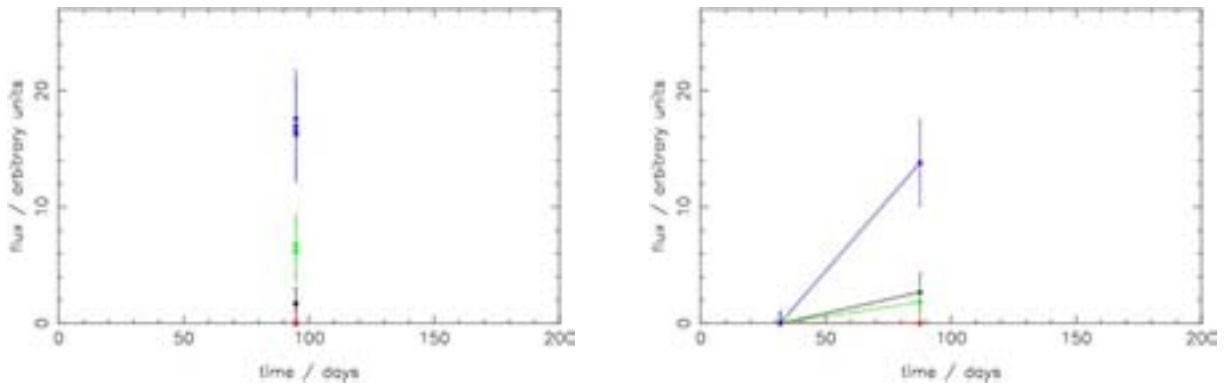


Figure 11: Two examples of poorly-sampled light curves, which result in apparent time delays of zero (filter  $r$ ).

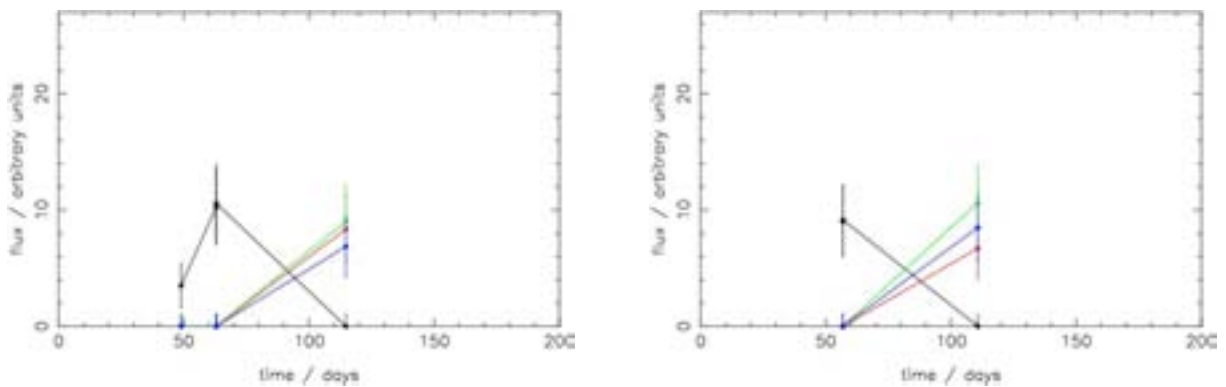


Figure 12: Two examples of poorly-sampled light curves, which result in apparent time delays of about 55 days (filter  $r$ ).

### 3.2.3 Filter $i$ (685-870 nm)

**Field conditions:** Figure 13 shows the dependence of the minimum detected magnitude as a function of seeing and sky brightness, in filter  $i$ . For this filter, the fields always involve days where the sky brightness is dimmer than about 20 magnitude arcsec<sup>-2</sup>, and the seeing is less than about 1 arcsec. Under these conditions, LSST images to magnitude 24 in almost all fields.

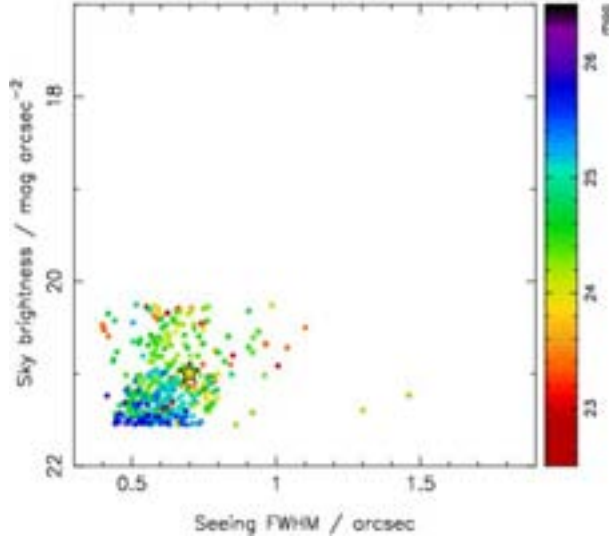


Figure 13: Minimum detected magnitude as a function of seeing and sky brightness, in filter  $i$  (Fig. 5 caption provides more detail).

**Visiting schedule:** Panels a) in Figs. 14–16 show histograms of the fractional time delay error,  $\delta^{1k}$  (Eq. 1), between the image pairs 1–2, 1–3 and 1–4 respectively. The variation of the error with number of visit days per field and number of detections is shown in panels b) of these figures. In contrast to the  $r$  filter histograms (Figs. 7a–9a), there are no longer clearly defined peaks centered about zero. The three histograms share the following two characteristics: a sharp, narrow peak at 1, and a broader, off-zero peak. This second feature suggests that the measured time delay is systematically shorter than the true time delay. There are few fields with greater than 50 observation days (Figs. 14b–16b), which, for the present analysis, marks the minimum required for good time delay measurements. (Improvements in the analysis will be discussed later.) Moreover, the sky brightness is somewhat higher for this filter than for filter  $r$  (compare Figs. 6 and 13).

**Discussion:** The reason for the peak at 1 in Figs. 14a–16a has been previously described in §3.2.2. The frequency of this occurrence is high since the majority of fields have a small number of observation days. Examples of light curves producing the systematic off-zero peak are shown in Fig. 17. These cases are due to a sparse sampling of around three measurements, with time intervals of about 20 days. These measurements systematically miss the image peaks, and create apparent equal time delays for the image pairs, leading to time delay errors of about 0.3, 0.4 and 0.5 between image pairs 1–2, 1–3 and 1–4, respectively. As before, these poorly-measured delays can be readily eliminated by applying a minimum quality cut on the data. In summary, therefore, this filter is not useful for time delay measurements, primarily due to the sparse visiting schedule.

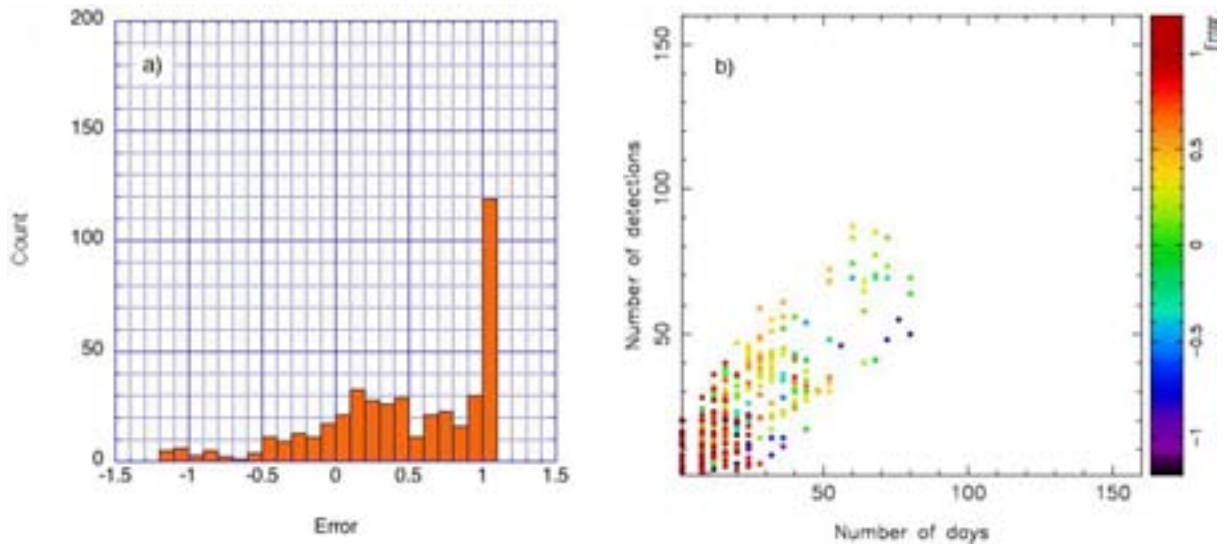


Figure 14: Measurements of image pair 1–2 with filter  $i$ : a) fractional error distribution, and b) number of visit days per field vs. number of detections made. In panel b), the colour of each data point indicates the fractional error obtained in that field.

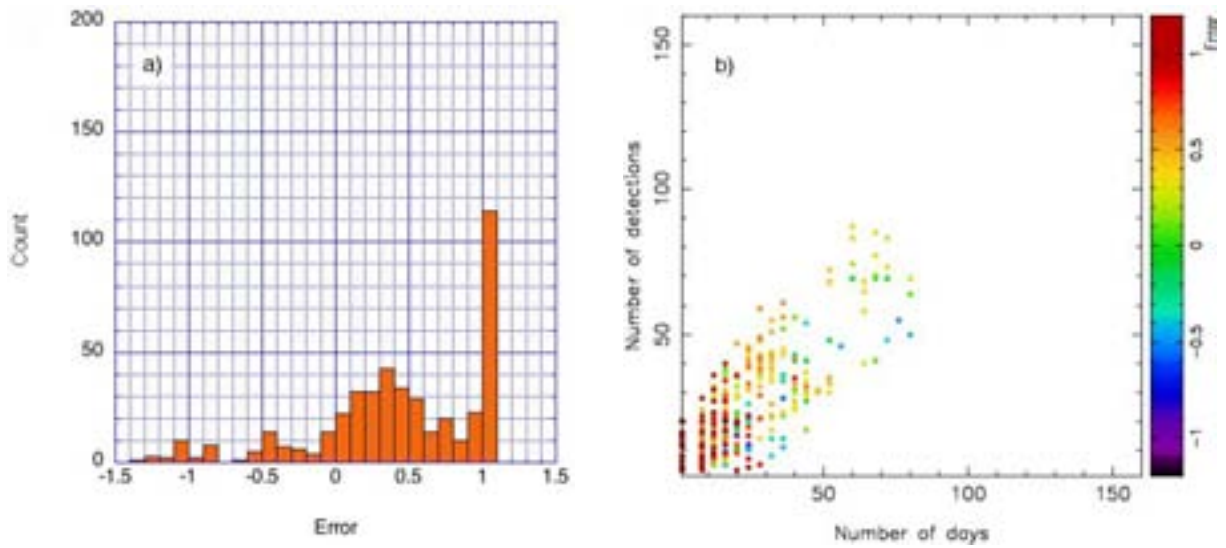


Figure 15: Measurements of image pair 1–3 with filter  $i$ : a) fractional error distribution, and b) number of visit days per field vs. number of detections made. In panel b), the colour of each data point indicates the fractional error obtained in that field.

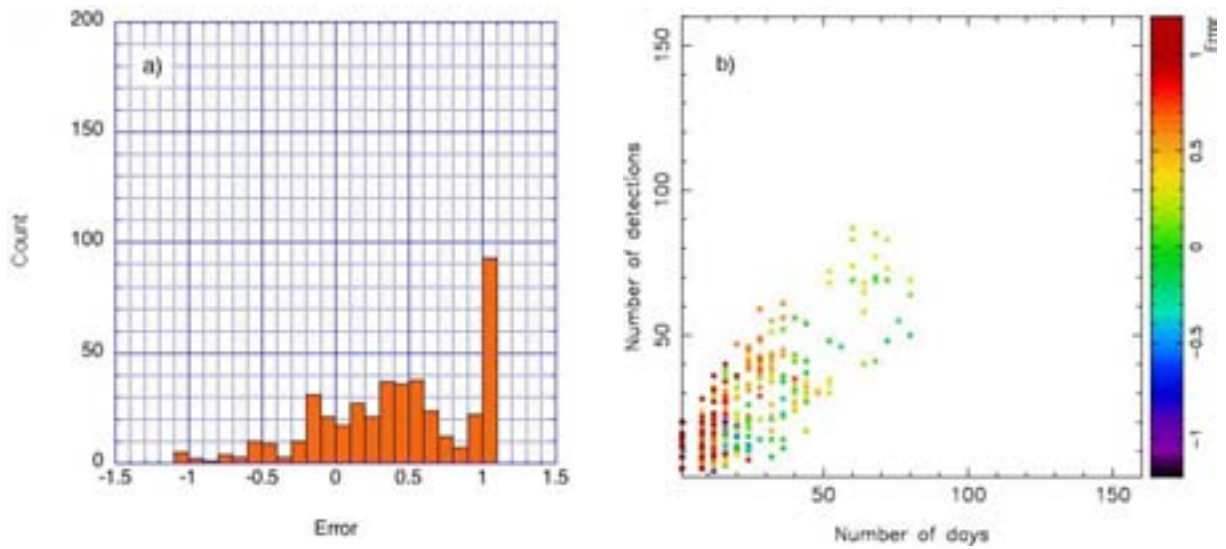


Figure 16: Measurements of image pair 1–4 with filter  $i$ : a) fractional error distribution, and b) number of visit days per field vs. number of detections made. In panel b), the colour of each data point indicates the fractional error obtained in that field.

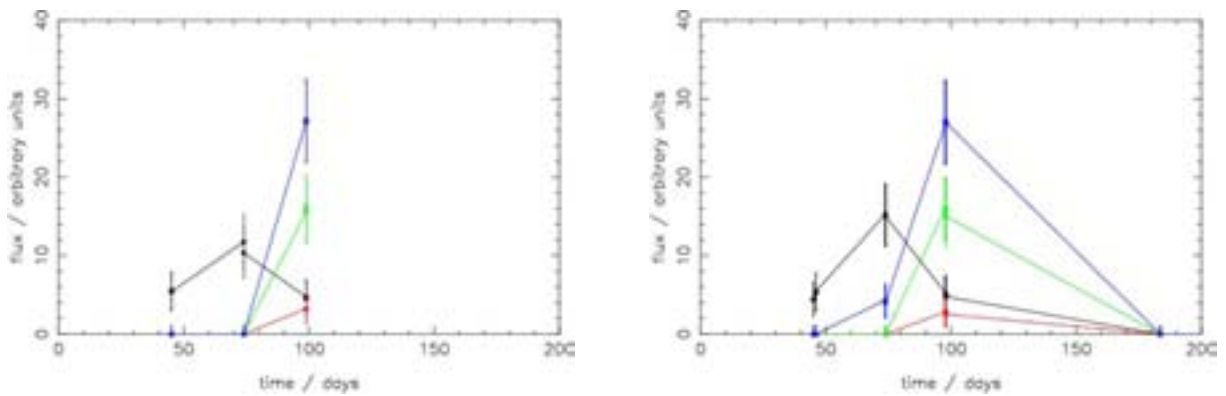


Figure 17: Two examples of poorly-sampled light curves with filter  $i$ , which result in apparent time delays of about 25–30 days.

### 3.2.4 Filter $z$ (840-950 nm)

**Field conditions:** Figure 18 shows the dependence of the minimum detected magnitude as a function of seeing and sky brightness, in filter  $z$ . There is a much larger scatter of data points compared with Figs. 5, 6 and 13, which are the corresponding plots for the  $g$ ,  $r$  and  $i$  filters respectively. Observations in filter  $z$  are no longer limited to a dim sky brightness; the range extends over 3 magnitudes, from about 21 to 18 magnitude  $\text{arcsec}^{-2}$ . In addition, there is a large range of seeing, from about 0.5 to 1.3 arcsec. The sharp cut-off at 1.3 arcsec suggests that LSST will not schedule observations in this filter if the seeing exceeds this value. Under these conditions, LSST can image only to magnitudes of between about 24.5 and 23, requiring significantly brighter sources than those for filters  $g$ ,  $r$  and  $i$ .

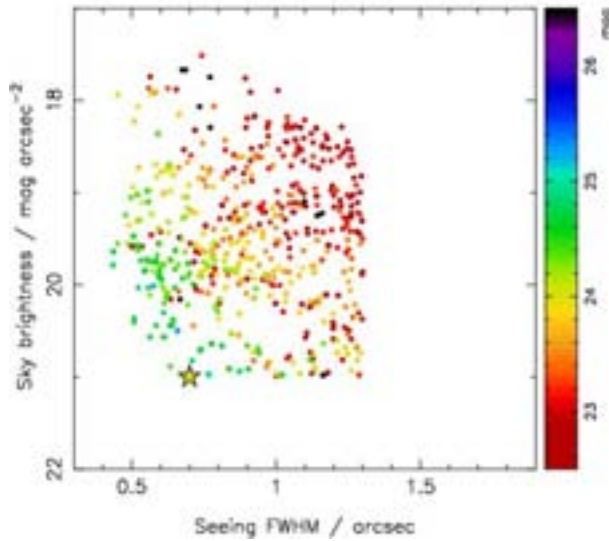


Figure 18: Minimum detected magnitude as a function of seeing and sky brightness, in filter  $z$  (Fig. 5 caption provides more detail).

**Visiting schedule:** Panels a) in Figs. 19–21 show histograms of the fractional time delay error,  $\delta^{1k}$ , between the image pairs 1–2, 1–3 and 1–4 respectively. The variation of the error with number of visit days per field and number of detections is shown in panels b) of these figures. The visit schedule is typically below 50 days per field, and is similar to filter  $i$  (Figs. 14b–16b). This leads to error histograms with similar characteristics to those for filter  $i$ , with a broad peak centered on positive values.

**Discussion:** As before, filter  $z$  is not useful for time delay measurements, primarily due to the sparse visiting schedule.

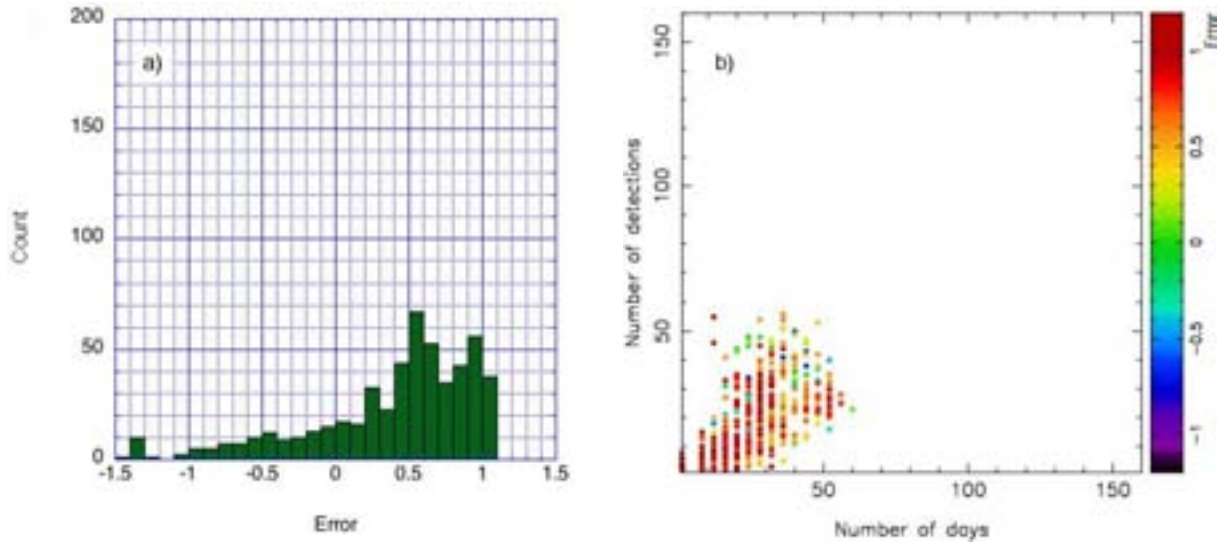


Figure 19: Measurements of image pair 1–2 with filter  $z$ : a) fractional error distribution, and b) number of visit days per field vs. number of detections made. In panel b), the colour of each data point indicates the fractional error obtained in that field.

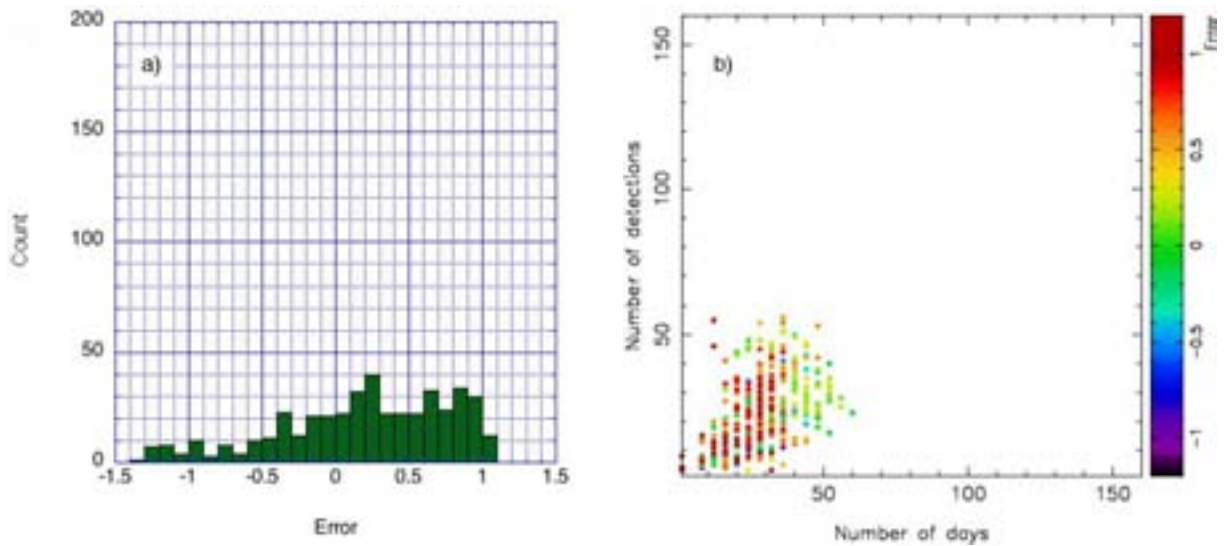


Figure 20: Measurements of image pair 1–3 with filter  $z$ : a) fractional error distribution, and b) number of visit days per field vs. number of detections made. In panel b), the colour of each data point indicates the fractional error obtained in that field.

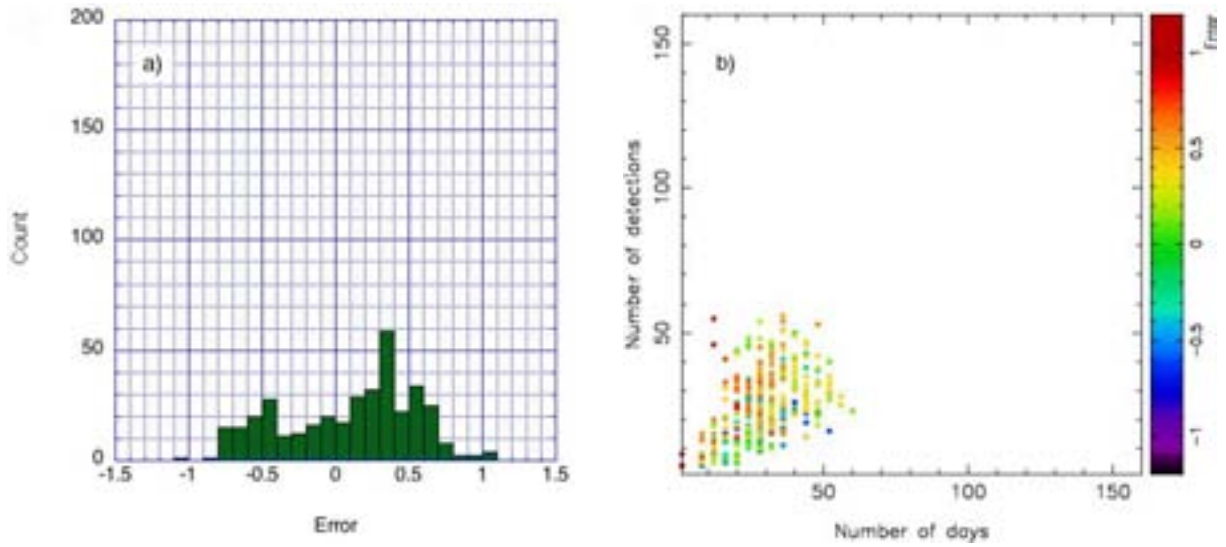


Figure 21: Measurements of image pair 1–4 with filter  $z$ : a) fractional error distribution, and b) number of visit days per field vs. number of detections made. In panel b), the colour of each data point indicates the fractional error obtained in that field.

### 3.2.5 Filter $Y$ (945-1030 nm)

**Field conditions:** Figure 22 shows the dependence of the minimum detected magnitude as a function of seeing and sky brightness, in filter  $Y$ , the far infra-red filter. As with the  $z$  filter, observations range over a sky brightness of 21 to 18 magnitude arcsec $^{-2}$ . Here, the seeing threshold appears to be 1 arcsec, in contrast with 1.3 arcsec for filter  $z$ . Measurements range from a minimum magnitude of about 25, when conditions are best (seeing about 0.5 arcsec, sky brightness about 21 magnitude arcsec $^{-2}$ ), to a maximum of about 23.

**Visiting schedule:** Panels a) in Figs. 23–25 show histograms of the fractional time delay error,  $\delta^{1k}$ , between the image pairs 1–2, 1–3 and 1–4 respectively. The variation of the error with number of visit days per field and number of detections is shown in panels b) of these figures. The visit schedule is typically below 50 days per field, which results in histograms that display similar characteristics as for filters  $i$  and  $z$ .

**Discussion:** The same conclusion is obtained as for the previous two filters, namely that filter  $Y$  is unsuitable for time delay measurements, owing to the sparse visiting schedule.

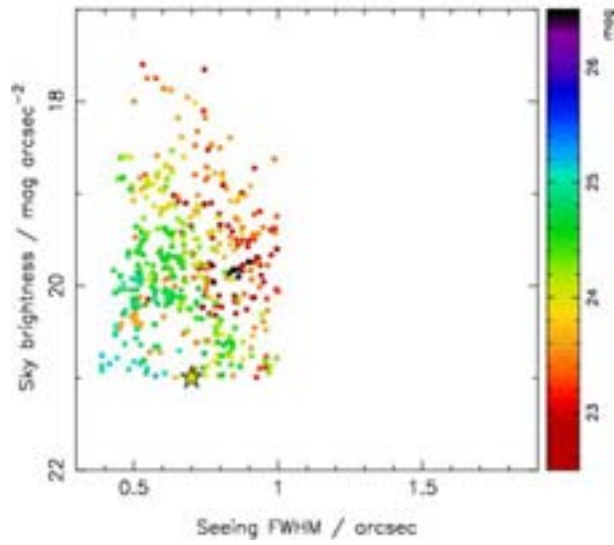


Figure 22: Minimum detected magnitude as a function of seeing and sky brightness, in filter Y (Fig. 5 caption provides more detail).

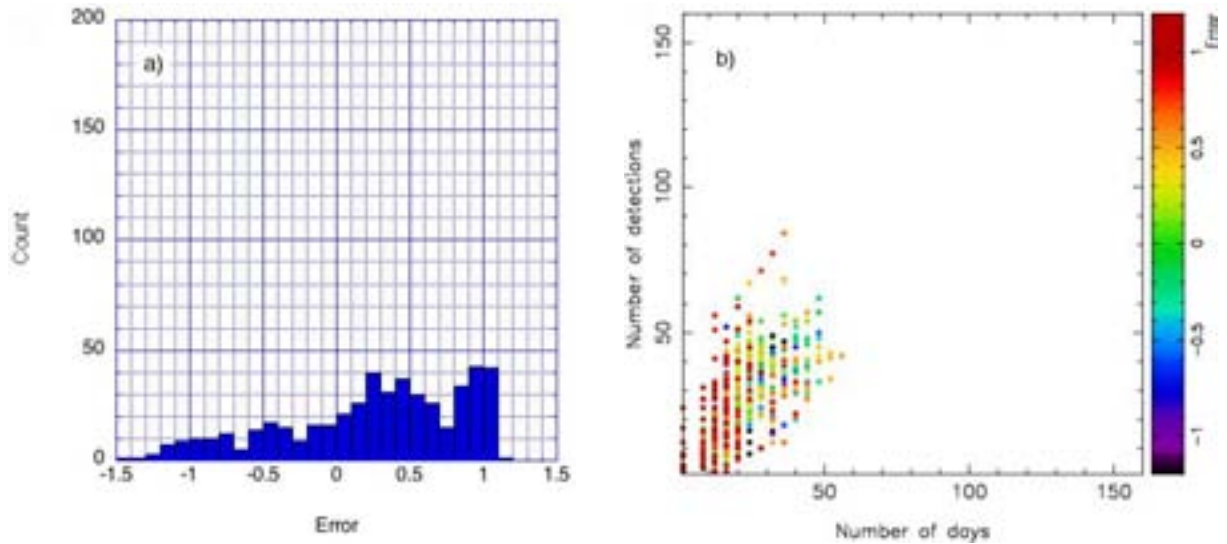


Figure 23: Measurements of image pair 1–2 with filter Y: a) fractional error distribution, and b) number of visit days per field vs. number of detections made. In panel b), the colour of each data point indicates the fractional error obtained in that field.

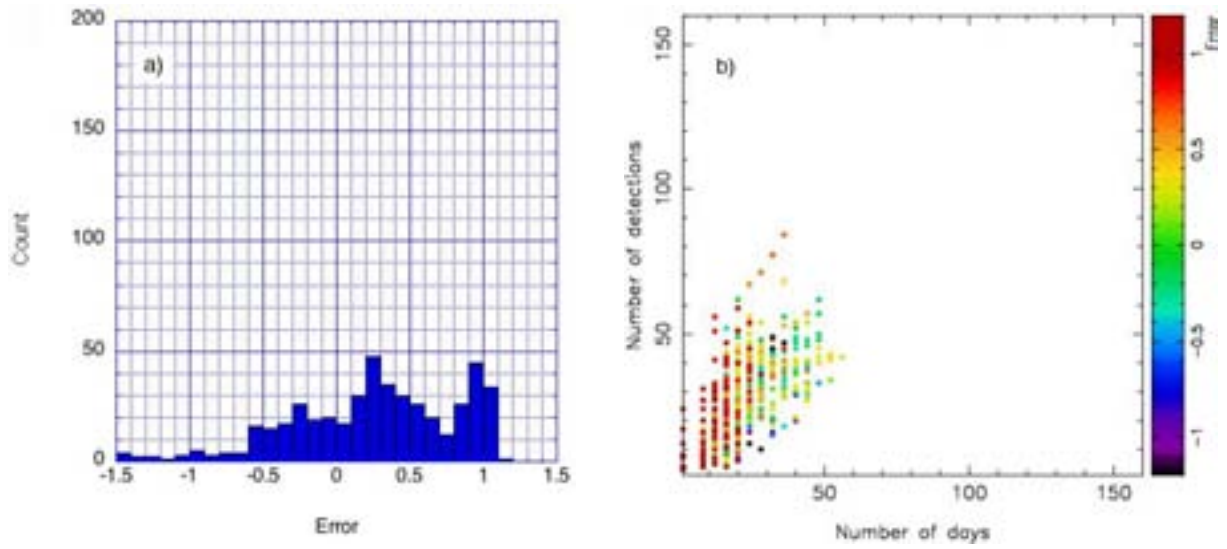


Figure 24: Measurements of image pair 1–3 with filter Y: a) fractional error distribution, and b) number of visit days per field vs. number of detections made. In panel b), the colour of each data point indicates the fractional error obtained in that field.

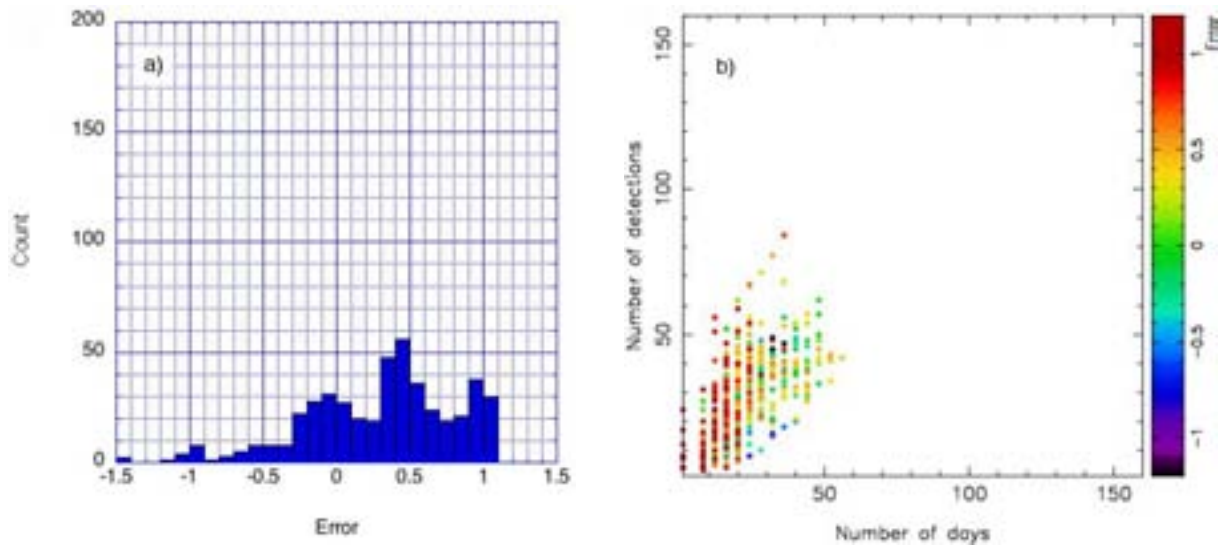


Figure 25: Measurements of image pair 1–4 with filter Y: a) fractional error distribution, and b) number of visit days per field vs. number of detections made. In panel b), the colour of each data point indicates the fractional error obtained in that field.

## 4 Conclusions

LSST can measure gravitational lens time delays to better than 10% precision per image-pair, under the following conditions:

1. **Threshold source peak-magnitude:** A minimum peak observed magnitude of about 22.5–22.0 is required. For typical galaxy-scale lenses providing magnifications of around 10, this corresponds to an intrinsic source magnitude of 24–25. The expected number of lensed supernovae visible with LSST is under investigation; the magnitude threshold measured here is a key ingredient of this calculation.
2. **Visiting schedule:** A minimum of about 50 visit days per field is required for a lensed Type Ia supernova. These visits must be evenly distributed over the duration of the event; the minimum visit frequency should be once approximately every 10–15 days. With the nominal LSST observing strategy, we find about 15% of all fields exceed 50 visit days: 13% in the  $r$  filter alone and 2% in all remaining filters combined. The  $r$  filter, with its high visit frequency and good spectral acceptance, provides ideal conditions for precise time delay measurements. Fig. 26 shows the fractional error distribution of these fields, integrated over all filters. The central peak indicates a time delay measurement precision,  $\sigma = 0.12$ .

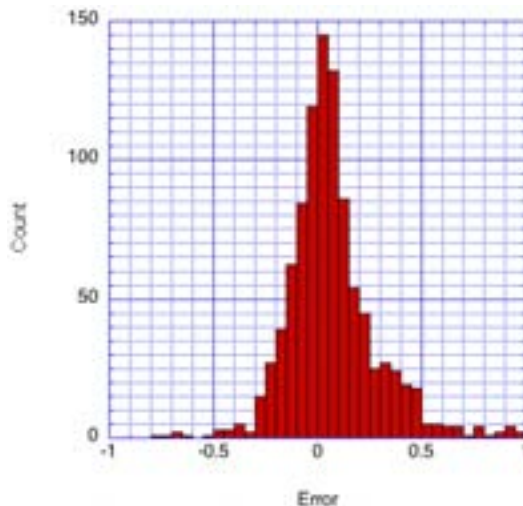


Figure 26: Fractional time delay error distribution for fields exceeding 50 visit days, for any filter. A Gaussian fit to the central peak gives  $\sigma = 0.12$  and  $\mu = -0.001$ .

3. **Field conditions:** At a sky brightness of 21 magnitude  $\text{arcsec}^{-2}$ , the LSST images permit point-source detections down to a magnitude limit of about 24.5 in 30 seconds exposure time. This fiducial limit is well below the threshold peak-magnitude of about 22 and so will allow good light curve measurements. The resolution of the lensed images will directly depend on the seeing. For the representative System LSN, a seeing of better than about 1 arcsec is required. For the proposed locations of LSST, the seeing is typically better than this value. Good seeing will also improve the sensitivity to weaker supernovae (those at greater distances).

The primary conclusion from this study is that the visiting schedule is the single most important parameter to optimise for time delay measurements. The proposed LSST schedule results in a

visiting frequency of typically 20 to 30 days per field, over the duration of the supernova event. This is inadequate for precision measurements. An alert system is therefore required and, once the supernova has been detected, frequent regular observations can be made. Cadences of approximately one week appear sufficient for high precision time delay measurements.

Significant improvements can also be made in the analysis. In particular, for this study the time delays were evaluated on the simple basis of weighted means of the light curves. The next step is to fit the measurements to the predicted supernovae light curves, once the type is known. This will improve the sensitivity to weaker systems and allow for sparse time sampling.

In summary, the proposed design and visiting schedule of the LSST should provide a large sample of precision gravitational lens time delay measurements—and significant improvements can be made with further optimisation.

## Acknowledgments

It is a pleasure to thank Marusa Bradac, Stuart Marshall, Liz Rivers, Masao Sako and, in particular, my supervisor Phil Marshall for their guidance and for many enjoyable and stimulating discussions. I would also like to express my appreciation to Helen and Dan Quinn, James Lindesay and my fellow SULI colleagues for their warm friendship and hospitality during my visit to SLAC. Finally, I would like to thank the the U.S. Department of Energy, Office of Science for creating, organising, and funding the SULI program, which made this work possible. This work was supported in part by the U.S. Department of Energy under contract number DE-AC02-76SF00515.

## References

- [1] LSST homepage: <http://www.lsst.org>
- [2] Marusa Bradac, *Substructure in the Gravitationally Lensed System B1422+231*, Bonn, Germany (2001).
- [3] Cerro Tololo Inter-American Observatory homepage: <http://www.ctio.noao.edu>
- [4] Dark Energy Task Force Committee, Rocky Kolb (chair), *The Large Synoptic Survey Telescope*, (2004).
- [5] E. Bertin and S. Arnouts, *SExtractor: Software for source extraction*, (1996).

# **Turn-by-Turn and Bunch-by-Bunch Transverse Profiles of a Single Bunch in a Full Ring**

Richard Kraus

Office of Science, Summer Undergraduate Laboratory Internship (SULI)

University of Nevada, Reno

Stanford Linear Accelerator Center

Menlo Park, California 94025

August 12, 2005

Prepared in partial fulfillment of the requirements of the Office of Science, Department of Energy's Science Undergraduate Laboratory Internship under the Direction of Dr. Alan S. Fisher in the Accelerator Division of the Stanford Linear Accelerator Center (SLAC).

Participant: \_\_\_\_\_  
Signature

Research Advisor: \_\_\_\_\_  
Signature

## TABLE OF CONTENTS

Abstract	iii
Introduction	1
Materials and Methods	3
Results	7
Discussion	8
Acknowledgements	10
References	10
Tables and Figures	11

## ABSTRACT

Turn-by-Turn and Bunch-by-Bunch Transverse Profiles of a Single Bunch in a Full Ring.

RICHARD KRAUS (University of Nevada, Reno, NV 89557) ALAN S. FISHER (Stanford Linear Accelerator Center, Menlo Park, CA 94025).

The apparatus described in this paper can image the evolution of the transverse profile of a single bunch, isolated from a full PEP-II ring of 1500 bunches. Using this apparatus there are two methods of single bunch imaging; bunch-by-bunch beam profiling can image every bunch in the ring a single bunch at a time with the images of sequential bunches being in order, allowing one to see variations in beam size along a train. Turn-by-turn beam profiling images a single bunch on each successive turn it makes around the ring. This method will be useful in determining the effect that an injected bunch has on a stable bunch as the oscillations of the injected bunch damp out. Turn-by-turn imaging of the synchrotron light uses a system of lenses and mirrors to image many turns of both the major and minor axis of a single bunch across the photocathode of a gateable camera. The bunch-by-bunch method is simpler: because of a focusing mirror used in porting the light from the ring, the synchrotron light from the orbiting electrons becomes an image at a certain distance from the mirror; and since the camera does not use a lens, the photocathode is set exactly at this image distance. Bunch-by-bunch profiling has shown that in the Low Energy Ring (LER) horizontal bunch size decreases along a train. Turn-by-turn profiling has been able to image 100 turns of a single bunch on one exposure of the camera. The turn-by-turn setup has also been able to image 50 turns of the minor axis showing part of the damping process of an oscillating injected charge during a LER fill. The goal is to image the

damping of oscillations of injected charge for 100 turns of both the major and minor axis throughout the damping process during trickle injection. With some changes to the apparatus this goal is within reach and will make turn-by-turn imaging a very useful tool in beam diagnostics.

## INTRODUCTION

PEP-II at the Stanford Linear Accelerator Center (SLAC) collides 9-Gev electrons stored in the high-energy ring (HER) with 3.1-Gev positrons stored in the low-energy ring (LER). PEP-II operates with currents of 2.50 A in the LER and 1.5 A in the HER. The collisions create  $B\bar{B}$  meson pairs for the purpose of measuring different decay rates due to charge-parity violation. The frequency of these collisions is dependent upon the luminosity in the rings, which depends both on the current and the transverse beam size. To gain more collisions one could increase the current in the rings, shorten the bunch length, shrink the transverse beam size, or focus the beam more tightly at the IP. However, it is impossible to increase the current in the ring above a certain level because there is not enough RF power available; and even before the current gets to the limit, equipment overheats and starts to malfunction. Shortening the bunch length by using higher RF voltages works except that heating from the increased peak current has caused some beam position monitors to loosen and fall off. And as beams are focused at the interaction point (IP) through a smaller waist the luminosity is limited by the “hourglass effect,” where the beams expand more quickly on either side of the focus [1]. The greatest gains in luminosity lie in shrinking the transverse profile of the beam.

Megawatt microwave generators called klystrons accelerate electrons and positrons at PEP-II; there are places in the microwave field where electron or positron bunches can be relatively stable, such places are called RF buckets. Within the HER or LER, bunches travel in trains where every other bucket is filled and each train has between 30 and 70 bunches for a total of typically 1588 bunches in a ring at one time.

This work images synchrotron light emitted by a single bunch of electrons or positrons onto a gateable intensified charge-coupled device (ICCD) camera. But because an ICCD camera does not have the ability to repeatedly store images at 136 kHz, the frequency that a bunch goes around the ring, an apparatus capable of imaging up to one hundred turns of the same bunch using only a few optical components and a gateable ICCD camera is used.

Past work with bunch-by-bunch beam profiling [2] has shown that horizontal beam size decreases with bucket number along a train. We have recently reproduced the experiment and found the same results (see Figure 1). Understanding why the beam decreases in size along the train could give insight into how to decrease the transverse size of every bunch in the train.

During injection, charge from the linear accelerator must be injected from above the PEP-II rings at an angle to the path of the stable bunches in the rings. These injected charges are focused towards the axis of the ring by quadrupole magnets causing them to oscillate. These oscillations will eventually damp out because the particles emit synchrotron radiation in their direction of travel but gain energy from the microwave field in the longitudinal direction. A major focus of this experiment is to understand charge injection damping. Questions that should be answered with this research include; what effect does the injected bunch have upon the stable bunch and specifically in the HER why is there greater background at BaBar a few milliseconds after trickle injection when the damping process takes 37.1ms? Imaging an injected bunch during trickle injection is not easy: the injected bunch is  $1/20^{\text{th}}$  the size of the stable bunch, the bunch will only be visible for the first part of the damping process as after a few milliseconds it will have blended in with the outer part of the stable bunch, and if the tune of the ring is such that the injected bunch is in plane with the stable bunch at the synchrotron light pick-off point, one would not be able to see it at all.

Alignment is crucial for such an experiment; any major deviation from the layout will cause the image to blur or increase in size such that the image will not fit on the photocathode. The most difficult part about this research will be the analysis of the data, there are 100 images of the major axis and 100 images of the minor axis stored in one frame; simple pixel addition will not suffice.

## MATERIALS AND METHODS

The synchrotron light used in this research comes from a bending dipole magnet on each ring; the light is initially diverted using a water cooled mirror set at grazing incidence with a slit through the center such that the x-rays will pass through to a beam dump and the maximum power on the mirror will be 200 W/cm. Synchrotron light is usually sent to an interferometer which measures vertical beam size [3]; however, using a button macro in the SLAC Control Panel (SCP) program the light can be diverted using servo-controlled mirrors onto an optical table in building 675 for the HER and 620 for the LER. A diagram of the experimental layout in the LER is shown in Figure 2; the apparatus in the HER uses the same components, the magnifications and beam sizes are different (see Table 1).

The goal of this optical setup is to manipulate the synchrotron light beam to a tall and thin image: thin so that many images will fit across the photocathode and tall so that measurements of the profile can be taken easily. Since the beam is originally an ellipse the major and minor axis measurements are not equal. This requires that the beam be split: to measure both the profile of the major axis and the minor axis (for clarification the beam which images the major axis shall be called the major axis beam and the beam which images the minor

axis shall be called the minor axis beam). Because there are now two beams on the table, there are four magnifications that need to be set; the major axis x (horizontal) and y (vertical) directions, and the minor axis x and y directions. Cylindrical lenses are used because they can magnify in one direction and leave the beam unaltered in the other direction. For each axis this allows magnification in one direction to be semi-independent from the other direction; semi because they must both come to a focus on the photocathode of the ICCD camera.

Once on the table the synchrotron light is filtered with a polarizer cube such that only the horizontally polarized light from the emission point continues on the set beam path. This is necessary because synchrotron light is horizontally polarized on the mid-plane of the curve and any vertically polarized light can cause a blurred image. Next the light is filtered with a 30 nanometer wide bandpass filter, centered around 450nm in the LER and 550nm in the HER: this is necessary because lenses have different indices of refraction for different wavelengths and thus if the imaging light has too broad a spectrum the image will never be in focus.

From there the light can be diverted, using a mirror mounted on an insertable (“flipper”) mount, to a gated camera for use in Bunch-by-Bunch beam profiling [1], for a sample image see Figure 3. Usually the light will pass over the “flipper” mirror and onto a nominally 50% beam splitter. Half of the beam will go through an out of plane periscope, which rotates the beam by 90° and brings it to the required height. The beam must be rotated so that both axes of the bunch can be imaged. The major axis beam goes through a cylindrical y-lens (lens that magnifies in the vertical direction) to achieve a slight magnification. The path which images the minor axis is a bit more complicated, to compensate for the additional path length and extra horizontal width of the minor axis beam (the major axis of the particle beam’s ellipse) a negative lens must be used to create a smaller virtual image 110mm downstream of the true image. Then the minor axis

beam will go through a magnifying cylindrical y-lens such that the beam's height will expand by a factor of almost three: to use more of the photocathode. At this point the minor axis beam is six millimeters above the major axis beam. Using two, 2-inch mirrors the beams shall be forced parallel above one another and through one last cylindrical x-lens that demagnifies the major axis beam in the x-direction by a factor of 10 and the minor axis beam in the x-direction by a factor of 20. The major and minor profiles of the beam have been manipulated to thin vertical stripes.

These stripes are reflected off a 14.2mm tall by 8.5mm wide mirror, attached to a scanning galvanometer, onto the photocathode of the ICCD camera. The purpose of the scanning galvanometer is such that in one exposure of the CCD the micro channel plate can be repeatedly gated so that light from only one bunch can be exposed onto the CCD and with the motion of the mirror the next time that bunch comes around the ring the light will be reflected to a new place on the photocathode.

An external trigger, defined as the injection trigger plus the delay between the trigger and the injected bunch less the time the rotating mirror takes to get into position, starts the rotation of the mirror by triggering an arbitrary waveform generator to begin its waveform; the waveform voltage is directly proportional to the rotation of the mirror. Once the light reflected from the rotating mirror has reached the left side of the photocathode another pulse is sent by a delay generator to both the camera and a second delay generator, signifying the injected bunch is here and the camera should begin gating; the second delay generator sends triggers to the camera every 7.32 s, the period of the ring, so as to image the injected bunch on every turn. The delay generator can also be set to trigger the camera every other turn or every third turn by increasing the delay to integer multiples of 7.32 s.

There is an injection trigger that is given from the Main Control Center (MCC) every time charge is inserted into the PEP-II rings. Due to transport there is a delay between the time the charge is actually injected into the ring and the time at which the delay generator receives the pulse. Finding the delay is quite tedious. The only optimal time to search for the injection delay is right after a ring abort when the ring is being filled one bunch at a time. However, it only takes about eight injections to fill a bunch, which means that the camera, triggered by the injection, can only be gated eight times during the bunch filling process. The period of the ring is  $7.32\mu\text{s}$  and thus each gate images  $0.915\mu\text{s}$ . Now the injected bunch is in a  $0.915\mu\text{s}$  time frame, which with the next abort can be narrowed down further to a  $0.114\mu\text{s}$  ( $1/8^{\text{th}}$  of  $0.915\mu\text{s}$ ) time frame, the process is continued till the injected bunch has been confined to a  $2.1\text{ns}$  time frame. The delay between the injection trigger and the injected bunch will be known once the delay to the injected bunch is identified.

For the purpose of watching the damping of an injected bunch only the minor axis of the particle beam's ellipse will be imaged, for that is the direction in which the injected charge oscillates. The beamsplitter is removed so that all of the synchrotron light will be used in imaging the minor axis. With the camera only gating the bucket that charge is being injected into, there are only a few things to vary. The section of the damping process which the camera images can be varied by changing the delay to the waveform and the length of the section imaged can be changed by having the camera postpone the gates for an integer number of turns.

No analysis software has been written yet for the turn-by-turn images. In bunch-by-bunch mode analysis is done using software written in C; the beams are fit to a gaussian profile.

## Results

Figure 4 shows 94 turns of a single bunch in the LER. The major axis is seen above the minor axis in the picture because the camera inverts the true image. Although the initial goal of this project was to see the largest number of turns possible, images are useless when one image cannot be distinguished from the next. For our present focusing abilities 100 turns seems to be about the limit in resolving one turn from the next in the major axis beam (see Figure 4). As one moves down to 60 turns, each turn is easily resolvable in both the major and minor axis as seen in Figure 5. And if there needed to be absolutely no question as to which photon belonged to which turn, 41 turns across the photocathode are quite well spaced, as seen in Figure 6.

In the LER a section of the damping process for an injected bunch was imaged during a ring fill after an abort. Figure 7 shows 50 sequential turns of an injected bunch oscillating around an empty bucket at the beginning of the filling process. Figure 8 shows another injected bunch oscillating around a small stable bunch in the LER. Figure 9 shows 50 sequential turns of an injected bunch oscillating about a stable bunch that is  $1/3^{\text{rd}}$  full; these images were taken at the beginning of the LER filling process.

Using the single bunch ring fill method the delay between the injection trigger and the injected bunch is 5649.7ns. For use in bunch-by-bunch mode the delay between the ring turn trigger and bucket zero is 5785.0ns.

## DISCUSSION

In the LER the minor axis beam does not image nearly as well as the major axis beam, for only at 60 turns does the minor axis beam become resolvable. This was expected for in the LER the minor axis beam started out close to six times as wide as the major axis beam and the negative lens in the minor path only demagnifies the minor axis beam by a factor of two. Thus the image of the minor axis is three times as wide as the image of the major axis. This will not be as great a problem in the HER for the minor axis beam is only three times as wide as the major axis beam.

Magnification and focus are two very important factors in being able to image many turns. This project required multiple changes to the layout in the LER to find magnifications capable of a suitable width and height, such that the major and minor axis beams fit on the photocathode. 100 turns across the photocathode in the LER did not come cheaply, two lenses were liberated from their positions in the HER apparatus for the benefit of the LER. The HER, which has not been completed, will most likely have to go through as many changes in both layout and lens choice. And after many iterations of changing the lenses and the layout it is all for naught without the correct focus: a difference of a millimeter in the position of the camera can mean the difference between 100 turns and 20.

It was only possible to image the injected bunch when all of the light was used in imaging the minor axis of the particle beam ellipse and when the LER was being filled after an abort. It is easier to image the injected bunches at the beginning of a fill because there is no stable charge to block the view of the injected charge. Although imaging injected charge during a fill was a large step, it is very important that charge injected during trickle injection be imaged;

for that is the charge that affects the colliding beams. Luckily, now that all the delays are set correctly it should be trivial to image the damping process during trickle injection. It is also important to be able to image the major axis of the particle beam ellipse during trickle injection: the oscillating charge should have some very interesting effects on the major axis as well as the minor axis of the particle beam's ellipse.

In order to image the effects of oscillating charge on both axes a greater amount of light will have to get to the camera. Small optics are not passing the full beam and are limiting the total light to the camera; larger, 2-inch optics are on order and will be able to pass most of the beam. A new beam splitter will be used to send the necessary amount of light to each path. Another option is to set the camera to accumulate mode, where images are superimposed on one another to increase the brightness of the image.

This apparatus is quite flexible in the fact that if one wanted to take one clear picture of a single bunch (see Figure 3) they would be able to do so without much effort in bunch-by-bunch mode. Once in turn-by-turn mode, the variations become even simpler: to view more turns all one has to do is lessen the slope of the waveform and increase the number of triggers to the camera. If there was a need to view a single bunch for a long period of time, the delay on the delay generator could be set to wait for any integer number of turns before it triggers the camera.

With the correct magnifications and foci the bunch-by-bunch and turn-by-turn single bunch imaging systems will become useful tools in beam diagnostics.

## ACKNOWLEDGEMENTS

First and foremost I would like to thank my mentor, Alan S. Fisher, for his guidance and assistance throughout this internship. I have learned a great deal from talking and working with him. I want to thank Mark Petree for his technical support and Benny Chan for his assistance in this research. I would like to thank Helen Quinn and James Lindesay for their support of the SULI program. I would also like to thank the Department of Energy's Office of Science and the Stanford Linear Accelerator Center for creating, organizing, and funding the SULI program.

## RESOURCES

- [1] A.S. Fisher, A. Novokhatski, J.L. Turner, U. Wienands, G. Yocky, R. Holtzapple, "Bunch-Length Measurements in PEP-II," presented at IEEE Particle Accelerator Conference, Knoxville, Tennessee, 2005.
- [2] Robert Holtzapple, Denis Dujmic, and Alan S. Fisher, "Single-Bunch Tune and Beam Size Measurements along Bunch Trains in PEP-II," presented at IEEE Particle Accelerator Conference, Knoxville, Tennessee, 2005.
- [3] A.S. Fisher, M. Petree, E. L. Bong, "A Synchrotron-Light Interferometer for PEP-II," presented at Beam Instrumentation Workshop, Cambridge, Massachusetts, 2000.

## FIGURES AND DIAGRAMS

HER Magnifications and Dimensions						Major	Minor
						(mm)	(mm)
Typical beam sigma (in collision) at source in vacuum chamber (from SLM)						1.5000	0.5000
Magnification from beampipe to image on table						0.3968	
Size of beam image on table						0.6000	0.2000
Size of CCD						9.7300	9.7300
Magnification in x-plane						0.0600	0.0178
Magnification in y-plane						0.4433	4.4592

LER Magnifications and Dimensions						Major	Minor
						(mm)	(mm)
Typical beam sigma (in collision) at source in vacuum chamber (from SLM)						2.4	0.38
Magnification from beampipe to image on table						0.2930	
Size of beam image on table						0.70	0.11
Size of CCD						9.7300	9.7300
Magnification in x-plane						0.2710	0.0339
Magnification in y-plane						0.2710	1.0746

**Table 1:** Magnifications and image distances for HER and LER.

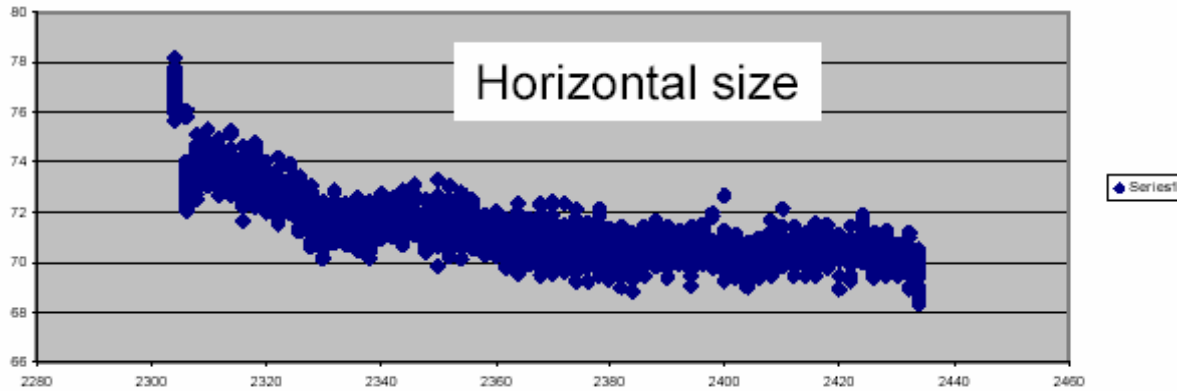


**Figure 1:** Bunch-by-bunch diagram showing decrease in beam size along bunch train in LER. X-axis shows bunch number, Y-axis in arbitrary units of size.

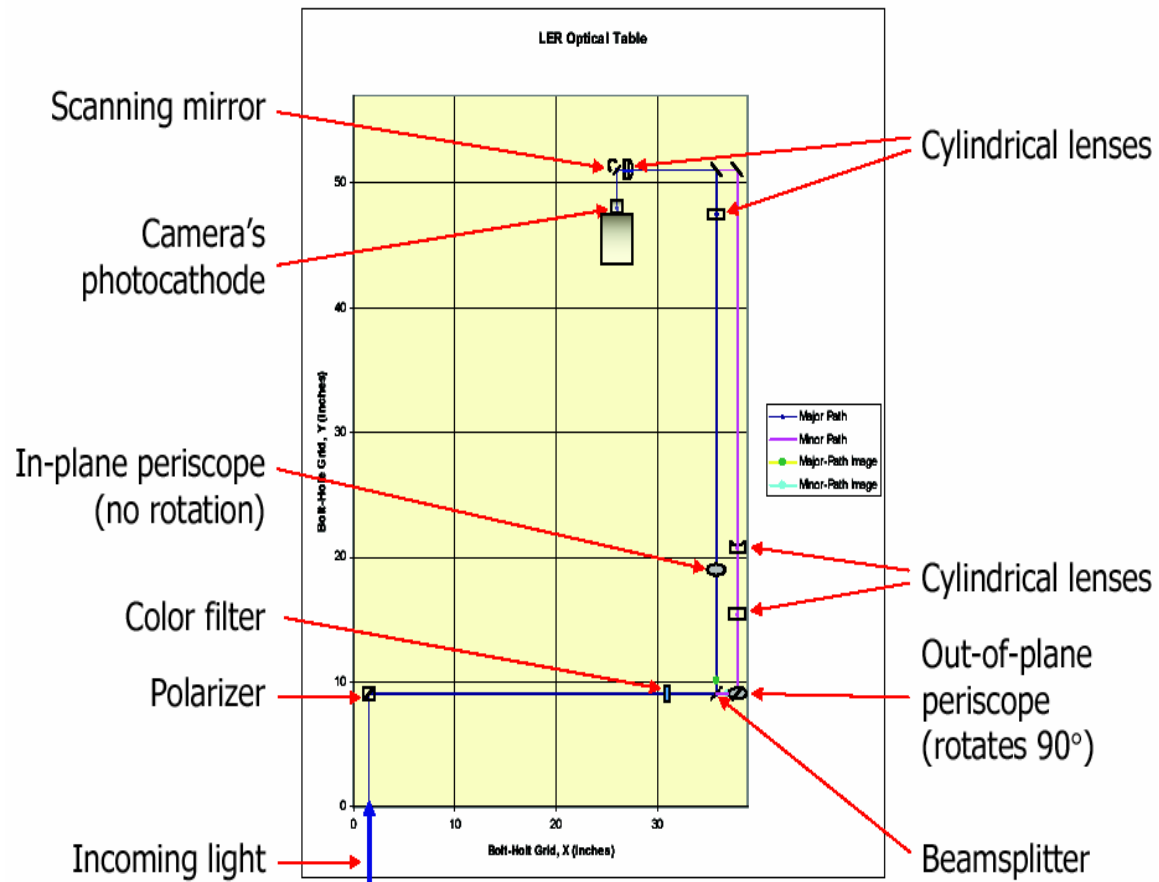


**Figure 2:** Diagram of turn-by-turn apparatus in the LER

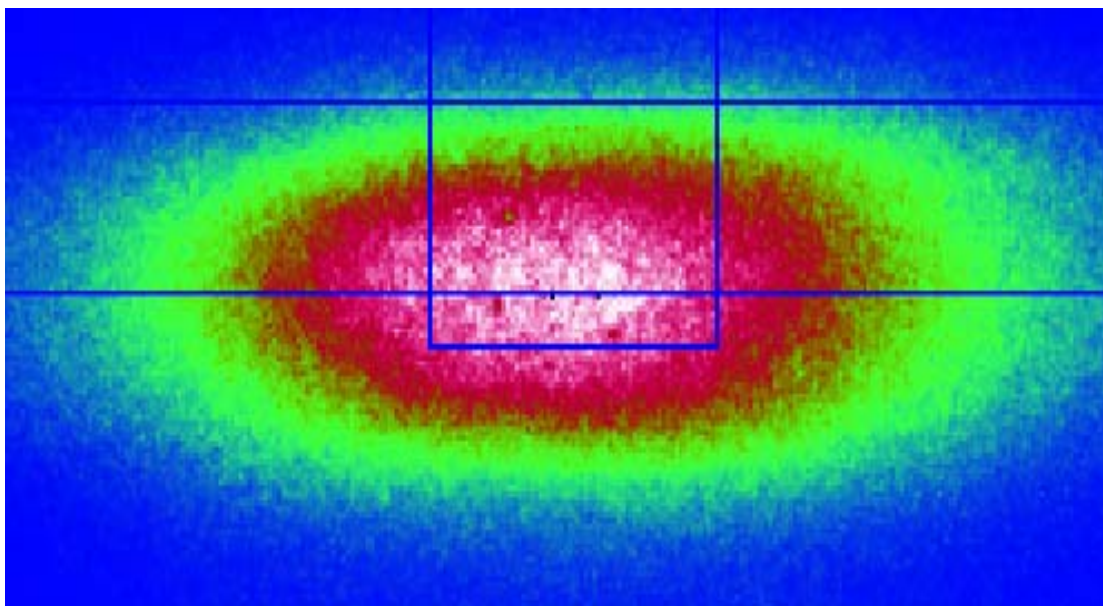


**Figure 3:** Transverse profile of a single bunch in LER using Bunch-by-bunch method, white shows highest intensity.

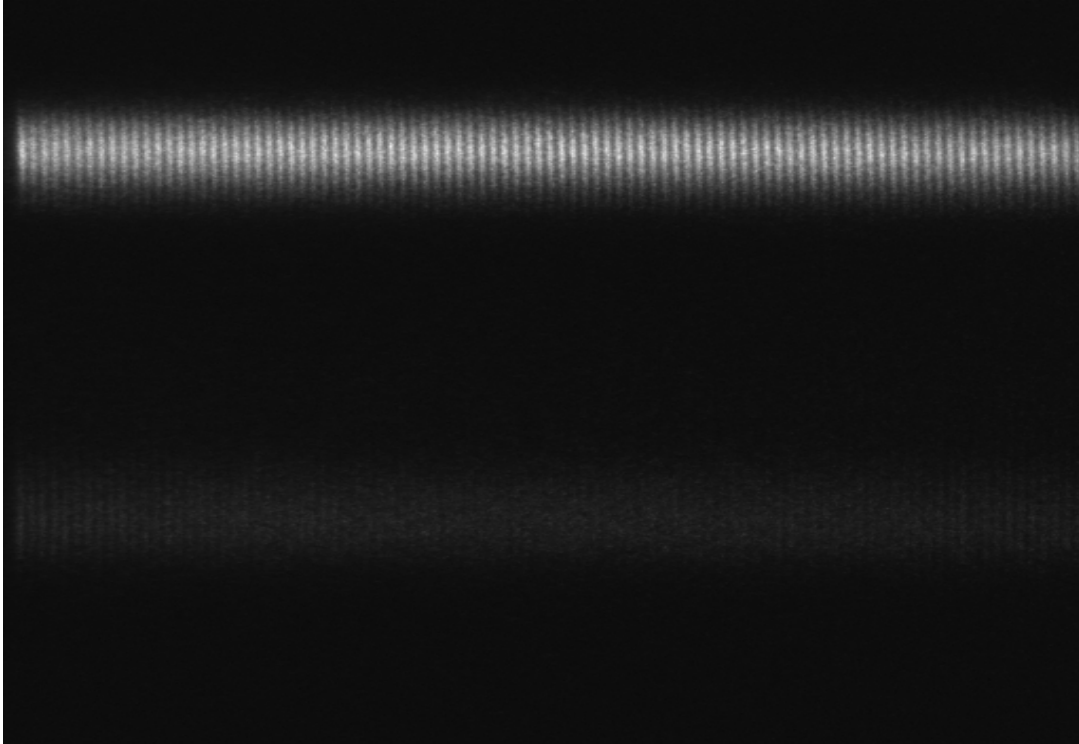


**Figure 4:** 94 turns of single bunch in LER, major axis shown above minor axis.

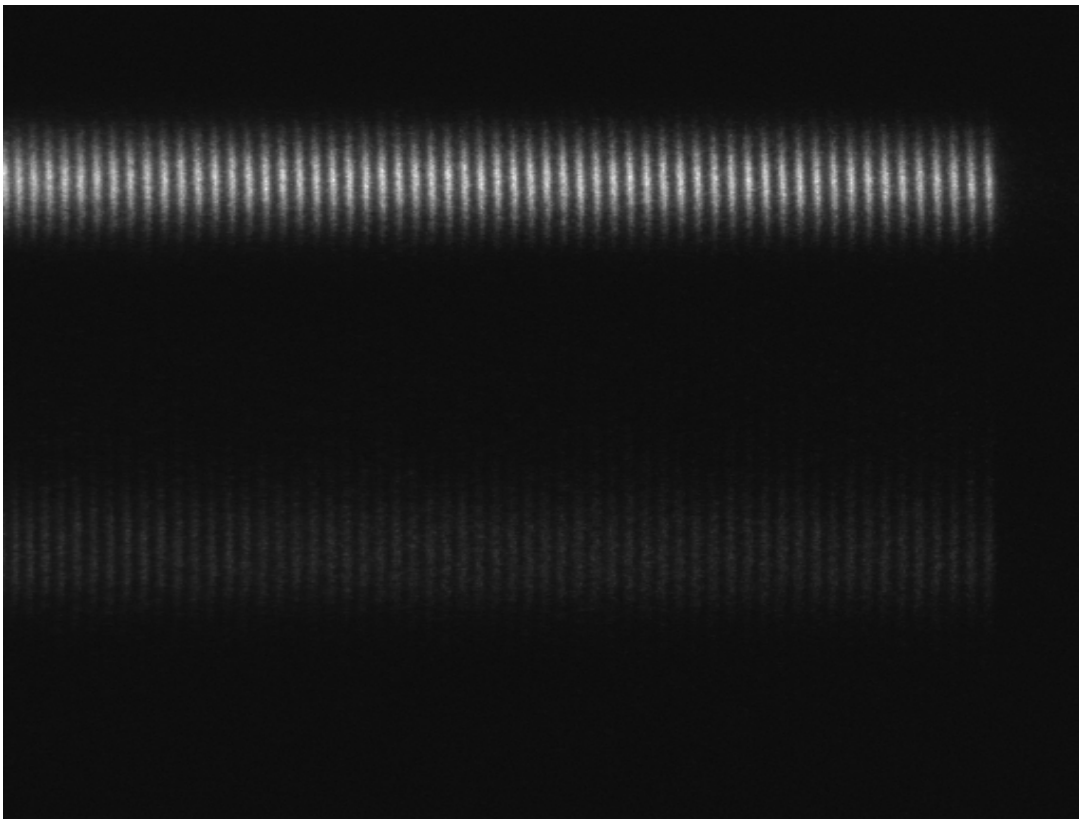


**Figure 5:** 60 turns of single bunch in LER, major axis shown above minor axis.

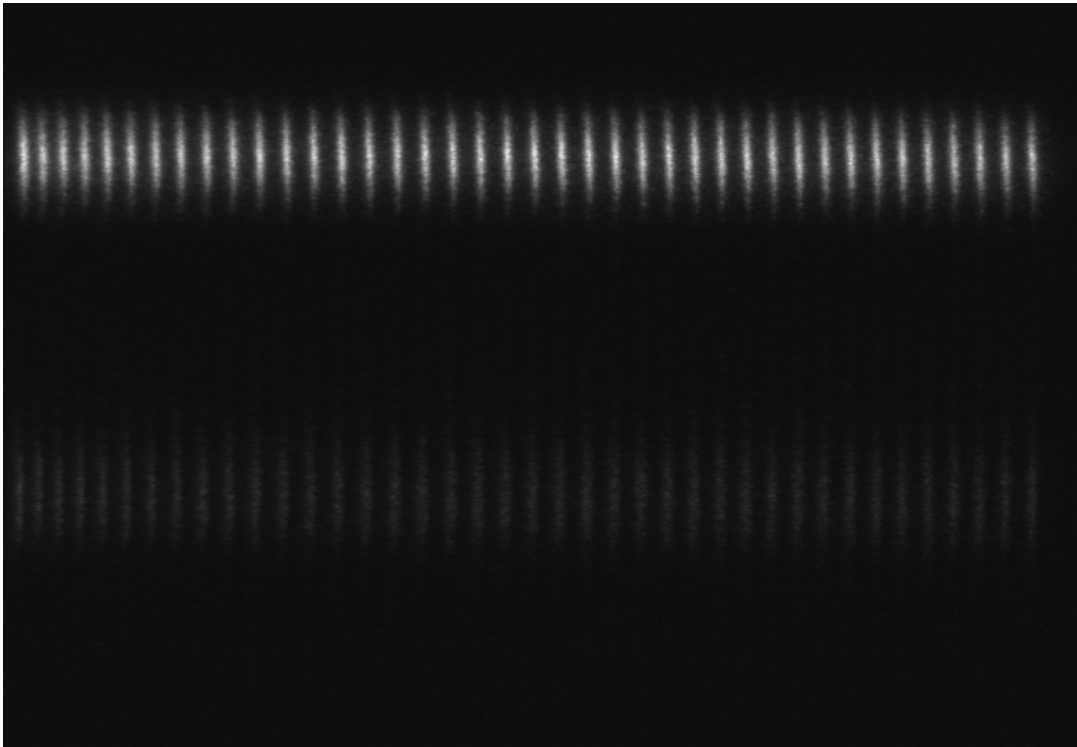


**Figure 6:** 41 turns of a single bunch in LER, major axis shown above minor axis.

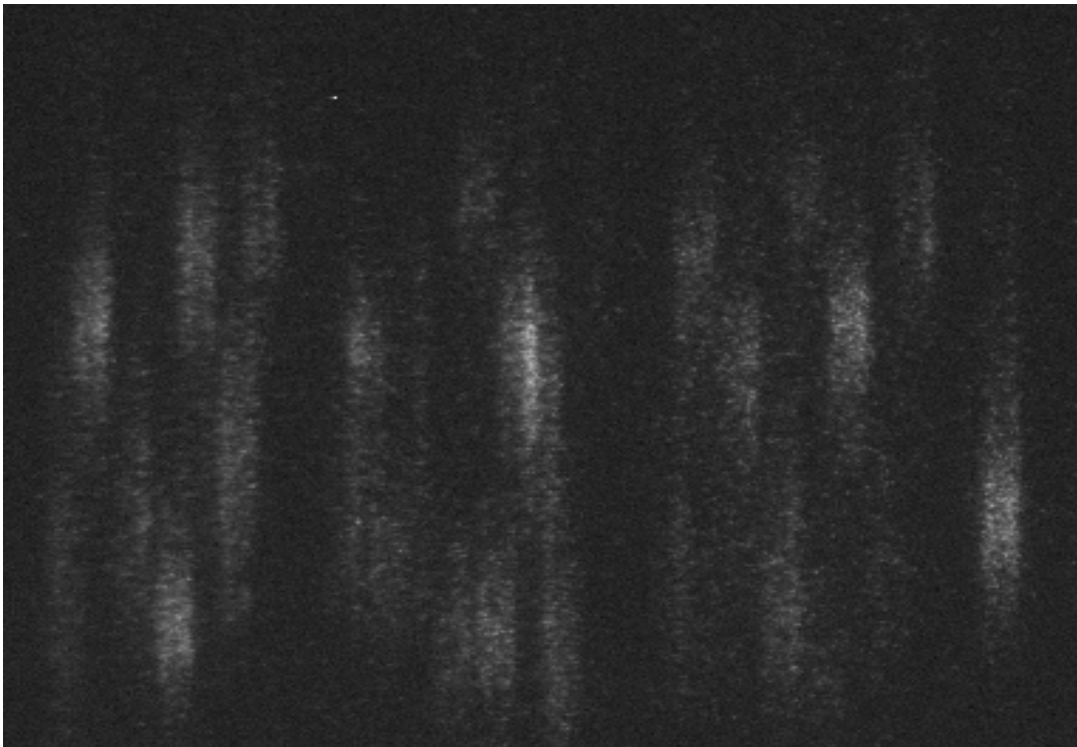


**Figure 7:** 50 turns of single injected bunch in LER, at beginning of ring fill.

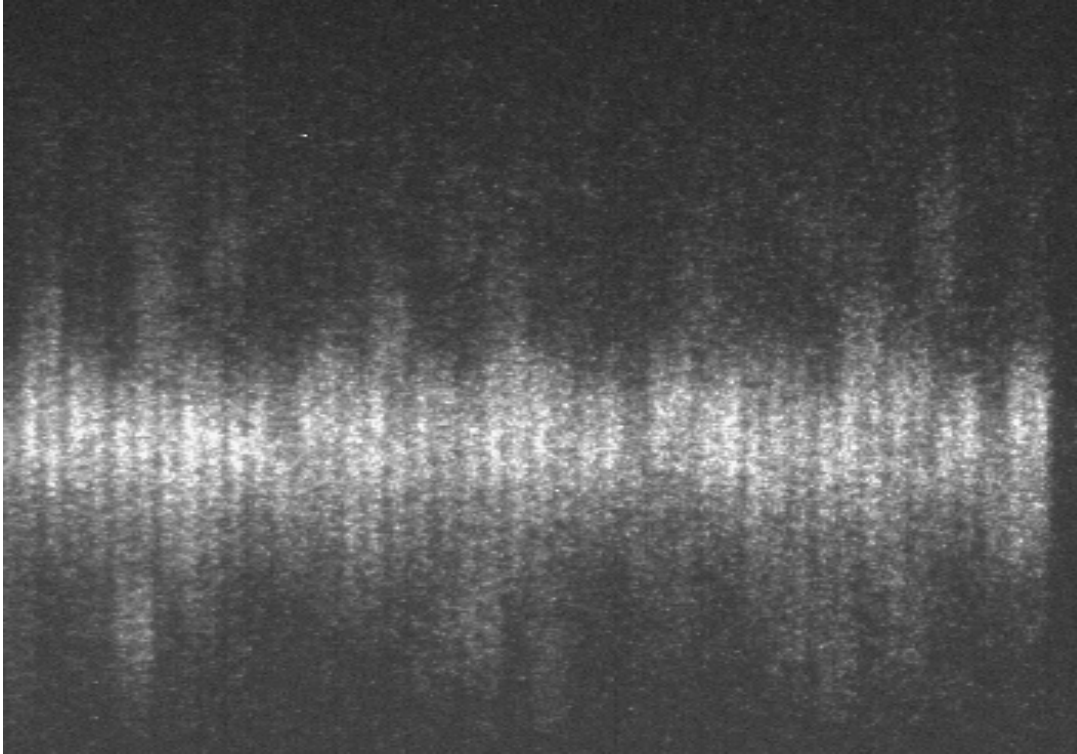


**Figure 8:** 50 turns of single injected bunch in LER oscillating around small stable bunch.

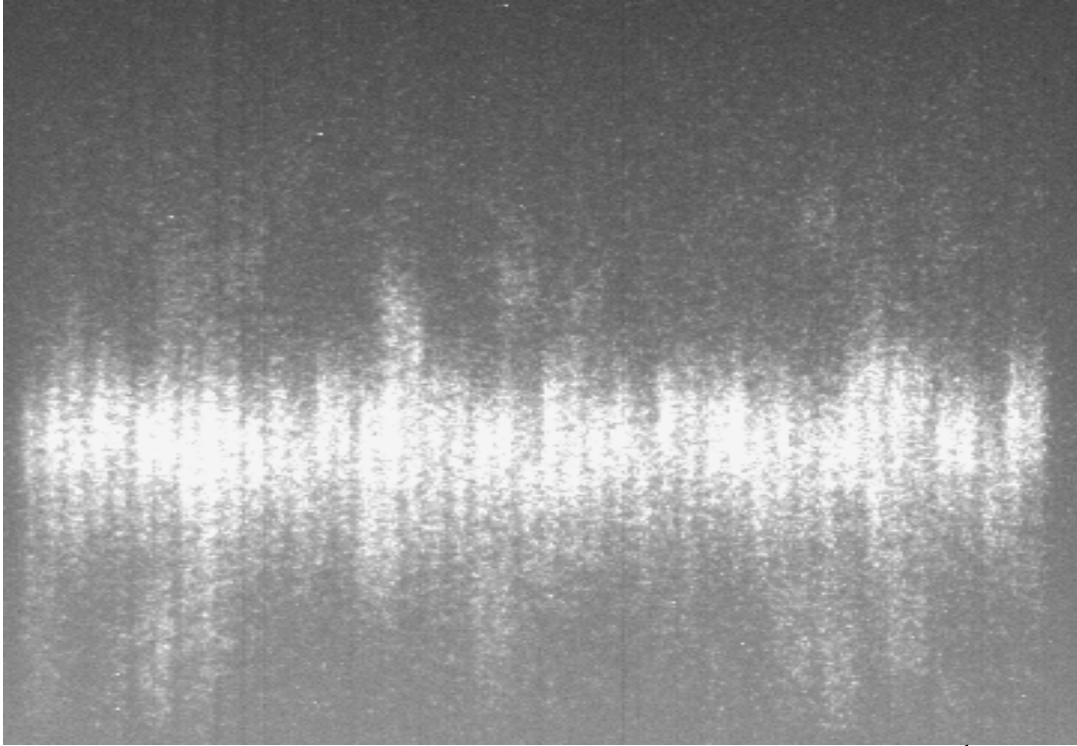


**Figure 9:** 50 turns of single injected bunch in LER oscillating around  $1/3^{\text{rd}}$  full stable bunch.

# Background Characterization for Thermal Ion Release

## Experiments with $^{224}\text{Ra}$

Helen Kwong

Office of Science, Science Undergraduate Laboratory Internship (SULI)

Stanford University

Stanford Linear Accelerator Center

Menlo Park, California

August 19, 2005

Prepared in partial fulfillment of the requirements of the Office of Science, Department of Energy's Science Undergraduate Laboratory Internship under the direction of Peter Rowson in the Research Division at the Stanford Linear Accelerator Center.

Participant: \_\_\_\_\_  
Signature

Research Advisor: \_\_\_\_\_  
Signature

# Table of Contents

<b>Abstract</b>	<b>ii</b>
<b>1 Introduction</b>	<b>1</b>
<b>2 Materials and Methods</b>	<b>3</b>
<b>3 Results</b>	<b>5</b>
3.1 In vacuum . . . . .	5
3.2 In xenon gas . . . . .	5
<b>4 Discussion and Conclusion</b>	<b>7</b>
4.1 Peak characterization . . . . .	7
4.2 Time decay . . . . .	9
<b>5 Acknowledgements</b>	<b>10</b>
<b>6 Tables and Figures</b>	<b>11</b>
<b>References</b>	<b>17</b>

## Abstract

Background Characterization for Thermal Ion Release Experiments with  $^{224}\text{Ra}$ . HELEN KWONG (Stanford University, Stanford, CA 94305) PETER ROWSON (Stanford Linear Accelerator Center, Menlo Park, CA 94025).

The Enriched Xenon Observatory for neutrinoless double beta decay uses  $^{136}\text{Ba}$  identification as a means for verifying the decay's occurrence in  $^{136}\text{Xe}$ . A current challenge is the release of Ba ions from the Ba extraction probe, and one possible solution is to heat the probe to high temperatures to release the ions. The investigation of this method requires a characterization of the alpha decay background in our test apparatus, which uses a  $^{228}\text{Th}$  source that produces  $^{224}\text{Ra}$  daughters, the ionization energies of which are similar to those of Ba. For this purpose, we ran a background count with our apparatus maintained at a vacuum, and then three counts with the apparatus filled with Xe gas. We were able to match up our alpha spectrum in vacuum with the known decay scheme of  $^{228}\text{Th}$ , while the spectrum in xenon gas had too many unresolved ambiguities for an accurate characterization. We also found that the alpha decays occurred at a near-zero rate both in vacuum and in xenon gas, which indicates that the rate was determined by  $^{228}\text{Th}$  decays. With these background measurements, we can in the future make a more accurate measurement of the temperature dependency of the ratio of ions to neutral atoms released from the hot surface of the probe, which may lead to a successful method of Ba ion release.

# 1 Introduction

Two fundamental questions in neutrino physics are the determination of the neutrino masses, and whether the neutrino is its own antiparticle. Successful detection of neutrinoless double-beta decay ( $0\nu\beta\beta$ ) will allow us to measure the average neutrino mass, and establish the Majorana nature of neutrinos, a discovery that would also have profound implications for other areas of physics. However, thus far no experiment has been able to establish unambiguously that  $0\nu\beta\beta$  occurs. The Enriched Xenon Observatory (EXO) seeks to observe  $0\nu\beta\beta$  decays in  $^{136}\text{Xe}$ , and in order to verify the occurrence of double-beta decay, EXO will attempt to detect ions of  $^{136}\text{Ba}$ , the daughter nucleus of  $^{136}\text{Xe}$ . This involves using ionization and scintillation light to determine the event location, extracting the barium ion from the event site by a probe, and transporting it to a cell for laser spectroscopy analysis. Among the current challenges for the EXO experiment, now in the R&D stage, is the release of the barium ion after its capture by the probe.

Since heated metal surfaces can release captured metal atoms in both the neutral or ionized state, one possible method of ion release is to heat the probe to high temperatures [1]. This method requires that the platinum surface is heated to a high enough temperature to liberate the barium ions, without releasing a significant proportion of neutral atoms. Therefore, the temperature dependency of the ratio of neutral to ionized atoms on a platinum surface has to be determined.

In our thermal ion release experiments, we will test a platinum surface with  $^{224}\text{Ra}$  ions, since the first and second ionization energies of radium are similar to those of barium, according to [1]. Our ion source will be  $^{228}\text{Th}$ , which produces  $^{224}\text{Ra}$  daughters and has a decay scheme that leads eventually to a stable  $^{208}\text{Pb}$  (see Figure 1) [2]. The experiments will be conducted in a cell filled with xenon gas, and background sources must be taken into account. In this paper, we report on our characterization of the background, measured both

with the cell in vacuum and with the cell filled with xenon gas.

## 2 Materials and Methods

The main part of our system is a chamber built almost entirely out of UHV-compatible materials, and Figure 2 shows a diagram of the chamber. Inside the chamber, in the center, is a small piece of platinum foil mounted on two tungsten rods, which allow the foil to be moved up and down, and are connected to a power supply that we will use to heat the foil. Facing the foil is the  $^{224}\text{Ra}$  source, with  $^{228}\text{Th}$  electroplated onto a platinum disk, and it is connected to a high voltage power supply. Below the source is an  $\alpha$  detector that is read out using standard pre- and post-amplification electronics. Between the source and the foil is a collimator plate; the plate has a hole in front of the detector, and is also connected to a high voltage power supply. Furthermore, the chamber is connected to a purifier that will reduce the impurities inevitably present in the system, and connected to the purifier is a turbomolecular pump.

In the actual thermal ion release experiments, the foil will receive the ions recoiled from the forward-biased source and then be heated by a current to temperatures over 1000 K, to release the radium ions. The ion yield is determined by counting the  $\alpha$  particles emitted in the  $^{224}\text{Ra}$  decay, along with those produced by the subsequent  $\alpha$  decays of  $^{220}\text{Rn}$ ,  $^{216}\text{Po}$ ,  $^{212}\text{Bi}$ , and  $^{212}\text{Po}$  (see Figure 1). We do not expect any detection of  $^{228}\text{Th}$   $\alpha$  decays, for the way the source is positioned above the detector makes it very unlikely that an  $\alpha$  particle from a  $^{228}\text{Th}$  decay would be received by the detector.

For the first part of our background measurement, we pumped the cell down to a  $5.0 \times 10^{-6}$  torr vacuum, had everything in the cell at zero voltage, and ran a background count for 68 hours. For the second part of the measurement, we pumped the cell down to a  $1.7 \times 10^{-8}$  torr vacuum and then filled the vessel with research-grade xenon gas (which is quoted as 99.999% pure by the supplier) at about 0.5 atm. The source was reversed-biased at -700 V, the collimator plate was at +500 V, and the foil was biased at +500 V with a temporary

device. With this setup, in the ideal situation, the  $^{224}\text{Ra}$  ions that resulted from  $^{228}\text{Th}$  decays would have been immediately attracted back to the source. A count with the foil placed in front of the source was run for 72 hours, one with it in front of the detector, for 12 hours, and one with it in front of the stopper plate, for 12 hours (see Figure 2). Complicating our measurement was that we used a different post-amplifier for our xenon gas background counts, because the original one was malfunctioning.

## 3 Results

### 3.1 In vacuum

Figure 3a shows a histogram of the pulse heights detected in vacuum. We can discern four clear peaks, and fitting them with Gaussian curves gives us mean values of 0.859 V, 0.957 V, 1.039 V, and 1.345 V, as shown in Figure 3b. While the peak at 1.345 V is well isolated, the other three are quite close to each other, with a shoulder between the two leftmost peaks. Restricting the data to the 0.8 V - 1.1 V range and fixing the mean values of the three peaks, we do a Gaussian fit to obtain a mean of 0.922 V at the shoulder (Figure 3c).

Figure 4 shows a histogram of the times at which pulses were recorded. The two bursts of activity at approximately 160,000 s and 235,000 s were likely due to equipment heating that we performed at those times. Discounting those bursts by restricting the data to 140,000 s and below, we graph the time distribution for each of the four peak ranges of pulses and fit each to an exponential curve. We find that their fitted slopes are quite small and have relatively large errors (the slope would be  $-k$  in a decay function  $N(t) = N_0e^{-kt}$ ). The values are  $7.01 \times 10^{-7} \pm 1.53 \times 10^{-6} \text{ s}^{-1}$ ,  $-1.57 \times 10^{-6} \pm 1.37 \times 10^{-6} \text{ s}^{-1}$ ,  $1.66 \times 10^{-6} \pm 1.33 \times 10^{-6} \text{ s}^{-1}$ , and  $-2.12 \times 10^{-6} \pm 1.21 \times 10^{-6} \text{ s}^{-1}$ .

### 3.2 In xenon gas

As mentioned in Section 2, we did three background counts in xenon gas, each with the foil in a different position. Figure 5a shows the superimposition of the signal histograms for the three counts - red indicates the 72-hour count with the foil in front of the source, blue, the 12-hour count in front of the detector, and green, the 12-hour count in front of the stopper plate (“discharge” position). The three histograms seem to exhibit the same patterns, showing peaks at similar positions, and doing Gaussian fits on the most obvious peaks for the 72-hour

count (see Figure 5b) gives us mean values of 0.885 V, 0.962 V, 1.029 V, 1.144 V, and 1.476 V.

Figure 6 shows the time histograms for the xenon gas counts, each fitted to an exponential curve. The slopes for the source, detector, and discharge foil positions are respectively  $-5.24 \times 10^{-7} \pm 1.39 \times 10^{-6} \text{ s}^{-1}$ ,  $-7.45 \times 10^{-7} \pm 1.64 \times 10^{-6} \text{ s}^{-1}$ , and  $-1.74 \times 10^{-6} \pm 1.58 \times 10^{-6} \text{ s}^{-1}$ .

## 4 Discussion and Conclusion

### 4.1 Peak characterization

Let us first look at the vacuum data and try to identify the peaks there. We can see from Figure 3b that the peak at 1.345 V is well isolated and has the highest energy; this appears to correspond to the  $^{212}\text{Po}$   $\alpha$  decay energy, which at 8.78 MeV is the highest energy in the decay scheme and is also well separated from the other energies (see Figure 1). On the other hand, assuming that the number of  $^{228}\text{Th}$  decays detected is negligible due to the relative positioning of the source and the detector (see Section 2), the lowest  $\alpha$  decay energy in the scheme is that of  $^{224}\text{Ra}$ , at 5.67 MeV. We therefore hypothesize that the peak with the lowest energy, at 0.859 V, represents  $^{224}\text{Ra}$   $\alpha$  decays. Assuming that our highest and lowest energies are represented by our highest and lowest pulse heights, we linearly calibrate the other four alpha decay energies in the scheme to obtain four predicted pulse voltages, displayed in Table 1. Comparing the pulse voltage predicted by calibration for  $^{220}\text{Rn}$  decays (0.956 V), and the voltage at which we observed the second peak (0.957 V), we find that their difference is small, much smaller than the  $\sigma$  value of 0.022 V obtained from the Gaussian fit for the second peak. Therefore it appears that the second peak represents the energies from  $^{220}\text{Rn}$  decays. Performing the same analysis, we find a similar correspondence between  $^{216}\text{Po}$  decays and the third peak also. Similarly, the two possible  $\alpha$  decays of  $^{212}\text{Bi}$  both seem to correspond to the apparent shoulder between the first and second peaks (see Figure 3c), the differences between the calibrated pulse voltages and the observed mean again well within the  $\sigma$  value. We also observe that the two predicted pulse voltages differ by only 0.006 V, about half of  $\sigma$ . With such a small difference, it seems that we cannot distinguish between the two energies with our data. The shoulder we see between the second and third peaks appears to represent a combination of the two possible  $\alpha$  decays from  $^{212}\text{Bi}$ .

Thus we are able to account for all the peaks and the shoulder observed in the vacuum

data and determine their corresponding  $\alpha$  decays (see Figure 3d). Since our assumption that the first peak represents a peak of  $^{224}\text{Ra}$  decays has resulted in a good calibration, we conclude that in a vacuum, the average pulse signal given by  $^{224}\text{Ra}$  decays is approximately 0.86 V, with the subsequent decays of  $^{212}\text{Bi}$ ,  $^{220}\text{Rn}$ ,  $^{216}\text{Po}$ , and  $^{212}\text{Po}$  giving pulse signals of 0.92 V, 0.96 V, 1.04 V, and 1.34 V, respectively.

Unfortunately, the xenon gas data are much more complicated and elude a similarly straightforward analysis. First, as mentioned in Section 2, we used a different pre-amplifier for the background counts in xenon gas, which might have had an effect on the size of the pulse signals. This seems to have been the case, as Figure 5c, with the vacuum background histogram drawn in black and the xenon gas histogram (at source position) drawn in red, shows that the peaks for the background in xenon gas have shifted higher. We attribute this increase to the pre-amplifier switch, because normally we would expect the peaks to shift down, as alpha particles should lose rather than gain energy in gas. With the shifted peaks, we cannot do a comparison of the absolute values as we had hoped to do. We attempted to resort to comparing the differences between peaks - for instance, the difference between the two rightmost peaks in vacuum is 0.306 V, and in xenon gas, 0.334 V - and see how they compare with the values predicted from the stopping power of alpha particles in xenon (according to [3]) and the density of xenon at 0.5 atm (according to [4]), but this approach did not work very well. The reason for this may be that the spectrum we are looking at is really much more complicated, with many peaks hidden inside. We can observe from Figure 5c that except for the rightmost peak, the peaks in the xenon gas histogram are not as well-defined as they are in the vacuum histogram, particularly in the lower range, which seem to have a combination of several peaks that are very difficult to differentiate. These peaks may be due to that in xenon gas, the particles accepted by the detector came from different parts of the chamber - some have traveled longer distances, and others shorter, so the energies they have lost to the gas might have been significantly different as well. This

would break up the well-defined peaks observed in vacuum and result in smaller peaks at points we would not expect. In the end we conclude that we cannot characterize the  $\alpha$  spectrum with so many ambiguities and complications. Perhaps in the future, by making a vacuum background count with the new amplifier, we can make a more accurate analysis.

## 4.2 Time decay

We are also interested in the decay rates that were observed. From Figure 4, we see that all four slopes from the exponential fits for our vacuum data are quite flat, with two of them positive and the other two negative. Of course, it is nonphysical to have a positive decay rate for a decaying element. However, we also see that all four slopes have relatively large errors, with considerable scattering in the data, and in each case, 0 lies within  $2\sigma$ s from the mean, so even in the cases of positive slopes, the actual value may well be a very small negative value. Since the slopes are relatively flat and the data seem to scatter around a constant level, we can reasonably say that the actual slope for the data is very close to zero, and that the decay rates observed in vacuum were very low, in accordance with  $^{228}\text{Th}$ 's long half-life of 1.9 years.

We observe similar results with the xenon gas background counts: the slopes are negative and very small, with errors that are larger or almost as large as the slopes. This is consistent with the decay rates being very nearly zero, due to  $^{228}\text{Th}$ 's half-life. This is actually not the result we expected - we anticipated the decay rate in xenon gas to follow that of  $^{224}\text{Ra}$ , because the reversed-biased source should have attracted back any Ra ions that decayed from the Th, so that the decays seen by the detector are only those from Ra atoms (and their daughter nuclei) already deposited on different parts of the chamber before the count was initiated. This then would result in the decay rate being determined by Ra, rather than Th. One possible explanation for the Th decay rate that we are observing is that a significant number of Ra ions recoiled from the source might have recombined quickly with electrons to become neutral again.

## 5 Acknowledgements

This research was conducted at the Stanford Linear Accelerator Center. I would like to take this opportunity to thank my mentor Peter Rowson for his guidance and support throughout the past weeks. I am also grateful for the help and enthusiasm from everyone else in EXO at SLAC. In particular, I would like to thank Kolo Wamba for his day-to-day guidance and patience. Finally, I thank the U. S. Department of Energy, Office of Science, and SLAC for organizing and funding the SULI program and making this tremendous learning experience possible.

## 6 Tables and Figures

Element	$E$ (MeV)	Predicted $V$ (V)	Observed $V$ (V)	$\Delta V$ (V)	$\sigma_V$ (V)
$^{224}\text{Ra}$	5.67	(0.859)	0.859	(0)	0.023
$^{212}\text{Bi}$ (25%)	6.05	0.919	0.922	0.003	0.012
$^{212}\text{Bi}$ (10%)	6.09	0.925	0.922	-0.003	0.012
$^{220}\text{Rn}$	6.29	0.956	0.957	0.001	0.022
$^{216}\text{Po}$	6.78	1.032	1.039	0.007	0.018
$^{212}\text{Po}$	8.78	(1.345)	1.345	(0)	0.022

Table 1: Decay Energy ( $E$ )-Pulse Voltage ( $V$ ) Calibration

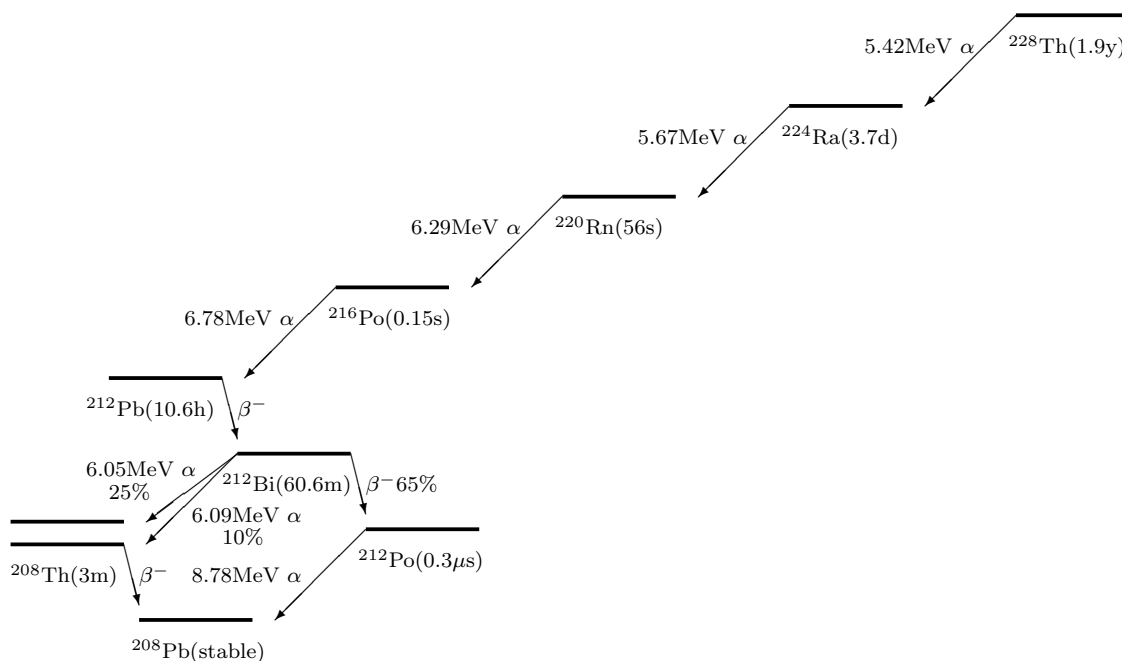


Figure 1: Level scheme for  $^{228}\text{Th}$ .

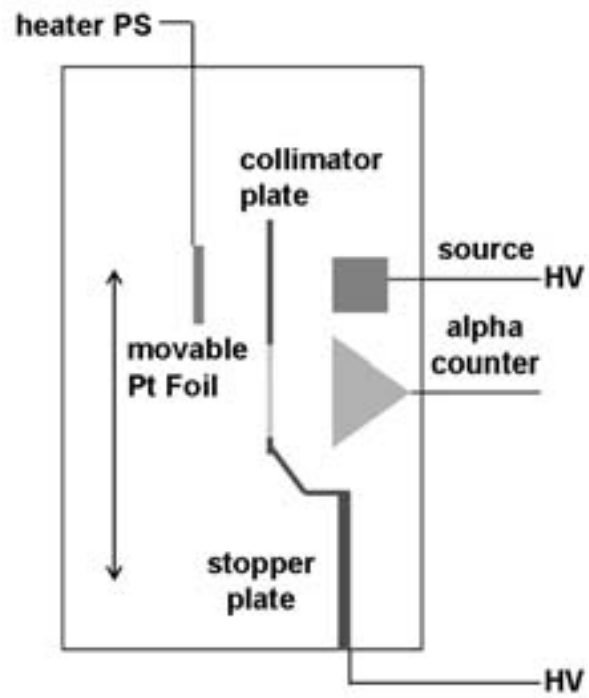
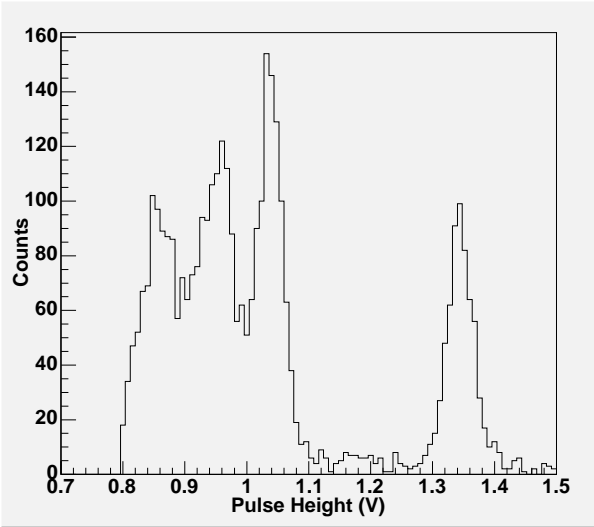
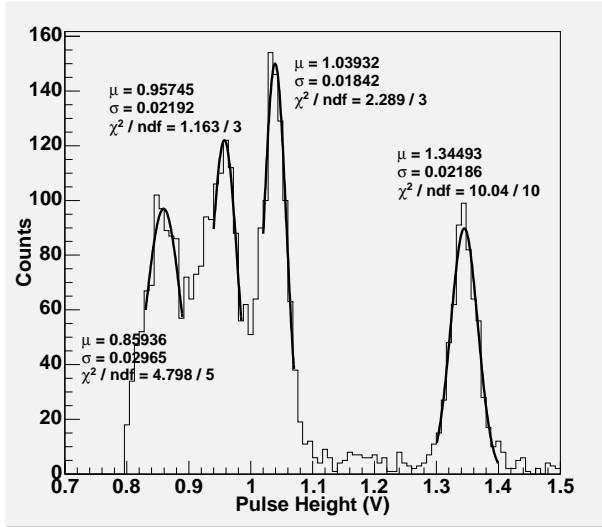


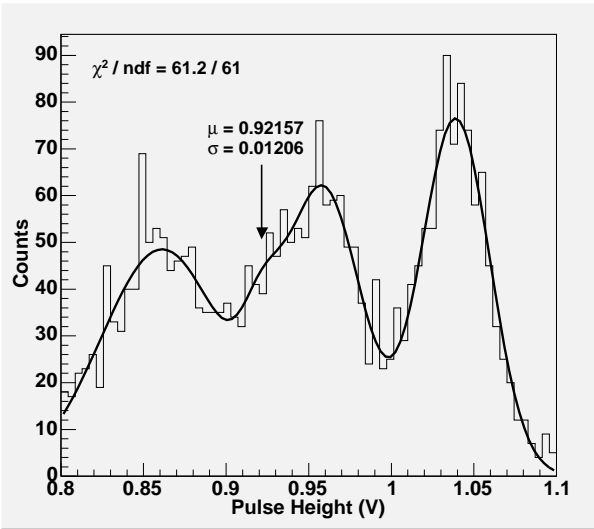
Figure 2: Diagram of the apparatus for the experiment.



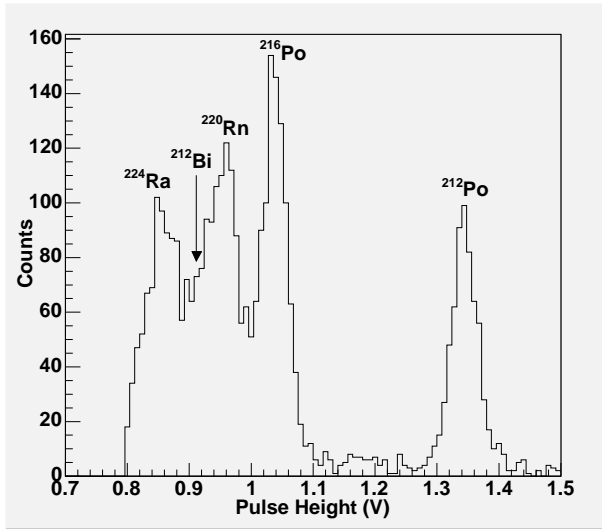
(a)



(b)



(c)



(d)

Figure 3: (a): Histogram of pulses observed in vacuum. (b): A Gaussian curve is fitted for each peak. (c): A sum of four Gaussian curves is fitted over a smaller range, for the first three peaks and the apparent shoulder between the two leftmost peaks. (d): The spectrum is labeled with corresponding decaying elements.

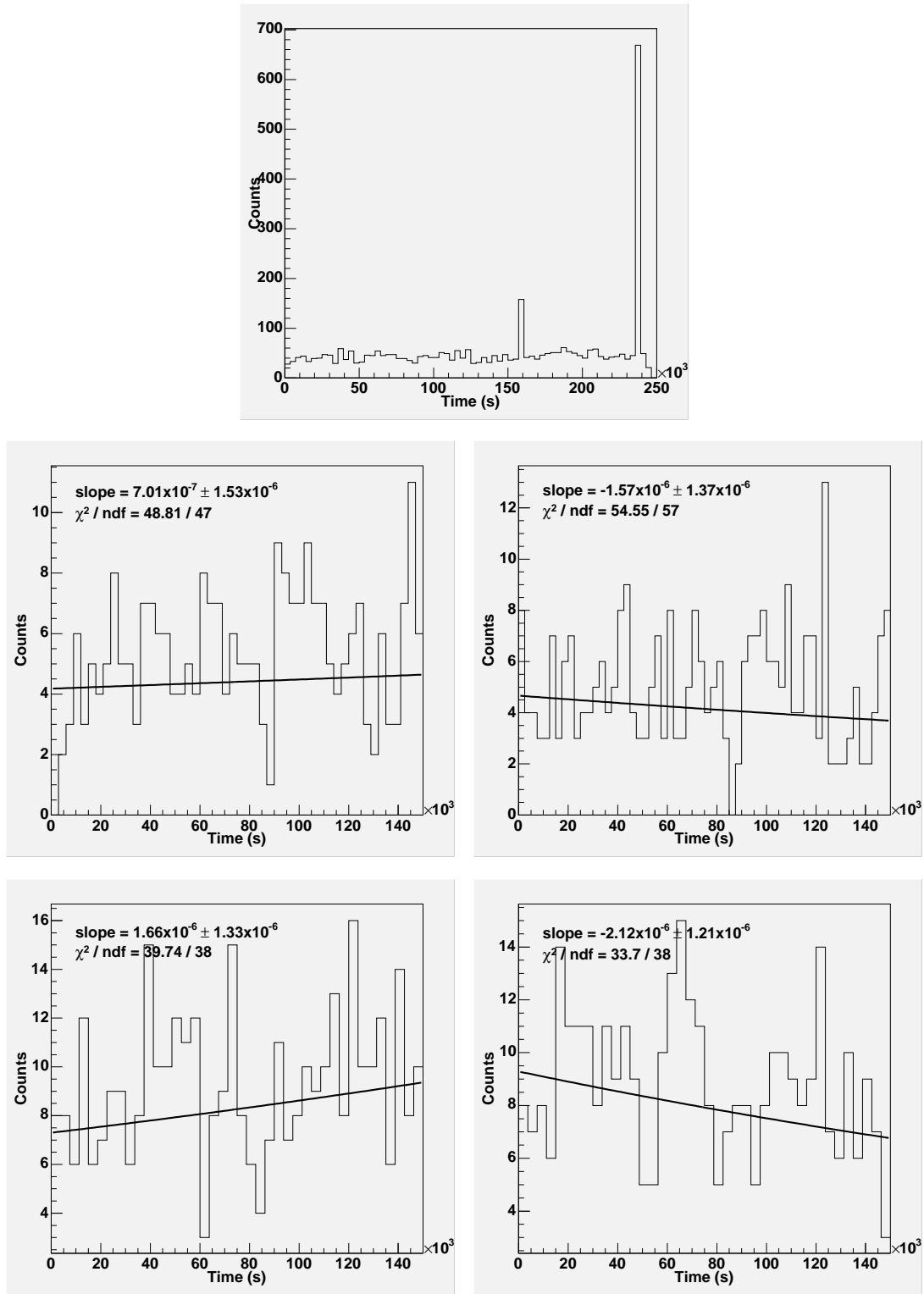


Figure 4: Histogram of times at which particular ranges of pulses were observed, in vacuum. Top: The entire range, 0.8 - 1.5 V. Middle left:  $^{224}\text{Ra}$  range, 0.83 - 0.89 V. Middle right:  $^{220}\text{Rn}$  range, 0.94 - 0.985 V. Bottom left:  $^{216}\text{Po}$  range, 1.02 - 1.07 V. Bottom right:  $^{212}\text{Po}$  range, 1.3 - 1.4 V.

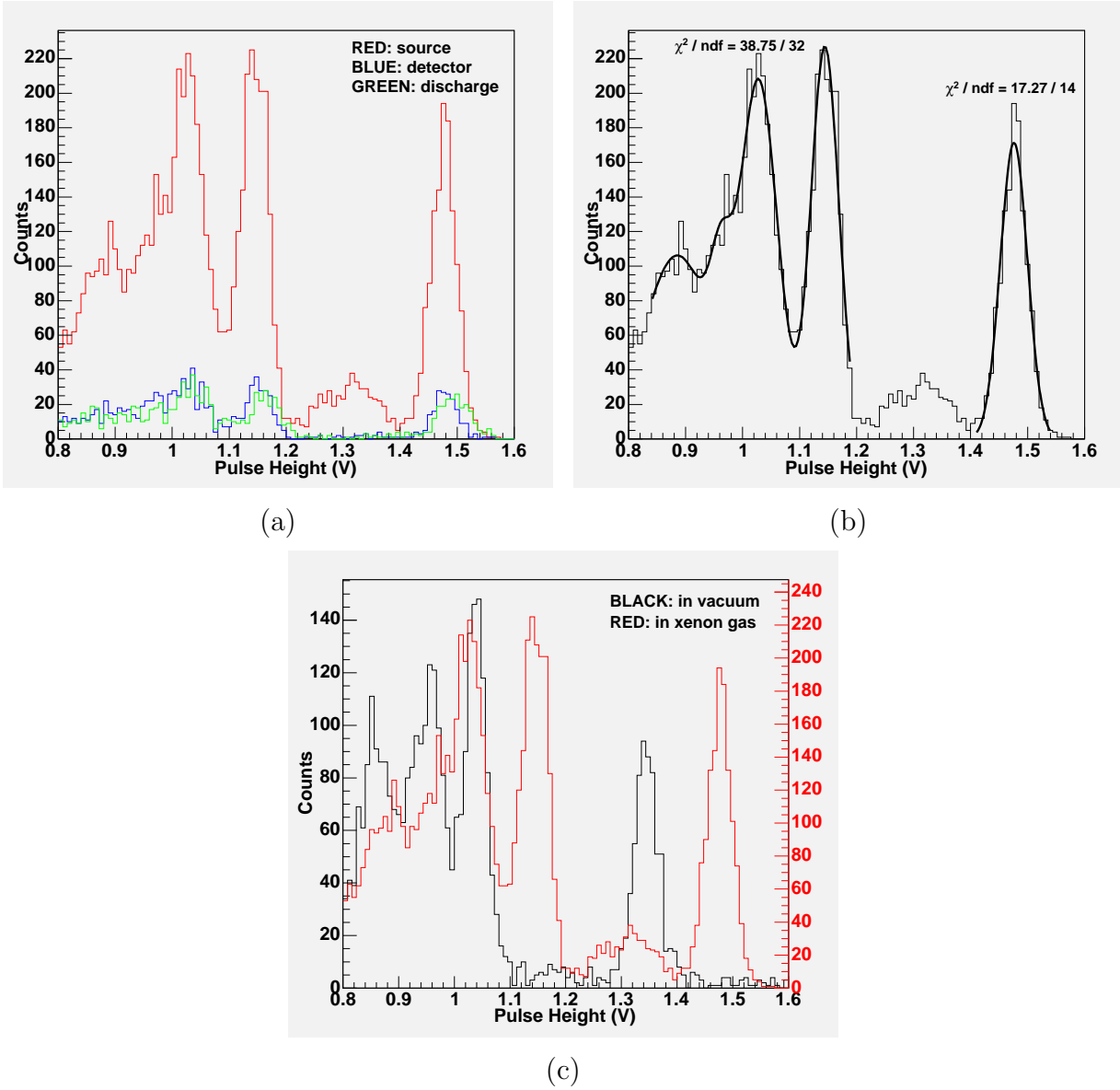


Figure 5: (a): Superimposition of the histograms for the three background counts done with the chamber filled with xenon gas; the foil is at a different position for each count, as indicated by the colors. (b): Histogram for the 72-hour count at source position, with Gaussian curve fits. (c): Scaled superimposition of the vacuum background histogram and the “source” xenon gas histogram.

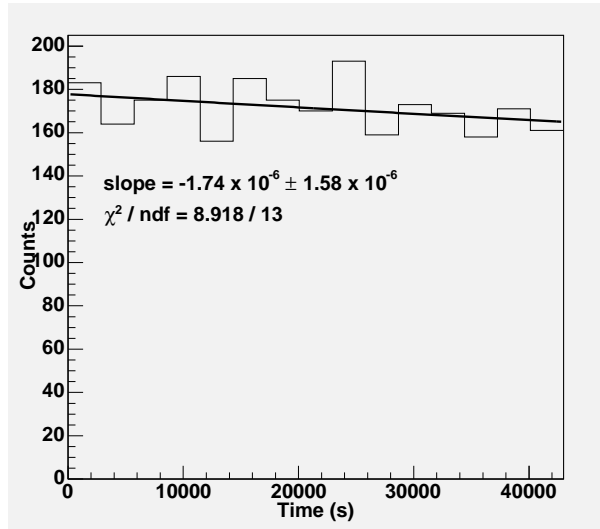
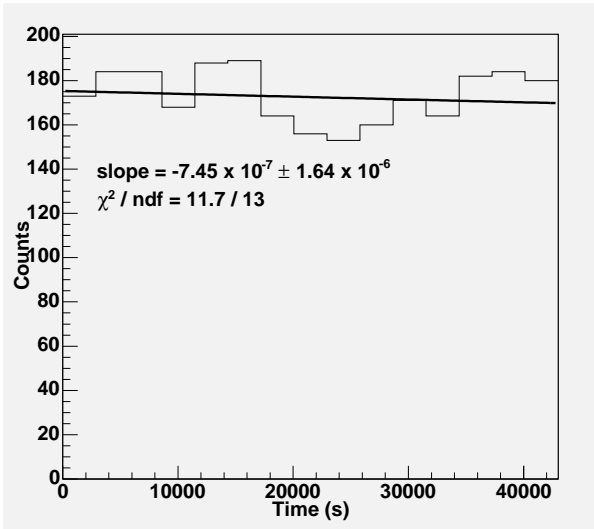
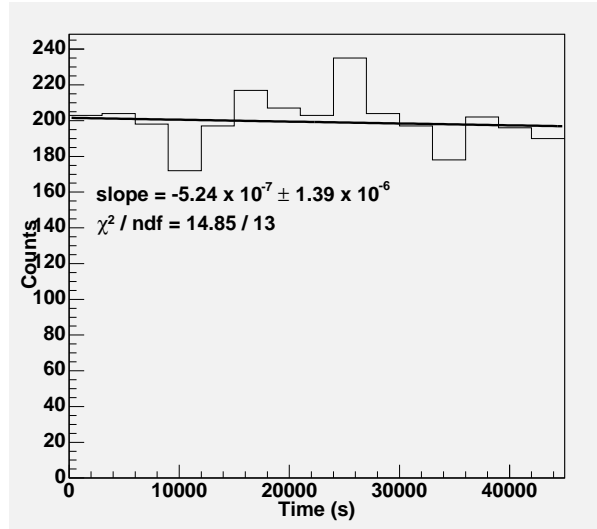


Figure 6: Time histograms for xenon gas background. Top: Source position. Bottom left: Detector position. Bottom right: Discharge position.

## References

- [1] P.C. Rowson, “Barium Ion Tagging: Ion Acquisition in LXe & Laser Fluorescence Identification,” presented at EXO Week, Stanford, CA, 2005.
- [2] K. Wamba, “Proposal for Ion Grabbing Experiments with a  $^{228}\text{Th}$  Source,” *EXO Collaboration ELOG*, no. 36.
- [3] M.J. Berger, J.S. Coursey, M.A. Zucker, and J. Chang, *ESTAR, PSTAR, and ASTAR: Computer Programs for Calculating Stopping-Power and Range Tables for Electrons, Protons, and Helium Ions*, [Online database] Gaithersburg, MD: National Institute of Standards and Technology, [2005 Aug 17], Available at HTTP: <http://physics.nist.gov/Star>
- [4] E.W. Lemmon, M.O. McLinden and D.G. Friend, “Thermophysical Properties of Fluid Systems” in *NIST Chemistry WebBook, NIST Standard Reference Database Number 69*, [Online database] Eds. P.J. Linstrom and W.G. Mallard, Gaithersburg, MD: National Institute of Standards and Technology, June 2005, [2005 Aug 17], Available at HTTP: <http://webbook.nist.gov>

# Localized PEP-II Storage Ring Optics Measurements

Jonathan Landy  
Office of Science, SULI Program  
California Institute of Technology  
Stanford Linear Accelerator Center  
Menlo Park, California

August 19, 2005

Prepared in partial fulfillment of the requirements of the Office of Science, DOE Science Undergraduate Laboratory Internship (SULI) Program under the direction of Dr. Yitong Yan in the Accelerator Research Department A at Stanford Linear Accelerator Center.

Participant:

---

Signature

Research Advisor:

---

Signature

Localized PEP-II Storage Ring Optics Measurements. JONATHAN LANDY (California Institute of Technology, Pasadena, CA 91126) YITON YAN (Stanford Linear Accelerator Center, 2575 Sand Hill Road Menlo Park, CA 94025)

### Abstract

The current technique employed to determine the parameters which specify the betatron oscillation in the PEP-II ring at SLAC is a global procedure in that the data from each *BPM* (Beam Position Monitor) is weighted equally. However for more accurate interaction point (IP) measurements it would be beneficial to weight the data from the *BPMs* closest to the IP much more heavily. Researchers are thus considering the possibility of developing a technique to determine the oscillation parameters near the IP using as few *BPMs* as possible. In this paper, allowing *BPM* gains and cross coupling, we show analytically that given data from  $N$  *BPMs* there remain  $6N + 2$  degrees of freedom in the matrices  $M_{A,A}$ ,  $M_{B,A}$ , ...,  $M_{N,N-1}$  unspecified by the observable data alone. From this we demonstrate that data from at least 3 *BPMs* is required to completely specify the system when the transfer maps between *BPMs* are assumed known, and that 4 *BPMs* may be more suitable.

# Contents

<b>1</b>	<b>Introduction</b>	<b>4</b>
<b>2</b>	<b>One-Dimensional Case</b>	<b>5</b>
2.1	Single BPM Analysis . . . . .	5
2.2	Multiple BPM Analysis . . . . .	10
2.3	Results in Terms of Standard Parameters . . . . .	13
2.4	Approximate Solution . . . . .	14
2.5	A Note on Rational Tunes . . . . .	15
<b>3</b>	<b>Two-Dimensional Case</b>	<b>15</b>
3.1	Single BPM Analysis . . . . .	15
3.2	Multiple BPM Analysis . . . . .	20
3.3	Approximate Solution and Future Work . . . . .	22
<b>4</b>	<b>Acknowledgements</b>	<b>23</b>

# 1 Introduction

As particles circle around a storage ring, such as the PEP-II ring at SLAC, they move longitudinally in a tight beam. The particles will also have transverse momenta and therefore will tend to diverge. To prevent this from happening, in addition to the required bending dipoles, a series of quadrupole magnets is used to alternately focus the beam and then defocus the beam. As the particles move around the ring they will then oscillate in transverse phase space and are prevented from diverging. This oscillation is known as the betatron motion of the beam and is uniquely determined at each  $BPM$  (Beam Position Monitor) by 10 beam parameters. In this paper we will be investigating how many of these parameters can be determined from orbit data.

The transverse phase space position of the beam at  $BPM_A$  and turn  $n$  around the ring is denoted by  $\overrightarrow{x_{n,A}} = (x, p_x, y, p_y)_{n,A}^T$ , although we will sometimes drop the subscript specifying the  $BPM$  when the meaning is clear. The position of the beam at  $BPM_A$  uniquely determines what it will be when it reaches  $BPM_B$ . Therefore we can define a function  $f_{B,A}$  as follows:

$$f_{B,A} : \overrightarrow{x_{n,A}} \rightarrow \overrightarrow{x_{n,B}} \quad (1)$$

Thus  $f_{B,A}$  maps the beam's phase space position at  $BPM_A$  to what it will be at  $BPM_B$ . In particular we can define the 1-turn map  $f_{A,A}$  which maps the phase space position at  $BPM_A$  at turn  $n$  to what it will be at turn  $n+1$ :

$$f_{A,A} : \overrightarrow{x_{n,A}} \rightarrow \overrightarrow{x_{n+1,A}} \quad (2)$$

These functions are known to be largely linear and therefore we may approximate these maps by 4x4 matrices which operate on the phase space. For example, the linear approximation of  $f_{A,A}$  will be denoted by  $M_{A,A}$ . If it were possible to measure all components of the beam's phase space position as it passed by the  $BPM$  it would be a simple matter to determine this matrix. We would only need to invert the orbit as follows:

$$M_{A,A} \begin{pmatrix} x_0 & x_1 & x_2 & x_3 \\ p_{x0} & p_{x1} & p_{x2} & p_{x3} \\ y_0 & y_1 & y_2 & y_3 \\ p_{y0} & p_{y1} & p_{y2} & p_{y3} \end{pmatrix}_A = \begin{pmatrix} x_1 & x_2 & x_3 & x_4 \\ p_{x1} & p_{x2} & p_{x3} & p_{x4} \\ y_1 & y_2 & y_3 & y_4 \\ p_{y1} & p_{y2} & p_{y3} & p_{y4} \end{pmatrix}_A \rightarrow$$

$$M_{A,A} = \begin{pmatrix} x_1 & x_2 & x_3 & x_4 \\ p_{x1} & p_{x2} & p_{x3} & p_{x4} \\ y_1 & y_2 & y_3 & y_4 \\ p_{y1} & p_{y2} & p_{y3} & p_{y4} \end{pmatrix}_A \begin{pmatrix} x_0 & x_1 & x_2 & x_3 \\ p_{x0} & p_{x1} & p_{x2} & p_{x3} \\ y_0 & y_1 & y_2 & y_3 \\ p_{y0} & p_{y1} & p_{y2} & p_{y3} \end{pmatrix}_A^{-1} \quad (3)$$

Knowing the phase space position at 5 consecutive turns thus gives you complete information about the map. Further, the position of the beam at any later time is in the space spanned by the first 4 positions. This implies that no new information can be obtained by looking at more turns of the orbit.

Unfortunately, the *BPMs* can only measure the spatial coordinates of the beam and cannot measure its transverse momenta. Thus we are only able to measure half of the coordinates of its phase space position. For this reason it has been assumed that the information one can get from orbit data is insufficient to solve for the parameters without some a priori information about the machine lattice. We confirm this is true; however, it may be possible that some of the information lost about the map which is contained in the momenta at each turn could be recovered by looking at the  $x$  and  $y$  positions at later turns in the orbit. In this paper we demonstrate rigorously the number of parameters left unspecified by the orbit data and further give a lower bound on the number of *BPMs* required to determine all the parameters when the matrices  $M_{B,A}$ ,  $M_{C,B}$ , etc. are assumed known.

## 2 One-Dimensional Case

We will begin by analyzing lattices which oscillate only in the  $x$ -direction. In section 2.1 we will look at what can be determined from data from 1 *BPM* alone. In section 2.2 we will analyze the case of data from 2 or more *BPMs*. In section 2.3 we will discuss our results in terms of the machine parameters. And in section 2.4 we will demonstrate how a natural assumption permits a solution.

### 2.1 Single BPM Analysis

In this section we will prove that given the  $x$ -orbit data from a single *BPM*,  $BPM_A$ , it is impossible to determine the map  $M_{A,A}$ . Further we will show that there are in fact 2 degrees of freedom in  $M_{A,A}$  left unspecified by this data alone.

#### Symplectic Matrices and Normalized Phase Space

A 2x2 symplectic matrix  $M$  is defined as one such that:

$$M^T S M = S, \quad \text{where } S = \begin{pmatrix} 0 & 1 \\ -1 & 0 \end{pmatrix} \quad (4)$$

In the 2x2 case, it is easy to show that the symplectic condition is equivalent to the condition  $\det(M) = 1$ .

One condition on the matrices  $M_{A,A}$ ,  $M_{B,A}$ , etc. is that they be symplectic. This is a consequence of the fact these matrices represent systems in which the hamiltonian is time-independent. Another condition on  $M_{A,A}$  is that its eigenvalues be complex-conjugates and of modulus 1. We can see that is true as follows:

As  $M_{A,A}$  is symplectic  $\rightarrow \lambda_1 \lambda_2 = 1$  where  $\lambda_1, \lambda_2$  are its eigenvalues. As the machine is designed so that the orbits of  $M_{A,A}$  will remain bounded it cannot be true that either  $|\lambda_1|$  or  $|\lambda_2| > 1$ , as this would result in an expanding orbit. This implies  $|\lambda_1| = |\lambda_2| = 1$ . If  $\lambda_1, \lambda_2$  are complex, then they are

necessarily conjugate by the conjugate root theorem. Also if they are real,  $\lambda_1 \lambda_2 = 1 \rightarrow \lambda_1 = \lambda_2$  and again they must be conjugate.

With these two conditions on  $M_{A,A}$  it can be shown that it is always possible to decompose  $M_{A,A}$  as follows:

$$M_{A,A} = A_A R_{A,A} A_A^{-1} \quad \text{with,} \quad (5)$$

$$A_A = \begin{pmatrix} \sqrt{\beta_A} & 0 \\ \frac{-\alpha_A}{\sqrt{\beta_A}} & \frac{1}{\sqrt{\beta_A}} \end{pmatrix} \text{ and } R_{A,A} = \begin{pmatrix} \cos \mu_A & \sin \mu_A \\ -\sin \mu_A & \cos \mu_A \end{pmatrix} \quad (6)$$

Thus the matrix  $A_A^{-1}$  transforms to a normalized space in which the one turn map is a simple clockwise rotation which induces circular orbits.

This decomposition explicitly shows that there are 3 parameters determining the matrix  $M_{A,A}$  in the 1-Dimensional case. The rotation angle  $\mu_A$  is set by the operators of the machine during runtime. This angle is always chosen so that the tune,  $\nu \equiv \frac{\mu_A}{2\pi}$ , is irrational for if the linear orbits were periodic, nonlinear effects would start to play a more important role. One consequence of this choice is that the eigenvalues of  $M_{A,A}$  are necessarily complex.  $\beta_A$  causes the orbit to become an ellipse when it differs from 1 while  $\alpha_A$  has the effect of skewing the ellipse.

### Number of Independent Orbit Data Sets

As mentioned above, the *BPMs* can only measure the spatial coordinates of the beam and cannot measure its transverse momenta. Therefore for a 1-Dimensional lattice a typical data set from an orbit may look like that in Table 2.1 below. At each turn the  $x$  position of the beam is recorded as it passes by *BPM<sub>A</sub>*, but the momentum  $p_x$  is unknown.

The goal is to determine as much as we can about  $M_{A,A}$  from this  $x$ -orbit data. The first question we might ask ourselves then is: How many independent  $x$ -orbit data sets can we use to determine  $M_{A,A}$ ? The answer is that (after normalization) all orbits are actually the same, in that any given orbit will contain all other orbits. Therefore no new information can possibly be gained by taking more than 1  $x$ -orbit data set. The proof follows:

Consider two  $x$ -orbit data sets taken at *BPM<sub>A</sub>*:  $x_0, x_1, \dots$  and  $X_0, X_1, \dots$ . The first step in the proof that the second orbit,  $X_0, X_1, \dots$ , is contained in the first is to discuss normalization:

<i>Turn</i> :	0	1	2	3	4	5	...
$x_A$	3.1623	3.0075	2.5583	1.8587	0.9772	0.0000	...
$p_{x_A}$	$p_0 = ?$	$p_1 = ?$	$p_2 = ?$	$p_3 = ?$	$p_4 = ?$	$p_5 = ?$	...

Table 1: Example *BPM<sub>A</sub>* data for a 1-Dimensional lattice

Consider the evolution of the orbit  $\vec{x}_0, \vec{x}_1, \dots$  instead in normalized space. That is consider the orbit:  $A_A^{-1}\vec{x}_0, A_A^{-1}\vec{x}_1, \dots \equiv \vec{x}_0^N, \vec{x}_1^N, \dots$ . In normalized space the transfer matrix is simply  $R_{A,A}$ , a clockwise rotation. Thus:

$$\vec{x}_{m+1}^N = R_{A,A} \vec{x}_m^N \rightarrow \quad (7)$$

$$|\vec{x}_{m+1}^N| = |\vec{x}_m^N| \equiv l \quad \forall m \quad (8)$$

as  $R_{A,A}$  conserves the norm. Similarly:

$$\vec{X}_{m+1}^N = R_{A,A} \vec{X}_m^N \rightarrow \quad (9)$$

$$|\vec{X}_{m+1}^N| = |\vec{X}_m^N| \equiv L \quad \forall m \quad (10)$$

Now:

$$\vec{x}_m = \begin{pmatrix} \sqrt{\beta_A} & 0 \\ \frac{-\alpha_A}{\sqrt{\beta_A}} & \frac{1}{\sqrt{\beta_A}} \end{pmatrix} \vec{x}_m^N \quad (11)$$

This implies that  $x_m$  is maximized when  $x_m^N$  is maximized. Now in normalized space  $\vec{x}_m^N$  is rotating around a circle of radius  $l$  in  $x^N - p^N$  space. As  $\nu$  is irrational  $\rightarrow$  the normalized orbit  $\vec{x}_0^N, \vec{x}_1^N, \dots$  gets arbitrarily close to the  $x^N$ -axis, as the orbit of an irrational rotation is dense on the unit circle [2]. Therefore:

$$\max |x_m^N| = l \rightarrow \quad (12)$$

$$\max |x_m| = \sqrt{\beta_A} l \quad (13)$$

Similarly:

$$\max |X_m^N| = L \rightarrow \quad (14)$$

$$\max |X_m| = \sqrt{\beta_A} L \quad (15)$$

Therefore, measuring  $\max |x_m| = \sqrt{\beta_A} l$  and  $\max |X_m| = \sqrt{\beta_A} L$  and then dividing the two we obtain:

$$\frac{\max |x_m|}{\max |X_m|} = l/L \equiv r \quad (16)$$

We can now multiply the second orbit by  $r$  to obtain a new orbit:

$$r\vec{X}_0, r\vec{X}_1, \dots \equiv \vec{X}_0^*, \vec{X}_1^*, \dots \quad (17)$$

$$r\vec{X}_0^N, r\vec{X}_1^N, \dots \equiv \vec{X}_0^{*N}, \vec{X}_1^{*N}, \dots \quad (18)$$

We now have two orbits whose normalized phase space positions have the same norm:

$$|\vec{x}_m^N| = |\vec{X}_n^{*N}| = l \quad \forall m, n \quad (19)$$

Once again, as  $\nu$  is irrational  $\rightarrow$  the orbit  $\overrightarrow{x_0^N}, \overrightarrow{x_1^N}, \dots$  is dense on the circle of radius  $l$ . As  $\overrightarrow{X_0^{*N}}$  lies on this circle  $\rightarrow$  the orbit  $\overrightarrow{x_0^N}, \overrightarrow{x_1^N}, \dots$  must get arbitrarily close to  $\overrightarrow{X_0^{*N}}$ . As it can get arbitrarily close, there must be some  $j(k)$  such that:

$$|\overrightarrow{x_{j(k)}^N} - \overrightarrow{X_0^{*N}}| < 10^k, \text{ for any } k \quad (20)$$

Therefore we can choose a  $k$  such that the difference between  $\overrightarrow{x_{j(k)}^N}$  and  $\overrightarrow{X_0^{*N}}$  is unmeasurable. Doing this we find:

$$\overrightarrow{x_{j(k)}^N} \simeq \overrightarrow{X_0^{*N}} \rightarrow R_{A,A} \overrightarrow{x_{j(k)}^N} = \overrightarrow{x_{j(k)+1}^N} \simeq R_{A,A} \overrightarrow{X_0^{*N}} = \overrightarrow{X_1^{*N}} \dots \quad (21)$$

$$\rightarrow A_A \overrightarrow{x_{j(k)}^N} = \overrightarrow{x_{j(k)}} \simeq A_A \overrightarrow{X_0^{*N}} = \overrightarrow{X_0^*}, \overrightarrow{x_{j(k)+1}^N} \simeq \overrightarrow{X_1^*} \dots \quad (22)$$

that is:

$$\overrightarrow{x_{j(k)}}, \overrightarrow{x_{j(k)+1}}, \overrightarrow{x_{j(k)+2}}, \dots \simeq \overrightarrow{X_0^*}, \overrightarrow{X_1^*}, \overrightarrow{X_2^*}, \dots \quad (23)$$

where of course the two orbits will stay close for more turns the larger  $k$  is chosen. This concludes the proof that any properly normalized second orbit will always be included (to an arbitrary degree of accuracy) within another arbitrarily chosen orbit. As a single orbit contains all other orbits, this implies we need only consider one when we are attempting to determine the parameters of our map.

### Specifying a Single $x$ -Orbit

We have seen above that you can get no new information about  $M_{A,A}$  by using more than 1  $x$ -orbit data set. The next thing we will show is that in fact, only the first 3  $x$  data points are required to specify an entire  $x$ -orbit. proof:

As  $M_{A,A}$  is a real matrix with complex eigenvalues, the eigenvectors of  $M_{A,A}$  must also be complex. As the zeroth turn of the orbit is a real vector, it cannot be an eigenvector of  $M_{A,A}$ . Therefore the first two turns of the orbit are independent and we can write, for some  $a$  and  $b$ :

$$\begin{pmatrix} x_2 \\ p_{x_2} \end{pmatrix} = \begin{pmatrix} x_0 & x_1 \\ p_{x_0} & p_{x_1} \end{pmatrix} \begin{pmatrix} a \\ b \end{pmatrix} \quad (24)$$

That is,  $\overrightarrow{x_2}$  is in the span of  $\overrightarrow{x_0}$  and  $\overrightarrow{x_1}$ . Multiplying on the left by  $M_{A,A}^n$  gives:

$$\begin{pmatrix} x_{n+2} \\ p_{x_{n+2}} \end{pmatrix} = \begin{pmatrix} x_n & x_{n+1} \\ p_{x_n} & p_{x_{n+1}} \end{pmatrix} \begin{pmatrix} a \\ b \end{pmatrix} \quad (25)$$

This gives 2 independent recursion relations for  $x_n$  and  $p_{x_n}$ . By definition:

$$\begin{pmatrix} x_{n+1} & x_{n+2} \\ p_{x_{n+1}} & p_{x_{n+2}} \end{pmatrix} = M_{A,A} \begin{pmatrix} x_n & x_{n+1} \\ p_{x_n} & p_{x_{n+1}} \end{pmatrix} \rightarrow \quad (26)$$

$$\det \begin{pmatrix} x_{n+1} & x_{n+2} \\ p_{x_{n+1}} & p_{x_{n+2}} \end{pmatrix} = \det \begin{pmatrix} x_n & x_{n+1} \\ p_{x_n} & p_{x_{n+1}} \end{pmatrix} \equiv Q \quad (27)$$

as  $\det M_{A,A} = 1$ . Note that  $Q \neq 0$  as the first two turns are linearly independent. From Eq.(27) we get the following two equations:

$$p_{x_1} = \frac{x_1 p_{x_0} + Q}{x_0} \quad (28)$$

$$p_{x_2} = \frac{x_2 p_{x_1} + Q}{x_1} = \frac{Q}{x_1} + \frac{x_2 Q}{x_1 x_0} + \frac{x_2 p_{x_0}}{x_0} \quad (29)$$

Plugging in Eq.(28) and Eq.(29) into Eq.(24) gives after a little manipulation:

$$Q\left(\frac{x_0}{x_1} + \frac{x_2}{x_1} - b\right) = p_{x_0}(ax_0 + bx_1 - x_2) \quad (30)$$

By Eq.(24)  $ax_0 + bx_1 - x_2 = 0 \rightarrow$

$$\frac{x_0}{x_1} + \frac{x_2}{x_1} - b = 0; \quad (31)$$

which finally gives:

$$b = \frac{x_0 + x_2}{x_1} \quad (32)$$

$$a = -1 \quad (33)$$

Plugging in then to Eq.(25) we see that the entire  $x$ -orbit is specified uniquely by  $x_0, x_1$ , and  $x_2$ . Further the  $x$ -orbit depends only on these 3  $x$  values and not at all on the  $p_x$  values.

### Conclusion of Single BPM Analysis

We are now ready to demonstrate that it is impossible to determine the matrix  $M_{A,A}$  from the  $x$ -orbit data alone. In order to do this we will show how to construct an infinite set of matrices, all of which are symplectic and could produce the observed  $x$ -orbit data. As our only assumption on the form of  $M_{A,A}$  is that it be symplectic we cannot determine which of the matrices in this set is the correct  $M_{A,A}$  when using only the  $x$ -orbit data:

Let us begin by considering an observed  $x$ -orbit data set:  $x_0, x_1, \dots$  with the momenta unspecified as usual. Then we know:

$$M_{A,A} = \begin{pmatrix} x_1 & x_2 \\ p_{x_1} & p_{x_2} \end{pmatrix} \begin{pmatrix} x_0 & x_1 \\ p_{x_0} & p_{x_1} \end{pmatrix}^{-1} \quad (34)$$

$M_{A,A}$  is symplectic  $\rightarrow$

$$p_{x_2} = \frac{p_{x_1}(x_0 + x_2)}{x_1} - p_{x_0} \quad (35)$$

This reduces the number of unknown parameters specifying  $M_{A,A}$  to 2, those being  $p_{x_0}$  and  $p_{x_1}$ . We are unable to measure these two momenta using the *BPMs*, but the question still remains if there is some way that you could find

out what these are. We see that one cannot: For if you guess at  $M_{A,A}$  by randomly choosing both a  $p_{xg_0}$  and  $p_{xg_1}$  and plug these into Eq.(34) you will obtain a different matrix:

$$G_{A,A}(p_{xg_0}, p_{xg_1}) = \begin{pmatrix} x_1 & x_2 \\ p_{xg_1} & p_{xg_2} \end{pmatrix} \begin{pmatrix} x_0 & x_1 \\ p_{xg_0} & p_{xg_1} \end{pmatrix}^{-1} \quad (36)$$

which is symplectic if  $p_{xg_2}$  is obtained by plugging into Eq.(35). By definition, given input phase space position  $\vec{x}_{g0} = (x_0, p_{xg_0})^T$  the orbit under  $G_{A,A}(p_{xg_0}, p_{xg_1})$  will have the same first three turn  $x$  positions:  $x_0, x_1, x_2$ . As the entire  $x_n$  orbit is determined by its first 3 values, this  $x_n$  orbit will match that of the observed data set. Therefore as each of these matrices,  $G_{A,A}(p_{xg_0}, p_{xg_1})$ , is symplectic and could produce the  $x$ -orbit observed we cannot determine which of them is the actual one turn map  $M_{A,A}$ .

We shall write  $\mathcal{D} = 2$ , to signify the fact that there are 2 degrees of freedom in  $M_{A,A}$  left unspecified by the observable data alone. Thus 2 extra constraints in addition to the  $x$ -orbit data from a single  $BPM$  are required to determine the 1-turn map  $M_{A,A}$  in a 1-dimensional lattice.

## 2.2 Multiple BPM Analysis

Now that we have proven that it is impossible to determine  $M_{A,A}$  given just the  $x$ -orbit data from  $BPM_A$  the next question we must answer is whether or not it may be possible to determine  $M_{A,A}$  using the  $x$ -orbit data from multiple  $BPMs$  around the ring in conjunction. The answer, as we shall see, is that again you cannot.

We begin by looking at a hypothetical storage ring which has 2  $BPMs$ . As the beam circles around the ring the  $x$ -position of the beam is recorded turn by turn as it passes by  $BPM_A$  and then again as it passes by  $BPM_B$ . We define an orbit data set as a complete set of data for all  $BPMs$  under consideration for a given run. Of course the transverse momenta is still unmeasurable at each of the  $BPMs$  and so a typical orbit data set may look like that in Table 2.2 below.

As in the single  $BPM$  proof above, our analysis of the double  $BPM$  case will hinge on the construction of an infinite set of symplectic matrices,  $G_{A,A}(a, b, \dots)$  and  $G_{B,A}(a, b, \dots)$ , which are capable of producing the  $x_n$ -orbits observed in the orbit data sets. First, however, we must turn our attention to the number of independent orbit data sets we may use.

<i>Turn :</i>	0	1	2	3	4	5	...
$x_A$	3.0046	3.0391	2.5351	1.5817	0.3480	-0.9473	...
$p_{xA}$	$p_0 = ?$	$p_1 = ?$	$p_2 = ?$	$p_3 = ?$	$p_4 = ?$	$p_5 = ?$	...
$x_B$	3.4580	3.4345	2.8022	1.6734	0.2479	-1.2215	...
$p_{xB}$	$p_0 = ?$	$p_1 = ?$	$p_2 = ?$	$p_3 = ?$	$p_4 = ?$	$p_5 = ?$	...

Table 2: Example  $BPM_A$  and  $BPM_B$  data for a 1-Dimensional lattice

### Number of Independent Orbit Data Sets

As in the analogous section above, we wish to show that all orbit data sets are contained (to any desired degree of accuracy) within every other orbit data set. We can easily extend the result we obtained above:

Consider two orbit data sets, each consisting of the orbit data from  $BPM_A$  and the data from  $BPM_B$ :

$$\text{set1} : (\overrightarrow{x_{0,A}}, \overrightarrow{x_{1,A}}, \dots; \overrightarrow{x_{0,B}}, \overrightarrow{x_{1,B}}, \dots) \quad \text{set2} : (\overrightarrow{X_{0,A}}, \overrightarrow{X_{1,A}}, \dots; \overrightarrow{X_{0,B}}, \overrightarrow{X_{1,B}}, \dots)$$

If we now plug in the orbits  $x_{n,A}$  and  $X_{n,A}$  into Eq.(16) we shall obtain the normalization ratio  $r_A$ . Multiplying both the orbit  $(\overrightarrow{X_{n,A}})$  and the orbit  $(\overrightarrow{X_{m,B}})$  by  $r_A$ , we obtain the normalized orbit data set,  $(\overrightarrow{X_{n,A}^*})$  and  $(\overrightarrow{X_{m,B}^*})$ . Now by Eq.(20) we can find a  $j(k)$  such that the following holds:

$$|\overrightarrow{x_{j(k),A}^N} - \overrightarrow{X_{0,A}^{*N}}| < 10^k, \text{ for any } k \quad (37)$$

If we choose a large  $k$  then, we have by Eq.(23) that:

$$\overrightarrow{x_{j(k),A}}, \overrightarrow{x_{j(k)+1,A}}, \overrightarrow{x_{j(k)+2,A}}, \dots \simeq \overrightarrow{X_{0,A}^*}, \overrightarrow{X_{1,A}^*}, \overrightarrow{X_{2,A}^*}, \dots \quad (38)$$

where the two orbits stay close for more turns the larger  $k$  is chosen. Multiplying on the left by  $M_{B,A}$  we obtain:

$$\begin{aligned} M_{B,A} \overrightarrow{x_{j(k),A}}, M_{B,A} \overrightarrow{x_{j(k)+1,A}}, \dots &= \overrightarrow{x_{j(k),B}}, \overrightarrow{x_{j(k)+1,B}}, \dots \\ &\simeq M_{B,A} \overrightarrow{X_{0,A}^*}, M_{B,A} \overrightarrow{X_{1,A}^*}, \dots = \overrightarrow{X_{0,B}^*}, \overrightarrow{X_{1,B}^*}, \dots \rightarrow \\ \overrightarrow{x_{j(k),B}}, \overrightarrow{x_{j(k)+1,B}}, \overrightarrow{x_{j(k)+2,B}}, \dots &\simeq \overrightarrow{X_{0,B}^*}, \overrightarrow{X_{1,B}^*}, \overrightarrow{X_{2,B}^*}, \dots \end{aligned} \quad (39)$$

showing that the 2nd orbit at  $B$  is contained in the first as well. Clearly this argument can be extended to any number of  $BPMs$  by proceeding inductively. In general we see that for 1-dimensional lattices a single orbit data set contains all others, implying we need only consider one when attempting to determine the matrices  $M_{A,A}$ ,  $M_{B,A}$ ,  $M_{C,B}$ , etc..

### Construction of Guess Matrices

By definition, the actual matrix  $M_{B,A}$  satisfies the following relation:

$$M_{B,A} \begin{pmatrix} x_{0,A} & x_{1,A} \\ p_{x_{0,A}} & p_{x_{1,A}} \end{pmatrix} = \begin{pmatrix} x_{0,B} & x_{1,B} \\ p_{x_{0,B}} & p_{x_{1,B}} \end{pmatrix} \quad (40)$$

from which we obtain,

$$M_{B,A} = \begin{pmatrix} x_{0,B} & x_{1,B} \\ p_{x_{0,B}} & p_{x_{1,B}} \end{pmatrix} \begin{pmatrix} x_{0,A} & x_{1,A} \\ p_{x_{0,A}} & p_{x_{1,A}} \end{pmatrix}^{-1} \quad (41)$$

$M_{A,A}$  is given by Eq.(34). Again the symplectic condition Eq.(35) still holds for  $M_{A,A}$ , while setting the determinant of Eq.(41) to 1 we see that the symplectic condition applied to  $M_{B,A}$  is equivalent to:

$$p_{x1,B} = \frac{x_{1,B}}{x_{0,B}}p_{x0,B} - \frac{x_{1,A}}{x_{0,B}}p_{x0,A} + \frac{x_{0,A}}{x_{0,B}}p_{x1,A} \quad (42)$$

Thus the symplectic condition reduces the number of unknown parameters to 3:  $p_{x0,A}$ ,  $p_{x1,A}$ , and  $p_{x0,B}$ . Choosing random values for these momenta we can construct the symplectic matrices  $G_{A,A}(p_{x0,A}, p_{x1,A}, p_{x0,B})$  and  $G_{B,A}(p_{x0,A}, p_{x1,A}, p_{x0,B})$  by plugging into Eq.(34) and Eq.(41):

$$G_{A,A} = \begin{pmatrix} x_{1,A} & x_{2,A} \\ p_{xg1,A} & p_{xg2,A} \end{pmatrix} \begin{pmatrix} x_{0,A} & x_{1,A} \\ p_{xg0,A} & p_{xg1,A} \end{pmatrix}^{-1} \quad (43)$$

$$G_{B,A} = \begin{pmatrix} x_{0,B} & x_{1,B} \\ p_{xg0,B} & p_{xg1,B} \end{pmatrix} \begin{pmatrix} x_{0,A} & x_{1,A} \\ p_{xg0,A} & p_{xg1,A} \end{pmatrix}^{-1} \quad (44)$$

By the above, given input data  $\overrightarrow{x_{g0,A}} = (x_{0,A}, p_{xg0,A})^T$  we know that the  $x_{n,A}$  orbit under  $G_{A,A}$  will match that of the observed orbit data set. By definition the  $x_{g0,B}$ , and  $x_{g1,B}$  values of the first two turns will also match the authentic data set, where:

$$\begin{pmatrix} x_{gn,B} \\ p_{xgn,B} \end{pmatrix} = G_{B,A} \begin{pmatrix} x_{n,A} \\ p_{xgn,A} \end{pmatrix} \quad (45)$$

If we could show that  $x_{g2,B}$  also matches the observed orbit data set, then the first 3  $x_{gn,B}$  values would match. This would then imply that the entire  $x_{gn,B}$  orbit matches the observed orbit data. Apply  $G_{B,A}$  to obtain the third x-value in the orbit:

$$\begin{pmatrix} x_{g2,B} \\ p_{xgn,B} \end{pmatrix} = \begin{pmatrix} x_{0,B} & x_{1,B} \\ p_{xg0,B} & p_{xg1,B} \end{pmatrix} \begin{pmatrix} x_{0,A} & x_{1,A} \\ p_{xg0,A} & p_{xg1,A} \end{pmatrix}^{-1} \begin{pmatrix} x_{2,A} \\ p_{xg2,A} \end{pmatrix} \quad (46)$$

By Eq.(24):

$$\begin{pmatrix} x_{0,A} & x_{1,A} \\ p_{xg0,A} & p_{xg1,A} \end{pmatrix}^{-1} \begin{pmatrix} x_{2,A} \\ p_{xg2,A} \end{pmatrix} = \begin{pmatrix} a \\ b \end{pmatrix} \quad (47)$$

Using Eq.(32), and Eq.(33) and plugging into Eq.(46) we get,

$$\begin{pmatrix} x_{g2,B} \\ p_{xgn,B} \end{pmatrix} = \begin{pmatrix} x_{0,B} & x_{1,B} \\ p_{xg0,B} & p_{xg1,B} \end{pmatrix} \begin{pmatrix} -1 \\ \frac{x_{0,A}+x_{2,A}}{x_{1,A}} \end{pmatrix} \quad (48)$$

Explicitly showing that  $x_{g2,B}$  depends only on  $x_{0,B}$ ,  $x_{1,B}$ ,  $x_{0,A}$ ,  $x_{1,A}$ , and  $x_{2,A}$  but is completely independent of all  $A$  and  $B$  momenta. As all of these  $x$  values match the authentic data, it follows that  $x_{g2,B} = x_{2,B}$  and therefore  $x_{gn,B} = x_{n,B} \forall n$ .

Thus we have shown that the matrices  $G_{A,A}(p_{x0,A}, p_{x1,A}, p_{x0,B})$ , and  $G_{B,A}(p_{x0,A}, p_{x1,A}, p_{x0,B})$  given in Eq.(43) and Eq.(44) are symplectic and could

produce the observed  $x_n$ -orbits at both  $BPM_A$  and  $BPM_B$  for any choice of the values  $p_{x_0,A}, p_{x_1,A}$ , and  $p_{x_0,B}$ . Therefore the observable  $x$ -orbit data from 2  $BPM$ s is insufficient to determine the matrices  $M_{A,A}$  and  $M_{B,A}$  and leaves the global number of undetermined parameters in these matrices at  $\mathcal{D} = 3$ .

### Extension to Multiple BPMs

We may extend this result to multiple  $BPM$ s by proceeding inductively. Take, for example, a storage ring consisting of 3  $BPM$ s. By the above, we need only consider a single orbit data set in the following.

Looking first at only  $BPM_A$  and  $BPM_B$  construct the matrices  $G_{A,A}$  and  $G_{B,A}$  using Eq.(43) and Eq.(44). Now construct  $G_{C,B}$  by randomly choosing  $p_{xg_0,C}$ :

$$G_{C,B} = \begin{pmatrix} x_{0,C} & x_{1,C} \\ p_{xg_0,C} & p_{xg_1,C} \end{pmatrix} \begin{pmatrix} x_{0,B} & x_{1,B} \\ p_{xg_0,B} & p_{xg_1,B} \end{pmatrix}^{-1} \quad (49)$$

Where  $p_{xg_1,B}$  is given by Eq.(42) and the symplectic condition on  $G_{C,B}$  gives  $p_{xg_1,C}$ :

$$p_{xg_1,C} = \frac{x_{1,C}}{x_{0,C}} p_{xg_0,C} - \frac{x_{1,B}}{x_{0,C}} p_{xg_0,B} + \frac{x_{0,B}}{x_{0,C}} p_{xg_1,B} \quad (50)$$

The symplectic condition on  $G_{A,A}$ ,  $G_{B,A}$  and  $G_{C,B}$  reduces the number of unknown parameters to 4. Similar to the above we can see that no matter what our choice is for these 4 parameters, we will generate a consistent set of symplectic matrices which could generate orbits with  $x_n$ -orbits matching that of the observed orbit data set. As the  $x$  data from the orbit data set is all the information we know, we cannot possibly reduce the number unknown parameters specifying the system to less than 4.

Continuing in this fashion we obtain the following result: The constraints supplied by the observable data from  $N$   $BPM$ s alone are insufficient to determine the symplectic matrices  $M_{A,A}$ ,  $M_{B,A}$ , ...,  $M_{N,N-1}$  and leaves the global number of unknown parameters specifying these matrices at  $\mathcal{D} = N + 1$ .

### 2.3 Results in Terms of Standard Parameters

In this section we will quickly describe the work above in terms of the machine parameters we are interested in determining, namely the  $\alpha$ 's,  $\beta$ 's, and  $\mu$ 's.

The only parameters that can be determined from the observable data alone are the  $\mu$ 's. We can see intuitively that  $\mu_A = \mu_B = \mu_C = \dots \equiv \mu$  and this can be proven mathematically without too much difficulty. To find  $\mu$  from the  $x$  data one need only set up the recursion relation Eq.(25) and solve for the roots of its characteristic equation. These roots will have the form  $e^{\pm i\mu}$ .

From Eq.(13), we see that  $\max|x_{m,A}| = \sqrt{\beta_A l}$  and  $\max|x_{m,B}| = \sqrt{\beta_B l}$ . From these two we may write:  $\beta_B = \left(\frac{\max|x_{m,B}|}{\max|x_{m,A}|}\right)^2 \beta_A$ . Similarly, we may write  $\beta_C$  in terms of  $\beta_A$  and so on. Therefore once  $\beta_A$  is specified, all other  $\beta$ s can be determined from the orbit data.

If there are  $N$  *BPMs* in our storage ring, then by the above, the measurable orbit data leaves  $N + 1$  parameters unspecified. Note that in terms of the  $\alpha_A, \alpha_B, \alpha_C, \dots, \beta_A, \beta_B, \beta_C, \dots$ , and  $\mu$  parameters, we have already reduced the number required to specify them all to  $N + 1$ , those being the  $N$   $\alpha$ s, (one at each *BPM*) and  $\beta_A$ . As these parameters completely specify our system, this must mean that the  $N$   $\alpha$ s and  $\beta_A$  are unspecified by the data and are independent: even if you somehow knew  $N$  of the parameters  $\alpha_A, \alpha_B, \dots, \alpha_N$ , and  $\beta_A$ , you still could not determine the  $N + 1^{\text{st}}$  from the observable data alone.

Note: To provide some physical intuition as to why we cannot determine all the parameters  $\alpha_A, \alpha_B$ , etc., consider a lattice with just a single *BPM*. We can measure only the  $x$ -orbit values and not the momenta. But the values  $x_n$  are simply given by,  $x_n = \sqrt{\beta_A} x_n^N$ , which is completely independent on  $\alpha_A$  and so we cannot hope (at least in the single *BPM* case) to get at  $\alpha_A$  from this data.

## 2.4 Approximate Solution

As we cannot determine the matrices  $M_{A,A}, M_{B,A}$ , etc. from the measurable data alone, we must resort to approximate solution techniques. A reasonable approximation can be obtained for 2 or more *BPMs* when the *BPMs* are spaced close to one another around the ring. We may approximate the transverse motion of the particle beam between the quadrupole magnets as being essentially a drift:

$$D = \begin{pmatrix} 1 & \delta \\ 0 & 1 \end{pmatrix} \quad (51)$$

where  $\delta$  is determined by measuring the distance between the two magnets. Meanwhile, as the beam passes by one of the quadrupole magnets it is either focused or defocused:

$$F_x = \begin{pmatrix} 1 & 0 \\ -k & 1 \end{pmatrix} \quad (52)$$

$$F_y = \begin{pmatrix} 1 & 0 \\ k & 1 \end{pmatrix} \quad (53)$$

$F_x$  represent an  $x$ -focusing matrix,  $F_y$  represents an  $x$ -defocusing matrix. If we approximate the matrix  $M_{B,A}$  as a product of these 3 types of matrices we can then easily determine  $M_{A,A}$ . Assuming  $M_{B,A}$  known:

$$\begin{aligned} M_{B,A} &= \begin{pmatrix} a & b \\ c & d \end{pmatrix} \rightarrow \\ \begin{pmatrix} a & b \\ c & d \end{pmatrix} \begin{pmatrix} x_{n,A} \\ px_{n,A} \end{pmatrix} &= \begin{pmatrix} x_{n,B} \\ px_{n,B} \end{pmatrix} \rightarrow \\ px_{n,A} &= \frac{1}{b}x_{n,B} - \frac{a}{b}x_{n,A} \end{aligned} \quad (54)$$

Plugging these momenta values into Eq.(34) we obtain  $M_{A,A}$  and the entire set of parameters is determined.

## 2.5 A Note on Rational Tunes

The results above assumed that the tune  $\nu = \frac{\mu}{2\pi}$  is irrational. As I mentioned before, this is the case in PEP-II as a rational tune would result in nonlinear resonance effects. However, if one chose a rational tune which would result in very large periods, e.g.  $\nu \equiv \frac{1}{10^{50}} \pmod{1}$ , then the resonance effects would be minimal. If  $\nu$  were chosen so, would it then be possible to determine the map  $M_{A,A}$ ? We prove below that it is not:

Assume that for some 1-turn map  $M_{A,A}$  with rational tune  $\nu$  you could determine the matrix  $M_{A,A}$  using only the observable data. The set of irrationals is dense in the set of reals and therefore we may find an irrational  $\nu_2$  infinitely close to  $\nu$ . Consider now a second 1-turn map  $M_{A,A,2}$  which is identical to  $M_{A,A}$  except that its tune is  $\nu_2$  rather than  $\nu$ . The orbit data you would measure under  $M_{A,A,2}$  would be infinitely close to that from  $M_{A,A}$  and therefore you would be able to use the same technique used to determine  $M_{A,A}$  to get an approximation to  $M_{A,A,2}$  which is infinitely accurate, if not exact. However, we have shown above that it is not possible to accurately determine the matrix  $M_{A,A,2}$  and therefore our original assumption must be wrong: it is not possible to determine the matrix  $M_{A,A}$  for any rational tune  $\nu$ . (further it's not possible to accurately determine anything with a rational  $\nu$  that you couldn't with an irrational  $\nu$ .) This result can easily be extended to lattices with multiple *BPMs* and applies to 2-dimensional lattices as well.

## 3 Two-Dimensional Case

We can now apply what we have learned from the 1-Dimensional lattice problem above to the more relevant 2-Dimensional problem which describes the lattice in PEP-II. In section 3.1 we shall look at what can be determined from data from a single *BPM* alone, in section 3.2 we will analyze lattices containing 2 or more *BPM's*, and in section 3.3 we will discuss how many *BPMs* are required to determine the machine parameters when the matrices  $M_{B,A}$ ,  $M_{C,B}$ , etc. are assumed known.

### 3.1 Single BPM Analysis

In this section we shall prove that given  $x$  and  $y$  orbit data from a single *BPM* it is impossible to determine the 1-turn map  $M_{A,A}$  and that there are 8 degrees of freedom left unspecified by the data alone.

## Symplectic Matrices Revisited

A 4x4 symplectic matrix  $M$  is defined as one such that:

$$M^T S_{4x4} M = S_{4x4} \quad (55)$$

where,

$$S_{4x4} \equiv \begin{pmatrix} S_{2x2} & 0_{2x2} \\ 0_{2x2} & S_{2x2} \end{pmatrix} \quad (56)$$

It can be shown [3] that in the 2-dimensional case the symplectic matrices  $M_{N,M}$  can be decomposed in a form analogous to that in Eq.(5):

$$\begin{aligned} M_{N,M} &= \tilde{A}_N R_{N,M} \tilde{A}_M^{-1} \\ &= C_N A_N R_{N,M} A_M^{-1} C_M^{-1} \end{aligned} \quad (57)$$

where  $R_{N,M}$ ,  $A_M$ , and  $C_M$  have the following forms:

$$R_{N,M} = \begin{pmatrix} R_{xN,M} & 0_{2x2} \\ 0_{2x2} & R_{yN,M} \end{pmatrix} \quad (58)$$

$$A_M = \begin{pmatrix} A_{x,M} & 0_{2x2} \\ 0_{2x2} & A_{y,M} \end{pmatrix} \quad (59)$$

$$C_M = \begin{pmatrix} I_{2x2} \cos \phi & -S_{2x2} W^T S_{2x2} \sin \phi \\ -W \sin \phi & I_{2x2} \cos \phi \end{pmatrix} \quad (60)$$

$R_{xN,M}$ ,  $R_{yN,M}$ ,  $A_{xM}$ , and  $A_{yM}$  have the same form as those in Eq.(6) and  $W$  is a  $2x2$  matrix:

$$W = \begin{pmatrix} a & b \\ c & d \end{pmatrix} \quad (61)$$

If we assume that all elements of  $W$  are nonzero, it can be shown that we can choose  $d \equiv d(a, b, c)$  such that  $C$  is symplectic. Thus there are 10 unknown parameters specifying the symplectic matrix  $M_{A,A}$ :

$$\alpha_x, \beta_x, \alpha_y, \beta_y, \mu_x, \mu_y, \phi, a, b, \text{ and } c$$

In addition to these 10, there are 4 unknown parameters describing errors in how the *BPM* measures the position of the beam. These are  $g_x$ ,  $g_y$ ,  $\theta_{x,y}$ , and  $\theta_{y,x}$  and they are defined as follows: if the actual transverse position of the beam is  $(x, y)$  then the *BPM* will read out:

$$\begin{aligned} x_R &= g_x x + \theta_{xy} y \\ y_R &= g_y y + \theta_{yx} x \end{aligned} \quad (62)$$

This brings the number of unknown parameters specifying the measurement error and the one turn map at  $BPM_A$  to 14.

Looking back at the decomposition Eq.(57), we see that  $C_M^{-1}$  transforms into an uncoupled space, consisting of two  $2x2$  subspaces, the  $x^U-p_x^U$  and  $y^U-p_y^U$

eigenplanes (the  $U$  superscript denoting the uncoupled space). Thus in this space the orbits may be decomposed as the conjunction of two independent 1-Dimensional lattice orbits, one in each eigenplane. Again the matrix  $A_M^{-1}$  transforms into the normalized space in which the orbits in each eigenplane are circular.

### Number of Independent Orbits

In this section we shall demonstrate that it is possible to manipulate an orbit data set by normalizing its two independent 1-dimensional orbits in the normalized space so that the new normalized orbit data set will be contained in a second orbit data set. For simplicity, we shall ignore the measurement errors associated with the parameters  $g_x$ ,  $g_y$ ,  $\theta_{x,y}$ , and  $\theta_{y,x}$  in this section. However, it can easily be seen that the same method described below is still applicable when these parameters are included. We begin by describing the normalization process:

In the normalized space we have,

$$\begin{pmatrix} x_n^N \\ p_{x_n}^N \end{pmatrix} = \begin{pmatrix} \cos n\mu_x & \sin n\mu_x \\ -\sin n\mu_x & \cos n\mu_x \end{pmatrix} \begin{pmatrix} x_0^N \\ p_{x_0}^N \end{pmatrix} \quad (63)$$

Multiplying on the left by  $A_x$  we must have,

$$\begin{pmatrix} x_n^U \\ p_{x_n}^U \end{pmatrix} = \begin{pmatrix} s & t \\ u & v \end{pmatrix} \begin{pmatrix} \cos n\mu_x \\ \sin n\mu_x \end{pmatrix} \quad (64)$$

for some constants  $s$ ,  $t$ ,  $u$ , and  $v$ . Similarly we have,

$$\begin{pmatrix} y_n^U \\ p_{y_n}^U \end{pmatrix} = \begin{pmatrix} w & x \\ y & z \end{pmatrix} \begin{pmatrix} \cos n\mu_y \\ \sin n\mu_y \end{pmatrix} \quad (65)$$

for some constants  $w$ ,  $x$ ,  $y$ , and  $z$ . Multiplying  $\vec{x}_n^U = (x_n^U, p_{x_n}^U, y_n^U, p_{y_n}^U)^T$  on the left by  $C_A$  we obtain:

$$x_n = j \cos n\mu_x + k \sin n\mu_x + l \cos n\mu_y + m \sin n\mu_y \quad (66)$$

$$y_n = n \cos n\mu_x + o \sin n\mu_x + p \cos n\mu_y + q \sin n\mu_y \quad (67)$$

$j$ ,  $k$ ,  $l$ ,  $m$ ,  $n$ ,  $o$ ,  $p$ , and  $q$  all constants. To determine these coefficients we must first find the values of  $\mu_x$  and  $\mu_y$ . These can be determined by setting up a recursion relation like that in Eq.(25) and then solving for the roots of its characteristic equation. Once the values of  $\mu_x$  and  $\mu_y$  are known we can determine the coefficients  $j$ ,  $k$ ,  $l$ ,  $m$ ,  $n$ ,  $o$ ,  $p$ , and  $q$  using the first 4 positions of the orbit. Noting the form of  $C_A$  and  $A_A$ , we must have:

$$j \cos n\mu_x + k \sin n\mu_x = \cos \phi \sqrt{\beta_x} x_n^N \quad (68)$$

$$p \cos n\mu_y + q \sin n\mu_y = \cos \phi \sqrt{\beta_y} y_n^N \quad (69)$$

Writing,  $|(x_n^N, p_{x_n^N})^T| \equiv l_x$  and  $|(y_n^N, p_{y_n^N})^T| \equiv l_y$  (which are independent of  $n$  as the normalized orbit in each eigenplane lies on a circle) and recalling that  $\mu_x$  and  $\mu_y$  are irrational we must have:

$$\max(j \cos n\mu_x + k \sin n\mu_x) = |\cos \phi| \sqrt{\beta_x} l_x \quad (70)$$

and,

$$\max(p \cos n\mu_y + q \sin n\mu_y) = |\cos \phi| \sqrt{\beta_y} l_y \quad (71)$$

Considering now a second orbit data set  $\vec{X}_n = (X_n, P_{x_n}, Y_n, P_{y_n})^T$ , we have:

$$X_n = J \cos n\mu_x + K \sin n\mu_x + L \cos n\mu_y + M \sin n\mu_y \quad (72)$$

$$Y_n = N \cos n\mu_x + O \sin n\mu_x + P \cos n\mu_y + Q \sin n\mu_y \quad (73)$$

with,

$$\max(J \cos n\mu_x + K \sin n\mu_x) = \cos \phi \sqrt{\beta_x} L_x \quad (74)$$

$$\max(P \cos n\mu_y + Q \sin n\mu_y) = \cos \phi \sqrt{\beta_y} L_y \quad (75)$$

Dividing Eq.(70) by Eq.(74) and Eq.(71) by Eq.(75) we obtain,

$$\frac{\max(j \cos n\mu_x + k \sin n\mu_x)}{\max(J \cos n\mu_x + K \sin n\mu_x)} = \frac{l_x}{L_x} \equiv r_x \quad (76)$$

$$\frac{\max(p \cos n\mu_y + q \sin n\mu_y)}{\max(P \cos n\mu_y + Q \sin n\mu_y)} = \frac{l_y}{L_y} \equiv r_y \quad (77)$$

If we now multiply all terms of the orbit  $\vec{X}_n$  containing  $\mu_x$  by  $r_x$  and all terms containing  $\mu_y$  by  $r_y$ , we obtain a new orbit  $\vec{X}_n^*$ . For example the  $X_n^*$  orbit will be given by:

$$X_n^* = r_x J \cos n\mu_x + r_x K \sin n\mu_x + r_y L \cos n\mu_y + r_y M \sin n\mu_y \quad (78)$$

In effect, we have constructed another observable orbit,  $\vec{X}_n^*$ , s.t.  $|(X_n^{*N}, P_{x_n^{*N}})^T| = l_x$  and  $|(Y_n^{*N}, P_{y_n^{*N}})^T| = l_y$ . Thus in normalized space,  $(X_n^{*N}, P_{x_n^{*N}})^T$  is rotating around in a circle which has the same radius as the circular orbit  $(x_n^N, p_{x_n^N})^T$  and  $(Y_n^{*N}, P_{y_n^{*N}})^T$  is rotating around in a circle which has the same radius as the circular orbit  $(y_n^N, p_{y_n^N})^T$ .

The rotation angles  $\mu_x$  and  $\mu_y$  are always chosen not equal as this results in resonances. As they are both irrational, it can then be shown that there must be some  $j(k)$  such that:

$$|(X_0^{*N}, P_{x_0^{*N}})^T - (x_{j(k)}^N, p_{x_{j(k)}^N})^T| < 10^k \quad (79)$$

and,

$$|(Y_0^{*N}, P_{y_0^{*N}})^T - (y_{j(k)}^N, p_{y_{j(k)}^N})^T| < 10^k, \text{ for any } k \quad (80)$$

Multiplying on the left by  $C_A A_A$  we find,

$$\vec{x}_{j(k)}, \vec{x}_{j(k)+1}, \vec{x}_{j(k)+2}, \dots \simeq \vec{X}_0^*, \vec{X}_1^*, \vec{X}_2^*, \dots \quad (81)$$

where the two orbits will stay close for more turns the larger  $k$  is chosen. Thus the second normalized orbit is contained in the first.

Although the "normalization" process described here is not as simple as the scaling factor used in the 1-dimensional process, they amount to the same thing: we can take a single orbit data set and from it construct all others. This implies no new information about the map can be obtained by taking more data and again we need only consider one orbit data set when attempting to determine  $M_{A,A}$ .

### Construction of Guess Matrices

Consider a single orbit data set  $\overrightarrow{x_{0,R}}, \overrightarrow{x_{1,R}}, \dots$ . We shall construct a set of symplectic guess matrices  $G_{B,A}$  which produce the observed  $x_{0,R}, x_{1,R}, \dots$  and  $y_{0,R}, y_{1,R}, \dots$  orbits. Begin by randomly choosing  $g_x, g_y, \theta_{xy}$ , and  $\theta_{yx}$ . Inverting Eq.(62) we obtain:

$$\begin{pmatrix} x_{n,g} \\ y_{n,g} \end{pmatrix} = \frac{1}{g_{x,g}g_{y,g} - \theta_{xy,g}\theta_{yx,g}} \begin{pmatrix} g_{y,g} & -\theta_{xy,g} \\ -\theta_{yx,g} & g_{x,g} \end{pmatrix} \begin{pmatrix} x_{n,R} \\ y_{n,R} \end{pmatrix} \quad (82)$$

obtaining a guess at the actual position of the beam for each turn of the orbit. Now randomly choose the parameters determining the matrix  $C_A$ . These are:  $a, b, c$ , and  $\phi$  (recall  $d \equiv d(a, b, c)$ ).

$$C_{A,g} = \begin{pmatrix} I_{2x2} \cos \phi_g & -S_{2x2} W_g^T S_{2x2} \sin \phi_g \\ -W_g \sin \phi_g & I_{2x2} \cos \phi_g \end{pmatrix} \quad (83)$$

Similar to Eq.(66) and Eq.(67) we may decompose  $x_{n,g}$  and  $y_{n,g}$  as follows:

$$x_{n,g} = j \cos n\mu_x + k \sin n\mu_x + l \cos n\mu_y + m \sin n\mu_y \quad (84)$$

$$y_{n,g} = n \cos n\mu_x + o \sin n\mu_x + p \cos n\mu_y + q \sin n\mu_y \quad (85)$$

for some new constants  $j, k, l, m, n, o, p$ , and  $q$  which can again be solved for by using the first 4 positions of the orbit. From Eq.(57) and Eq.(60) we obtain,

$$x_{n,g} = \cos \phi_g x_{n,g}^U + d_g \sin \phi_g y_{n,g}^U - b_g \sin \phi_g p_{y_{n,g}}^U \quad (86)$$

$$y_{n,g} = \cos \phi_g y_{n,g}^U - a_g \sin \phi_g x_{n,g}^U - b_g \sin \phi_g p_{x_{n,g}}^U \quad (87)$$

comparison with Eq.(84) and Eq.(85) gives:

$$x_{n,g}^U = \frac{1}{\cos \phi_g} (j \cos n\mu_x + k \sin n\mu_x) \quad (88)$$

$$y_{n,g}^U = \frac{1}{\cos \phi_g} (p \cos n\mu_y + q \sin n\mu_y) \quad (89)$$

Plugging these back into Eq.(86) and Eq.(87),

$$\begin{aligned} p_{x_{n,g}}^U &= \frac{-1}{b_g \sin \phi_g} [n \cos n\mu_x + o \sin n\mu_x + a_g \frac{\sin \phi_g}{\cos \phi_g} (j \cos n\mu_x + k \sin n\mu_x)] \\ &= -[\frac{a_g j}{b_g \cos \phi_g} + \frac{n}{b_g \sin \phi_g}] \cos n\mu_x - [\frac{a_g k}{b_g \cos \phi_g} + \frac{o}{b_g \sin \phi_g}] \sin n\mu_x \\ &\equiv r \cos n\mu_x + s \sin n\mu_x \end{aligned} \quad (90)$$

Similarly we find:

$$\begin{aligned}
p_{y_{n,g}}^U &= \left[ \frac{d_g p}{b_g \cos \phi_g} - \frac{l}{b_g \sin \phi_g} \right] \cos n\mu_y + \left[ \frac{d_g q}{b_g \cos \phi_g} - \frac{m}{b_g \sin \phi_g} \right] \sin n\mu_y \\
&\equiv t \cos n\mu_x + u \sin n\mu_x
\end{aligned} \tag{91}$$

From  $x_{n,g}^U$  and  $p_{x_{n,g}}^U$  we obtain  $A_{x_g,A}$  and  $R_{x_g,A}$ . From  $y_{n,g}^U$  and  $p_{y_{n,g}}^U$  we obtain  $A_{y_g,A}$  and  $R_{y_g,A}$ . Now we can construct the entire guess matrix.

$$\begin{aligned}
G_{A,A} &\equiv G_{A,A}(g_{x,g}, \theta_{xy,g}, g_{y,g}, \theta_{yx,g}, a_g, b_g, c_g, \phi_g) \\
&= C_{A,g} A_{A,g} R_{A,G} A_{A,g}^{-1} C_{A,g}^{-1}
\end{aligned} \tag{92}$$

With the initial condition  $\overrightarrow{x_{0,g}} = C_{A,g}(x_{0,g}^U, p_{x_{0,g}}^U, y_{0,g}^U, p_{y_{0,g}}^U)^T$  we see by working backwards from Eq.(90) and Eq.(91) that the symplectic matrices  $G_{A,A}$ , given by Eq.(92), will all produce the same  $x_n$  and  $y_n$  orbits as those in the observed orbit data set. As 8 parameters are randomly chosen to obtain the  $G_{A,A}$ , the  $x$ -orbit data from a single  $BPM$  alone must be insufficient to determine the 1-turn map  $M_{A,A}$ . Further we must have  $\mathcal{D} = 8$  exactly as all the remaining  $14 - 8 = 6$  parameters are uniquely determined once these 8 are specified.

### 3.2 Multiple BPM Analysis

We begin by considering a 2-Dimensional lattice consisting of 2  $BPM$ s. Again we shall show that the constraints supplied by the observable data are insufficient to determine the matrices  $M_{A,A}$ , and  $M_{B,A}$ . We shall then extend this result to the general storage ring consisting of  $N$   $BPM$ s.

#### Number of Independent Orbits

To show that we need only consider a single orbit data set we may use the same argument as was used in the 1-dimensional lattice case.

Consider two orbit data sets, each consisting of the  $x$  and  $y$  data from  $BPM_A$  and  $BPM_B$ :

$$\text{set1} : (\overrightarrow{x_{0,A}}, \overrightarrow{x_{1,A}}, \dots; \overrightarrow{x_{0,B}}, \overrightarrow{x_{1,B}}, \dots) \quad \text{set2} : (\overrightarrow{X_{0,A}}, \overrightarrow{X_{1,A}}, \dots; \overrightarrow{X_{0,B}}, \overrightarrow{X_{1,B}}, \dots)$$

Looking first at only the data from  $BPM_A$  we may normalize the second orbit data set, obtaining a new one,  $(\overrightarrow{X_{0,A}^*}, \overrightarrow{X_{1,A}^*}, \dots, \overrightarrow{X_{0,B}^*}, \overrightarrow{X_{1,B}^*}, \dots)$ , which is contained in the first:

$$\overrightarrow{x_{j(k),A}}, \overrightarrow{x_{j(k)+1,A}}, \overrightarrow{x_{j(k)+2,A}}, \dots \simeq \overrightarrow{X_{0,A}^*}, \overrightarrow{X_{1,A}^*}, \overrightarrow{X_{2,A}^*}, \dots \tag{93}$$

as in the above. Now multiplying on the left by  $M_{B,A}$  we obtain:

$$\begin{aligned}
M_{B,A} \overrightarrow{x_{j(k),A}}, M_{B,A} \overrightarrow{x_{j(k)+1,A}}, \dots &= \overrightarrow{x_{j(k),B}}, \overrightarrow{x_{j(k)+1,B}}, \dots \\
&\simeq M_{B,A} \overrightarrow{X_{0,A}^*}, M_{B,A} \overrightarrow{X_{1,A}^*}, \dots = \overrightarrow{X_{0,B}^*}, \overrightarrow{X_{1,B}^*}, \dots \rightarrow \\
\overrightarrow{x_{j(k),B}}, \overrightarrow{x_{j(k)+1,B}}, \overrightarrow{x_{j(k)+2,B}}, \dots &\simeq \overrightarrow{X_{0,B}^*}, \overrightarrow{X_{1,B}^*}, \overrightarrow{X_{2,B}^*}, \dots
\end{aligned} \tag{94}$$

showing that the 2nd orbit is contained in the first at  $BPM_B$  as well. This argument can be extended to any number of  $BPM$ s by proceeding inductively. In general we see that for 2-dimensional lattices it is possible to normalize an orbit data set so that it will be contained in another. As a single orbit data set contains all others (up to this normalization), this implies we need only consider one when attempting to determine the matrices  $M_{A,A}$ ,  $M_{B,A}$ ,  $M_{C,B}$ , etc..

### Construction of Guess Matrices

Consider a single orbit data set  $\overrightarrow{x_{A0,R}}, \overrightarrow{x_{A1,R}}, \dots, \overrightarrow{x_{B0,R}}, \overrightarrow{x_{B1,R}}, \dots$ . Using only the data from  $BPM_A$  we could proceed as in the above and find a family of matrices which could produce the observed data at  $BPM_A$ . Similarly using the data from  $BPM_B$  we could find another family of matrices which produce the observed data at  $BPM_B$ . For each choice of the symplectic guess matrices  $G_{A,A}$  and  $G_{B,B}$  we obtain a different guess at the actual phase space orbits of the beam and thus a different guess matrix  $G_{B,A}$ ,

$$G_{B,A} = (\overrightarrow{x_{B,0}}, \overrightarrow{x_{B,1}}, \overrightarrow{x_{B,2}}, \overrightarrow{x_{B,3}})(\overrightarrow{x_{A,0}}, \overrightarrow{x_{A,1}}, \overrightarrow{x_{A,2}}, \overrightarrow{x_{A,3}})^{-1} \quad (95)$$

(the fact that  $G_{B,A}$  will map the entire orbit at  $A$  to the orbit at  $B$  can be shown easily, by considering the map in the uncoupled space.) We must apply the symplectic condition to  $G_{B,A}$  to determine which of the  $G_{A,A}$  and  $G_{B,B}$  are valid guesses. We may simplify the application of the symplectic condition to these matrices by first factoring them. Note that we can decompose the  $G_{B,A}$  in the following form,

$$G_{B,A} = \tilde{A}_{B,g} U \tilde{A}_{A,g}^{-1} = C_{B,g} A_{B,g} U A_{A,g}^{-1} C_{A,g}^{-1} \quad (96)$$

for some matrix  $U$  as the matrices  $A_g$  and  $C_g$  are all invertible. By definition:

$$\begin{aligned} G_{A,A} &= G_{B,A}^{-1} G_{B,B} G_{B,A} \rightarrow \\ C_{A,g} A_{A,g} R_{A,A} A_{A,g}^{-1} C_{A,g}^{-1} &= G_{B,A}^{-1} C_{B,g} A_{B,g} R_{B,B} A_{B,g}^{-1} C_{B,g}^{-1} G_{B,A} \quad (97) \end{aligned}$$

Plugging in Eq.(96) we get:

$$R_{A,A} = U^{-1} R_{B,B} U \quad (98)$$

The rotations  $R_{A,A}$  and  $R_{B,B}$  share the same 4 eigenvectors, namely:  $(1, \pm i, 0, 0)^T$  and  $(0, 0, 1, \pm i)^T$ . As these matrices are similar under  $U$  it follows that  $U$  maps this set of eigenvectors to itself modulo some scalar factors. Further, as  $U$  is real, it maps complex conjugate vectors to complex conjugate vectors. Therefore either  $U(1, \pm i, 0, 0)^T = a(1, \pm i, 0, 0)^T$  or  $U(1, \pm i, 0, 0)^T = a(0, 0, 1, \pm i)^T$ . However, we know that  $G_{B,A}$  will not swap the  $x - p_x$  and  $y - p_y$  eigenplanes implying that  $U(1, \pm i, 0, 0)^T = a(1, \pm i, 0, 0)^T$  and similarly  $U(0, 0, 1, \pm i)^T = b(0, 0, 1, \pm i)^T$  so that  $U$  is block diagonal.

$$U = \begin{pmatrix} U_x & 0_{2 \times 2} \\ 0_{2 \times 2} & U_y \end{pmatrix} \quad (99)$$

We may now easily apply the symplectic condition to the matrices  $G_{B,A}$ . The  $C_g$  and  $A_g$  matrices are symplectic by construction. Therefore by Eq.(96), requiring  $G_{B,A}$  symplectic is equivalent to requiring the block diagonal matrix  $U_g$  to be symplectic. Plugging in Eq.(99) to Eq.(55), we see this is equivalent to requiring each of the diagonal matrices of  $U$  to be symplectic. Thus we get the following two symplectic constraints:

$$\det U_{g,x} = \det \begin{pmatrix} x_{0,g} & x_{1,g} \\ p_{x0,g} & p_{x1,g} \end{pmatrix}_B \begin{pmatrix} x_{0,g} & x_{1,g} \\ p_{x0,g} & p_{x1,g} \end{pmatrix}_A^{-1} = 1 \quad (100)$$

$$\det U_{g,y} = \det \begin{pmatrix} y_{0,g} & y_{1,g} \\ p_{y0,g} & p_{y1,g} \end{pmatrix}_B \begin{pmatrix} y_{0,g} & y_{1,g} \\ p_{y0,g} & p_{y1,g} \end{pmatrix}_A^{-1} = 1 \quad (101)$$

Applying these constraints we obtain the symplectic matrices  $G_{A,A}$  and  $G_{B,B}$  which are consistent with a symplectic map  $G_{B,A}$  and produce the observed orbit data. As 14 parameters are randomly chosen to obtain these matrices (8 from each of the two 1-turn maps, minus 2 due to the symplectic conditions, Eq.(100) and Eq.(101)), the  $x$ -orbit data from 2  $BPM$ s alone must be insufficient to determine the maps  $M_{A,A}$  and  $M_{B,A}$ . Further  $\mathcal{D} = 14$  exactly as the remaining  $28 - 14 = 14$  parameters are uniquely determined once these 14 are chosen.

### Extension to Multiple BPMs

The extension to a lattice with  $N$   $BPM$ s follows very easily. By the above we need only consider a single orbit data set,

$$\overrightarrow{x_{A0,R}}, \overrightarrow{x_{A1,R}}, \dots; \overrightarrow{x_{B0,R}}, \overrightarrow{x_{B1,R}}, \dots; \dots; \overrightarrow{x_{N0,R}}, \overrightarrow{x_{N1,R}}, \dots,$$

when attempting to determine the matrices  $M_{A,A}, M_{B,A}, \dots, M_{N,N-1}$ . We may construct with 8 degrees of freedom each, the matrices  $G_{A,A}, G_{B,B}, \dots$ , and  $G_{N,N}$ . Applying the  $2(N-1)$  symplectic constraint equations similar to Eq.(100) and Eq.(101) on the matrices  $G_{B,A}, G_{C,B}, \dots, G_{N,N-1}$ , we are left with the infinite set of matrices  $G_{A,A}, \dots, G_{N,N}$ , which are consistently symplectic and produce the observed  $x_n$  and  $y_n$  orbit data. The constraints supplied by the observable data are again insufficient to determine the matrices  $M_{A,A}, M_{B,A}, \dots, M_{N,N-1}$  and leave the global number of undetermined parameters in these matrices at  $\mathcal{D} = 8N - 2(N-1) = 6N + 2$ .

### 3.3 Approximate Solution and Future Work

For a 2-dimensional lattice consisting of  $N$   $BPM$ s, we saw above that the observable data supplies an insufficient number of constraints to specify correctly the matrices  $M_{A,A}, M_{B,A}, \dots, M_{N,N-1}$ . We must therefore turn to the method described in section 2.4 to determine these matrices.

Suppose we have  $x$  and  $y$ -orbit data from both  $BPM_A$  and  $BPM_B$  and further that we have knowledge of the symplectic matrix  $M_{B,A}$ . As there are 10 independent elements in a  $4 \times 4$  symplectic matrix, knowledge of  $M_{B,A}$  supplies

10 constraint equations. However, the system is still under-constrained as the observable data leaves the number of unknown parameters at  $\mathcal{D} = 14$ . Therefore, even if  $M_{B,A}$  is known, we still cannot determine  $M_{A,A}$ ; a result which differs from its 1-dimensional analog.

If we have  $x$  and  $y$ -orbit data from 3 *BPMs* and knowledge of both  $M_{B,A}$  and  $M_{C,B}$  it may then be possible to determine the matrix  $M_{A,A}$ : The observable data leaves the number of unknown parameters at  $\mathcal{D} = 20$  but we also obtain 20 additional constraint equations from knowledge of  $M_{B,A}$  and  $M_{C,B}$ . Although it may be theoretically possible to determine  $M_{A,A}$  using just 3 *BPMs*, an over-constrained system would be preferable as the use of some least squares fitting approach would enable the reduction of error. Therefore we have proven that 3 is a lower bound on the number of *BPMs* required to have a properly constrained system while we recommend 4 as the minimum to be used in practice.

The use of 4 *BPMs* will soon be tested numerically here at SLAC. Pending those results, 2 new *BPMs* may be installed near the interaction point of the LER and HER rings, in the hope that using a localized measurement approach in conjunction with the current global scheme may improve beam position measurements and ultimately increase the efficiency of the machine.

## 4 Acknowledgements

I would like to thank my advisor, Dr. Yiton Yan, who has been an excellent mentor, Dr. James Lindesay and Dr. Helen Quinn, the directors of the SULI program here at SLAC, Deji Akinwande, Dr. Tom Knight, and William Colocho, who have all helped me in various ways this summer, and lastly, the United States Department of Energy - Office of Science for providing funding towards what has been for me a very rewarding and educational summer internship.

## References

- [1] Y. T. Yan, Y. Cai, F-J. Decker, et. al., *Virtual Accelerator for Accelerator Optics Improvement*. SLAC-PUB-11209, May 2005
- [2] Robert L. Devaney, *An Introduction to Chaotic Dynamical Systems*. Westview Press, Massachusetts, 2nd Edition, 2003.
- [3] Philip Tanedo, *Modeling of the Transverse Linear Optics of a Charged Particle Storage Ring*. SLAC-TN-03-016, Sep 2003.
- [4] Y. T. Yan, *The Use of Lie Algebra Methods to Analyze and Design Accelerator Beamlines. Notes from the U.S. Particle Accelerator School; Rice University, Houston, Texas*. January, 2001.

**Relative Humidity in Limited Streamer Tubes for Stanford Linear Accelerator Center's  
BABAR Detector**

Mary-Irene Lang

Office of Science, Science Undergraduate Laboratory Internship Program

Massachusetts Institute of Technology

Stanford Linear Accelerator Center

Stanford, California

August 19, 2005

Prepared in partial fulfillment of the requirements of the Office of Science, U.S. Department of Energy Science Undergraduate Laboratory Internship (SULI) Program under the direction of Dr. Mark Convery and Dr. Wolfgang Menges in the BABAR Experiment at the Stanford Linear Accelerator Center.

Participant: \_\_\_\_\_

Signature

Research Advisors: \_\_\_\_\_

\_\_\_\_\_  
Signatures

## Table of Contents

Abstract	iii
Introduction	1
Materials and Methods	3
Results	6
Discussion and Conclusions	9
Acknowledgements	10
References	11
Tables	12
Figures	13

## ABSTRACT

Relative Humidity in Limited Streamer Tubes for Stanford Linear Accelerator Center's BABAR Detector. MARY-IRENE LANG (Massachusetts Institute of Technology, Cambridge, MA 02139) MARK CONVERY (Stanford Linear Accelerator Center, Stanford, CA 94309) WOLFGANG MENGES (Queen Mary, University of London, London, UK).

The BABAR Detector at the Stanford Linear Accelerator Center studies the decay of B mesons created in  $e^+e^-$  collisions. The outermost layer of the detector, used to detect muons and neutral hadrons created during this process, is being upgraded from Resistive Plate Chambers (RPCs) to Limited Streamer Tubes (LSTs). The standard-size LST tube consists of eight cells, where a silver-plated wire runs down the center of each. A large potential difference is placed between the wires and ground. Gas flows through a series of modules connected with tubing, typically four. LSTs must be carefully tested before installation, as it will be extremely difficult to repair any damage once installed in the detector. In the testing process, the count rate in most modules showed was stable and consistent with cosmic ray rate over an approximately 500 V operating range between 5400 to 5900 V. The count in some modules, however, was shown to unexpectedly spike near the operation point. In general, the modules through which the gas first flows did not show this problem, but those further along the gas chain were much more likely to do so. The suggestion was that this spike was due to higher humidity in the modules furthest from the fresh, dry inflowing gas, and that the water molecules in more humid modules were adversely affecting the modules' performance. This project studied the effect of humidity in the modules, using a small capacitive humidity sensor (Honeywell). The sensor provided a humidity-dependent output voltage, as well as a temperature measurement from a thermistor. A full-size

hygrometer (Panametrics) was used for testing and calibrating the Honeywell sensors. First the relative humidity of the air was measured. For the full calibration, a special gas-mixing setup was used, where relative humidity of the LST gas mixture could be varied from almost dry to almost fully saturated. With the sensor calibrated, a set of sensors was used to measure humidity vs. time in the LSTs. The sensors were placed in two sets of LST modules, one gas line flowing through each set. These modules were tested for count rate v. voltage while simultaneously measuring relative humidity in each module. One set produced expected readings, while the other showed the spike in count rate. The relative humidity in the two sets of modules looked very similar, but it rose significantly for modules further along the gas chain.

## INTRODUCTION

The imbalance found in the universe between matter and antimatter is extremely remarkable: because matter and antimatter annihilate upon collision, equal quantities of the two would make the known universe impossible. Instead of galaxies, stars, life—all composed largely of matter—the universe would be filled with radiation resulting from the collision of matter and antimatter. The asymmetry in matter and antimatter is therefore truly fundamental, and, in fact, so familiar that to many it may seem obvious. From a theoretical standpoint, however, the difference in relative amounts is not easy to understand. The Stanford Linear Accelerator Center's BABAR experiment is studying the decays of B and  $\bar{B}$  mesons, hoping to gain insight into the problem.

BABAR studies the products of electron-positron collisions occurring at the site of a large detector, specifically B and anti-B mesons. As these mesons move through the detector they decay, leaving tracks in each of the detector's components. The tracks are then analyzed for information about the probabilities of a B "mixing" with a  $\bar{B}$  (i.e. changing quark content to become the anti-particle) before reaching the final state in the decay. The hope is that understanding differences in the decay rates will give insight into fundamental differences of matter and antimatter [1].

BABAR's detector consists of numerous layers to track different characteristics of the particles: an innermost silicon vertex detector, a drift chamber, a particle identification system, a cesium-iodide calorimeter, and a solenoidal magnet with instrumented flux-return (IFR) at the outermost layers. For those layers of the detector furthest from the initial collision, BABAR has been using Resistive Plate Chambers (RPCs) within the inter-iron gaps to detect muons and long lived neutral K-mesons. These chambers have suffered deterioration in performance over past few years and are being replaced by Limited Streamer Tube (LST) chambers in the barrel. Each

layer of the system consists of a set of up to 10 LST modules, providing the muon's coordinate. When a muon passes through a cell, it ionizes the gas and the resulting electron is accelerated towards the wire by the electric field. This electron in turn ionizes more gas molecules, resulting in a cascade of electrons and ions that is detected as a signal on the wire. Below each layer of modules, copper strips running orthogonal to the wires receive an induced signal to provide the z coordinate [2,3]. As it is difficult to access LST modules after they are in place, it is crucial to test them carefully before installation.

In the testing process, muons from cosmic rays were used in place of the muons that will be found in the detector. Ideally, as the voltage is incrementally increased up to 6000V, more and more muons are detected until muon count rates v. voltage reaches saturation (known as a plateau). Most modules have plateaus ~500 V wide. It was discovered, however, that some of the modules would plateau briefly, then the count number would spike upward dramatically for voltages above the operation point of 5500V. Figure 1 shows an extreme example of this behavior, with the spike already beginning at 5600V. As modules most likely to give unexpected readings are furthest from the inflow of gas, one suggested explanation is higher humidity in the modules furthest from the dry, inflowing gas. If water vapor inside the modules were to mix with the gas as it flowed from module to module, those modules furthest from the gas inflow would have higher humidity. At high voltage, it is possible that water molecules could interfere with the signal readout on the wire.

To test this, we configured and calibrated a set of humidity sensors for a set of modules in a gas line. We used a gas line filled with known (and variable) humidity to correlate the sensor's output voltage to the gas's relative humidity for one sensor, then assembled a set of sensors. We examined the voltage readings from each of these sensors to determine how the humidity varied

in each of the modules, and thus to see if humidity is a reasonable cause for the unusual spike in the number of counts.

## MATERIALS AND METHODS

The BABAR group's LST modules are built on a PVC "profile," which contain seven or eight 1.4 cm x 1.4 cm long cells. These cells are coated in graphite, with silver-plated wire strung down the length of each cell. The graphite provides a resistivity of between .2 and 1 M $\Omega$ /square. The wires are connected to a high voltage source of 5500V, and through each cell flows a gas mixture of 89% CO<sub>2</sub>, 8% Isobutane, and 3% Argon. Either two or three tubes are connected together to make a module, and gas flows through a series of modules, typically four (see Figure 2) [2,3].

The humidity sensor used is model HIH-3602-A from Honeywell. It consists of a planar capacitor housed in a TO-5 cylindrical case of 9.14 mm diameter and 6.60 mm height, with six 8.89-mm-long pins for input and output. The casing holds a silicon substrate, followed by layers of platinum, thermoset polymer, platinum, and second thermoset polymer, respectively (see Figure 3). A thermistor, suitable between 0° C and 50° C, is contained within the sensor casing [4].

The sensor was connected to an IC socket, soldered to six-wire cable and placed inside a 3/8-inch Teflon pipe plug with .4-inch hole drilled through the center. Heat-shrink tubing provided insulation—both on individual wires and over each cable—and Devcon 2-Ton Epoxy was used for gas-tightness. The pipe plug was screwed into a Tee gas fitting, which could be placed into the 1/4-inch Poly-Flo Tubing gas line. All cables were connected to a General Monitoring Board (GMB) extender board, and to allow each cable to be connected or removed individually the

cable was interrupted partway along its length with an inline connector made with Molex crimp pins and a Molex shroud (see Figures 4a,5, 6). The wiring map is shown in Table 1.

To calibrate the sensors, a Panametrics Hygrometer (System 5) was measured the relative humidity in a gas line containing the sensor. Feeding into the hygrometer gas line from a Quincy Labs model 12-140 incubator (see Figure 4b), dry gas could be mixed in controlled proportions with gas flowed through water at roughly 30° C—aimed to be near saturation. This was done in an attempt to keep the saturated gas at constant temperature, as gas bubbled through water at room temperature would have a dew point very near current room temperature. Therefore, to avoid difficulties arising from fluctuations in ambient temperature, the essentially saturated gas was kept at constant temperature.

The flow rates of wet and dry gas were used to estimate a desired relative humidity, which was then measured more accurately by the hygrometer. The hygrometer provided temperature and dew point data, and the National Weather Service Forecast Office’s website “Dewpoint” [5] was used to convert this information to relative humidity. Each sensor’s individual calibration was then used to determine the relative humidity. Eq. 1 shows this conversion, based on input ( $V_I$ ) and output ( $V_O$ ) voltage, thermistor compensation  $G$ , and the individual sensor’s particular slope ( $m$ , in mV/% RH) and offset ( $b$ , in V):

$$(Eq.1) \quad \text{Relative Humidity} = \frac{5000}{m} \left( \frac{V_O}{V_I} - \frac{b}{5} \right) \cdot G$$

The temperature correction  $G$  (equation supplied by the manufacturer) at a temperature  $T$  (in K) is given by the manufacturer as:

$$(Eq.2) \quad G = \left( \frac{1}{1.0546 - .00216 \cdot (T - 273.15)} \right)$$

This dependence is illustrated in Figure 10. Figure 10a shows the ratio of the corrected value to the original value, while Figure 10b shows the value for  $RH_{corrected} - RH_{initial}$ .

To determine the value of T, the thermistor was placed in series with a 100 kΩ resistor on the GMB (see Figure 7). The thermistor's resistance ( $R_T$ ) could therefore be calculated from the GMB voltage across the thermistor  $V_T$  and the input voltage  $V_I$ , as  $R_T / 100 \text{ k}\Omega = V_T / (V_I - V_T)$ . Thus, based on manufacturer's equation for dependence of  $R_T$  on temperature:

$$(Eq.3) \quad T = \left( \frac{4143}{\frac{4143}{298.15} + \ln\left(\frac{R_T}{100 \text{ k}\Omega}\right)} - 273.15 \right) = \left( \frac{4143}{\frac{4143}{298.15} + \ln\left(\frac{V_T}{V_I - V_T}\right)} - 273.15 \right)$$

$V_I$ ,  $V_O$ , and  $V_T$  were measurements made in the lab, while m and b were supplied by the manufacturer. In the final stages of verifying the manufacturer's calibration, 33% and 75% relative humidity calibration salts were used for greater accuracy at those values for relative humidity. This allowed for verification of the calibration at higher relative humidity than possible with the hygrometer.

For the electronic readout of the multi-sensor configuration, the GMB connected through a CAN Bus cable to an Input Output Controller (IOC), feeding the data into the Data Online Detector Control System. The readout interface was an Epics control panel, built into the existing system for monitoring the LSTs. The primary software programs used in analysis were StripTool, AmbientExplorer and Excel.

The supplied calibration was tested at a variety of values for relative humidity. For single sensors, a test board was created with BNC cable connectors to each output and to the requisite 5V input. For preliminary testing, sensor 98 was soldered in place on the board and epoxy used to secure a metal Tee gas fitting over the sensor. Further into the project, a small piece of cable was connected to the board with appropriate wiring to connect to the Molex shroud. Readings

were taken with a multimeter, and compared after calculation with the readings from the hygrometer.

For multiple sensors placed in a gas line, relative humidity in the gas line was varied and a representative equilibrium data point chosen for each sensor. The thermistor temperature correction was calculated from raw data, and the average value at each humidity calculated. To find the average, relative humidity for each sensor as calculated by Ambient was multiplied by the thermistor-compensation factor  $G$ .

Two models were employed to fit the data. In one, the individual sensors' relative humidity points were mapped to the average value based on a linear fit. In the other, each sensor's value for  $V_O/V_I$  was plotted against the same average values and a linear fit made for each sensor (see Figure 12, Table 2). The quality of the fits was compared using data taken at a later point in time and the one with the lowest average spread chosen for correct calibration (see Figure 11). Spread at any moment in time was calculated as  $Q = |\text{highest reading} - \text{lowest reading}| / (\text{average of all readings at that time})$ . The time average of all  $Q$ 's for the two methods was used to determine each method's spread with a data set.

Once calibration finished, the sensors were placed in the gas lines of the LSTs and relative humidity measured over time. Simultaneously, data was taken using the BABAR LST system to determine count rate v. voltage. Finally, the results were compared with data taken on a smaller LST connected in the hygrometer line. For these modules, the relative humidity of the gas in the modules was varied and the count rate graphed as voltage increased.

## RESULTS

Table 2 shows the calculated slopes and offsets for a best-fit line between voltage ratio and relative humidity. These were calculated for each individual sensor.

Figure 1 was taken from the BABAR LST database, and shows the number of counts detected by Module 1312 in each channel as the voltage is increased. There is one channel for every two cells. Data collection time was 100 seconds. (These measurements were taken prior to testing relative humidity.)

Figure 8 shows data taken for single-sensor relative humidity calibration before final modifications to the configuration. It shows the time evolution of the difference between the hygrometer and sensor readings, for a number of relative humidity values. Calculated humidity values were obtained using Eq. 1. Readings were recorded every three minutes. A response time of about 15 minutes was evident simply from visual interpretation of graphs.

Figure 9 shows one of the calibration curves used to relate relative humidity values measured with sensor 98 and the hygrometer. The sensor readings were plotted against the hygrometer ones (assumed correct for initial calibration) and a best-fit linear equation used to describe the correlation. Data for this graph were taken every three minutes. Data from the first 15 minutes after an adjustment in the gas were not used due to the observed sensor response time.

Figure 11 shows calibration corrections to data taken over 6 ½ hours with seven sensors simultaneously in the hygrometer line. The flow rates were adjusted twice, approximately 1590 and 6630 seconds after data collection began. The same raw data are used for both graphs, and then adjusted by the calculated slopes and offsets for best-fit lines from the two potential methods of calibration. The average value of  $Q$  for the humidity calibration is .054, and for the ratio calibration is .039.

Figure 12 shows two of seven voltage-ratio calibration curves for the multi-sensor configuration, with all sensors placed in the controlled-humidity hygrometer line. Eight representative data points were selected for each sensor, with data taken every 10 seconds and

subsequently averaged over 60 seconds. A linear fit was used to relate the ratio of input and output voltages to the average temperature-corrected value for relative humidity over all sensors at that time.

Figure 13 shows readings from two sets LST modules in a single gas chain: modules 454, 455, 457 & 456 in 12a and 23, 24, 1035 & 1058 in 12b. This data was taken using the existing data collection system at BABAR for measuring count rate v. voltage [6]. The set in 12a contains seven cells in each tube, and accordingly it is expected that the fourth channel—connected to only one tube instead of two—will measure roughly half the count rate of the other channels. The set of modules in 12b have channels all connected to two tubes. The fourth module in 12b is shown on a different scale for count rate to allow for relevant data from all channels to be viewed. (Channel four continues upward to a count rate of 70,121 at 5900V.) These module sets were selected based on a their history of count spikes, as one had previously shown a spike and the other had not.

Figure 14 shows humidity readings taken simultaneously with the data in Figure 13. Sensor 34 measured humidity before gas enters any of the modules. Sensor 57 measured input to the second module in the gas chain, sensor 98 to the third module, 99 output from the third module, 129 input to the fourth module, and 192 output from the fourth module. 219 was open to the atmosphere. The ordering of the modules in the gas chain for the first module set was 454, 455, 457, & 456 and for the second set was 1058, 1035, 23 & 24.

Figure 15 shows data taken by the BABAR LST group, running tests on a small LST placed in the hygrometer line at 19.45% and 28.99% relative humidity. Data were taken every 100 seconds. As with the measurements for Figure 13, the voltage was increased in 100V-increments from 4600-5900V, and the count rate measured.

## DISCUSSION AND CONCLUSION

By studying a single sensor on a test board, it was possible to determine the proper treatment of different elements in to the sensor configuration. Prior to final modifications it was difficult to extract meaningful data, as errors were significant and lacking consistency. It was noted that deviations from the hygrometer measurements increased with relative humidity, and that a linear fit was able to provide a good model for sensor readings v. hygrometer readings. However, the required correction was large, sometimes as much as 30% (see Figures 8, 9). To insure accurate and reliable readings, the sensor required an input voltage above 4V, which could only be achieved with sufficiently low resistances on the GMB. Additionally, gas-tightness was crucial. Appropriate hardware modifications were able to greatly reduce error and to produce far more consistent readings.

The thermistor correction was small, but comparable in scale to the accuracy of the measurements (see Figure 10). It least affected readings near 25°C, where the ratio of corrected and original value was very near to 1. However, at 10°C a relative humidity reading of 40% would be offset by 1.3% and at 30°C a 60% relative humidity reading by .62%. (The ambient temperature during testing is roughly between 20°C and 24°C.) As the thermistor may make a correction that is not significantly smaller than the error, it is useful to include thermistor compensation in the data analysis.

Using the thermistor compensation, the two calibration curves (for relative humidity against the average and voltage ratio against the average) gave similar results. As the average Q of the calibration for relative humidity was larger than for voltage ratios, the voltage ratio provides a better method of calibration. This required a slope of between roughly 104 and 122, with vertical translations ranging from -23.0 to -32.7. The gap between lowest and highest readings at any given point in time increased with relative humidity (see Figure 11). After calibration, the gap

between readings near 80% relative humidity was 2.9%. Therefore, we believe the calibration to be accurate within at least  $\pm 3\%$ .

Given this accuracy, the LST modules furthest from the inflowing gas showed a significant difference in relative humidity (see Figure 14). The increase in humidity was smaller for each subsequent module, and by far the largest increase came as gas flowed through the first module in the chain. The humidity in the modules was fairly sensitive to changes in the ambient temperature, as the trend in ambient humidity change was mirrored by a humidity change within the module. Those at highest humidity were most sensitive to changes in ambient humidity.

There did not appear to be any large variation in the humidity of a module set that showed the count rate spike as opposed to one that did not (see Figure 13, 14). However, this does not discount high humidity as a cause for count rate spikes. Based on the count rates taken by the BABAR LST group (see Figure 15), higher humidity appears to be able to cause a spike in the voltage. Even at a humidity value as low as 28.99%, the spike was notably increased. It is therefore quite possibly that humidity is responsible for the count rate spikes: higher humidity appears to cause a spike and those modules more likely to spike (at the end of the gas chain) have higher humidity.

The investigation into humidity of the modules should continue for some time. A larger data set should allow for more conclusive results, and help to determine if perhaps those modules that spike are more susceptible to high humidity than those that do not. (For example, a susceptible module could have dust in the cell that might allow for condensation). Based on those conclusions, it should be possible to decide how best to configure the gas chains and what length of gas chain is appropriate, as well as what future humidity monitoring will be necessary.

## ACKNOWLEDGMENTS

This research was conducted at the Stanford Linear Accelerator Center. I thank the U. S. Department of Energy, Office of Science for providing me with the chance to participating in a rewarding and instructional research experience. Special thanks, of course, are due to my supervisors Dr. Mark Convery and Dr. Wolfgang Menges for their patience and willingness to provide instruction, advice, and materials. Thanks also to Dr. Charlie Young, and Dr. Sanjay Swain of the BABAR LST group, to Dr. Gabriele Benelli and Dr. Nikolai Sinev for their help with the computer interface for data readout, and to the SLAC electronics lab for their help with the construction of the sensors. Finally, I would like to express my appreciation of the work done for all the SLAC SULI students by Dr. Helen Quinn and Dr. James Lindesay.

## REFERENCES

- [1] M.I. Williams, C. Hee, K. Onaga, K. Webb and T. Glanzman, "BABAR Collaboration Homepage," Jun. 1 2005, [cited 2005 Aug 19], Available HTTP: <http://slac.stanford.edu/BFROOT>.
- [2] BABAR Collaboration LST Team, "A Barrel IFR Instrumented with Limited Streamer Tubes," *Stanford Linear Accelerator Center Experimental Program Advisory Committee*, Stanford, CA, May 2003.
- [3] S. Smith, "Limited Streamer Tubers for the IFR Barrel," *Stanford Linear Accelerator Center Experimental Program Advisory Committee*, Stanford, CA, Jun. 2003.
- [4] Honeywell Sensing and Control, "Humidity Sensors, Relative Humidity," [cited 2005 Aug 19], Available HTTP: [http://content.honeywell.com/sensing/prodinfo/humiditymoisture/catalog/c15\\_95\\_0913.pdf](http://content.honeywell.com/sensing/prodinfo/humiditymoisture/catalog/c15_95_0913.pdf).
- [5] T. Brice and T. Hall, "Dewpoint, National Weather Service Forecast Office, El Paso Area" May 3 2002; <http://www.srh.noaa.gov/elp/wxcalc/dewpoint.shtml>.
- [6] C. Young and BABAR Collaboration LST Team, "Singles Rates Measurement," Jun 2004, [cited 2005 Aug 19], Available HTTP: <http://www.slac.stanford.edu/BFROOT/www/Detector/LST/QC/SLAC/SinglesRate/index.html>.

## TABLES

	Thermistor	Thermistor Ground	+5 V	Ground	Output Voltage	Case Ground	
Sensor <sup>1</sup>	A	B	C	D	E	F	
Sensor Cable	Red	Black <sub>Red</sub>	White	Black <sub>White</sub>	Green	Black <sub>Green</sub>	
Cable Connector <sup>2</sup>	2	1	4	5	6	Shielding/ Insulation	
GMB Cable	Black <sub>Red</sub>	Red	Black <sub>White</sub>	Green	Black <sub>Green</sub>		White
Extender Board Input <sup>3</sup>	2	1	4	5	6		3
Extender Board Output	2	1	3 & 4 (shorted)	5	6		3 & 4 (shorted)
GMB	IN0 <sup>+</sup>	IN0 <sup>-</sup>	IN1 <sup>-</sup> & IN1 <sup>+</sup>	IN2 <sup>-</sup>	IN2 <sup>+</sup>		IN1 <sup>-</sup> & IN1 <sup>+</sup>

<sup>1</sup>Read counterclockwise, beginning at sensor tang and with pins facing upward

<sup>2</sup>Read beginning with 1 at arrow

<sup>3</sup>Beginning from upper left corner and reading down columns

**Table 1.** Wire connection map.

Sensor	34	57	98	99	129	192	219
Slope	103.77	121.56	105.78	114.86	117.46	107.97	108.46
Offset	-22.998	-32.742	-24.868	-28.971	-31.111	-24.784	-24.792

**Table 2.** Final calibration for multi-sensor configuration.

## FIGURES

Singles Rate of Module 1312 tube A with FERRARA configuration in a 100 s counting time at SLAC\_CEH at 12-Jul-2005 16:48:46

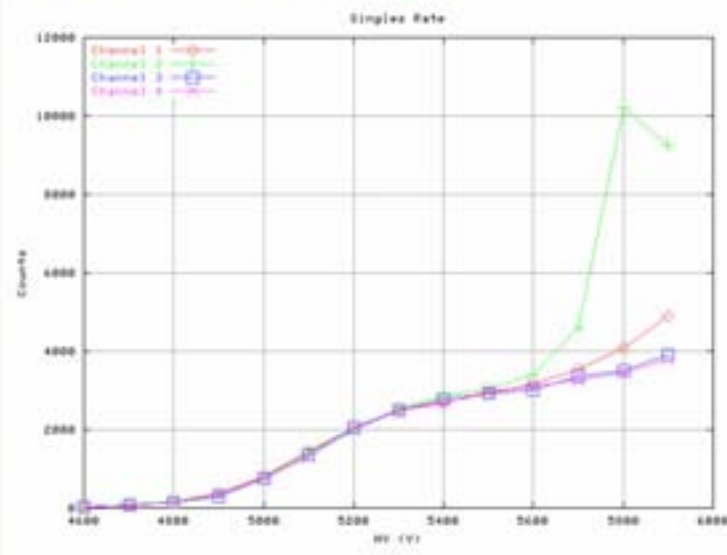


**Figure 1.** Spike in count rate near 5600V (Image courtesy of BABAR LST Group database).

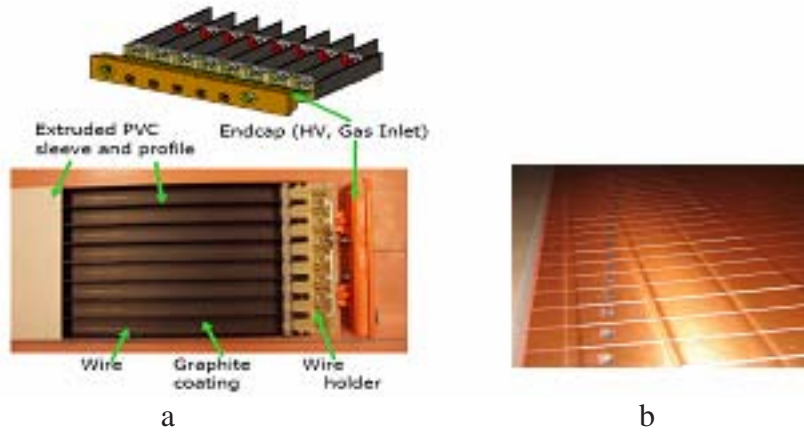


**Figure 2.** **a.** Top and side views of single LST (8 cells). **b.** Copper z-plane. (Images courtesy of BABAR LST Group.)

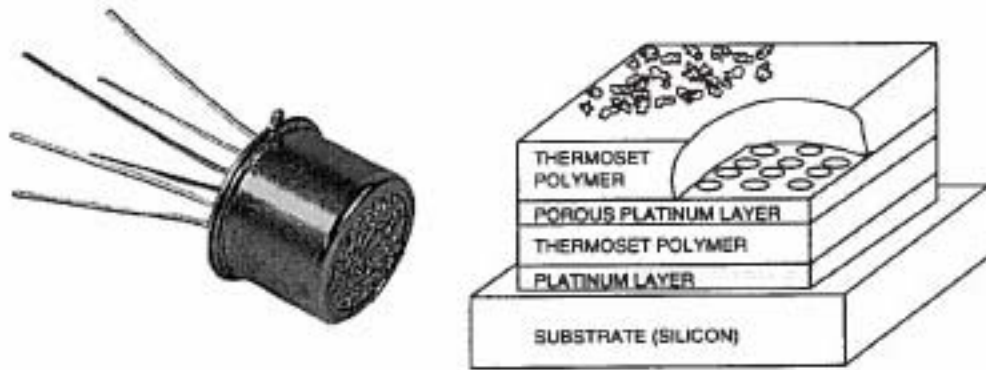


**Figure 3.**Honeywell sensor and diagram of internal layers (images from manufacturer catalog).

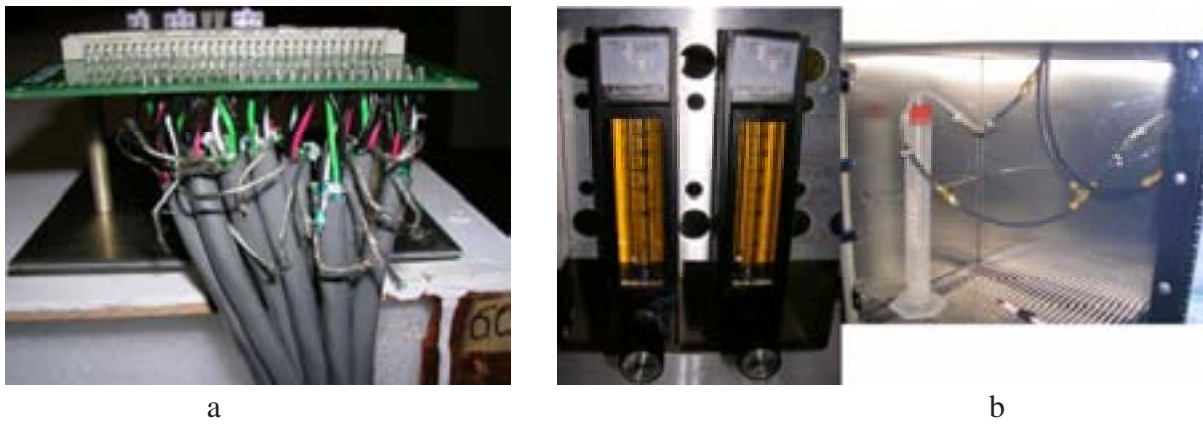


**Figure 4.**a.Side view of GMB extender board. b.Hygrometer flow control and Polyflow Tubing.



**Figure 5.**IC socket and individual wire heat-shrink, Molex crimp pins, Molex shroud with heat-shrink.



**Figure 6.**Completed multi-sensor configuration.

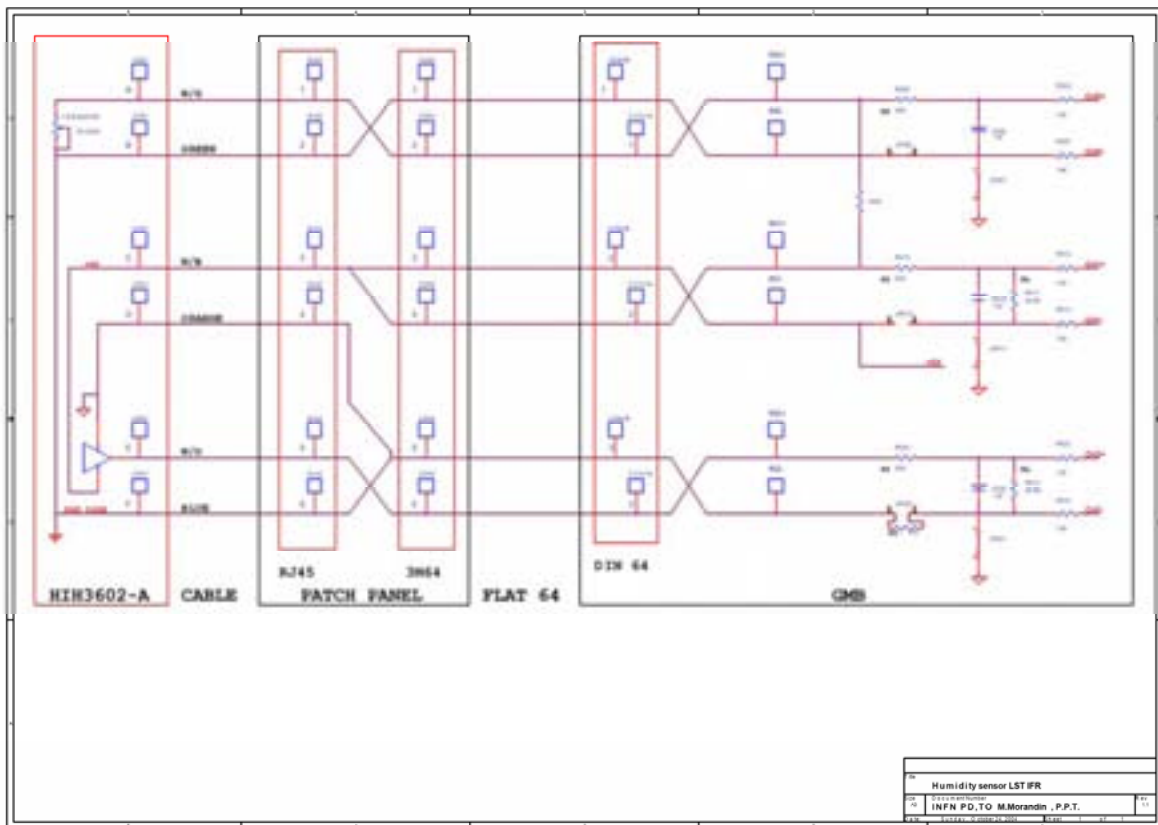


**Figure 7.**Schematic of GMB (image courtesy of BABAR LST Group).

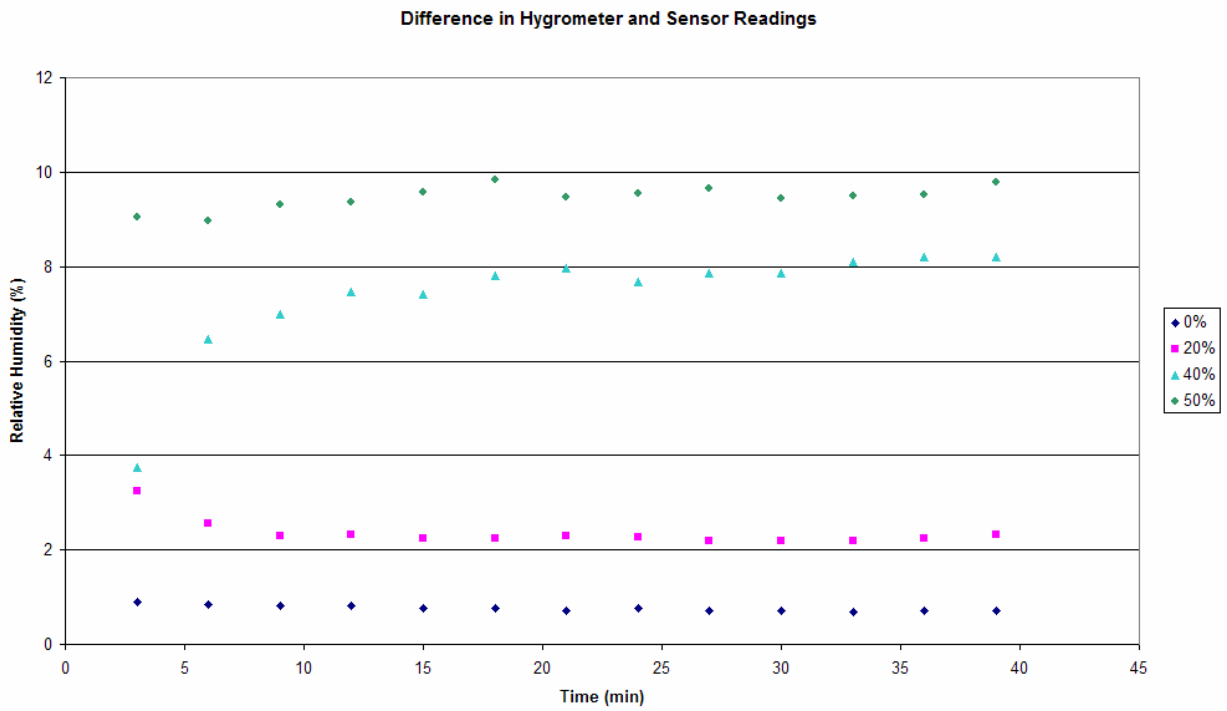


**Figure 8.** Time evolution of errors before modifications.

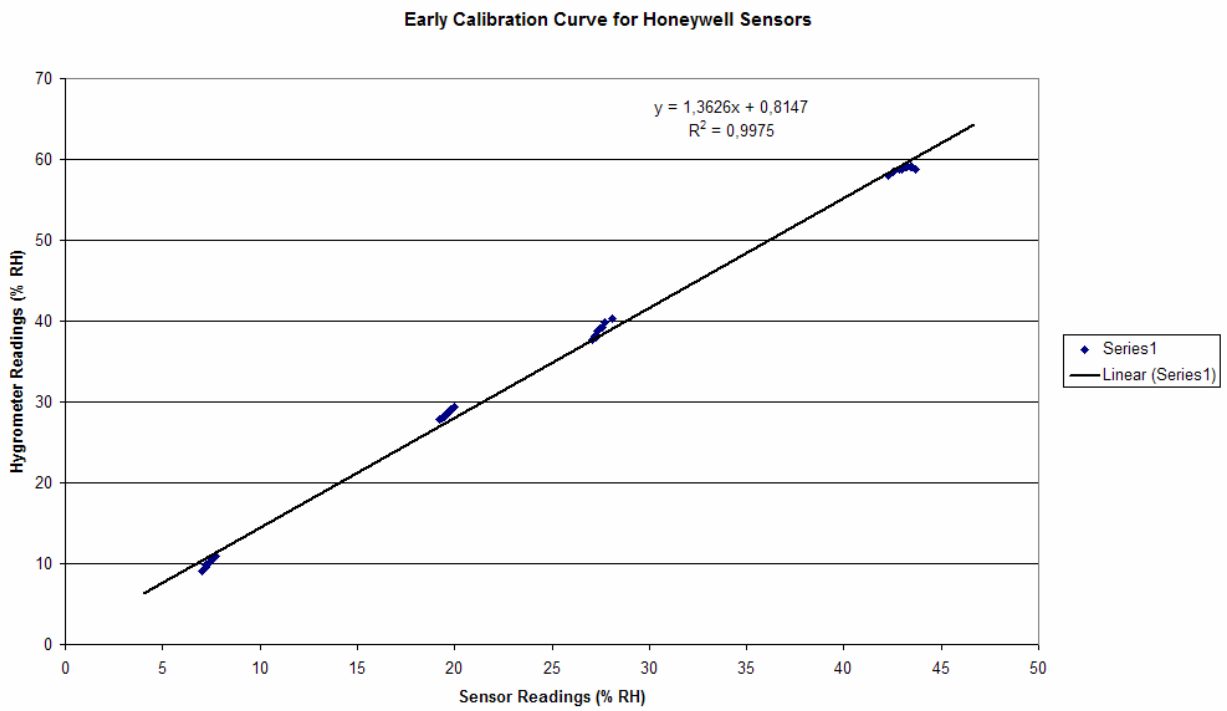


**Figure 9.** Early linear fit to correlate sensor 98 and hygrometer readings.

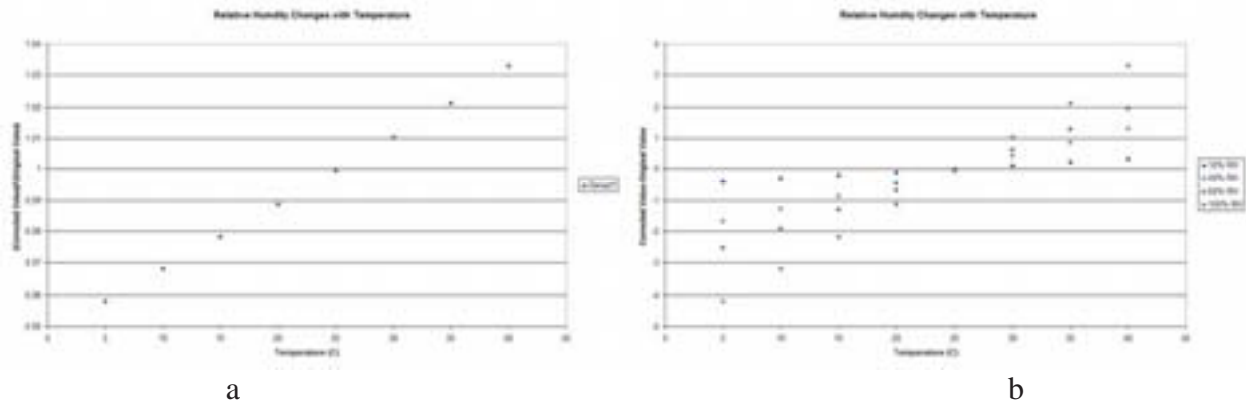


**Figure 10.a.**Ratio of corrected and original values for thermistor compensation **b.**Difference between corrected and original values.

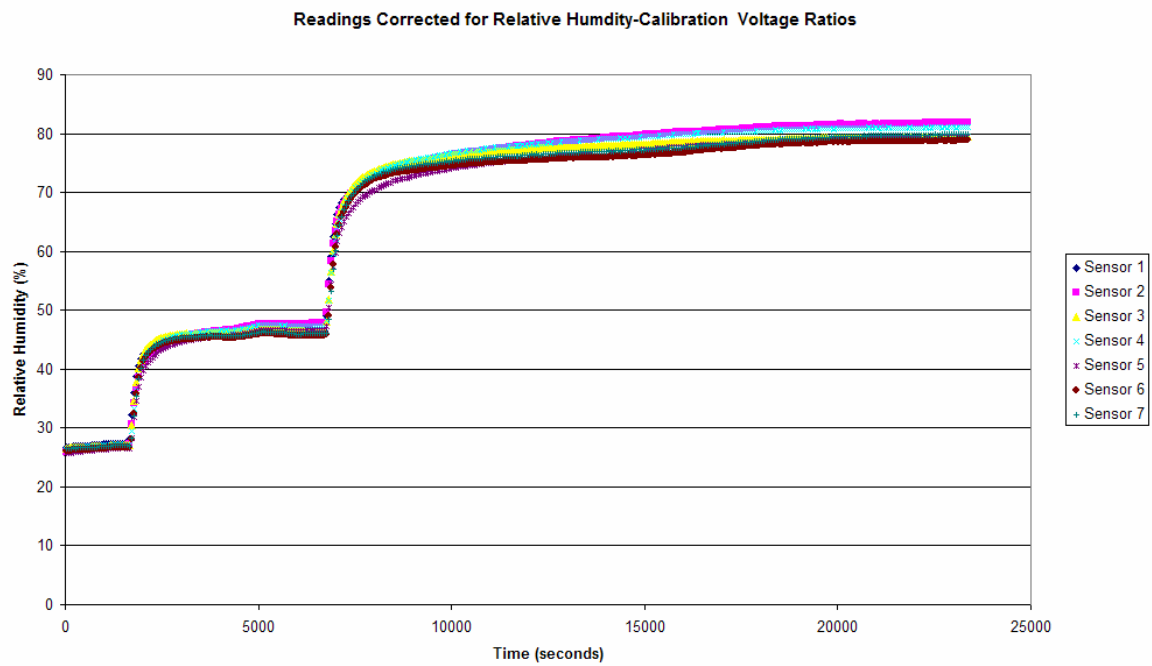
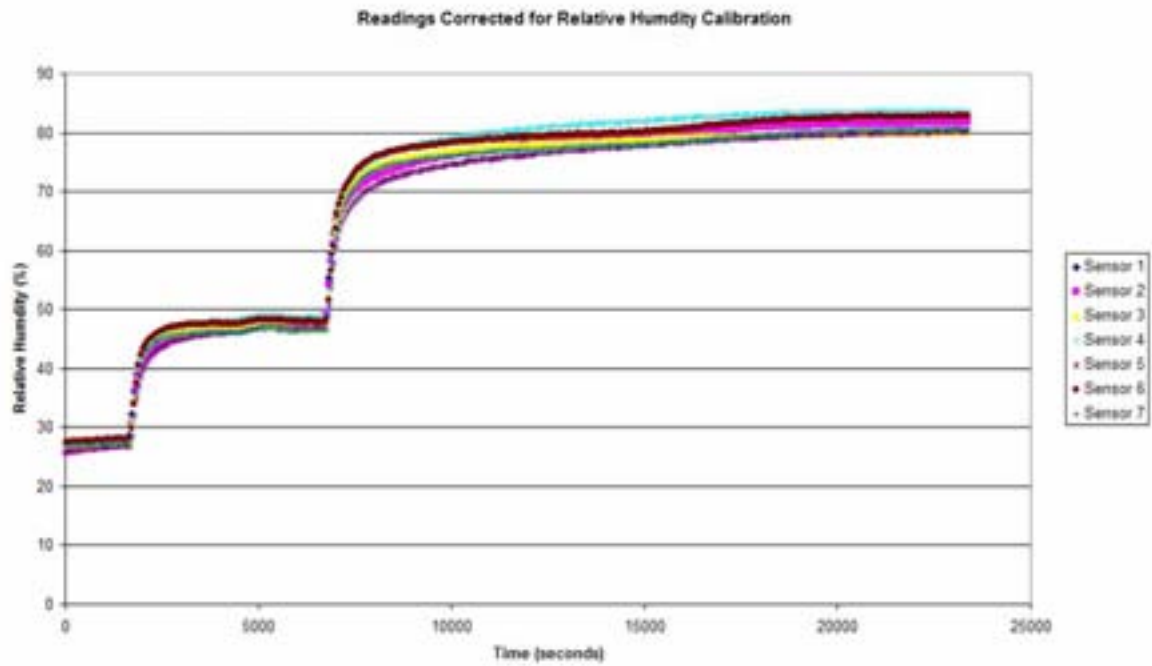


**Figure 11.** Comparison of potential calibration curves correcting one data set.

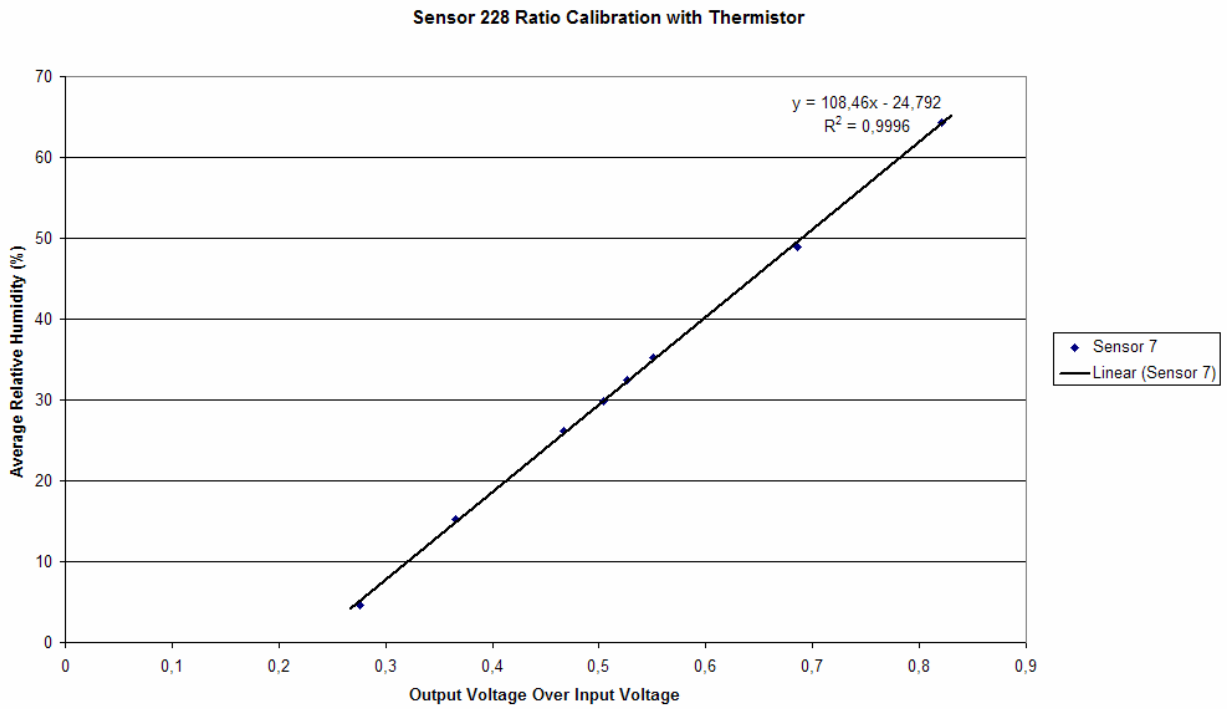
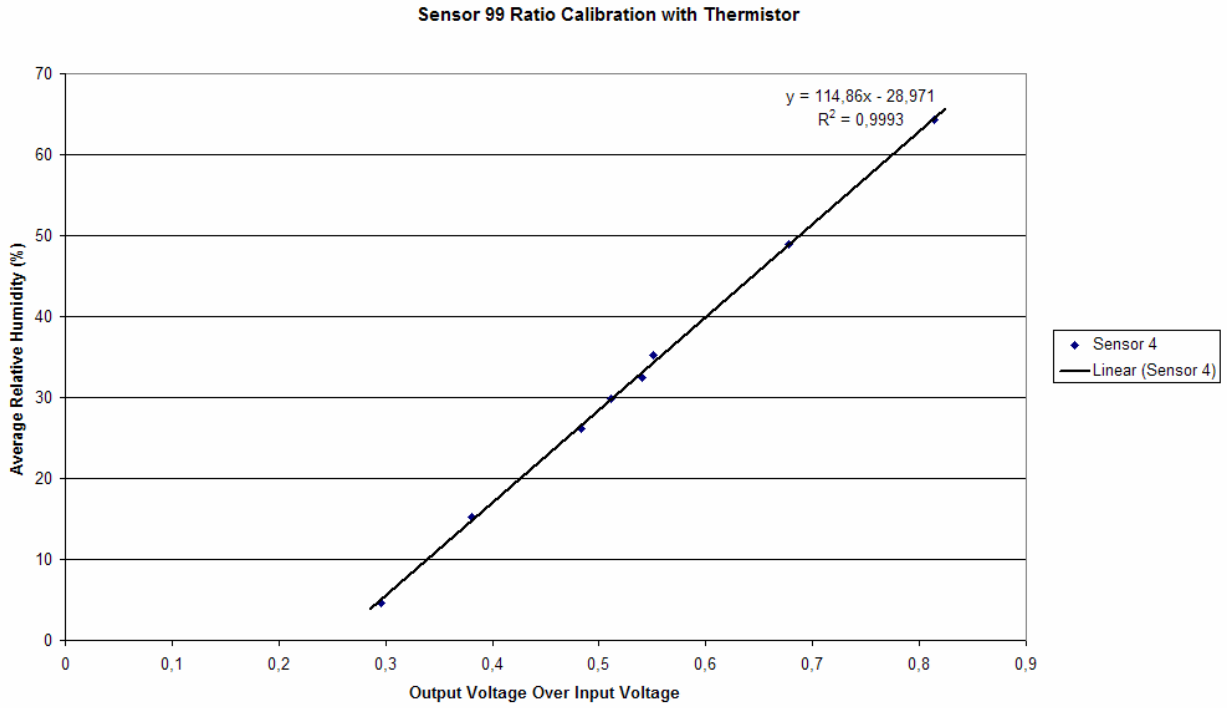
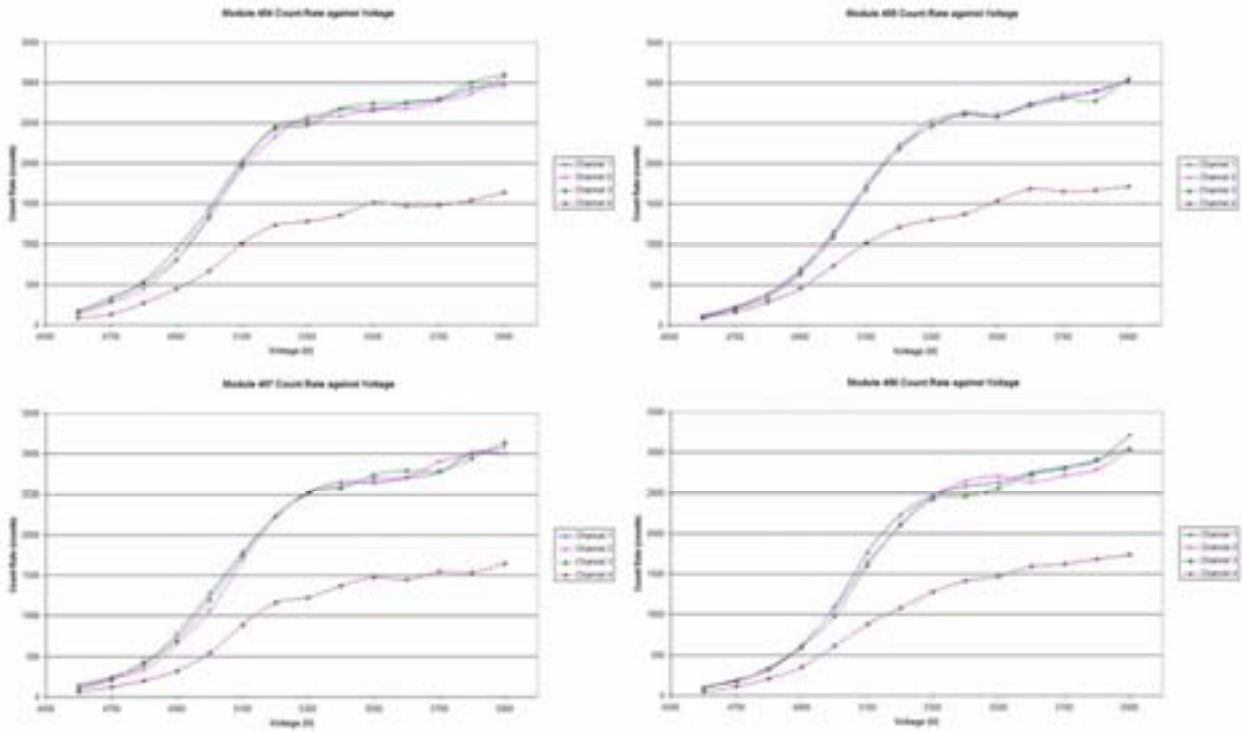
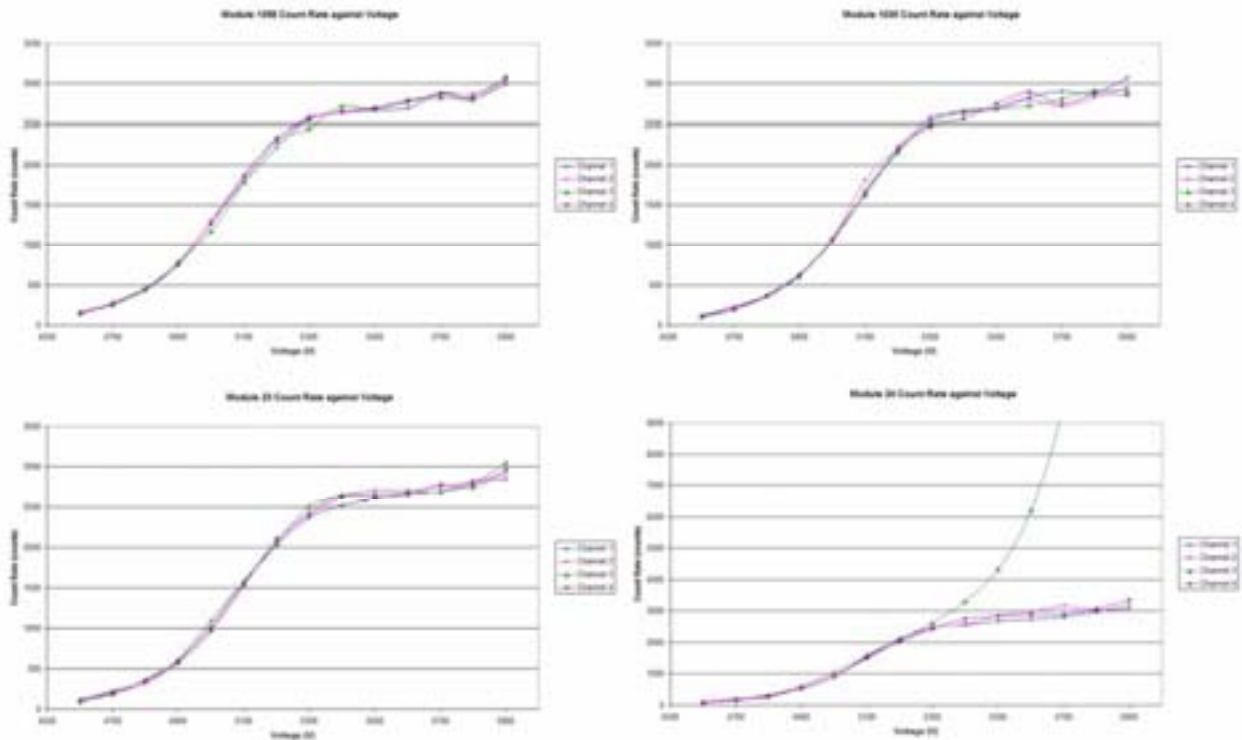


**Figure 12.** Two voltage ratio calibration curves for multi-sensor configuration.



a



b

**Figure 13.a.**Count rate v. voltage for four 7-cell modules in gas chain **b.**Count rate v. voltage for four 8-cell modules in gas chain.

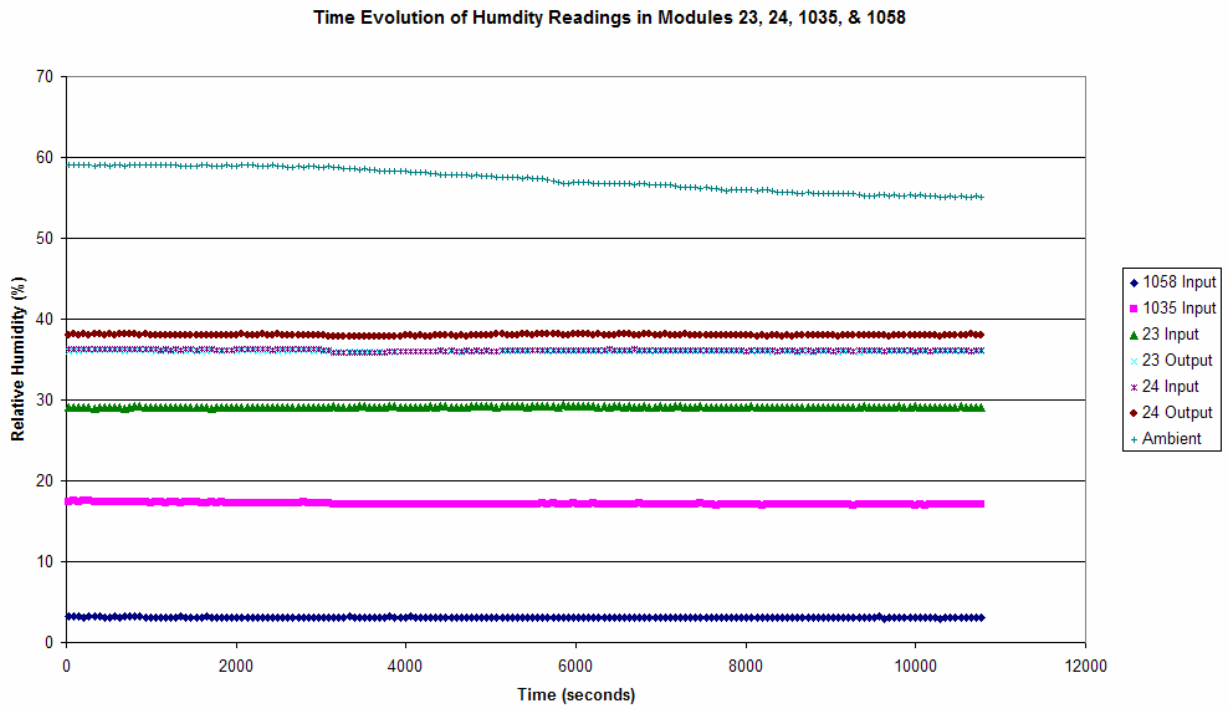
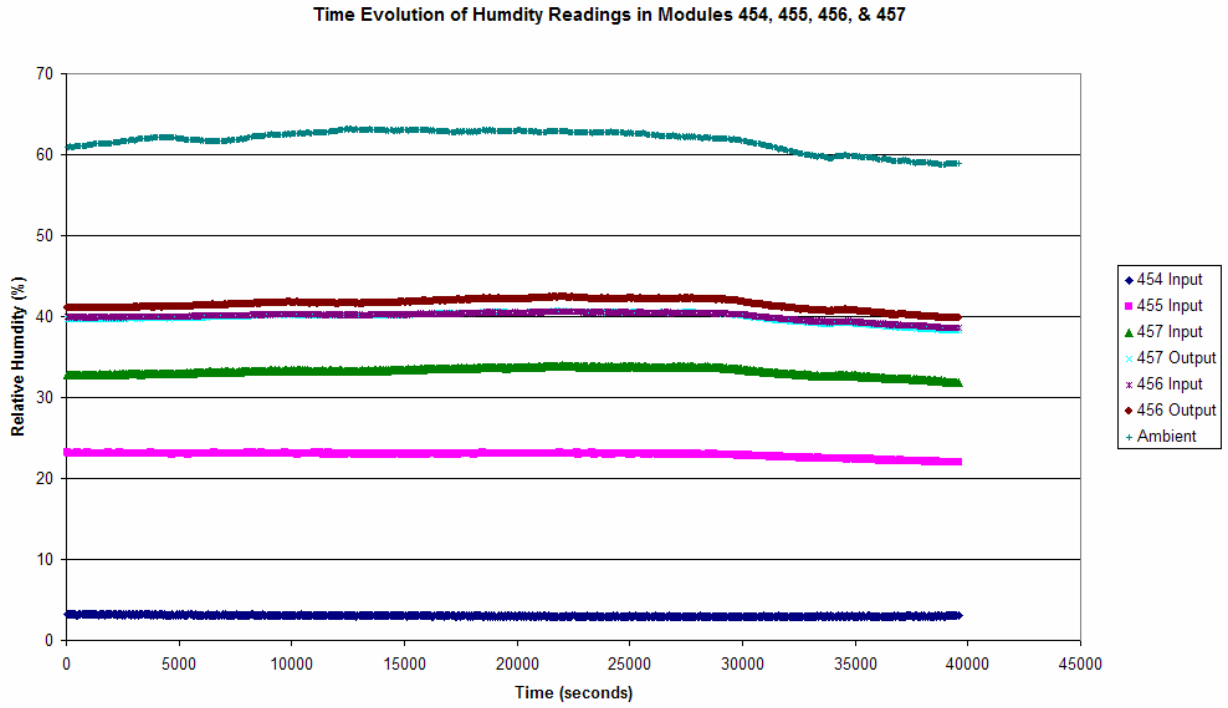
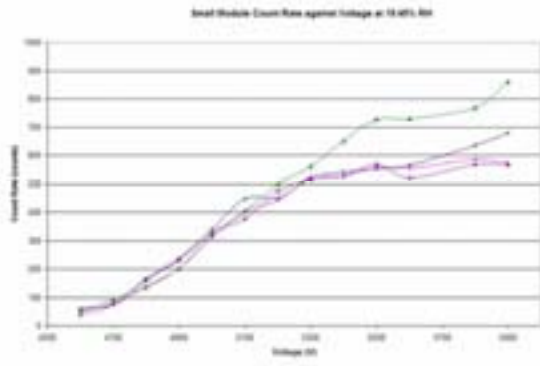
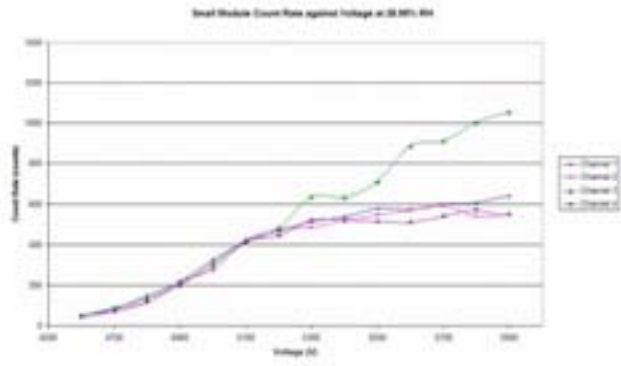


**Figure 14.** Humidity readings taken simultaneously with count rate data for two sets of modules.



a



b

**Figure 15. a.**Count rate for small LST at 19.45% RH. **b.**At 28.99% RH.

## Monitoring SLAC High Performance UNIX Computing Systems

Annette K. Lettsome

Office of Science, SULI Program

Bethune-Cookman College

Stanford Linear Accelerator Center

Menlo Park, California

August 19, 2005

Prepared in partial fulfillment of the requirements of the Office of Science, U.S. Department of Energy Science Undergraduate Laboratory Internship (SULI) Program under the direction of Mr. Adeyemi Adesayna in the Systems Group of the SLAC Computing Services (SCS) at Stanford Linear Accelerator Center (SLAC).

Participant: \_\_\_\_\_

Signature

Research Advisor: \_\_\_\_\_

Signature

## ABSTRACT

Monitoring SLAC High Performance UNIX Computing Systems. ANNETTE K. LETTSOME (Bethune-Cookman College, Daytona Beach, FL 32114) ADEYEMI ADESANYA (Stanford Linear Accelerator Center, Menlo Park, CA 94025).

Knowledge of the effectiveness and efficiency of computers is important when working with high performance systems. The monitoring of such systems is advantageous in order to foresee possible misfortunes or system failures. *Ganglia* is a software system designed for high performance computing systems to retrieve specific monitoring information. An alternative storage facility for *Ganglia*'s collected data is needed since its default storage system, the round-robin database (RRD), struggles with data integrity. The creation of a script-driven MySQL database solves this dilemma. This paper describes the process took in the creation and implementation of the MySQL database for use by *Ganglia*. Comparisons between data storage by both databases are made using *gnuplot* and *Ganglia*'s real-time graphical user interface.

## INTRODUCTION

Stanford Linear Accelerator Center (SLAC) is a large particle physics laboratory that performs various government-funded experiments. Computers, mainly UNIX platforms, aid some of our experiments by collecting data, storing results, and calculating the findings. When working in a large environment such as SLAC, with experiments and projects that spit out information to its corresponding workstation constantly, it is important to monitor the performance of those computer systems. UNIX has some special commands—like *top* (provides an ongoing look at processor activity in real time), *iostat* (monitors system input/output device loading by observing the time the devices are active in relation to their average transfer rates), *vmstat* (reports information about processes, memory, paging, block IO, traps, and cpu activity), and *ps* (gives a snapshot of the current processes)—that provide various monitoring information. The health and stability of any computer system—no matter its platform, memory capacity, or age—are very important and should be monitored to avoid and prevent mishaps from occurring.

*Ganglia* is a software system that provides monitoring capabilities for high performance computing systems. *Ganglia* is comprised of two daemons, a process that runs in the background generally unaware to and not affecting users, called *gmond* and *gmetad*. These daemons are responsible for the retrieval of various monitoring information, known as metrics, over specified intervals. Some examples of metrics are percent CPU usage, current process/load size, host name, last boot time, etc.

The *Ganglia* system works on a federation of clusters [1], meaning a group of clusters that are each comprised of computers. *Ganglia* uses its daemons in a chain of command method to retrieve the metrics. Each computer or host has its own *gmond* and it sends its monitoring info

in the form XML to the *gmond* of the computer in its cluster that has been designated ‘delegate’. It is then the delegate’s responsibility to retrieve the monitoring info and keep it until *gmetad* retrieves it. After *gmetad* gets the information, it stores it in a round-robin database.

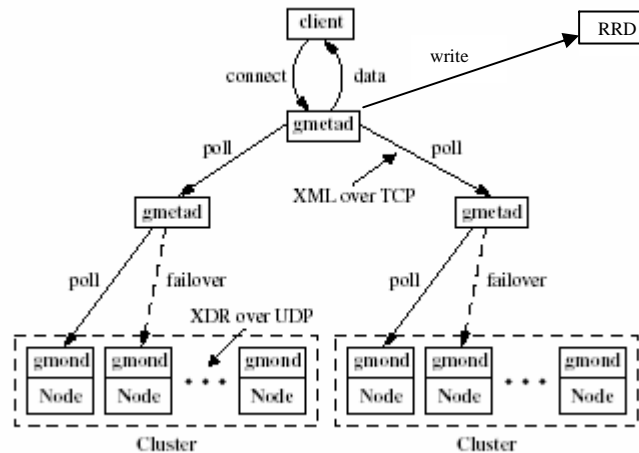


**Figure 1 Ganglia Architecture [6]**

*Ganglia* currently works hand-in-hand with the round-robin database (RRD), a database storage system with a fixed size [2]. Therefore, the initialized size is the size it will remain; it is not capable of growing or shrinking. The advantage of this is that the problem of not having enough space to house its expanding info is never an issue. In addition, the RRD manages time-oriented measurements, so working with *Ganglia*’s periodic output is a strong suit.

Unfortunately, the downfall of the RRD is its advantage. Being that the nature of the round-robin database is to remain fixed in size, when there is no longer space available for the incoming information, the not so current data that it presently holds is compacted. By doing so, the accuracy of the older information is lost. Therefore, when querying the database to find the memory usage of a particular host on a date exactly one year ago today, the resultant data would be an estimation rather than the exact figure. Since the round-robin database does this, it is

advantageous to find a more adequate storage system, even though other methods increase the risk of infinite growth.

The alternative way of storing the information is to use a traditional relational database, specifically MySQL. To design and create the tables, the monitoring info that needed storage—the XML dump of the metrics delivered by the *gmond* and *gmetad* daemons—was studied. The obvious relationships found to model the tables after are as follows:

- A ganglia system has many clusters.
- A cluster has many related hosts.
- A host has many monitored metrics.

## **PROJECT OVERVIEW**

Two methods taken to study the *Ganglia* system and learn exactly what it does were by:

1. Logging on remotely to various hosts and using commands like *top* and *iostat* to see the monitoring info that *Ganglia* collected at the source, and by
2. Viewing the real-time graphical web interface *Ganglia* produced with the information gathered and stored in the round-robin database.

After the basic understanding of *Ganglia* was developed, the creation of a database that would hold the relevant monitoring information proceeded. The database's purpose was to become a medium to query different monitoring information from various hosts, clusters, and metrics. The control of the database and its activities became the responsibility of a program, since the database is unable to differentiate between which information is to store where and how without assistance. The program's task was to initially create tables as needed, fill the tables

with its corresponding information by deciphering the XML output from *Ganglia* and convert it into structured query language (sql) statements, and constantly update the tables with new information.

## DATABASE

The design of a database is the first, most difficult, and longest stage in the creation of a database. This is because it involves planning and numerous revisions to make it normalized. “In relational database design, normalization is the process of organizing data to minimize redundancy. Normalization usually involves dividing a database into two or more tables and defining relationships between the tables. The objective is to isolate data so that additions, deletions, and modifications of a field can be made in just one table and then propagated through the rest of the database via the defined relationships” [3].

As stated earlier, when designing the database for *Ganglia*, the structure of the XML output helped in identifying the relationships. The first design plan consisted of six tables, which was to hold all the information ever created for every grid, cluster, host and metric. This first design wasted memory space because all of the values in the metric tables were to be stored as string, even though some values were actually numeric and would take up less if they were stored effectively.

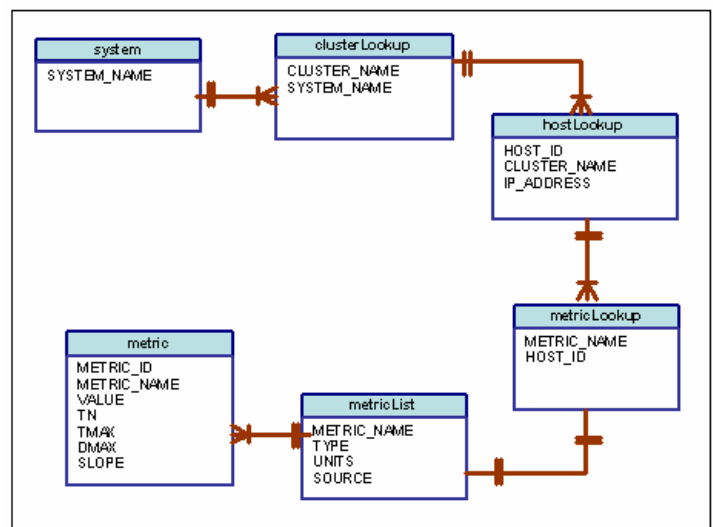


**Figure 2 Design Schema #1**

With that epiphany, the table designs that followed split the metric table into smaller tables depending on its type. The latest design of this method consisted of eight tables accommodating string, numerical, floating point, and time metrics. This method's downfall was its potential growth factor and scalability issues. Scalability "refers to how well a hardware or software system can adapt to increased demands. For example, a scalable network system would be one that can start with just a few nodes but can easily expand to thousands of nodes" [3]. This method had a scalability flaw since each metric table held more than one metric and the addition of rows due to updates overtime would slow down its search time when querying even if indexed.

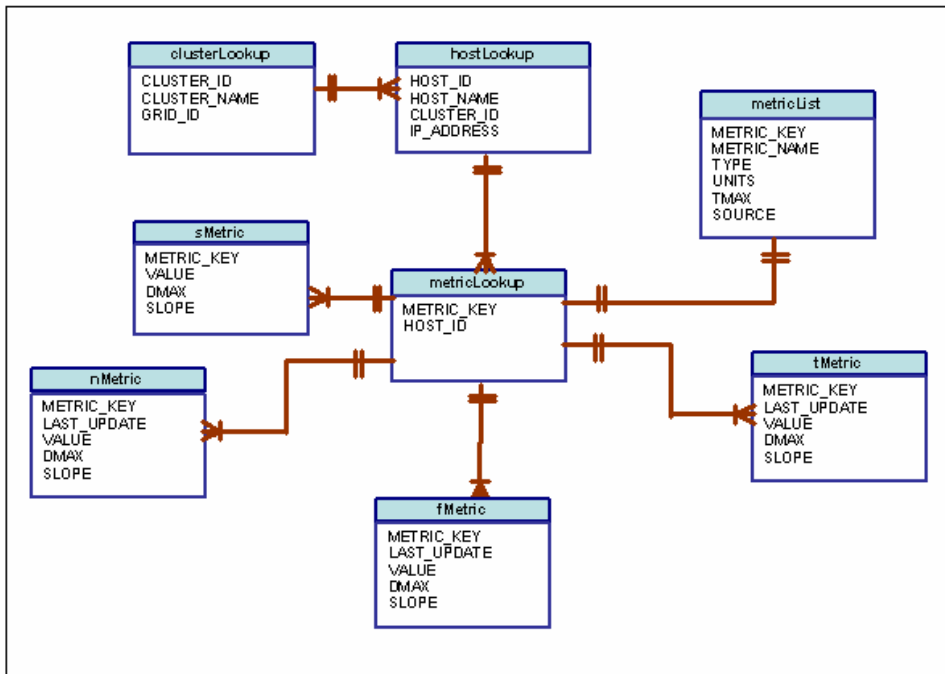


**Figure 3**  
**Design Schema #4**

When thinking on the potential growth of any individual table over time and its decrease in search time, it became evident not to concern so much about the amount of tables, but rather the size of each table. This new philosophy led to the final design of the tables. The idea of the

design was to create tables specifically for a given metric belonging to a particular host. There are currently 350 distinct metrics and 2350 monitored hosts in *Ganglia* thus far. Not all hosts have the same amount of monitored metrics, but they do share the basic 28 metrics. Therefore, there would be at least 65,800 metric tables in addition to the basic four tables in the database.

Since *Ganglia* checks for changes in metric values according to its tmax (the maximum time in seconds between metric calls), a calculation was done to see how big a given metric table would increase over time. The table below shows the amount of rows added if the information gathered each time was different from its predecessor.

**Table 1 Per Metric Per Host Row Calculation**

	tmax (s)	# of rows / hr	# of rows /day	# of rows/month	# of rows / year
[all gmetrics]	60	60	1440	43848	526176.00
load_one	70	51.42	1234	37584	451008.00
cpu_nice	90	40	960	29232	350784.00
mem_free	180	20	480	14616	175392.00
pkts_out	300	12	288	8769.6	105235.20
load_five	325	11.07	265.8	8095.015	97140.18
load_fifteen	950	3.789	90.34	2769.34	33232.16
bootime	1200	3	72	2192.4	26308.80

The current design of the tables (Fig. 4) is economical and scalable. It is economical in that each value type corresponds with the appropriate information being stored and scalable since only the specific metric info will be stored in a given table thus making expansion easier.

With the current design completed, the implementation proceeded. Direct MySQL implementation created the database itself and the four basic tables—cluster, host, metric and metricList. The program dealt with everything else—from the creation of the specific metric tables to the insertion and comparison of data.

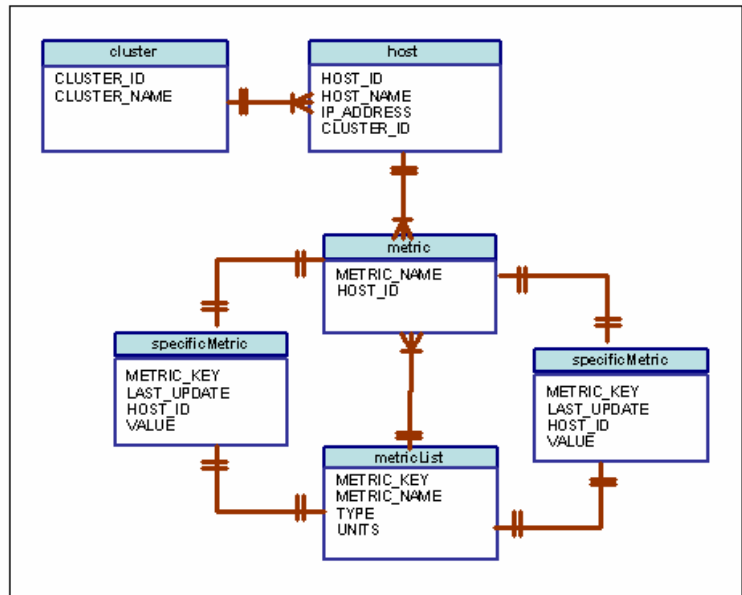


Figure 4 Second to Last Design Schema

## PROGRAMMING

The programming played an instrumental role in the project. Without a program, some data entry clerk would have the grueling task of reading through the XML output and manually inserting the new information into the database. That task in itself would not be a one-man's job and would take forever especially since the metric values updates are available at least every 60 seconds.

A C++ structure guide for the program, created by my mentor, jump-started the coding process. The guide included the header file of the *Expat XML Parser*. A parser is “a program that dissects source code so that it can be translated into object code” [3]. Specifically, *Expat* “is a stream-oriented parser in which an application registers handlers for things the parser might find in the XML document (like start tags)” [4]. This parser, written in C, helped with the

deciphering of the XML code. The guide also used some functions from the MySQL C API, an application program interface that “allows C programs to access a database” [5]. After studying the guide for basic understanding, it became apparent that a good bit of the code needed the MySQL C API itself.

The program initially needed to read the XML code in order to populate the four basic tables (see Tables 2 thru 5 for descriptions). During the initial population of the metric and metricList tables, the specific metrics tables were to be simultaneously created and filled. To distinguish the specific metric tables from each other, a naming scheme was created. The metric name and host identification number of each specific metric table would be its identifier. For instance, if the hostID for gala002 was 144 and one of its metrics were mem\_buffers, then that metric table’s name would be “mem\_buffers\_144.” This method allowed the creation of uniquely named tables that also served an identification purpose. (See Appendix A for the table creation code.)

In order to update the table with new info, a comparison between the last value and the newly retrieved value occurs. The word ‘update’ in this context refers to the addition of new rows rather than replacing old value with new ones. If that were the case, the database would not hold a history of info. The program is to parse through the XML code every 60 seconds, which is the minimum tmax for the metrics. Recall that some metrics have a tmax as great as 1200 and that the values do not necessarily change after each metric call. If there were no comparison statement, duplications would occur in the table and waste space. The code therefore compares the new info with the last input and if it has changed, it will be stored. Data redundancy in the aspect of rows 1, 5, & 8 being identical is wanted because the purpose of the database is to note the fluctuations. On the other hand, it is unwanted if rows 7, 8, & 9 are identical because the

data could have just been saved in one row instead of the three. This is the comparison code's main purpose. (See Appendix B for update function containing the comparison code.)

The update function marks the end of the basic code. All programming details mentioned thus far lies in an infinite loop. With each iteration, the XML dump will be parsed and everything will repeat over again, after sleeping for 60 seconds. The addition of cluster, host, and metric information happens if and only if new information appears. Creation of new specific metric tables occurs whenever the dump reveals a new metric, while updates occur with justification of the comparison statement.

## **IMPLEMENTATION AND ANALYSIS**

Implementaion of the MySQL database with driver program proceeded on August 3. First, I manually created the basic four tables—cluster, host, metric and metricList. Next, the program was compiled and executed using the main gmetad daemon, ganglia01. The specificMetric tables were created as described and all tables received their appropriate data.

After running the program for a week, I noticed that my metricKey from both the metricList and corresponding specificMetric tables were larger than what my calculation said it should be. Realizing the problem, I knew exactly where the mishap occurred, fixed it, and restarted the implementation process on August 13.

Everything seems to be ruuning smoothly thus far with the current implementation. The database has 68449 tables, being that it is storing info from 2349 hosts. It takes my program approximately 13 minutes to parse through the XML dump provided by *Ganglia*. I expect the database to increase by atleast 224 tables since my previous implementation showed that there

are atleast 2357 hosts being monitored. There is uncertainty with the amount of host being monitored because when a host has a heavy load it does not produce its heartbeat. The heartbeat is used by *Ganglia* to report whether a host is up and they are usually pegged as 'down' when the heartbeat is not retrieved. Moreover, I believe that if a host is marked as 'down' for a long time span *Ganglia* temporarily forgets that it was being monitored and decreases its host monitoring total.

## **FUTURE / FURTHER WORK**

The database could probably be fined tuned somemore to decrease search time. The program has the ability to indefinitely create and update tables in the database as long as they are being monitored by *Ganglia*. Also, if there needs to be a change in the columns of a table to either stop collecting a particular piece of information or to add a piece, the code can be altered. The code has commented explanations of what is being done every step of the way. Therefore, anyone should be able to pick up where I left off and continue the project if further work needs to be done in the future.

If I had more time to with this project, I would figure out how to shorten the hostName for each host instead of adding the common extenstion for all 2349+ hosts. I would also add a grid table to show which clusters belonged to which grids. It was not included in my final design plan because at the time *Ganglia* did not provide that info in its XML dump. In addition, I would add a clause to the code that would only check for an update when that particular metric's tmax was due instead of checking all specificMetric tables with each iteration. This method should decrease the current iteration length of 13 minutes. Finally, I wish I had more time to see my

program run. Being that its final implementation began so late, I was unable to get enough data to make a thorough comparison of the two storage systems. Maybe I would get a chance after a year's span of time to see if the database accomplished its main goal of storing accurate data that could be retrieved in the future.

## **ACKNOWLEDGEMENTS**

This project was conducted at the Stanford Linear Accelerator Center. First and foremost, I would like to thank GOD for giving me air to breathe, food to sustain me, and shelter to protect me while I was at this internship. I want to thank my mentor, Adeyemi Adesanya, for putting up with me for the entire eight weeks. I know that I can be a hand-full at times. I also want to thank my computer science professors at Bethune-Cookman College for telling me about this program and sending me off with acquired knowledge. Special thanks to my parents for answering their cell phones at least three times a day to speak with their lonely child. In addition, I want to thank the SULI program especially the people at SLAC for choosing me. Finally yet importantly, I would like to thank myself, Annette Kamilah, for accomplishing the goals that were set and succeeding.

## REFERENCES

- [1] F. D. Saceroti, M. J. Katz, M. L. Massie, and D. E. Culler, "Wide Area Cluster Monitoring with Ganglia," presented at the IEEE Cluster Conference, Hong Kong, China, 2003.
- [2] M. L. Massie. (2005, March 24). [Online]. Ganglia. Available: <http://ganglia.sourceforge.net/> June 22, 2005 [date accessed].
- [3] Jupitermedia Corporation. (n.d.). [Online]. Webopedia: Online Computer Dictionary for Computer and Internet Terms and Definitions. Available: <http://www.webopedia.com> July 30, 2005 [date accessed].
- [4] <eXpat/>: The Expat XML Parser. (2005, Jan 28). [Online]. Available: <http://expat.sourceforge.net> July 27, 2005 [date accessed].
- [5] MySQL AB. (n.d.). [Online]. MySQL Reference Manual. Available: <http://dev.mysql.com/doc/mysql/en/index.html> July 5, 2005 [date accessed]
- [6] M. L. Massie, B. N. Chun, and D. E. Culter, "The Ganglia Distributed Monitoring System: Design, Implementation, and Experience," *Parallel Computing*, vol. 30, pp.817-840, July 2004.

## FIGURES AND TABLES

Field	Type	Null	Key	Default	Extra
clusterID	int(10) unsigned		PRI	NULL	auto_increment
clusterName	varchar(20)		UNI		

**Table 2 Cluster Table Description**

Field	Type	Null	Key	Default	Extra
hostID	int(10) unsigned		PRI	NULL	auto_increment
hostName	varchar(20)		UNI		
IP	varchar(15)		UNI		
clusterID	int(10) unsigned		MUL		

**Table 3 Host Table Description**

Field	Type	Null	Key	Default	Extra
hostID	int(10) unsigned		PRI	0	
metricKey	int(10) unsigned		PRI	0	

**Table 4 Metric Table Description**

Field	Type	Null	Key	Default	Extra
metricKey	int(10) unsigned		PRI	NULL	auto_increment
metricName	varchar(40)		UNI		
type	enum('uint8','int8','uint16','int16','uint32','int32','float','double','timestamp','string')	YES	MUL	NULL	
units	varchar(15)	YES		NULL	
source	enum('gmond','gmetric')	YES	MUL	NULL	

**Table 5 metricList Table Description**

Field	Type	Null	Key	Default	Extra
metricKey	int(10) unsigned			0	
hostID	int(10) unsigned		MUL	0	
lastUpdate	Timestamp	YES	PRI	CURRENT_TIMESTAMP	
value	int(10) unsigned [if type is integer] varchar(25) [if type is string] double [if type is floating point] datetime [if type is time]		MUL	0	

**Table 6 specificMetric Tables Description**

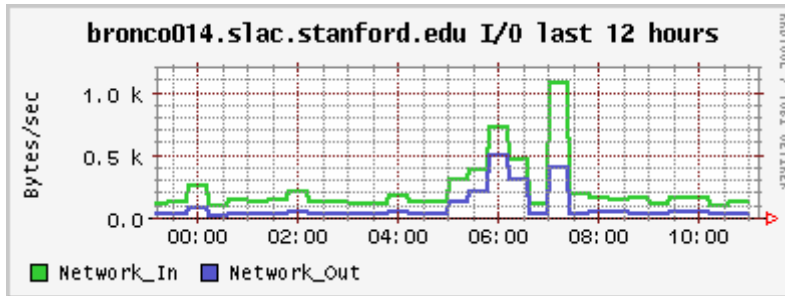


Figure 5 Comparison #1—Ganglia's RRD data

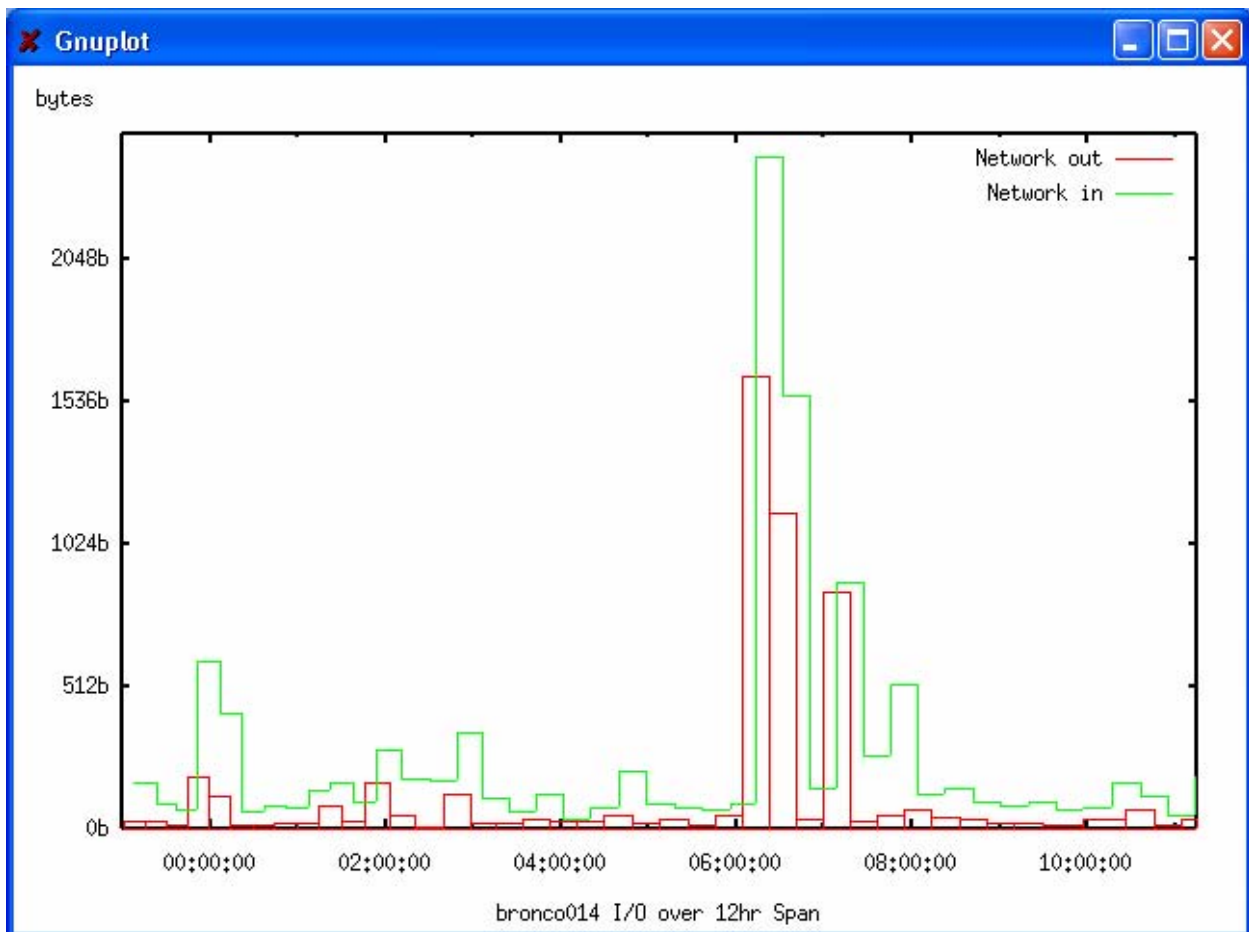


Figure 6 Comparison #1—MySQL data

The graphs of Comparison #1 compare the input/output for bronco014 over a 12 hours span. Specifically, ["08/14/05 23:00:00":"08/15/05 11:15:00"].

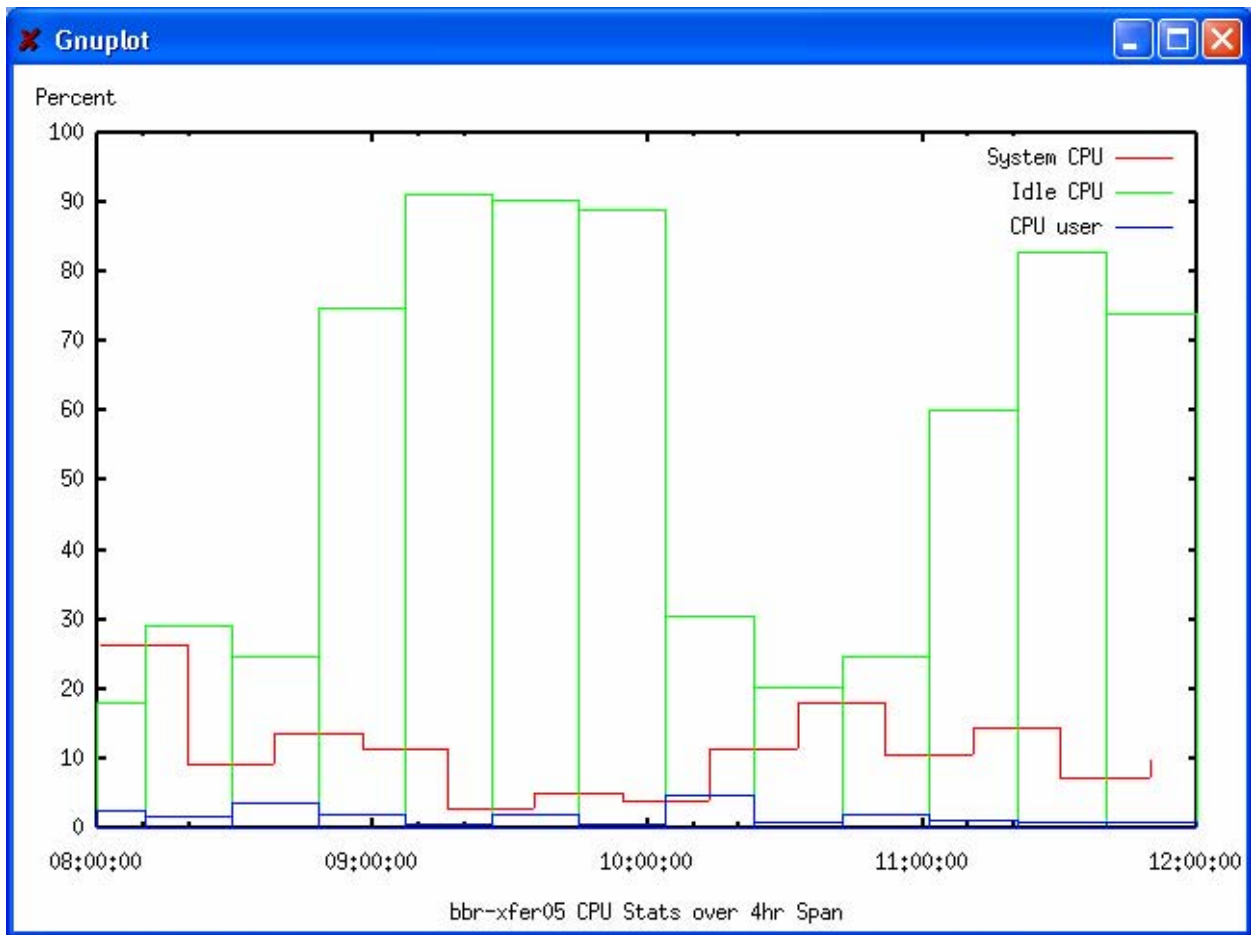


Figure 7 Comparison #2—MySQL data

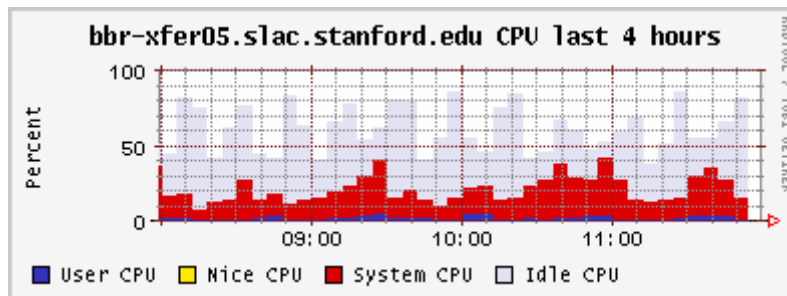


Figure 8 Comparison #2—Ganglia's RRD data

The graphs of Comparison #2 compare various CPU stats for bbr-xfer05 over a 4-hour span. Specifically, ["08/15/05 08:00:00":"08/15/05 12:00:00"].

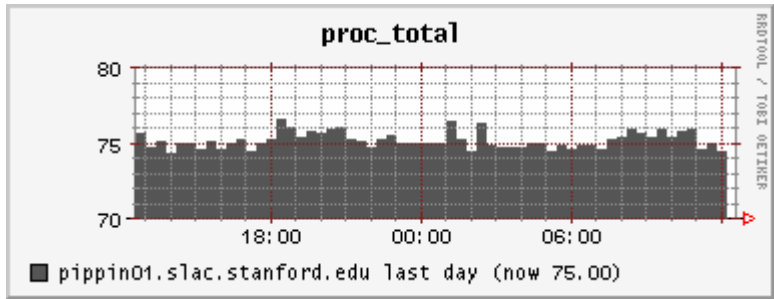


Figure 9 Comparison #3—Ganglia’s RRD data

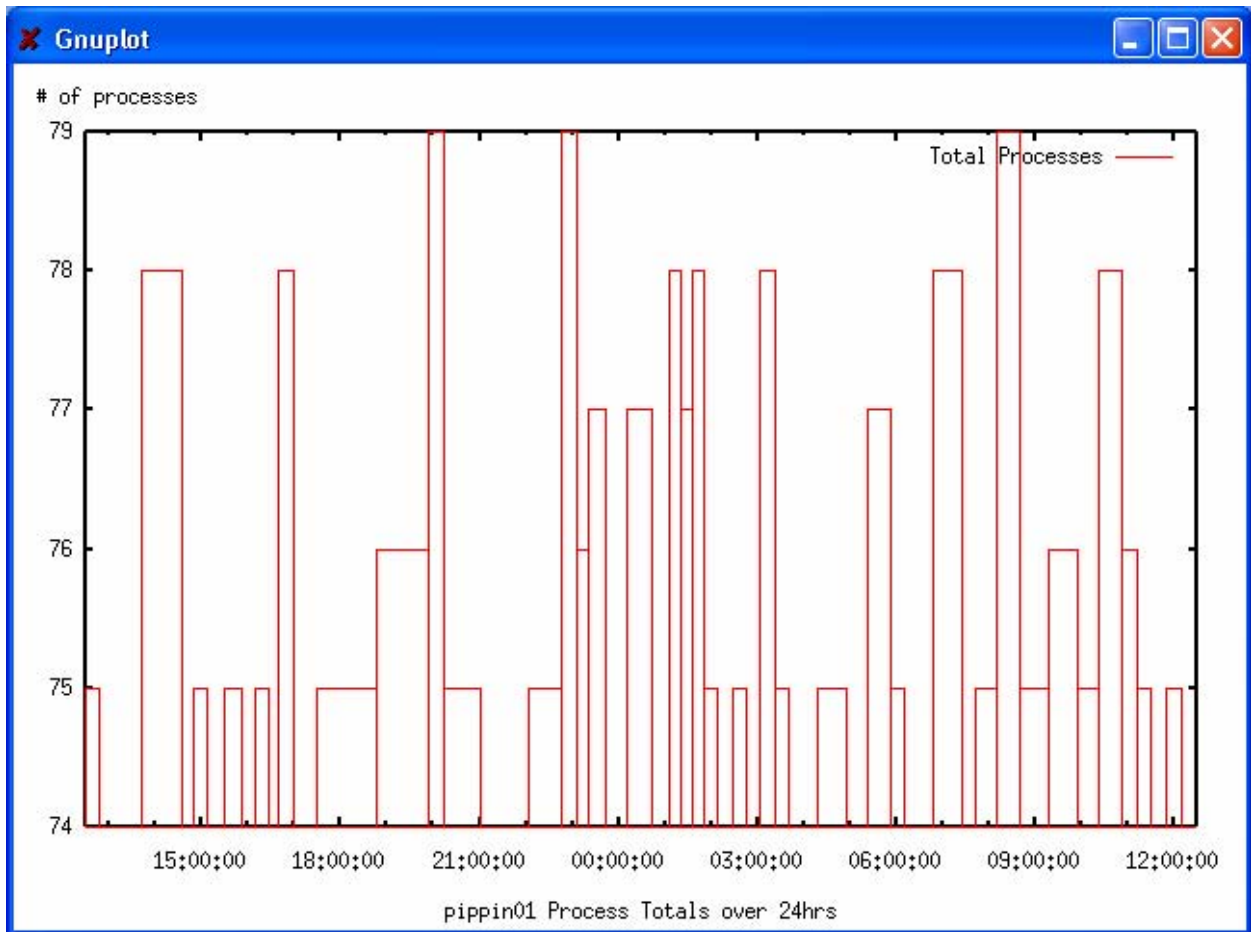


Figure 10 Comparison #3—MySQL data

The graphs of Comparison # 3 compare the total processes for pippin01 over a 24-hour span. Specifically, ["08/14/05 12:30:00":"08/15/05 12:30:00"].

## APPENDIX A

```
void GangliaDB::createSpecificMetricTable(const char **attr, int hostID)
{
    char queryBuffer[BUFFERSIZE];
    char *setValue;

    // condition statements figure out which type the particular value needs to be stored as and saves it as setValue

    if(strcmp(attr[5],"uint8")==0) setValue = "tinyint unsigned NOT NULL";
    else if(strcmp(attr[5],"uint16")==0) setValue = "smallint unsigned NOT NULL";
    else if(strcmp(attr[5],"uint32")==0) setValue = "int unsigned NOT NULL";

    else if(strcmp(attr[5],"int8")==0) setValue = "tinyint NOT NULL";
    else if(strcmp(attr[5],"int16")==0) setValue = "smallint NOT NULL";
    else if(strcmp(attr[5],"int32")==0) setValue = "int NOT NULL";

    else if(strcmp(attr[5], "string") == 0) setValue = "varchar(25) NOT NULL";

    else if(strcmp(attr[5], "float")==0 || strcmp(attr[5], "double")==0) setValue = "double NOT NULL";

    else if(strcmp(attr[5], "timestamp")==0) setValue = "datetime NOT NULL";

    // statement allows the creation of tables along with its indices; setValue used here for database statement
    sprintf (queryBuffer, "Create table IF NOT EXISTS %s_%u ( metricKey int unsigned , hostID int unsigned, lastUpdate timestamp PRIMARY KEY,
value %s, INDEX indx1 (value, lastUpdate, metricKey, hostID), INDEX indx2 (value, metricKey, hostID), INDEX indx3 (lastUpdate, metricKey,
hostID), INDEX indx4 (value, hostID, metricKey), INDEX indx5 (hostID, metricKey))", attr[1], hostID, setValue);

    if(mysql_real_query(mysqlSess, queryBuffer, strlen(queryBuffer))){
        cerr << "Create statement: " << queryBuffer << " did not work. " << endl;
    }
} // end void createSpecificMetric
```

## APPENDIX B

```
void GangliaDB::updateSpecificMetricTable(const char **attr, int hostID, int mKey)
{
    char queryBuffer[BUFFERSIZE];

    int hID;    // holds holdID; used just for verification purposes
    char *mName; // holds metricName; used just for verification purposes

    char* mValue; // holds value from specificMetric
    int rowCounter; // use to control the loop to place first values into tables

    sprintf(queryBuffer, "Select COUNT(metricKey) from %s_%u", attr[1], hostID);
    if(mysql_real_query(mysqlSess, queryBuffer, strlen(queryBuffer))){
        cerr << "Select statement: " << queryBuffer << " did not work. " << endl;
    }

    result = mysql_store_result(mysqlSess);
    if(!result){
        cerr << "store_result Failed" << endl;
    }

    if(!mysql_num_rows(result)){
        cerr << "No rows; count =0 " << endl;
    }

    row = mysql_fetch_row(result);
    rowCounter =atoi(row[0]); // convert to integer

    // free results
    mysql_free_result(result);

    if(!rowCounter){ // meaning that the table is empty
// insert into specificMetric table according to its type; must be converted differently if float, integer, etc.

        if (strcmp(attr[5],"uint8")==0 || strcmp(attr[5],"uint16")==0 || strcmp(attr[5],"uint32")==0){
            sprintf(queryBuffer, "insert into %s_%u (metricKey, hostID, value) values(%u,%u, %u)", attr[1], hostID, mKey, hostID, atoi(attr[3]));
        }
    }
}
```

```

else if(strcmp(attr[5], "int8")==0 || strcmp(attr[5], "int16")==0 || strcmp(attr[5], "int32")==0){
    sprintf(queryBuffer, "insert into %s_%u (metricKey, hostID, value) values(%u, %u, %d)", attr[1], hostID, mKey, hostID, atoi(attr[3]));
}
else if(strcmp(attr[5], "string") == 0 || strcmp(attr[5], "timestamp")==0){
    sprintf(queryBuffer, "insert into %s_%u (metricKey, hostID, value) values(%u, %u, \"%s\")", attr[1], hostID, mKey, hostID, attr[3]);
}
else if(strcmp(attr[5], "float")==0 || strcmp(attr[5], "double")==0){
    sprintf(queryBuffer, "insert into %s_%u (metricKey, hostID, value) values(%u, %u, %f)", attr[1], hostID, mKey, hostID, atof(attr[3]));
}
else{
    cout << "My unknown type is " << attr[5] << endl;
    // clear free queryBuffer just incase;
    sprintf(queryBuffer, "");
}

if( mysql_real_query(mysqlSess, queryBuffer, strlen(queryBuffer))) {
    cerr << " failed to execute mysql query: " << queryBuffer << endl;
}
}

// select rows from specified place and sort them with the most recent update first; then only retrieve that first rows and use it for comparison
else{
    sprintf(queryBuffer, "select value, metricName, hostID from %s_%u INNER JOIN metricList ON %s_%u.metricKey = metricList.metricKey where lastUpdate < CURRENT_TIMESTAMP order by lastUpdate DESC", attr[1], hostID, attr[1], hostID);

    if( mysql_real_query(mysqlSess, queryBuffer, strlen(queryBuffer))) {
        cerr << " failed to execute mysql query: " << queryBuffer << endl;
    }

    result = mysql_store_result(mysqlSess);
    if(!result){
        cerr << "store_result Failed" << endl;
    }

    if(!mysql_num_rows(result)){
        cerr << "No rows, but why?; count =0 " << endl;
    }
}

```

```

row = mysql_fetch_row(result);
mValue = row[0];
mName = row[1];
hID = atoi(row[2]);

// free results
mysql_free_result(result);

// verify that input goes into current table; comparison uses mValue at last part of if statement

if(hID == hostID && strcmp(mName,attr[1]) ==0) // this verification is probably not necessary
{
    if ((strcmp(attr[5],"uint8")==0 || strcmp(attr[5],"uint16")==0 || strcmp(attr[5],"uint32")==0) && atoi(mValue) != atoi(attr[3])){
        sprintf(queryBuffer, "insert into %s_%u (metricKey, hostID, value) values(%u, %u, %u)", attr[1], hostID, mName, hostID, atoi(attr[3]));
    }
    else if((strcmp(attr[5],"int8")==0 || strcmp(attr[5],"int16")==0 || strcmp(attr[5],"int32")==0) && atoi(mValue) != atoi(attr[3])){
        sprintf(queryBuffer, "insert into %s_%u (metricKey, hostID, value) values(%u, %u, %d)", attr[1], hostID, mName, hostID, atoi(attr[3]));
    }
    else if((strcmp(attr[5], "string") == 0 || strcmp(attr[5], "timestamp")==0) && strcmp(mValue, attr[3]) != 0){
        sprintf(queryBuffer, "insert into %s_%u (metricKey, hostID, value) values(%u, %u, \"%s\")", attr[1], hostID, mName, hostID, attr[3]);
    }
    else if((strcmp(attr[5], "float")==0 || strcmp(attr[5], "double")==0) && atof(mValue) != atof(attr[3])){
        sprintf(queryBuffer, "insert into %s_%u (metricKey, hostID, value) values(%u, %u, %f)", attr[1], hostID, mName, hostID, atof(attr[3]));
    }
    else{ // mValue == attr[3], so do nothing → need to clear free queryBuffer; it should contain select statement;
        sprintf(queryBuffer, "");
    }

    if( mysql_real_query(mysqlSess,queryBuffer,strlen(queryBuffer))){
        cerr << " failed to execute mysql query because attr[3] == mValue " << endl;
    }

} //end internal if statement

} // end else

} // end update specificMetric

```

**Hardware Testing of the BaBar Drift Chamber  
Electronics Upgrade**

Bryce Littlejohn<sup>1</sup>, Yiwen Chu<sup>2</sup>, Liv Wiik<sup>3</sup>

Office of Science, SULI Program

1) Principia College, 2) Massachusetts Institute of Technology,

3) Universität Hamburg

Stanford Linear Accelerator Center

Menlo Park, California

August 4, 2005

Prepared in partial fulfillment of the requirements of the Office of Science,  
U.S. Department of Energy Science Undergraduate Laboratory Internship  
(SULI) Program under the direction of Jochen Dingfelder and Mike Kelsey  
in Experimental Group C at the Stanford Linear Accelerator Center (SLAC).

Participants: \_\_\_\_\_

Signatures

Research Advisor: \_\_\_\_\_

Signature

# Contents

<b>1</b>	<b>Abstract</b>	<b>3</b>
<b>2</b>	<b>Introduction</b>	<b>4</b>
<b>3</b>	<b>Methods and Materials</b>	<b>8</b>
3.1	Overview . . . . .	8
3.2	Component Test Stand . . . . .	9
3.3	Calibration Test Stand . . . . .	11
3.4	DCT Test Stand . . . . .	12
3.5	Test Records . . . . .	13
<b>4</b>	<b>Results and Discussion</b>	<b>14</b>
<b>5</b>	<b>Conclusion</b>	<b>19</b>
<b>6</b>	<b>Acknowledgements</b>	<b>20</b>

# 1 Abstract

**Hardware Testing of the BaBar Drift Chamber.** BRYCE LITTLE-JOHN(Principia College, Elsau, IL 62028) YIWEN CHU(Massachusetts Institute of Technology, Cambridge, MA 02139) LIV WIIK(Universität Hamburg, Germany) JOCHEN DINGFELDER AND MIKE KELSEY(Stanford Linear Accelerator Center, Stanford, CA 94025).

The BaBar drift chamber provides position, timing, and  $dE/dx$  measurements for charged decay products of the  $\Upsilon(4S)$  resonance at 10.58 GeV. Increasing data collection rates stemming from higher PEP II luminosities and background have highlighted dead time problems in the drift chamber's data acquisition system. A proposed upgrade, called Phase II, aims to solve the problem with the introduction of rewritable, higher-memory firmware in the DAQ front-end electronics that lowers dataflow through the system. After fabrication, the new electronics components were tested to ensure proper function and reliability before installation in the detector. Some tests checked for successful operation of individual components, while others operated entire sections of the upgraded system in a mockup drift chamber environment. This paper explains the testing process and presents results regarding performance of the upgrade electronics.

## 2 Introduction

The BaBar detector makes precision measurements of rare  $B$ ,  $D$ , and  $\tau$  decays by collecting large amounts of collisional data at the  $\Upsilon(4S)$  resonance. An efficient data acquisition system is essential if approximately 3000 events per second are to be successfully collected. Thus, an important criterion in BaBar detector design is minimization of dead time. Despite a previous upgrade, referred to as Phase I, the drift chamber (DCH) has consistently been the experiment's largest dead time contributor. At the current beam luminosity of  $8 \times 10^{33} \text{cm}^{-2} \text{s}^{-1}$ , average dead times peak at 10% over short periods, but are generally closer to 2% [1]. However, as PEP II upgrades bring about increases in luminosity and potentially background, dead time has become a noticeably limiting factor in detector efficiency, and will continue to increase until further changes are implemented.

In the drift chamber, each of 7104 sense wires is surrounded by six field wires that create a logarithmically decreasing electric field centered roughly radially about the sense wire [2]. Incident charged particles ionize fill gas inside the drift chamber. The produced electrons drift towards the sense wire, causing secondary ionizations at small distances from the sense wire as electrons are accelerated by the strong electric field. Continued ionization creates a charge avalanche that induces an electric pulse in the sense wire. This signal, along with inherent background, is fed from the sense wires to sixteen azimuthally symmetric groups of three Front End Assemblies (FEAs). FEA 1, the radially innermost assembly, holds two Front End Elements (FEES), while FEA 2 and FEA 3 contain one each. The FEAs extract timing and charge information from pulses and prepare accepted events for further selection and storage. The large amount of data generated in the FEA can be regarded as one of the causes of dead time in the detector.

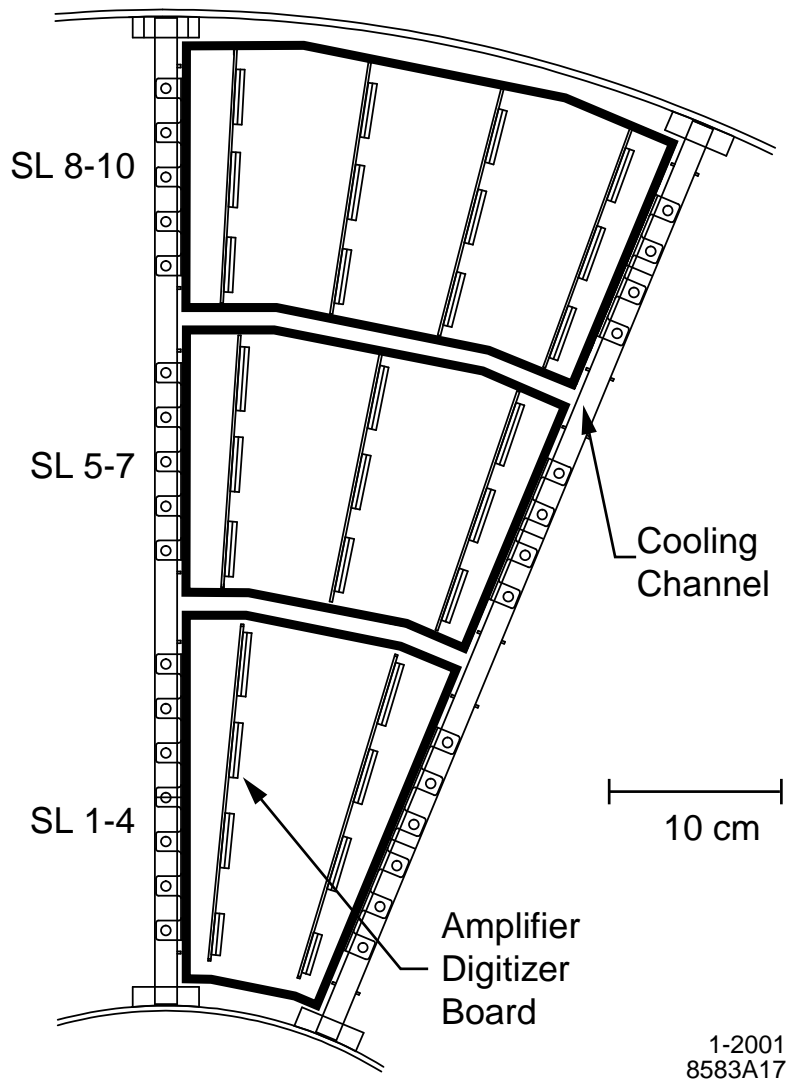


Figure 1: An end-on view of 1/16 of the front-end electronics. The numbers of ADBs per FEA and ELEFANTS per ADB are clearly visible. Taken from [2].

The FEAs, shown in Figure 1, are housed in aluminum boxes of three different sizes that conform to the DCH endplate's circular geometry. In the FEAs, an analog signal is first sent to an amplifier-digitizer board (ADB), where it is amplified and transferred to an ELEFANT (ELEctronics For Amplitude aNd Timing) IC. In the ELEFANT, the pulse can be digitized by a Flash Analog-to-Digital Converter (FADC) and marked at its leading edge with a timestamp by a Time-to-Digital Converter (TDC). Created data are then stored in a 12.9 microsecond buffer. Another continuous stream of raw data is concurrently sent through the FEA and provides the necessary information to decide when an acceptable event (Level 1 Accept) has occurred. Once triggered, a readout interface board (ROIB) accepts data from the ELEFANT buffers and sends them to a data input output module (DIOM). The DIOM sequences all accepted data and sends them to the readout module (ROM) for further storage and analysis via a 1 gigabit fiber-optic link. An abstract block diagram of this system can be seen in Figure 2.

The cables connecting the FEAs to the DIOM are essentially the bottleneck in the data acquisition system. The data for each of the 16 FEAs that compose a quadrant of the DCH electronics are transmitted on 1/16 of the cable. Dead time occurs when the data volume generated per unit time by the large amount of accepted events in one FEA is greater than the carrying capacity of 1/16 of the cable. These ratios are not adjustable; thus, if one channel is producing more data than 1/16 of the cable can carry, and another FEA is producing little or no data, the system will experience dead time. The solution to this problem is either to increase the system's clocking speed, to enhance the cable capacity, or to redesign the system so that the amount of data sent through does not exceed the cable's carrying capacity. Advances in chip technology and availability of extra ROMs have made the second option

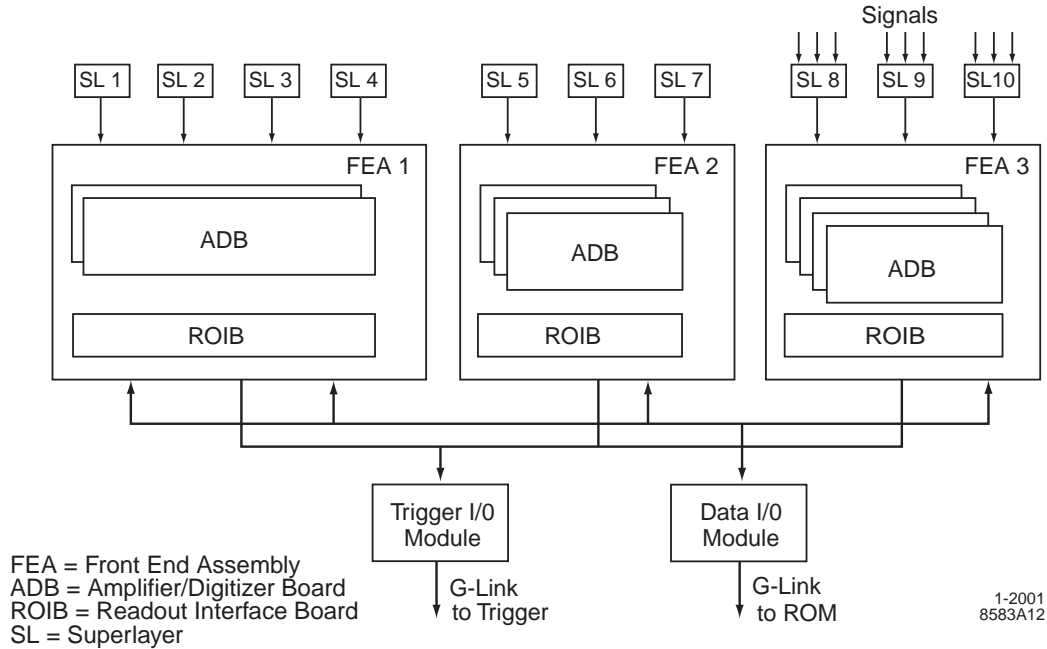


Figure 2: A block diagram of the DCH DAQ system. Taken from [2].

the most cost-effective and realistic.

The Phase II upgrade being implemented in the FEAs is the physical replacement of an older ROIB chip with a newer ball-grid array FPGA that uses increased memory and rewritable firmware to perform more tasks and lower the dataflow through the system. Pulse-height integration and pedestal removal functions that were previously performed in the ROM can now take place in the FEA. Thus, instead of sending a digitized, tagged waveform through the system, data are reduced to a single set of numbers that indicates the total deposited charge and location of trigger hits in the buffer. Whereas the initial DCH electronics setup produced 32 bytes of data per wire hit, the Phase II configuration will create a variable package size that averages to about 6.5 bytes per wire hit. Even at higher expected future luminosities, this change, along with respective alterations in data flow parallelism, will lower the dead times to less than 5%, .

In the first four years of BaBar's operation, most of the 4% dead time was caused by detector component malfunctions. Therefore, it is imperative that accepted changes in the BaBar detector are completely operational before they are implemented. The purpose of this paper is to explain the process by which Phase II changes in DCH ROIB boards were tested and to present and discuss the results of those tests.

## 3 Methods and Materials

### 3.1 Overview

For the DCH electronics upgrade, 81 new ROIB boards were fabricated to fill the 48 available spaces in the DCH FEAs. The 33 extra boards will be used to provide hardware for a DCH prototype and replacements for possible future failures. In order to make sure the upgraded DCH electronics are operational before their implementation, a series of tests can be performed on all functions and features of the new ROIBs. Real-time processes and final results of tests must also be catalogued in log files and databases for review and analysis.

Tests on the ROIBs are conducted using three computer-controlled test stands, some of which were used for tests of the original DCH FEAs and their components. On the component and calibration test stands, no modification is necessary for Phase II upgrade testing. The Drift Chamber Trigger (DCT) test stand was built after the initial construction of BaBar to provide a rigorous testing environment for all new BaBar hardware and software changes. The FEAs, test stands, and software were thoroughly tested beforehand to ensure that any failures in the testing process could be attributed to the ROIB boards themselves, rather than to testing apparatus and software.

This allows for easy identification of badly manufactured boards.

On each day of testing, six new ROIBS are connected into six previously tested FEAs after a thorough visual inspection of each board. Next, the FEAs are attached one at a time in any order to the component test stand and the calibration test stand. For these stands, the board is tested by using a computer terminal to input commands into an IOC directly or via UNIX protocols. If the performance of each board in these two test stands is deemed acceptable, the six FEAs are then placed simultaneously in the DCT test stand and run as a group. Each stand conducts a variety of tests; their names and basic functions are listed in Table 1.

## **3.2 Component Test Stand**

Also known as the VROM test stand, the component test stand is designed to check the functionality of specific FEA processes. The FEA is not physically situated in the test stand, but is plugged into a power supply and incorporated into the test stand hardware via a serial data cable. Fans placed on either side of the FEA keep temperatures within an acceptable operating range. For this stand, pulses of known duration and size are generated by discharging calibration circuits surrounding ELEFANT chips inside the FEA. Thus the signal input pins, normally the sources of incident pulses, are left unattached. A metal covering protects them from being accidentally bent or broken.

The individual components of the FEAs are checked by six separate tests in the VROM stand. The first, fifth, and sixth tests (featest 1, featest 5, and featest 6) are devoted to checking how an FEA and its components respond individually. Individual responses of registers and ELEFANTs are examined in featests 1 and 6, while featest 5 checks buffer readout of individual ELEFANTs.

Test Stand	Test Name	Function of Test
Component	Featest 1	Checks response of individual registers
	Featest 2	Checks that ELEFANTs go into count mode correctly when prompted
	Featest 3	Makes sure that trigger hits read out as expected
	Featest 4	Tests pulse-height readout; Checks for proper signal gain
	Featest 5	Checks individual ELEFANT buffer readouts
	Featest 6	Calls each ELEFANT individually and checks for its response
Calibration	Internal/External Gain (G)	Tests signal gain; similar to featest 4
	Noise Floor (NF)	Finds and examines pedestal height of every channel
	Slew (S)	Checks amplitude versus threshold crossing time of pulses
	Internal/External Linearity (L)	Checks that time offsets between pulses are properly sent
DCT	Trigger Pattern Calibration (T)	Displays visually the agreement between raw data and TDC hits
	Synch-Pulse (SP)	Checks buffer readout of four nearly simultaneous events
	Long-Term (LT)	Looks for similarity of ELEFANT output for millions of events

Table 1: A summary of tests and their functions

If the correct ELEFANT or register responds in an acceptable manner when called, the test is successful. Featests 2, 3, and 4 are tests that, when passed, will result in the return of identical output from all channels. Featest 2 tests whether or not all ELEFANTS can be brought into count mode; success in this test assures that the system’s clocking is correctly configured and operational. Once proper clocking is assured, triggering and pulse-height portions of the FADC data can be monitored for proper readout in featests 3 and 4, respectively. Differing output between any channels in these tests will result in a failure.

During the testing process, each featest is entered into the computer terminal individually, and then, if all pass, tests can then be repeated in sequence by using the command “featest 99”. After approximately ten successful repetitions, testing can be considered complete.

### **3.3 Calibration Test Stand**

Initially used to calibrate gain, triggering, and pedestal height for the original DCH FEAs, the calibration test stand is now used to check the functionality of the FEA as a whole. Unlike the component test stand, pulses are generated externally and fed from stand-based electronics into the FEA via the back-end signal inputs. Because of this, the FEA must be screwed tightly into place on a water-cooled structural frame resembling that of the DCH’s. To reduce backgrounds in the tests, the FEA is left to cool down for fifteen to twenty minutes before testing.

Triggered test signals are read out from the front of the FEA through a serial-link cable and interpreted differently depending on the test. For the internal and external analog gain tests, a failure occurs when the gain of an outgoing signal from an FEA is different than expected. The noise floor test

measures pedestal heights and compares them to reference values. The cause of a failure in this test is an excessively high pedestal, which results from noise in the test stand, increased background because of high temperatures, or because of improper wiring in new or old FEA components. Linearity tests check to see if time offsets corresponding to various known delay lengths between pulses are transferred properly through the FEA.

### **3.4 DCT Test Stand**

After the FEAs have been run through the component and calibration test stands, they are sent in a group of six to the DCT test stand area. The test stand is an operating mockup of the BaBar drift chamber; it incorporates identical software and sections of the DCH hardware. For example, instead of running sixteen azimuthally symmetric electronics sections for data acquisition, the DCT test stand runs only two. It contains one DIOM and one trigger input output module (TIOM), whereas the drift chamber has four DIOMs and eight TIOMs. Because of the similarity between the test stand and the full DCH, new software for the DCH can be tested on the DCT system before being implemented in the detector. Parts can also be swapped directly out of the DCT stand into the DCH. The one main difference between the two setups besides size is signal source: as in the component test stand, signals are generated by calibration circuits inside the FEA itself.

Three tests are run by the DCT test stand. The trigger pattern calibration test attempts to match raw data trigger hits on groups of channels from the TIOM with subsequent trigger data read from ELEFANT buffers to the ROMs via the DIOM. BaBar DCH software visually plots incoming data from the two systems in an end-on view of the DCH; if the test is successful, all raw trigger hits correspond to TDC hits in the same location. The synch-pulse test

addresses a problem identified in some of the current ELEFANT ICs. When four events are read out as fast as possible in one ELEFANT buffer, clocking information and FADC data are often confused with one another. By sending in four quick pulses, the synch-pulse test determines whether or not this is also the case with the new boards. The long-term test runs ELEFANTs in count mode overnight and logs upwards of  $2 \times 10^8$  events, allowing the reliability of the ELEFANTs to be tested very rigorously.

### **3.5 Test Records**

In order to keep track of new boards and their performance history, various forms of documentation have been created. To record in-test processes, a log file is created in the ROM window where commands are executed and data is returned from the FEA. All successes and failures are documented in this file; unfortunately, one must search through many lines of code to find them. The advantage of log files is that they contain the exact messages the software returns upon finding a failed event. This allows easy access for troubleshooting.

To have an overview of the entire testing process on all boards, hardware and testing databases have been created. Directly after a test on an FEA is concluded, the FEA serial number, ROIB number, and test start and end time are recorded in the testing database, along with information on which tests, if any, the FEA failed. Comments concerning test results can also be recorded. This simple system allows boards to be tested in an efficient and organized manner.

## 4 Results and Discussion

The purpose of testing the Phase II electronics upgrade is to identify badly manufactured boards and to uncover any noteworthy behavior in the new components before they are put into the DCH. Bad boards are sent back to the manufacturer, while unreliable ones are relegated to serving as backups for more dependable new units.

Out of the 81 new ROIB boards tested, 17 failures were documented in the testing database. However, the database was only marginally helpful in gauging how many problems actually occurred during the course of testing. In some cases, immediate troubleshooting of the test stands and FEAs after a failure solved the problem. For this situation, the test was recorded as successful in the database, despite the initial problems. Some events recorded in the database as failures were problems of the same nature as the ones just previously mentioned, only that the failed status was reported before troubleshooting solved the problem. Ultimately, log files for the tests were the best places to look for actual errors that occurred during the testing process. A short list of commonly failed tests and their reasons for failure can be seen in Table 2.

The component test stand identified one operational problem that occurred in some of the FEA 1 ROIBs. During featest 3 on ROIB boards 20004738, 20004782, 20004798, 20004807, and 20004818, read and predicted values on a small number of trigger buffers did not agree with one another, resulting in failed tests. During the troubleshooting process, it was observed that the delay chips on all failing ROIBs were manufactured at different times than the delay chips on the rest of the boards. The discrepancy in delay caused by the different chips was reconciled by putting an extra jumper on all offending boards. After the addition of this new part, the boards proceeded to behave

Test Name	Reason for Failure
Featest 3	Triggers not in sync; differing delay chips
Featest 4	Box not grounded; ambient noise
Internal and External Gain	Probable bad component on ADB
Noise Floor	Temperature-dependent background; improper ADB connection
Slew	Temperature-dependent background
Internal and External Linearity	Not fully understood; test stand-related
DCT tests	Network and database issues, delay chips, badly written data from ROIBs, lack of control over the DCT environment
Visual	various causes; errant soldering, etc.

Table 2: A short summary of failed tests and their reasons for failure

normally. These 2-jumper ROIBs will be kept as backups for DCH FEAs when the Phase II upgrade is installed.

The remaining featests on the component test stand were relatively uneventful. Featests 1, 2, 5, and 6 had no failures at any point. Featest 4 failed intermittently. Over the course of testing 81 boards, 43 one-channel featest 4 failures occurred at a rate of approximately one error for every 2000 to 4000 channels tested, depending on the FEA type. The failures were the result of ungrounded FEAs; on the component test stand, signal input pins were left floating, which allowed baseline fluctuations in the signal from ambient noise. Such a fluctuation contributes to an incorrect signal gain and pulse-height readout.

The calibration test stand, while incurring some fairly frequent failure modes, did not uncover any abnormal ROIB behavior. A ubiquitously occurring error was reported by the noise floor test. Despite waiting fifteen to twenty minutes for temperature-related background to dissipate, the reported pedestal remained at unacceptable values. As boards flawlessly passed triggering and pulse-height tests on other test stands, the problem was attributed to noise in the test stand itself. Any noise floor test with less than ten errors was disregarded. Two occurrences of higher noise floor problems, 36 and 42, for boards 20004788 and 20004782, occurred when ADB boards were not properly mounted on their FEA. The slew test failed intermittently, but these problems were also temperature-related and disregarded if problems occurred on an isolated basis.

More non-ROIB related failures were also noted on the linearity and gain tests. Three out of twelve gain tests on FEA #127 failed only at the highest settings, most likely due to a malfunctioning component on an ADB board. One board failed all gain tests for four channels and all linearity tests for all

channels. The offending FEA had passed related tests on other stands, so the problem was attributed to the test stand once again. The cause of failure has yet to be specifically determined. Later calibration tests on the same ROIB were completely successful.

The DCT test stand had more failures per test than either of the other two test stands, some of which were attributable to bad readout input boards. A chart of all ROIB failures can be found in Table 3. Board 20004764 was found to be improperly communicating its synchronization status: although it was locked with the system's clocking times, it was reporting that it was out of synchronization. This problem displayed itself as damage on the trigger pattern calibration test. Along with a delay chip problem, board 20004798 occasionally wrote tag bits and header bits in incorrect locations, causing a similar kind of failure. These problems could be the result of bad soldering in the ROIB board itself. These two ROIBs, as well as another board (20004783) with a massive shorting solder found during visual tests, are the only completely non-functioning boards.

The rest of the DCT failures were not ROIB-related. The complexity of the DCT test is one reason so many failures were encountered. Rather than running independently from other systems, the DCT stand has to communicate with ROMs from various locations, which means that all ROMs, databases, and networks must be operational in order for testing to proceed successfully. The DCT stand is also used for a variety of purposes, including trigger and software experimentation. If non-ROIB-related work on the DCH mockup has altered any DCT operating procedures or environments, Phase II upgrade tests will return failures. It is also worth noting that some of the failures on this test stand are recurrences of problems found on previous test stands. For example, the delay chip problem first identified on the VROM stand caused

ROIB #	Visual	F1	F2	F3	F4	F5	F6	G	NF	S	L	T	SP	LT
20004738	.	.	.	×	.	.	.	.	.	.	.	.	.	.
20004764	.	.	.	.	.	.	.	.	.	.	.	×	×	-
20004782	.	.	.	×	.	.	.	.	.	.	.	.	.	.
20004783	×	-	-	-	-	-	-	-	-	-	-	-	-	-
20004798	.	.	.	×	.	.	.	.	.	.	.	×	×	-
20004807	.	.	.	×	.	.	.	.	.	.	.	.	.	.
20004812	.	.	.	×	.	.	.	.	.	.	.	.	.	.
20004818	.	.	.	×	.	.	.	.	.	.	.	.	.	.

Table 3: Bad or unusually behaving boards and their failed tests. Symbol key: ., passed test; ×, failed test; -, not tested.

Test name abbreviations: F, Featest; G, Internal/External Gain; NF, Noise Floor; S, Slew; L, Internal/External Linearity; T, Trigger Pattern Calibration; SP, Sync-Pulse; LT, Long-Term.

data to be improperly written from board 20004812 in the DCT stand.

To summarize overall ROIB performance the results from all three test stands and visual testing should be viewed as a whole. Three boards were completely non-functional, and five others displayed slightly different but fixable delay behaviors. Nine boards need to be tested more thoroughly, either because they missed certain test stands or because they experienced some unpredictable and possibly anomalous failures during the testing process. Four boards have yet to be assembled or tested.

## 5 Conclusion

Overall, the functionality and short-term reliability of the ROIB boards has been proven through the course of testing, with few exceptions. Out of 81 boards, the three completely non-functional boards will likely be sent back to the manufacturer for replacement. The five FEA 1 boards with delay problems only will be used as backups for more reliable failure-free boards. Thus, 73 completely functional and reliable boards remain to be used for various purposes. Six ROIBs will be installed permanently on the DCT test stand to be used for developing or troubleshooting triggering and software problems in the DCH. Two will be integrated into the Proto-2 drift chamber prototype, which is located near the DCT test stand. The remaining boards will either be installed into the 48 available ROIB slots on the front end of the BaBar drift chamber electronics or will serve as spares for failed boards in the DAQ system. In the event of massive drift chamber electronics failures, many replacements will be ready and available for installation to restart the experiment as soon as possible.

Besides checking for functionality of ROIB boards in the Phase II upgrade, hardware testing has also served other important purposes. First, it has

allowed the BaBar group to observe the performance of new ROIBs without having to use them in the drift chamber itself. This experience with the upgrade allows for easier and quicker troubleshooting of problems during drift chamber operation. In addition, testing has identified important problems in other aspects of the electronics. Software and non-ROIB related hardware problems, such as incorrectly connected or malfunctioning ADB boards, were noticed and will be fixed before implementing the upgrade. Without testing the ROIBs, these problems could have gone unnoticed, causing failures in the drift chamber and interruptions in data-taking.

Future work will include longer-term testing of all FEA components. When it is certain that the properly tested Phase II upgrade can operate reliably in the BaBar detector, the changes will be implemented. In its operation, the upgrade will reduce dataflow through the system, significantly decreasing dead time without sacrificing detector reliability.

## 6 Acknowledgements

I would like to acknowledge Karl Bouldin and Mike Kelsey for their help in learning about and operating the DCH electronics system and test stands, and for solving all those problems that were beyond my expertise. I also want to thank Jochen Dingfelder, Vera Luth, and the rest of SLAC Research Group C for their help and guidance during the course of the project, and the Department of Energy, Office of Science for making my internship possible.

## References

- [1] DCH DAQ upgrade Working group, Jessop *et al.* "Proposal to Upgrade the BaBar Drift Chamber Electronics." February 6, 2004.

- [2] *BABAR* Collaboration, B. Aubert *et al.* “The BABAR detector,” in Nuclear Instruments and Methods in Physics Research A, Vol. 479, pp. 1-116.

Analysis of Old Copper Synchrotron Light Absorbers from the Stanford Positron  
Electron Accelerating Ring

Sara R Marshall

Office of Science, SULI Program

Franklin W. Olin College of Engineering

Stanford Linear Accelerator Center

Menlo Park, California

August 3, 2005

Prepared in partial fulfillment of the requirements of the Office of Science, U.S.  
Department of Energy Science Undergraduate Laboratory Internship (SULI) Program  
under the direction of Benjamin Scott in Accelerator Systems Development Engineering  
& Technology Services of the Stanford Synchrotron Radiation Laboratory at the Stanford  
Linear Accelerator Center.

Participant:

\_\_\_\_\_  
Signature

Research Advisor:

\_\_\_\_\_  
Signature

## Table of Contents

Abstract	v
Introduction	1
Methods and Materials	2
Results	4
Discussion and Conclusions	5
Acknowledgements	7
References	8
Tables	9
Figures	11

## Tables

Table 1: Properties of each absorber observed	9
Table 2: Polish repetitions	9
Table 3: Corrosion depth and absorber diameters	10
Table 4: Chemical composition of absorbers	10

## Figures

Figure 1: Sample location diagram	11
Figure 2: SEM image of surface scratches	11
Figure 3: SEM image of outer surfaces	12
Figure 4: BE image of outer surfaces	12
Figure 5: Outer edges of samples	12
Figure 6: Inner edges of samples	13
Figure 7: Cross-section of experimental sample	13
Figure 8: Grain structure of samples	13
Figure 9: Surface of inner tube	14

## **Abstract**

Analysis of Old Copper Synchrotron Light Absorbers from the Stanford Positron Electron Accelerating Ring. SARA MARSHALL (Olin College of Engineering, Needham, MA 02492) BEN SCOTT (Stanford Linear Accelerator Center, Menlo Park, CA 94025).

Synchrotron light absorbers intercept synchrotron radiation to protect chamber walls from excessive heat. When subjected to the high temperature of the beam, these absorbers undergo thermal stress. If the stress is too great or fatigues the material, the absorbers may fail. These absorbers are designed to last the lifetime of the machine. Any premature cracking could result in a leak and, consequently, loss of the ultra high vacuum environment. Using secondary and backscattered electron techniques, several sections of a used copper absorber were analyzed for material damage. Chemical analyses were performed on these samples as well. Comparing the unexposed sections to the sections exposed to the electron beam, few cracks were seen in the copper. However, the exposed samples showed heavy surface damage, in addition to crevices that could eventually result in material failure. Significant corrosion was also evident along the water cooling passage of the samples. These findings suggest that further investigation and periodic inspection of absorbers in SPEAR3 are necessary to control corrosion of the copper.

## INTRODUCTION

Synchrotron light absorbers protect the beam chamber walls from excessive heat due to the radiation given off by the accelerated beam. Some of these absorbers use oxygen free electronic (OFE) grade copper tubes, cooled with water, to mask the beam section walls. The current design practice is to limit the thermal stress in these absorbers to less than the fatigue strength of copper. Any cracks along the grain boundaries jeopardize the performance of the copper and may cause a catastrophic water leak into the high vacuum environment. Copper has no defined fatigue limit; any number of cycles could damage the structure. So, in practice, this means that many absorbers employ GLIDCOP, a dispersion hardened alloy, as the primary heat conducting material because of the high yield strength.

In this investigation, the absorber used in Beam Line 10 (BL10) of the second Stanford Positron Electron Accelerating Ring (SPEAR2) for 16 years was analyzed to determine whether the absorbers experienced any critical damage. The analysis included the observation of select sections of the copper tubing (see Figure 1) under the scanning electron microscope (SEM), using secondary (SE) and back-scattered (BE) electron techniques to search for material damage due to continuous thermal stress. In addition, energy dispersive x-ray spectrometry (EDS) was used to analyze material compositional changes. Using this technology, the properties of new copper were compared to the property data of the fatigued copper. Absorbers from BL11 were also observed to provide additional evidence for corrosion. The properties of each absorber are listed in

Table 1, some of the values of which were taken from a previous study [1]. Further investigation could shed light on the mechanical situation of the copper absorbers.

## **MATERIALS AND METHODS**

All samples were OFE copper taken from the SPEAR2 storage ring. Using a low stress-inducing water-cooled Buehler Abrasimet 2 diamond blade saw, six samples were cut from one absorber: 2 control cross-sections, 1 control surface, 2 experimental cross-sections, and 1 experimental surface. The control samples were taken from the part of the absorber that was not exposed to the electron beam. The experimental samples were taken from the exposed part (see Figure 1).

After cutting, the samples were mounted in 25 cubic centimeters of Buehler transoptic powder using a Simplimet 3 mounting press in preload mode. The resin mount allows for easier observation of the samples. The press operated for 5.5 minutes with a temperature of 150°C and a pressure of 3900psi.

Each sample was prepared for analysis according to ASTM standard E3 [2]. This allows for uniform sample preparation. Rough grinding was done using a Power Pro 5000 water cooled system with Buehler metallurgical grade silicon carbide paper at 150 reps per minute (RPM) for 40 second intervals. Paper was replaced after each cycle. The grit sizes used and their respective repetitions are listed in Table 2.

After grinding, the samples were coarsely polished using a Power Pro 5000 system with Struers diamond suspension in 6 $\mu$ m, 3 $\mu$ m and 1 $\mu$ m sizes at 120 RPM. Samples ran once for each size. Nylon 1000 cloth loaded with  $\frac{3}{4}$  gram of Buehler Metadi

paste was used for the 6 $\mu$ m run for 5 minutes. Struers MOL woven wool cloth loaded with Metadi paste was used for the 3 $\mu$ m interval for 4 minutes. Buehler Microcloth synthetic cloth was used for the 1 $\mu$ m run for 3.5 minutes.

Each sample was finish-polished using a Power Pro 5000 system with Struers 0.06 $\mu$ m OP-S colloidal silica suspension on an OP-CHEM porous neoprene cloth surface for 3 minutes at 100 RPM.

Vibratory polish was used to remove fine scratches at a setting of 35. Using a Microcloth loaded with 150ml of 0.02 $\mu$ m Mastermet 2 non-crystallizing colloidal silica suspension, the samples were polished for 2.5 hours. The polishing procedure removed most of the surface scratches, leaving a few small ones behind.

Observation of the samples took place after the completion of polishing. Cross-sections were viewed using the optical microscope at magnifications ranging from 25 to 200x. The SEM was used to analyze the surface samples at magnifications ranging from 15 to 5000x. Chemical analysis was performed on the surface samples using EDS techniques.

The absorbers from BL11 were cut using a Buehler band saw. After deburring the edges of each cut, the sections were observed with a magnifying glass and then followed the same preparation procedure discussed above. Corrosion depth was estimated by using Vermont Gage Series C Plus gauges to measure the inner diameters of the tubing. The valleys of the corrosion ring were measured using electronic calipers from the gauge to the tip of the valley. Measurements taken from the cut samples are listed in Table 3.

## RESULTS

The three observation techniques each gave a snapshot of the mechanical and thermal damage withstood by the absorber. The SE method showed extensive surface scratches on the control and the experimental samples (see Figure 2). At 1000x magnification, the experimental sample showed heavy grooves along the surface. Figure 3 compares the control sample surface to the experimental sample surface at this magnification.

Figure 4 displays the surface of each sample using the BE technique. The BE method constructs an image of the surface of a sample according to atomic number, as opposed to the SE method, which builds an image based on topography.

Table 4 shows the results of the chemical analysis. Each sample contained carbon and oxygen in addition to copper. The amount of carbon stayed around the same level; however the experimental sample showed greater amounts of oxygen than did the control.

The outer edge of each sample was observed using the optical microscope. Figure 5 illustrates the mechanical damage sustained by the sample exposed to the intensity of the electron beam.

Figure 6 displays the edge of the water cooling passage of the absorber. Each sample showed heavy indentation. The extent of this mechanical damage for each absorber is listed in Table 3. Figure 7 shows the overall cross-section of the experimental sample.

Using the optical microscope, grain structure was observed. Figure 8 illustrates the effect of heating on water-cooled OFE copper. The experimental sample sustained substantial grain growth and thus thermal damage.

Table 1 lists the properties of each absorber. Values noted with \* were taken from a previous study [1]. Thermal stress data was determined by using a two-dimensional ANSYS model. Flow velocity was calculated by dividing the flow rate by the area of the cross-section of the water passage ( $v = \frac{q}{A}$ ).

The corrosion depth and diameter of Table 3 were measured using the procedure discussed in *Materials and Methods*.

Figure 9 illustrates the plating discovered on the inner surface of the BL10 near absorber. Plating of this type was found on each absorber studied.

## **DISCUSSION AND CONCLUSION**

In order for OFE copper to fail, extensive grain movement must occur. When individual grains move within a material, they push into each other. Often the force causes the grains to slip and pull apart from one another. This movement results in the cracks characteristic of failure. When intense heat is added to the system, the grains begin to fuse together, leaving behind larger and fewer grains. This grain growth weakens the material as there are fewer grains to support the structure. The investigation of the BL10 absorber showed evidence of high grain activity. Comparing the control to the experimental sample in Figure 3, it is clear that the structure of the copper changed during its exposure to the electron beam.

Despite the surface scratches, distinct grooves can be seen in the experimental sample (see Figure 5). These features could be deeper surface scratches, or could be the result of grain separation. But since these grooves do not seem to occur along grain boundaries, they may be deeper surface scratches.

The experimental sample experienced substantial grain growth during its time in operation, as evidenced by Figure 8. As copper is formed into a tube, grains break up, leaving vast amounts of small grains. As a result of this work-hardening, the material strengthens. Heat undoes this hardening, fusing grains together.

An unexpected result of the absorber usage was the significant corrosion experienced by the inner surface of the tube. This corrosion could be the result of fast flowing or stagnant water. According to an outside study [3], when oxides form on the copper surface and carbon dioxide is present in the water, the  $\text{CO}_2$  forms an acid that breaks down into hydrogen atoms and  $\text{HCO}_3^-$ . The hydrogen atoms react with the oxygen atoms on the surface of the copper to form water. The copper dissolves and the process continues. In addition, the water flowing through the far BL10 tube ran with a velocity of 22.1 ft/s. Typically, the flow velocity is set at 15 ft/s to provide a high heat transfer coefficient and reduced cavitation. The velocities experienced by these absorbers fall in the undesired range. At these speeds, the copper tends to corrode at a faster rate than a normal absorber.

Interestingly, the absorbers from BL10 and 11 appear to have material deposited inside the tubes. Before use, the BL11 absorbers were gun-bored with a 0.25" diameter. As seen from Table 3, the diameters of these samples decreased, indicating that material was deposited and plated to the inside of the tube during use. This plating can be seen

along the inside of each tube (see Figure 9). The composition of the deposit was found to be copper oxide. An EDS test performed on the inner surface showed high levels of oxygen and copper. This indicates that the high velocity of the water forced some of the corroded material onto the walls of the water passage.

One way to prevent the copper from severely corroding would be to slowly circulate the water through the absorbers during shutdown periods. This would help prevent stagnation. Another way would be to keep the velocities of the water at reasonable levels during each run. Taking an unused SPEAR3 absorber and subjecting it to controlled high flow velocities as well as stagnant water would provide additional information as to the severity of these problems under optimal operating conditions.

This research has provided valuable information concerning the effects of high temperatures on the synchrotron light absorbers used in the SPEAR storage ring. With this knowledge of corrosion and material weakening, the engineers of the Stanford Synchrotron Radiation Laboratory can take greater steps to prevent catastrophic failure in the future.

## **ACKNOWLEDGEMENTS**

This research was conducted at the Stanford Linear Accelerator Center. I would like to thank my mentor Ben Scott for his knowledge and support. Also I thank my colleagues Rebecca Armenta and Matthew Crockett for their enthusiasm and input. Many thanks go to Bob Kirby, Will Glesener, and Mike Swanson for preparing the samples. I also thank Stacey Block for her support. Finally, I would like to extend my

gratitude to the U.S. Department of Energy, Office of Science for granting me the opportunity to participate in the exceptional SULI Program and the chance to have an exciting internship.

## REFERENCES

- [1] Ross, Max, *Synchrotron Radiation Mask Temperature and Stress Results and Analysis: SPEAR2 Masks in the Beam Line 5, 9, 10, 11 Insertion Device Vacuum Chambers*, SSRL Engineering Note M485, 2004.
- [2] ASTM E3: Standard Methods of Preparation of Metallographic Specimens.
- [3] Dortwegt, R., "Low-Conductivity Water Systems for Accelerators," *2003 IEEE Particle Accelerator Conference*, pp 630-634, 2003.

## TABLES

Absorber	Service Length (yrs)	Material	Power input* (watt/cm)	$\Delta T$ metal/metal-water interface* ( $^{\circ}C$ )	LCW velocity (ft/sec)	Thermal Stress* (ksi)
BL10 far	16 run cycles Inst 87 Rem 04	OFE Cu	78.9	27.1/57.9	13.5gpm 22.0	11.5
BL10 near		OFE Cu	46.6	19.2/35.2		8.1
BL11 far	5 run cycles Inst 98 Rem 04	OFE Cu	59.0	31.4/126.9	4.7gpm 30.9	13.3
BL11 mid		OFE Cu	47.9	28.0/106.7		11.8
BL11 near		OFE Cu	62.6	40.8/144.4		17.3

**Table 1:** Properties of each absorber observed. Each value corresponds to the maximum current experienced by these absorbers (200mA). Inst stands for installed, Rem stands for removed. \* Taken from previous study [1].

Grit	# of Repetitions
320	3
400	3
600	5
800	5

**Table 2:** Number of times samples were run for each grit size.

<b>Absorber</b>	<b>Corrosion Depth (in)</b>	<b>Original Diameter* (in)</b>	<b>Measured Diameter (in)</b>
BL10 far	0.018	0.5 <sup>#</sup>	0.462
BL10 near	0.018	0.5 <sup>#</sup>	0.475
BL11 far	0.017	0.25	0.227
BL11 mid	0.008	0.25	0.225
BL11 near	0.012	0.25	0.242

**Table 3:** Corrosion depths and diameters of the absorbers studied. \*Original diameter taken from drawing.  
<sup>#</sup>Drawing not available, value is estimated.

<b>Sample</b>	<b>Chemical Composition (in order of abundance)</b>
Control	Cu, C, O, S
Experimental	Cu, O, S, C

**Table 4:** Chemical composition of each sample.

## FIGURES

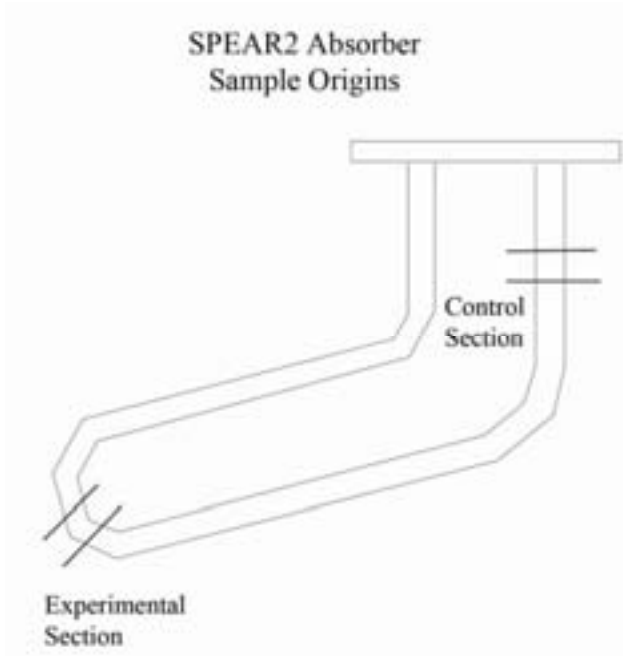


**Figure 1:** Image identifying original locations of samples.

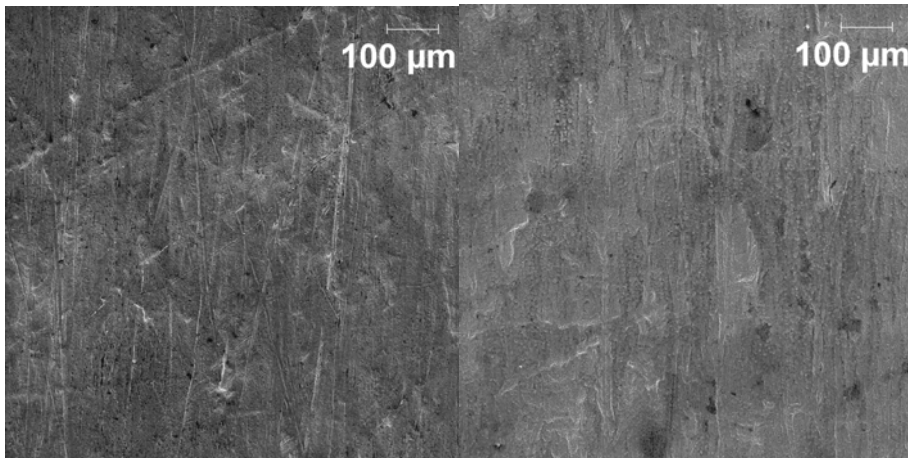


**Figure 2:** SEM image of surface scratches on both samples, control (left) and experimental (right) at 100x magnification

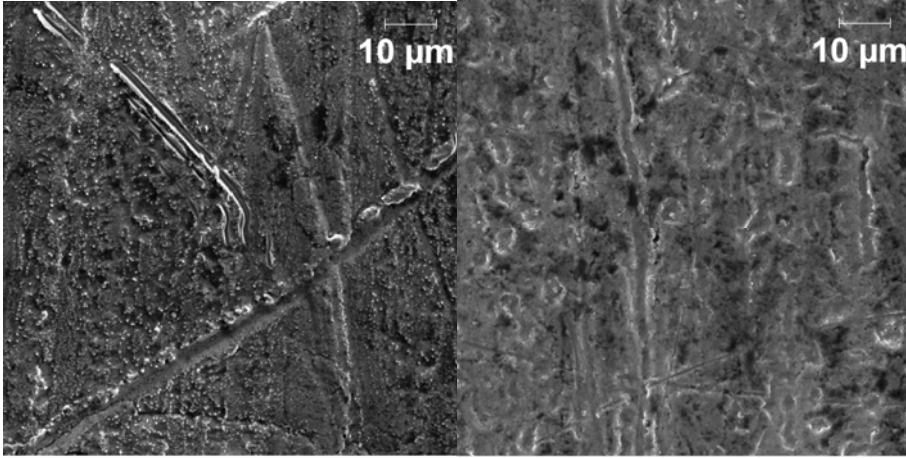


**Figure 3:** SEM image of outer surface of samples at 1000x magnification. Experimental (right) shows grain movement and structure change.

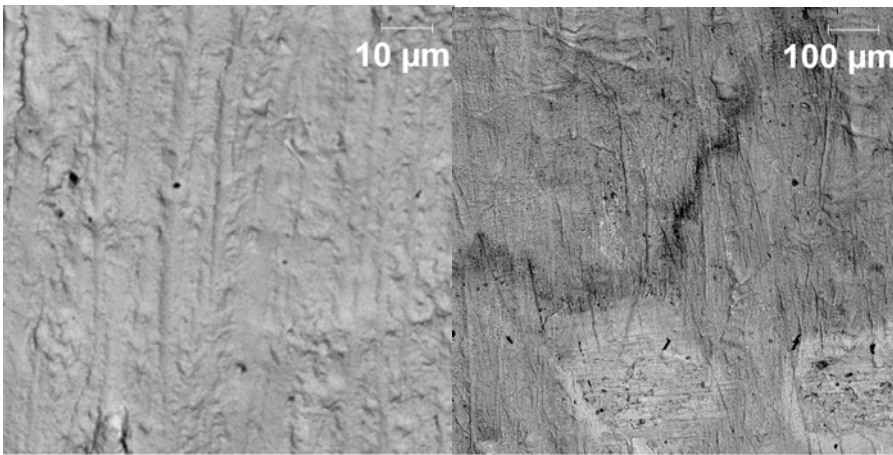


**Figure 4:** BE image of sample surfaces. Control (left) at 1000x magnification. Experimental (right) at 100x magnification. Experimental shows greater color change.

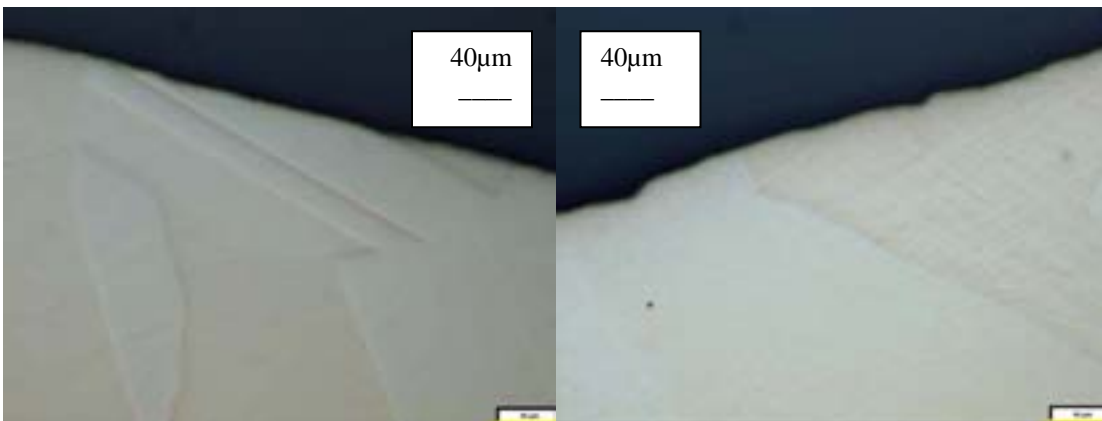


**Figure 5:** Outer edge of samples seen through optical microscope at 200x magnification. Control (left) shows a smoother edge than experimental (right).



**Figure 6:** Inner edge of absorber at 25x magnification showing water corrosion. The experimental (right) shows greater damage.

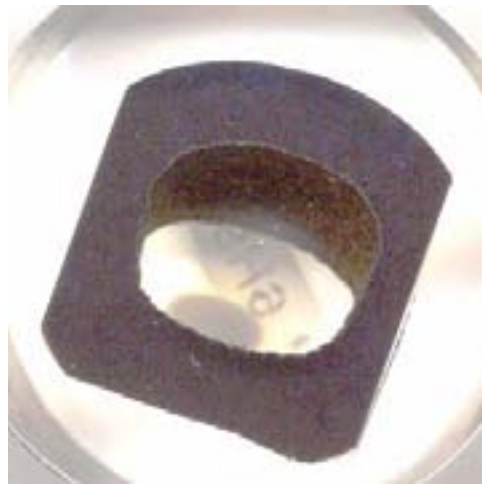


**Figure 7:** Cross-section of experimental sample. Corrosion is evident along the inner edge of the section. Figure 6 experimental sample enlarges this section. Image enlarged 2.5 times.

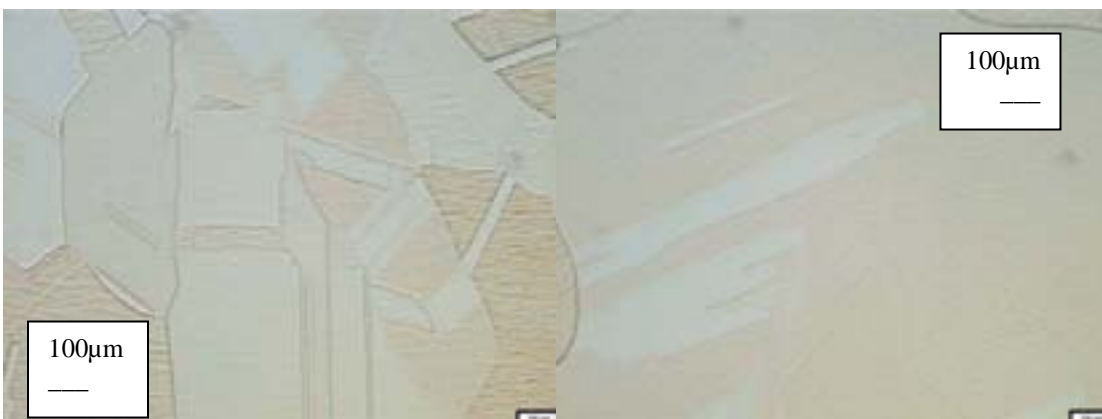


**Figure 8:** Grain structure of samples at 25x magnification. Control (left) has an overall smaller grain size than the experimental sample (right).

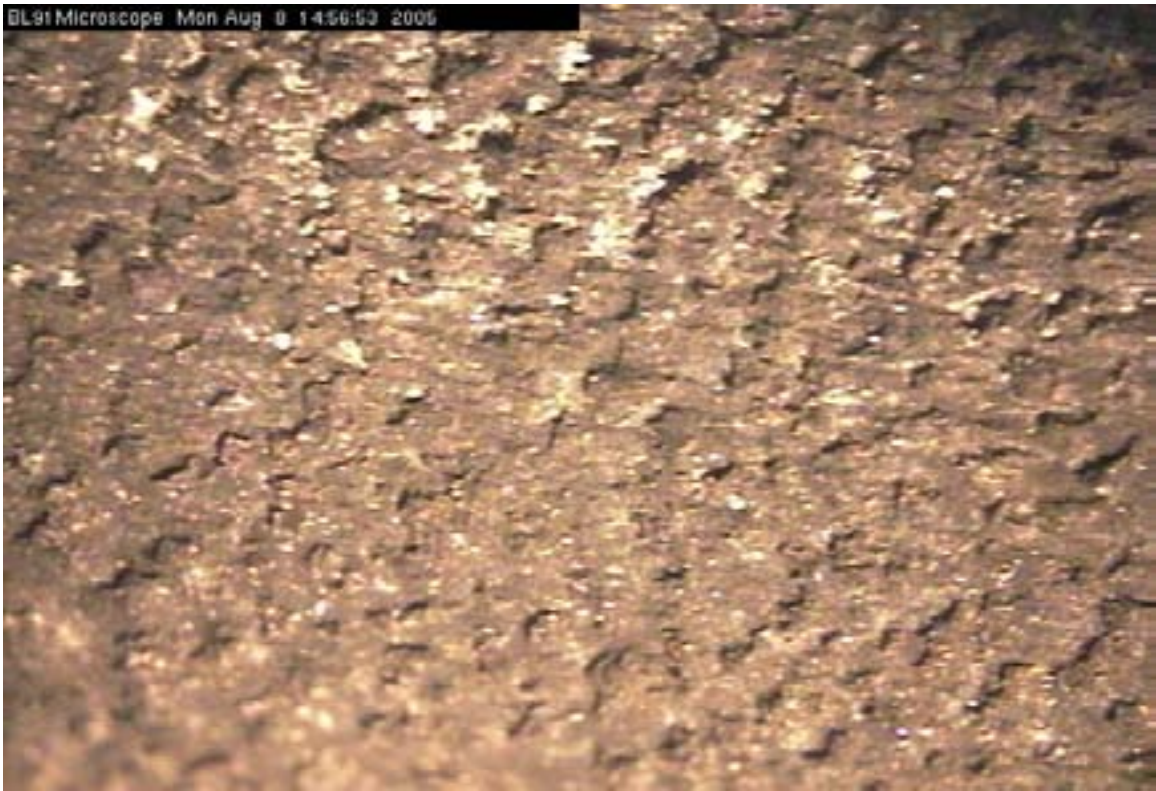


**Figure 9:** Image taken from BL9-1 microscope showing black deposit on water cooling passage, 12.5x magnification.

## Study the Z-plane strip capacitance

Harshil Parikh

Office of Science, Science Undergraduate Laboratory Internship

University of Illinois at Urbana-Champaign

Stanford Linear Accelerator Center

Menlo Park, CA

August 4<sup>th</sup>, 2005

Prepared in partial fulfillment of the requirements of the Office of Science,  
Department of Energy's Science Undergraduate Laboratory Internship under the  
direction of Dr. Sanjay Swain in the High-Energy department at Stanford Linear  
Accelerator Center.

Participant: \_\_\_\_\_

Research Advisor: \_\_\_\_\_

## **Table of Contents**

Abstract	3 - 4
Introduction	4 - 6
Materials and Methods	6 - 11
Results	11 - 14
Discussion and Conclusions	15 - 16
Acknowledgements	16
References	17

## **Abstract**

Study of the Z-plane strip capacitance. Harshil Parikh (University of Illinois at Urbana-Champaign, Urbana, IL 61801) Dr. Sanjay Swain (Stanford Linear Accelerator Center, Menlo Park CA 94305)

The BaBar detector at the Stanford Linear Accelerator Center is currently undergoing an upgrade to improve its muon and neutral hadron detection system. The Resistive Plate Chambers (RPCs) that had been used till now have deteriorated in performance over the past few years and are being replaced by Limited Streamer Tube (LSTs). Each layer of the system consists of a set of up to 10 streamer tube modules which provide one coordinate ( $\phi$  coordinate) and a single "Z-plane" which provides the Z coordinate of the hit. The large area Z-planes (up to  $12 m^2$ ) are 1mm thick and contain 96 copper strips that detect the induced charge from avalanches created in the streamer tube wires. All the Z-planes needed for the upgrade have already been constructed, but only a third of the planes were installed last summer. After installing the 24 Z-planes last year, it was learned that 0.7% of the strips were dead when put inside the detector. This was mainly due to the delicate solder joint between the read-out cable and the strip, and since it is difficult to access or replace the Z-planes inside the detector, it is very important to perform various tests to make sure that the Z-

planes will be efficient and effective in the long term. We measure the capacitance between the copper strips and the ground plane, and compare it to the theoretical value that we expect. Instead of measuring the capacitance channel by channel, which would be a very tedious job, we developed a more effective method of measuring the capacitance. Since all the Z-planes were built at SLAC, we also built a smaller 46 cm by 30 cm Z-plane with 12 strips just to see how they were constructed and to gain a better understanding about the solder joints.

### **Introduction**

The BaBar detector at Stanford Linear Accelerator Center (SLAC) is a device that studies  $e^+e^-$  collisions at the  $\Upsilon(4s)$ . The detector group proposed an upgrade in May 2003 which was intended to improve muon and neutral hadron detection in the Instrumental Flux Return (IFR) barrel region of the BaBar detector. Muon detection is vital for analyses such as semi-/leptonic decays and lepton tagging for CP violation. Initially, Resistive Plate Chambers (RPCs) were used, but several persistent problems in the RPCs resulted in continuous drop in the efficiency of the muon identification. To improve the efficiency, the proposed upgrade introduced a completely new technology of Limited Streamer Tubes (LSTs). There are two components of LSTs: the streamer tube chamber array and an associated Z-plane made up of copper strips and copper planes. A gas flows through the streamer tubes, and when a  $\mu$  passes through the tube, it

ionizes the gas which produces electron/ion pairs. The electric field causes the pairs to accelerate towards the anode which causes the electrons to gain energy. This gain causes further ionization, and high voltage causes large amounts of charge multiplication (Townsend effect) that results in an avalanche. The secondary electron/ion pairs create an electric field comparable to the applied field. The avalanche gets saturated, but there is an electric field between the avalanche tip and the anode wire. New avalanches form from photoionized electrons, and the streamer propagates to the anode wire producing a signal. A current is also induced in the Z-plane below the tubes, and this current is detected through the cable soldered with the Cu strip.

During the summer of 2004, streamer tubes and Z-planes were installed in 2 of the 6 sections of the IFR barrel region. Several important lessons were learned while installing the 24 Z-planes in the detector. Firstly, handling and moving the Z-planes sometimes broke the solder joint, and these broken solder joints were only found after they were put into the detector. Secondly, a device was needed to quickly and efficiently check whether the solder joints are broken before we put them into the detector. The Z-planes are made in a novel but complicated method using mylar sheets, copper strips, ribbon cables, and copper sheets. The copper strips have been soldered to the ribbon cables, but from previous experience, they are known to easily break and make that part of the Z-plane essentially useless. In order to solve this problem, we measure the

capacitance of the Z-planes with respect to the ground plane, and we use the results of the capacitance to determine the status of the solder joints.

### **Materials and Methods**

Since the Z-plane consists of a Cu ground plane below the 96 Cu strips, one can theoretically approximate the capacitance between a strip and the plane, and measure it experimentally. An approximate formula to calculate the

capacitance between the strip and the plane is given by:  $C = \frac{2 \epsilon_o A_1 A_2}{(A_1 + A_2) d}$  where

$A_1$  is the area of the strip,  $A_2$  is the area of the ground plane and  $d$  is the distance between them. If one plugs in an approximate value for the three variables, one gets an approximate capacitance value  $C \approx 4.55 nF$ . Since the ribbon cable that carries the signal is soldered to the Cu strip, the capacitance between the ribbon cable and the ground plane should approximately be equal to the capacitance between the Cu strip and the ground plane. Therefore, one can conclude that if one measures the capacitance between the ribbon cable and the ground plane, one should measure a value close to  $C \approx 4.55 nF$ . For any given strip in the Z-plane, if the solder joint is intact and the strip is well connected to the cable, one should measure a capacitance value close to the calculated approximate value. On the other hand, if one measures a capacitance value that is much less than the theoretical value, then one can conclude that the solder joint is loose and it must be fixed before the Z-planes are installed inside the

detector. Since there were 48 Z-planes (4 Layer 18 Z-planes) that need to be installed, and each Z-plane has 96 strips (except Layer 18), that's a total of 4568 strips, or in other words, 4568 measurements. We realized that with a little ingenuity, we can take these measurements in a much more effective manner than manually measuring channel-by-channel using a capacitance meter. Moreover, if we can measure the capacitance of one Z-plane in a time efficient manner, we can check for bad solder joints very quickly and that would help us tremendously during installation. If we build an electrical box that takes in the signal from the ribbon cable, and use a switch to swap between the 16 channels, we can take these 4568 measurements in an effective manner. In order to build the box, several materials were needed: 2 12-position single pole rotary switches, a 16 channel signal cable, a transition board, an output BNC connector, a capacitance meter, and a small box to mount the switches and the connector.



*Figure 1 shows the transition board that takes in the white ribbon cable from the Z-plane, a 16 channel blue & white signal cable and 2 12-position single pole rotary switches*

Figure 1 shows most of the materials that were used to build the box. We first strip the insulation off the blue and white signal cable and determine which color wires carry the signal and which color wires act as ground. After some testing, it is determined that the white color wires are the signal wires, and now, we needed to figure out how to solder to solder on 16

signal wires on the 2 12-position rotary switches. Since the switch has 12 input and one output positions, we decided to do the following: solder 11 signal cables (first white cable onto position 1, second white cable onto position 2, etc.), onto positions 1 – 11 on the switch (switch A), then use another wire to connect the out of the 2<sup>nd</sup> switch (switch B) onto the 12<sup>th</sup> position of the first switch. Then, if we connect the remaining 5 signal cables onto position 1 – 5 on the second switch, we have completely connected the 16 channel signal cable to the 2 rotary switches. We now collected all the ground wires together (blue wires), and soldered them onto the box using a solder log. The solder log is then screwed onto the box, hence acting as a ground. We then took another wire and connected the output of the first switch (the one with 11 signal wires) to a BNC output connector. We then use a BNC wire cable to connect from the BNC connector to the capacitance meter, which then reads out the value of the capacitance. One final step was needed to connect the ground plane to the box: we took another wire and soldered it to a solder log, and connected the other end of the wire to an alligator clip. Now, we can clip the ground plane to the box using the wire with the alligator clip, and our box is complete.

Figure 2 shows the final picture of the box, with all its components. After the box has been completed, we needed to figure out a convention on how to rotate the switch to swap between channels 1 -16. Since 11 signal wires are connected to one switch, channels 1 – 11 can be accessed by rotating switch A



*Figure 2 shows the complete box, with the 16 channel signal cable connected to the transition board, the blue wire with the alligator clip that connects to the ground plane, and the black wire which connects from an out BNC connector to the capacitance meter*

in the counterclockwise direction. In order to access channels 12 – 16, one needs to place switch A on position 12, and then rotate Switch B in the counterclockwise direction. Finally then, we now had a capacitance box that we could use to measure the capacitance

between the output ribbon cables and the Cu ground plane. In order to take a measurement, we insert the 2 ribbon cables

from the Z-plane into the transition board, attach the BNC cable to a capacitance meter, and rotate the switches to get the measurements.

A second major part of my project involved actually making a small Z-plane. This small Z-plane had 16 strips (8 on each side), and it was made using the same materials as the actual Z-planes that were made last year. The motivations for making the Z-plane are multi-fold: to grasp a better understanding about the structure of the Z-plane, to learn more about the solder joints and why they are so delicate and break easily, and to gain new knowledge in a novel technique of vacuum thermal lamination. Figure 3 shows the precise makeup of the Z-plane, and we followed this structure while making our smaller Z-plane. We first cut out 3mil, 5mil, and 10 mil mylar film to the size of the Z-plane (60 cm x 24 cm), and a Cu foil just a bit smaller than the size of the Mylar

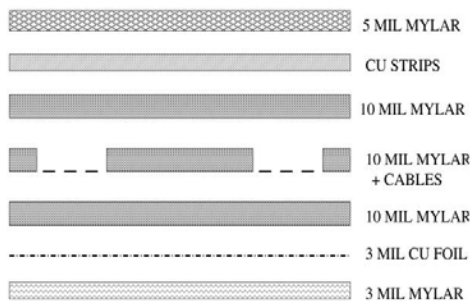


Figure 3: Detailed make up of the Z-plane

film. We first placed the 3 Mil Mylar adhesive side up, then placed a Cu Foil on top of the mylar. We then added a 10 Mil mylar adhesive side face down, another 10 Mil mylar adhesive side face down with holes, and 2 ribbon cables with solder on them at 8 different wires at 8 spots. Therefore, each cable had 8 solder spots on 8 different wires (1 solder spot per wire), and these solder spots matched the holes in the 10 mil mylar. Then, we added Cu strips

on top of the 10 Mil mylar film with holes, so that we could feel the solder spots from the cable to the strips. We then carefully cut out the Cu strip just enough so that the solder spot passes through the strip, and then we melted the solder spot onto the Cu strip. The ribbon cable was now soldered onto the Cu strip, and we added another 5 mil mylar adhesive side face down on top of the Cu strip to protect the strip (Figure 4) . We now needed to take all the air out from the Z-plane, so we used this new process of thermal vacuum lamination to suck all the air out from the plane.

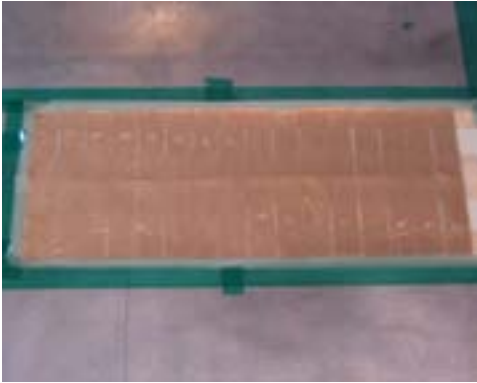


Figure 4



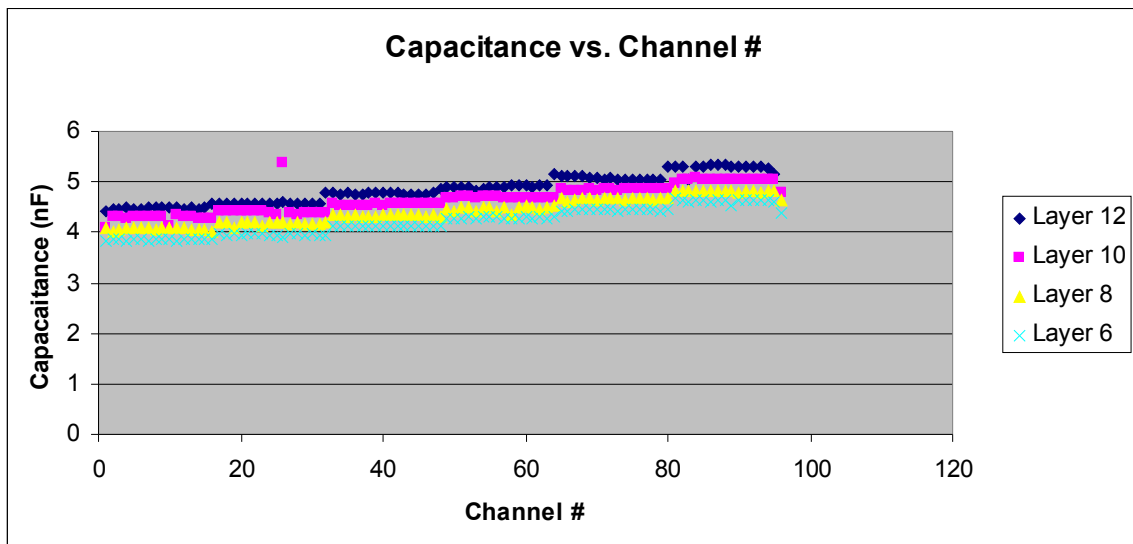
Figure 4, 5, 6: Z-plane before cloth was put on; Z-plane covered in cloth and taped to make it air tight; Z-plane after the thermal vacuum lamination process

We covered the entire Z-plane with a large piece of cloth, and and taped the cloth to the surface so that the Z-plane is air-tight (Figure 5). Before we placed the cloth, we inserted a small tube through a hole in the machine so that the vacuum could suck all the air from the region, and it would travel through that tube. After letting the vacuum runs for about 3 hours, we carefully opened up the Z-plane again, and cut off the extra side edges of the mylar (which had now formed a covering over the strips and the plane). Our Z-plane was finally ready. Figure 6 shows a picture of the Z-plane after it was completed.

## Results

Since the capacitance of the Z-planes had never been studied before, we thought it was a good idea to take some measurements manually first, instead of using the box right away. Firstly, by taking measurement manually first, we were able to get a good idea of the capacitance measurements as we measure from channel 1 – 96. We

took hand-by-hand measurements of 12 Z-planes, and the graph below shows the capacitance (in nF) as a function of channel number for 4 of the 12 Z-planes. This graph proves that our theoretical value of  $C \approx 4.55 \text{ nF}$  is a good approximation for the capacitance, since most of the capacitance values for these 384 strips (4 planes x 96 strips) lies close it.

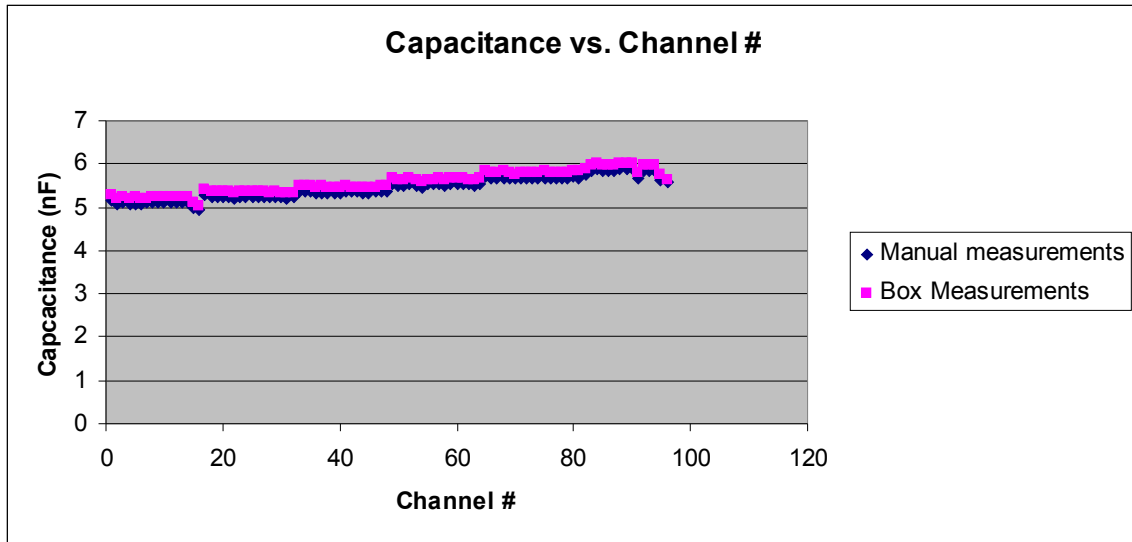


Picture 1 | Capacitance vs. Channel #

This graph also proves our suspicions that the cable length does affect the capacitance. Since the length of the cable is equal for 16 strips, and then increases for the 17<sup>th</sup> one, it makes sense that the capacitance stays constant for the first 16 channels and then increases for the 17<sup>th</sup> one.

Since we took capacitance measurements for 12 Z-planes manually, we used this data to check whether our box is working or not. We took capacitance measurements of the same 12 Z-planes using the box, and compared our

measurements to those from the manual data. The graph below compares the capacitance measurements for one layer.



Picture 1 2Capacitance vs. Channel #

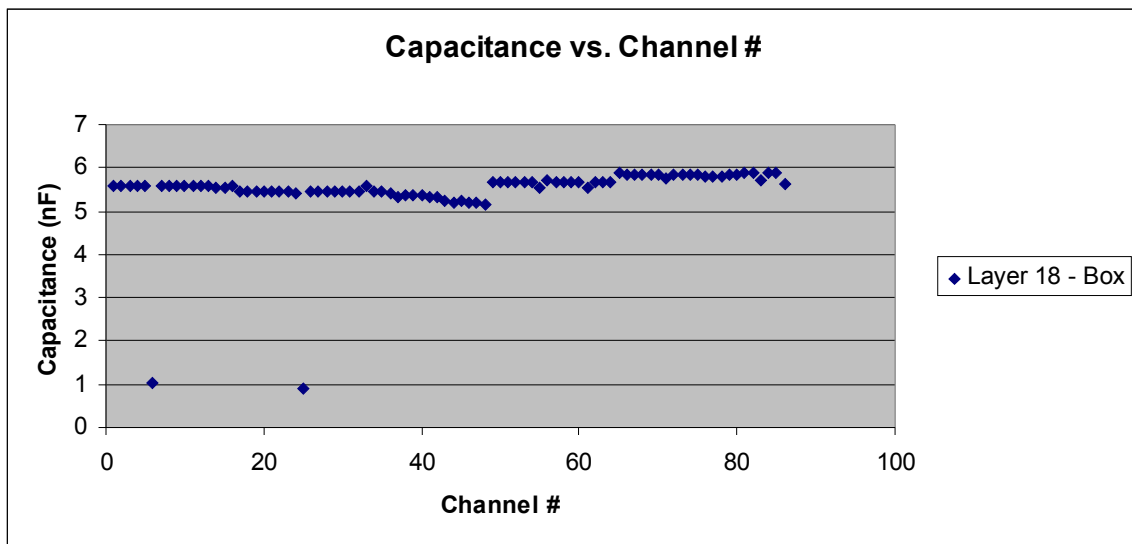
The graph above shows that our box is working well. The manual data and the box data follow the same pattern for one of the layers measured, except for an additional constant in all measurements in the box data. This graph proves to us that we can take measurements of the remaining 36 planes using the capacitance box. After taking measurements of the remaining 36 planes, I was able to form a loose relationship between capacitance value and the status of the solder joint. The table below describes this relationship, and shows the status of all the solder joints from the 48 Z-planes.

<i>Capacitance (nF)</i>	<i>Status</i>	<i>Total #</i>
3.0 – 6.5	Good joint	4561

<i>Capacitance (nF)</i>	<i>Status</i>	<i>Total #</i>
< 3.0	Loose joint	5
> 3.0	2 shorted strips	2

Table 1 Shows the total number of good and bad joints

The 5 joints that were loose were easy to find because their capacitance measurement was  $C < 2.0 nF$ . The graph below shows the capacitance measurements of one of the 4 layer 18 Z-planes. This Z-plane had 2 loose solder joints, as seen from this graph:



Picture 1 3 Capacitance vs. Channel #

This graph clearly shows the 2 loose solder joints. These results were verified when we pressed these particular strips near the solder joint, the capacitance suddenly increased, but again decreased when we stopped pressing near the solder joint.

## Discussion and Conclusion

Using the capacitance box was clearly a more efficient way to taking the capacitance measurements of these Z-planes. When we took the measurements manually, 12 Z-planes required 10 hours and two people to complete the job, while I was able to take capacitance measurements of 48 Z-planes in 10 hours without using anyone's help using the box. Using the box, I was able to finish my measurements almost 4x faster. Before I could use the box, however, I had to make sure that the box was working correctly since there are many delicate solder joints attached to the switch and the BNC connector and the chances of mechanical errors are high. The agreement between the manual and box measurements allowed us to conclude that the box was working accurately. All the measurements from the box were a little higher than the manual measurements, and the source of this additive constant of  $C \approx 0.12 \text{ nF}$  is from the white signal cable wires that have been soldered to the switch. The cables have a small capacitance of their own, but since it is present in the measurements of every strip, we can ignore it. After measuring all the 48 Z-planes, our results show that a total of 7 were found as bad joints. 5 of the 7 bad joints were loose, and therefore, they must be resoldered before the next installation. The remaining 2 joints were shorted together, and these will be harder to fix. Somehow, these joints have been connected together and we need to find it, which will certainly not be easy. Nevertheless, this is not a bad result

considering such a large number of Z-planes since we are still only 0.15% inefficient. While making the Z-planes, I realized how delicate the solder joint is and how easily it could break or disconnect from the strip. Since the solder joint is melted onto the Cu strip, if the melting does not cover the entire hole, the solder joint could potentially break very easily while moving and handling the Z-plane. Since the installation for the remaining streamer tubes and Z-planes is not planned till next summer, continuous testing of the Z-plane capacitance while they move around from one place to another will be necessary. Once these solder joints are fixed, regular testing will probably be helpful in order to gain a better understanding of how Z-planes withstand movement. When installation time does come next summer, the box will be of tremendous help to determine the status of a solder joint quickly before putting the Z-planes into the detector.

### **Acknowledgements**

This research was conducted at the Stanford Linear Accelerator Center. I would like to thank the United States Department of Energy, Office of Science for giving me the opportunity to participate in such a learning and rewarding research internship. I would like to thank Dr. Sanjay Swain for guiding me in the right direction throughout my project, challenging my intellectual curiosity , and helping me in making my research experience a great learning experience. I would also like to thank Dr. Mark Convery, Dr. Charlie Young, and Dr. Wolfgang Menges for their continuous support and help throughout my project.

## References

[1] BABAR Collaboration LST Team, "A Barrel IFR Instrumented with Limited Streamer Tubes," *Stanford Linear Accelerator Center Experimental Program Advisory Committee*, Stanford, CA, May 2003.

[2] S. Smith, "Limited Streamer Tubers for the IFR Barrel," *Stanford Linear Accelerator Center Experimental Program Advisory Committee*, Stanford, CA, Jun. 2003.

# Photometric Supernova Typing for the SDSS SN Survey

Elizabeth S. Rivers

Wellesley College

Office of Science, SULI Program

Stanford Linear Accelerator Center

Stanford, California

August 12, 2005

Prepared in partial fulfillment of the requirements of the Office of Science, U.S. Department of Energy Science Undergraduate Laboratory Internship (SULI) Program under the direction of Dr. Masao Sako of the Kavli Institute for Particle Astrophysics and Cosmology (KIPAC) at the Stanford Linear Accelerator Center (SLAC).

Participant

---

Signature

Adviser

---

Signature

# Table of Contents

Abstract	3
Introduction	4
Methods	6
Results	7
Conclusion	7
Acknowledgments	9
References	9
Tables & Figures	10

## ABSTRACT

SN Typing for the SDSS SN Survey. Elizabeth S. Rivers (Wellesley College, Wellesley, MA, 02481) Masao Sako (KIPAC/Stanford, Stanford, CA)

In the fall of 2004 the Sloan Digital Sky Survey (SDSS) 2.5m telescope scanned the southern equatorial stripe for approximately 20 nights over the space of two months. Light curves for over four dozen supernovae (SNe) were collected over time using five colored filters *ugriz* that together had a range of approximately 3000Å to 10500Å. 22 SNe were spectroscopically confirmed with follow-up observation. Using the data obtained in the Fall 2004 campaign, preparations are now being made for the Supernova Survey of the SDSS II, a three-year extension of the original project. One main goal of the Supernova Survey will be to identify and study type Ia SNe of up to redshift  $\sim 0.4$ , the intermediate 'redshift desert,' as well as enabling further study of other types of SNe including type 1b/c and peculiar SNe. Most of the SNe found will not have spectra taken, due to time and cost constraints. Thus it would be advantageous to be able to robustly type SNe solely from the light curves obtained by the SDSS telescope prior to, or even without ever obtaining a spectrum. Using light curves of well-observed SNe templates were constructed for comparison with unknown SNe in order to photometrically type them.

*Red and bloated spheres  
Explode like hot tomatoes.  
  
I'm watching stars die*

# 1 Introduction

## SUPERNOVA CLASSIFICATION

Supernovae (SNe) come in a great variety, ranging in magnitude, redshift and light curve shape. Due in main part to the history of SN discovery, classification is typically based on optical spectra taken of the SNe near maximum light [1]. By definition type II SNe show strong hydrogen emission lines, absent in type I SNe. The types are further broken down into several subtypes – Ia, the famous standard candles that allow astronomers to measure distances to distant galaxies, distinguished by Si II lines in their spectra; Ib which shows no Si II, and Ic, with no Si II and also no helium. Type II are sometimes subclassified based on the profile of the hydrogen line (II<sub>n</sub> showing a narrow H line) as well as on their light curveshapes.

In reality Ib/c SNe share more in common with type II SNe than they do with Ia. Both type II and type Ib/c SNe mark the deaths of massive stars. When a star reaches the end of its life of hydrogen burning there are a few paths it may take depending on the mass of the star in question. If it is a relatively light star, around three solar masses or less, then it goes out with the proverbial whimper, collapsing down into a white dwarf with little to mark its passing. If the star is a bit heavier, then it becomes a red giant, fusing hydrogen, helium and heavier elements into iron. Once the giant has fused all that it is able, it dies in a rather complicated manner – cooling, contracting and then blowing its outer layers outward in a massive explosion that leaves behind the collapsed core in the form of a neutron star or a black hole. It is theorized that type Ib/c SNe show differences in their spectra due to the loss of their outer atmospheres prior to going nova.

The mechanism behind a type Ia SN is quite different from that of the core-collapse SNe

and is unique in the degree of homogeneity it gives to Ia light curves. It is believed that a type Ia SN is caused by a white dwarf, essentially a small, dead star, becoming heavy enough that the electron-degeneracy pressure keeping it up can no longer balance the gravitational force pulling it in and the star collapses into a neutron star, expelling its atmosphere in a massive SN. This process however only occurs when a white dwarf grows to a certain size by accreting mass from a larger star in a binary system. Since this occurs at the same size for any white dwarf, type Ia SNe are necessarily homogeneous, showing very nearly identical light curves from one occurrence to another and virtually always peaking at the same magnitude of brightness. Consequently they make excellent standard candles – that is since their absolute magnitude is already known, their distance can be calculated from their apparent magnitude in the sky. It might be expected that all type Ia SNe are exactly identical. This, however, is not the case. Some type Ia's are brighter than others and some have peculiarly shaped light curves. It is still possible to determine absolute magnitude from algorithms using the decay rate of the light curve, but further study is required to understand the causes of the observed diversity.

## THE SLOAN DIGITAL SKY SURVEY

The Sloan Digital Sky Survey (SDSS) II will begin observing in the fall of 2005 and will survey the southern equatorial stripe for periods of three months in the falls of 2005 – 2007. It will cover 350 square degrees of sky, taking data for each section every other observing night. The Supernova Survey will be a major subcomponent of this study, and its primary goal is to obtain high-quality, multi-color light curves of  $\sim 200$  Ia SNe in the intermediate redshift interval of  $z = 0.05 - 0.35$  [2]. The survey will provide multi-band light curves measured with the SDSS 2.5m telescope at Apache Point Observatory. The SDSS focal plane camera is equipped with 5 filters *ugriz* [figure] that together cover a wavelength range of approximately  $3000\text{\AA}$  to  $10500\text{\AA}$ .

During the first Supernova Survey light curves were inspected manually, comparing the curves with standard models of the homogeneous type Ia looking for matches. Spectra were

taken of 22 SN candidates that were suspected of being type Ia and of these 16 SNe were spectroscopically confirmed to be Ia. The rest were found to be 1 type Ib/c and 5 type II SNe. Our goal is to improve upon this classification of SNe observed by the SDSS telescope for the upcoming survey.

## 2 Methods

One way to type SNe lacking spectra is to compare the measured light curves with those of other known spectroscopically confirmed SNe. This is, however, not very straightforward, since the light curves of most SNe in the literature have been measured in the Johnson/Cousins filter set  $UBVRI$ , which have filter transmission curves that differ quite markedly from those of the SDSS filters. Transformation of magnitudes in one filter set to another is not easy to do unless you know the underlying spectrum well. This is also problematic when comparing SNe at different cosmological redshifts, since strong spectral features may shift in and out of filter band passes.

Additionally, the diversity of SNe makes it difficult to create a truly standard model for any class, with the possible exception of type Ia. SNe resulting from the core-collapse of a giant stars tend to show a wide range of properties, particularly in the many different light curveshapes they exhibit. Type II SNe are sometimes broken down into subtypes based on light curveshape: type IIP and type IIL, 'P' for the  $\sim 100$  day plateau following peak brightness and 'L' for the linear decay of IIL light curves.

We choose to construct a library of multi-epoch template spectra in the SDSS filters and calculated on a grid of redshift  $z$  up to 0.4 and extinction  $A_V$  up to 0.5. This library is built of template spectra from P. Nugent (UC Berkely, CA) and  $UBVIR$  light curves and spectra from [4] transformed into the SDSS filter set. Each light curve observed by SDSS can now be compared with the templates, shifted on the grid of  $z$  and  $A_V$ , fitting the data to each model curve. The best fit (lowest  $\chi^2$ ) template is chosen as the most likely SN type. If and when new SN are uncovered with sufficient photometric and spectral data they can be added

to the library for improved accuracy in typing.

### 3 Results

Using the *ugri* filters we calculate the  $\chi^2$  for the SNe light curve in each filter [Figures 1&2]. We can then select the lowest  $\chi^2$  value as the most likely SN type using 3, 6 or 10 epochs. Applying this to the 22 confirmed SNe we find that 20/22 are typed correctly with maximum number of epochs [Table 1] and 19/22 are typed correctly with only 3 epochs.

We also used our photometric method to type nearly 60 SNe lacking spectra, finding 40 Ia, 5 Ibc and 10 type II SNe. 23 type Ia were confidently typed using all available epochs [Table 2] and a number of these will receive follow-up work.

### 4 Conclusion

For the 22 spectroscopically confirmed SNe from the initial run of the SDSS Survey we are able to type with  $\sim 90\%$  accuracy. Given only 22 test cases, each with good data, the percent-accuracy is likely to change when the method is applied to large numbers of SNe.

Of the 58 unconfirmed SN candidates that we attempted to type, three were completely ambiguous and several jumped suddenly in  $\chi^2$  from 6 to 10 epochs, adding doubt to the confidence of their typing. Additionally, none of the confirmed SNe was stamped with a Ibc type, so it is difficult to say what kind of accuracy we should really expect out of the five unconfirmed SNe that received this type. However several of the unconfirmed SNe appear to have been well-typed. We plan to obtain spectra of host galaxies of a few of these SN Ia candidates that have good photometric data. If the host galaxy spectroscopic redshift is consistent with the redshift estimated from the light curves, we will include them in the sample of confirmed SNe.

Given the volume of the SDSS and the expense involved with taking spectra, it would seem best to implement additional parameters when choosing Ia candidates for spectral

analysis. Placing an upper limit on the  $\chi^2$  value, a lower limit on the distance between the best and second-best fit light curves and limiting our candidates to the ones with the best photometry (in this case, smoothest curve and smallest error-bars) should greatly increase our chances of actually sifting out the best Ia Supernovae for study.

## Acknowledgments

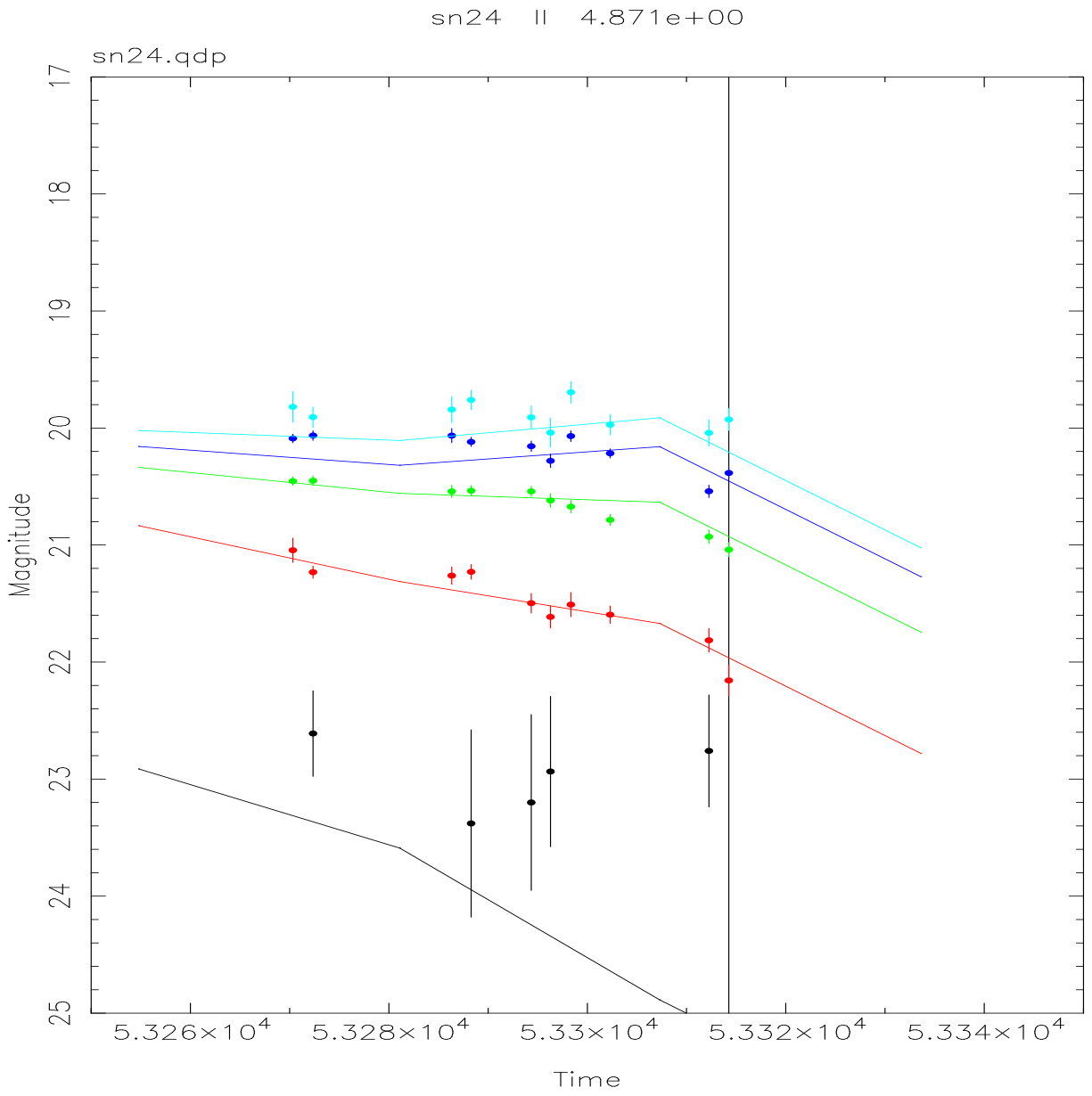
The US. Dept. of Energy, Office of Science for opportunity and funding. Masao and Phil for excellent mentoring, Peter Nugent whom I have never met, My father for his lovely tech support, Lowry, Vidya and the people in the office next door for all the rest.

Thanks guys.

## References

- [1] Filipppenko A. F. "Optical Spectra of SNe." *Annu. Rev. Astron. Astrophys.* 1997.
  
- [2] Sako, M. et al. "The Fall 2004 SDSS SN Survey." Dec, 2004. 22nd Texas Symposium on Relativistic Astrophysics, Stanford, CA, 2004.
  
- [3] The Online Supernova Spectrum Website. [Online Database] Available HTTP:  
<http://bruford.nhn.ou.edu/suspect/index1.html>

# Tables & Figures



sn30 Ia 8.589e+00

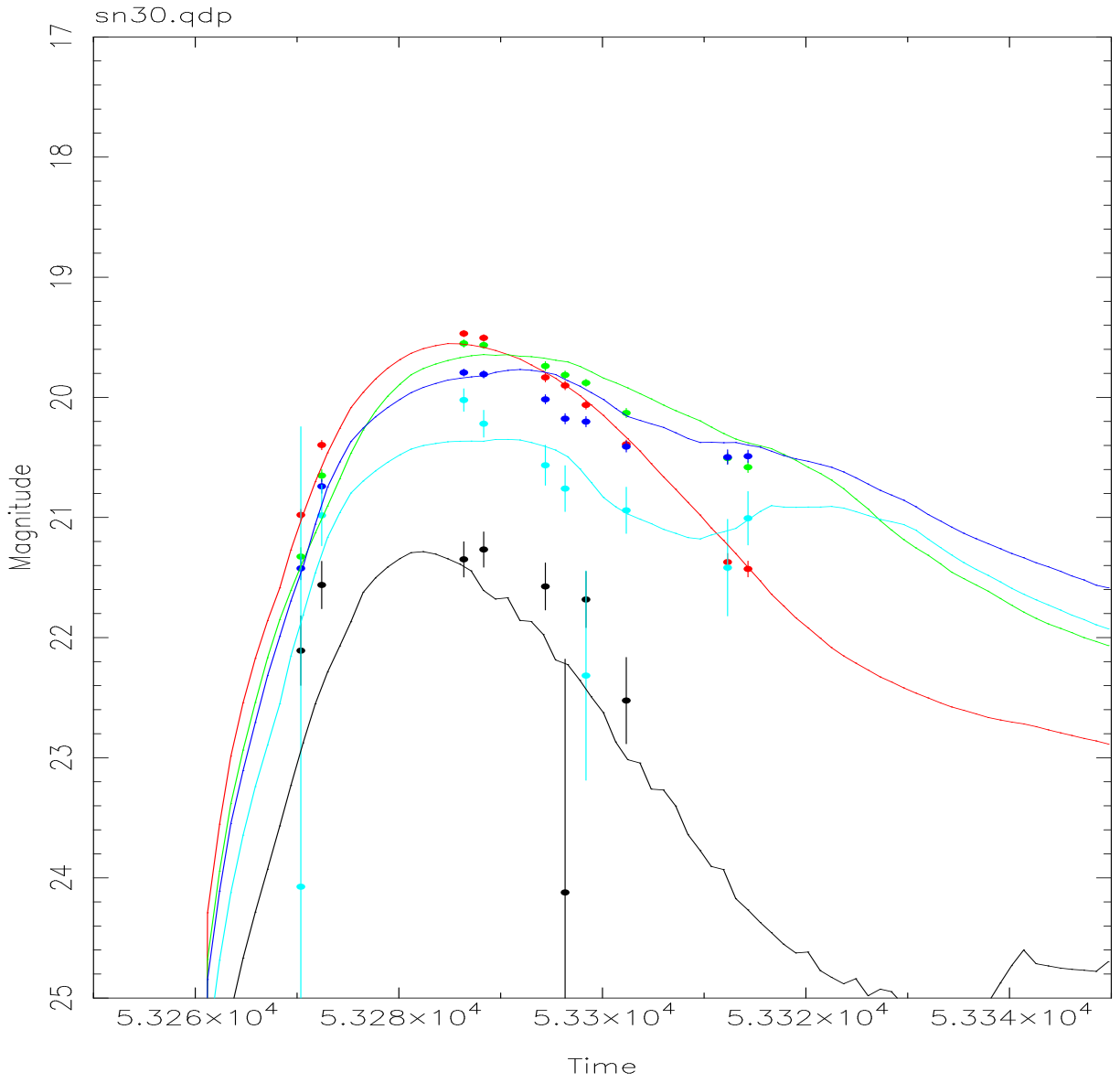


Table 1: Confirmed Supernovae

SN	Type	Best-Fit Type	Best-Fit $\chi^2$ (max epochs)
5	Ia	Ia	1.231e+01
9	II	II	2.960e+01
10	Ia	Ia	5.893e+00
12	II	II	1.304e+01
15	Ia	Ia	1.819e+01
18*	II	Ia	1.111e+02
19	Ia	Ia	4.586e+01
20*	Ib	Ia	1.641e+01
24	II	II	4.871e+00
25	Ia	Ia	5.316e+00
30	Ia	Ia	8.589e+00
83	Ia	Ia	2.403e+01
111	II	II	1.211e+01
128	Ia	Ia	8.701e+01
133	Ia	Ia	4.608e+01
171	Ia	Ia	1.207e+02
172	Ia	Ia	3.537e+01
176	Ia	Ia	7.317e+01
191	Ia	Ia	4.372e+01
194	Ia	Ia	4.708e+01
242	Ia	Ia	1.922e+01
247	Ia	Ia	3.334e+00

Table 2: Unconfirmed Supernovae: Well-Typed Ia Supernovae

SN	Best-Fit $\chi^2$ (max epochs)	SN	Best-Fit $\chi^2$ (max epochs)
<b>108</b>	8.591e-02	<b>35</b>	3.605e+00
<b>100</b>	1.309e+00	<b>123</b>	4.112e+00
<b>93</b>	1.693e+00	<b>96</b>	4.658e+00
<b>117</b>	1.698e+00	<b>32</b>	5.023e+00
<b>4</b>	2.343e+00	<b>94</b>	5.209e+00
<b>33</b>	2.446e+00	<b>51</b>	5.669e+00
<b>28</b>	2.869e+00	<b>37</b>	5.760e+00
<b>130</b>	3.057e+00	<b>41</b>	6.334e+00
<b>116</b>	3.070e+00	<b>91</b>	6.349e+00
<b>88</b>	3.366e+00	<b>86</b>	8.398e+00
<b>125</b>	3.429e+00	<b>29</b>	8.622e+00
<b>110</b>	3.453e+00		

**Extended Source Gamma-Ray Emission from WIMP Annihilation in the  
Sagittarius Dwarf Elliptical Galaxy**

**VIDYA VASU-DEVAN**  
Columbia University

OFFICE OF SCIENCE, SCIENCE UNDERGRADUATE LABORATORY INTERNSHIP (SULI)  
STANFORD LINEAR ACCELERATOR CENTER  
Menlo Park, CA 94025

August 20, 2005

Prepared in partial fulfillment of the requirements of the Office of Science, Department of Energy's Science Undergraduate Laboratory Internship under the direction of DR. LARRY WAI in Group K of the Kavli Institute of Particle Astrophysics and Cosmology (KIPAC) at the Stanford Linear Accelerator Center (SLAC).

Participant: \_\_\_\_\_  
Signature

Research Advisor: \_\_\_\_\_  
Signature

# Contents

<b>1</b>	<b>INTRODUCTION</b>	<b>3</b>
<b>2</b>	<b>INSTRUMENT AND OBSERVATIONS</b>	<b>5</b>
2.1	EGRET . . . . .	5
2.2	GLAST . . . . .	6
<b>3</b>	<b>METHOD OF ANALYSIS</b>	<b>7</b>
3.1	Determination of the Background Model . . . . .	7
3.1.1	Background Origination . . . . .	7
3.1.2	Method of Extrapolating Background From Data . . . . .	8
3.1.3	Combining Viewing Periods . . . . .	8
3.1.4	Monte Carlo Generation of Point Sources . . . . .	8
3.2	Addition and Application of Models . . . . .	10
3.2.1	Point Source Model . . . . .	10
3.2.2	Extended Source Model . . . . .	11
3.2.3	Variations of Extended Source Model . . . . .	12
3.3	Hypothesis Testing . . . . .	12
<b>4</b>	<b>FUTURE ANALYSIS</b>	<b>13</b>
4.1	Expansion of Analysis to GLAST . . . . .	13
4.2	Extension to Different Energy Range . . . . .	13
<b>5</b>	<b>RESULTS AND CONCLUSIONS</b>	<b>14</b>
<b>6</b>	<b>ACKNOWLEDGMENTS</b>	<b>15</b>
<b>7</b>	<b>TABLES AND FIGURES</b>	<b>17</b>

## Abstract

Extended Source Gamma-Ray Emission from WIMP Annihilation in the Sagittarius Dwarf Elliptical Galaxy. VIDYA VASU-DEVAN (Columbia University, New York, NY 10027-8361) LARRY WAI (Stanford Linear Accelerator Center, Menlo Park, CA 94025).

The proximity of the dark matter dominated Sagittarius Dwarf Elliptical Galaxy (position  $(l,b) = 5.6^\circ, -14^\circ$ ) allows it to act as an ideal laboratory for the exploration of extended gamma-ray emission from Weakly Interacting Massive Particle (WIMP) annihilation processes in a dark matter-dominated system. Since the matter in our universe is predominantly dark, exploring such processes as WIMP annihilation will lead to a better understanding of cosmology. In order to study this gamma-ray emission, a model for the diffuse background gamma-radiation in the dwarf galaxy's region is extracted from the Energetic Gamma Ray Experiment Telescope (EGRET) data. After validating this model and comparing it to the EGRET diffuse model, the background model is added to effective bleeding-contamination from external point sources and multiple models for the signal-above-background emission. Various models of this emission are tested: a)no source located in region, b)unidentified point source 3EG J1847-3219 from the *Third EGRET Catalog* responsible for the emission and c)extended emission resulting from WIMP annihilation responsible for the signal above background. These models are created through the employment of Monte Carlo simulation methods, utilizing the response functions of the EGRET instrument to simulate the point spread function, energy dispersion and effects of variable effective area depending on angle of incidence. Energy spectra for point sources are generated from the best predictions of spectral indices listed in the *Third EGRET Catalog* and the spectrum for the extended dark matter source is generated from Pythia high energy annihilation simulations. Hypothesis testing is conducted to assess the goodness-of-fit of these models to the data taken by EGRET. Additionally, we hope to expand our analysis by employing the response functions of the imminent Gamma Ray Large Area Space Telescope (GLAST) to our models. This extension should highlight the sensitivity disparities between GLAST and EGRET and show GLAST's potential enhancement of this analysis. This process will allow for forecasting of extended WIMP annihilation emission signatures for the GLAST detector.

## 1 INTRODUCTION

Current understanding of the universe leads to the prediction that the universe is at critical density (i.e. has a flat geometry) with baryonic matter accounting for approximately 4% of this density, dark matter responsible for approximately 23% and the mysterious dark energy accounting for approximately 73%. Thus, as the matter which inhabits the universe is predominantly non-baryonic

(i.e. dark), pinpointing and exploring the elusive nature of dark matter is of the utmost importance in understanding the composition, dynamic systems and origin and development of our universe. Dark matter is largely responsible for the gravitational binding of large-scale structures such as galaxies and clusters of galaxies. Though many theories suggest plausible models for the nature of dark matter, including its interaction processes and characteristics, the actual constituent particles have not been identified with any level of certainty. Weakly-Interacting Massive Particles (WIMPs) are likely candidates for cold dark matter - or dark matter particles, which were not moving at relativistic speeds during the formation of galaxies. This naming device reflects the fact that these particles do not exhibit any electromagnetic or strong interaction and only interacts with baryonic matter through gravitation. The originally low speeds of cold dark matter allow for eventual clumping into structures. For a universe with critical density, the cross section of interaction among WIMPs is on the electroweak scale [1]. In order to compensate for problems with the Standard Model, supersymmetric theory postulates the neutralino, the lightest supersymmetric partner to bosons like photons, as a particle which interacts on the electroweak scale. Thus, the neutralino is a likely candidate for the Weakly-Interacting Massive Particle (WIMP). Dark matter can be both directly and indirectly detected in a variety of experimental methods. This paper will focus on the indirect detection of WIMP annihilation processes through the detection of astrophysical gamma-rays.

The fortunate proximity of many galactic satellite dwarf galaxies provides favorable targets for exploring galactic processes. The Sagittarius Dwarf Elliptical Galaxy (SagDEG) is particularly interesting since its lack of significant disruption over the course of its  $\geq 10$  orbits around the Milky Way suggests that the galactic baryonic matter is enveloped by a dark matter halo. Though the galactic center also possesses a great density of dark matter, the abundance of other varied gamma-ray emitting astrophysical processes creates a region so complex and polluted, these annihilation processes are extremely difficult to isolate. Thus the location of the dark matter dominated SagDEG, which orbits the center of our galaxy and is situated off of the galactic plane, provides a more unadulterated view of the dynamics of dense clumps of dark matter. N-body simulations predict that particles, which only experience gravitational interaction, clump into dense structures [2]. Since the WIMP annihilation cross-section is proportional to the square of the WIMP density, regions like SagDEG are ideal for exploring WIMP annihilation. WIMP annihilations produce

a quark/anti-quark final state, which fragments into hadrons. We will focus on the annihilation process which leads to the production of  $\pi^0$ ,  $\pi^-$  and  $\pi^+$  particles. The  $\pi^0$  particles subsequently decay into a pair of gamma-rays while the charged  $\pi$  particles decay into neutrinos and leptons, which produce gamma radiation through inverse Compton scattering off of starlight as well as synchrotron radiation [3]. In this paper, we will focus on only the gamma-radiation resulting from the  $\pi^0$  decays. This radiation is expected to have an extended signature due to the SagDEG's proximity and composition.

This paper will explore the application of a model of an extended source of WIMP annihilation in contrast to other hypotheses for the emission above background originating in the region of SagDEG. These models will be compared with data taken by the Energetic Gamma Ray Experiment Telescope (EGRET). In order to complete this analysis, we must model the diffuse gamma-ray emission background. We choose to approach this challenge by extracting a background model from the data itself. We then look at the background model and external point source contamination coupled with our models and compare with raw EGRET data. We hope to explore the signatures of extended emission, which have not been explored for the SagDEG system to date.

Additionally, we plan to conduct the same analysis for the Gamma Ray Large Area Space Telescope (GLAST). We will extrapolate the sensitivity of GLAST to such models, forecasting the signatures of dark matter annihilation which GLAST should expect to see and the potential amelioration to our analysis GLAST will allow.

## 2 INSTRUMENT AND OBSERVATIONS

### 2.1 EGRET

EGRET, located on the Compton Gamma Ray Observatory (CGRO), was a space-based instrument designed to detect gamma-rays between 20 MeV and 30 GeV. The 2.25m x 1.65 m detector was composed of a spark chamber tracking system, which reconstructed the direction of gamma-rays through the monitoring of pair-production in the chamber, and a NaI calorimeter, which reconstructed the energy of incoming photons. The entire detector was enclosed in a plastic scintillator anticoincidence dome, which flagged charged particles to avoid false identification of gamma-rays. Certain EGRET response functions must be corrected for when using raw EGRET counts data. First, the

effective area of EGRET was approximately  $1500 \text{ cm}^2$  and fell off completely at  $40^\circ$  off-axis (See FIGURE 1). EGRET's point spread function could be well approximated as an energy-dependent Gaussian function. Additionally, energy dispersion has to be taken into account. EGRET operated through localized pointing for 2 week periods (a.k.a. Viewing Periods). Due to the orbit of CGRO, the Earth would obstruct EGRET's field of view to various extents over the 2 week viewing periods, thus telescope modes need to be taken into account when using EGRET data, specifically when attempting to simulate data for a specific viewing period.

EGRET's scientific objectives included the search for gamma-ray emitting point sources and the identification of locations, energy spectra and variability. Additionally, EGRET aimed to probe supernovae remnants and investigate their cosmic ray acceleration processes, to explore the galactic and extragalactic diffuse background and to search for extragalactic high energy sources. EGRET succeeded in locating and specifying the energy distributions of 271 point sources. Among these point sources are pulsars, galaxies, solar flares, AGNs and 170 unidentified astrophysical objects [4]. However, *Third EGRET Catalog* only positively identified one extended source, which required a highly specialized analysis [5]. Additionally, EGRET data was used to create the first sensitive map of diffuse emission.

## 2.2 GLAST

GLAST, which will be launched in 2007, is the next generation space-based gamma-ray detector. It is designed to detect gamma-rays in the approximate range of 10 MeV to 300 GeV. The GLAST Large Area Telescope (LAT) will have approximately 50 times the sensitivity and twice the field of view of EGRET. The effective area as a function of angle off-axis is plotted in FIGURE 1. LAT contains 16 towers of silicon detectors, which track the pair-production electrons and positrons. The CsI calorimeter employs scintillation and photoelectric conversion to determine the energy of the detected photons. Like EGRET, GLAST is entirely surrounded by an anticoincidence shield, which discriminates between actual gamma-ray events and the charged particle background. Also like EGRET, future GLAST raw data will need to be corrected for the effective area, energy dispersion and point spread function. However, GLAST will be a scanning mission and thus will not have viewing periods. As a result, the complex rotation and movement of the instrument, while in orbit, will need to be taken into account.

GLAST aims to investigate the acceleration processes in such high energy emitting astrophysical sources as supernovae remnants, AGN and pulsars. Additionally, GLAST aims to improve upon the EGRET model of diffuse emission and extend the catalog of gamma-ray point sources. GLAST also plans on using the detection of gamma-rays to probe the interaction of dark matter. Due to increased sensitivity, GLAST will be able to explore extended emission of such interactions in great detail, hopefully uncovering much of the mystery of the dark matter, which dominates our universe.

## 3 METHOD OF ANALYSIS

### 3.1 Determination of the Background Model

#### 3.1.1 Background Origination

In order to carry out this analysis, an appropriate model for the background diffuse emission has to be created. The galactic diffuse emission results primarily from the interaction of cosmic rays with the interstellar medium. The cosmic ray electrons produce gamma-rays through bremsstrahlung radiation while the protons are involved in nucleon-nucleon processes. Additionally, a contribution arises from these charged particles producing gamma-rays through inverse Compton scattering off of Cosmic Microwave Background (CMB) photons and starlight. The heavily gamma-ray emitting galactic plane does not allow for the demarcation and identification of possible point sources located along the galactic plane. These unresolved sources also contribute to the galactic diffuse emission [6]. There is also an indication that cosmic rays interact with molecular gas clouds, which are prevalent in our galaxy [7]. These gas clouds (primarily molecular hydrogen) are a likely candidate for a portion of the composition of the baryonic dark matter. Cosmic rays interact with these gas clouds producing  $\pi^0$  particles. These  $\pi^0$ s subsequently decay into two gamma-rays. The preceding components of the galactic diffuse emission are represented in the following equation, in which  $q$  represents a gamma-ray source function,  $N_{HI}$  and  $N_{HII}$  represent neutral and ionized hydrogen, respectively, and  $I_{IC}$  and  $I_{EG}$  represent the inverse Compton and extragalactic contributions [7]:

$$I = I_{clouds} + (q_{pp \rightarrow \pi^0} + q_{brems})(N_{HI} + N_{HII}) + I_{IC} + I_{EG} \quad (1)$$

### 3.1.2 Method of Extrapolating Background From Data

We choose to extract our background model directly from the EGRET data. Since the source region is located at a significant distance from the galactic plane ( $b=-14$ ), it is possible to well-model the background originating in the highly-emitting galactic plane in the area around the source region. Thus, it is possible to take regions located on either side of the source region in longitude and then interpolate a background model across the source region.

The following region fully contains the source, SagDEG:  $0^\circ < l < 8^\circ$  and  $-18^\circ < b < -10^\circ$ . We select the following regions as the two surrounding background regions: 1)  $-8^\circ < l < 0^\circ$  and  $-18^\circ < b < -10^\circ$  and 2)  $8^\circ < l < 16^\circ$  and  $-18^\circ < b < -10^\circ$ . We create a step function for  $2^\circ$  latitude steps, which slopes between the average value of counts in region 1 and the average value in region 2. Thus the interpolated background model consists of four independent background slopes across the  $8^\circ$  in longitude (one for each step down in latitude). Stepping down over latitude is necessary since the number of counts decreases as the latitude value moves further away from the galactic plane.

In order to extract this step function, we must remove both the EGRET point sources located in these surrounding regions and the point sources located outside of these regions, which bleed in due to the point spread function of the detector.

### 3.1.3 Combining Viewing Periods

In order to conduct an analysis, which maximizes EGRET sensitivity, we choose to merge data from multiple viewing periods, which provides much higher statistics. After looking at the *Third EGRET Catalog*, we selected the viewing periods which have flagged  $\geq 30$  counts for unidentified source 3EG J1847-3219 which EGRET located at  $(l,b) = 3.21^\circ, -13.37^\circ$ , which corresponds to signal generated from our source region. The viewing periods and their locations are located in TABLE 1.

### 3.1.4 Monte Carlo Generation of Point Sources

To remove the bleeding sources, we run a Monte Carlo simulation for each point source to recreate the photon events seen by the detector in each viewing period. The energies of the photons originating from this source must be distributed from the power-law spectrum associated with the

source. These power-law indices and their associated errors are contained in the *Third EGRET Catalog*. Additionally, the counts and locations need to be “spread” using the appropriate EGRET response functions (point spread function, energy dispersion function, and effective area correction). Additionally, to accurately recreate the data from each viewing period, we extract the amount of live time spent in each telescope mode and generate the photon events accordingly. Thus, 10,000 photon events per viewing period are Monte Carlo generated from the source spectrum, with the correct proportion coming from each telescope mode. We spread these counts’ locations and energies using the response functions and smear in the effective area function to account for the falling off effect for photons detected off-axis. The parameters associated with each of the point sources, which bled into the background regions, are contained in TABLE 2.

Sources 3EG J1800-3955 and 3EG J1911-2000 have been identified as AGNs, while the other seven sources are unidentified. As forementioned, the unidentified 3EG J1847-3219, located at  $l = 3.21$ ,  $b = -13.37$ , lies inside the source region. Thus the bleeding effects of this source into the outside background regions also needs to be taken into account. Plots of the true power-law energy spectrum, dispersed energy spectrum and point spread function for an example point source, highlighting the effects of the detector on the data, are shown in FIGURE 2, FIGURE 3, & FIGURE 4.

Once the simulation has been completed, the events that fall into the viewing period field and energy range (100 MeV - 10 GeV) must be calculated. That total number is then scaled down to the total number of source events detected by EGRET for each viewing period. For many sources, the *Third EGRET Catalog* only lists upper limits for counts detected from the source in the viewing period, thus we must calculate the best normalization factor from the source flux value. EGRET lists flux values associated with each source, corresponding to the average value over the first four phases of data. We take this value and convolve it with the viewing period exposure at the location of the point source to determine the best number of events EGRET could attribute to the source. These values are our scaling factors for the Monte Carlo counts. In the case that this value exceeds the upper limit of viewing period counts listed in the *Third EGRET Catalog*, we choose to use the upper limit. Similarly, for variable sources like AGNs, we choose to use listed absolute count values rather than the flux-calculated values since the average flux value is inaccurate. Once we normalize our simulated sources, we add the photons detected in each  $.5^\circ \times .5^\circ$  bin from all of the bleeding

point sources and viewing periods.

It is now possible to model the background. In order to do this, we take the merged raw EGRET counts data from the five viewing periods and subtract this totaled point source contribution. The resulting counts are considered the background values for each bin. It is at this point that we calculate the average number of counts for  $2^\circ$  latitude slices in each background region and then interpolate a crooked step function across the source region. A three-dimensional plot of the background model is located in FIGURE 5.

## 3.2 Addition and Application of Models

The background model is now added to the external point source contamination in the source region and hypothesis models. In order to determine the likely source of the signal above background, we consider three separate hypotheses. First, no source lies in signal region; only our background model lies in the region. Second, the EGRET point source 3EG J1847-3219 is responsible for all emission from this region. And third, the extended WIMP annihilation source in SagDEG is responsible for the signal in this region.

The first model involves only the background model obtained from the data as delineated above.

### 3.2.1 Point Source Model

First, we hypothesize that a point source lying in the source region corresponds to the EGRET data. Since EGRET flagged 3EG J1847-3219 as a point source located in the signal region, we used the catalog's precise location and the EGRET power-law index to Monte Carlo generate a model. In order to correct for the detector effects we follow the same process as previously described for dealing with external point source contamination. Similarly, we follow the same process to scale the Monte Carlo counts down to an appropriate value to compare with the EGRET data.

Once we scale this model we generate a plot, which shows the raw EGRET counts and the model to facilitate easy comparison. We choose to show our data and model in longitude and latitude profiles. Taking the longitude summed into one-degree wide bins, we sum all of the data over the eight-degree latitude source region. The same process is followed for the latitude profile. We then plot the raw EGRET counts with statistical errors (black), the background value associated with each bin (red), the background model (the average of the values for each bin) (blue), the background

model with external point source contamination within the source region (green), and finally the point source model: the background model with the external point source contamination and the model for the point source signal (cyan). FIGURE 6 & FIGURE 7 show plots of the longitude and latitude counts profiles associated with the signal region for this point source.

Additionally, we create an alternate model for the point source utilizing a different normalization process. Since we are using a different background model than the EGRET diffuse model, the normalization counts value will differ. Thus, we choose to conduct the analysis again by choosing a normalization value, which corresponds to the minimum  $\chi^2$  value. This requires looping through various normalization (EGRET total count values for the point source) and calculating the corresponding  $\chi^2$  values. FIGURE 8 shows the normalization values and their corresponding  $\chi^2$  values. We find that 210 is the optimal normalization value and plot the longitude and latitude profiles for this model in FIGURE 9 & FIGURE 10.

### 3.2.2 Extended Source Model

Our alternative hypothesis states that extended emission generated by WIMP annihilation in the dark matter dominated SagDEG region accounts for the signal seen in our source region. In order to create a model for such emission, we need the WIMP annihilation cross section at non-relativistic velocities and the spectrum of annihilation products [3]. WIMP annihilation can be approximated as a  $q/\bar{q}$  final state. Using Pythia, a program which simulates final quark state decays, we simulate  $b/\bar{b}$  final states (since the WIMP is expected to have mass in the GeV-TeV range, we chose the most massive quark final state) [8]. These final states hadronize into  $\pi^0$ ,  $\pi^-$  and  $\pi^+$  particles in roughly even branching fractions. We ignore the charged pions decay into leptons (which produce gamma rays through inverse Compton scattering off of present photons) and focus on the direct  $\pi^0$  decays. Thus, for the purposes of our model, we consider only the  $\pi^0$ s and their subsequent decay into gamma-rays. Using Pythia, we generated the energy spectrum, seen in FIGURE 11, for WIMP annihilation. This figure shows spectra for WIMP masses of 10 GeV, 100 GeV and 1000 GeV.

Extrapolating broken power-laws from the 100 GeV mass spectrum, we Monte Carlo simulate events from this distribution for each viewing period. Since SagDEG has a large extent in the sky, we do not generate the photons from a point location but rather an ellipse with  $a=4.0$  and  $b=3.0$  centered at  $l=5.0$  and  $b=-14.0$  [2]. We then spread these events as previously described and add in

the effective area effects of the detector. We choose to scale the Monte Carlo counts based on the minimum  $\chi^2$  value for the model as previously described. FIGURE 12 shows a plot of  $\chi^2$  value as a function of this normalization factor.

We choose a value of 120 EGRET counts as our optimal normalization factor. FIGURE 13 & FIGURE 14 show the longitude and latitude profiles for photon events generated by this extended source in the source region, with each color representing the same intermediate portions of the model as in the point source profiles.

### 3.2.3 Variations of Extended Source Model

We also choose to vary our extended source hypothesis by modeling differing WIMP masses, location of the center of the source and extent. We consider the location of our original extended source model as well as the location of 3EG J1847-3219 ( $l=3.21$  and  $b=-13.37$ ). Additionally, we consider the original extent of an ellipse with  $a=4.0$  and  $b=3.0$  and half-extent with  $a=2.0$  and  $b=1.5$ .

We also consider the original extent and location with WIMP masses of 10 GeV and 1000 GeV. Finally, we look at the scenario where the EGRET point source within the source region, 3EG J1847-3219, is considered part of the external (or in this case internal) point source contamination within the source region and the extended source accounts for the emission above the background model added to this contamination. The  $\chi^2$  values associated with each of these varied models are located in TABLE 3.

## 3.3 Hypothesis Testing

We conduct  $\chi^2$  testing for these different models. We use the standard comparison between the expected (model counts) values and those observed by EGRET (raw counts). For the case of the various extended source models, we choose to normalize in order to minimize the  $\chi^2$  value, so these normalization factors present the most likely EGRET count values associated with these source models for best consistency with the data.

## 4 FUTURE ANALYSIS

### 4.1 Expansion of Analysis to GLAST

We would like to explore the increased sensitivity GLAST will bring to high-energy astrophysics and specifically our analysis of extended source WIMP annihilation in SagDEG. In order to do this, we have decided to modify our previous method through the utilization of GLAST response functions.

Since no GLAST data has been taken, we cannot extract an apt background model from real data. Thus in order to run an analysis, which aims to simply highlight the improvement GLAST will offer, we plan to scale our current background model and EGRET count values to values appropriate for GLAST.

We will also model the various extended source models using the GLAST detector response functions. Since the LAT is more sensitive than EGRET, this will allow for a much more detailed analysis of this region.

After scaling the counts data (increasing count statistics decreases the statistical error), we will add the point source contamination within the source region and our new GLAST-treated extended source model and compare to the GLAST-scaled EGRET data.

### 4.2 Extension to Different Energy Range

We would like to increase the sensitivity of our analysis in the future by fine-tuning our analysis into different energy bands, which minimize the errors. In order to determine an optimal energy cut, we have conducted signal to background analysis for various energy cuts. We hope to split our analysis into two different energy bands, one which minimizes statistical error while the other minimizes systematic error. We took the WIMP annihilation spectra created by Pythia and integrated  $\frac{dN}{dE}$  from the energy cut value to  $\infty$  for each WIMP mass value. Utilizing the same cut values, we integrate a simplified function for the diffuse background. We use a power law spectrum with  $\gamma=2.1$  [6]. Finally, we plotted the signal to background ratio and signal to  $\sqrt{\text{background}}$  ratio and selected the cuts, which will minimize the two previously mentioned errors.

We have selected the following two bins in which to conduct our analysis of the 100 GeV mass WIMP: 1) 100 MeV to 1 GeV and 2) 1 GeV to 10 GeV. The analysis will be repeated in these two

bands in future work.

## 5 RESULTS AND CONCLUSIONS

We find that our method of extracting a background model from the data is both successful and simple. We were not forced to consider the varying portions of the diffuse background and thus posed with the challenge of adequately modeling these manifold contributions. In subtracting only point source bleeding, we were certain that we did not remove anything from the EGRET data that could be considered signal. Thus we truly created an upper bound of the background model, which allowed us to be sensitive to pure signal. Additionally, since the model was extracted from the viewing periods we chose to focus on, it is tailored specifically to our local analysis. The simplicity of our background model also allows for easy integration of the background with our source models.

However, since the background model is different from the EGRET diffuse model, we face the challenge of dealing with normalization values for our Monte Carlo simulations. The implementation of a different background model requires that the number of counts attributed to any source above the background will differ from the EGRET values (which are based on the diffuse value). Thus, our modeling of the point source and extended source hypotheses was limited to a selection of normalization factors depending on minimum  $\chi^2$  values. This is simply one method to deal with this delicate issue.

TABLE 3 lists the  $\chi^2$  values associated with each of the models we tested. We found that the various extended source models (with exception of the half-extent model at the original location) generate lower  $\chi^2$  values than the no source or original point source values. The half-extent, point-source located extended source has the lowest  $\chi^2$  value, followed by the original extent and location with 3EG J1847-3219 as part of the background. We found that the  $\chi^2$  values of the various extended source models (including those of the varying WIMP masses) are very similar to each other.

These results reflect our use of a  $\chi^2$  minimization normalization process for the extended source models, while the point source model was constrained to the normalization calculated from the *Third EGRET Catalog*. When we allow the point source normalization to vary according to the corresponding minimum  $\chi^2$  value, it becomes the lowest  $\chi^2$  value, again highlighting the impact

of this normalization process. However, this analysis indicates that an extended source could be responsible for the emission seen in this region and specifically a source corresponding to the extent and spectrum of WIMP clump located in the SagDEG fits the data within errors. This result pushes for further analysis of this region using methods mentioned above and hopefully GLAST data in the future.

Using 31 degrees of freedom (32 bins in our analysis with the normalization optimization process eliminating one), we find that we cannot reject either our point source or extended source models (we can only reject the model displaying no source in the region). Thus we have succeeded in corroborating EGRET's identification of 3EG 1847-3219 as a point source, using entirely different methods. Additionally, our half-extended and point source located extended source's low  $\chi^2$  value suggests that the dark matter distribution within SagDEG might be uneven, with most of the clumping in the area of the EGRET unidentified point source.

We hope to minimize systematic and statistical errors through the expansion of our analysis into two different energy bands. We think that this process will allow us to maximize our exploration of an extended source model since its spectrum is much harder than that of the diffuse background model, thus analyzing the data in a higher energy band (e.g.  $>1$  GeV) will allow us to focus on pure signal in the source region.

We also hope to see the potential GLAST has for improving the sensitivity of this analysis. In our GLAST analysis, we plan on using a modified version of our background model, which was taken from EGRET data. We feel that this process will enable us to adequately show the capabilities of GLAST in the capacity of this analysis. However, with the possibility of obtaining a much more robust and intricate background model taken from the more sensitive GLAST data, we speculate that this analysis will provide more conclusive results with smaller error bars. We hope that this fact will allow GLAST to delve further into the exploration and understanding of dark matter.

## 6 ACKNOWLEDGMENTS

This research was conducted at the Stanford Linear Accelerator Center (SLAC). I would like to thank the U.S. Department of Energy, Office of Science, for providing me with the unique oppor-

tunity of participating in the SULI program. I would especially like to thank my mentor Larry Wai for his enthusiasm, guidance and insight. I would also like to thank James Lindesay and Helen Quinn for providing a great experience and environment. Special thanks to Seth Digel, Jim Chiang and Reshmi Mukherjee for their EGRET expertise.

## References

- [1] Griest, K. 1996, *Gateway Reviews*, No. 2.
- [2] Helmi, A. & White, Simon D.M. 2001, *MNRAS*, 323 (529H).
- [3] Baltz, E.A. & Wai, L. 2004, *Phys. Rev. D*, 70 (023512).
- [4] Hartman, R.C., et al. 1999, *ApJS*, 123 (79H).
- [5] Sreekumar, P., et al. 1992, *ApJ*, 400 (67S).
- [6] Hunter, S.D., et al. 1997, *ApJ*, 481 (205H).
- [7] Ohishi M., Mori, M. & Walker, M. 2002, *Universal Academy Press*, Inc. (1-8).
- [8] Sjostrand, T., Eden, P., Friberg, L. Lonnblad, G. Miu, Mrenna, S. & Norrbin, E. 2001, *Computer Phys. Commun.*, 135 (238, LU TP 00-39, hep-ph/0010017)
- [9] Combi, J.A., Romero, G.E., Benaglia, P. & Jonas, J.L. 2001, *A&A*, 336 (1047C)
- [10] Grenier, I.A., Casandjian, J.M., & Terrier, R. 2005, *Science*, 307 (1292).
- [11] Jaffe, T.R., Bhattacharya, D., Dixon, D.D., & Zych, A.D. 1997, *ApJ*, 484L (129J).
- [12] Nolan, P.L., Tompkins, W.F., Grenier, I.A., & Michelson, P.F. 2003, *ApJ*, 597 (615N).
- [13] Peirani, S., Mohayaee, R., & de Freitas Pacheco, J.A. 2004, *Phys. Rev. D*, 70 (3503P).
- [14] Sreekumar, P., et al. 1998, *ApJ*, 494 (523S).
- [15] Wai, L. 2005, *NewAR*, 49 (307W).

## 7 TABLES AND FIGURES

<i>ViewingPeriod</i>	<i>Start</i>	<i>End</i>	<i>l</i>	<i>b</i>	<i>3EGJ1847 – 3219 Counts</i>
5.0	1991 <i>Jul</i> 12	1991 <i>Jul</i> 26	0.00	−4.00	< 67
209.0	1993 <i>Feb</i> 09	1993 <i>Feb</i> 22	0.24	−34.01	35
226.0	1993 <i>Jun</i> 19	1993 <i>Jun</i> 29	355.00	5.00	< 34
232.0	1993 <i>Aug</i> 24	1993 <i>Sep</i> 07	347.50	0.00	< 40
323.0	1994 <i>Mar</i> 22	1994 <i>Apr</i> 05	356.84	−11.29	< 50

Table 1: Viewing Periods: number, starting and ending dates, longitude and latitude of instrument z-axis, and number of counts associated with 3EG J1847-3219.

<i>Source</i>	<i>l</i>	<i>b</i>	$\gamma$
<i>3EGJ1736 – 2908</i>	358.79	1.56	2.18±0.12
<i>3EGJ1744 – 3011</i>	358.85	−0.52	2.17±0.08
<i>3EGJ1746 – 2851</i>	0.11	−0.04	1.70±0.07
<i>3EGJ1800 – 3955</i>	352.05	−8.24	3.10±0.35
<i>3EGJ1834 – 2803</i>	5.92	−8.97	2.62±0.20
<i>3EGJ1850 – 2652</i>	8.58	−11.75	2.29±0.45
<i>3EGJ1858 – 2137</i>	14.21	−11.15	3.45±0.38
<i>3EGJ1911 – 2000</i>	17.03	−13.29	2.39±0.18
<i>3EGJ1847 – 3219*</i>	3.21	−13.37	2.67

Table 2: Parameters associated with point sources: EGRET source name, galactic longitude and latitude, and power-law index  $\gamma$ . \*Point Source 3EG J1847-3219 is located within source region.

<i>Model</i>	<i>l</i>	<i>b</i>	<i>a</i>	<i>b</i>	<i>OptimalNormalization</i>	$\chi^2$
<i>NoSource</i>	−	−	−	−	−	69.1256
<i>PointSource</i>	3.21	−13.37	−	−	−	39.2362
<i>AlternativePointSource</i>	3.21	−13.37	−	−	210	25.7097
<i>Orig.Ext.Src.</i>	5.0	−14.0	4.0	3.0	120	36.1757
<i>Orig.atNewLoc.</i>	3.21	−13.37	4.0	3.0	130	34.0208
<i>Half – ExtentatOrig.Loc.</i>	5.0	−14.0	2.0	1.5	50	44.0358
<i>Half – ExtentatNewLoc.</i>	3.21	−13.37	2.0	1.5	100	28.3630
<i>10GeVmass</i>	5.0	−14.0	4.0	3.0	130	36.7441
<i>1000GeVmass</i>	5.0	−14.0	4.0	3.0	120	36.9587
<i>Orig.withPSinBG</i>	5.0	−14.0	4.0	3.0	80	32.2346
<i>Half – ExtentwithPSinBG</i>	5.0	−14.0	2.0	1.5	60	35.8630

Table 3:  $\chi^2$  values associated with each model considered: Model, longitude and latitude, semi-major and semi-minor axis of extent, optimal normalization count value and  $\chi^2$  value.

EGRET AND GLAST: Angle of Incidence vs. Effective Area for 100 MeV

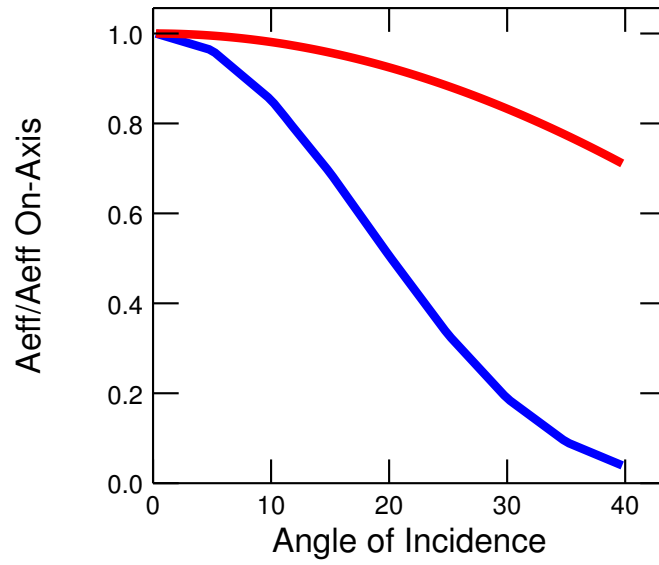


Figure 1: Effective area/effective area on-axis of EGRET (BLUE) and GLAST (RED) as a function of angle of incidence for energy of 100 MeV.

3EG J1850-2652 MC Spectrum of True Energies

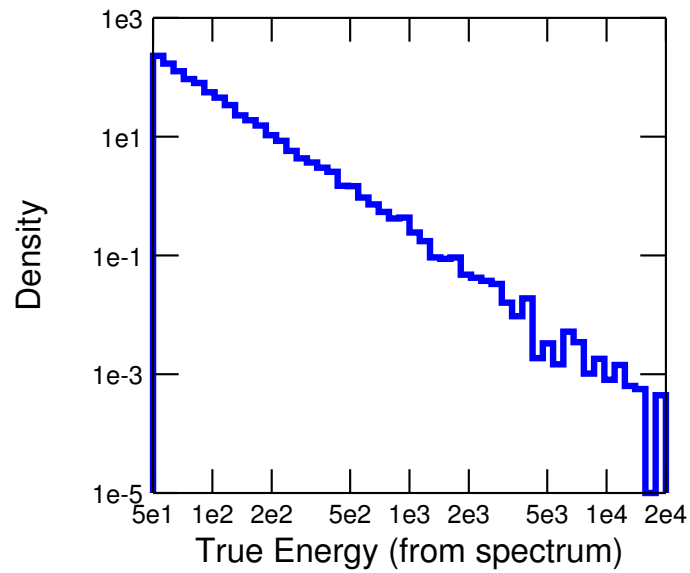


Figure 2: True Energy Spectrum of 3EG J1850-2652. (MEV)

3EG J1850-2652 MC Spectrum of Energies Corrected for Dispersion

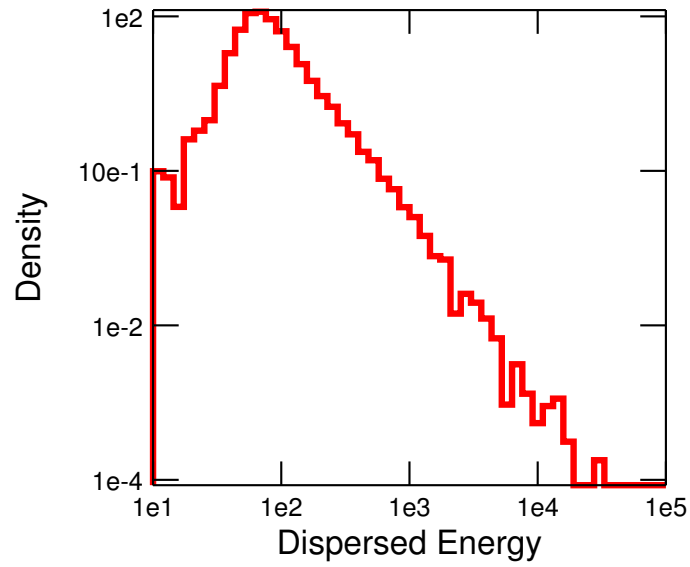


Figure 3: Energy spectrum after dispersion function employed on 3EG J1850-2652. (MEV)

3EG J1850-2652 Histogram of Stheta

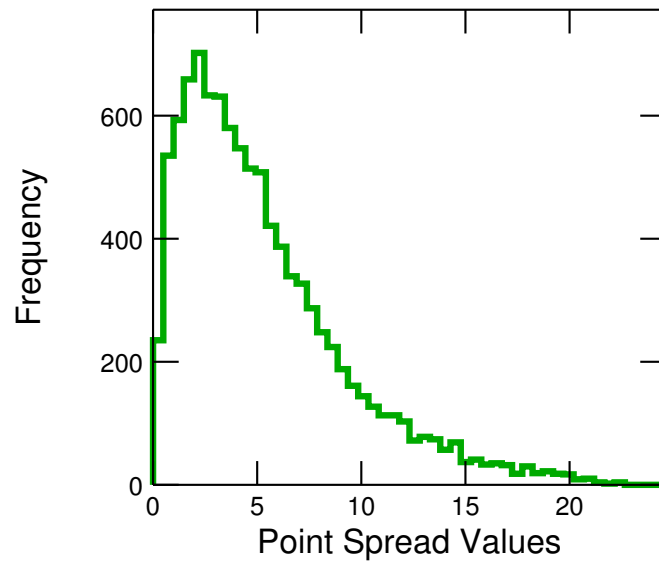


Figure 4: Counts as a function of angular distance (Point Spread Function) for 3EG J1850-2652. (DEGREES)

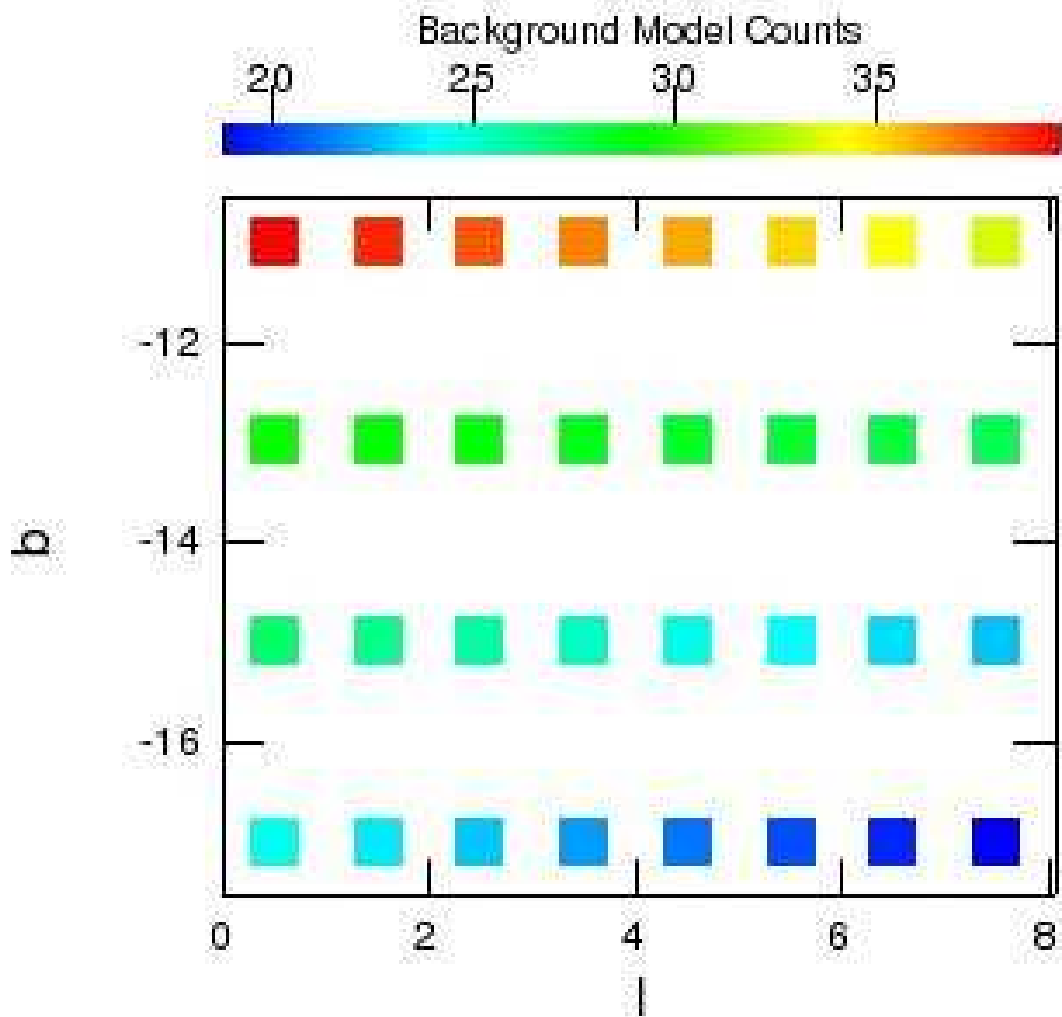


Figure 5: Three-dimensional background step-function model.

l x EGRET VP5 Counts (SOURCE REGION) - Point Source Model

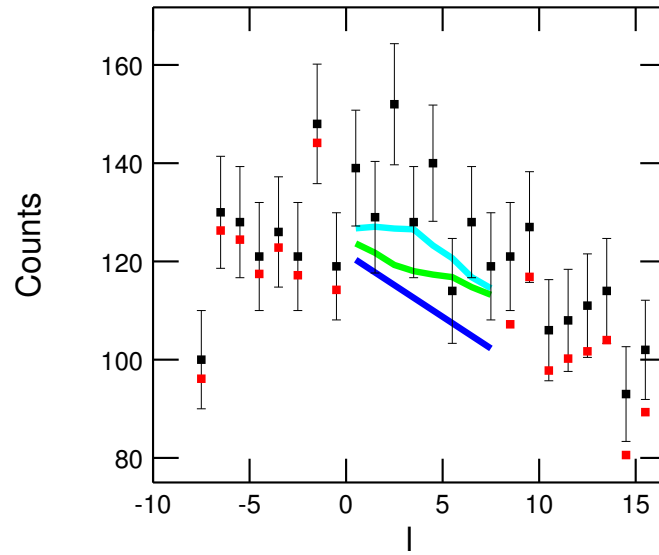


Figure 6: Longitude profile of point source emission. (Different colors explained in SECTION 3.2.1)

b x EGRET VP5 Counts (SOURCE REGION) - Point Source Model

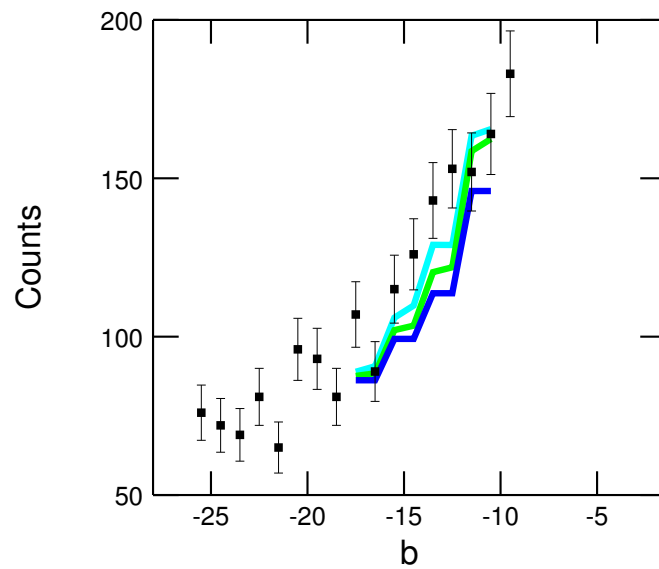


Figure 7: Latitude profile of point source emission. (Different colors explained in SECTION 3.2.1)

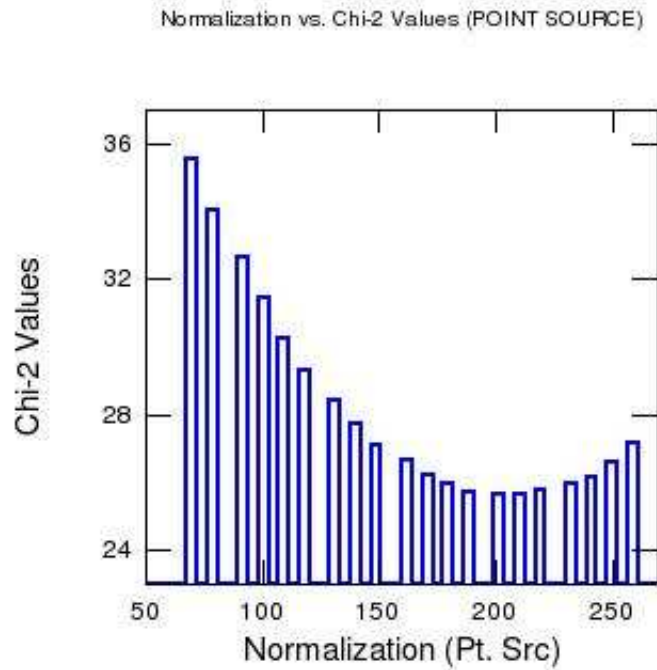


Figure 8:  $\chi^2$  value as a function of scaling normalization value for point source model.

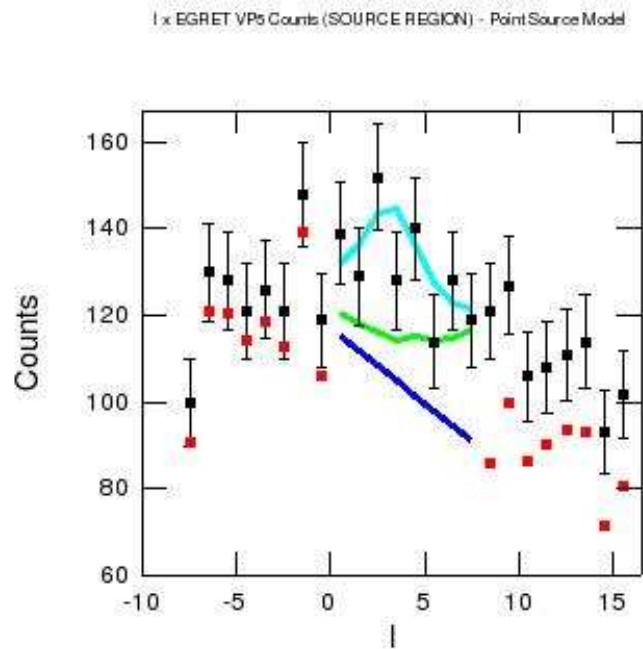


Figure 9: Longitude profile of alternate point source model. (Different colors explained in SECTION 3.2.1)

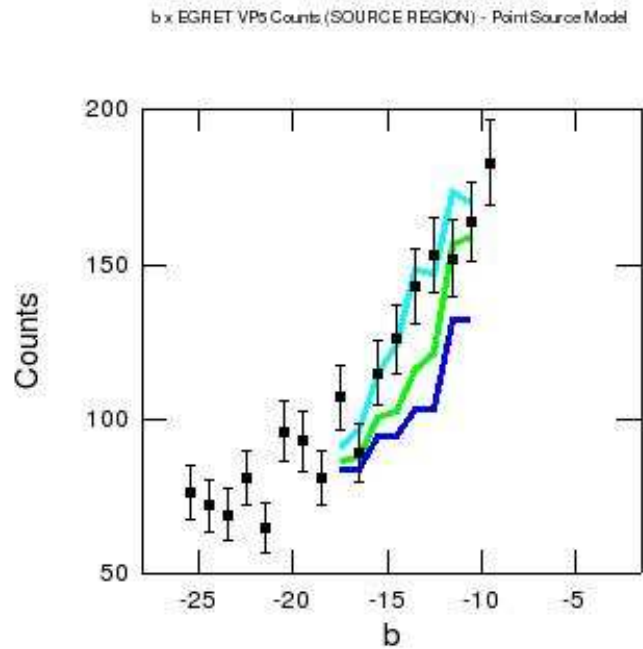


Figure 10: Latitude profile of alternate point source model. (Different colors explained in SECTION 3.2.1)

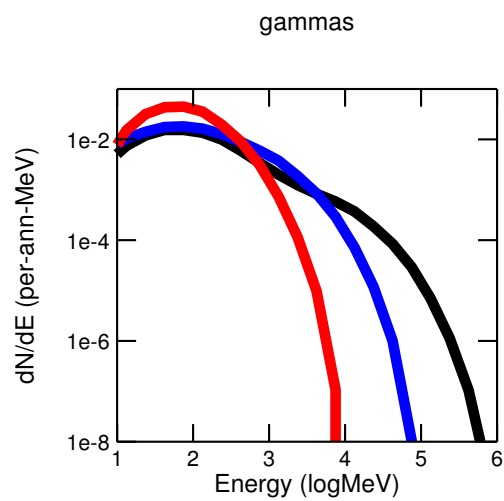


Figure 11: Energy spectra for WIMP annihilation for varying WIMP mass. red: 10 GeV, Blue: 100 GeV, and Black: 1000 GeV. [Plot generated by Larry Wai]

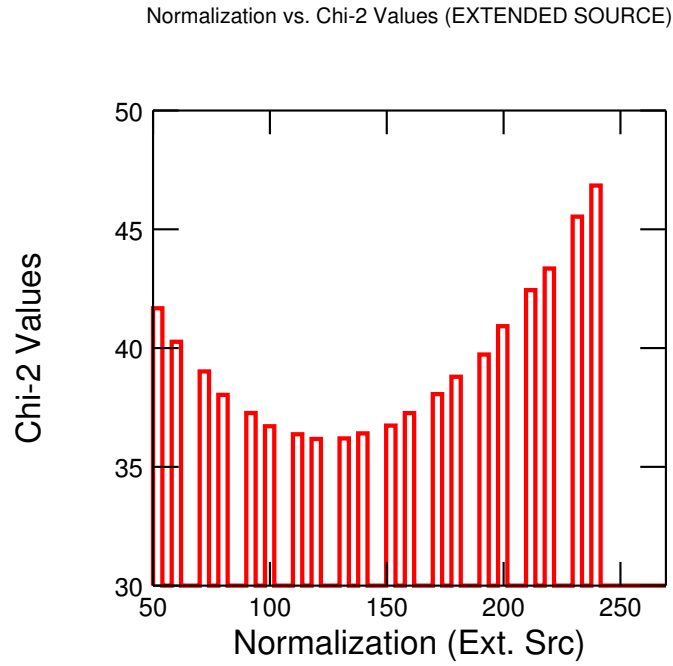


Figure 12:  $\chi^2$  value as a function of scaling normalization value for extended source model.

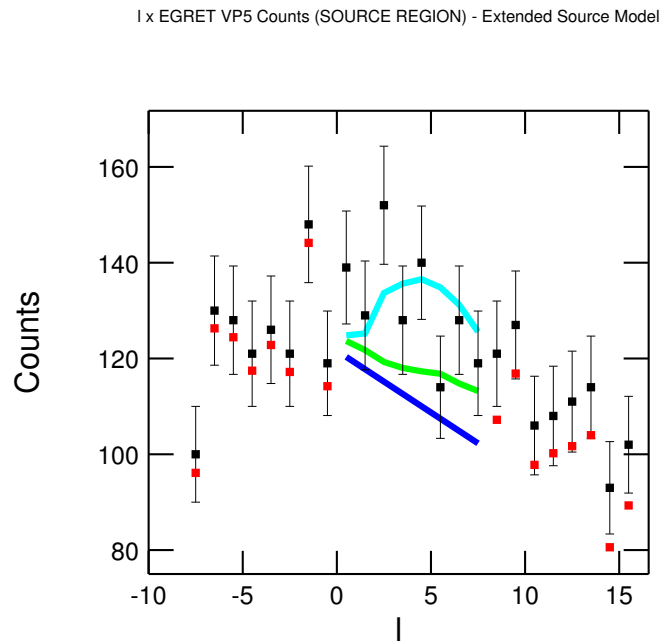


Figure 13: Longitude profile of extended source emission. (Different colors explained in SECTION 3.2.2)

b x EGRET VP5 Counts (SOURCE REGION) - Extended Source Model

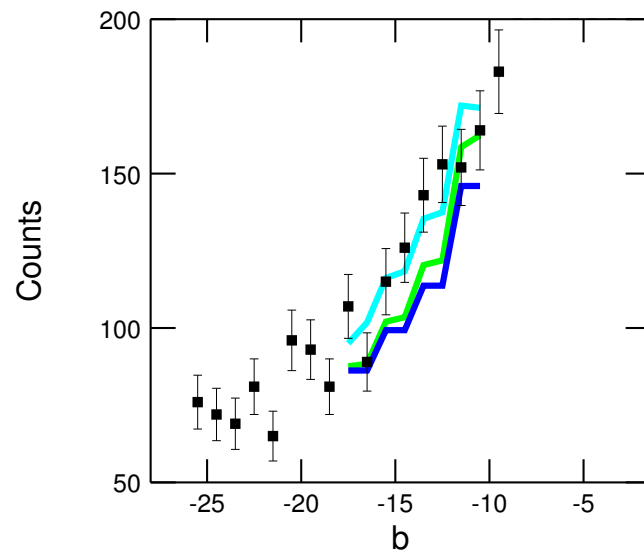


Figure 14: Latitude profile of extended source emission. (Different colors explained in SECTION 3.2.2)

# Study of Hydrogen Bonding in Small Water Clusters with Density Functional Theory Calculations

Johanna Wendlandt

Office of Science, Science Undergraduate Laboratory Internship (SULI)

University of Wisconsin

Stanford Synchrotron Radiation Laboratory  
Stanford Linear Accelerator Center  
Menlo Park, CA

August 19, 2005

Prepared in partial fulfillment of the requirements of the Office of Science,  
Department of Energy's SULI program under the mentorship of  
Professor Anders Nilsson at the Stanford Synchrotron Radiation Laboratory

Participant:

---

Research Advisor:

---

## **ABSTRACT**

The unique characteristics of hydrogen bonding have left our understanding of liquid water far from complete in terms of its structure and properties. In order to better describe the hydrogen bond in water, we seek to understand the electronic states which show sensitivity to hydrogen bonding. We investigate the structure of unoccupied valence states by performing X-ray Absorption calculations on water clusters using Density Functional Theory. For each water cluster, studying how valence electronic structure is perturbed by changes in the local hydrogen bonding environment facilitates our description of the hydrogen bond. Also in this framework, we move toward a depiction of local structures in liquid water by comparison to experimental X-ray absorption spectra. We find consistent localization along internal bonds in the electronic structures of pre- and post-edge states for single-donor species. In addition, we propose a molecular orbital bonding-antibonding picture to explain this directional localization from dimer calculations, and show that the pre- and post-edge spectral regions have a resulting relationship.

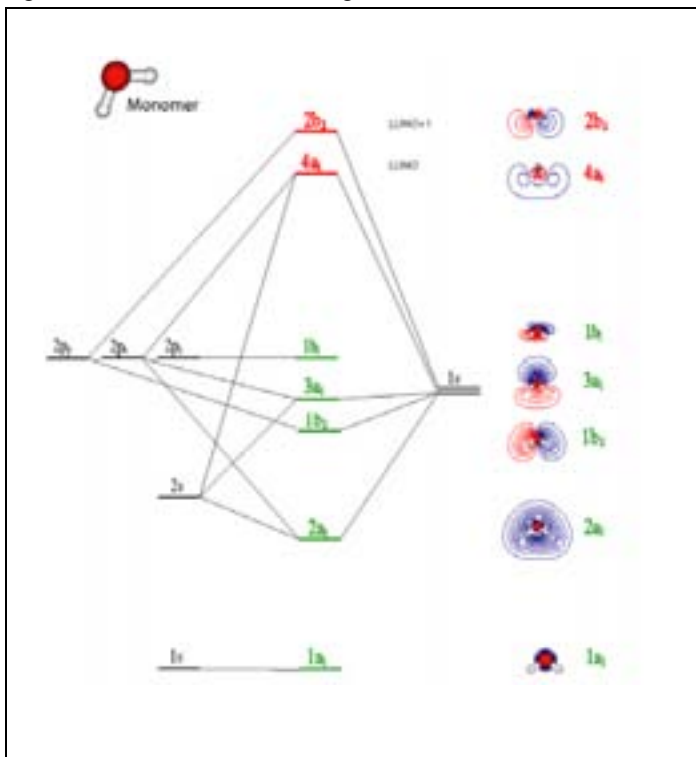
## **INTRODUCTION**

Water is central to countless biological and chemical processes in nature. Despite its extensive importance and its crucial role in living organisms, however, the structure and chemistry of liquid water are not fully understood. Liquid water molecules are associated through a hydrogen bonding network, formed as a result of internal polarization of covalent bonds. The hydrogen bond is much weaker than internal covalent bonds, but strong enough that well-defined structures could form in liquid water.

A model that proposes organized structure in water is a sharp departure from the traditional continuum model of a disordered molecular network, but is supported by the work of [1]. Addressing the question of local structure and organization in water depends strongly upon a deeper understanding of the hydrogen bond. Its intermediacy in strength between strong covalent and weak intermolecular forces, as well as cooperativity effects, has made the electronic nature of the hydrogen bond difficult to characterize.

The application of X-ray Absorption Spectroscopy (XAS) to liquid water is a promising development toward characterization of the hydrogen bond [2]. XAS locally probes the nature of the unoccupied electronic states, which have been shown to be sensitive to changes in the hydrogen bonding network [3]. Figure 1 shows the molecular

Figure 1: Molecular Orbital Diagram for Water Monomer



Fully occupied states (labeled in green) localize near oxygen atoms while unoccupied states (red) localize near hydrogens. The LUMO and LUMO+1 exhibit pure  $a_1$  and  $b_2$  symmetries, respectively.

orbital diagram for a free water molecule. Due to internal polarization of the molecular OH bond, occupied molecular orbitals tend to localize near the highly electronegative oxygen atom, while the unoccupied orbitals localize near the hydrogen atoms [4]. For different hydrogen-bonding environments, XAS can be used to locally probe the nature of unoccupied states

through excitation of a core O1s electron. From the simple dipole selection rule, transitions are allowed into p-like states. Transition intensities reflect the extent of p-character in the unoccupied orbitals, and information regarding the mixing and symmetry of these orbitals can be gained. Thus, XAS is an experimentally sensitive technique to locally study the symmetry-resolved character of unoccupied states in different hydrogen-bonding configurations [5]. Additionally, core electron excitations take place on the attosecond timescale, orders of magnitude faster than molecular motions in liquid water. This advantage allows investigation of electronic structure in frozen molecular geometries [6].

In this study, theoretical calculations are performed to generate X-ray absorption spectra based on density functional theory (DFT). DFT is an *ab initio* quantum chemistry approach which was introduced as an alternative to wavefunction based methods. Underlying DFT is the principle that a system's ground state energy, and other expectation values of observables, are functionals of the electron density  $\rho(\mathbf{r})$ . The variational principle for total energy holds within DFT, giving energy as a function of  $\rho$  such that  $E[\rho] \geq E[\rho_0]$  [7]. This method yields the ground state energy as a function of electron density through a series of self-consistent field calculations. Additionally, electron correlation and exchange energy are accounted for as functionals of electron density [5].

Dipole transition elements are obtained using the dipole operator for solved states of transition. The dipole approximation holds, where the wavelength of light is orders of magnitude larger than atomic dimensions. This allows for a simplification of transition elements to the form  $|\langle \varphi_f | p | \varphi_i \rangle|^2$ , where  $p$  is the dipole operator. This simplification

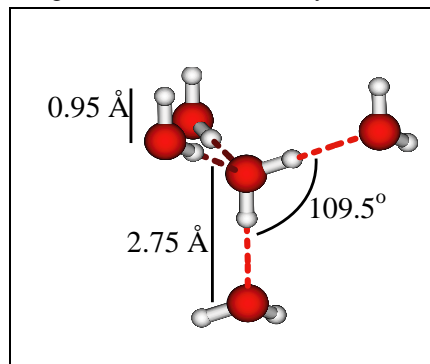
yields atom-like selection rules, wherein the excited O1s electron is allowed transition into a p-like orbital [5]. Through the dipole selection rule, intensities of transition provide a direct method to resolve the p-character of the unoccupied valence orbitals.

The unoccupied valence states are here investigated through DFT calculations of small systems of water clusters. We begin with a water monomer and build up the hydrogen bonding network to larger clusters (up to 11 molecules) in effort to understand the changing local electronic structure that results from various bonding environments. Focus has been placed on single-donor species, in effort to concentrate on configurations we believe contribute most significantly to structure in liquid water [1]. At each step, we compare calculated spectra to the experimental spectra of liquid water. This extended approach will eventually allow exclusion of some structures as primary contributors to the overall liquid water structure, and brings others forth in contention.

## METHODS

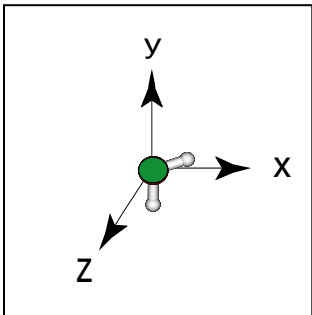
Density Functional Theory calculations were performed on small water clusters. Clusters were chosen such that the immediate hydrogen-bonding environment of the central water molecule was varied, placing emphasis on single-donor species. All clusters were arranged in a fixed ice-like geometry, where the water molecule to be excited was associated with others to reflect the tetrahedral arrangement of ice, as shown in Figure 2. All HOH bond angles were fixed at  $109.5^\circ$ , and all

Figure 2: Ice-like Geometry



internal oxygen-hydrogen bond distances were 0.95 Å. Oxygen-oxygen (hydrogen bond) distances were fixed at 2.75 Å. In all cases, the coordinate system was chosen as shown

Figure 3: Coordinate system



in Figure 3, where the three atoms of the excited water molecule define the xy plane and one OH bond is in the pure y-direction.

All computed X-ray absorption spectra were generated using the StoBe-deMon DFT code [8]. The calculations involved creation of a core hole by removing

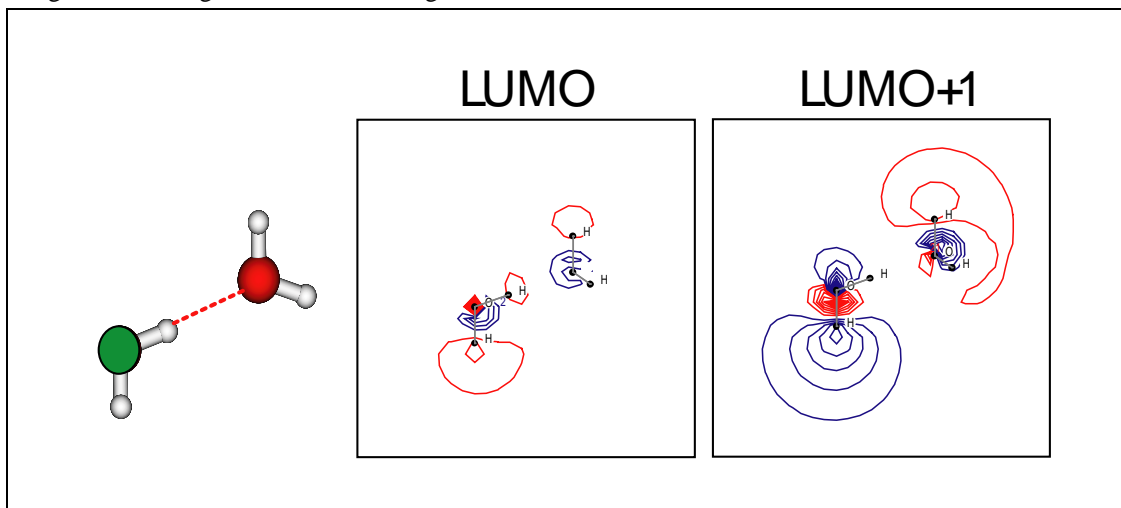
half an electron from the 1s orbital of the central oxygen atom. This approach has been shown to generate reliable XA spectra from DFT calculations [9]. The StoBe-deMon code employs a double basis set procedure to describe electron density with Gaussian Type Orbitals of the general form  $\sigma = Nx^ay^bz^c \exp(-\alpha r^2)$ . The first basis set describes the initial electron density prior to excitation, while a larger, more diffuse (19s, 19p, 19d) basis set describes the density in extended regions above the ionization potential for the core-excited oxygen [5]. The core-excited oxygen was described with the full-electron III\_IGLO basis set [10]. Effective core potentials were used to describe the chemically inert core electrons of all other oxygen atoms.

The transition matrix elements were obtained in each direction and in total. An  $r^2$  operator was used to compute the density of s-like states and evaluate relative contributions to solved energy states. The total oscillator strengths were broadened using gaussian functions of increasing full width at half maximum (fwhm) to simulate experimental spectra, unless otherwise noted.

## RESULTS AND DISCUSSION

For all single-donor type clusters, a visible pre-edge is observed in the generated X-ray absorption spectra, though the relative intensities and energy positions corresponding to the LUMO and LUMO+1 vary widely and the pre-edge is seldom sharply defined. Across these configurations, we see similarities in electronic structure of states contributing to the pre-edge. Figure 4 shows a representative example of orbital pictures from a single-donor water dimer. The LUMO resembles an  $a_1$  symmetry, distorted slightly toward the free OH bond and delocalized from interaction with the other water molecule. The LUMO+1 orbital localizes along the free OH bond.

Figure 4: Pre-edge States for Donating Water Dimer

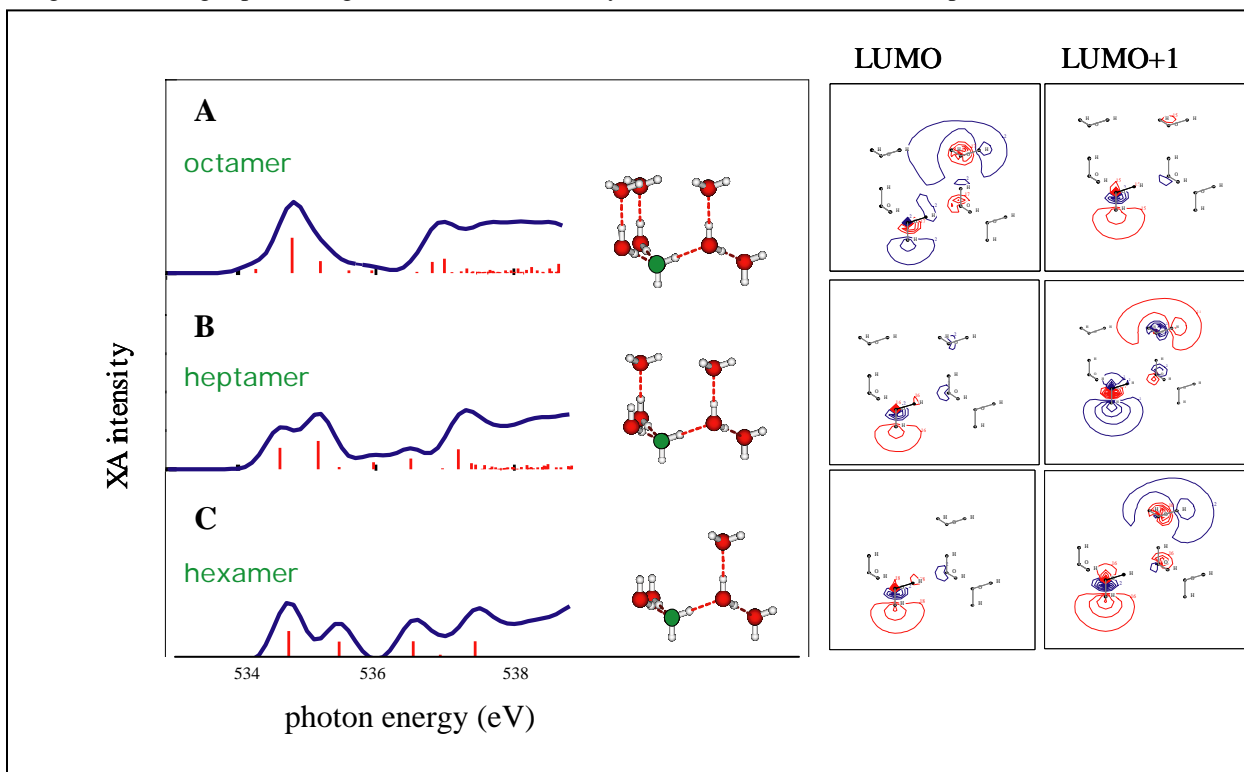


The excited water molecule (green) donates a hydrogen bond. The LUMO exhibits a slightly distorted  $a_1$  symmetry, and the LUMO+1 density is directional and more highly localized along the free OH bond of the donating water molecule.

Figure 5 shows an example of a computed spectra for an octamer with a well-defined pre-edge due to suppression of the LUMO oscillator strength (Figure 5; A). When water molecules are selectively removed from the second shell on the accepting side of the central water, the LUMO oscillator strength gains intensity (Figure 5; B, C).

Simultaneously, the transition intensity for the LUMO+1 decreases. Increasing localization along the free OH bond is observed in the LUMO, with increasing delocalization in the LUMO+1 from the octamer to the hexamer. Calculations of larger clusters in which free OH bonds were closed with donating hydrogen bonds confirmed that observed delocalization was not due to surface effects. We can thus obtain a preliminary understanding of pre-edge character by observing the symmetry origins of the states to be of  $a_1$  and  $b_2$  symmetries. More study is needed to connect changes in the hydrogen bonding configuration with the corresponding changes in electronic structure.

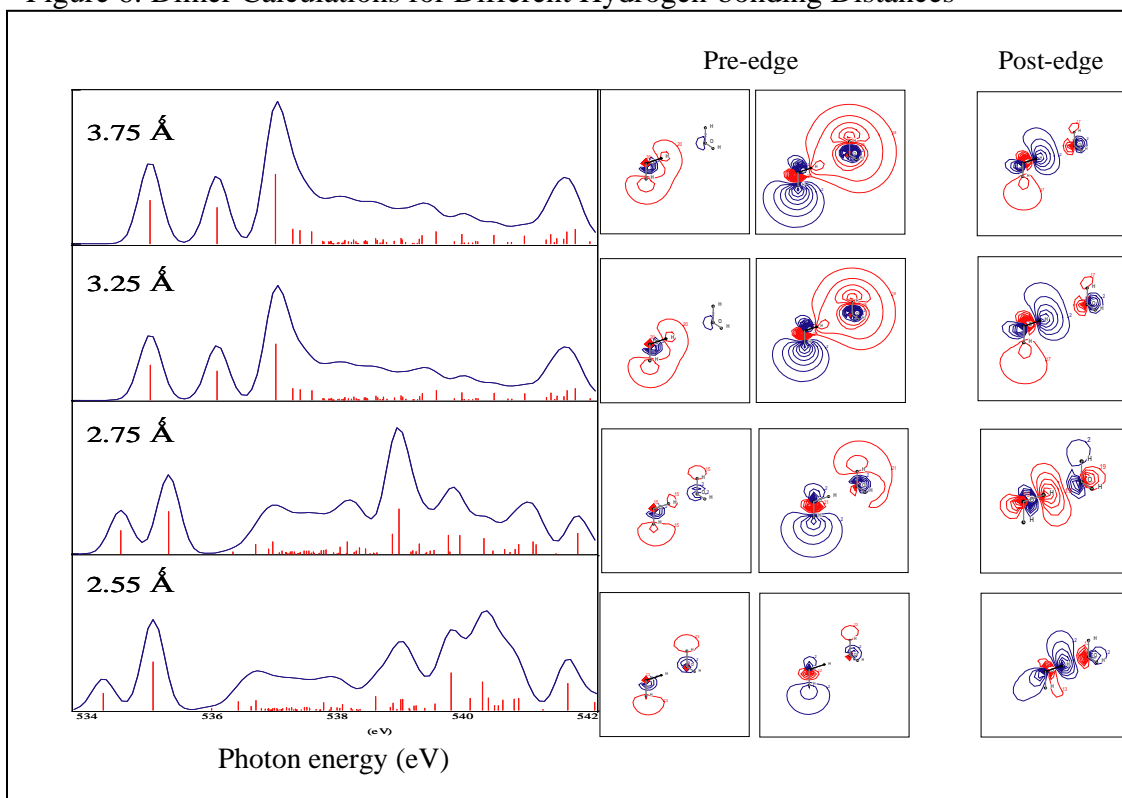
Figure 5: Pre-edge spectral regions and electron density states for selected octamer, heptamer, and hexamer



The pre-edge sharpness in the octamer spectra is lost as water molecules on the accepting side of the excited water are removed and there is a higher intensity transition to the LUMO and a weaker transition to the LUMO+1 state.

Computed spectra for a water dimer, where the distance between oxygen atoms varies and the central molecule donates a hydrogen bond, are shown in Figure 6. In these cases, the spectra have been broadened with gaussians of a constant fwhm of 0.5 eV to emphasize strong transitions. An increasing separation in energy is observed between the pre-edge and a sharp post-edge as the water molecules are brought closer together. The

Figure 6: Dimer Calculations for Different Hydrogen-bonding Distances

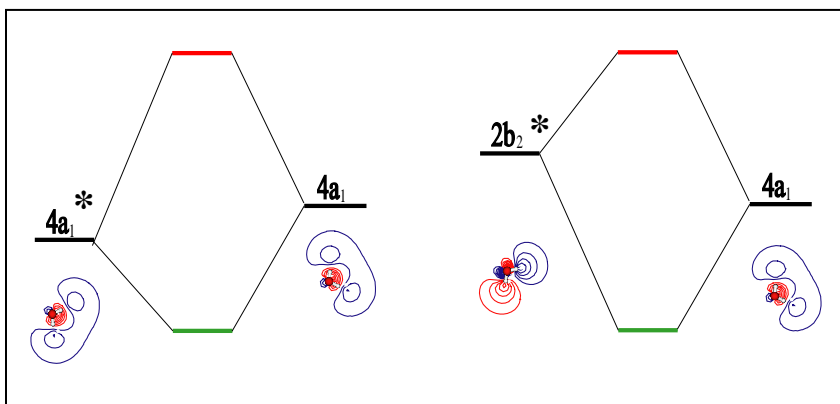


As the Oxygen-oxygen distance is decreased, greater molecular orbital overlap leads to a mixing of symmetries (observed as localization along internal OH bonds) and greater splitting of bonding and anti-bonding combinations (observed as increasing distance between the pre- and post-edges).

pre-edge orbitals (LUMO and LUMO+1) and the orbital corresponding to the highest oscillator strength in the post-edge region are shown alongside their spectra. Clear localization along the free OH bond is observed in the LUMO+1 orbitals, and localization along the donating OH bond is observed in the post-edge orbitals. This localization

reflects a loss of  $b_2$  symmetry in the LUMO+1 orbitals, and an increase in  $p_y$  character. Similarly, the localized orbitals in the post edge reflect mixing of  $a_1$  and  $b_2$  type symmetries. We can understand these observations in electronic structure with a bonding-antibonding description of molecular orbital interaction between the two water molecules, as shown in Figure 7. As the water molecules are brought closer together, there is greater overlap of their molecular orbitals, and the interaction produces bonding-

Figure 7: Molecular Orbital Mixing in the Water Dimer



Symmetry mixing can be understood as bonding and antibonding combinations from the mixing of the  $4a_1$  and  $2b_2$  excited states (denoted by asterisks) with the  $4a_1$  state of the accepting water molecule.

antibonding orbitals which are observed as localized states with mixed symmetries. At shorter distances, the energy splitting between bonding and antibonding

combinations increases as molecular orbital overlap increases. We see the spectral expression of the bonding and antibonding interactions as an increasing separation between pre-edge and post-edge peaks, in Figure 6.

## CONCLUSION

We have found similarities in electronic structure for unoccupied valence states of all single-donor species computed. Specifically, we see that LUMO states are of a slightly distorted  $a_1$  symmetry toward the free OH bond, and the LUMO+1 is localized

directly along the free OH bond when there is sufficient interaction of molecular orbitals. We have begun to decipher the nature of the pre-edge in terms of the symmetry origins and localization patterns of the LUMO and LUMO+1 states. We have proposed a simple bonding-antibonding picture to describe this localization by a mixing of core-excited molecular orbitals with other valence states, observing that the localized states along the free OH bond contribute to pre-edge intensities, while localized states along the donating OH bond contribute strongly to post-edge transitions.

## ACKNOWLEDGMENTS

This research was conducted at the Stanford Synchrotron Radiation Laboratory in Menlo Park, CA. I would like to thank Professor Anders Nilsson for his mentorship and guidance, and for his continued support as I continue my work on this research project. I would also like to thank Dennis Nordlund for his daily time, guidance, and teaching during the course of the summer. I extend my thanks to the Office of Science, the Department of Energy, and the Stanford Linear Accelerator Center for their support of the SULI program and for giving me the opportunity to participate.

## REFERENCES

- [1] Ph. Wernet, *et. al.*, “The Structure of the First Coordination Shell in Liquid Water,” Science, Vol. 304, Issue 5673, 14 May 2004, pp. 995-999.
- [2] A. Nilsson, *et. al.*, “The hydrogen bond in ice probed by soft x-ray spectroscopy and density functional theory,” Journal of Chemical Physics, Vol. 122, April 2005, 154505.
- [3] J. Stöhr, NEXAFS Spectroscopy, Berlin, Heidelberg: Springer-Verlag, 1992.

- [4] M. Cavalleri, *et. al.*, “The interpretation of X-ray absorption spectra of water and ice,” Chemical Physics Letters, Vol. 364, 2002, pp. 363-370.
- [5] D. Nordlund, “Core Level Spectroscopy of Water and Ice,” Philosophy Doctor Thesis. Stockholm University; Stockholm, Sweden, 2004.
- [6] S. Myneni, *et. al.*, “Spectroscopic probing of local hydrogen-bonding structures in liquid water,” Journal of Physics: Condensed Matter, Vol. 14, 2002, pp. L213-L219.
- [7] W. Koch and M. C. Holthausen, A Chemist’s Guide to Density Functional Theory, Weinheim: Wiley-VCH, 2002.
- [8] K. Hermann, LGM Pettersson, M. Casida, C. Daul, A. Goursot, A. Koester, E. Proynov, A. St-Amant, and D. Salahub, *STOBE Software*, 2002.
- [9] Cavalleri, *et. al.*, “Half or full core hole in density functional theory X-ray absorption spectrum calculations of water?” Physical Chemistry Chemical Physics, Vol. 7, Issue 15, 2005, pp. 2854-2858.
- [10] W. Kutzelnigg, U. Fleischer, and M. Shindler, NMR—Basic Principles and Progress, Heidelberg: Springer, 1990.